THE GEOLOGY OF SHEAR-ZONE HOSTED GOLD DEPOSITS IN NORTHEAST BRAZIL

Maria Glícia da Nóbrega Coutinho

A thesis submitted for the degree of Doctor of Philosophy
at the University of London

Department of Geology
Royal Holloway and Bedford New College
University of London

September, 1994

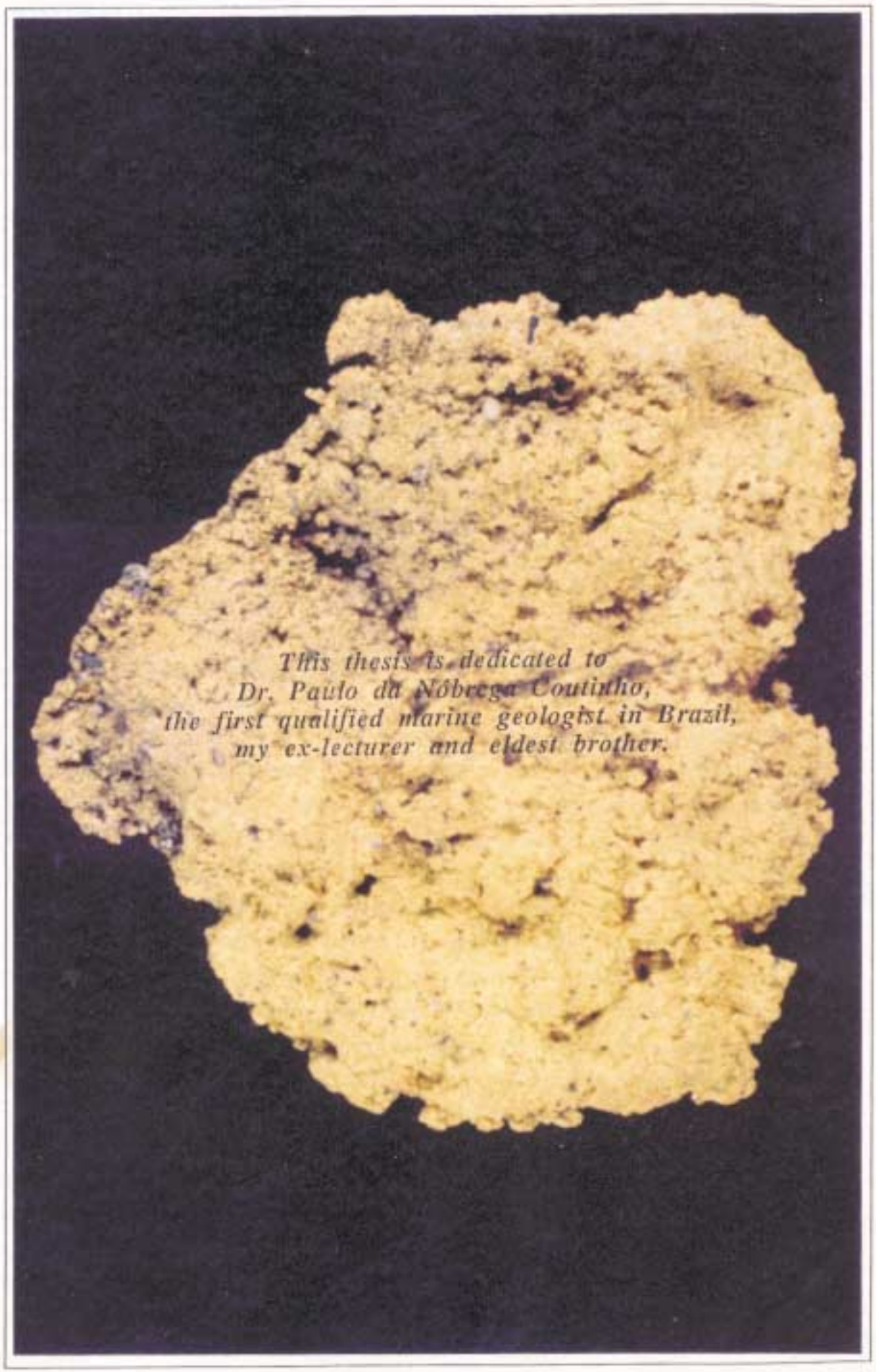
This thesis is dedicated to
Dr. Paulo da Nóbrega Coutinho,
the first qualified marine geologist in Brazil,
my ex-lecturer and eldest brother.

ABSTRACT

Mesothermal gold-bearing quartz veins are widespread in the Borborema Province in N.E. Brazil, and well exposed in two active mines: São Francisco mine and Cachoeira de Minas mine.

Although the Borborema Province shows a complex crustal evolution, the general structure consists of a mosaic of Archaean-Early Proterozoic massif terranes surrounded by Proterozoic fold belts. The major tectonic features are the development of crustal-scale shear zones and the emplacement of batholiths and stocks of granitoid related to the Brasiliano-Pan African thermal-tectonic event (0.9-0.5 Ga). The province is a medium to high-grade metamorphic zone cut by two E-W crustal-scale lineament systems or first order shear zones, about 150 km apart. These structures developed a complex anastomosing network of thrust faults and subsidiary strike-slip shear zones. Deformation is predominantly in the plastic regime, although plastic-brittle deformation also occurs. Many subsidiary N to NE trending structures are characterised as second-order shear zones, which allowed the migration of metal-bearing hydrothermal fluids and provided sites for mineralization. Mesothermal lode gold deposits occur either within the shear zones, on the limbs of folds commonly associated with thrust faults and strike-slip faults, or in close association with major shear zones. The relationship between the quartz veins and the deformation indicates that mineralization and shearing overlapped in time.

Gold-bearing quartz veins occur in a variety of host rocks: Archaean basement, Early Proterozoic metavolcanic-sedimentary fold belts, and Early to Late Proterozoic granitoids that intruded both the supracrustal and basement rocks. The basement consists of gneiss-migmatite-granite terranes and is characterised by a transition from granulite to upper amplibolite facies (720°C and 4.0 kb). The Proterozoic supracrustals consist of schists and gneisses, and minor amphibolite, and are predominantly mylonitic with a penetrative foliation. Schists contain a high component of felsic, and minor mafic volcanics and greywackes, and gneisses are predominantly granite-derived. Maximum metamorphic conditions for metavolcanic-sedimentary rocks are estimated at 5.5 kb and 600°C, suggesting a depth of ≈ 25 km and characteristic of amphibolite facies. A lead isotope study of the host rocks to the mineralization has yielded a Pb-Pb isochron age of ≈ 1.0 Ga, regarded as the time of regional high-grade metamorphism, and stabilisation of amphibolite facies crust. Mineral assemblages in all lithologies confirm that these rocks were subsequently subjected to retrogressive metamorphism in the sub-greenschist facies (350° C).

Calc-alkaline magmatism associated with the Brasiliano Orogeny resulted in hybrid S-I type granites, the chemistry of which is consistent with derivation in either a continent-continent collision or continental magmatic arc tectonic setting. The

widespread gold-bearing quartz veins hosted by calc-alkaline magmatism reflect a genetic link between the magmatism and the gold mineralization.

Ore-mineral studies have placed constraints on the gold metallogenesis and these, combined with the structural information, suggest three stages of mineralization. In the first stage, during brittle deformation, the mineral assemblage is characterised by titanium, iron oxides and the early sulphides (pyrrhotite and pyrite), which were formed by the destabilisation of mafic minerals in the host lithologies. Fluids enriched in CO_2 and S provided conditions for the precipitation of metals, and gold occurs as submicron particles associated with pyrite and chalcopyrite. In the second stage there is a greater input of additional elements, particularly those which indicate a granitic influence (e.g. Bi, Te, Mo, F and B). The gold liberated from the sulphides during this stage occurs as visible gold associated with recrystallised sulphides or intergrowths with bismuth and selenium/tellurium minerals. The last stage developed under an extensional tectonic regime and is characterised by an enrichment in lead, tellurium and gold. The mineralization occurs in fine to medium-grained annealed sulphides. The gangue mineralogy is dominated by quartz and tourmaline.

The geochemistry of the wallrock alteration indicates massive additions of K, and less Ti, Fe and Mn. The mineralized areas are enriched in a distinctive suite of trace elements: Ba, Pb, Th, V, Zn, Sc, Ga, Y, Rb, Nb, and Nd. Depletions in Ca and Na are typical. The high values of K, Ba, Rb, and B in the potassic and tourmaline-rich alteration suggest a magmatic-hydrothemal paragenetic association. The same pattern of wallrock alteration occurred in different host lithologies, suggesting that the rocks were all subjected to the same metasomatic processes and also that the hydrothermal fluid composition was not controlled by the chemistry of the host rocks.

The relationships between deformation, gold mineralization, and wallrock alteration indicate that the wallrock alteration took place before the gold mineralization, possibly at the same time as some of the early sulphide-rich mineralization. The gold mineralization overprints regional metamorphism and is contemporaneous with, and/or later than, retrogressive metamorphism and the terminal plutonic-deformation event.

Lead isotope results from sulphides associated with gold-bearing quartz veins show a model age of 0.6-0.8 Ga. The lead isotope data suggest that gold mineralization was formed after peak metamorphism.

The hydrothermal fluid from which the gold-bearing quartz veins crystallised is CO_2-rich (3.0-23.0 mole %) and characterised by low salinity ($\approx$ 6.0 eq. wt % NaCl) and minor amounts of CH_4 (3-10 mole %). The fluid was originally homogeneous and CO_2-rich, but the subsequent immiscibility process caused separation of CO_2-rich and CO_2-poor or H_2O-CO_2 phases. The unmixing of fluids was related to episodic hydraulic fracturing which provided pressure fluctuations during the growth of the veins by multi-increment crack-seal deformation .

P-T conditions during mineralization have been constrained by a variety of methods (chlorite geothermometry, ore mineral assemblages and pyrite texture, temperature of fluid inclusion homogenization and fluid inclusion isochores) and indicate that gold precipitated at 270-350 °C and 1.0-3.4 kb.

Stable isotope analyses of fluid inclusions in gold-bearing quartz veins indicate that the carbon has a magmatic, possibly mantle, derivation. There is a large scatter in the δ^{18} O quartz values (7.0 to 14.5 $^{o}/_{oo}$), suggesting mixing of fluids from different sources, including that of meteoric water.

On the basis of these studies the Borborema Province is shown to have had a complex geological evolution. The model for mineralization invokes several sources for the fluids and the ore components; the importance of granitic magmatism and convecting meteoric fluids is highlighted. Further exploration should be concentrated in fold belts which represent former back-arc basins, and particularly where these contain subsidiary shear zones.

TABLE OF CONTENTS

		Page
Title Page		i
Frontispiece		ii
Abstract		iii
Table of Contents		vi
List of Figures		x
List of Tables		xviii
List of Appendices		xx
List of Abbreviations		xxii
Acknowledgements		xxvi
CHAPTER 1 Introduction		**1**
1.1	Statement of the Problem	1
1.2	Aims of the Thesis	2
1.3	Methods of Research	2
3.1.1	Fieldwork Programme	2
3.1.2	Laboratory Work	3
1.4	Structure of the Thesis	3
CHAPTER 2 Geological and Geotectonic Setting of the Borborema Province		**5**
2.1	Introduction	5
2.2	Regional Geology of the Borborema Province	7
2.2.1	Structural Framework	7
	a) Massif Terranes or Microplates	8
	b) Fold Belts or Mobile Zones	12
2.2.2	Tectonism and Age of the Deformation Events	15
2.2.3	Deformation and Metamorphism	18
2.2.4	Magmatism	20
	a) Pre-Brasiliano Magmatism	20
	b) Brasiliano Magmatism	23
	c) Volcanism	25
2.3	Plate Tectonics and the Borborema Province	26
CHAPTER 3 Geology and Structure of the Mineralized Areas		**31**
3.1	Introduction	31
3.2	São Francisco Mine	33
3.2.1	Introduction	33
3.2.2	Geology	33
3.2.3	Deformation and Metamorphism	37
3.2.4	Shear Zones and the Emplacement of the Gold-Bearing Quartz Veins	37
3.3	Cachoeira de Minas Mine	41
3.3.1	Introduction	41
3.3.2	Geology	41
3.3.3	Deformation and Metamorphism	45
3.3.4	Shear Zones and the Emplacement of the Gold-Bearing Quartz Veins	45
3.4	Itapetim District	51
3.4.1	Introduction	51
3.4.2	Geology	51
3.4.3	Deformation and Metamorphism	53

3.4.4 Shear Zones and Emplacement of the Gold-Bearing Quartz Veins 57
3.5 Gold Occurences Hosted by Granitoids 66
3.5.1 Introduction 66
3.5.2 Santo Aleixo Area 66
3.5.3 Igarape Garapa Occurrence 69
3.5.4 Canaffstula 'Garimpo' 70
3.5.5 Cacimba Salgada Occurrence 71
3.6 Gold Occurence in the Archaean Basement 71
3.7 Relationships Between the Shear Zones and Veining 75
3.8 Vein Growth Processes 76
3.8.1 Introduction 76
3.8.2 Vein Growth in the Borborema Province 78
3.9 Vein Development Related to Fluid Dynamics 81
3.10 Conclusions 83

CHAPTER 4 Petrology, Geochemistry and Metamorphic Grade of the Host Rocks 86

4.1 Introduction 86
4.2 Methods of Study 86
4.3 Granitoids Rocks 88
4.3.1 Introduction 88
4.3.2 Mineralogical Composition 89
4.3.3 Mineral Assemblage and Texture 89
4.3.4 Chemical Composition 91
4.3.5 Geochemistry 94
4.3.6 Petrogenesis and Geotectonic Setting 99
4.3.7 Isotopic and Rare-Earth Element Constraints 109
4.3.8 Discussion 111
4.4 Supracrustal Rocks 115
4.4.1 Introduction 115
4.4.2 Petrography 115
a) Gneisses 115
b) Schists 117
c) Amphibolites 119
4.4.3 Geochemistry 122
4.4.4 Geotectonic Setting 132
4.4.5 Discussion 139
4.5 Metamorphic Grade 144
4.5.1 Introduction 144
4.5.2 Metamorphic Facies 145
a) Granulite-Upper Amphibolite Facies 145
b) Amphibolite Facies 148
c) Retrogressive Metamorphism 151
d) Discussion 152
4.5 Conclusions 156

CHAPTER 5 Mineralization and Wallrock Alteration 157

5.1 Introduction 157
5.2 Methods of Study 158
5.3 Ore-Minerals 158
5.3.1 Mineral Assemblages 158
a) Oxides 158
b) Sulphides 160
c) Intergrowths of Native Bismuth, Selenium/Tellurium Minerals and alloys

of Gold-Silver and Gold-Bismuth 168
d) Tellurides 170
e) Native Gold 173
5.3.2 Microstructure of Pyrite and Marcasite 178
5.3.3 Mineralization Evolution 183
a) The First Stage of the Mineralization 184
b) The Second Stage of the Mineralization 186
c) The Third Stage of the Mineralization 186
5.4 Geothermometry 187
5.4.1 Introduction 187
5.4.2 Evidence from Ore Minerals 187
5.5 Gangue Mineral Assemblages 188
5.6 Wallrock Alteration 189
5.5.1 Introduction 189
5.5.2 Wallrock Alteration in the Granitoids 190
5.5.3 Wallrock Alteration in the Supracrustal Rocks 197
5.5.4 Relationships Between Wallrock Alteration, Deformation and Gold Mineralization 201
5.7 Conclusions 202

CHAPTER 6 Lead Isotope Studies 204

6.1 Introduction 204
6.2 Principles 204
6.3 Methods of Study 205
6.3.1 Sampling 205
6.3.2 Analytical Procedure and Error 207
6. 4 Discussion of Lead Isotope Data 207
6.4.1 Lead Isotopic Characteristics of the Host Lithologies 207
6.4.2 Lead Isotopic Characteristics of the Mineralization 213
6.5 Economic Implications 218
6.6 Conclusions 219

CHAPTER 7 Hydrothermal Fluids 221

7.1 Introduction 221
7.2 Fluid Inclusion Study 222
7.2.1 Introduction 222
7.2.2 Method of Study 222
7.2.3 Fluid Inclusion Types and Mode of Occurrence 224
7.2.4 Microthermometric Results 227
a) H_2O-CO_2 Fluid Inclusions 231
b) H_2O-rich Fluid Inclusions 231
c) CO_2 Monophase Fluid Inclusions 238
7.2.5 Bulk Composition of the Fluid Inclusion 238
7.2.6 Fluid Inclusion Pressure and Temperature 243
7.2.7 Discussion of the Fluid Inclusions Data 247
7.3 Stable Isotopes 251
7.3.1 Introduction 251
7.3.2 Method of Study 252
7.3.3 Discussion of the δ^{13} C Analyses of Fluid Inclusions 252
7.3.4 Discussion of the δ^{18} O Isotope Results in Quartz 253
7.3.5 Discussion of the δ^{18} O Values of Water 256
7.4 Conclusions 258

CHAPTER 8 A Model for the Gold Mineralization in Boborema Province **261**

8.1 Geological Setting and Evolution of the Area 261
8.1.1 The Extensional Regime: Rifting (Archaean-Early Proterozoic) 261
8.1.2 Convergent Plate: The Subduction Stage (Middle Proterozoic) 263
8.1.3 Convergent Plate: The Continent-Continent Collision Stage (Late Proterozoic) 264
8.2 A Model for Gold Mineralization 267
8.2.1 Source of the Gold 267
8.2.2 Hydrothermal Fluids 268
a) Nature and Compostion of the Fluid 268
b) Source of the Fluids and P-T Constraints 269
8.2.3 Gold Transport and Deposition 270
8.2.4 The Model for the Gold Mineralization 271
8.3 Comparisons World-Wide 274
8.4 Exploration Significance 281

REFERENCES **284**

APPENDICES **300**

Paper 'A lead isotope study of metamorphism and associated gold mineralization in N.E. Brazil' submitted for MINERALIUM DEPOSITA

LIST OF FIGURES`

Chapter 2

			Page
Fig.	**2.1**	Sketch map of Brazil showing the distribution of Precambrian and Phanerozoic units and structural provinces	6
Fig.	**2.2**	View of the central domain of Borborema Province along the Patos to Teixeira road	6
Fig.	**2.3**	Simplified geological map of N.E. Brazil, showing the limits of Borborema Province	9
Fig.	**2.4a**	Radar imagery showing major structures in N.E. Brazil	10
Fig.	**2.4b**	Interpretative sketch of radar imagery (Fig. 2.4a), showing the distribution of gold deposits	11
Fig.	**2.5**	Sketch map of N.E. Brazil showing the distribution of Archaean and Proterozoic units and highlighting the distribution of Brasiliano age igneous rocks	22
Fig.	**2.6**	Photograph of an early to syn-tectonic granite transformed to ultramylonite along the Patos Lineament	24
Fig.	**2.7**	Photograph of porphyritic syn- to late-tectonic granite in the Itapetim District	24
Fig.	**2.8**	Photograph of syn- to late-tectonic granite within the shear zone (Itapetim District)	24
Fig.	**2.9**	Photograph of late tectonic leucocratic pegmatitic veins intruded along a sinistral shear (Riacho Verde to Fava de Cheiro road, Itapetim)	24
Fig.	**2.10**	Map showing the Pan African belt and the Borborema Province in a Pre-Mesozoic drift reconstruction	28

Chapter 3

Fig.	**3.1**	Shear zone system and gold mineralization in N.E. Brazil (Interpretation from radar imagery)	32
Fig.	**3.2**	Geological framework of the Seridó Fold Belt, N.E. Brazil	34
Fig.	**3.3a**	Photograph of a porphyroblast of cordierite rotated and wrapped by foliation S_2 and displaying dextral shear sense	36
Fig.	**3.3b**	Sketch of Fig. 3.3a showing kinematic indicators of dextral shear	36
Fig.	**3.4a**	Photograph of refolded earlier fabric developed in polydeformed garnet-biotite-quartz-feldspar schist in Seridó Formation	36
Fig.	**3.4b**	Sketch of Fig. 3.4a displaying the F_3 folding	36
Fig.	**3.5**	Photograph of inclined conjugate reverse kink bands (F_4) developed in deformed mica schist in Seridó Formation	36
Fig.	**3.6**	Photograph of the Morro Pelado thrust fault showing the large gold-bearing quartz vein	36
Fig.	**3.7**	Structural framework of the São Francisco mine area	39
Fig.	**3.8a**	View of the Morro Pelado thrust fault	40
Fig.	**3.8b**	Sketch of Fig. 3.8a showing C and S fabric	40
Fig.	**3.9a**	Photomicrograph of the contact between the quartz-muscovite schist and the auriferous quartz vein in the Morro Pelado thrust	40
Fig.	**3.9b**	Sketch of Fig. 3.9a illustrating the geometry	40
Fig.	**3.10**	Photomicrograph of layering in a ribbon textured gold-bearing quartz vein, São Francisco mine	40
Fig.	**3.11**	Photomicrograph of laminae of wall rock parallel to the vein walls, São Francisco mine	40
Fig.	**3.12**	View of the Cachoeira de Minas mine	42
Fig.	**3.13**	Cross section of the Cachoeira de Minas deposit	42
Fig.	**3.14**	Geological framework of the Piancó/Alto Brígida Fold Belt,	

		N.E. Brazil	43
Fig.	**3.15**	Structural framework of the Cachoeira de Minas mine area	47
Fig.	**3.16a**	Photograph of S_2 foliation deformed by F_3 folds, Cachoeira de Minas mine, Covico area	49
Fig.	**3.16b**	Sketch of Fig. 3.16a showing two phases of deformation	49
Fig.	**3.17a**	Photograph of pinch-and-swell structures in quartz veins in the Cachoeira de Minas mine area	49
Fig.	**3.17b**	Sketch of Fig. 3.17a illustrating the boudin shape of the quartz vein	49
Fig.	**3.18**	Photomicrograph of biotite-chlorite schist showing sigmoidal feldspar porphyroclasts, Cachoeira de Minas mine	49
Fig.	**3.19a**	View of the main mineralized quartz vein in the Covico area.	50
Fig.	**3.19b**	Sketch of Fig. 3.19a interpreting the deformation	50
Fig.	**3.20a**	Photomicrograph of the contact between the quartz-muscovite-sericite schist and the auriferous quartz vein in the Covico area	50
Fig.	**3.20b**	Sketch of Fig. 3.20a illustrating the fabric developed during shearing	50
Fig.	**3.21**	Geological framework of the Itapetim gold District	52
Fig.	**3.22a**	Block diagram showing the distribution of the Irajaí facies in the Itapetim gold district	54
Fig.	**3.22b**	Photograph of well developed banding in folded paragneisses of the Irajaí Formation, São José do Egito to Itapetim road	54
Fig.	**3.22c**	Photograph of well developed vertical schistosity transposed into the N65°E foliation in the Irajaí Formation	54
Fig.	**3.23a**	Photograph of the contact between the syn- and late tectonic granite and the Irajaí metasediments at Piedade dam, Itapetim District	56
Fig.	**3.23b**	Photomicrograph of porphyritic granite shown in the Fig. 3.23a	56
Fig.	**3.23c**	Photomicrograph of the muscovite-biotite schist shown in Fig. 3.23a	56
Fig.	**3.24**	A cross section through the Itapetim shear zone: (**A**) Flow structures and very thin mylonitic zones; (**a**) Photomicrograph of (A); (**B**) Sinistral sense of shear movement; (**b**) Photomicrograph of (B); (**C**) Augen gneiss with flattened K-feldspar (pink colour) porphyroclasts; (**c**) Photomicrograph of (C)	58
Fig.	**3.25**	Structural framework of the Itapetim Gold District	59
Fig.	**3.26**	Photomicrograph of a feldspar crystal deformed by microfracturing, Itapetim shear zone, central domain	60
Fig.	**3.27**	Photomicrograph of stretched ribbon quartz wrapping around a porphyroblast of feldspar, Itapetim area	60
Fig.	**3.28**	Photomicrograph of a mica flake deformed by crystalpastic flow in a high-grade shear zone	60
Fig.	**3.29a**	Photograph of shear bands transecting the main foliation in strongly deformed augen gneiss, Itapetim shear zone	61
Fig.	**3.29b**	Sketch of Fig. 3.29a showing the geometry of the C and S fabric	61
Fig.	**3.30a**	Photograph of redirection of movement developing C and S planes in moderately deformed granite, Itapetim shear zone	61
Fig.	**3.30b**	Sketch of Fig. 3.30a illustrating the C-S fabric	61
Fig.	**3.31**	Photograph of a syn-shearing mineralized quartz vein developed in mica schist	63
Fig.	**3.32**	Photograph showing folding of the S_3 foliation that has produced a transposed foliation S_4	63
Fig.	**3.33**	Photomicrograph of a gold-bearing quartz vein showing intense deformation, Itapetim District, Sertãozinho	63
Fig.	**3.34**	Vein pattern in the Itapetim gold District showing the predominant direction parallel to the regional shear	64

Fig.	**3.35**	Geological map (**A**) and vertical sections (**B**) in the central area (Sertãozinho domain) in the Itapetim shear zone	65
Fig.	**3.36a**	Photograph of augen gneiss displaying intense mylonitic foliation, Santo Aleixo area, Guilhermina 'garimpo'	67
Fig.	**3.36b**	Photomicrograph of mylonitic texture in augen gneiss, Santo Aleixo area, Guilhermina 'garimpo'	67
Fig.	**3.37**	Vein pattern in the Santo Aleixo area indicating inhomogeneous shear	68
Fig.	**3.38a**	Photograph of a gold-mineralized regional extensional vein at Igarape Garapa occurrence	67
Fig.	**3.38b**	Photomicrograph of the granitoid in Fig. 3.38a	67
Fig.	**3.39a**	Photograph of outcrop showing gold-bearing quartz veins hosted by orthogneisses, Canafístula 'garimpo'	67
Fig.	**3.39b**	Photomicrograph of tourmaline fibres showing a ribbon texture, Canafístula 'garimpo'	67
Fig.	**3.40a**	Photograph of a regional extensional quartz vein (N 70°E) mineralized with pyrite and gold, Cacimba Salgada area	72
Fig.	**3.40b**	Detail of Fig. 3.40a showing deformed enclaves of quartz diorite	72
Fig.	**3.40c**	Photograph showing shearing in granodiorite that contains quartz diorite enclaves, Cacimba Salgada occurence	72
Fig.	**3.40d**	Sketch of Fig. 3.40c illustrating sinistral movement	72
Fig.	**3.41a**	Photograph of two differently oriented quartz veins passing through a shear zone, Boqueirão dos Cochos area	74
Fig.	**3.41b**	Sketch of Fig. 3.41a	74
Fig.	**3.41c**	Photograph of quartz-eye phyllonite, Boqueirão dos Cochos area	74
Fig.	**3.42**	Sequence of events in the development of a typical ribbon gold-bearing quartz-tourmaline-vein in Canafistula 'garimpo'	79
Fig.	**3.43**	Sketches from photomicrographs of the tourmaline-bearing quartz vein showing the complexity of the growth process	80
Fig.	**3.44**	Photomicrograph of crack-seal developed in the quartz vein at the São Francisco mine	82
Fig.	**3.45a**	Photomicrograph: crack-seal at Cachoeira de Minas mine.	82
Fig.	**3.45b**	Detail of Fig. 3.45a	82
Fig.	**3.46**	Photomicrograph of crack healing, Itapetim District	82
Fig.	**3.47**	Photomicrograph of quartz vein showing chlorite and opaque minerals developed along the crack healing, Itapetim: Pimenteiras area	82
Fig.	**3.48**	Photograph of mineralized crack healing in a quartz vein, Itapetim: Sertãozinho area	82

Chapter 4

Fig.	**4.1**	Geological map of Itapetim area showing the granite sample lable	87
Fig.	**4.2**	CIPW normative feldspar proportions for ETG, ESTG and SLTG	90
Fig.	**4.3**	CIPW normative quartz-(orthoclase+albite)-anorthite proportions for granites	90
Fig.	**4.4a/d**	Thin sections of granitoids	92
Fig.	**4.5**	Major element contents (XRF analyses) of granites	95
Fig.	**4.6**	Diagram ASI against SiO_2 for granites	96
Fig.	**4.7**	The ratio Ga/Al against SiO_2 for granites	96
Fig.	**4.8**	Diagram ASI against Rb/Sr for granites	96
Fig.	**4.9**	Diagram Sr against Rb for granites	96

Fig.	**4.10a/c**	Chondrite-normalised incompatible element 'spidergrams' for the ETG	97
Fig.	**4.10d/e**	Chondrite-normalised incompatible element 'spidergrams' for the ESTG	97
Fig.	**4.10f/g**	Chondrite-normalised incompatible element 'spidergrams' for the SLTG	97
Fig.	**4.11**	Rb-Ba-Sr diagram for ETG, ESTG and SLTG (Pearce *et al.*, 1984) for granitoids	101
Fig.	**4.12**	Discriminant diagrams showing Rb versus Nb+Y (Pearce *et al.*, 1984) for granitoids	101
Fig.	**4.13**	Discriminant diagrams showing Nb versus Y (Pearce *et al.*, 1984) for granitoids	101
Fig.	**4.14**	ACF diagram (Takahashi *et al.*, 1980) showing the I-and S-type granite	101
Fig.	**4.15**	Range of K/Ba and K/Rb ratios selected from publications for comparison with Borborema Province granitoids	104
Fig.	**4.16**	Diagram FeO*/MgO against (Zr+Nb+Ce+Y) for granitoids	105
Fig.	**4.17**	Diagram (K_2O+Na_2O/CaO) against (Zr+Nb+Ce+Y) for granitoids	105
Fig.	**4.18**	Tectonic discrimination diagrams after Maniar and Piccoli (1989)	107
Fig.	**4.19**	Tectonic discrimination diagrams after Muller and Groves (1993)	108
Fig.	**4.20**	K_2O aginst SiO_2 diagram showing the tholeiitic, calc-alkaline, high-k calc-alkaline and shoshonitic affinity granitoids (Peccerillo and Taylor, 1976)	113
Fig.	**4.21a/l**	Thin sections of rocks showing the different petrographic types of gneiss, schist and amphibolite	116/8/20
Fig.	**4.22**	Amphiboles classified according to formula ions calculated from electron microprobe analyses	121
Fig.	**4.23**	Major element variation diagrams for schist	123
Fig.	**4.24**	Major element variation diagrams for gneiss	124
Fig.	**4.25**	Variation of trace elements in schist	125
Fig.	**4.26**	Variation of trace elements in gneiss	126
Fig.	**4.27**	Scandium contents of (**a**) schist and (**b**) gneiss plotted against silica contents	128
Fig.	**4.28**	Trace element ratio discrimination diagrams after Winchester and Floyd (1977) for schists (**a**) and gneisses (**b**)	129
Fig.	**4.29**	Major and minor element contents of amphibolites plotted as Harker-type diagrams	130
Fig.	**4.30**	Comparison of the amphibolite chemistry to volcanic rocks (LeMaitre, 1984) in (**a**) and AFM diagram for amphibolites in (**b**); In (**c**) the ternary diagram CaO-MgO-FeO*	130
Fig.	**4.31**	Chondrite-normalised incompatible trace elements diagrams for amphibolites	131
Fig.	**4.32**	(**a**) Chemistry of schists (silica and alkali content) compared to volcanic rock classification and (**b**) (FeO*+MgO) content compared to 'peraluminicity'	133
Fig.	**4.33**	Werner (1987) major element discrimination diagrams for (**a**) schist and (**b**) gneiss	134
Fig.	**4.34**	Rb-Ba-Sr ternary plots for (**a**) gneiss and (**b**) schist.	135
Fig.	**4.35**	Range of K/Rb and K/Ba ratios for volcanics reported in the literature (**a**) compared to Borborema rocks (**b**)	137
Fig.	**4.36**	Variation of K versus Ba and K versus Rb in gneiss compared data from literature (**a**) to the Borborema gneisses (**b**)	138
Fig.	**4.37**	Tectonomagmatic discrimination diagrams (Pearce *et al*, 1973) for amphibolites (**a**) Ti-Y-Zr and(**b**) Ti against Zr; and (**c**) TiO_2 -P_2O_5-MnO (Mullen, 1983)	140

Fig. 4.38a/h Thin sections of rocks showing the range of metamorphic grade 147/9
Fig. 4.39 Petrogenetic P-T grid showing common reactions in Itapetim District-Pimenteiras area; São Francisco mine; and Boqueirão dos Cochos 153
Fig. 4.40 Pressure-temperature diagram showing the fields of the various metamorphic facies and the distribution of the rocks from this study 155

Chapter 5

Fig. 5.1 Photomicrograph of a polished block of magnetite with exsolution lamellae of maghemite in both PPL and XPL 161
Fig. 5.2 (**a**) Photomicrograph of polished block of rutile, (**b**) X-ray spectrum and (**c**) SEM mapping of Si, Ti, Mn, and Fe 162
Fig. 5.3 (**a**) Photomicrograph of polished block of rutile elongated along its c axis, and (**b**) SEM mapping showing Ti, Fe, Ti, and Fe 163
Fig. 5.4 (**a**) Photomicrograph of a polished block of hematite with pyrite from Itapetim District, Sertãozinho; (**b**) Same view as the Fig. 5.4a but in XPL 165
Fig. 5.5 Photomicrograph of pyrite surrounded by hematite with chalcopyrite occuring as inclusions in both minerals 165
Fig. 5.6 Photomicrograph of polished block showing hematite rhythmically replaced by goethite during weathering 165
Fig. 5.7 Photomicrograph of polished block showing pyrite crystal surrounded by hematite associated with small grains of covellite: Santo Aleixo 165
Fig. 5.8 Photomicrograph of a polished block showing allotriomorphic chalcopyrite infiltrated along cracks in pyrite from São Francisco mine 165
Fig. 5.9 Photomicrograph of polished block of pyrrhotite with chalcopyrite filling cracks: São Francisco mine 166
Fig. 5.10 Photomicrograph of polished block of galena displaying deformed cleavage pits: Santo Aleixo 166
Fig. 5.11 Photomicrograph of polished block of galena whose cleavage pits do not show any evidence of deformation: Igarape Garapa 166
Fig. 5.12 Photomicrograph of polished block of galena with cerussite forming a zoned weathering texture: Sertãozinho 166
Fig. 5.13 Photomicrograph: disintegration of chalcopyrite to form a network of covellite, Santo Aleixo 166
Fig. 5.14 Photomicrograph of chalcopyrite replaced along fractures by covellite and magnetite replaced by maghemite 166
Fig. 5.15 (**a**) Photomicrograph of polished block showing an idiomorphic pyrite crystal partly replaced by xenomorphic chalcopyrite, in part along cleavage. The SEM image is shown in the (**b**). (**c**) shows the X-ray spectrum. Itapetim District, Sertãozinho area 167
Fig. 5.16 (**a**) Photomicrograph (PPL) of a polished block containing idiomorphic marcasite enclosed in pyrite and (**b**) is a XPL view: Itapetim District, Sertãozinho area 167
Fig. 5.17 (**a**) Photomicrograph of a polished block of pyrite enclosing native bismuth with uncharacterised selenium minerals, exsolution laths of selenium/tellurium minerals, and bismuth from São Francisco mine. (**b**) is a sketch of (a) with microprobed points and analyses, (**c**) gives X-ray spectra, and (**d**) shows SEM mapping 169
Fig. 5.18 (**a**) Photomicrograph of galena enclosing a small grain of hessite intergrown with greenockite from Igarape Garapa. (**b**) and (**c**) are X-ray images of hessite and greenockite; (**d**) and (**e**) are X-

	ray spectra of greenockite and hessite); (**f**) is SEM mapping of Ag and Te for hessite, and Cd and S for greenockite	171
Fig. 5.19	(**a**) X-ray mapping of chalcopyrite showing Cu and Fe; (**b**) Au, Te, Ag and S; (**c**) BSE image displaying Ag-telluride-bearing phases at the edges of grain, and (**d**) microprobe analyses: Itapetim District	172
Fig. 5.20	(**a**) Gold within sulphides: pyrite and chalcopyrite. (**b**) X-ray mapping showing an image and the distribution of gold and sulphur	174
Fig. 5.21	Photomicrographs show gold occuring as random (**a**) distribution and filling crack healing (**b**)	175
Fig. 5.22	Photomicrograph of gold filling tiny holes in pyrite associated with chalcopyrite	175
Fig. 5.23	Photomicrograph of coarse gold associated with fractured pyrite	175
Fig. 5.24	Photomicrograph of quite coarse gold enclosed in pyrite associated with native bismuth from São Francisco mine	175
Fig. 5.25	Photomicrograph of symplectic intergrowth of gold, bismuth, and uncharacterised selenium/tellurium minerals in a pyrite 'matrix'	175
Fig. 5.26	Photomicrograph of native gold associated with silver and copper and disseminated in quartz with SEM mapping	176
Fig. 5.27	X-ray mapping showing the distribution of the elements associated with native gold in quartz: Au, Ag, Cu. From Cachoeira de Minas mine	176
Fig. 5.28	Photomicrograph of relict primary spheroidal rhythmic texture in pyrite and marcasite	181
Fig. 5.29	Photomicrograph of brecciated texture developed in pyrite and marcasite suggesting britlle deformation	181
Fig. 5.30	Photomicrograph of zoned euhedral overgrowths of pyrite on cores of pyrrhotite from São Francisco mine	181
Fig. 5.31	Photomicrograph of overgrowth texture on pyrite from São Francisco mine	181
Fig. 5.32	Photomicrograph of deformation texture in pyrite showing filament-structure from São Francisco mine	181
Fig. 5.33	Photomicrograph of plastic deformation texture in pyrite from São Francisco mine	181
Fig. 5.34	Photomicrograph of deformation texture suggesting folding in porphyroblastic euhedal pyrite: Santo Aleixo	182
Fig. 5.35	Photomicrograph of recrystallised pyrite showing truncated grain boundaries which form 120° dihedral angles: Santo Aleixo	182
Fig. 5.36	Photomicrograph of recrystallisation products of pyrite forming idiomorphous crystals: Igarape Garapa	182
Fig. 5.37	Detail of Fig. 5.36 showing a recrystallised pyrite crystal enclosing a coarse grain of gold	182
Fig. 5.38	Sketch of Fig. 5.46a showing wallrock alteration sampling in São Francisco mine	192
Fig. 5.39	Sketch of the Fig. 5.47a showing wallrock alteration sampling in the Itapetim District area	192
Fig. 5.40	Illustration of the Fig. 5.42a showing sampling in the potassic-silicified zone of Canafistula 'garimpo'	192
Fig. 5.41	Illustration of Fig. 5.43a depicting sampling in the tourmaline-silicified-potassic zone at Canafistula 'garimpo'	192
Fig. 5.42a	Photograph of a potassic-silicified zone mineralized with gold and sulphides: Canafístula 'garimpo'	194
Fig. 5.42b	Photomicrograph of the above mentioned potassic-silicified zone	194
Fig. 5.42c	Photomicrograph of thin section showing the enrichment in K-feldspar for Canafístula 'garimpo'	194

Fig. 5.43a	Photograph of the tourmaline-silicified-potassic zone at Canafístula 'garimpo'	194
Fig. 5.43b	Detail of the tourmaline-silicified-potassic zone showing the rhythmic alternation of tourmaline, K-feldspar, and silicified zones	194
Fig. 5.43c	Photomicrograph of kinked tourmaline in gold-bearing tourmaline-quartz vein at Canafístula 'garimpo'	194
Fig. 5.44	Enrichment/depletion diagrams for Canafístula potassic-silicified-tourmaline zone	195
Fig. 5.45	Enrichment/depletion diagrams for Canafístula tourmaline-silicified-potassic zone	196
Fig. 5.46a	Photograph of silicified-potassic-tourmaline zone at Morro Pelado, São Francisco mine	198
Fig. 5.46b	Photomicrograph of thin section of the schist wallrock at Morro Pelado	198
Fig. 5.46c	Photomicrograph of the iron oxide rich mineralized quartz vein at Morro Pelado shear zone	198
Fig. 5.47a	Photograph of silicified-potassic-tourmaline zone at Pimenteiras-Desterro, Itapetim	198
Fig. 5.47b	Photomicrograph of gneiss wallrock shown in Fig. 5.47a.	198
Fig. 5.47c	Photomicrograph of amphibolite wallrock in Fig. 5.47a.	198
Fig. 5.48	Enrichment/depletion diagrams for alteration zones of São Francisco mine	199
Fig. 5.49	Enrichment/depletion diagrams for Itapetim area	200

Chapter 6

Fig. 6.1	Diagrams showing lead isotopic ratios of rocks and sulphides at present time	209
Fig. 6.2	$^{207}Pb/^{204}Pb$ against $^{206}Pb/^{204}Pb$ present day ratio diagram showing the Pb-Pb isochron	212
Fig. 6.3	$^{232}Th/^{204}Pb$ against $^{206}Pb/^{204}Pb$ present day ratio diagram showing the Th-Pb isochron	212
Fig. 6.4	Diagrams showing lead isotopic ratios in rocks and in sulphides calculated for 0.8 Ga time	216

Chapter 7

Fig. 7.1	Photomicrographs and sketches of fluid inclusions showing different trapping mechanisms and the relationships between intra-grain diffusion, crack-seal and crack healing	226
Fig. 7.2	Photomicrograph of a doubly-polished section of a gold-bearing quartz vein showing fluid inclusions (type I) associated with diffusion processes inter grains	228
Fig. 7.3	Photomicrograph of a doubly-polished section of a gold-bearing quartz vein showing fluid inclusions (type II) associated crack-seal mechanism	229
Fig. 7.4	Photomicrograph of a doubly-polished section of a gold-bearing quartz vein showing fluid inclusions (type III) as trails related to crack healing	230
Fig. 7.5	Photomicrographs and sketches of fluid inclusions showing H_2O-CO_2 inclusions with different DF, CO_2 monophase and H_2O-rich fluid inclusion	232
Fig. 7.6	Distribution of CO_2-H_2O, CO_2-rich and H_2O-rich phase fluid inclusions in gold-bearing quartz veins	233

Fig. 7.7	Histograms of H_2O-CO_2 fluid inclusions showing degree of fill, size, temperature of solid CO_2 melting, and clathrate melting	235
Fig. 7.8	Histograms of H_2O-CO_2 fluid inclusions showing temperature of liquid-vapour CO_2 homogenization, total homogenization, and density	236
Fig. 7.9	Histograms of H_2O-CO_2 fluid inclusions showing salinity and amounts of methane and carbon dioxide	237
Fig. 7.10	Histograms of CO_2 monophase fluid inclusions showing degree of fill, size, temperature of solid CO_2 melting, temperature of liquid-vapour homogenization of CO_2, density of fluid, and amount of methane and carbon dioxide	240
Fig. 7.11	Histograms of H_2O fluid inclusions showing degree of fill, size, temperature of first melting of the aqueous phase, temperature of last melting of aqueous phase, and salinity of the fluid	242
Fig. 7.12	Evidence of CO_2 effervescence by coeval CO_2-rich and H_2O-CO_2 inclusions indicating different CO_2 contents	249
Fig. 7.13	Compositions of H_2O-CO_2 and monophase CO_2-rich fluid inclusions in relation to the solvus for the H_2O-CO_2-NaCl system at 2.0 k bars and 6 % eq. wt NaCl	250
Fig. 7.14	Variation of the pressure and temperature of the CO_2 in H_2O-CO_2 and monophase CO_2 fluid inclusions	250
Fig. 7.15a	δ^{13} C data from fluid inclusions for gold-bearing quartz veins in Borborema Province	255
Fig. 7.15b	δ^{13} C values from fluid inclusions for gold-bearing quartz veins compared with other data source	255
Fig. 7.16a	δ^{18} O values for gold-bearing quartz veins in Borborema Province	257
Fig. 7.16b	δ^{18} O values for gold-bearing quartz veins compared with other data source	257
Fig. 7.17	The δ^{18} O and δ^{13} C isotope fields of varions δ^{13} C reservoirs used for comparison with the Borborema data	259

Chapter 8

Fig. 8.1	Borborema Province evolution	262
Fig. 8.2	Diagram showing lead isotopic ratios in supracrustal and granites and the fields for rocks from the lower and upper continental crust	265
Fig. 8.3	A model for the gold mineralization modelling in Borborema Province	272

LIST OF TABLES

Chapter 2 *Page*

Table 2.1	Regional geological evolution and granitoid emplacement in Borborema Province	16
Table 2.2	Tectonic/metamorphic events in Borborema Province	19
Table 2.3	Main occurrences of mafic and ultramafic rocks in Borborema Province	21

Chapter 3

Table 3.1	Deformation and metamorphism in the São Francisco Mine area	38
Table 3.2	Deformation and metamorphism in the Cachoeira de Minas Mine area	46
Table 3.3	Deformation and metamorphism in the Itapetim gold district	55

Chapter 4

Table 4.1	Description of granioitds from the Borborema Province: Central Domain	93
Table 4.2	Geotectonic characteristics of the granitoids from Itapetim area	100
Table 4.3	Rare-earth elements and isotopic characteristics of granitoids from Borborema Province: Central Domain	110
Table 4.4	Schists and their possible protoliths	137
Table 4.5	Gneisses and their possible protoliths	138
Table 4.6	Amphibolite petrochemistry	143
Table 4.7	Mineral assemblages diagnostic of metamorphic facies in Borborema Province: Central Domain	146
Table 4.8	Rock pressure-temperature data	154

Chapter 5

Table 5.1	Mineral assemblages in the gold-bearing quartz veins in Borborema Province	159
Table 5.2	Gold/silver ratios and true fineness	179
Table 5.3	Paragenetic sequences for gold mineralization in Borborema Province	185
Table 5.4	Wallrock alteration: enrichment/depletion	191

Chapter 6

Table 6.1	Sample location and geological setting	206
Table 6.2	Rock and sulphide lead isotopic ratios	208
Table 6.3	Sulphide lead isotopic ratios and model-age data	214
Table 6.4	Lead isotopic ratios of rocks at 0.8 Ga calculated from their Th/U ratios	217

Chapter 7

Table 7.1	Gold-bearing quartz vein sampling for fluid inclusions and stable isotope studies and relationship to geological setting	223

Table 7.2 Microthermometric data of CO_2-H_2O fluid inclusions in quartz veins hosted by granitoids, supracrustals and amphibolite 234
Table 7.3 Microthermometric data of CO_2 monophase fluid inclusions in quartz veins hosted by granitoids and supracrustals 239
Table 7.4 Microthermometric data of H_2O-rich fluid inclusions in quartz veins hosted by granitoids and supracrustals 241
Table 7.5 Bulk composition, density, temperature of homogenization and predicted pressure for CO_2-H_2O fluid inclusions in gold-bearing quartz veins 245
Table 7.6 Bulk composition, density, and predicted temperature of homogenization and pressure for CO_2 monophase fluid inclusions in gold-bearing quartz veins 246
Table 7.7 Oxygen and carbon isotope data for quartz and fluid inclusions hosted by gold-bearing quartz veins 254

Chapter 8

Table 8.1 Comparison of geological features of Archaean lode gold deposits 275
Table 8.2 Comparison of geological features of Phanerozoic lode gold deposits 280
Table 8.3 Comparison of geological features of Archaean, Phanerozoic and Borborema mesothermal gold deposits 282

LIST OF APPENDICES

Chapter 1

A	1.1	Sample descriptions	300

Chapter 4

A	4.1	Petrographic and geochemical methods of study	305
A	4.1a	Procedure for making fusion beads for X-ray fluorescence analysis for major elements	308
A	4.1b	Procedure for pressed pellet preparation for X-ray fluorescence analysis for trace elements	309
A	4.2	Chemical analyses of standards (XRF)	310
A	4.3	Chemical analyses of granites (XRF)	311
A	4.4	Granites: CIPW normalised data	312
A	4.5	Ga/Al ratios and their interpretation for granite study	313
A	4.6	Chemical anlyses of gneisses (XRF)	314
A	4.7	Chemical anlyses of schists (XRF)	316
A	4.8	Chemical anlyses of amphibolites (XRF)	319
A	4.9	Microprobe analyses of amphiboles	320
A	4.10	Methods of calculation of P-T conditions	322
A	4.11	Microprobe analyses used for P-T calculations	323
A	4.12	Chlorite microprobe analyses used for P-T calculations	325
A	4.13	Geochemical database	326

Chapter 5

A	5.1	Electron microscope analyses of gold within sulphides: pyrite	328
A	5.2	Electron microscope analyses of native gold	329
A	5.3	Electron microscope analyses of maldonite	330
A	5.4	Microprobe analyses of sulphides: pyrite	331
A	5.5	Microprobe analyses of sulphides: chalcopyrite	332
A	5.6	Microprobe analyses of bismuth minerals, native gold and selenium/tellurium minerals	333
A	5.7	Microprobe analyses of gangue minerals	334
A	5.8	Major and trace element geochemistry of wallrock alteration assemblages	335

Chapter 6

A	6.1	Lead isotope extraction methods	337

Chapter 7

A	7.1	Microthermometry standards	338
A	7.2	Graphs used to calculate density (**a**), the amount of CH_4 (**b**), and salinity (**c**) of CO_2 phases (Shepherd *et al.*, 1985)	339
A	7.3	Diagram after Schwartz (1989) to predict temperature of homogenization and pressure for fluid inclusions	340
A	7.4	Microthermometric data CO_2-H_2O fluid inclusions in quartz veins hosted by SLTG (Igarapé Garapa)	341
A	7.5	Microthermometric data CO_2-H_2O fluid inclusions in the quartz veins hosted by SLTG (Cacimba Salgada 'garimpo')	432
A	7.6	Microthermometric data CO_2-H_2O fluid inclusions in quartz	

		veins hosted by SLTG (Santo Aleixo area)	343
A	7.7	Microthermometric data CO_2-H_2O fluid inclusions in quartz veins hosted by ETG (Canafístula 'Garimpo')	344
A	7.8	Microthermometric data CO_2-H_2O fluid inclusions in the quartz veins hosted by supracrustal (Cachoeira de Minas mine)	345
A	7.9	Microthermometric data CO_2-H_2O fluid inclusions in the quartz veins hosted by supracrustal rock (São Francisco mine)	346
A	7.10	Microthermometric data CO_2-H_2O fluid inclusions in the quartz veins hosted by supracrustal rock (Itapetim District)	347
A	7.11	Microthermometric data CO_2-H_2O fluid inclusions in the quartz veins hosted by amphibolite (Boqueirão dos Cochos)	348
A	7.12	Microthermometric data CO_2 monophase fluid inclusions in quartz veins hosted by granites	349
A	7.13	Microthermometric data CO_2 monophase fluid inclusions in quartz veins hosted by supracrustal rocks	349
A	7.14	Microthermometric data H_2O-rich fluid inclusions in quartz veins hosted by granites	350
A	7.15	Microthermometric data H_2O-rich fluid inclusions in quartz	351
A	7.16	Bulk composition of H_2O-CO_2 monophase fluid inclusions in gold-bearing quartz veins	352
A	7.17	Bulk composition of CO_2 monophase fluid inclusions in gold-bearing quartz veins	358
A	7.18	δ^{13} C data for fluid inclusions in gold-bearing quartz veins	359

LIST OF ABBREVIATIONS

The reader will find several types of abbreviations used in this thesis. In general, abbreviations from the original source have been used.

GENERAL

CPRM	Mineral Resources Exploration Company (Ministry of Mines and Energy of Brazil)
CNPq	Brazilian Research Council (Ministry of Education)
DNPM	Mineral Production National Department (Ministry of Mines and Energy of Brazil)
MG-T-001	Sample label; (MG = author name; T = drill core sample)
MG-R-001	Sample label; (MG = author name; R = surface sample)
RHBNC	Royal Holloway and Bedford New College (University of London)

FLUID INCLUSIONS

Aq	Aqueous phase
cp	Critical point
DF	Degree of fill
ρ CO_2	CO_2 density (g cm^{-3})
ρ H_2O	H_2O density (g cm^{-3})
NFI	Number of fluid inclusion measurements
L CO_2	CO_2 liquid phase
PVTX	Pressure-volume-temperature-composition
P-pred	Predicted pressure
Th CO_2	Temperature of liquid-vapour homogenization of carbon dioxide phase
Tm Cl	Temperature of clathrate melting
Tm CO_2	Temperature of solid carbon dioxide melting
T-fm Aq	Temperature of first melting of the aqueous phase
T-lm Aq	Temperature of the last melting of the aqueous phase
T-Th	Temperature of total homogenization of the fluid inclusion
Th-pred	Temperature of predicted total homogenization
V CO_2	CO_2 vapour phase

LEAD ISOTOPES

μ	$^{238}U/^{204}Pb$
ω	$^{232}Th/^{204}Pb$
SRM 981	Pb standard
%/amu (2 se)	% atomic mass unit (standard error)
%amu (2sd)	% atomic mass unit (standard deviation)
Re filament	Rhenium filament

MICROSCOPY

BSE	Back-scattered electron image
n	Refractive index
PPL	Plane polarised light
RL	Reflected light
SEM	Scanning electron microscopy
TL	Transmitted light
XPL	Cross polarised light
WOF	Width of field (for photomicrograph)

MINERALS

Ab	Albite
Aegir	Aegirine
Alm	Almandine
Allan	Allanite
An	Anorthite

Ann	Annite
And	Andalusite
Andes	Andesite
Apat	Apatite
Biot	Biotite
Cal	Calcite
Cel	Celadonite
Ch	Chlorite
Chp	Chalcopyrite
Clinoz	Clinozoisite
Cord	Cordierite
East	Eastonite
Epid	Epidote
Fe ox	Iron oxide
Flu	Fluorite
Gal	Galena
Gar	Garnet
Gr	Grossular
Hfls	Hornfels
Horn	Hornblende
Ilm	Ilmenite
K-feldsp	K-feldspar
Ky	Kyanite
Marcs	Marcasite
Mg	Magnetite
Microcl	Microcline
Molyb	Molybdenite
Musc	Muscovite
Or	Orthoclase
Olig	Oligoclase
Pa	Paragonite
Phl	Phlogopite
Plag	Plagiolcase
Preh	Prehnite
Py	Pyrite
Pyro	Pyrope
Pyrr	Pyrrhotite
Pump	Pumpellyite
Px	Pyroxene
Qz	Quartz
Staur	Staurolite
Ser	Sericite
Sill	Sillimanite
Tit	Titanite
Tu	Tourmaline
Op min	Opaque minerals
Zr	Zircon

PETROCHEMISTRY

AFM	Alkalis (K_2O + Na_2O), total iron, magnesium diagram normalized to 100
ASI	Aluminium saturation index
A/CNK	{molar [Al_2O_3/(CaO+Na_2+K_2O)]}; CaO has the amount of CaO inclued in apatite subtracted; = CaO-3.3P_2O_5.
BIF	Banded iron formation
CAF	Alkalis (K_2O + Na_2O), aluminium and total iron modal diagram normalized to 100
Fe_2O_3*	Total iron expressed as Fe_2O_3
GSB	Greenstone belt
HFS	High field strength elements (e.g. Ti, P, Zr, Hf, Nb, Ta, Y)
HREE	Heavy rare-earth elements (e.g. Hy, Nd, Eu)
QAP	Quartz, alkali feldspar, and plagioclase modal diagram normalized to 100
LIL	Large-ion lithophile elements (e.g. K, Rb, Sr, Ba, Th, Pb, U, Cs)
LOI	Loss on ignition

LREE	Light rare-earth element (e.g. Ce, Yb)
REE	Rare-earth elements
Sr (i)	Strontium initial isotope ratio

Basalts:

ARC	Active island arc
CAB	Calc-alkaline basalt
IAT	Island arc tholeiite
LKT	Low potassic tholeiitic
MORB	Mid-ocean ridge basalt
OIA	Ocean island alkalic
OIB	Ocean island basalt
OFB	Ocean floor basalt
OIT	Ocean island tholeiite
WPB	Within plate basalt

Granites:

VAG	Volcanic arc granite
COLG	Collision granite
TTG	Tonalite-trondhjemite-granodiorite
WPG	Within plate granite

STABE ISOTOPE

δ^{13} C	Carbon isotopic composition
δ^{18} O	Oxygen isotopic composition
$^{0}/_{00}$	Per mil
f CO_2	CO_2 fugacity
f H_2S	H_2S fugacity
f O_2	Oxygen fugacity
PDB	Pee Dee Belemnite
SMOV	Standard mean ocean water

TECTONICS/STRUCTURAL

C	Plane of shear
D_1	Deformation
ETG	Early-tectonic granite
ESTG	Early-syn-tectonic granite
F_1	Fold
L_1	mineral lineation
LTG	Late tectonic granite
SLTG	Syn-late tectonic granite
SZ	Shear zone
S_0	Bedding and layering
S_1	Foliation
S	Plane of schistosity
$\sigma_1, \sigma_2, \sigma_3$	Principal stress, intermediate, least compressive stress

UNITS / MEASUREMENTS

cm	Centimetre
Ga	Giga (factor = 10^9)
m	Metre
Mole %	Molarity percentage
MSWD	Mean standard weighted deviation
ng	Nano (= 10^{-9})
km	Kilometre
ppb	Parts per billion
ppm	Parts per million
P	Pressure (expressed as kb = kilo bar)
T	Temperature (expressed as °C or °K)

UTM	Universal Transverse Mercator grid system
vol. %	Per cent by volume
wt %	Per cent by weight
μm	Micro (10^{-6})

REFERENCES

Acad. Sci. Fr.	Académie des Sciences de France
Amer. J. Sci.	American Journal Sciences
Amer. Geophys. Union	American Geophysical Union
Amer. Mineral.	American Mineralogist
Australas. Inst. Min. Metall.	Australasian Institute of Mining and Metallurgy
Can. Geol. Surv. Bull.	Canadian Geological Survey Bulletim
Can. Inst. Mining Metall.	Canadian Institute of Mining and Metallurgy
Can. J. Earth Sci	Canadian Journal of Earth Sciences
Can. Mineralog.	Canadian Mineralogist
Clay Miner.	Clay Minerals
Chron. Rer. Min.	Chronique de la Recherche Miniere
Chem. Geol.	Chemical Geology
Contrib. Mineral. Petrol.	Contribution to Mineralogy Petrology
Econ. Geol.	Economic Geology
Earth Planet. Sci. Lett.	Earth and Planetary Sciences Letters
Earth Sci. Rev.	Earth Science Reviews
Geol.	Geology
Geochim. Cosmochim. Acta	Geochimica et Cosmochimica Acta
Geochem. Int.	Geochemical Institute
Geol. Assoc. Can.	Geological Association of Canada
Geol. Rundschau	Geologische Rundschau
Geol. Soc. Amer.	Geological Society of America
Geol. Soc. Amer. Bull.	Geological Society of America Bulletim
Geol. Soc. Aust. Abstr.	Geological Society Australia Abstract
Geol. Soc. London	Geological Society of London
Epis.	Episodes
J. Chem. Thermody.	Journal of Chemical Thermodynamics
J. Geophys	Journal of Geophysics
J. Geophys Res.	Journal of Geophysics Reserch
J. Geol. Soc. London	Journal of Geological Society of London
J. Metamorph Geol.	Journal of Metamorphic Geology
J. Petrog.	Journal of Petrology
J. Pure Appl. Geophys.	Journal Pure Application Geophysics
J. Struct. Geol.	Journal of Structural Geology
J. Volc. Geother. Res.	Journal of Volcanology and Geothermal Reserch
Lithos	Lithos
Mem. Sci. de la Terre	Memorium Science de la Terre
Mineral. Depos.	Mineralium Deposita
Min. Assoc. Can.	Mineralogical Association of Canada
Mineral. Mag.	Mineralogical Magazine
Min. Sci. Eng.	Minerals Sciences Engineering
Nat.	Nature
Nevada Bur. of Mines	Nevada Bureau of Mines
Ontario Geol. Surv.	Ontario Geological Survey
Ore Geol. Rev.	Ore Geology Reviews
Phil. Trans. Royal Soc. London	Philosophical Transactions of the Royal Society of London
Precamb. Res.	Precambrian Reserch
Rev. Bras. Geoc.	Revista Brasileira de Geociencias
Rev. Eng. Min. Met.	Revista Engenharia Mineração e Metalurgia
Sci.	Science
Soc. Bras. Geol.	Sociedade Brasileira de Geologia
Tectonophy.	Tectonophysics
Terra Abst.	Terra Abstracts
Univ. W. Aust.Pub.	University of Western Australia Publication
US Geol. Surv.	United States Geological Survey
Z. Geol. Paleont.	Zoology Geology Paleontology

ACKNOWLEDGEMENTS

I would like to acknowledge help from the following people who contributed greatly to this research and supported me throughout:

- My supervisor: Dr. David H.M. Alderton who helped me a great deal throughout by providing valuable and constant guidance, discussion and comments about different aspects of gold mineralization. I really appreciated his advices and continuous help. His patience with this student was a constant source of encouragement.

- Dr. I. Davison and Dr. J. Keller who helped with the structural aspects of the area. Their criticism in editing the structural chapter was useful.

- Academic staff of the Department of Geology, Royal Holloway, University of London, who helped me were: Dr. M.F. Thirlwall for reading the manuscript and commenting on aspects of the lead isotope study; Dr. G.F. Marriner (geochemical analyst) for tuition in XRF sample preparation, analysis and data processing, and Dr. D. Mattey and Dr. I. Fitzsimons for their assistance with stable isotope analysis.

-Jennifer Riddell and Fiona Nelson in the RHBNC Electron Microscopy Unit for teaching me the use of the electron microscope and for their friendly guidance and assistance in SEM analysis.

-Technical staff of the Geology Department, RHBNC: Mr. K.W. Stephens, Departmental Superintendent; Mr. Neil Holloway, Mr. I. Gill, and Miss C. Warren for help during the preparation of polished blocks for ore-mineral study and polished sections for probe and fluid inclusion research; Mr. K. Salzedo and Mr. C. Jenkins for teaching me XRF sample preparation and geochemical data processing using the VAX computer system, and Mr. G. Ingram for his help in lead isotope sample preparation.

- Mr. Colvine (RHBNC) and the Geologists Grigore Simon (Bucharest University) and Gu Lianxing (Nanjing University) for discussion the ore mineral indentification.

- The Natural Environment Research Council, Isotope Geosciences Laboratory in Keyworth, Nottingham, for analysis of oxygen isotopes.

- Dr. Terry Williams of the Natural History Museum for help during microprobe analysis of ore minerals.

- The Open University academic staff: Dr. A. Tindle for helping with microprobe analyses of rocks and minerals; N. Williams for assistance in using the BSE electron microscope and Dr. H. Prichard who provided analytical facilities at that university.

- Dr. T. Liverton for help with the photomicrographs, discussion, and editing of this thesis. His guidance and help were greatly appreciated.

- The Geologist April Harper for reviews and critical comments and Miss Sandra Muir for her help in layout the thesis.

- Thanks must go to all my friends and collegues at RHBNC who have put up with me over the years, especially those who provided encouragement and discussion of

many aspects of this thesis: Shariff Omang, Luiz D'el Rey, Dennis Brown and Mohamed Al-Kadasi. Andrew Long and Joel Baker deserve thanks for their help when I was working in the Radiogenic Isotope Lab. A special mention is reserved for Bill Wilks and Chris Dart, with whom I shared the writing-up room and for Christine Perrin, Angeliki Skamvetsaki, Moyra Wilson, Richard Symms, Neil Frewin, Damien Strogen, Karim Al'Subbary, Kadrim and Nigel Blade who have endured a great deal of mumbling and muttering.

- At RHBNC, the successive Heads of the Geology Department, Prof. A.J. Smith and Prof. D.J. Blundell, who allowed access to facilities.

- Special gratitude is reserved for Prof. De Morais, his wife Dr. Selene and their family for help in settling me in this country. Further thanks are required for their hospitality.

- Throughout this research, assistance and discussion were provided by the Brazilian geologists: Dr. Brito Neves from the University of São Paulo and Dr. Santos and Geologist Silva Filho from CPRM in Recife respectively, who helped me to elucidate the stratigraphy and geochronological aspects of Borborema Province.

- Geologist Carlos Vasconcellos at the Open Univesrity for his help during the calculation of the pressure and temperature of the rocks.

- Companhia de Pesquisa de Recursos Minerais-CPRM for their support and assistance and particularly: Dr. Eduardo Machado, the ex-president, who allowed me to undertake the PhD; Dr. Carlos Oiti Berbert, the President, who supported me during this time; and the technical staff of the Mineral Laboratory who helped with powder sample preparation; thin sectioning of rocks and polished ore blocks; Dr. Tania Freire head of the Library and her staff and Dr. Fanny for helping with references and mapping support during all of this period.

- From the CPRM office in Recife: my gratitude to Dr. Mascarenhas for providing logistical and other support during the fieldwork; my colleagues H.Torres, H.Gomes and S. Muntesuma for their assistance in the fieldwork and for discussion and comments about the stratigraphy and geology of Borborema Province; geologists Benício Montenegro and Expedita Torres who discussed the petrography of the area; the and the taxi driver Rene who helped through two journeys during the fieldwork.

- To Prof. Octavio Barbosa from CPRM-Rio and Prof. J. Cassedanne from the University of Rio de Janeiro for their criticism about the original project.

- The Conselho Nacional de Desenvolvimento Científico e Tecnológico, the Brazilian Research Council-CNPq for sponsoring this research.

- Finally to my Family whose patience, guidance and support provided the strength to complete this research: my parents, and my brothers and my sisters and their families.

'Thank you so much and God bless you all'

CHAPTER 1 INTRODUCTION

1.1 STATEMENT OF THE PROBLEM

Many Pre-Cambrian shield areas, and some younger metamorphic terranes, contain gold-bearing quartz veins, the development of which seems to be closely related to that of shear zones. Such mesothermal, 'lode' deposits are widespread and are of great economic significance (their cumulative production in the world is estimated to be second only to that of the Witwatersand deposits; Woodall, 1988). However, in spite of the extensive research into these deposits, they have many features that remain poorly understood. It is appreciated that these shear zones represent important conduits for fluid movement through crustal rocks and that they are often the site of retrogressive metamorphism and metasomatic alteration, in addition to gold mineralization. However, there are still some relationships between shear zones and the mineralized fluids that are not entirely clear. In addition, the potential sources of both the metals and the mineralizing fluids which formed these gold deposits still remain a matter for debate, even though the amount of information available is quite large (e.g. Colvine *et al.*, 1988; Kerrich, 1989).

The Borborema Province in N.E. Brazil contains several examples of shear zone hosted gold deposits, including two active mines: São Francisco and Cachoeira de Minas. The major tectonic feature of relevance is a sinuous, anastomosing shear system which is related to the Brasiliano-Pan African tectonic event. This crustal-scale shear system divides the province into elongate domains characterised by diverse and distinctive lithologies, metamorphic grades and structures. Gold-bearing quartz veins are widespread and occur in a variety of geological environments (Archaean basement, Early Proterozoic supracrustal sequences, Early to Late Proterozoic granitoids).

Although gold was first discovered in the province in the early 1940's and exploration has continued for the past 50 years, no research has yet attempted to characterise these deposits and to determine their genesis. A large amount of money and effort has been expended in past exploration programmes in the province, although the lack of any cohesive understanding of the geology and mechanism of gold precipitation has usually resulted in the failure to discover an economic deposit, and a consequent loss of investment. There is thus an urgent need to understand the geology of the gold deposits of the Borborema Province, so as to enable an efficient exploration philosophy to be developed.

1.2 AIMS OF THE THESIS

This thesis has two main aims. The first is simply to characterise the mineral deposits, both as regards their economic mineralization, and their geological setting. The second aim is to examine the mechanism and controls of gold precipitation in these deposits. As shown later, effort has also been expended in characterizing economic targets, and thus providing a guide to minimise investment risks for prospecting such an enormous area.

There is a plethora of complex models that have been formulated to explain mesothermal gold deposits, and no unifying hypothesis appears to encompass and take into account all the geological and geochemical observations (Kerrich, 1989). Until fairly recently, the consensus view was that hydrothermal fluids were generated by dehydration of silicates during peak metamorphism; gold and other metals were presumed to be derived by leaching of appropriate lithologies, mainly basic rocks. However, some recent studies have advocated a different mechanism for mineralization: one that involves granite-related fluids produced some time after peak metamorphism (e.g. Spooner and Fyfe, 1973; see Wilkins, 1993). As shown later, this present study confirms that later granite-related hydrothermal activity plays an important role in the genesis of shear zone-related gold mineralization. Although the genetic model developed here has been derived from studies in the Borborema Province, it may also have relevance in other regions.

1.3 METHODS OF RESEARCH

1.3.1 Fieldwork Programme

In order to achieve the aims of this study, two periods of fieldwork were undertaken in Borborema Province: the first one during the months of June and July 1990, the second in October-November 1991. Altogether, approximately 16 weeks were spent in the field. Detailed field observations were made of the mineralized veins and their host lithologies, and more than 300 rock and ore samples were collected from surface exposures and from drill cores. The locations of those samples referred to in the text are given in Appendix A1.1.

The granites occur in the upland regions and are generally well-exposed. The supracrustals occur in the lowland regions and are less well-exposed. However, because the climate is fairly arid, only a thin weathering profile occurs above these lithologies. No major problem exists in gaining access in the region.

1.3.2 Laboratory Work

The rock and ore samples collected during the fieldwork were described and prepared for petrographic study using both transmitted and reflected light microscopy. Approximately 100 samples were powdered for determination of major and trace elements using X-ray fluorescence, and 22 samples were further utilised for radiogenic Pb isotopic analysis. Samples of ore and rock were selected for electron microscope analysis (X-ray mapping and quantitative determinations). Fifteen samples of mineralized quartz vein were used in a combined fluid inclusion - stable isotope (δ^{13} C and δ^{18} O) study.

Most of the sample preparations, for example the powder, thin sections (300 samples) and polised block (87 samples), were performed at the CPRM laboratories in Rio de Janeiro and in Recife, N.E. Brazil. All the laboratory work was performed at Royal Holloway, except for some of the microprobe and δ^{18} O analyses. Details of each of the analytical techniques used during this research will be described separately in the relevant chapters.

1.4 STRUCTURE OF THE THESIS

This thesis contains eight chapters. Chapter 1 contains the introduction to the thesis. Chapter 2 provides a review of the geological and geotectonic setting of Borborema Province and its tectonic evolution. The geology and structure of the mineralized areas are covered extensively in Chapter 3, where each mineral deposit is discussed separately. Chapter 4 deals with the geochemical and petrographic analysis of the host rocks to the mineralization and presents a discussion of the nature of the important pre-mineralization metamorphic events. Chapter 5 discusses the characteristics of the mineralized veins: their ore-mineral assemblages and associated gangue minerals, their textures and paragenesis, and the associated wallrock alteration. A lead isotope study was carried out on rocks and sulphides in an attempt to date the metamorphism and related gold mineralization, and to provide constraints on the source of the metals. The results of this study are presented in Chapter 6. An understanding of the mechanism of, and processes responsible for, the deposition of the gold requires a characterization of the P-T properties of the hydrothermal fluids. This aspect has been tackled in Chapter 7 by the study of fluid inclusions in quartz. In addition, isotopic analyses of quartz and fluid inclusions have allowed some constraints to be placed on the source of the hydrothermal fluids. Finally, Chapter 8 develops a genetic model for gold mineralization in the Borborema Province, discusses the application of this model to

mineral exploration in N.E. Brazil, and compares the gold mineralization in N.E. Brazil with other gold deposits worldwide.

CHAPTER 2 REGIONAL GEOLOGICAL AND GEOTECTONI(SETTING OF THE BORBOREMA PROVINCE

2.1 INTRODUCTION

Northeast Brazil is dominated by two structural provinces (Fig. 2.1): (i) the Parnaíba province in the north comprises the São Luiz Craton, a probable extension of the former West African Craton into Brazil (Hurley *et al.*, 1967), and the Gurupi Fold Belt (Hasui *et al.*, 1984); and (ii) the Borborema Province (Fig. 2.2), which occupies an area of about 450,000 km^2 and covers much of the northeast area.

Regional geological and geophysical investigations confirm the assertion that the extent of the Borborema Province is limited by cratonic areas: in the NW the São Luiz Craton, and to the south the São Francisco Craton. These two areas have formed stable geological units since the Late Proterozoic (Almeida *et al.*, 1981). A large extension of the province is buried by Phanerozoic cover on the western side (Parnaíba Basin) and, at the eastern and northeastern sides, by sediments distributed along the continental margin (see Fig. 2.3).

The Borborema Province is composed of two fundamentally different terranes: (i) the gneiss-migmatite-granite terranes of Archaean to Middle Proterozoic age which represent massifs or microplates; and (ii) the folded metavolcanic-sedimentary terranes with a Late Proterozoic, or an Early to Late Proterozoic polycyclic evolution (Jardim de Sá, 1988).

The Archaean basement (3.5-2.9 Ga; Brito Neves and Cordani, 1991) consists of migmatitic gneisses banded with biotite gneiss, granite-granodiorite orthogneiss, and calc-silicate rocks. These high-grade metamorphics are surrounded by metavolcanic-sedimentary rocks consisting of orthogneiss, paragneiss, schist, amphibolite, quartzite and calc-silicate lenses and metavolcanic rocks.

The major tectonic feature of Borborema Province is a sinuous and branched, anastomosing shear zone (Caby *et al.*, 1990), which divides the province into three structural domains (see Fig. 2.3):

(i) The Northern Domain, where several N-NE trending fold belts occur such as: Médio Coreau, Jaguaribeano and Rio Curu/Independencia.

(ii) The Central Domain, where three N-NE-trending fold belts are present: Seridó, Pajeú/Paraíba and Piancó/Alto Brígida.

(iii) The Riacho do Pontal and the Sergipano ESE-WNW mobile zones which border the São Francisco craton (Santos and Brito Neves, 1984).

Lode gold deposits are widespread and occur in different geological environments.

Figure 2.1. Sketch map of Brazil showing the distribution of Precambrian and Phanerozoic units (Schobbenhaus *et al.*, 1984) and structural provinces (Almeida *et al.*, 1981).

Figure 2.2 View of Borborema Province in the central domain (along the Patos toTeixeira road). Note the higher ground represented by the batholiths and stocks of granitoids.

Deposits with gold occur predominantly in the fold belt terranes. Gold-bearing quartz veins are also present in the basement rocks and the granitoids, the latter intruding both the supracrustal sequences and the basement rocks. However, the fold belts are the important geological setting for the gold mineralization. Gold is related to shear zones which provided conduits for mineralizing fluids and represent important sites of ore deposits. The mineralization occurs predominantly in sheared quartz veins, preferentially associated with mylonitic rocks (Figs. 2.4a and 2.4b).

The gold deposits of the Borborema Province are limited to the region to the north of the Pernambuco Lineament, and are predominantly concentrated in the Central Domain (Fig. 2.4b). This study focusses on the Central Domain, consisting of the Pajeú/Paraíba, Piancó/Alto Brígida and Seridó fold belts.

2.2 REGIONAL GEOLOGY OF THE BORBOREMA PROVINCE

2.2.1 Structural Framework

The Borborema Province consists of a mosaic of Archaean to Early Proterozoic granitic, gneissic and migmatitic terranes (massifs or microplates) which are surrounded by mobile zones or fold belts of Proterozoic age (Fig. 2.3). The province was reworked during the 0.9-0.5 Ga Brasiliano thermal-tectonic cycle, which was characterised by widespread emplacement of granitic rocks (Brito Neves, 1975; Santos and Brito Neves, 1984; Brito Neves, 1986). Evidence of an earlier tectonic evolution (the Trans-Amazonian thermal-tectonic cycle), starting at around 2.1-1.8 Ga (Brito Neves, 1975), has also been documented in some fold belts (Jardim de Sá *et al.*., 1988; Jardim de Sá, 1988).

Although the Early Proterozoic fold belts were subjected to Pre-Brasiliano deformation, most of the evidence for this event was subsequently obliterated by the Late Proterozoic Brasiliano event. This produced a complex structural pattern, characterized by polyphase folding, NE, E-W and WNW-ESE-trending ductile strike-slip faults, and horizontal stretching consistently parallel to the trend of the belts (Corsini *et al.*, 1991).

Two E-W trending, crustal-scale lineament systems, about 150 km apart, cross-cut the province: the Patos (north) and Pernambuco (south) lineaments (Ebert, 1970; see Figs. 2.4a and 2.4b). A complex anastomosing network of E-NE-trending strike-slip shear zones is also linked with the main lineaments and these form many subsidiary structures (Santos and Brito Neves, 1984; Santos *et al.*, 1984; Corsini *et al.*, 1991). This network is composed of NE-trending dextral strike-slip faults in the northwestern domain, and by E-W trending dextral strike-slip faults associated with N to NE-

trending metasedimentary fold belts, in the central and southeastern domains (Fig. 2.4a and 2.4b). The N to NE trending branches display evidence of transpression, whereas the E-W-trending shear zones are infilled by syntectonic magmas, more suggestive of transtension (Vauchez *et al.*, 1992). In this regard, Hollister and Crawford (1986) point out that the melts themselves may be important in terms of lubrication of shear zones in the lower crustal environment.

These systems developed under low pressure-high temperature metamorphic conditions and were subsequently reactivated under decreasing temperature conditions, with the development of strike-slip faults in the Central Domain, which are characterised by E-W dextral and N-NE sinistral trending faults (Vauchez *et al.*, 1992).

The Patos shear has been linked to the tectonic evolution of the Seridó Fold Belt during the 0.9-0.5 Ga Brasiliano Cycle (Corsini *et al.*, 1991), while the Pernambuco Lineament is related to reactivation of the Trans-Amazonian-age Riacho do Pontal Fold Belt during the Brasiliano Cycle (Gomes, 1990).

a) Massif Terranes or Microplates

The granitic, gneissic and migmatitic terranes were consolidated by the end of the Trans-Amazonian thermal-tectonic cycle (2.1-1.8 Ga) and reworked by the Brasiliano Orogeny (0.9-0.5 Ga). They consist largely of upper amphibolite to granulite metamorphic facies assemblages, although often they have suffered the effects of granitoid emplacement (Brito Neves, 1975; Santos and Brito Neves, 1984).
Usually the massifs occur in irregular oval forms with sheared contacts (Fig. 2.3). They consist of: (i) migmatite/gneiss terranes associated with metamorphosed mafic and ultramafic rocks (Almeida *et al.*, 1981; Caby *et al.*, 1990); (ii) granite and granodiorite batholiths (Jardim de Sá *et al.*, 1981); and (iii) folded cover consisting of supracrustal terranes (Santos *et al.*, 1984).

The gneisses consist mostly of plagioclase-hornblende-biotite gneisses. They were probably derived from a predominant tonalite-trondjemite-granodiorite (TTG) plutonic association and later subjected to ductile deformation (Myers, 1978). Migmatites are dominated by leucosome, with evidence of intrusion of additional anatectic melt material. They were most likely derived from the reworking of the associated ('grey') gneisses. The granitoids consist of porphyritic granite grading into augen-gneiss through increasing deformation ('G-1' type). Metasediments associated with minor 'greenstones' consist of mafic rocks with Mg-rich amphibolite, associated with volcanic breccias, tremolite schists, calc-silicate rocks, and Al-rich metapelitic schists.

A lack of gechemical, geophysical and geochronological information means that these terranes are poorly understood. However, an age at 3.5-2.9 Ga has been proposed for these massif terranes, based on Rb-Sr whole rock isochrons (Santos and Brito Neves,

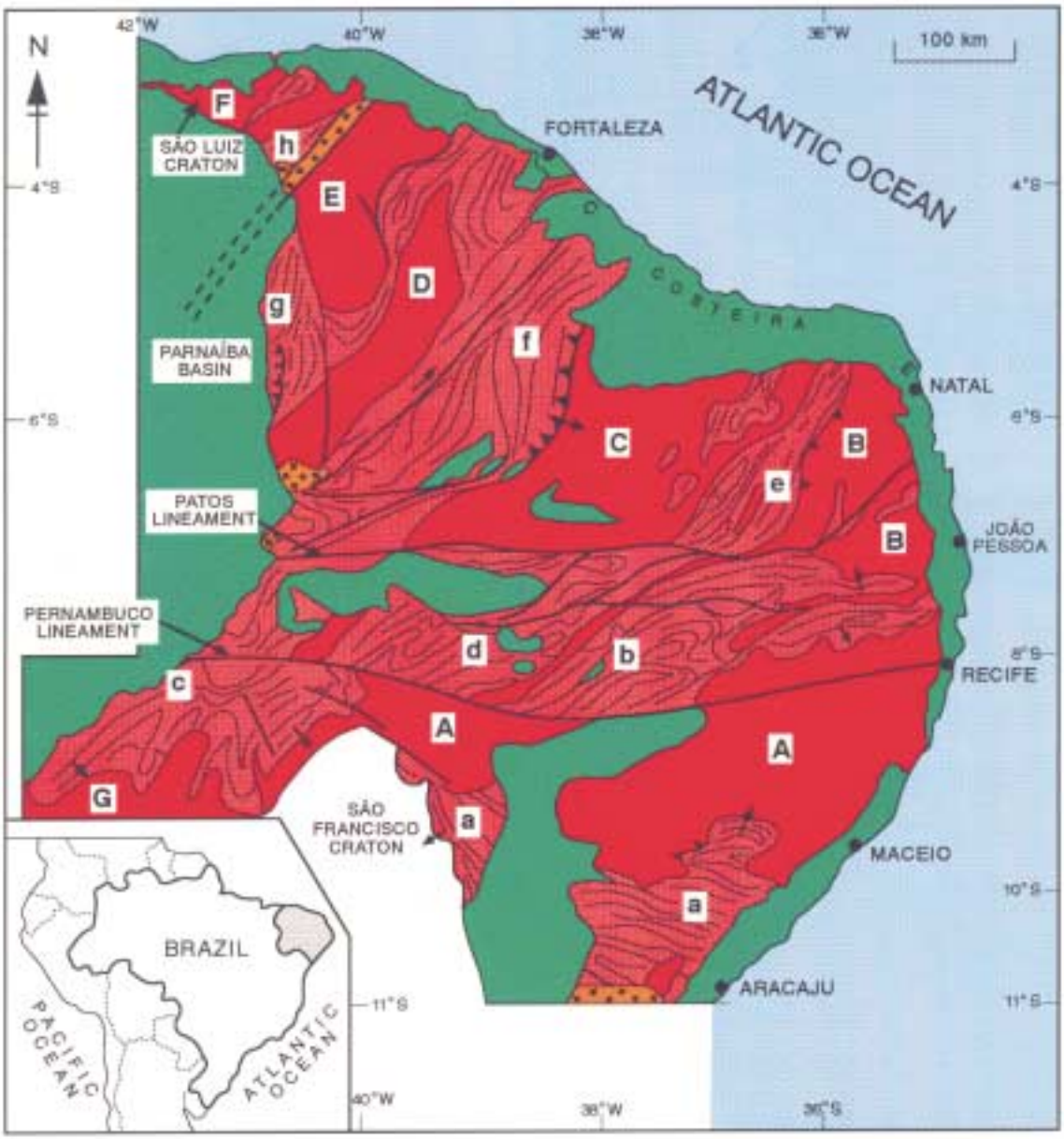

Figure 2.3 Simplified geological map of N.E. Brazil, including the Borborema Province and its limits (Modified from Santos and Brito Neves, 1984).

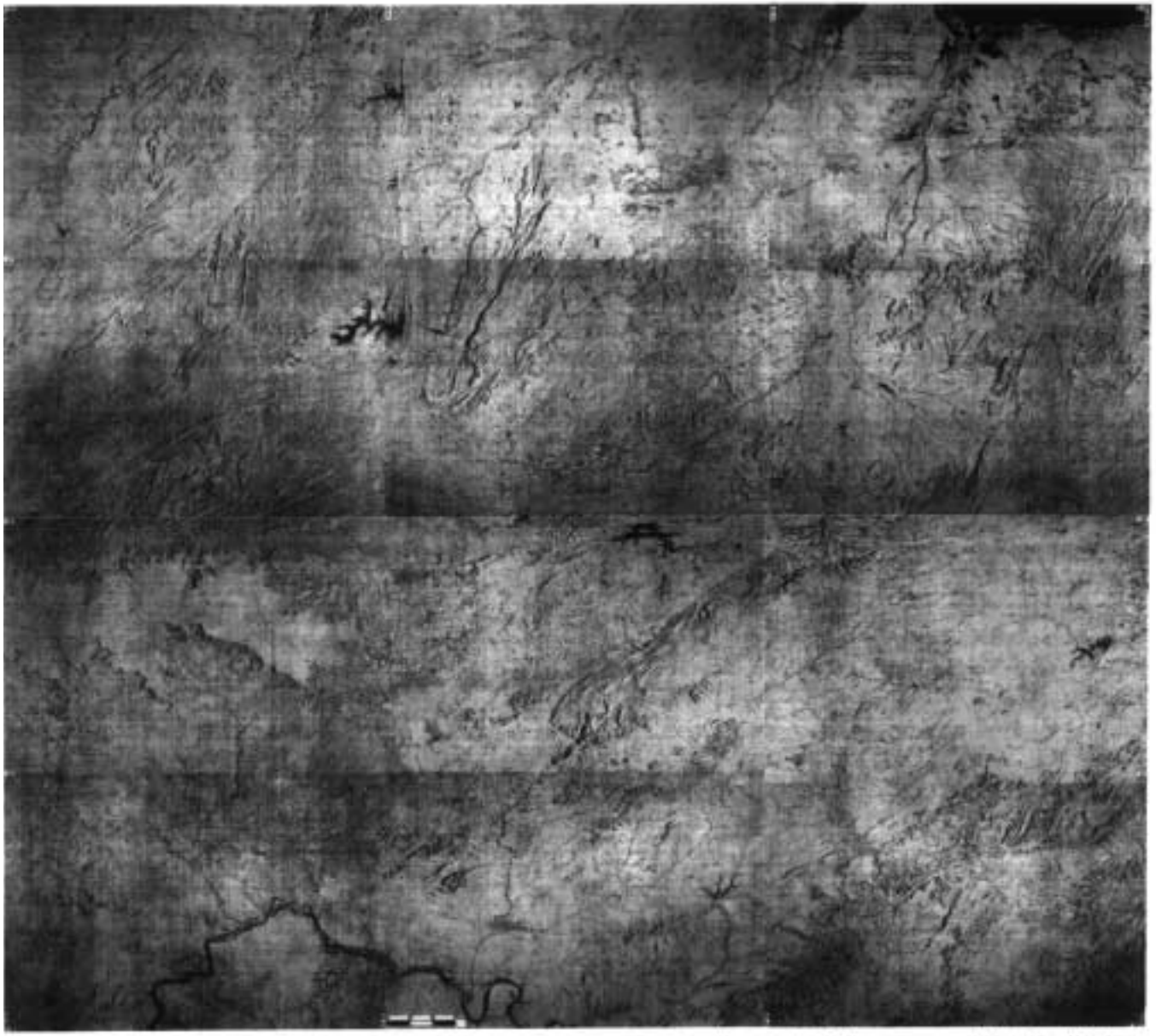

Figure 2.4a Radar imagery showing extension of major structures in N.E. Brazil. Note the E-W trending, crustal-scale lineament systems: the Patos (north) and Pernambuco (south). A system of E-NE-trending strike-slip shear zones are also linked with the main lineaments and these form many subsidiary structures.

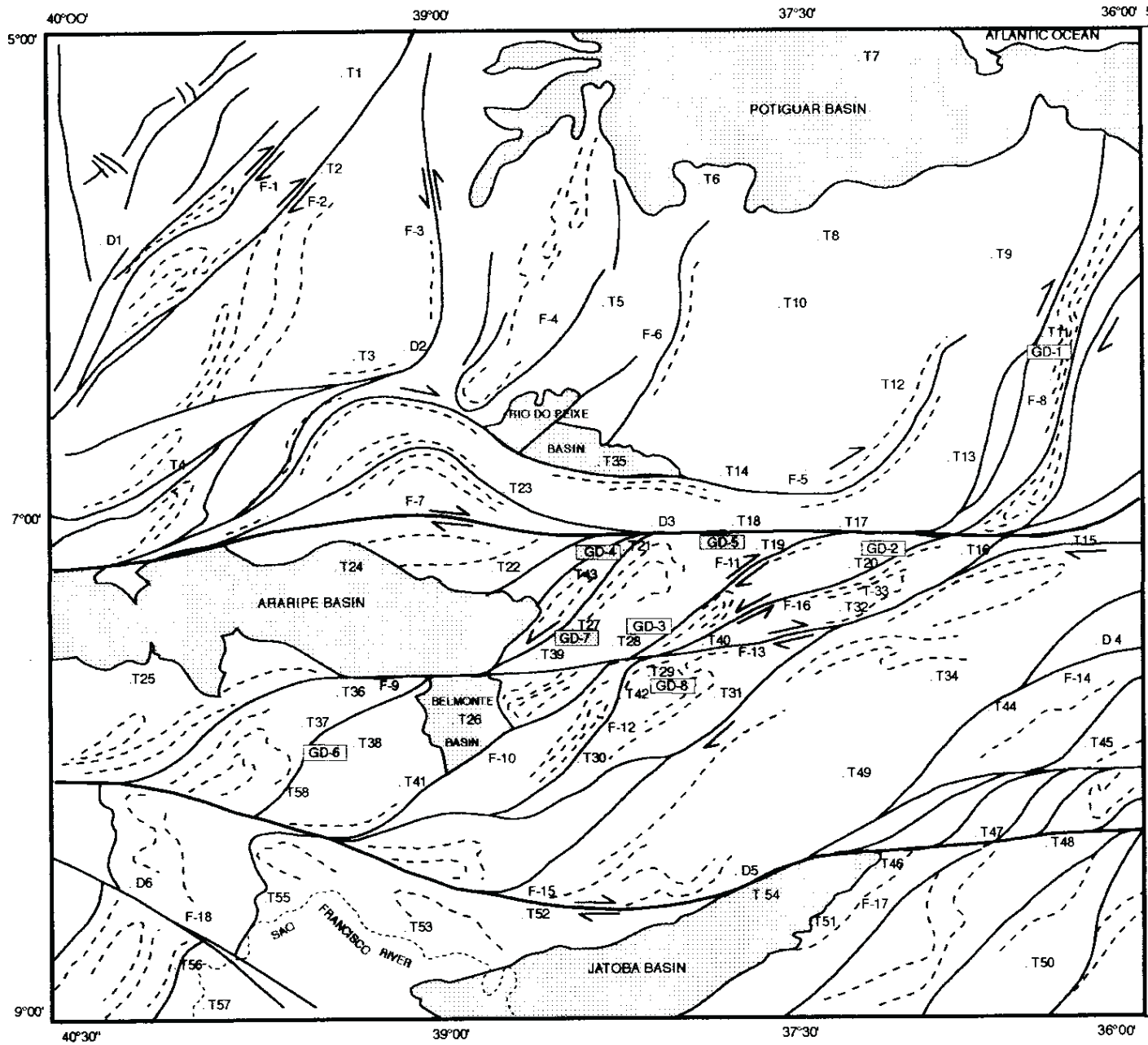

LEGEND

GOLD DEPOSIT

GD-1 S. FRANCISCO MINE	GD-5 ITAJUBATIBA
GD-2 ITAPETIM DISTRICT	GD-6 SERRITA
GD-3 CACHOEIRA DE MINAS	GD-7 IBIARA
GD-4 BOQUEIRAO DOS COCHOS	GD-8 PRINCESA ISABEL

MAJOR FAULT

F-1 SABONETE	F-10 SALG.-CACH. MINAS-PATOS
F-2 SENADOR POMPEU	F-11 JARU
F-3 OROS	F-12 SERRA TALHADA-MANAIRA
F-4 TATAJUBA-JAGUARIBE	F-13 AFOGADOS DA INGAZEIRA
F-5 MALTA	F-14 CONGO
F-6 RIO DO PEIXE	F-15 PERNAMBUCO LINEAMENT
F-7 PATOS LINEAMENT	F-16 ITAPETIM
F-8 SERIDO	F-17 BUIQUE-ARCO VERDE
F-9 CEDRO-BOQUEIRAO COCHOS	F-18 SANTA MARIA BOA VISTA

PHANEROZOIC BASIN

MAJOR FAULT

MINOR FAULT

FOLDING

SHEAR SENSE

GEOGRAPHY LOCALITY

T : TOWN; D: DAM

T1 QUIXERAMOBIM	T30 SERRA TALHADA
T2 SENADOR POMPEU	T31 AFOGADOS INGAZEIRA
T3 IGUATU	T32 SAO JOSE DO EGITO
T4 ANTONINA DO NORTE	T33 ITAPETIM
T5 PAU DE FERRO	T34 SUME
T6 APODI	T35 SOUZA
T7 MOSSORO	T36 CEDRO
T8 AUGUSTO SEVERO	T37 IPUEIRA
T9 SANTANA DO MATO	T38 SERRITA
T10 JUNCO	T39 CONCEICAO
T11 CURRAIS NOVOS	T 40 JARU
T12 CAICO	T41 SALGUEIRO
T13 PARELHAS	T42 MANAIRA
T14 POMBAL	T43 S. JOSE DE CAIANA
T15 SOLEDADE	T44 CONGO
T16 TAPEROA	T45 STA. CRUZ CAPIBARIBE
T17 PATOS	T46 ARCO VERDE
T18 ITAJUBATIBA	T47 PESQUEIRA
T19 CATINGUEIRA	T48 BELO JARDIM
T20 TEIXEIRA	T49 SERTANIA
T21 BOQUEIRAO DOS COCHOS	T50 GARANHUNS
T22 MONTE OREBE	T51 BUIQUE
T23 CAJAZEIRAS	T52 FLORESTA
T24 JUAZEIRO DO NORTE	T53 BELEM DO S. FRANCISCO
T25 IPUBI	T54 IBIMIRIM
T26 S. JOSE DO BELMONTE	T55 OROCO
T27 IBIARA	T56 STA. MARIA DA BOA VISTA
T28 CACHOEIRA DE MINAS	T57 CURACA
T29 PRINCESA ISABEL	T58 PARNAMIRIM

D1 VAZEA DO BOI	D4 BOQUEIRAO
D2 OROS	D5 POCO DA CRUZ
D3 COREMAS	D6 SACO II

Km
0 30

Figure 2.4b Interpretative sketch of Radar imagery (Fig.2.4a). Note the distribution of the gold deposits.

1984; Brito Neves and Cordani, 19991). An Rb-Sr isochron dated the TTG plutonic association at 2.7 Ga (Wanderley, 1990).

b) Fold Belts or Mobile Zones

The supracrustal, metavolcanic-sedimentary sequences are widespread throughout the province. They occur surrounding the massifs/microplates, and represent the most important sites for the economic gold-bearing quartz veins.

The Seridó Fold Belt (see letter e, Fig. 2.3) outcrops as a rectangular area, limited on its western and eastern sides by basement areas (Rio Piranhas and Caldas Brandão massifs). The northern boundary is buried under Phanerozoic sediments (Potiguar Basin). It displays a N-NE to E-W structural trend which extends ≈ 300 km southward towards the Patos Shear Zone. The Seridó Belt consists of Archaean basement, which outcrops as elongate domes of banded granodiorite augen gneiss, amphibolite and garnet-biotite schist (Caicó Complex: Meunier, 1964). This is overlain by supracrustal rocks of the Proterozoic Seridó Group (the Jucurutu, Equador and Seridó Formations) comprised of paragneiss, amphibolite, quartzite, polymict conglomerate, mica schist with calc-silicate lenses, and mafic rocks associated with felsic metavolcanics (Jardim de Sá, 1984). The supracrustal rocks are present in synformal structures associated with sinuous shear zones that converge toward the Patos Lineament in the south.

The Seridó Formation, host rock of the gold mineralization, is a monotonous semi-pelitic and pelitic unit several kilometres in thickness, with some quartzite, calc-silicate and amphiblolite layers. Rhythmic bedding is preserved and is taken to indicate that these rocks were originally deposited as turbidites (Caby *et al.*, 1990).

The N-NE-trending Seridó Belt was subjected to polyphase deformation and its evolution was related to a progressive transition to the Brasiliano-age, E-W-trending, Patos Lineament (Brito Neves, 1975). Satellite imagery shows that the Patos-Santa Luzia area, where this bending occurs, has no transverse structures, thus suggesting a continuity between the E-W-trending Patos Shear Zone and the the N-NE-trending transpressional Seridó Belt (Corsini *et al.*, 1991). This concept is consistent with the views of Moreira *et al.*, (1989) who used the presence of gravity and magnetic anomalies to show that the junction area contains no transverse features. In the southern part of the fold belt the N-NE structural trend was rotated to an E-W direction and now penetrates the Patos regional-scale strike-slip shear zone; this suggests a progressive transition from E-W-trending structures (transcurrent shear) to N- or NE-trending structures (transpressional fold belt). The deformation in both zones was broadly contemporaneous and locally accompanied by crustal melting. The Brasiliano evolution overprints the earlier deformations with successive generations of folds and faults.

Geochemical studies of the 'G-3' (Brasiliano-age) granitoids (see below) provide

constraints on the later geodynamic evolution of the Seridó Belt. They suggest that these diorite and granite suites may have been generated and emplaced during the same geodynamic event along an active continental margin and collision zone (Leterrier *et al.*, 1990).

The Piancó/Alto Brígida Fold Belt (Brito Neves, 1975) is limited by massifs on the northern (Rio Piranhas), southern (Pernambuco-Alagoas) and western (Floresta) sides and by the Late Proterozoic Teixeira batholith to the east (see letter d, Fig. 2.3). This fold belt is composed of a high grade migmatitic-gneiss basement of Archaean age (the Uauá Group: Barbosa *et al.*, 1970) overlain by two sequences. The lower sequence of metavolcanic sedimentary rocks contains gneiss, biotite-muscovite-chlorite and graphitic schist, amphibolite, quartzite, and lenses of marble, and is characterised by bimodal volcanism and amphibolite facies metamorphism (Salgueiro Group; Silva Filho *et al.*, 1985). The upper sequence is composed of metasediments affected by low-grade metamorphism (Cachoeirinha Group: Silva Filho *et al.*, 1985). The Salgueiro schists represent the host rocks of the gold mineralization encountered in this belt.

The Cachoeirinha and Salgueiro Groups are correlated with the Seridó Group (Jardim de Sá and Hackspacher, 1980; Caby *et al.*, 1990) and represent a monotonous flysh-type unit which was subjected to greenschist facies metamorphism. Load structure, slumps, convolute and graded bedding, brittle beds and incomplete Bouma sequences have all been observed, suggesting that these pelitic sediments may represent distal turbidites. Metagreywackes and a bimodal volcanic suite (spilitic metabasalt and felsic volcanics, with calcareous and volcaniclastic deposits) are also associated with these units (Munis and Santos, 1980). The acid to intermediate Salgueiro meta-rhyolites were dated at 1.10 Ga (using U-Pb analyses of zircons), and the rock Rb-Sr isotopes analysed for the same meta-volcanic rocks have yielded an age of 0.95 Ga. These data were interpreted as the age of volcanism and the regional metamorphism respectively, the latter being correlated with the main phase of deformation under the amphibolite facies conditions (Brito Neves *et al.*, 1990).

The Piancó/Alto Brígida Belt has an overall NE-SW trend extending for ≈ 200 km and is located between the two E-W trending, crustal-scale lineament systems or transcurrent faults: Patos in the north and Pernambuco in the south. The shape of this belt is sinuous and shows a succession of NE- and EW-trending segments. The belt is connected with the Seridó Fold Belt in the north and with the Riacho do Pontal Belt in the south (Southern domain; Santos *et al.*, 1984; Santos and Brito Neves, 1984; see Fig. 2.3).

According to Caby *et al.* (1990) the overall NE-SW structural orientation of the belt is a result of the late stages of the tectonic evolution of the region. The Cachoeirinha and Salgueiro Groups could represent different crustal levels of the same orogen. In the northern part of the belt asymmetric folds are associated with a steeply-dipping incipient

slatey cleavage. To the south, a gently dipping foliation suggests deeper crustal levels. However, Silva Filho *et al.* (1985) have mapped the Salgueiro and Cachoeirinha groups as two different units. They considered the Salgueiro Group to be a higher-grade metamorphic (amphibolite facies) equivalent of the Cachoeirinha Group (greenschist facies).

The Pajeú/Paraíba Fold Belt (see b, Fig. 2.3) displays a long axis (≈ 250 km length) which trends NE and is limited on its northern and western sides by a Late Proterozoic granitoid (the Teixeira batholith) and in the south and east by an Archaean massif (the Pernambuco-Alagoas Massif). It comprises an Archaean basement of mafic-ultramafic affinity, with lenses of calc-silicate, amphibolite, and marble intercalations (Caicó Complex: Meunier, 1964). It is overlain by a metavolcanic-sedimentary sequence (Irajaí Complex: Wanderley, 1990) with gold-bearing quartz veins. This sequence consists of paragneiss, orthogneiss, biotite-muscovite-, biotite- or chlorite-schist, amphibolite and rare calc-silicate rocks.

Brito Neves (1975) highlighted the intense magmatism which had occurred at different stages of the evolution of the Pajeú/Paraíba Belt:

(i) stocks of gabbro and diorite, dykes and lenses of ortho-amphibolite and meta ortho-pyroxenite; these mark an early phase of magmatism.

(ii) syn-orogenic granitoids.

(iii) late stocks of syenite and quartz-syenite, dated at 0.54 Ga.

Subduction mechanisms associated with island-arc evolution have been postulated to explain the tectonic environment of the Pajeú/Paraíba Fold Belt. This is supported by the following evidence:

(i) The chemistry of the subalkaline volcanics indicate an island-arc tectonic environment, as do the clastic-chemical metasediments associated with subalkaline volcanic rocks (Wanderley *et al*, 1992).

(ii) A suite of mafic and ultramafic rocks (anorthosites, gabbros) associated with Fe-Ti mineralization described by Beurlen (1988) is interpreted as an ophiolite suite by Caby (1989).

(iii) The Brasiliano intrusive magmatism of shoshonitic affinity within the boundary zone between the Pernambuco-Alagoas Massif and the Pajeú/Paraíba Fold Belt (Sial, 1987; Jardim de Sá *et al.*, 1987; Da Silva Filho and Guimarães,1990) indicates a late-orogenic setting and a deep, partly crustal source.

(iv) Negative Bouguer anomalies combined with geochemical signature of the rocks indicate an island-arc environment for the Toritama region (located on the boundary zone between the Pernambuco-Alagoas Massif and the Pajeú/Paraíba Belt). This could be related to the subduction of oceanic lithosphere (Da Silva Filho and Guimarães, 1990).

(v) A strip of negative Bouguer anomalies striking in a general NE-SW direction and coincident with a major strike-slip fault marks the northern boundary of the Pajeú/Paraíba Belt, (Brito Neves *et al.*, 1982).

The age of the fold belts has been determined on the basis of their different phases of deformation and their structural relationships with dated granitoid rocks (Table 2.1). Orthogneiss and augen gneiss which intrude both the 2.7 Ga Archaean basement (Brito Neves, 1975) and the basal sequence of the supracrustals (Jucurutu Formation) have been dated at 2.0 Ga (Macedo *et al.*, 1984). Thus the supracrustals sequences are interpted as Early Proterozoic in age (Brito Neves, 1983; Jardim de Sá and Hackspacher, 1980).

2.2.2 Tectonism and the Age of the Deformation Events

The concept of a Pre-Brasiliano age for the main metamorphism and polyphase deformation in the Early Proterozoic of Borborema Province has been continuously challenged by several researchers (Jardim de Sá *et al* ., 1981; Caby and Arthaud, 1986; Jardim de Sá, 1987a). However, nowadays, a polyphase deformation is recognised in the province, the evidence for which will be discussed below.

Three major tectonothermal events have been recognised in Borborema Province:

(i) Archaean, or Pre-Trans-Amazonian (2.6 Ga; Brito Neves, 1975).

(ii) Early Proterozoic, related to the Trans-Amazonian Cycle (2.1-1.8 Ga; Brito Neves and Cordani, 1991).

(iii) Late Proterozoic, related to the Brasiliano Cycle (0.9-0.5 Ga; Almeida *et al.*, 1981), during which the province was finally cratonised (Table 2.2).

However, the intensity of the reactivation of Pre-Brasiliano basement rocks is variable, and distinction between poly- and mono-cyclic evolution (Ferreira, 1967) has been intensely debated.

Two main types of tectonism have been characterised in the province:

(i) Low angle, thin-skinned tectonics, resulting typically in a recumbent pattern of folding, which has produced tight to isoclinal folds.

(ii) Transcurrent tectonics, characterised by strike-slip fault zones that have very strong, penetrative foliation and contain folds with axial planes that are subvertical to vertical.

A lack of geochronological data for unravelling the history of the polydeformed terranes in the province makes the age of the deformation a matter of controversy. Determination of the age of various deformations is based upon observation of overprinting of successive phases of folding or faulting, with heavy reliance placed on

Table 2.1 Regional Geological Evolution and Granitoid Emplacement in Borborema Province

Granite Type	Classification and Composition	Event and Deformation Type	Types of Plutonism	Xenolith	Metamorphism	Thermal-Tectonic Event	P-T (kb - °C) Conditions	Age (Ga)	Tectonic Setting	Data Source (s)
'G-4'	Granite to granodiorite Bi > Hb	D_4: Brasiliano granite G-4; late plutonism (leucovein) Crenulation, kinks (F_4) assoc. w/ strong cleavage (S_{13}); sub-vert. shear zones w/ local strike-slip	Stocks and dykes	Supracrustal, porphyritic granite	Retrogressive (M_4): mineral assemblage: albite, epidote, musc., biotite alter. to chlorite, sericite	Brasiliano	2.0-3.5 kb 350 °C	G-4: 0.55-0.51	Active margin and collision zone	Almeida et al., 1981 Jardim de Sá et al., (1981) Galindo, 1984 Almeida et al. 1967 Sial, 1984; Sial and Ferreira, 1988
'G-3'	Granitoids w/ ultra-mylonitic texture w/ porphyrocl. amphib.; Porph. gr.; alk. gr.; gr. to granodiorite Suite w/ sheshonitic affinity	D_3: Emplacement of Brasiliano granite G-3; K-feldsp. orient. by F_2 w/ vertical or sub-vertical axial folded (F_3) plane; remnant porphyroblasts of hornb. and ribbons qz. orientated (F_2). M_3 low P high T (andalusite+cordierite)	Stocks and dykes, irregular diapirs	Basic, ultrabas., supracrustal, granite 'G-2'	Retrogressive (M_4): mineral assemblage: albite, epidote, musc., biotite alter. to chlorite, sericite	Brasiliano	2.0-3.5 kb 350 °C	G-3: first phase: 0.76 - 0.55 second phase: 0.57 - 0.55	Subduction mechanism associated with magmatic arc	Almeida et al., 1981 Jardim de Sá et al., (1981) Letterier et al., (1990) Legrand and Sá, 1986 Guimarães, 1989
'G-2'	Augen-gneiss and orthogneiss, porphyroblastic. Granodiorite to tonalite	D_2: Emplacement of 'G-2'(augen-gneiss- produced by M_2); recumbent fold (F_2) in supracrustal; gneissic foliat. (S_2); biot. fabric paral. to gneissic foliat. (S_2); porphyroblasts of hornb.	Sheets and dykes; Schollen and schlieren structures	Basement amphibolite, gabbro, orthogneiss, supracrustal	Upper amphibolite-granulite (M_3): Mineral assemblage: albite, epidote, biotite, muscovite, opaque minerals, andalusite, garnet, cordierite. Breakdown of mica produce K-feldspar, magnetite, sillimanite and H_2O	Trans-Amazonian	4.5 kb 720°C	G-2: 2.0	Rifting phase	Jardim de Sá et al., (1981) Macedo et al., (1984)
'G-1'	Orthogneiss; Granodiorite, tonalite and diorite	D_1: Biotite fabric (S_1) folded by F_2 Gneissic banding (D_1) overpriated by F_2. G-1 intrusive in the Archaean Basement	Xenoliths in the augen-gneiss 'G-2' or as sheet in amphibolite basement	Amphibolite basement	Granulite facies : (M_2): Feldspathic layers formed by anatexis (M2)	Pre-Trans-Amazonian		G-1: intruded in the basement > 2.7		Brito Neves (1975) Santos and Brito Neves, 1984

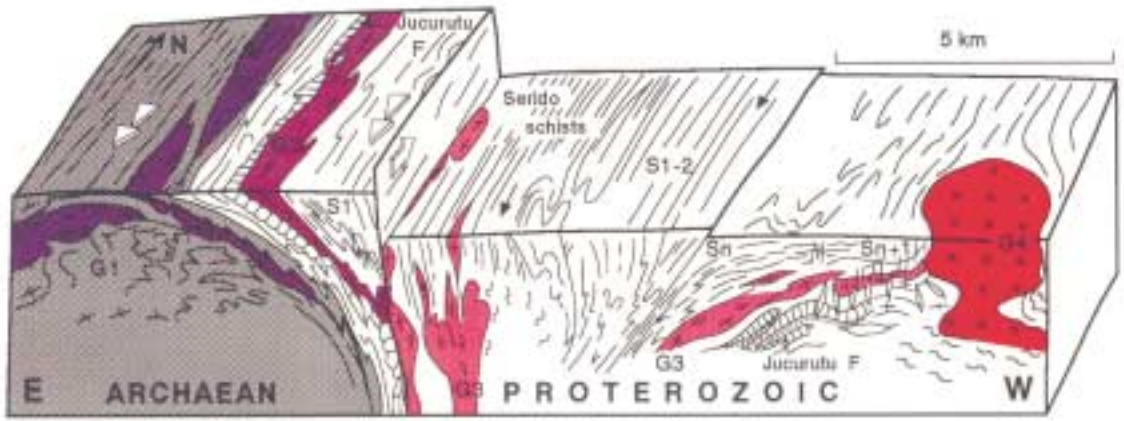

Block diagram showing geometric relationships of the different generations of granites G1 to G4 (Jardim de Sá, et al., 1987). Note the relationships between the horizontal tectonics and strike-slip tectonics in Seridó Fold Belt. (Modified from Caby, 1989).

Granites:

- G-4: Late Tectonic (PLG)
- G-3: Early-to Syn Tectonic (ESTG) & Syn and Late Tectonic (SLTG)
- G-2: Early Tectonic (ETG)
- G-1: Archaean Granitoids

the relationships of deformation to variously dated granitoids.

Deformation related to thin-skinned tectonics was recognised as Trans-Amazonian in age (2.1-1.8 Ga) based on the Rb-Sr rock isochrons from the orthogneisses and augen gneiss ('G-2' type; Jardim de Sá *et al.*, 1981) dated at 2.0 Ga (Macedo *et al.*, 1984) that intruded rocks of the Early Proterozoic Seridó Fold Belt. The age of 2.0 Ga is interpreted to be the time of the earliest deformation related to the Trans-Amazonian event which affected the intrusive granitoids in the supracrustal rocks and transformed them into orthogneiss and augen gneiss. The 2.0 Ga age for the orthogneiss and augen gneiss was also supported by the correlation of the Salgueiro schist (Riacho do Pontal Fold Belt) with the Seridó schist (Seridó Belt). The Salgueiro rocks were deformed by thin-skinned tectonics and occur unconformably overlain by sandstone of the Tombador Formation, dated as Middle Proterozoic (Jardim de Sá and Hackspacher, 1980). Then, using this stratigraphic correlation, a polyphase evolution for the Borborema Province was postulated that comprised a D_2 event related to the Trans-Amazonian Cycle, with subsequent reworking during the Brasiliano Cycle (0.9-0.5 Ga).

Some authors favour a model of monocyclic deformation and do not agree with a Pre-Brasiliano age for the recumbent deformation. They consider that the 'G-2' type granites are anorogenic (Caby, 1989) and therefore that they have intruded the Late Proterozoic belt.

Stable isotopes (oxygen) from the marble of the Jucurutu Formation (the lowest unit of Seridó Group) indicate that its composition is consistent with data from other sediments deposited in the Early Proterozoic (Torquato and McReath, 1983).

Volcanic rocks in the Salgueiro Group of the Piancó/Alto Brígida Fold Belt were extruded at 1.10 Ga and then metamorphosed at 0.95 Ga. The metamorphism is considered to have been associated with the main phase of deformation that produced recumbent folds or metamorphic nappes. The mineral assemblage of the metavolcanic rocks (quartz-plagioclase-garnet-staurolite) indicates initial amphibolite facies metamorphism; the secondary mineral association of chlorite, sericite, biotite and carbonate is consistent with subsequent retrogressive metamorphism (Brito Neves *et al.*, 1990).

In the Serra do Machado, southwest of Jabitacá and near Patos (within the Pajeú/Paraíba Belt) orthogneisses intruded the Irajaí rocks of Early Proterozoic age. Isotope data (Rb-Sr) from the orthogneisses have yielded an age of 1.0 Ga (Scheid and Ferreira, 1991). These granitoids could represent a new phase of Pre-Brasiliano granitoids.

2.2.3 Deformation and Metamorphism

The Borborema Province has a complex polyphase deformation evolution with two regionally significant events which are recognised as the D_2 and D_3 deformation phases (Jardim de Sá *et al.*, 1981; Jardim de Sá, 1987a; see Table 2.2).

An early thermal-tectonic cycle is indicated in the granitic, gneissic and migmatitic terranes (massifs) where an early-developed gneissic banding (D_1) was overprinted by D_2. Deformation D_2 is interpreted to be related to the Trans-Amazonian Cycle (2.1-1.8 Ga), which resulted in emplacement of the early tectonic granitoids ('G-2' type; Jardim de Sá and Sá, 1987) dated at 2.0 Ga (Macedo *et al.*, 1984). Metamorphism occurred during both the regional D_1 and D_2 deformation events. However D_2 metamorphism has penetratively overprinted and reset D_1 effects and consequently, little is known about the D_1 conditions.

The metamorphism (M_2) developed in the granitic gneisses produced a tectonic banding with a penetrative regional foliation (S_2), which shows mineral segregation into quartzo-feldspathic layers, probably formed by anatexis, and mica layering oriented parallel to the original bedding.

On a regional scale this event folded the original fabric (S_1) in tight to isoclinal and recumbent folds (F_2) which produce an axial planar and penetrative foliation S_2 (Jardim de Sá, 1984). A lineation is apparent with mineral orientation, quartz ribbons and boudins elongated along the fold axes. Detailed studies still need to be carried out in order to characterise this regional event.

The third phase of deformation (D_3; Jardim de Sá and Hackspacher, 1980; Jardim de Sá, *et al.*, 1981) produced an axial planar cleavage (S_3) defined by, crenulation cleavage and a penetrative mica schistosity and quartz shape fabric. D_3 deformation locally overprinted the D_1 and D_2 structural elements and resulted in the development of folding (F_3). The metamorphic conditions are consistent with amphibolite facies.

A fourth event (D_4) can be recognised regionally and is characterised by sub-vertical strike-slip shear zones and retrogressive metamorphism (Jardim de Sá *et al.*, 1981; Jardim de Sá, 1987a). The event produced shear zones associated with horizontal WNW/ESE compression, thrusting, and emplacement and uplift of the Brasiliano granites ('G-3' and G-4'; Jardim de Sá *et al.* , 1987). These granites are related to the Brasiliano-Pan African event, dates at 0.76 to 0.55 Ga; Almeida *et al.*, 1967). The metamorphism recrystallised sericite, chorite, albite and epidote. D_4 also resulted in the emplacement of the post tectonic granites, consisting of leucoveins dated at 0.55 Ga (Galindo, 1984), and which represent the end of Brasiliano magmatism.

Table 2.2
Tectonic Metamorphic Events in Borborema Province : Central Domain

Age (Ga) (Bdy. Ages *)	Eon	Era	Event (Bdy. Ages**)	Deformation & Granitoid Emplacement	Metamorphism	Volcanism	Geotectonic Unit	Tectonic Setting	Data Source (s)
0.90-0.57	Proterozoic	Late	Brasiliano (0.9 - 0.5 Ga)	Transcurrent; shear zones with strike-slip and thrust faults. Granit. emplacement: (G3 & G4 types) at 0.76 to 0.51 Ga Diorite and granite suite; K calc-alkaline, calc-alkaline magmatism suggests upper crust; granitic suite (monzon.-syenite.) w/ shoshonitic affinity	Sub-greenschist facies accompanied by retrogressive processes Low pressure and medium temperature	'Jaibaras Volcanism' at 0.53 Ga (***)	Molasse Basins Brasiliano Plutonism: (Syn and Late-tectonic granites-SLTG and Early-Syn-tectonic granites-ESTG)	Active margin and collision zone	Almeida et al ., 1981; Brito Neves and Cordani, 1991; Brito Neves et al., 1990; Galindo, 1984; Jardim de Sá et al., 1981; Jardim de Sá, 1984; Jardim de Sá et al., 1987; Leterrier et al., 1990; Novais et al., 1979; 1979; Santos et al.,1984; Sial 1984; 1986; Sial and Ferreira, 1988
1.6-0.9	Proterozoic	Middle	Pre-Brasiliano (1.4 - 1.0 Ga)	Recumbent folding; Granitoid emplacement at 1.0 Ga (Serra do Machado, Limoeiro, Afieção types)	Medium pressure and high temperature amphibolite facies	'Salgueiro Volcanism' at 1.10 Ga	Fold Belt: Pianco/Alto Brígida (Cachoeirinha Group) Seridó (Seridó Group) Plutonic rocks (Pre-Brasiliano granitoids)	Back arc basin & Lithosphere-activated rifts (?)	Almeida, 1967; Brito Neves et al., 1982; 1990; Brito Neves, 1986; Brito Neves and Cordani, 1991; Caby et al., 1991; Corsine et al., 1991; Ebert, 1970; Gomes,1990; Jardim de Sá,1987a; Sá et al., 1991; Silva Filho et al, 1981; 1985; Santos et al., 1984
2.5-1.6	Proterozoic	Early	Trans-Amazonian (2.1 - 1.8 Ga)	Low-angle thin-skinned compression tectonics Recumbent folding with tight to isoclinal folds Augen gneiss and ortho-gneiss emplacement at 2.0 Ga (G-2 type)	Granulitic to upper amphibolite facies accompanied by anatexis	'Irajaí Volcanism' 'Orós Volcanism' at 1.70 Ga (***)	Fold Belts: Seridó: (Jucurutu Formation); Pianco/Alto Brígida (Salgueiro Group); Paje/Paraíba (Irajaí & Sertania Compl.); Plutonic rocks (Early tectonic granites (ETG)	Subduction mechanism associated with magmatic arc	Almeida, 1967; Beurlen et al., 1991; Brito Neves,1975; Brito Neves et al., 1990; Brito Neves, 1986; Da Silva and Guimarães 1989; Ebert, 1970; Legrand and Sá, 1986; Ferreira, 1967; Gomes, 1990; Jardim de Sá, 1987a; Jardim de Sá et al., 1988; Moreira et al., 1989; Scheid and Ferreira, 1991; Macedo et al., 1984; Santos et al., 1984; Vouchez et al., 1992; Wanderly, 1990
>2.5	Archaean	Late	Pre-Trans-Amazonian (>2.2 Ga)	Archaean granitoids at 2.5 Ga (G-1 type)			Microplate (or Massifs): Rio Piranhas; Caldas Brandão; Pernambuco-Alagoas	Rifing stage	Almeida et al. 1967; Brito Neves,1975; 1975; Brito Neves and Cordani, 1991; Caby et al., 1981; Caby et al., 1990; Ebert, 1970; Ferreira 1968; Hackspacher et al., 1987; Jardim de Sá et al., 1987; Santos and Brito Neves, 1984; Santos at al, 1984

Observations:
* Data source of boundary ages: Geological Time Scale, North America Geology (1983); Geol. Soc. of America
** Data source of boundary ages: Geochronological time-scale for the Precambrian of South America; Brito Neves and Cordani (1991).
*** Used as reference (not observed in the Central Domain; occurs in the North Domain)

2.2.4 Magmatism

Two types of magmatism related with the thermal-tectonic cylcles can be recognised in Borborema Province (Fig. 2.5):

(i) Ultramafic to acid magmatism associated with the Trans-Amazonian event.

(ii) Granitic magmatism associated with the Brasiliano Cycle (Almeida *et al.*, 1981).

However, there has been a continuous debate whether the Proterozoic magmatism is monocyclic or polycyclic in character, based on relationships between the granitic intrusions and the deformation of the country rocks (Jardim de Sá *et al* ., 1981; Caby and Arthaud, 1986; Jardim de Sá, 1987a;). The Brasiliano Cycle, the latest orogenic event, is characterised by strike-slip or transpressive plastic deformation, and widespread emplacement of plutonic intrusions with different magmatic signatures at low pressures and high temperatures (Leterrier *et al.*, 1990).

a) Pre-Brasiliano Magmatism

Pre-Brasiliano-age mafic and ultramafic rocks (Fig. 2.5) occur commonly in the granitic, gneissic and migmatitic terranes (Santos *et al.*, 1984). However, these rock types are not large and usuallly form bodies < 1km in size. Usually the exposures (see Table 2.3) occur near the junctions between the massifs and the fold belts, where the contacts are characterised by thrust faults (e.g. the contact between the NW Pernambuco-Paraíba Massif and Pajeú/Paraíba Fold Belt; Beurlen, 1988; Beurlen *et al.*, 1991; Guimarães, 1989). The magmatism occurs either as a suite of mafic and ultramafic rocks (anorthosite, amphibolite and gabbro, associated with Fe-Ti-V mineralization; e.g. the Limoeiro-Passira occurrence in the Pajeú/Paraíba Fold Belt), or as a sequence of acid, basic and ultrabasic rocks, alternating with clastic and chemical sediments (e.g. lower São Francisco river area; Santos *et al.*, 1984). Mafic and ultramafic intrusions also commonly occur as sills, lenses or sheets hosted by biotite gneiss and tonalite gneiss, and are usually associated with chromite (Bodocó, PE area; Santos *et al.*, 1984).

The mafic to ultramafic magmatism has been dated using conventional rock Rr-Sr techniques on amphibolite associated with anorthosite, gabbro and Fe-Ti-V mineralization from the Limoeiro-Passira occurrence. The data indicate an age of 2.9-2.6 Ga (Dantas and Brito Neves, 1980). However, Trans-Amazonian/Ebournean ages (1.8-1.7 Ga) have also been obtained from the same suite (Brito Neves *et al* ., 1982).

Granitic augen gneiss, orthogneiss, tonalite and granodiorite ('G-2' type; Jardim de Sá and Sá, 1987) related to the Trans-Amazonian Cycle represent the early tectonic granites (ETG) of the Borborema Province. They occur as sheets, locally emplaced

Table 2.3
Main Occurrences of Mafic and Ultramafic Rocks in Borborema Province

Locality (*)	Lithology	Relationship	Data source (s)
Lower São Francisco river	Metavolc.-sediment. sequen.(acid, basic, ultrabasic) assoc. w/ clastic and chemical sediment. cross-cut by late granite and syenite	Border of PE-AL massif contact w/ fold belt (Pajeú / Paraíba) by thrust fault	Silva Filho et al., 1981
Limoeiro-Passira, Pernambuco	Meta-anorthosite, meta-amphibolite, meta-gabbro associated w/ Fe-Ti-V mineralization	Border of PE-AL massif contact w/ fold belt (Pajeú / Paraíba) by thrust fault	Sial and Menor, 1969 Da Silva Filho and Guimarães, 1989
Floresta, Pernambuco	Meta-anorthosite, meta-gabbro, meta-amphibolite, eclogite associated w/ Fe-Ti-V mineralization	Contact PE-AL massif with Pajeú / Paraíba fold belt	Angel and Riera 1959; Dantas, 1971; Beurlen, 1988; Beurlen et al., 1991
Custodia, Pernambuco	Meta-gabbro, meta-norite, meta-diorite, anorthosite associated w/ Fe-Ti mineralization	Contact PE-AL massif with Pajeú / Paraíba fold belt	Santos et al., 1984
45 km N from Bom Jardim Complex, Pernambuco	Meta-gabbro, gabbro w/ garnet, anorthosite, pyroxenite, eclogite associated w/ Fe-Ti mineralization	Lenses in massif (granulite terrane) concord. w/ massif struct. NE-SW	Costa et al., 1979 Beurlen, 1988; Beurlen et al., 1991
Contact: PE-AL massif and Pajeú-Paraíba fold belt	Anorthosite assoc. w/ mafic and ultrmafic (eclogite)	Lenses in massif (granulite terrane) concord. w/ massif struct. NE-SW	Beurlen, 1988; Beurlen et al., 1991
W border of Pajeú/ Paraíba w/ Piancó /Alto Brigída Fold Belts	Meta-gabbro, gabbro w/ garnet, anorthosite, pyroxenite, eclogite assoc. w/ Fe-Ti mineralization	Contact Pajeú / Paraíba w/ Piancó /Alto Brígida fold belt	Angel and Riera, 1959) Beurlen, 1988; Beurlen et al., 1991
Tróia area, Ceará	Ultramafic (anorthosite) with chromite hosted by biotite gneiss and tonalitic gneiss	Pods and sheets in massif terrane (Tróia massif)	Brito Neves, 1975
W-SE Caicó and São Rafael, Rio Grande do Norte	Diorite, gabbro, metabasite, amphibolite	Sheet hosted in gneiss that occur in Piancó / Alto Brígida fold belt	Santos et al., 1984
Bodocó, Pernambuco	Ultramafic w/ chromite hosted by gneiss	Sheet hosted in gneiss	Santos et al., 1984
Tauá, Ceará	Diorite and gabbro	Stock in Rio Piranhas massif	Santos et al., 1984
Serra dos Dois Irmãos-Cavaleiro Complex	Gabbro and meta-gabbro assoc. w/ Fe-Ti mineralization hosted by talc-schist	Sill and intrusions in supracrustal	Caldasso et al., 1973 Sá and Tinoco Sobrinho, 1979
Monte Orebe, Pernambuco	Meta-basalt intercalated with quartzite	Flood basalt in supracrustal	Santos et al., 1984

Observation: (*) for locality see Figures 2.4b and 2.5.; PE-AL massif = Pernambuco-Alagoas massif

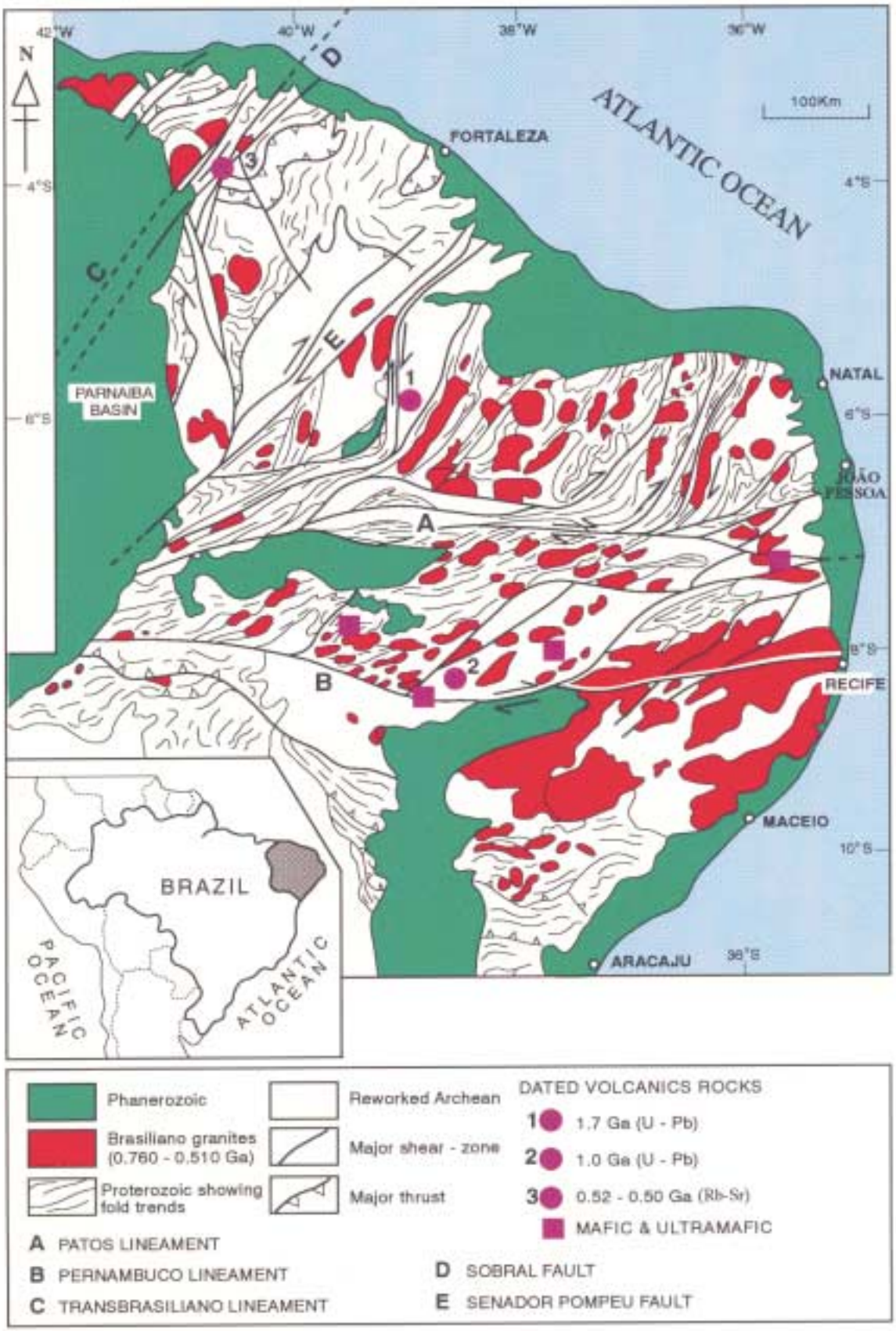

Figure 2.5 Geological map of N.E. Brazil showing the distribution of Archaean and Proterozoic units and highlighting the distribution of Brasiliano age granites, volcanic rocks, and mafic/ultramafic rocks (modified, after Sial, 1987).

along F_2 axial planes, or as complex batholiths along a NW-verging, NE- striking thrust belt.

These rocks intruded the Archaean basement and have been dated at 2.0 Ga (Macedo *et al.*, 1984). Caby *et al.* (1987) interpreted these granitoids as anorogenic intrusions emplaced into the Early Proterozoic sequences.

b) Brasiliano Magmatism

In Borborema Province, intrusive granitoids related to the Brasiliano cycle ('G-3' and 'G-4' types; Jardim de Sá *et al.*, 1987) form batholiths and stocks which are widespread predominantly in the fold belt (Sial, 1986; Sial and Ferreira, 1988; Jardim de Sá *et al.*, 1987; Hackspacher *et al.*, 1987: see Fig. 2.5). (Note: the various types of granite found in the Borborema Province are summarised in Table 2.1).

Two intense phase of plutonism occurred during the Brasiliano Cycle in this area: (i) the earlier phase at 0.76-0.55 Ga with I-type porphyritic granitoids, predominantly (Almeida *et al.*, 1967); (ii) the later phase occurred between 0.66-0.51 Ga and resulted in the intrusion of S-type granitoids (Jardim de Sá *et al.*, 1987; Jardim de Sá *et al* ., 1988). The I-type granites are widespread, while the S-type granites occur predominantly in the Piancó/Alto Brígida (Sial, 1984) and Pajeú/Paraíba fold belts.

The Brasiliano granitoids are usually associated with shear zones, and the following types of granite occur:

(i) Early to syn-tectonic granites (ESTG), streaked out along shear zones (predominantly along the subsidiary shears between the Pernambuco and Patos lineaments). They have been transformed to ultramylonite, with ribbons of recrystallised quartz and feldspar and remnant porphyroclasts of amphibole. These granites intrude sheared Archaean gneisses, and show well developed planar fabric with occasional asymmetrical folding (Fig. 2.6). This type of granite is correlated with the earlier phase of magmatism, dated at 0.76-0.55 Ga (Almeida *et al.*, 1967);

(ii) Syn- and late tectonic granites (SLTG), which represent the dominant type. These granites can occur either as porphyritic or non-porphyritic granitoids intruded through the shear zones. The porphyritic type (Fig. 2.7) is typically coarse-grained and is dominated by porphyroclasts of potassic feldspar in a fine mass of feldspar, quartz and minor amphibole and mica, with a protomylonitic texture, and showing well-developed planar and linear fabric elements. The alkali granite and syenogranite are undeformed and show no significant foliation where they intrude the country rocks outside the shear zones, but have a well-developed foliation and lineation where they have intruded adjacent to, or within, the shear zones (Fig. 2.8). The porphyritic

Figure 2.6 Early to syn-tectonic granite (ESTG), transformed to ultramylonite granitoid showing the extremely fine granulation and well developed planar fabric (along Pernanbuco Lineament).

Figure 2.7 Syn- and late-tectonic granite (SLTG), porphyritic with coarse-grained, dominated by porphyroclasts of K-feldpar (Itapetim District, along the S. José do Egito to Brejinho road).

Figure 2.8. Syn-and late-tectonic granite (SLTG), showing a well developed foliation and lineation, intruded within the shear zone (Itapetim District, along the Desterro to Itapetim road).

Figure 2.9 Late tectonic granite (LTG), consisting of leucocratic pegmatitic veins forming along the sinistral shear, cross-cuts the porphyritic granitoid with dextral shear sense (along the Riacho Verde to Fava de Cheiro road, Itapetim District).

Figure 2.6

Figure 2.7

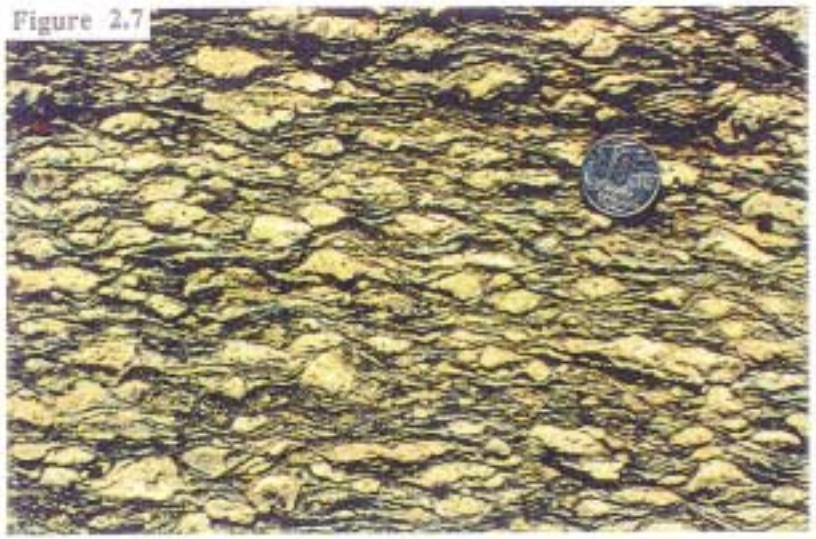

Figure 2.8

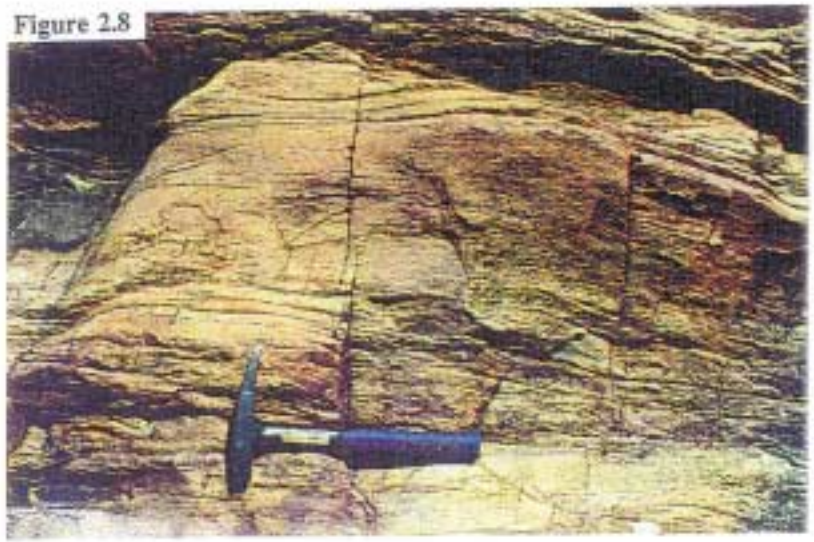

Figure 2.9

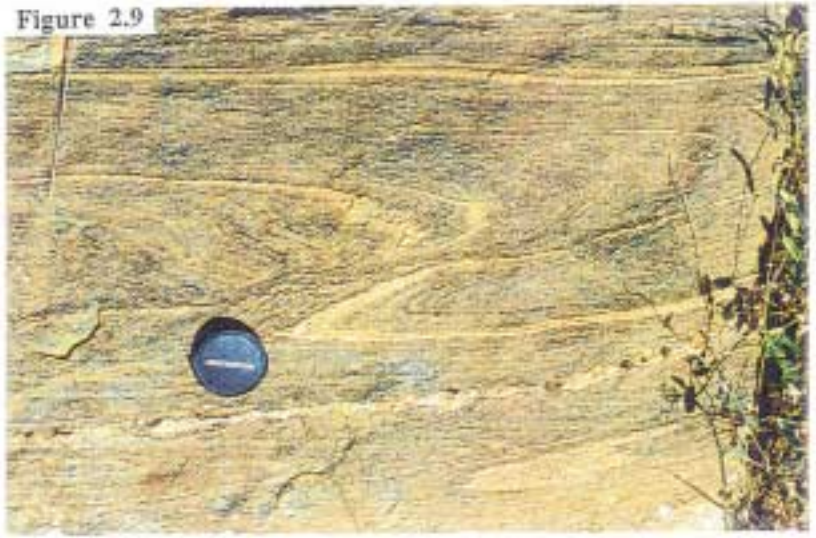

type correlates with the second phase of magmatism dated at 0.57-0.51 Ga (Jardim de Sá *et al.*, 1987; Jardim de Sá *et al.*, 1988). Stabe isotopes ($^{18}O/^{16}O$), rare earth (R.E.), major, and trace elements, and petrological studies (McMurry *et al.*, 1987) place constraints on the protoliths of the syn- to late-tectonic Brasiliano granites. These indicate involvement of the upper mantle in magma genesis by a mixing of calc-alkaline magma with a more mafic, dioritic melt contribution.

(iii) Late-tectonic granites (LTG) cross-cut both basement and the porphyritic granitoids, and occur as leucoveins (Fig. 2.9). They consist of leucocratic aplite, mesocratic aplite, and pegmatite (sometimes with Li, Be, and B mineralization; Santos and Brito Neves, 1984). Their thickness can vary from a few mm to 2 m, and they cross-cut the main deformational fabric at low angles. The mineralogy of these leucoveins is indicative of hydrous melts (presence of tourmaline and amphibole). This type represents the final stage of magmatism and is dated at 0.55-0.51 Ga (Galindo, 1984).

The late-tectonic granites have alkaline/peralkaline compositions and crustal signatures (Sr initial ratios > 0.710; Sial and Ferreira, 1988).

The geochemical signatures (Sr and Nd isotopic data) provide constraints on the emplacement conditions of the G-3 granites. The potassic-subalkaline (shoshonitic and monzonitic) to alkaline (syenite) affinities suggest emplacement associated with an active margin and collision zone. During ascent and emplacement within the continental crust the magma was submitted to a complex evolution process, combining crystal fractionation, wallrock assimilation and mixing with contemporaneous granite magmas (Leterrier *et al.*, 1990; Guimarães, 1989).

c) Volcanism

Three different phases of acid to basic volcanism, with predominantly alkaline/calc-alkaline affinity, have been dated in Borborema Province (Fig. 2. 5):

(i) A metavolcanic-sedimentary, Early Proterozoic sequence (Orós Unit) in the Jaguaribeano Fold Belt (see letter f, Fig. 2.3), located in the northern domain of the province, contains thick sheets of layered orthogneiss in which meta-rhyolites can be identified. The orthogneiss and the meta-rhyolite ('Orós Volcanism') predate regional deformation and metamorphism (marked by almandine and staurolite in metapelite), and have been dated at 1.7 Ga (Sá *et al.*, 1991).

(ii) A metavolcanic-sedimentary, Proterozoic sequence in the Piancó/Alto Brígida Fold Belt (see letter d, Fig. 2.3), extends along a NE-SW axis in the central

domain of the province. This rhyolitic volcanism ('Salgueiro volcanism') has been dated at 1.1 Ga using U-Pb in zircons (Brito Neves *et al.*, 1990).

(iii) Late Proterozoic, metavolcanic-sedimentary sequence in the Médio Cureau Fold Belt, or mainly in the Jaibaras graben (Martinópolis Group; see letter h, Fig. 2.3), located in the N domain of the province, where molasse sediments with interlayered volcanics occur (Coccoci Basin; São Julião, SE Piauí). These metavolcanic rocks consisting of basalts, andesite and rhyolite (low-grade prehnite-pumpelleyite facies), have been dated at 0.53 Ga (Novais *et al.*, 1979).

2.3 PLATE TECTONICS AND THE BORBOREMA PROVINCE

The operation of plate tectonics in the Phanerozoic seems unquestionable and evidence is also growing in quantity and quality for its operation in Proterozoic times (Hoffman, 1988). Examples of the application of plate tectonics in Archaean terranes are rare, but some concrete evidence is now appearing (e.g. Condie, 1982; Helmstaedt *et al.*, 1986; Sawkins, 1990).

The operation of Wilson Cycle tectonics (ocean opening and closing events) during the Early Proterozoic and Archaean times in Borborema Province is still poorly understood. A lack of petrological, geochemical, geophysical and isotopic studies for unravelling the history of these polydeformed terranes, now obscured by metamorphism and tectonic activity, makes the reconstruction of their evolution extremely difficult. The reconstruction of early plate interactions in ancient terranes has to be made on the basis of comparison between older lithological assemblages and those of a later period in which the complete evolution of the Wilson Cycle can be identified.

A definite suture zone has not been observed in Borborema Province (Jardim de Sá, 1984). The distribution of anorthosite associated with Fe-Ti mineralization may be considered to be related to either the Trans-Amazonian age (1.8-1.7 Ga; Brito Neves *et al.*, 1982) or the Archaean age at 2.9-2.6 Ga (Dantas and Brito Neves, 1980). These anorthosite belts might be interpreted as representing the early products of rifting in a supercontinent.

The eclogites that occur at the contact between the Pajeú/Paraíba Fold Belt and the Pernambuco-Alagoas Massif (see Fig. 2.5) in the Central Domain (as noted by Beurlen *et al.*, 1991) might have formed in a subduction zone.

The presence of a Brasiliano granitic suite (monzonite-syenite) with a shoshonitic affinity in the Central Domain (Pernambuco-Alagoas Massif) is considered to be consistent with a magma source from within a metasomatized lithospheric mantle below

a subduction zone. Field observations, combined with geophysical and geochemical data, suggest that this suite represents a late phase of magmatism, which occurred during the period of transition between the collision and post-collision phases of the evolution of an active continental margin, now represented by the Pernambuco-Alagoas Massif (Guimarães, 1989).

This evidence might be interpreted as representing the early products of rifting in a supercontinent. This supercontinent would have comprised the West African and the São Francisco cratons and the massifs, which were later broken up into several micro-plates (Caby, 1989; see Fig. 2.10).

Burke and Dewey (1973) suggested that a cryptic suture existed along the boundary of the West African and São Luiz cratons (northern part of the Borborema Province). The interpretation was based on a collision tectonic model, from observation that along strike from Dahomey (Hoggar Shield in Africa) to Brazil, parts of the postulated suture are characterised by the lack of exposures of eugeosyclinal material and, also the fact that both reactivated and unreactivated crustal material occur in contact with each other. These authors also pointed out the evidence for existence of a completely different earlier tectonic regime (pre 2.5 Ga) and that the transition between these two different regimes is marked by an exceptional suite of rocks, including aulacogens and thick sequences of supracrustal sedimentary and volcanic material (Fig. 2.10).

Porada (1989) recognised the Pan-African-Brasiliano fold belts as a system established within the Proterozoic supercontinent at 1.0-1.1 Ga, with an evolution similar to that of the Mesozoic North Atlantic rift system. The author also postulated a continental bridge across the northern part of the São Francisco (southern part of the Borborema Province) and Congo cratons around 1.1-1.0 Ga. This feature may have extended further to the north between Brazil and Africa, and may have been formed as long ago as 2.0 Ga, on the basis of structural, lithological and radiometric continuity between the two continents (Hurley *et al.*, 1967; Torquato and Cordani, 1981). Such a single land mass, grouping part of the Borborema Province, the São Francisco Craton and West Africa, is also in agreement with existence of a long-lived Proterozoic supercontinent proposed by Piper (1976; 1987) on the basis of paleomagnetic data. Moreover an Early Proterozoic connection is also suggested by the possible continuity of the granulitic rocks of the São Francisco Craton, the Pernambuco-Alagoas Massif and the Chailu Massif of the Congo Craton (Brito Neves *et al* ., 1977).

The polycyclic evolution of the Brasiliano and Pan-African Late Proterozoic fold belts (Gomes, 1990; Corsini *et al.*, 1991) implies that these cyclic events occurred at essentially the same locations. Nance *et al.* (1988) postulated that Proterozoic plate tectonics was related to a regular cyclical process of continuous disaggregation and amalgamation of a Proterozoic supercontinent along the same tectonic zones. Heat is postulated by these authors to be the primary engine of this process, and heat diffusion

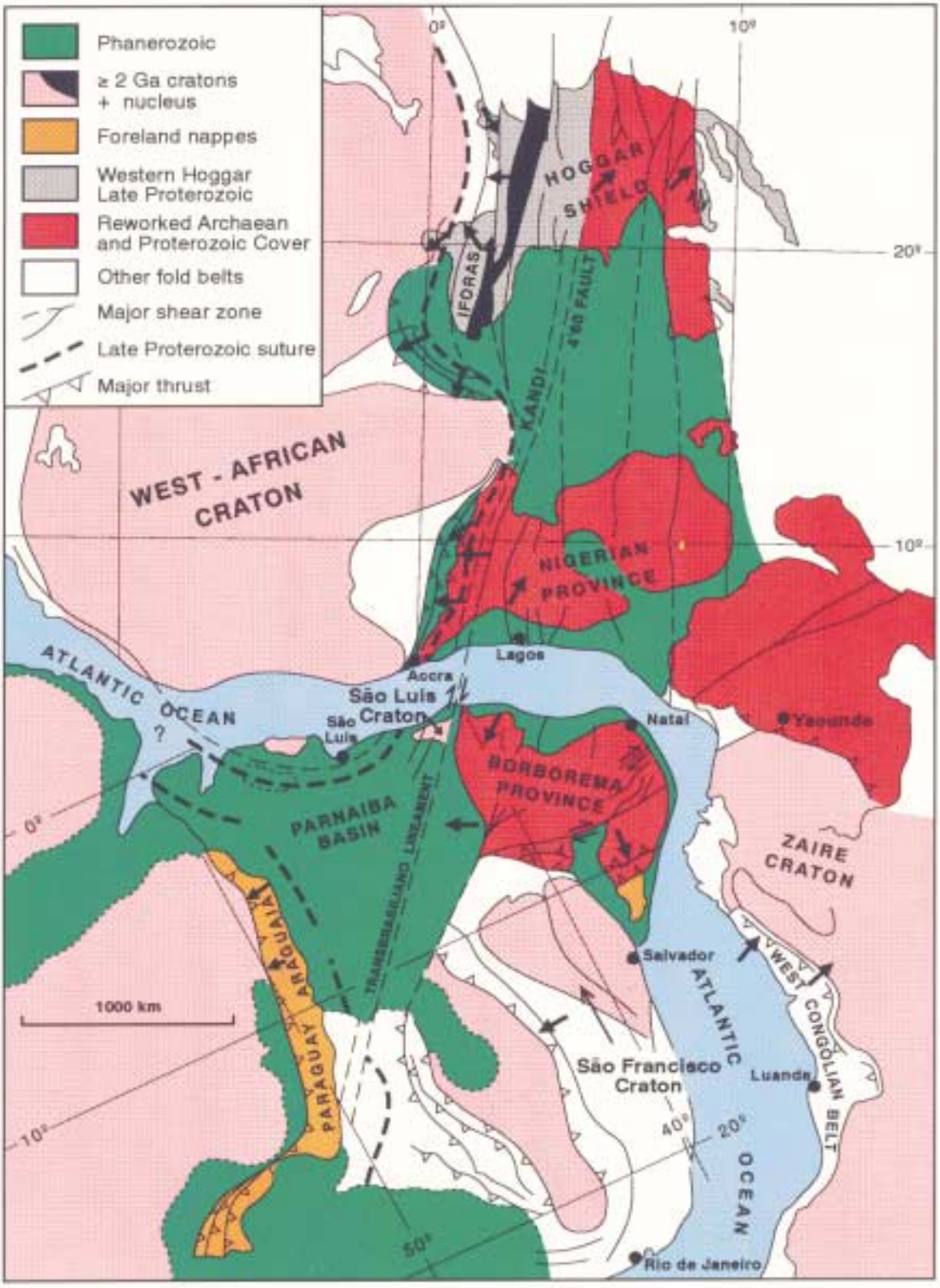

Figure 2.10 Map showing the West African Craton, Hoggar shield and Nigerian Province of the Pan African Belt and the Brasiliano Belt in the Borborema Province using the Pre-Mesozoic drift reconstruction. Arrows indicate movement directions in nappes and along shear zones (Caby, 1989).

through the continental crust as the key for its understanding. Cox (1991) suggested a causal relationship between the upwelling of the mantle plumes, continental break-up and the mechanism which triggers subduction. On the other hand, the attempts at understanding the stratigraphic and tectonic evolution of the terranes that constituted this hypothetical Proterozoic supercontinent have resulted in a considerable debate as to whether the basins that are now incorporated into Proterozoic fold belts were formed in intracratonic or oceanic settings (Windley, 1978).

In Borborema Province it seems that syn-extensional deposition processes occurred in intracratonic basins since the Early Proterozoic. In the different fold belts, multiple extension-based igneous events occur, their ultimate evolution being related to the Brasiliano Cycle (Table 2.2). This might suggest that a rift basin is the likely geotectonic environment for the Early Proterozoic metasedimentary-volcanic sequences.

While the operation of plate tectonics during early times in the Borborema Province is unclear the existence of such processes seems more likely during the Late Proterozoic period (Jardim de Sá, 1984; Porada, 1989; Brito Neves and Cordani,1991).

According to Murphy and Nance (1990) the Late Proterozoic fold belts throughout the world are evidence of crustal accretion and dispersal of a Proterozoic supercontinent. These authors recognised two types of fold belts: (i) the internal orogen related to supercontinental amalgamation with the destruction of the interior oceans; and (ii) the external orogen related to the destruction of wide oceans peripheral to the supercontinent.

Despite a different evolution in each individual orogen, subduction probably started everywhere during the Late Proterozoic. The Pan-African-Brasiliano fold belts represent an internal orogen, whilst the Avalonian-Cadomian belt of North America, western Europe and the Arabian shield is a group of external orogens (Brito Neves and Cordani, 1991).

In this model, at around 0.76-0.55 Ga the internal belts culminated in continent-continent collision which produced calc-alkaline magmatism, crustal thickening and regional thrusting, following by erosion and sedimentation in the cratonic areas (Murphy and Nance, 1990). At the margins of the supercontinent, oblique subduction and closure of the wide oceans generated the peripheral fold belts and produced widespread volcanism and synorogenic volcanoclastic sediments.

The amalgamation of West Gondwana (basically represented by Africa and South America in a pre-drift reconstruction) was part of a much larger Late Proterozoic supercontinent. The geological history of West Gondwana is dominated by the events related to the Pan-African-Brasiliano tectonomagmatic cycle (Brito Neves and Cordani; 1991) which encompasses the entire Late Proterozoic and ceased effectively by Cambro-Ordovician time (Cowie and Basset, 1989). These authors discuss the Late Proterozoic evolution and the amalgamation of the South American continent in the light

of plate tectonics and recognise that although many of the Pan-African-Brasiliano belts are intracratonic, some may have formed from oceanic basins. The marginal orogens evolved from oceanic basins are characterised by pelitic-carbonatic rocks and discrete volcanism. These were thrust by collision onto the margin of the plates (transcurrent tectonics). The intracratonic orogens (internal belt within the continental masses) consist predominantly of clastic and minor sedimentary carbonates and are characterised by bimodal volcanism and calc-alkaline plutonism. They represent flysch-type volcano-sedimentary wedges within smaller blocks which evolved to branching fold belt systems during collision.

Jardim de Sá (1984) suggested that the reconstruction of the Gondwana continent shows a pattern of folding and major lineaments of Brasiliano age (0.9-0.5 Ga) in Borborema Province that can be correlated with the Nigerian Shield lineaments. Caby *et al.* (1981) pointed out using geophysical evidence that these structures can be extrapolated 1500 km under the Phanerozoic sediments to the Hoggar Shield (Fig. 2.10).

The 4°50' E Hoggar lineament divides the Hoggar Shield into two distinct domains: (i) the reworked Archaean and Proterozoic Cover; and (ii) the Western Late Proterozoic (Fig. 2.10). The projection of this lineament to the south as far as the Dahomey region, where it has been identified by geophysical data (Caby *et al.*, 1981), suggests continuity with the Sobral Lineament within the northern Borborema Province. The Hoggar lineament is dextral in nature and located in the east part of the Hoggar Shield; it can be correlated with the NW trend in the Medio Cureaú Fold Belt in the northern part of Borborema Province (Jardim de Sá, 1984).

A complete evolution of the Wilson Cycle has been recognised in the west part of the Hoggar Shield (Caby *et al.*, 1981), with the opening of an oceanic basin at around 0.8 Ga (Eburnean time) followed by continental collision between the West African Craton and the Hoggar Shield during the Later Pan-African Cycle (0.64-0.61 Ga). The end of the cycle was marked by deposition of molasse and late-orogenic plutonism, including mafic, rhyolitic and alkaline dykes swarms, at 0.59 Ga. The Pan-African Event in Borborema Province is marked by intense granitic plutonism, ranging between 0.76 to 0.55 Ga in age (Almeida *et al.*, 1967). Cambro-Ordovician molasse sediments occur in the Medio Cureaú, Jaguaribeano and Sergipano fold belts (Santos *et al.*, 1984; see Fig. 2.3).

CHAPTER 3 GEOLOGY AND STRUCTURE OF THE MINERALIZED AREAS

3.1 INTRODUCTION

Gold-bearing quartz veins occur in all geological environments in the Borborema Province of northeast Brazil: preferentially in fold belts or basement terranes, but also hosted by granitoids which intrude the supracrustal sequences (Fig. 3.1). Some of these deposits are large enough to be economic (for example, the São Francisco and Cachoeira de Minas mines located in the Seridó and Piancó/Alto Brigída fold belts respectively), whilst in other environments, such as basement terranes (e.g. Boqueirão dos Cochos occurrence) or in granitoids (e.g. Santo Aleixo area, Cacimba Salgada, Canafístula and Garapá occurrences, all located in Itapetim District) the deposits are small and non-economic. In the Itapetim District, located in the Pajeú/Paraíba Belt, there are several small occurrences of gold but no workable deposits are known. In this district gold quartz veins hosted by supracrustal rocks form very small prospects which have only been exploited using rudimentary processes (in 'garimpos').

To investigate gold deposition and its mechanism of concentration in the Borborema Province, a selection of different geological environments has been studied. The following gold deposits or occurences were examined: São Francisco and Cachoeira de Minas mines, both related to fold belts; Itapetim District, where gold occurs either hosted by supracrustals (Sertãozinho-Pimenteiras areas) or granitoids (Santo Aleixo area, Cacimba Salgada, Canafístula and Garapá occurrences); and Boqueirão dos Cochos where gold-bearing quartz veins occur hosted by Archaean basement. A review of the local geology and structure of these eight gold deposits/occurrences is presented in this Chapter. A discussion of sealed cracks, highlighting the differences between the crack-seal and crack-healing mechanisms in quartz veins and their relationships with the fluid dynamics, are presented at the end of this Chapter.

This study has employed the techniques of structural analysis in regions of polyphase deformation (Ramsay, 1967). It is based on the recognition that the deformation of the rock can be conveniently divided into a number of discrete events which occur in chronological order. So, the first deformation event (D_1) is associated with structural elements such as folds (F_1), cleavage (S_1) and lineation (L_1). The next phase (D_2) produces F_2, S_2 and L_2, and so on. Bedding and layering are represented by S_0. The strike convention used in this thesis considers all planes as members of a family oriented clockwise from true north.

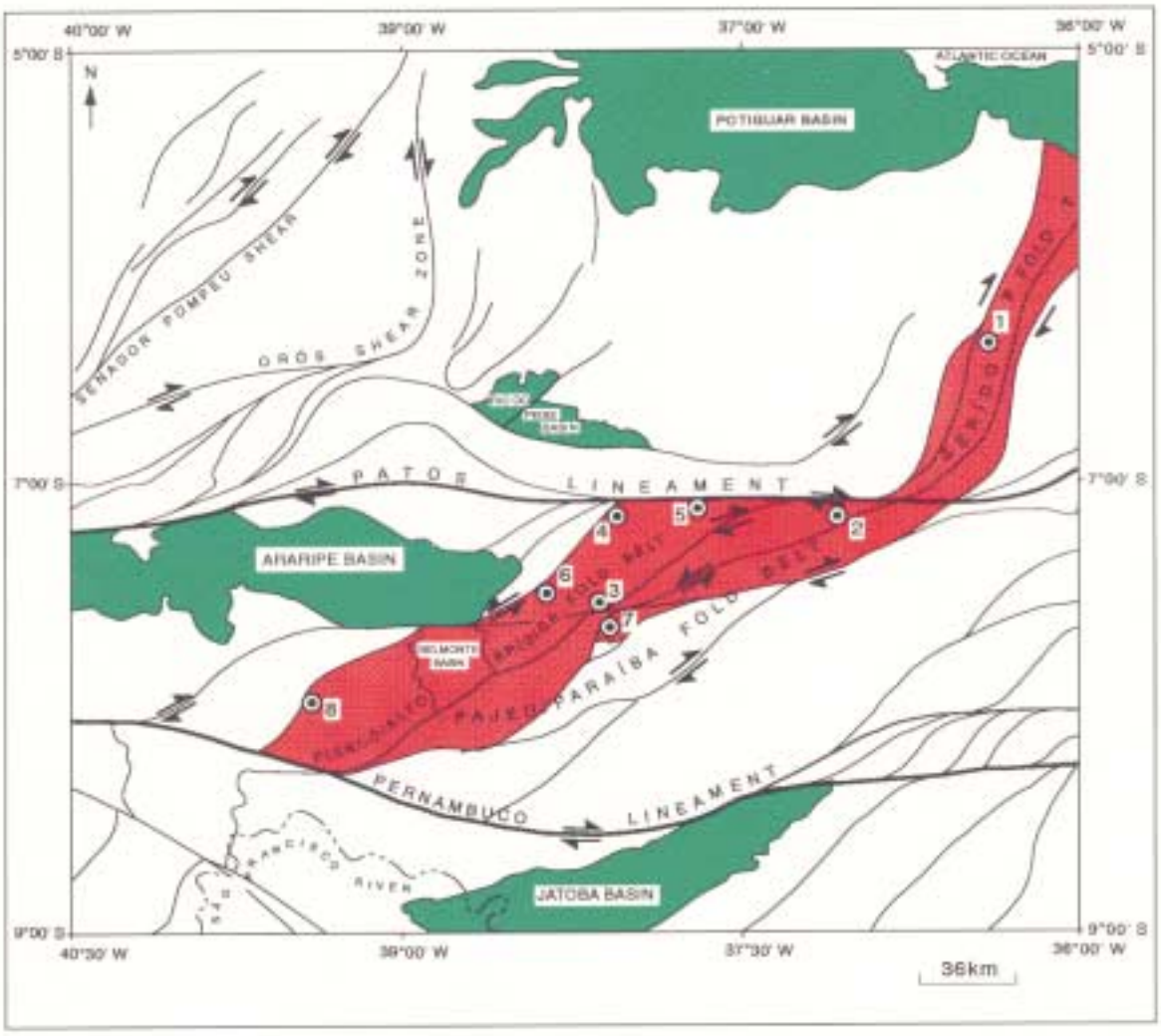

Figure 3.1 Shear zone system and gold mineralization in N.E. Brazil. (Interpretation from radar imagery).

The boundary ages used come from the Geochronological Time-scale for the Precambrian of South America, according to Brito Neves and Cordani (1991), the limits of which are: Late Archaean: > 2.5 Ga; Early Proterozoic: 2.5-1.8 Ga; Middle Proterozoic: 1.8-1.0 Ga; and Late Proterozoic: 0.9 -0.5 Ga.

3.2 SAO FRANCISCO MINE

3.2.1 Introduction

The São Francisco mine is located to the northeast of Currais Novos, in the state of Rio Grande do Norte. The area comprises the highly-deformed Seridó Fold Belt of Early Proterozoic age (Brito Neves, 1983; Leterrier *et al.*, 1990) which consists predominantly of polydeformed schists (Jardim de Sá and Hackspacher, 1980; see Fig. 3.2).

3.2.2 Geology

Located in the Seridó Fold Belt, the São Francisco mine area is comprised of an Archaean basement and a Proterozioc supracrustal sequence intensely intruded by plutons. Gold-bearing quartz veins are hosted by the supracrustal rocks.

The main units in the area are: (i) the high grade Archaean basement known as the Caicó Complex (Meunier, 1964); (ii) the Proterozoic supracrustal sequence represented by the Seridó Group; (iii) granitoid intrusions and pegmatite veins intruded at several stages during the Trans-Amazonian and Brasiliano events; and (iv) the Phanerozoic units (Leterrier *et al* ., 1990; see Fig. 3.2).

The basement consists primarily of granitic to gneissic rocks. The unit outcrops northward from a point 7 km north of São Francisco mine. The complex consists of granodiorite augen gneiss, banded amphibolite and garnet-biotite schist, lithologies which represent high-grade metamorphism of Archaean and Trans-Amazonian (Early Proterozoic) age (Brito Neves, 1975).

The Seridó Group (Santos and Brito Neves, 1984) comprises the Proterozoic metamorphic cover and is subdivided into three units represented in stratigraphic ascending order, by the Jucurutu, Equador and Seridó formations.

The Jucurutu Formation (Ferreira, 1967) occurs at the margins of the Caicó Complex, trending NNE to the northwest of Currais Novos. It is composed predominantly of quartz-feldspathic gneiss and abundant lenses of marble, calc-silicate rocks, quartzite, itabirite and mica schist. The lenses have lengths that vary from 2 to 6

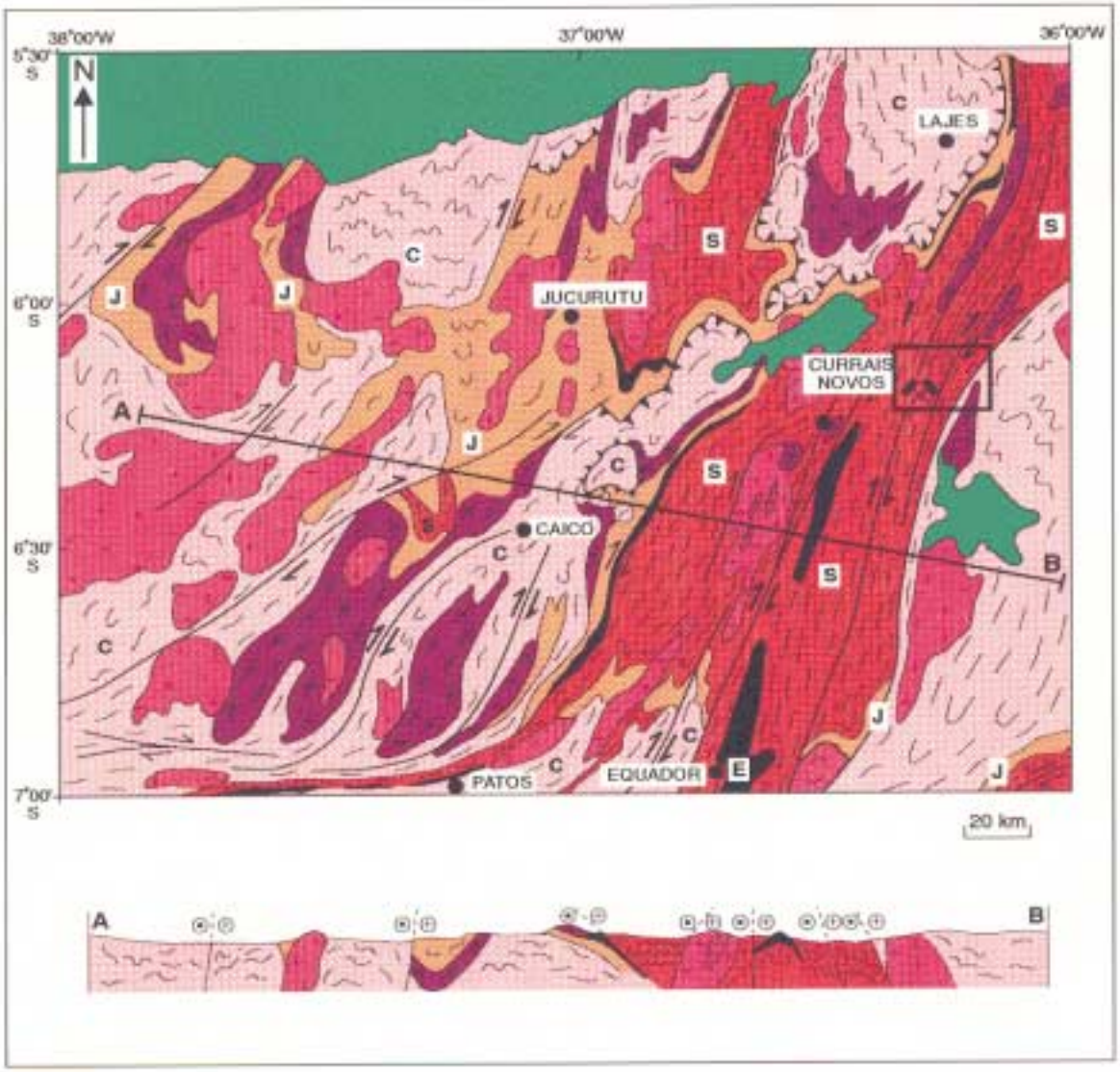

Figure 3.2 Geological framework of the Seridó Fold Belt, N.E. Brazil. Note the location of the São Francisco mine. (After Leterrier *et al.*, 1990)

m. Skarn and calc-silicate rocks contain scheelite (the principal tungsten ore mineral of the region; Maranhão *et al.*, 1986).

The Equador Formation (Jardim de Sá *et al* ., 1987) trends in a NNE-SSW direction and forms deeply-carved mountains around 600 m high. The formation consists essentially of pure quartzite associated with lesser amounts of muscovite-quartzite, muscovite-feldspar-quartzite and biotite-quartzite.

The Seridó Formation is widespread in the central part of the area (see Fig. 3.2) trending N to NE in the northern and NNE-SSW in the southern parts (Jardim de Sá *et al* ., 1987). The uppermost Seridó schists are the host rock for the gold mineralization and outcrop continually along the strike of the shear zones.

Four types of schist occur: garnet-biotite schist; garnet-cordierite-biotite schist; garnet-andalusite schist; and garnet-biotite-quartz-feldspar schist. Usually the schists form bands or layers of a metre to several tens of metres in thickness. They are highly-deformed with a strong preferred mineral orientation parallel to banding which is partly lithological and partly originated from metamorphic processes. The gneissic texture is well-defined by a rhythmic centimetric alternation of mica or quartz-feldspar rich bands. In the lithologies where porphyroblasts of andalusite or cordierite are present (10 cm in diameter; see Figs. 3.3a and 3.3b) the foliation wraps around these crystals and the deflected bands display anastomosing structures. Pure and impure layers of quartzite commonly occur intercalated in the schists.

Calc-silicate rocks do not occur in the mine area, but are important regionally. They usually occur as lenses up to one metre thick and several tens of metres in length, and are oriented parallel to the regional foliation.

Pressure and temperature conditions of metamorphism were estimated at 4.5-5.9 kb and 490-510 °C respectively in the biotite-garnet schist (Legrand and Sá, 1986). Evidence of retrogressive metamorphism occurs in all lithologies (e.g. choritization of biotite and garnet; saussuritisation of plagioclase; muscovitisation of andalusite, and pinnitisation of cordierite; see Chapter 4).

A large volume of plutonic rocks is found intruding both the Archaean basement and the Proterozoic supracrustal sequences. The structural imprint of one of the major deformation phases (F_2 or F_3) recognized in their country rocks dates these intrusions as Early Trans-Amazonian granitoids: G-2 (Jardim de Sá *et al* ., 1981; Macedo *et al* ., 1984) and Late Proterozoic Brasiliano granitoids: G-3 and G-4 (Jardim de Sá *et al.*, 1981). The early intrusions consist of orthogneiss and augen gneiss (the early tectonic granite: ETG) while the Brasiliano granitoids comprise early-syn tectonic (ESTG) and syn and late tectonic granites (SLTG). Late tectonic pegmatites (LTG) dated at 0.55 Ga (Galindo, 1984) are very common in the mine area and these have one phase of deformation. Details of the granitoids are found in Chapter 2 (Table 2.1).

Figure 3.3a Porphyroblast of cordierite rotated and wrapped by the foliation S_2. It displays dextral shear sense. Developed in cordierite-garnet schist of the Seridó Formation (MG-R-228C, São Francisco mine, Morro Pelado thrust fault).

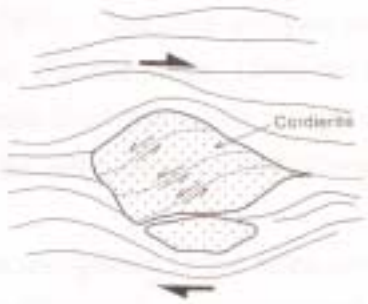

Figure 3.3b Sketch of Fig. 3.3a showing kinematic indicators of dextral shear and the fragmented porfipyroblast of cordierite displaying antithetic slip on the fracture planes in the grain.

Figure 3.4a Refolded earlier fabric developed in polydeformed garnet-biotite-quartz-feldspar schist in Seridó Formation. (the Currais Novos to São Francisco mine road: BR-226).

Figure 3.4b Sketch of Fig. 3.4a displaying the F3 folding. Note S1 paralell to S2 and S1 perpendicular to S3 (metamorphic banding).

Figure 3.5 Inclined conjugate reverse kink bands (F4) developed in deformed mica schist in Seridó Formation. The S3 (schistosity) is refolded during D4. (São Francisco mine).

Figure 3.6 Morro Pelado thrust fault showing the large gold-bearing quartz vein above the shear developed in quartz-muscovite schist. Note the tourmaline wallrock alteration (arrowed) on the top right (São Francisco mine).

3.2.3 Deformation and Metamorphism

The tectonic style of the Seridó area is dominated by mega-structures seen as synforms and antiforms with vertical axial planes (Ebert, 1970). Structural analysis has shown that the Seridó schists have a polyphase evolution (Jardim de Sá, 1984; see Figs. 3.4 and 3.5) linked to the tectonic evolution of the Seridó Fold Belt which was produced by strain transfer from the E-W Patos shear zone to the NNE-trending belt (Corsini *et al.*, 1991).

During this research a polyphase evolution was recognised in the mine area and its surroundings, and the four phases of deformation identified are summarised in Table 3.1.

3.2.4 Shear Zones and the Emplacement of the Gold-Bearing Quartz Veins

São Francisco mine is located on the long right-way-up limb of a large anticlinal structure characterised by a polyphase deformation evolution (Jardim de Sá, 1984). This structure represents an overturned limb of a F_3 fold with an axial plane dipping 50° SE. In the mine area the main structures are N to NE-trending thrust faults with NW vergence. The contact between the Seridó fold belt and basement on the east side is marked by a shear zone. On the west side, the fold belt domain is also limited by a strike-slip zone (Santa Monica shear zone; see Fig. 3.7).

The São Francisco deposit lies approximately 2 km NW of the Santa Monica shear and is located on the Morro Pelado thrust fault. Both structures are parallel to the regional structure and display NNE strikes with steep ESE dips. The whole deformed zone is approximately 4 km wide (Fig. 3.6).

The Morro Pelado thrust (Figs. 3.8a and 3.8b) is up to 50 m wide with reverse sense and dips 50° SE. The shear fabric is well-defined by the shear plane (C) and schistosity plane (S) sometimes forming very small angles. The C and S bands suggest oblique overthrusting to the NW (Figs. 3.9a and 3.9b). The thrust sense can be compared with the dextral movement of the porphyroblasts of cordierite or andalusite in the schists that occur around the mine area which are flattened parallel to the shear plane and dip 50°SE. The Morro Pelado thrust deformed the F_3 structures, suggesting that F_3 was refolded during overthrusting.

Jardim de Sá (1987b) recognised in São Francisco mine area a dextral movement in the plastic-brittle shear zones in combination with transpression and possibly a slightly inclined normal fault component. According to I. Davison (personal commun., 1993) the Morro Pelado thrust appears to be the last deformation feature, refolding the F_3, and

Table 3.1
Deformation and Metamorphism in the São Francisco Mine Area

Event	Description of the Structural Features	Metamorphism
	S0: consists of quartzitic layering, relicts of the sedimentary bedding with a superposed metamorphic layering under high P-T conditions	
D1	S1: consists of mica-rich (dark) and qz. feldsp. (lighter) layers that occur parallel to the original S0 and form N to NE-trending tectonic banding Lithological contact with amphibolite or calc-silicate rocks parallel to this banding (S1) indicates that S1 is parallel to original banding (S0)	
D2	F2: centimetric-scale, penetrative and axial planar foliation Layering S1 is transposed into S2 with S1 features preserved in porphyroblasts of cord. rotated and wrapped by S2 S2: develops tight to isoclinal folds F2	M2: high metamorphic grade: anatexis resulting in migmatization
D3	S3: N to NE-trending folding which formed the main regional structures F3: occurs from cm to metre-scale with the axial plane foliation folded The axial plane cleavage S3 produced by F3 folding dips 40°-60° SE and is well defined by crenulation or by a penetrative foliation shown by mica and quartz fabric orientation D3 produced tight to isoclinal upright folds F3 and also recumbent folds D3 transposed S1+S2 into S3 plane explained by the minerals being constrained to growth within the maximum stretching direction in the S1 plane	M3: amphibolite facies Mineral assemblage: staur., and., sill., gar., and K-felds.
D4	F4: overthrusting producing shear zones and folding of F3. Shear zones dip 50° SE. Shear sense can be compared to the dextral movement of porphyroblas. of cord. or and. in schist that occur flattened parallel to the shear. C and S fabric suggests dextral sense shear F4 form also crenulation, kink bands and isoclinal open folds	M4: sub-greenschist facies Mineral assemblage: Choritization of gar. and biot.; saussuritization of plag.; muscovitization pinnitisation of cord.

Observation:
For further information see List of Abbreviations.

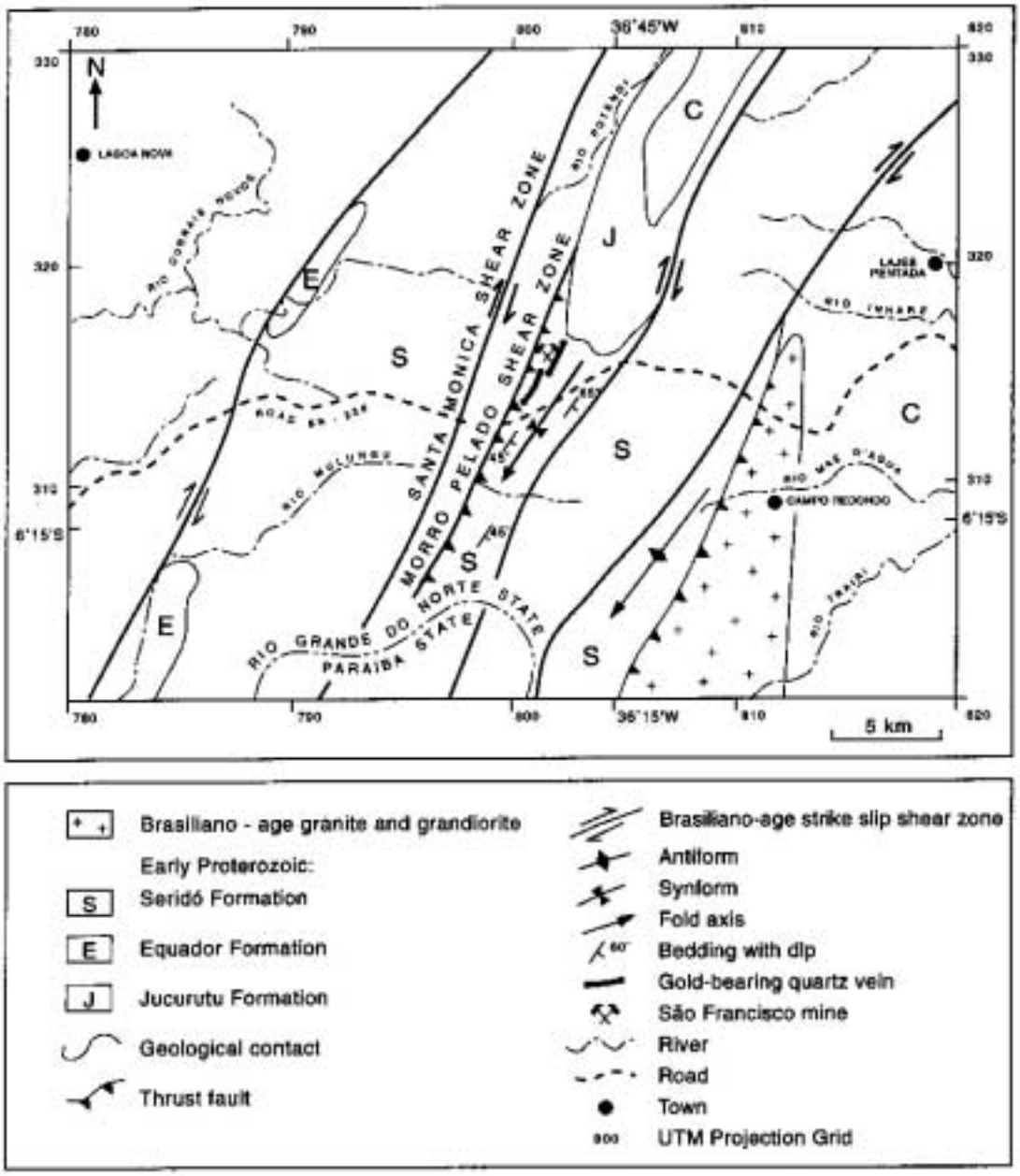

Figure 3.7 Structural framework of the São Francisco mine area. The mine lies on a SE dipping reverse shear zone. Note the location of the gold-bearing quartz veins. (Interpretation from radar imagery; structural information added from fieldwork).

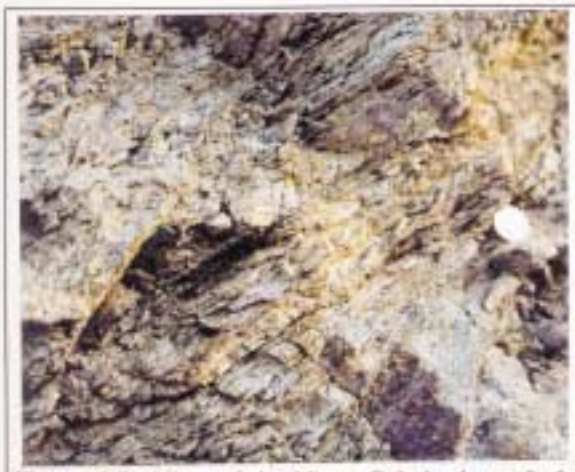

Figure 3.8a View of the Morro Pelado thurst fault developed in strongly foliated quartz-muscovite schist.

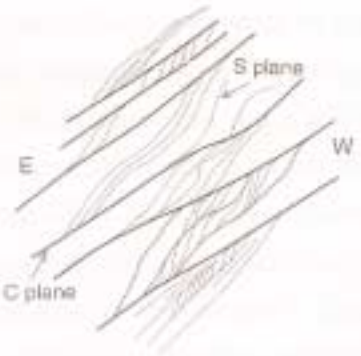

Figure 3.8b Sketch of Fig. 3.8a with details of the C (shear plane) and S (schistosity plane) fabric indicating a shear thrust sense movement to the west in the Morro Pelado shear zone.

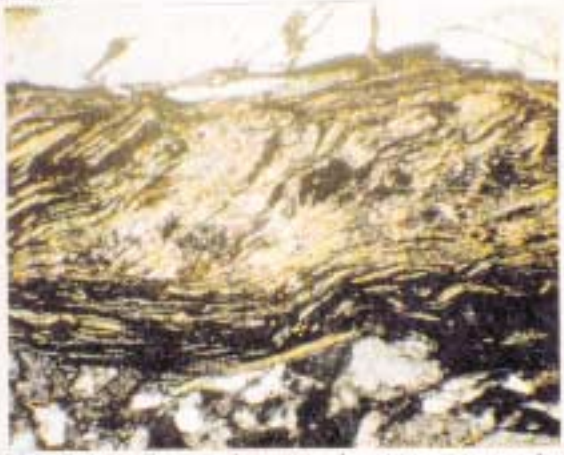

Figure 3.9a Contact between the quartz-muscovite schist and the auriferous quartz vein (on the top) in the Morro Pelado thrust where evidence of C and S fabric can be seen (XPL.; TL; WOF = 2500 μm; MG-R-225C, Morro Pelado, São Francisco mine).

Figure 3.9b Sketch of Fig. 3.9a illustrating the sigmoidal geometry of the C (plane of shear) and S (plane of schistosity) fabric developed during the thrusting towards the west.

Figure 3.10 Layering in gold-bearing quartz vein showing ribbon texture and matrix (grains < 0.5 mm) produced by syn-tectonic crystal-plastic processes. This shows the pervasive recovery, with extensive annealing and less than 10% of megacrysts forming an ultramylonitic to blastomylonitic texture (XPL; TL; WOF = 2500 μm; MG-R-225B, Morro Pelado, São Fracisco mine).

Figure 3.11 Laminae of wall rock parallel to the vein walls, where quartz grains appear massive and tabular with equigranular texture of random orientation indicating open-space filling. This texture implies high dilatation rates for large individual increments of deformation within the lode. Note the different optical orientation of the grains. (XPL; TL WOF = 2500 μm; MG-R-225C; Morro Pelado, São Francisco mine).

it may be intersected by Santa Monica strike-slip at depth.

In the São Francisco mine area (Morro Pelado thrust fault) two types of mineralized veins are distinguished according to the structural relationships: (i) large quartz veins (Fig. 3.6) with a thickness of 30-40 cm, situated 200 m above the shear and extending along strike for 140 m. These veins are slightly discordant to the regional foliation S_3 and occcur parallel to the thrust; and (ii) smaller veins of ≈ 0.5 cm thickness that intruded along C planes in the thrust, and were emplaced during the shearing (F_4).

The veins show ribbon texture and a matrix produced by syn-tectonic crystal-plastic processes. Some of the quartz crystals display pervasive recovery with annealing, while others still retain a mylonitic to ultramylonitic texture (Fig. 3.10). The veins are sub- parallel to the wallrock and the grains form equigranular random orientations, indicating open-space filling, but usually highly fractured (Fig. 3. 11). The fractures were formed during late D_3 and early-syn D_4 deformation, which is consistent with the refolding of F_3 by overthrusting (F_4) in the Morro Pelado area. It suggests that the emplacement of the gold-bearing quartz veins in São Francisco mine was pre-syn-shearing.

3.3 CACHOEIRA DE MINAS MINE

3.3.1 Introduction

The Cachoeira de Minas mine (Fig. 3.12) is located at 7°36'S and 38°03' W, NW of the Princesa Isabel area, in the southeastern part of Paraíba State. The area comprises complex polydeformed terranes of the Piancó/Alto Brigída Fold Belt of Early to Middle Proterozoic age (Brito Neves, 1975).

3.3.2 Geology

The geology of the the Cachoeira de Minas mine area comprises Archaean basement and Proterozoic supracrustal sequences, both intruded by plutonic rocks (Serra Talhada, Folha SB.24-Z-C; CPRM in press).

A N to NE trending structural pattern, defined by the Jaru shear zone, is the main structure in the area (Fig. 3.14). It is characterised by polyphase folding, longitudinal stretching and strike-slip faulting, consistently parallel to the regional trend. Gold-bearing quartz veins hosted by the supracrustal rocks occur towards the southern end of the Jaru shear.

Figure 3.12 View of the Cachoeira de Minas mine. Gold is recovered by cyanide heap leaching .

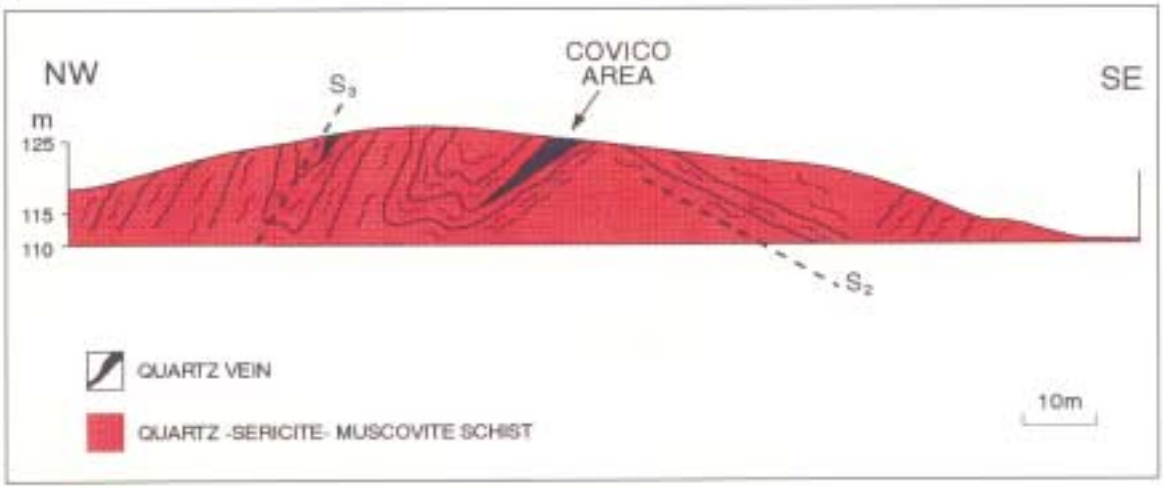

Figure 3.13 Cross section of the Cachoeira de Minas deposit (Covico area) showing the relationships between the folding in the Salgueiro schist and the gold-bearing quartz vein. (Cross section derived from field studies).

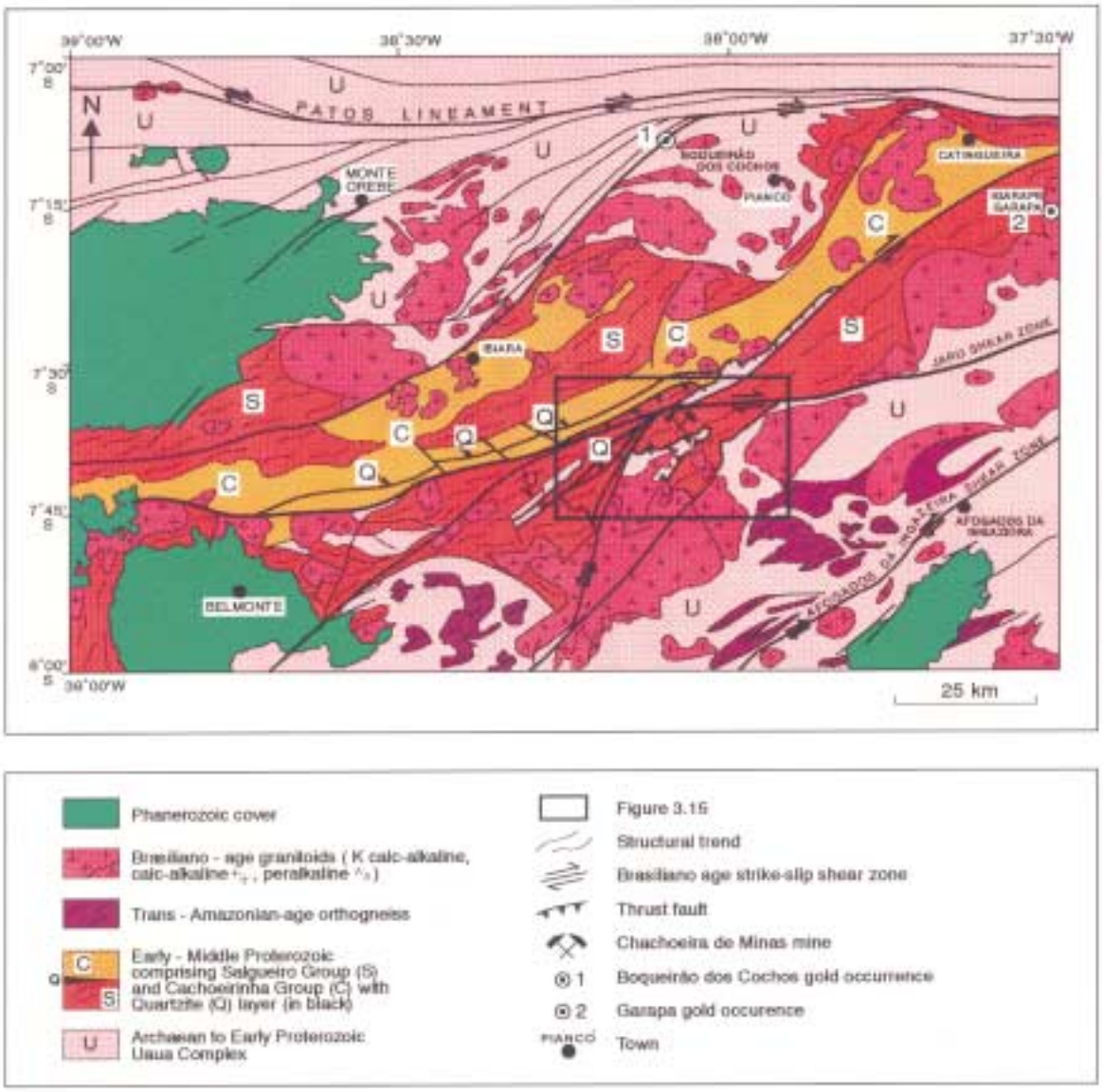

Figure 3.14 Geological framework of the Piancó/Alto Brígida Fold Belt, N.E. Brazil, showing the location of Cachoeira de Minas mine, Boqueirao dos Cochos and Igarape Garapa. (Modified from Serra Talhada, Folha SB. 24 - Z - C, CPRM; in press).

The main units in the area of the mine are: (i) the Archaean basement, composed of a migmatitic-gneiss complex (Uauá Group; Barbosa *et al.*, 1970); (ii) Proterozoic supracrustal sequences represented by the Salgueiro and Cachoeirinha groups (Silva Filho *et al.*, 1985); and (iii) granitoid intrusions and syenitic dykes intruded at several stages during Trans-Amazonian and Brasiliano times (Sial and Ferreira, 1988; Fig.3.14).

The basement consists of orthogneisses with protomylonitic textures. The unit is found in the NNE of the area and outcrops 3 km southeast of the Cachoeira de Minas mine. A NNE striking thrust fault on the southeast side of the complex forms the contact between the fold belt and the basement. Usually the unit exhibits a main foliation (S_2) oriented N 40°-60° E and dips to the SE.

The Salgueiro Group (Silva Filho *et al.*, 1985) is the predominant lithology in the mine area (Fig. 3.13) and occurs both sides (SE and NW) of the N-NE Jaru shear zone. The unit extends in a NNE direction (regional trend) and has faulted contact relationships with the basement in the SE, and in the NW it is overlain by the Cachoeirinha supracrustal rocks. It represents the lowermost supracrustal sequence (see Fig.3.14).

The Salgueiro Group is subdivided into five units (Silva Filho *et al.*, 1985) represented in ascending stratigraphic order by the following units: (i) the basal muscovite quartzite; (ii) sericite-mica schist with graphitic and marble layers, associated with acid and basic volcanic rocks; (iii) metavolcanic acid to intermediate sequence; (iv) meta-sandstone associated with basic metavolcanic rocks; and (v) quartz-muscovite schist associated with basic volcanic rocks.

In the local geological context of the mine area only three units occur. The quartz-muscovite schist associated with the basic rocks (unit v) is widespread toward the NW of the Jaru shear zone while the basal quartzite (unit i) occurs predominantly at the contact between the basement and the Salgueiro schists to the SW. The sericite-mica schist (unit ii) is widespread to the SW of the Jaru shear zone and extends toward the contact with the basement; it represents the predominant lithology in the mine area.

Five types of schist occur in the mine area (unit ii): biotite-sericite schist; biotite-muscovite-sericite schist; chlorite-sericite schist; muscovite-chlorite-garnet schist; and muscovite-quartz schist with graphitic lenses. These rocks consist predominantly of quartz, sericite and muscovite and minor chlorite, biotite, opaques, and plagioclase; accessories include garnet, epidote and carbonate. The schists are highly deformed with a strong preferred mineral orientation parallel to the banding. The texture (S_1) is well-defined by a rhythmic alternation of mica or quartz-rich bands, with predominance of the first. The banding may be either lithological or have originated by metamorphic processes which usually have produced a well-defined foliation in the region. Occasionally the mica crystals are folded and develop kink bands indicative of

refolding.

The sericite-muscovite-quartz schist is the main host of the gold mineralized veins (Fig. 3.13) and it is well-exposed in the Covico mine area. Lenses of graphite schist of 5 m thickness are intercalated parallel to the main foliation and are commonly associated with the main host rock. Prismatic crystals of graphite parallel to the main foliation S_2 or reoriented and refolded by the foliation S_3 can be seen in the graphite schist. Lenses of marble (30 m thickness) and amphibolite (around 1 m) intercalated in the muscovite-quartz schist also occur oriented parallel to regional foliation.

The Cachoeirinha Group (Silva Filho *et al.*, 1985) overlies the Salgueiro schist and is widespread in the area north of the Jaru shear zone (Fig.3.14). Stratigraphically this unit represents the uppermost supracrustal rocks, and is dominated by metapsammite (metagraywacke and metasandstone) and phyllonite, with rare acid metavolcanics and conglomerate. The phyllonite consists of sericite, quartz, chlorite, opaques, plagioclase, and biotite and tourmaline as accessories. Evidence of the original banding occurs in the rhythmic alternation of light and dark layers. The metaconglomerate is usually overlain by the phyllonite and occurs as lenses of 10 to 50 m thickness.

Plutonic rocks (see Chapter 2) are found intruding both the Archaean basement and Proterozoic supracrustal sequences in the mine area. The early tectonic granites (ETG, Trans-Amazonian age granites) consist of orthogneiss and augen gneiss and only intrude the basement complex. Later Brasiliano-age granitoids which are syn- and late-tectonic (ESTG and SLTG) are followed by syenite dykes (late tectonic; LTG).

3.3.3. Deformation and Metamorphism

The Cachoeira de Minas mine area is dominated by folds and faults that show reverse displacement (Pires *et al.*, 1984). Folding occurs from centimetre to kilometre scales throughout the region, but in the mine area microfolding is predominant. In the mine area the foliation is parallel to S_2 and dips towards the SE (Fig. 3.13).

Four phases of deformation were recognised in the mine area and its surroundings, during this study. The four deformation phases are summmarised in Table 3.2.

3.3.4 Shear Zones and the Emplacement of the Gold-Bearing Quartz Veins

The Cachoeira de Minas area is bounded by the N-NE Jaru dextral transcurrent fault on its north side. The Jaru shear zone forms intense mylonitic zones and puts in contact the Salgueiro and Cachoeirinha formations with different metamorphic grade. On the

Table 3.2
Deformation and Metamorphism in the Cachoeira de Minas Mine Area

Event	Description of Structural Features	Metamorphism
D1	S0 is marked by extensive layers of limestone and quartzite showing original bedding transformed into metamorphic layering S1: NE-SW-trending foliation in migmatite gneisses defined by qz.-feldsp.-rich and mica-rich layers parallel to S0. S1: gneissic banding evident by mica orientation (biot.+musc.) and deformed qz. in Salgueiro schist in the SW of the area S1: oriented N40°-60°E and dips 60° SE	
D2	S2: penetrative foliation forms isoclinal folds (F2) with reverse limbs in the SW of the area in the contact basement/ Salgueiro F2: tight to isoclinal folds containing stretched minerals along S2 S2 foliation in quartzite oriented musc. layers (S1) and forming crenulated fabric (S2) S2 foliation in Salgueiro schist cross-cuts S1 and forms angle 30° to S1. S2 foliation in marble with light/dark layers rhythmic alternation forming isoclinal folds (F2) w/ axial planes dipping 60° SE	M2: granulite/upper amphibolite facies Mineral assemblage: sill., gar., biot., qz., K-felds.
D3	S3 folded the main foliation S2 and produced asymetric folding (F3) with penetrative axial-planar foliation S3 Along S3 plane gar. and plag. altered to epid., ch. and ser.	M3: amphibolite facies Mineral assemblage: horn., epid., clinoz., gar., K-feldsp., ky., biot., musc..
D4	D4: refolded F3 producing NE-SW strike-slip, reverse fault, open folds with vertical to subvertical axial planes, crenulation and kink bands. Streched feldspar and ribbon quartz parallel to regional shear. Lineation formed by recrystallisation of musc. and ser. along S4 planes. S3 in the basement gneisses is folded and developed a slight foliation in the axial plane S3 perpendicular to S2 highlighted by recrystallised qz., ser., epid.	M4: sub- greenschist facies Mineral asssemblage: Chloritization of biot., saussuritization of plag., muscovitization

Observation:
For further information see List of Abbreviations

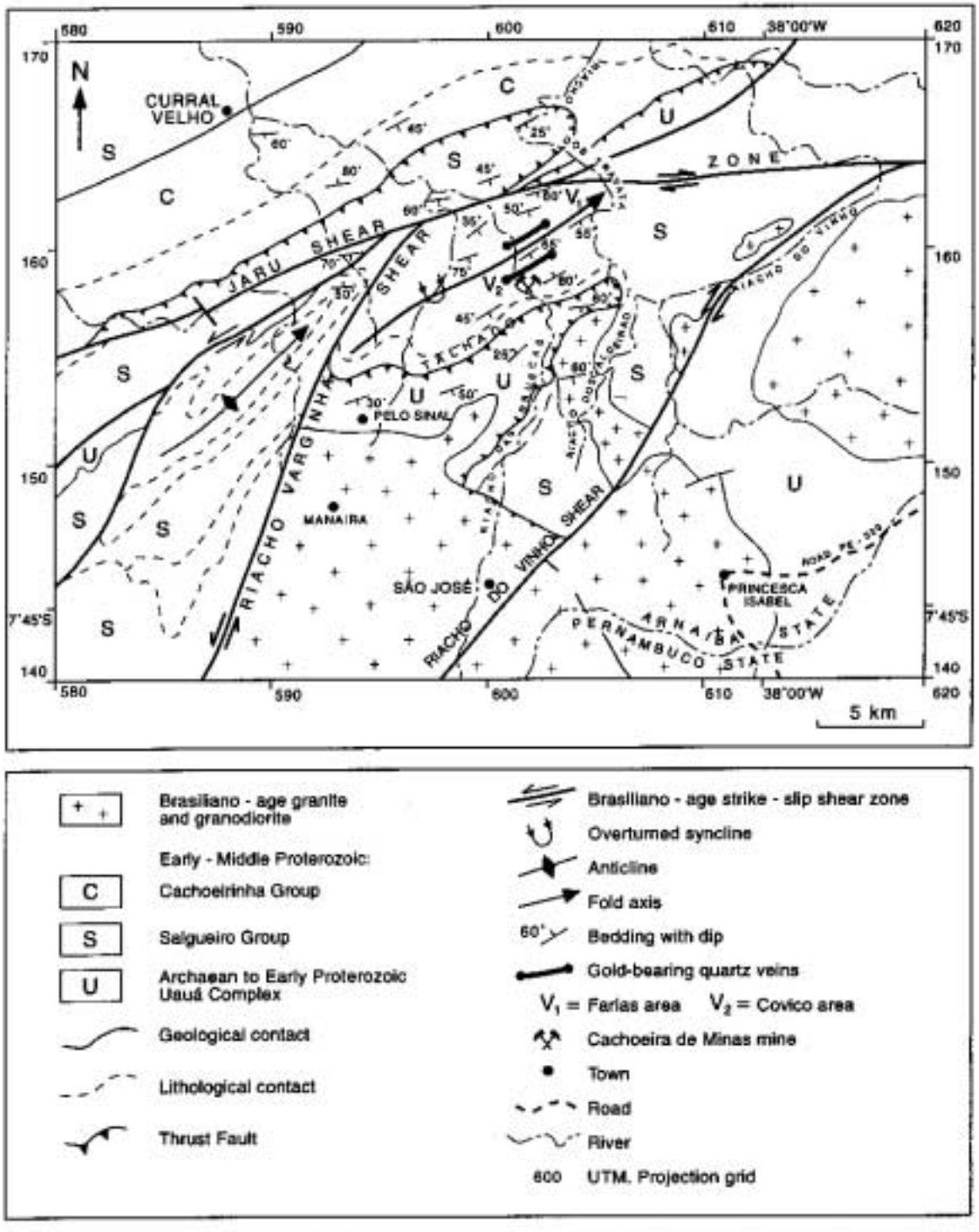

Figure 3.15 Structure framework of the Cachoeira de Minas mine area. The mine lies on a shear zone. Note the location of the gold-bearing quartz veins. (Based on Serra Talhada, Folha SB. 24-Z-C, CPRM; in press. Structural information in the mine area added from this study).

southern side of the Jaru shear, two NE-SW-trending sinistral strike-slip shear zones occur. These shears are 16 km apart in the eastern (Varginha shear) and in the western (Riacho do Vinho) sides and both connect with the Jaru shear (see Fig. 3.15) .

On the southern side of the Jaru shear, in the area limited by the Riacho Varginha and Riacho do Vinho shears (see Fig. 3.15), a ENE-trending thrust fault (Talhado thrust fault) forms the contact between the fold belt (Salgueiro rocks) and the gneissic basement. The Talhado fault is sub-parallel to the Jaru shear and displays an important vertical component since the gneissic basement is juxtaposed against schists along a vertical contact with intense mylonitisation.

The mine area is characterised by a NE-SW-trending overturned syncline that plunges to to the NE, where the mineralized quartz veins occur (the Covico/Farias area). The mine area is marked by small faults oriented parallel to the regional NW-SE structure, and dipping 70-80° SE (Fig. 3.13). The F_2 foliation was folded producing F_3 with axial planes dipping 15° to 30° NW to SE (Figs. 3.16a and 3.16b). The quartz boudins are stretched and oriented NE-SW, the same direction as the regional shear. Sigmoidal boudinaged quartz veins folded by F_4 (Figs. 3.17a and 3.17b) and extensional fractures filled by sigmoidal quartz veins, are common in the mine area.

The polycrystalline annealed texture of the quartz ribbons and the arrangement of the mineral fabric, showing porphyroclasts of K-feldspar with tails wrapped around by biotite altered to chlorite (Fig. 3.18), suggest a regime of plastic deformation.

The Cachoeira de Minas mine lies on the overturned limb of a NE-SW-trending syncline, with an axial plane dipping 60°SE. The mineralization zone is defined by the presence of deformed regional foliation (S_3) within which the quartz veins (at least two parellel systems: Covico and Farias) are found.

The gold-bearing quartz vein in the mine area (Covico area) is about 60 cm thick (Figs. 3.19a and 3.19b) and extends along strike for 1 km parallel to the regional S_3 foliation, striking 60°-70°, and with a dip of 40° to the NW. Mica and quartz stretching lineation plunges 10°SW and is interpreted as a transport direction. The D_4 deformation produces changes in the regional foliation (S_3) trend from NE-SW to E-W, resulting in discontinuity in the quartz vein thickness. Thus, the thickness of the veins is not constant but is interrupted either by boudinage or, more commonly, by extensional faults. Around the mine area quartz veins with boudinage, or those completely folded, indicate an association of extensional and compressional fields. In thin section the quartz veins show a recrystallised texture with lobate contacts between the grains. The veins occur parallel to the wallrock and the quartz grains are stretched parallel to the main foliation of the rock. These characteristics are consistent with post-crystalline deformation and suggest that the veins were folded during D_4 (Figs. 3.20a and 3.20b).

A system of fractures trending E-W is well exposed along the trench in the mine area. Gold mineralized quartz veins represent extensional fractures in a zone of intense

Figure 3.16a S_2 foliation deformed by F_3 folds producing the NE-SW (N 60°E) trend parallel to the regional structures in chlorite-biotite schist in Salgueiro Formation. A penetrative axial plane foliation is formed by the F_3 folding. (Cachoeira de Minas mine, Covico area).

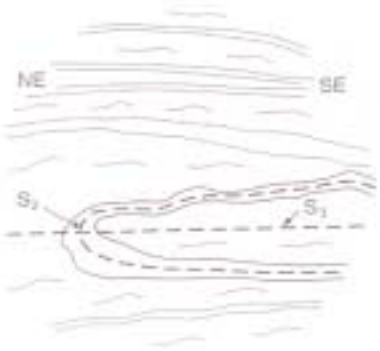

Figure 3.16b Sketch of Fig. 3.16a showing two phases of deformation D_2 and D_3.

Figure 3. 17a Pinch-and-swell structures in quartz veins developed in chlorite schist in the Salgueiro Formation in Cachoeira de Minas mine area.

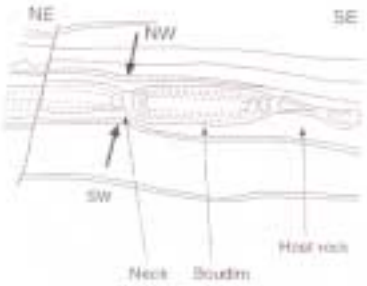

Figure 3. 17b Sketch of Fig. 3.17a illustrating the boudin shape of the quartz vein .

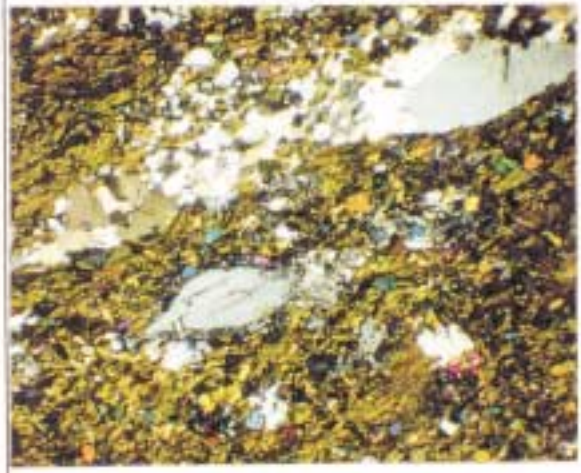

Figure 3.18 Biotite-chlorite schist showing sigmoidal feldspar porphyroclasts with tails wrapped around by biotite and chlorite flakes. Ribbons of quartz are marked by a polycrystalline annealed texture due to crushing and plastic deformation. The rock fabric is oriented parallel to the regional shear direction (N60°E; XPL; TL; WOF = 4500 µm; Cachoeira de Minas mine; MG-R-224).

Figure 3.19a View of the main mineralized quartz vein in the Covico area (about 60 cm thick) emplaced parallel to the NE-SW-trending regional foliation S3 (N60°E). The vein shows the same slight folding as the foliation S3 and dips 60°-70° SE (MG-R-224B, Cachoeira de Mineas mine, Covico area).

Figure 3.19b Sketch of Fig. 3.19a displaying D3 deformation folding the S_2 and producing asymmetric folding F3 whose axial plane forms the penetrative foliation S3 at an angle of 60°-80° to S_2.

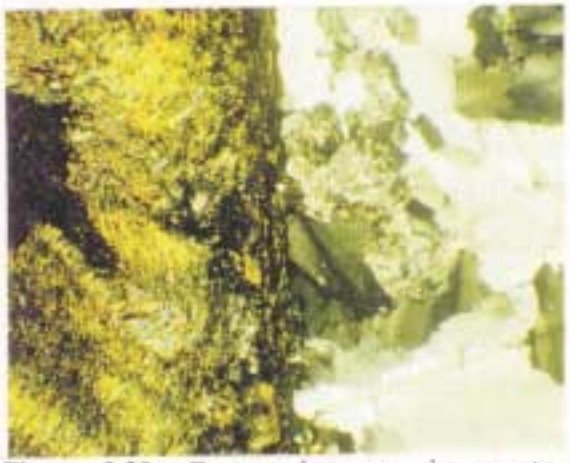

Figure 3.20a Contact between the quartz-muscovite-sericite schist and the auriferous quartz vein (on the right) in the Covico area. Note the F4 kink bands and the recrystallised texture, and the stretching of the quartz grains. Laminae of wallrock parallel to the vein wall indicate opening of the lode perpendicular to its boundaries (XPL; TL; WOF = 4500 µm; MG-R-224A; Cachoeira de Minas mine).

Figure 3.20b Sketch of Fig. 3.20a illustrating the fabric developed during shearing: polyclinal kink bands in the schist and sutured lobate texture in the stretched quartz grains due to slight post-crystalline deformation (syn-post shearing).

movement (late D_3 and syn D_4). This timing is consistent with the refolding of F_3 by reverse movement along the Talhado fault (F_4). A lineation was formed by recrystallization of muscovite, sericite and chlorite along the axial plane F_4. The emplacement of the quartz veins is related to the development of extensional fractures that resulted from thrusting. Thus the gold-bearing quartz veins in Cachoeira de Minas mine were formed pre-syn shearing, under plastic-brittle conditions and retrogressive metamorphic processes.

3.4 ITAPETIM DISTRICT

3.4.1 Introduction

The Itapetim gold district area is situated south of Patos and north of São José do Egito towns on the border between Paraíba and Pernambuco states (Fig. 3.21).

In Itapetim the mineralized areas occur within a strike-slip shear zone with NE-SW strike. The gold distribution is concentrated in three main areas: (i) the eastern, Pimenteiras; (ii) the central, Sertãozinho; and (iii) the western, Degredo, with an extension to the west in the Santo Aleixo area. (Fig. 3.21). The mineralization in the first two domains is related to supracrustal rocks (schists and gneisses), whilst in the latter area the gold is predominantly hosted by orthogneisses. The gold distribution defines a very extensive but narrow NE-SW regional trend that extends discontinuously for 30 km at the contact between the granitoids and supracrustal rocks (Fig. 3.21).

In this district, gold-bearing quartz veins are also found in close association with the major shear zone. They are hosted by competent rocks (granitoids), as for example the occurrences of Canafístula, Cacimba Salgada (Fig. 3.21) and Igarapé Garapa (see Fig. 3.13). This granitoid-related environment will be discussed later.

3.4.2 Geology

The Itapetim gold district is located in the Pajeú/Paraíba Fold Belt and comprises the Archaean basement and an Early Proterozoic metavolcanic-metasedimentary sequence (Brito Neves, 1975) which has been pervasively intruded by three Early to Late Proterozoic granite suites (Scheid and Ferreira, 1991). The main structure is a N to NE-trending belt of strike-slip shear zones that are parallel to the regional trend.

The main units in the district are: (i) granite to gneissic complex of high metamorphic grade that forms the Archaean basement (Caicó Complex; Meunier, 1964); (ii) Early Proterozoic supracrustal sequence represented by the Irajaí Complex (Wanderley,

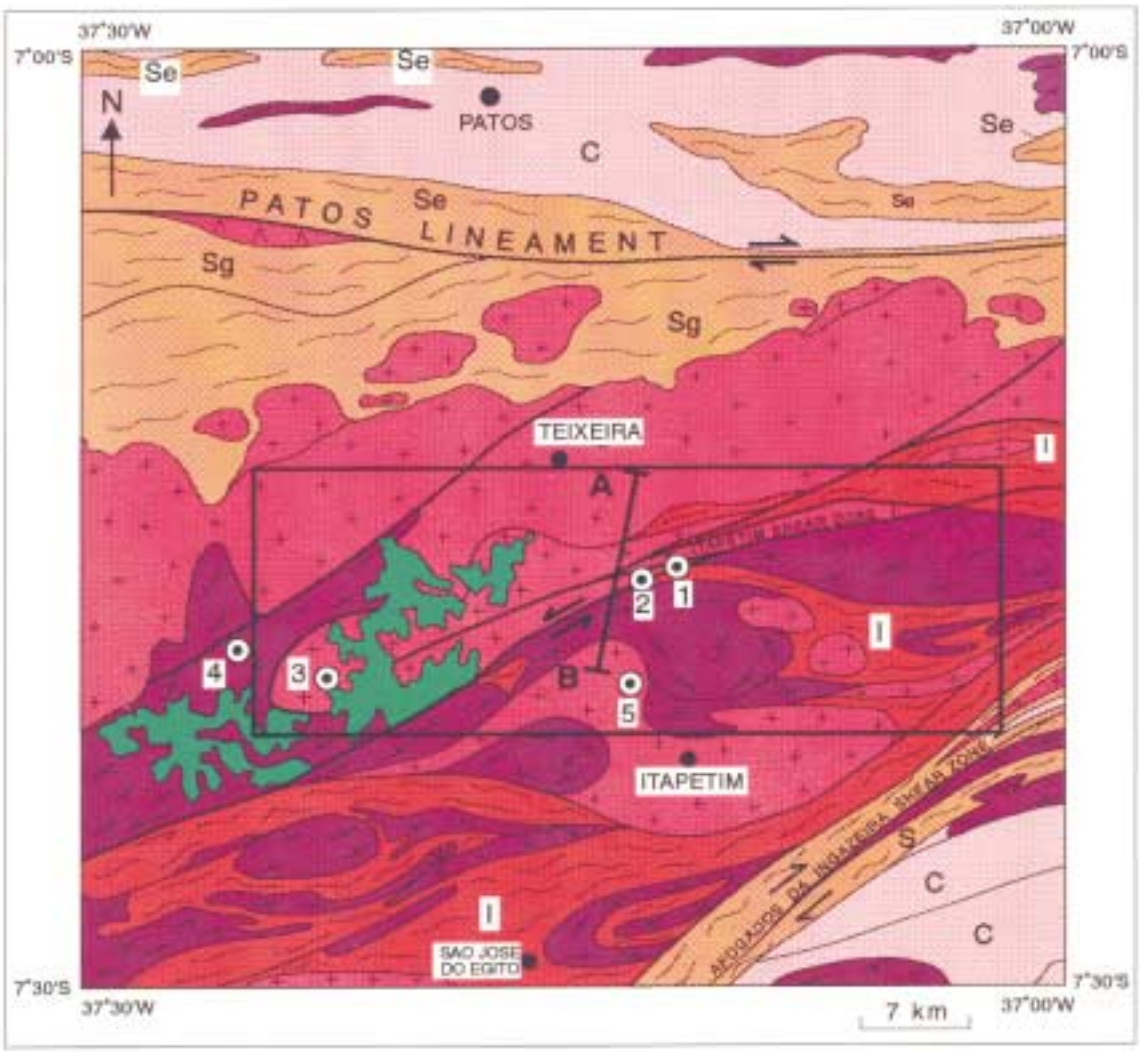

Figure 3.21 Geological framework of the Itapetim gold District, showing the location of the gold mineralized areas: (1) Pimenteiras, (2) Sertãozinho, (3) Santo Aleixo, (4) Canafístula, (5) Cacimba Salgada. (Modified from Patos, Folha SB. 24-Z-D.I., DNPM; 1991). Cross section obtained during this study.

1983); and (iii) granitoids intruded at several stages during Trans-Amazonian and Brasiliano times (Scheid and Ferreira, 1991; Fig. 3.21).

The granite-gneissic complex is overlain by the Irajaí metasediments and consists of banded biotite gneiss with amphibolite and calc-silicate intercalations and orthogneisses of granitic to granodioritic composition. These rocks represent high-grade metamorphism of Archaean to Trans-Amazonian (Early Proterozoic) age (Brito Neves, 1975).

The best exposures of the orthogneisses occur close to Patos town where they outcrop over an area of 200 km^2. The biotite gneiss is usually completely weathered.

The Irajaí Complex consists of two units (Fig. 3.22a) on a regional scale: (i) the clastic sequence, consisting of feldspathic-paragneisses (Fig. 3.22b) with minor intercalations of schist, limestone, calc-silicate, graphite and amphibolite rocks; and (ii) the metavolcanic sequence represented by volcanoclastics, mafic rocks, metagabbro, metadiorite and metavolcanics (Fig. 3.22c; Wanderley, 1990).

The Irajaí Complex is the predominant host rock for the main gold-bearing quartz veins in the east (Pimenteiras) and central (Sertãozinho) areas of the Itapetim District. The unit crops out continually along a 1.5 km wide and 4.0 km long, N to NE trending strike-slip shear zone, and consists predominantly of gneisses (in the central area) and abundant schists (in the east). The following lithologies occur in the mineralized areas: biotite gneiss; chlorite-biotite gneiss; biotite-quartz schist; garnet-muscovite-biotite schist and biotite-graphite schist. They form bands made up of alternating biotite and quartz-feldspathic layers of a centimetre to metre in thickness. They are highly deformed with a strong preferred mineral orientation parallel to banding which could be either lithological or have originated from metamorphic processes (Fig. 3.23). The gneissic texture is well defined by a rhythmic alternation of mica (mainly biotite) or quartz-feldspathic bands.

A large volume of plutonic rocks is found in the Itapetim area intruding both the Archaean basement and the Proterozoic supracrustal sequences. The intrusions have been classified (Scheid and Ferreira, 1991) according to geochronology and regional deformation regime (D_2 or D_3) into low-angle, thin-skinned, compressive tectonic granites (Trans-Amazonian granites; 'G-2' type; Macedo *et al.*, 1984) and transcurrent shear granitoids (Brasiliano granites; 'G-3' and 'G-4'; Jardim de Sá *et al.*, 1981; see Chapter 2).

3.4.3 Deformation and Metamorphism

The most important tectonic events recognised in the Itapetim area are : (i) low angle, thin-skinned compression tectonics with thrust faulting related to the Pre-Brasiliano

Figure 3.22b Well developed banding consisting of quartz-feldspathic and biotite-rich bands in folded paragneisses of the Irajaí Formation. The rocks are highly deformed with a strong gneissic preferred foliation parallel to the banding N60°E (regional shear direction). Note quartz veins discordant with the foliation (Along the São José do Egito to Itapetim road; MG-R-142).

Figure 3. 22a Block diagram (based on the 1 : 25,000 mapping from Santos *et al.*, 1985) showing the distribution of the Irajaí facies in the Itapetim area: gneisses with minor mafic intercalations (schists) predominate in the central area (Sertãozinho) and muscovite-biotite schist in the east side (Pimenteiras).

Figure 3.22c Well developed vertical schistosity transposed into the N65°E foliation in muscovite-biotite schist of the Irajaí Formation. Note the quartz veins which are concordant with the foliation, showing the development of sigmoidal or boudin forms (Itapetim District, Pimenteiras area; MG-R-219).

Table 3.3.
Deformation and Metamorphism in the Itapetim Gold District

Event	Description of Structural Features	Metamorphism
D1	S1: N-NE gneissic banding parallel to S0 consisting of qz.-rich (light) and biot.-rich (dark) layers. Sometimes S1 forms slight anastamosing banding in the basement lithologies cross-cuts S0 at low angle. Regionally D1 produced banded gneisses displaying anatexis/mobilisation of leucocratic material resulting in migmatization	M1: granulitic Anatexis resulting in migmatization
D2	S2: Penetrative foliation or banding at low angle consisting of biot., qz., musc., feldsp., gar. and sill. L2: Stretched lineation and mineral lineation on S2 F2: km-scale recumbent folds with tight to isoclinal folds whose axial planes dip 50° SSE and plunge NE .	M2: granulite/upper amphibolite facies Mineral assemblage: K-feldsp., gar. sill., biot.
D3	S3: Penetrative foliation parallel to the axial plane (F3) vertical to sub-vertical and strikes from NE to E-W with steep dip SE	M3: Amphibolite facies. Mineral assemblage along S2: sill., gar., K-feldsp., biot., epid. musc., qz.
D4	F4: produced strike-slip with regional N to NE-trending that oriented the rocks parallel to the regional shear F4: forms shear bands and kink bands overprint S3, well-developed in Irajaí biotite schist. Mineral assemb. ser., ch., alb., epid., and musc. suggest retrogressive metamorphic processes.	M4: sub-greenschist facies. Mineral assemblage along S4: Chloritization of biot. saussuritization of K-feldspr., musc.

Observation:
For further information see List of Abbreviations.

Figure 3.23a

Figure 3.23b

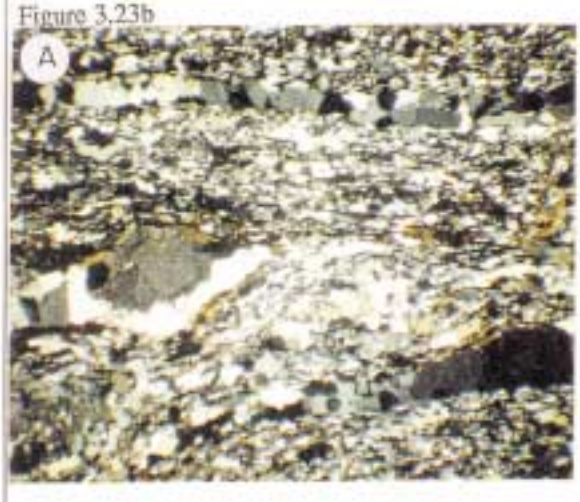

Figure 3.23c

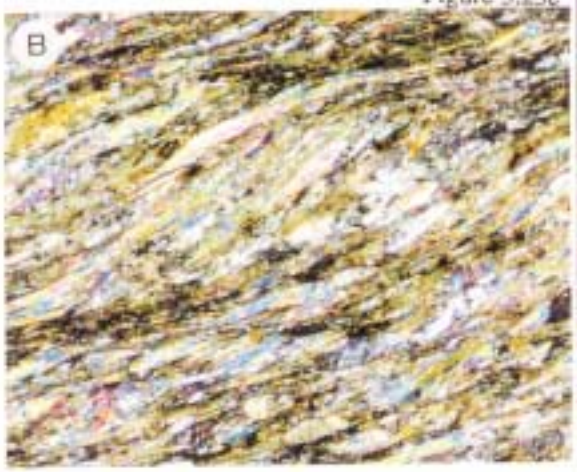

Figure 3.23a Contact between the syn- and late tectonic granite (A) and the Irajaí metasediments (B) which consists of muscovite-biotite schist and biotite schist within the shear zone. Note the well developed foliation N60°E parallel to the regional shear direction (MG-R-193, Piedade dam; Itapetim District, eastern side).
Figure 3.23b Porphyritic granite shown in the Fig. 3.23a displaying a foliation produced by the aligment of the flattened and streched porphyroclasts of K-feldspar and quartz resulting in a mylonitic texture. The sigmoidal arrangement of the fabric (quartz ribbons and granoblastic-polygonal texture) suggests plastic deformation. (XPL.; TL; WOF = 4500 µm; MG-R-192, Piedade, Itapetim District, eastern side).
Figure 3.23c Photomicrograph of the muscovite-biotite schist shown in Fig. 3.23a displaying C and S fabric in Irajaí schists. Note that the sigmoidal shapes of some of the quartz and feldspar are stretched out by the plastic shearing. A **dextral** shear sense is indicated (XPL; TL; WOF = 3000 µm; MG-R-190B, Piedade, Itapetim District, eastern side). This point is located in the cross section Fig. 3.24 as letter D.

Orogeny; and (ii) the transcurrent tectonics of the Brasiliano event, responsible for the shear zone evolution, which is characterised by high angle, strike-slip faults (Scheid and Ferreira, 1991).

The Brasiliano Orogeny deformed and reorientated the Pre-Cambrian units. Evidence for this seen in the field is: (i) horizontal stretching and strike-slip faulting in the supracrustal sequence; (ii) low angle compressional deformation of the orthogneisses; (iii) mylonitic foliation in the Brasiliano-age granitoids; (iv) emplacement of the Brasiliano granitoids (SLTG); and (v) NNE-trending stretching lineation with elongated porphyroclasts of K-feldspar and quartz ribbons. Some of this evidence is illustrated in the cross section of the Itapetim shear zone in Figure 3.24.

The Itapetim area is dominated by a trend which is predominantly parallel to the NE-SW shear direction. The structures are polydeformed with a strong preferred orientation parallel to the regional trend, defined by a mylonitic foliation and a gneissic banding preserved in country rocks and plutons (Fig. 3.23).

Linear and planar structural elements associated with D_2+D_1 developed by the low angle thin-skinned tectonics were reoriented by the strike-slip faults (F_4) which overprinted the oldest structures.

Four phases of deformation were recognised in the Itapetim gold district during this study. A summary of all the phases and their characterisc are presented in Table 3.3.

3.4.4 Shear Zones and the Emplacement of the Gold-Bearing Quartz Veins

The regional trend in the Itapetim area is defined by two main structures: the E-W Patos Lineament in the north and the NE-SW-trending strike-slip shear zone of Afogados da Ingazeira in the southeast (Vauchez *et al.*, 1992). According to Leterrier *et al.* (1990), these shear zones are characterised by the development of extensive mylonites and emplacement of granites, and show a sinistral and a dextral shear sense respectively (Vauchez *et al.*, 1992; see Fig. 3.21). The Itapetim strike-slip shear zone trends ENE-WSW and is situated between the two main shears. It is approximately 100 km in length and oriented sub-parallel to the main shears; it connects with the Patos Lineament in the north (see Fig. 3.21). The shear zone is roughly 200 m in width, and the mineralized quartz veins are located in the central part of the shear (Fig. 3.25).

Mylonitic deformation parallel to the border zones has a 70° south easterly dip and a lineation formed by bent quartz boudins with a low rake. The matrix of the mylonitic rocks has undergone extensive syntectonic recrystallization to a finer grain size, where large grains remain as porphyroclasts of K-feldspar or more rarely of garnet. 'Mortar' texture of the feldpar is consistent with recrystallization. The quartz (Fig. 3.27) and the

Figure 3.24 Cross section of the Itapetim shear zone oriented NNE to SSW and appearance of associated rock types. (upper case latters refer to views in the field, lower case to thin sections). For location see Fig. 3.21. (A) Flow structures and very thin mylonitic zones developed in undeformed to moderately deformed granite (SLTG). Mafic and felsic compositional banding is oriented by the flow. These elements are aligned according to the regional shear direction (N 70°E; Fava de Cheiro farm close to Riacho Verde village; MG-R-211). In (a) the rock exhibits an igneous appearence with the plagioclase grains still retaining their original texture. (XPL.; TL.; WOF = 4500 μm; MG-R-211). (B) Sinistral sense of shear movement indicated by the porphyroblasts of K-feldspar in strongly deformed porphyritic granite. The deformation produced asymmetric trails of recrystallised K-feldspar and oriented the fabric parallel to the regional shear (N 70° E). Stretched quartz grains also occur. (Piedade town; MG-R-191). In (b) the rock is partly mylonite and partly protomylonite (Sibson, 1977). Deformation processes have disrupted original K-feldspar phenocrysts to produce porphyroclasts with extinction and fracturing. (XPL; TL; WOF = 2500 μm; MG-R-191). (C) Augen gneiss with flattened K-feldspar (pink colour) porphyroclasts. The fabric represents a strongly to intensely deformed granite (ESTG). The strain gradient has produced a predominantly symmetrical movement in the porphyroclast of feldspar (foliation N 80 ° E; Piedade town; MG-R-214). In (c) the plagioclase feldspar survives as porphyroclasts but quartz has undergone syntectonic recrystallisation and produced fine oriented grains to form pronounced ribbon textures. Biotite has also been reduced to fine-grained material surrounding the ribbons. (XPL;TL; WOF = 2500 μm; MG-R-214). The location (D) represents the view in the point Fig. 3.23.

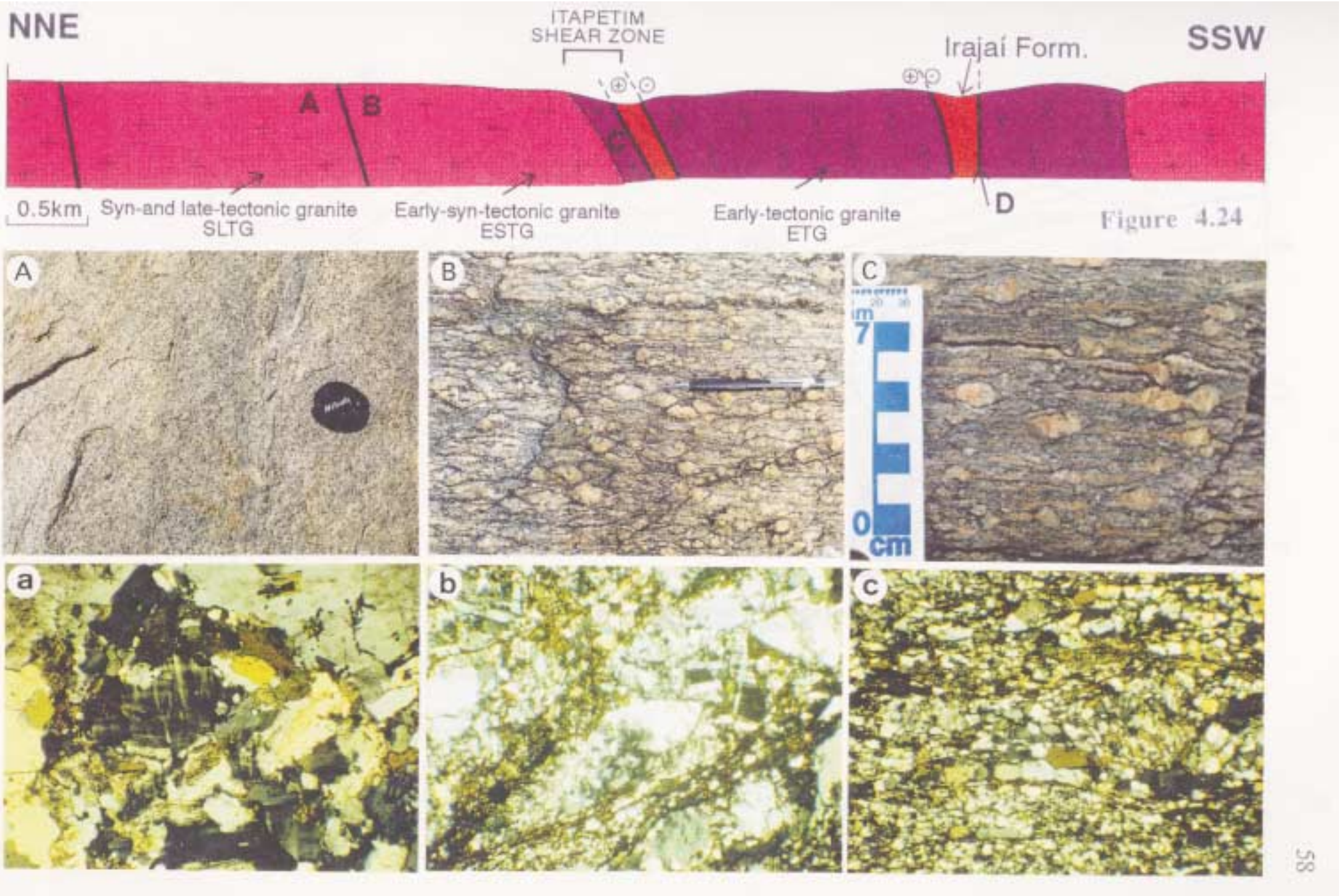
NNE
ITAPETIM
SHEAR ZONE
Irajaí Form.
SSW
A
B
C
D
0.5km
Syn-and late-tectonic granite
SLTG
Early-syn-tectonic granite
ESTG
Early-tectonic granite
ETG
A
B
C
a
b
c

Figure 4.24

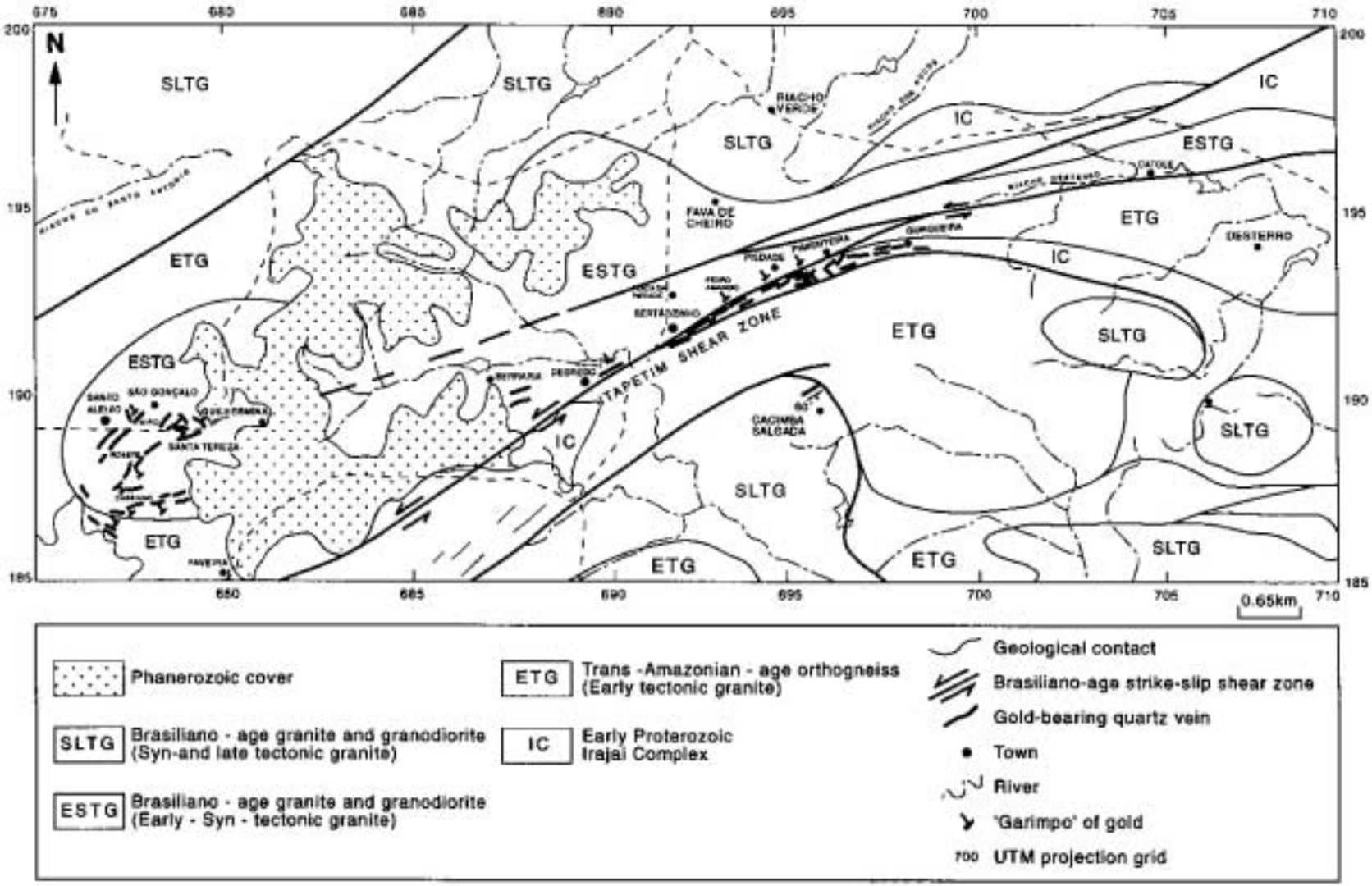

Figure 3.25 Structural framework of the Itapetim Gold District. Note the distribution of the gold-bearing quartz veins along the Itapetim shear zone. (Modified from Santos *et al.*, 1985; Structural information from this study).

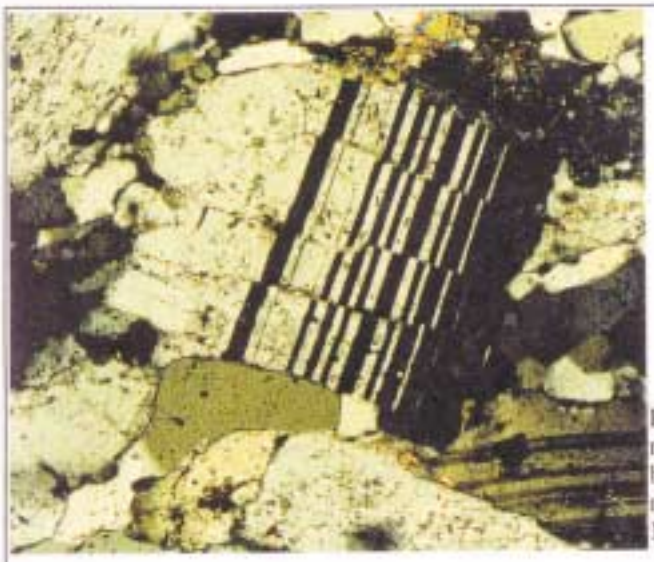

Figure 3.26 Feldspar crystal deformed by microfracturing characteristic of the transition between plastic and semi-brittle deformation in mylonitic gneiss. (XPL; TL; WOF= 2500 μm; MG-T-103; Itapetim shear zone, central domain).

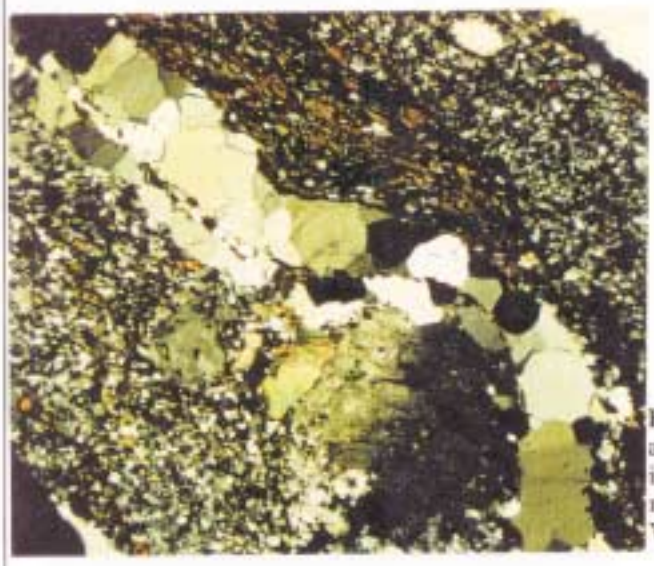

Figure 3.27 Stretched ribbon quartz wrapping around the porphyroblast of feldspar.The quartz is deformed by crystalline plasticity and produces ribbon texture. (Itapetim shear zone; XPL.; TL; WOF = 4500 μm; MG-T- 058; Itapetim area).

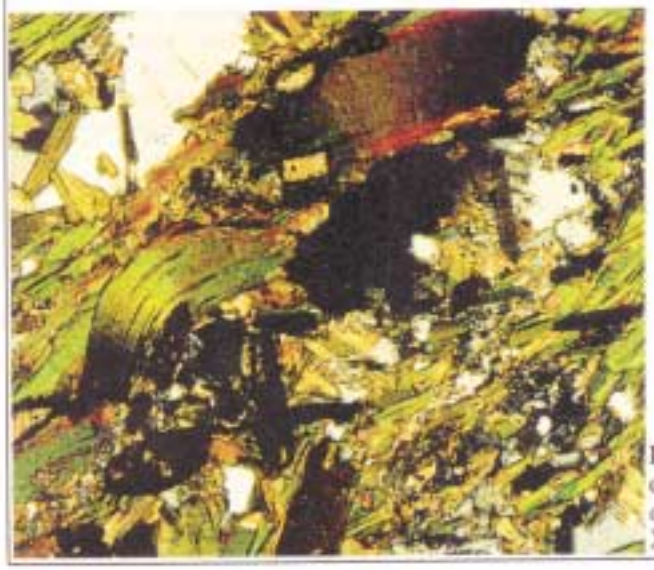

Figure 3.28 Mica flake (biotite) deformed by crystalpastic flow in high-grade shear zone developed in biotite schist. (Itapetim shear zone; XPL; TL; WOF = 1500 μm; MG-T-095).

Figure 3.29a Shear bands transect the main foliation in strongly deformed augen gneiss (ESTG). Note the sinistral sense of shear moviment. The direction of the shear plane is N 80°E. (Itapetim shear zone, Piedade dam area).

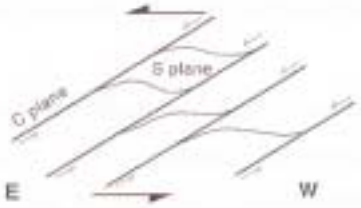

Figure 3.29b Sketch of Fig. 3.29a showing the geometry of the C (plane of shear) and S (plane of schistosity) fabric. The C plane has an extensional geometry with respect to the sense of shear. Note the sinistral sense of shear. (Itapetim shear zone, Piedade dam area).

Figure 3.30a Redirection of movement developing C and S planes in moderately deformed granite (SLTG) suggesting a plastic shear zone regime. Along the shear plane (C) whose direction is N 70°E very thin layers of mylonite occur, where chlorite can be seen. (Itapetim shear zone, Riacho Verde area).

Figure 3.30b Sketch of Fig. 3.30a illustrating the C (plane of shear) and the S (plane of schistosity) fabric. Note the sinistral sense of shear and the extensional geometry of the C plane. (Itapetim shear zone, Riacho Verde area).

mica (Fig.3.28) have been flattened and banded to produce a new fabric oriented parallel to the regional shear. Poikilitic minerals, triple point grain boundaries and quartz overgrowths indicate post-kinematic annealing. The deformation pattern in the mineral fabric suggests a plastic regime of deformation. On the other hand, evidence of brittle deformation is seen in the feldspar (Fig. 3.26). However, it is probable that the more rigid minerals tend to deform in a brittle manner and often fail to recrystallize even when quartz and mica are deformed extensively.

In the augen gneisses, porphyroblasts of K-feldspar are flattened and stretched (see Fig. 3.24). Redirection of movement developed C and S fabrics in moderately deformed granite (Figs. 3.30a and 3.30b). Although, the K-feldspar shows a tendency towards symmetry, sometimes asymmetric recrystallised tails around feldspar show rotated porphyroclasts indicating a sinistral shear sense (Fig. 3.24b). Evidence of C and S fabrics in mica schist (Fig. 3.23b) and shear bands in augen gneiss (Figs. 3.29a and 3.29b) are also consistent with sinistral sense shearing. Sigmoidal quartz veins show the same kinematic indicators as in the regional shear zone (Fig. 3.32).

The gold-bearing quartz veins in the Itapetim shear zone have a NE-SW strike and display evidence of high strain and predominantly strike-slip movement. Two very discontinuous mineralized trends occur, both with an orientation of N 65°E : (i) one from the eastern area (Pimenteiras area) to the central part (Sertãozinho area near Degredo); (ii) the other on the east side, having a more limited distribution (Pimenteiras-Gurgeia; see Fig. 3.34).

The thickness of the mineralized veins ranges from 0.05 m to 0.50 m and they can be concordant or discordant to the foliation (S_3). The concordant veins are more common and are hosted by mylonitic rocks e.g. muscovite-biotite schist (Fig.3.31) or orthogneiss with mafic intercalations (Sertãozinho area). In thin section the quartz shows annealed texture with the quartz grains completely stretched, aligned and banded, to produce banded ribbon forms. Tourmaline and quartz predominantly display a sigmoidal arrangement. These relationships suggest an emplacement under plastic deformation conditions (Fig. 3.33).

Three types of shear-related quartz veins were recognised during this study: (i) early-syn deformation veins which are concordant with the gneissic foliation and show evidence of deformation; (ii) syn-deformation veins which are slightly discordant (10°) with the gneissic foliation and show boudin structures; and (iii) post-deformation veins which are discordant with the gneissic foliation and lack any evidence of deformation. Gold mineralization occurs in the two first types (the early and syn-tectonic shear veins). Relationships between veins and host rocks in the central domain (Sertãozinho) are displayed in Figure 3.35.

It is interpreted that the emplacement of the gold-bearing quartz veins in the Itapetim District was during pre-syn-deformation D_3, and that these veins are related to fractures

Figure 3.31 Mineralized quartz vein (syn-shearing) developed in mica schist concordant to the S3 foliation (Shaft, Gurgueia area, Itapetim gold District, east domain; MG-R-165A).

Figure 3.32 Folding of the S3 foliation has produce a transposed foliation S4 (see the kink bands arrowed) and also sigmoidal arrangement of the quartz vein. (The Itapetim to Desterro road).

Figure 3.33 Gold-bearing quartz vein showing very intense degree of deformation. Recrystallisation has produced subgrains surrounding the margins of some grains, forming discrete bands of very fine quartz. Less recrystallised quartz ribbons occur showing annealed texture. These two quartz textures indicate that the degree of crystallisation is not constant. Note the needles of tourmaline included in the K-feldspar grains. Black areas (on the bottom left) are tourmaline fibres (XPL; TL; WOF = 3000 µm; MG-R-157B, Itapetim District, Sertãozinho).

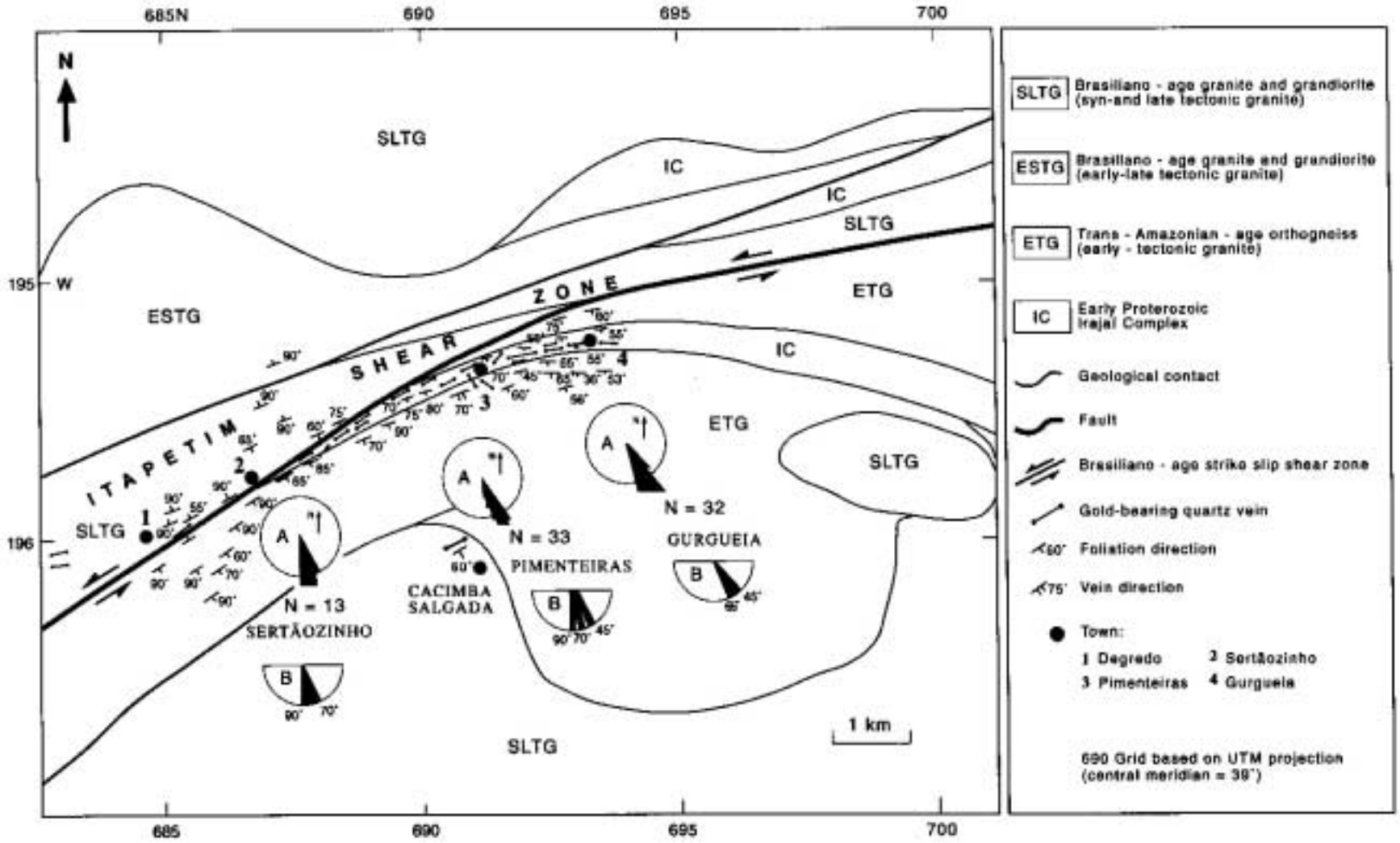

Figure 3.34 Vein pattern in the Itapetim gold District showing the predominant direction N70°E parallel to the regional shear direction. The stereo plots display (A) the dip direction of the foliation and (B) the amount of dip.

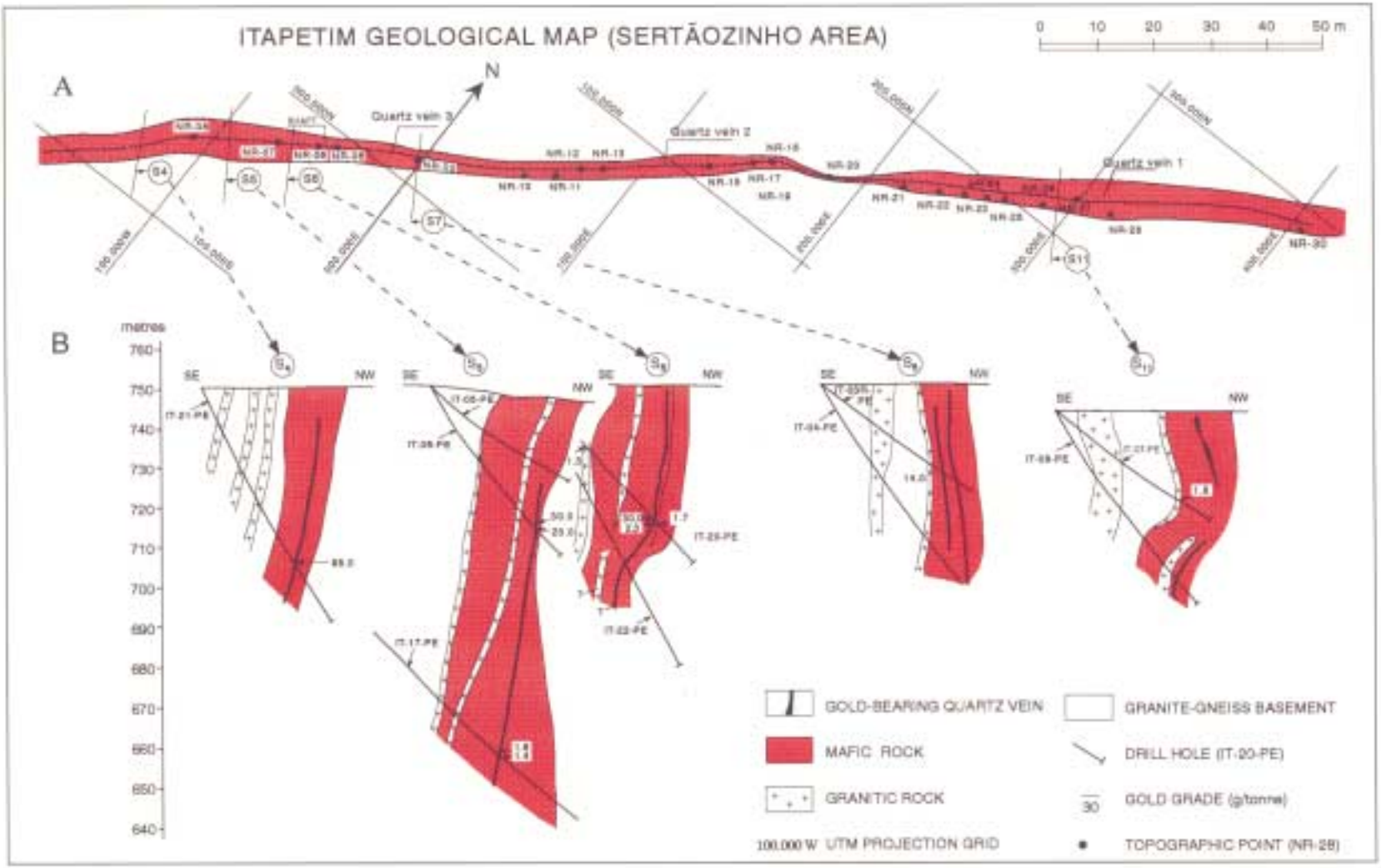

Figure 3.35 Geological map view (A) and vertical section NE - SW (B) in the central area, (Sertãozinho domain) in the Itapetim shear zone. Note that the shear direction is NE - SW (Redrawn from Itapetim Prospect, CPRM, 1984).

developed during strike-slip shearing, under conditions of plastic deformation and retrogressive metamorphism.

3.5 GOLD OCCURRENCES HOSTED BY GRANITOIDS

3.5.1 Introduction

Granitoids hosting mineralized quartz veins occur in four localities in the Itapetim District: Santo Aleixo, Cacimba Salgada, the Canafístula 'garimpos' (see Fig. 3.21), and the Igarape Garapa occurrence (Fig. 3.13). Santo Aleixo lies within the Itapetim shear zone and it is an extension of the N-NE Pimenteiras-Sertãozinho-Degredo trend to the east, while the others are related to plutonic bodies which are widespread in the belt. Although the last three occurrences do not lie within shear zones, they are in close association with major shear zones.

Gold-bearing quartz veins hosted by granitoids occur either in Trans-Amazonian or Brasiliano age granitoids. None of them form economic metal concentrations and their thickness (around 0.3 m) and length (about 5 m) are not extensive. These veins can occur either hosted by less acidic (e.g. Santo Aleixo and Cacimba Salgada occurences) or acidic (e.g. Igarape Garapa occurence) granitoids.

3.5.2 Santo Aleixo Area

The host rock for the gold-bearing quartz veins consists predominantly of augen gneisses (Fig. 3.36a) which display an intense mylonitic foliation, in which flattened K-feldspar porphyroclasts occur (Fig. 3.36b). Evidence of shear processes can also be deduced from the rotated foliation. This granitoid is interpreted as syn- and late-shear (SLTG Brasiliano granite, see Chapter 2).

The gneisses have symmetric deformed porphyroclasts of K-feldspar with their Z axes oriented N 70° E. The quartz has undergone syntectonic recrystallisation and fine grains are oriented to form a pronounced ribbon texture. Sigmoidal arrangement is common in the mineral fabric. The porphyroclasts of K-feldspar are embedded in a fine-grained matrix and locally mortar texture can form (Fig. 3.36b). Biotite has been reduced to fine-grained material surrounding the porphyroclasts of K-feldspar. Sometimes the gneisses display moderate to strongly deformed texture, and form partly mylonitic and partly protomylonitic texture (Sibson, 1977).

A progressive transition from undeformed plutonic rocks, in which irregular biotite-rich mafic enclaves are occasionally present, to strongly deformed banded gneiss

Figure 3.36a Augen gneiss (host rock for gold quartz veins) displaying intense mylonitic foliation (S_3) with flattened and symmetric porphyroclasts of K-feldspar oriented by shearing. (MG-R-205A, Santo Aleixo area, Guilhermina 'garimpo').

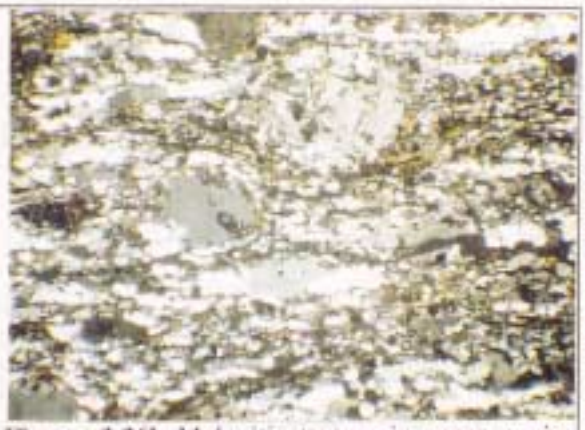

Figure 3.36b Mylonitic texture in augen gneiss (Fig. 3.36a) with quartz grains which have undergone syntectonic recrystallization to produce fine grains oriented to form a pronunced ribbon texture. (XPL; TL; WOF = 4500 μm; MG-R-205A, Santo Aleixo area, Guilhermina 'garimpo').

Figure 3.38a Regional extensional vein (N 70° E) mineralized with gold and sulphides (galena and pyrite) hosted by undeformed to moderately deformed leuco-granitoid (Igarapa Garapa occurrence; MG-R-197A).

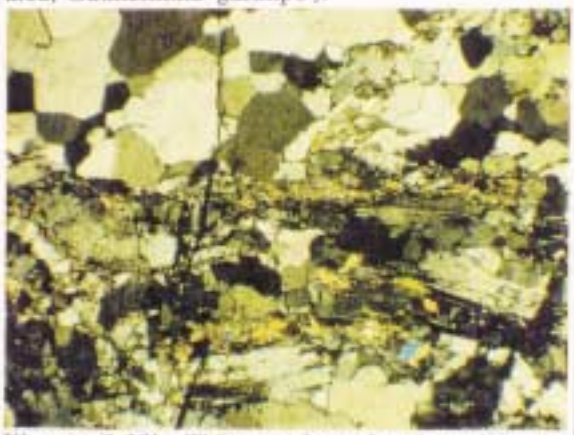

Figure 3.38b Thin section showing that the granitoid (Fig. 3.38a) still retains an igneous appearence with the plagioclase retainning its original texture. The rock is a hornblende granite. Note the contact (on the top) with the quartz vein. (XPL; TL; WOF = 4500 μm; MG-R-197A; Igarape Garapa occurrence).

Figure 3.39a Outcrop showing gold-bearing quartz veins hosted by orthogneisses which display an intense foliation oriented N 70° E
Note the tourmaline altered zone (dark colour) concordant with the foliation (S_3); Canafístula 'garimpo'; MG-R-204).

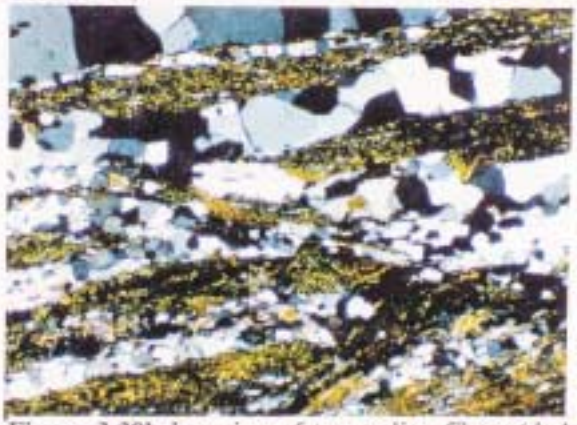

Figure 3.39b Layering of tourmaline fibres (dark colour; Fig. 3.39a) and very abundant quartz laminae giving an overall ribbon quartz appearence. The sigmoidal shapes of the layers produce a ribbon texture orientated parallel to the regional shear. Note the annealed texture in the quartz ribbons. (XPL; TL; WOF = 4500 μm; MG-R-203B; Canafístula 'garimpo').

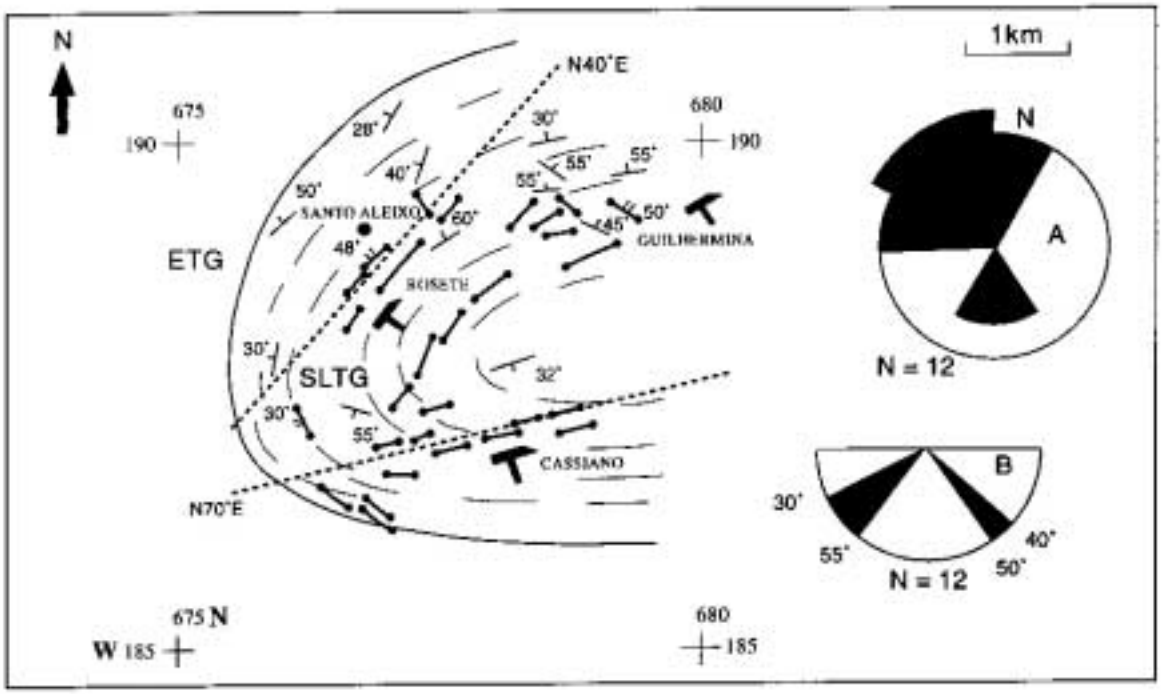

SLTG	Brasiliano - age granite and grandiorite (syn - and late tectonic granite)		Foliation
			Geological contact
ETG	Trans - Amazonian - age orthogneiss (early - tectonic granite)		Gold-bearing quartz vein
			'garimpo' of gold
40°	Foliation direction		Town
50°	Vein direction	675	Grid based on UTM projection (Central meridian = 39°)

Figure 3.37 Vein pattern in the Santo Aleixo area indicating inhomogeneous pure shear and showing two directions: N 70° E, the regional shear direction, to which the majority of veins are parallel, and N 40° E. The stereo plots display (A) the dip direction of the foliation and (B) the amount of dip.

occurs. The enclaves have an abundance of biotite and amphibole. Usually the gneisses form sheets with a characteristically intense recrystallisation similar to a medium to fine textured protomylonite. Mineralogy of the enclaves is essentially comprised of K-feldspar, plagioclase associated with epidote, hornblende and greenish biotite. Plagioclase-quartz rich bands are intercalated with quartz-rich bands. Enrichment in muscovite, carbonate, chlorite and sericite indicates retrogressive metamorphic processes, probably related to the shear processes. This rock is classified as a syenogranite to monzogranite (Chapter 4).

In the Santo Aleixo area two types of quartz veins are distinguished according to their mode of emplacement (Fig. 3.37): (i) veins parallel to the N 70° E regional shear or the foliation (S_3); and (ii) veins discordant to the regional foliation S_3 that form a small angle with S_3 and are predominantly emplaced along N40°E extensional fractures. The N 40° E oriented veins show dextral movement of emplacement whislt the N 70° E veins show a sinistral sense. This distribution may reflect a conjugate shear system. The veins usually do not have a thickness greater than 0.20 m. The presence of sinistral and dextral quartz veins in augen gneiss may reflect a plastic-semi-britle deformation regime. Along the NW-SE shear plane, where mylonitic layers are well developed, the mylonitic foliation F_3 is completely rotated (in a dextral sense) as a result of the quartz emplacement. This indicates that the veins are post -F_3 and syn-shear (F_4). These veins are also highly fractured. These fractures are interpreted to be extensional fractures that were formed during the intense movement of the shearing under a plastic-brittle regime.

3.5.3 Igarape Garapa Occurrence

The Igarape Garapa gold quartz veins (see Fig. 3.13 for location) occur in a syn- and late-shearing granite (SLTG, Brasiliano granite; see Chapter 2) known as the Teixeira granitoid (Almeida *et al.*, 1967), which is oriented E-W and has a length of 0.5km (Fig. 3.38a).

The rock is a hornblende granite (Fig. 3.38b) and consists of quartz, feldspar (microcline), biotite and hornblende. Saussuritization, sericitisation and hornblende altered to biotite indicate processes of change from amphibolite facies to greenschist metamorphic conditions (see Chapter 4). Xenoliths of mafic rocks are common.

The granites are moderately deformed to undeformed, and no significant foliation can be observed; some flow structures occur, as for example orientated xenoliths are parallel to the regional shear direction (N 70 ° E).

Three gold-bearing quartz veins occur along fractures oriented N 70° E, with thicknesses around 0.20 m and lengths no longer than 0.5 km. The veins are commonly 0.50 m apart. A lack of shearing in the veins points to a post-shearing

emplacement.

3.5.4 Canafístula 'Garimpo'

Canafístula is the largest 'garimpo' (Fig. 3.39a) in production in Itapetim District (for location see Fig. 3.21). Gold is recovered from tourmaline-quartz veins (Fig. 3.39b) developed in a potassic and tourmalinised alteration zone in granites. Gold-bearing quartz veins are hosted by biotite orthogneisses which display a penetrative foliation highlighted by biotite. The same fabric orientation may also be observed in the stretched K-feldspar porphyroclasts. Quartz-K-feldspar-rich bands are very common. Associated with these bands are abundant tourmaline and magnetite. Xenoliths of supracrustal rocks and enclaves of mafic rocks occur.

The granitoids are thought to be Trans-Amazonian age and G-2 type (ETG.; see Chapter 2), which were deformed during the low-angle thin-skinned compression tectonics (D_2) and characterised by superposition of S_1+S_2 foliation with a very shallow dip. D_3 deformation can be observed in the rock fabric as stretching of quartz grains and as well as boudins and quartz veins (Fig. 3.39a) with a consistent strike (S 40°E) and dip (70°NW). This direction represents the extensional fractures related to the regional shearing. The rock shows a protomylonitic to mylonitic texture where quartz ribbons are abundant and occur parallel to the mylonitic foliation. This granitoid has a syenogranite to monzogranite composition (see Chapter 4).

In the Canafístula area the orthogneiss occurs in pods (low strain zones) surrounded by a mylonitic zone. At the contact with the mylonitic zone the S_1+S_2 fabric is well-preserved and affected by a later fabric (S_3) defined by the stretching of the minerals (e.g. quartz, porphyroclasts of feldspar, mica) and also in the quartz boudins. This deformation (D_3) is oriented S 40° E and reflects extensional fracturing associated with the N 70° E regional shear direction. The gold-bearing quartz veins were developed within the altered zone and were oriented parallel to the S_3 or S 40° E direction and dip 70°NW. Their emplacement is interpreted as being associated with pre- or syn-shear fracturing.

Gold-quartz veins in Canafístula area have a thickness of around 0.5 m. Sigmoidal forms are very common. Rotated porphyroclasts of K-feldspar indicate a sinistral sense of movement. Evidence of a plastic regime can be also seen in the sigmoidal shapes and stretching layers of tourmaline associated with ribbon quartz. Annealing of the quartz texture and the presence of folded tourmaline crystals suggest recrystallisation after shearing (Fig. 3.39b).

3.5.5 Cacimba Salgada Occurrence

The Cacimba Salgada gold-quartz veins (Fig. 3.40a) are hosted by a granite known as the Itaporanga type (Almeida *et al.*, 1967). This granite is K_2O-rich and characterised by a porphyritic texture. The rock consists of a cream coloured quartz-feldspar matrix with zoned microcline phenocrysts (size ranges between 1 cm to 10 cm) and abundant enclaves of porphyritic granodiorite or quartz diorite (see Chapter 4) with 2 cm to 20 cm size and black colour (Fig. 3.40b). The mineralogy of this rock is essentially comprised of phenocrysts of microcline dispersed in the quartz-feldspar matrix, associated with epidote, hornblende and greenish biotite. Enrichment in muscovite, carbonate, chlorite and sericite is evidence of retrogressive metamorphism. The enclaves consist predominantly of plagioclase, hornblende and biotite.

The Cacimba Salgada granitoid is classified as syn- and late- shear (SLTG; see Chapter 2) where xenoliths of supracrustal rocks can be seen. Evidence of shearing processes within the granitoid is present, but the amount of deformation is not extreme. Stretching of the mafic enclaves, which display a common N 60° E orientation, is an indicator of some regional shear (Fig. 3.40c). Rock foliation, where obviously stretched quartz crystals have a preferred orientation, is further evidence. The sigmoidal outcrop pattern can be observed on the geological map (see Fig.3.21) and suggests emplacement related to deep extensional NE-SW oriented shear zones (N 70 ° E) which were associated with sinistral movement (as shown in Figs. 3.40c and 3.40d). The petrographic studies suggest emplacement in a low strain environment where the minerals are not intensely deformed or recrystallised.

The mineralized quartz veins have dimensions of about 0.20 m thickness and length of 5 m. They are related to extensional fractures with a N 70° E orientation. Evidence of sinistral shearing of the veins suggests emplacement was pre- to syn-shear.

3.6 GOLD OCCURRENCE IN THE ARCHAEAN BASEMENT

The Boqueirão dos Cochos area comprises highly deformed Archaean basement (Brito Neves, 1975) containing gold-mineralized quartz veins. The area is situated approximately 20 km NW of Piancó, in the northwestern part of the State of Paraíba (see Fig. 3.13 for location). Auriferous quartz veins are associated with amphibolite lenses that occur intercalated in the basement rocks.

The main unit in the mineralized area is the high grade Archaean migmatitic-gneissic complex with lenses of mafic rock, which was consolidated by the end of the Trans-Amazonian thermal-tectonic cycle and reworked by the Brasiliano Orogeny (Brito Neves, 1975; Santos and Brito Neves, 1984). The main structural feature of the area is

Figure 3.40a Regional extensional quartz vein (N 70°E) mineralized with pyrite and gold and hosted by porphyritic granodiorite with quartz diorite enclaves. The occurrence is in close association with a major shear (edge of the Itapetim shear zone).Enclaves are oriented by the regional shear (direction N 70°E; Cacimba Salgada; MG-R-218)

Figure 3.40b Detail of Fig. 3.40a showing the deformed enclaves of quartz diorite (dark colour) in a moderately deformed porphyritic granodiorite (SLTG), the host of the gold mineralized quartz vein. Note the phenocrysts of microcline (middle of the photo) from 2 cm to 20 cm size. (Cacimba Salgada area; MG-R-218).

Figure 3.40c Shearing evidence in granodiorite (cream coloured) that contains quartz diorite enclaves (dark coloured). This shows a zone with left hand shear sense running from the bottom right to the top left side. Mylonitic rock with chlorite occurs along the shear plane. (Cacimba Salgada occurrence).

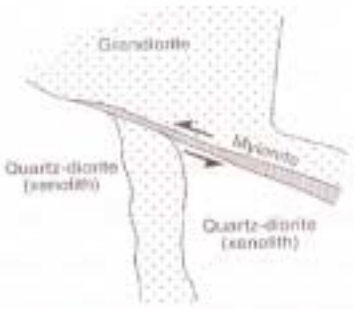

Figure 3.40d Details of the Fig. 3.40c illustrating the sense of sinistral movement and the indication of a mylonitic zone. (Cacimba Salgada occurence).

the N to NE-trending Cedro-Boqueirão dos Cochos shear zone (see Figs. 3.1 and 3.14) which extends northwards to connect with the Patos Lineament. This shear occurs at the boundary between the Piancó/Alto Brigída Belt and the Archaean basement. Its trend is approximately parallel to that of the Jaru shear in the Cachoeira de Minas mine area. While the Jaru shear zone has a dextral transcurrent shear sense (Silva Filho *et al.*, 1985) with intense mylonitic zones, this shear has a sinistral sense of movement (as shown by kinematic indicators, e.g rotated porphyroblasts of K-feldspar or quartz-eyes sheared in phyllonite; Fig. 3.41c).

The mineralized area consists of biotite-garnet gneiss associated with garnet-amphibolite lenses (Fig. 3.41a) that could be relicts of mafic rock. The mineral assemblage in the biotite gneiss, besides biotite and quartz, consists of both prismatic and fibrolitic sillimanite, plagioclase, K-feldspar and almandine, indicating a grade sufficient for anatexis to occur. Petrographic studies indicate that garnet is partially replaced by biotite, indicative of retrogressive metamorphic conditions (see Chapter 4). The biotite gneisses display mylonitic foliation and a prominent banding of micas alternating with quartz-feldspar-rich layers; bending of these suggests plastic deformation. The biotite gneiss has been transformed into recrystallised quartz-eyes and strongly sheared in a mica-rich phyllonitic matrix (Fig. 3.41c). This deformation is indicated by newly recrystallised biotite and polycrystalline quartz and plagioclase porphyroclasts that are stretched and oriented N70°E (i.e. parallel to the Jaru shear).

The mineralized area is characterised by an intensely deformed zone where three parallel quartz veins are hosted by a garnet amphibolite lens whose foliation strikes N 60° E and dips 75°SE. The minerals show stretching and are oriented parallel to the main foliation. Two types of quartz veins are distinguished according to their thickness and emplacement relative to the main foliation: (i) large quartz veins, 0.30 m in thickness, and concordant with regional foliation, S_3; (ii) smaller veins of approximately 0.5 cm thickness, discordant to the main foliation, striking N 60 ° E and dipping 75° SE. The first vein type is mineralized whilst the second is barren (Figs. 3.41a and 3.41b).

Gold-bearing quartz veins oriented parallel to the regional shear (N 60° E) are cut by smaller quartz veins with a S 60° E orientation, and which are probably extensional fracture fillings. These fractures produced a banding in the mineralized vein which is concordant with the main foliation of the host amphibolite (N 60° E) and indicative of a plastic-semi brittle regime of deformation. A symmetrical sense of sinistral movement can be observed from these two directions (see Fig. 3.41b). The relationships between the mineralized vein and the metric-scale shear zone indicate that the mineralized quartz veins predated the regional sinistral strike-slip shearing.

Figure 3.41a Two differently oriented quartz veins passing through a shear zone developed in garnet-rich amphibolite (foliation is N 60 ° E and dips 75° SE). The concordant vein (large) is mineralized with gold while the discordant (smallest) is barren.(Boqueirão dos Cochos area; MG-R-208B).

Figure 3.41b Sketch of Fig. 3.41a illustrating the concordant gold mineralized quartz vein (V_1; S 60 ° E) banded when cross-cut by the discordant vein (V_2; N40 ° E) indicating a sinistral sense of movement (Boqueirão dos Cochos area; MG-R-208B).

Figure 3.41c Quartz-eye phyllonite comprised of a strongly sheared quartz vein (on the right top; see the arrow) in a mica-rich phyllonite matrix produced by shearing (N 60 ° E). The rock is a biotite-garnet gneiss and displays a mylonitic foliation and a prominent banding of micas alternating with quartz-feldspar-rich layers; this indicates a fromation by plastic deformation oriented parallel to the shear. (Boqueirão dos Cochos area).

3.7 RELATIONSHIPS BETWEEN THE SHEAR ZONES AND VEINING

Two types of shear-related gold-bearing quartz veins occur in Borborema Province: (i) those that lie within the shear zones (e.g São Francisco and Cachoeira de Minas mines and the deposits related to the fold belt in Itapetim District); and (ii) those that occur in close association with major shear zones (e.g. gold occurences hosted by competent rocks related to either granitoids or basement).

The relationship between the mineralized quartz veins and the deformation indicates that the mineralization and the development of the shear zones overlapped in time. Two phases of gold-bearing quartz vein emplacement were found: (i) the pre-syn shearing emplacement within the shear zones; and (ii) the syn-late shear emplacement in undeformed to moderately deformed granites (SLTG), but in close association with the major shear. The first type occurs in the fold belt environment and represents the first phase of mineralization, while the second type is related to the end of shearing and may represent a second phase of mineralization.

The mineralized areas within the shear are intensely deformed, characterised by mylonitic rocks (protomylonite to ultramyonite), and marked by shear fabric crenulation, cleavage, lineations, microfolds, shear bands and a C-S fabric. The geometrical features of the mineralized shear zones as described earlier in this chapter comprise: (i) internal features of the shear zones observable in hand specimen or thin section or; (ii) features visible in geological maps. The fabric of the minerals and the metamorphic assemblage characterise the shear as anastomosing zones of medium-grade deformation developed predominantly under a plastic regime (Ramsay, 1980), although some evidence of brittle deformation occasionally occurs. However, in polycrystalline aggregates under greenschist facies conditions different crystal phases may exhibit different mechanisms of deformation. For instance, feldspar may deform cataclastically whereas quartz exhibits intercrystalline plasticity. As a result quartz and micas deformed by crystal plastic flow (see Figs. 3.27 and 3.28) while feldspar deformed predominantly by microfracturing (Sibson, 1977). At temperatures in excess of 300° C, quartz begins to flow plastically, whereas feldspar remains brittle until about 450° C (Voll, 1976).

Characteristic features of shearing are very common, such as: (i) rotation of individual mineral grains (e.g. porphyroblasts and porphyroclasts of cordierite, garnet and K-feldspar); (ii) mineral stretching and alignment of quartz ribbons parallel to the regional shear direction; (iii) matrix produced by syntectonic, crystal-plastic processes, and annealed texture marked by the reduced grain-size and recovery due to mylonitisation; (iv) shear bands; and (v) C-S fabric. Where veins are hosted by competent rocks such as gneisses or granites little evidence of plastic deformation is present, but where the wall rocks are deformed (supracrustal domain) the veins are

invariably sub-parallel or parallel to the foliation. Evidence of recrystallisation is very common (e.g. Figs. 3.10 and 3.33). In many cases several major veins are hosted by the same shear zone (e.g. 3 in Cachoeira de Minas, and 2 in São Francisco). All of these veins can be defined as shear veins by the terminology of Ramsay and Huber (1983) and lie at a high angle to the direction of compression established in the shear zone.

The position of the veins within the shear zones classifies them as central shear type veins (Hodgson, 1989). Three sets of mineralised veins occur: (i) central and oblique shear fractures (Itapetim District associated with strik-slip shear zone; Fig. 3.31); (ii) extension veins (associated with the reverse faults in São Francisco, see Fig. 3.11, and Cachoeira de Minas mines; and (iii) conjugate-set extension veins, in Santo Aleixo area, Fig.3.37.

The mineralized quartz veins which developed in competent rocks in close association with major shear zones (gneiss and granitoid) are predominantly extension veins. Two types are present: (i) extensional veins characterised by a typical ribbon vein, developed in the early tectonic granite (e.g.Canafístula 'garimpo'); and (ii) extension veins filling fractures developed in syn- and late-tectonic granites that border the shear zone (e.g. Igarape Garapa and Cacimba Salgada). Veins are characterised by irregular masses of equigranualr grains, straight boundaries, and triple junctions. Undulose extinction is common (Figs. 3. 38b and 3. 39b).

The most common textures in the mineralized veins are ribbon layering and laminated textures. However, crustified orbicular textures are also present in all deposits although these can only be seen in doubly polished thin sections (Fig. 3.43 and 3.45b). Sometimes ribbon quartz veins are truncated against vein walls which appear to be sealed. The vein fabric is predominantly antiaxial and veins are filled with minerals with different composition from those in the wall rocks. The growth occurs by a process of crack-seal associated with a subsequent healing mechanism (see below), resulting in bands of minerals aligned parallel to the walls.

3.8 VEIN GROWTH PROCESSES

3.8.1 Introduction

Vein growth processes comprise two very important concepts (Cox *et al.*, 1986): (i) mobilisation and mass balance during deformation; and (ii) rock fracturing processes and their significance.

During metamorphic processes aqueous mass-transport mechanisms are associated

with dissolution and precipitation processes (Fyfe *et al.*, 1978; Kerrrich, 1978). The dissolution process involves a range of reactions. These may result in volume loss whilst some material is added or remains and crystallises as new phases (Beach, 1979; White and Johnston, 1981). Dissolution and mass loss are partly or wholly balanced by precipitation in a range of sites. Evidence of mass gain is the overgrowth on grains or the development of mineral-filled microfractures (Cox and Etheridge, 1982; 1983) which on a large scale produce the veins (Sibson, 1980).

Two types of vein growth may be recognised (Ramsay, 1980): (i) simple or narrow veins; (ii) and large or crack-seal veins. The process of simple vein growth involves a stage of fracture growth and opening associated with essentially continuous crystallization of phases. If the fluid pressure within the fluid-filled fracture is maintained at sufficiently high levels to keep the vein wall apart and the fluid remains supersaturated, the growth process will continue and forms the large veins with the development of all textures characteristic of open space growth. If the fluid pressure is not always maintained at sufficiently high levels to keep the fracture walls separated, or if the rate of mineral growth is faster than the rate of fracture-wall separation over a sufficient period, the vein will become sealed. Ramsay (1980) has demonstrated that vein growth is by an accretionary process involving numerous repeated increments of microcrack opening, followed by sealing due to crystallisation of material from solution. This mechanism, defined as *crack-seal*, most frequently occurs in rocks deformed at different metamorphic grades and where the stress-induced chemical transfer (pressure solution) of materials seems to be relatively common (Ramsay, 1980; Cox *et al.*, 1986). Crack-seal mechanisms occur when dissolved material is transported in one direction by infiltration process via the pore fluid, and subsequently precipitated on the fracture surface, eventually sealing the crack (Batzle and Simmons, 1976).

Subsequent to quartz vein growth tectonics induces elastic strain in the veins and provides conditions for fracture development. The principles of fracture generation related to vein development has been extensively discussed (Secor, 1968; Phillips, 1972; Sibson, 1981) and can be illustrated by a Mohr diagram (Cox *et al.*, 1986). The mechanism that brings about tensile, *hydraulic-extension-* fractures is intrinsically associated with high fluid pressure and consequently low effective stresses. There is evidence that the fluid phase is present during fracturing and that the mechanism can be initiated when the fluid pressure equals the tensile strength of the rock (Ramsay, 1980). Some of the basic results of fracture mechanics provide significant insights into how and why fractures develop and the controls on the distribution and orientations of veins. To form vein-type ore deposits the development of hydraulic fracture regime must have access to a large fluid volume, providing a high fluid/rock ratio (Cox *et al.*, 1986).

When new cracks are not being produced in rocks at elevated temperature and

pressure, macrofractures transport most of the fluid volume and seal relatively slowly, whereas microcracks or microfractures allow pervasive penetration of fluid into the rock mass but heal quickly (Brantley *et al.*, 1990). This mechanism, termed as *crack healing* is also an example of a sealed crack mechanism (Walther and Orville, 1982; Brantley *et al.*, 1990). Crack healing apparently involves the local transport of material by diffusion processes, predominantly in two directions, with exchange between adjacent rock-types through stagnant pore fluids as it reforms a fractured lattice or grain boundary (see Smith and Evans, 1984). Where the porosity has a nonequilibrium shape (e.g. cracklike), gradients in chemical potential due to surface tension will always exist and may result in crack healing (Brantley *et al.*, 1990). Crack healing is a high temperature (± 300°C) process which results in the reorganization of initially planar cracks into arrays (Smith and Evans, 1984) and the formation of secondary fluid inclusions (Hollister, 1981; Roedder, 1981).

3.8.2 Vein Growth in the Borborema Province

The tourmaline-quartz-bearing gold veins in Borborema Province are interpreted as the results of two mechanisms: crack-seal and crack healing. The crack-seal process is depicted in detail in Fig. 3.42.

The veins show characteristics of antiaxial vein growth. The most remarkable feature of these is displayed in the double polished sections, and consists of the presence of very regularly-oriented lines of solid inclusions, mostly consisting of tiny crystals of tourmaline arranged sub-parallel to the walls of the quartz vein (Fig. 3.44). These inclusion bands (Figs. 3.45a and 3.45b; see Ramsay, 1980) form an undulated surface parallel to the adjacent bands and produce a structure similar to ripple marks. The lines are arranged at distances of just 1 μm apart and usually are enriched in abundant and tiny (< 15 μm) fluid inclusions with a random distribution. Crustifed textures are particularly common and result in orbicular forms (Fig. 3.45b) consisting predominantly of tourmaline. It appears to have formed at relatively deep crustal levels (Hodgson, 1989), and is similar to textures noted in the gold veins of the Campbell and Dickenson mines of the Red Lake area of Ontario (MacGeehan and Hodgson, 1982). Other types of tourmaline texture also occur (tourmaline occurring as fibres, sintaxial overgrowths, and needles included in the porphyroclasts of K-feldspar) and this shows the complexity of the growth process. Kinked tourmaline crystals also occur (Fig. 3.43)

Later, extremely irregular microfractures (Fig. 3.46) are also common. From the observations of double-polished sections, fluid inclusions are aligned as trails along these microfractures and formed late in the development of the individual increments.

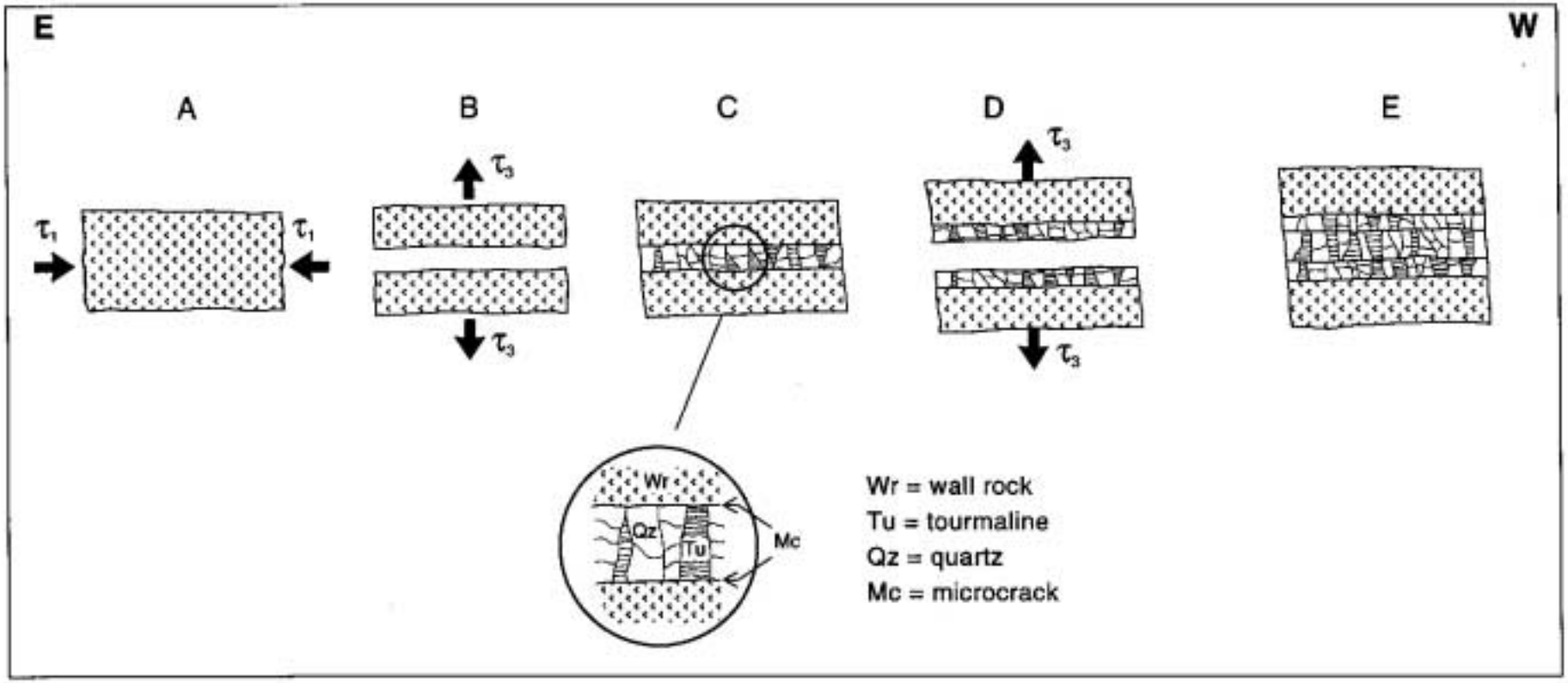

Figure 3.42 Sequence of events (A to E) in the development of typical ribbon tourmaline-bearing quartz vein in Canafistula 'garimpo' involved in fibre growth by a mechanism of crack-seal: (A) strain accumulation; (B) initial stage of hydraulic microfracture growth and opening to produce the release of strain, and providing the transport of mineral material such as quartz (Qz) and the development of inclusion bands consisting of solid material (tourmaline: Tu) into microcrack; (C) sealing of the microcrack and strain accumulation; (D) second stage of development of microcrack growth and opening with release of the strain; (E) development of syntaxial material on the microcrack wall producing the seal and forming a compound vein. Repeat of the crack-seal process may build up incremental vein structures.

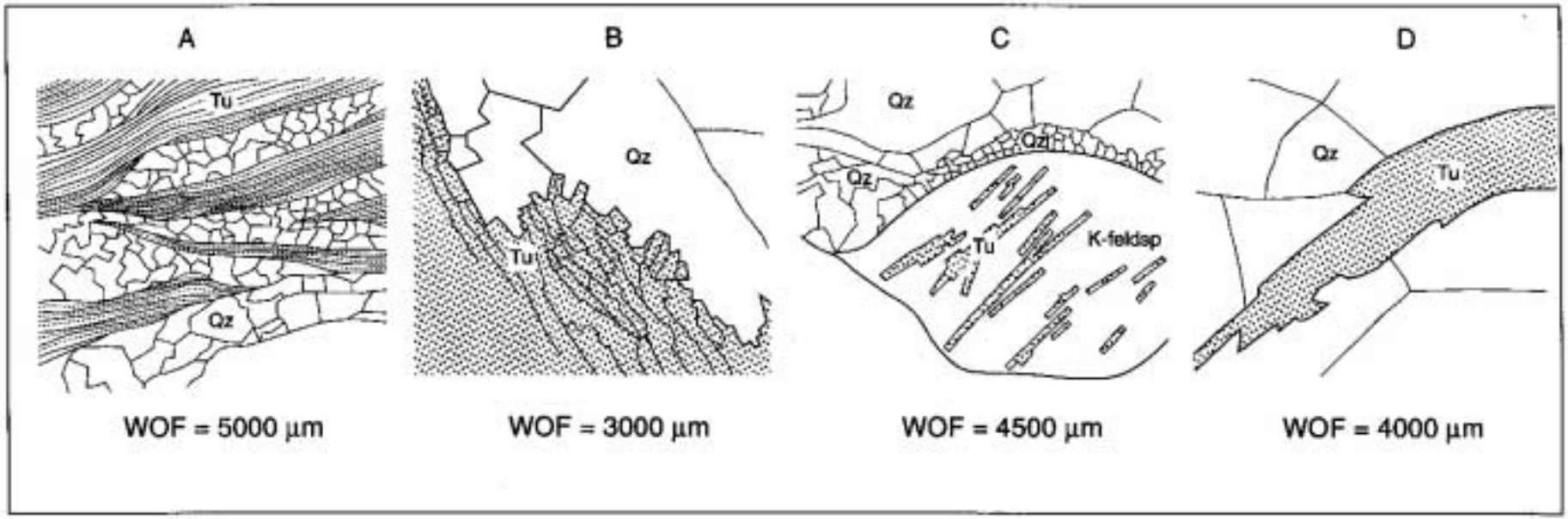

Figure 3.43 Sketches from photomicrographs of the tourmaline-bearing quartz vein showing the complexity of the growth process: (**A**) folded tourmaline fibres associated with medium-grained ribbons of quartz; (**B**) syntaxial tourmaline overgrowth; (**C**) needles of tourmaline as inclusions in porphyroclast of K-feldspar which occurs associated with ribbon quartz. Intense degree of deformation is shown: in (**C**) by two phases of quartz recrystallization consisting of very fine grains of quartz sourrounding porphyroclast of K-feldspar or by annealed texture showing by the medium-grained quartz ribbons; In (**D**) by a kinked tourmaline crystal. Plastic deformation (**A**) is suggested by the ribbons of quartz. Photomicrographs: MG-R-203 and MG-R-224D Canafistula 'garimpo'; WOF: (A) = 5000 µm ; (B) = 3000µm; (C) = 4500µm and (D) = 4500µm.

They usually occur cutting across both sutured grain quartz boundaries. The microfractures are invariable partially healed with fine trails of small secondary vapour inclusions, in association with chlorite, native gold and sulphides (Figs. 3.47 and 3.48). These microfractures display no consistent orientation within the samples, however they commonly occur as conjugate-sets. They are interpreted as healed cracks, developed by a crack healing process (Smith and Evans, 1984). Bouiller and Robert (1992) pointed out that these microcracks occur in the σ_1-σ_2 plane, an interpretation consistent with the high angle that these microfractures form with the vein wall (see Fig. 3.44). However, these microfractures suggest subhorizontal compression has produced extensional veins. Such a range of deformation patterns is consistent with the abundant refolded and boudinaged quartz veins.

The range of characteristic crack healing microstructures discussed above indicates that the growth of a typical 0.5 m thick vein involves several hundred crack healing growth increments. The association of the gold with crack healing highlights the late nature of the gold mineralization in Borborema Province.

3.9 VEIN DEVELOPMENT RELATED TO FLUID DYNAMICS

Eisenlohr *et al.*'s (1989) study of the relationship between the crustal-scale shear zones and the gold mineralization in Western Australia showed that the fluid originated from a deep source. It followed a complex path, re-equilibrated with different lithologies (granitoids and supracrustal rocks), and mixed with metamorphic fluid during migration to higher crustal levels. The multi-source origin and continous re-equilibration of the fluid with the crustal rocks is reflected in the diverse isotopic and geochemical signature of the gold deposits. In a large crustal-scale shear-system the larger first-order shear zones would be expected to be the regions of greatest fluid flow and highest fluid/rock ratios. However, there is growing evidence that in shear zone systems the second-order shears represent the best sites for mineralization, as shown in the lode-gold deposits of Western Australia (Eisenlohr *et al.*, 1989). These authors invoked the metamorphic model of Groves and Phillips (1987) to attribute the highest fluid/rock ratios to the abundance of fluids from the greenstones rocks associated with the second-order structures, whereas the first-order shears trapped the mantle and the deeper source fluids (magmatic model of Viljoen, 1984).

Temperature differences between the first and the second-order structures could provide a mechanism for selective gold deposition. Temperature has a strong influence on the precipitation of gold from a fluid (Groves *et al.*, 1984; Groves and Phillips, 1987) and the first-order shear zones are at higher temperatures than the second-order shears. If this is correct then gold will be more soluble in fluids of the main zones than


Figure 3.44

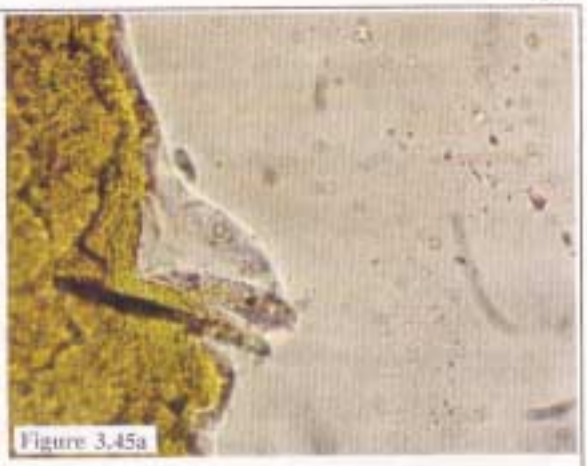
Figure 3.45a

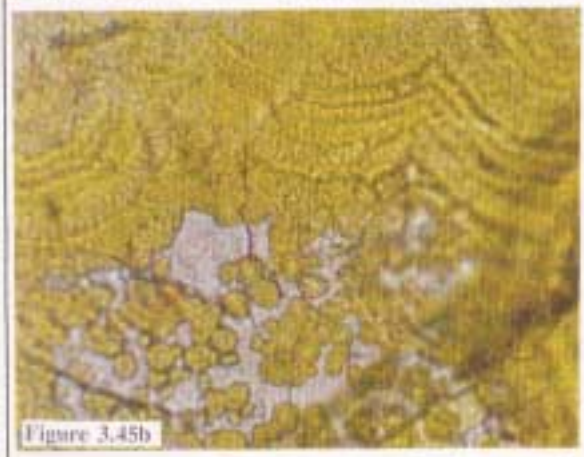
Figure 3.45b


Figure 3.46

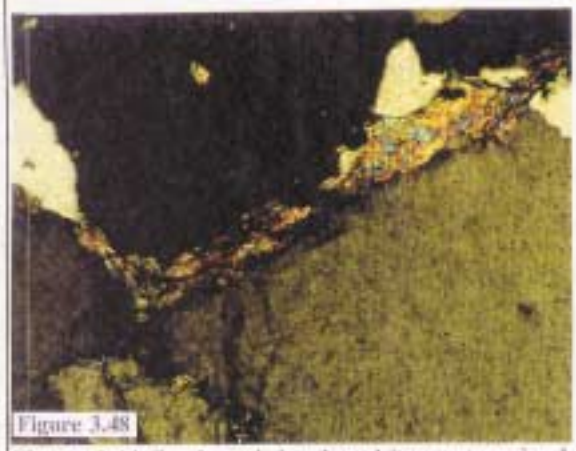
Figure 3.48

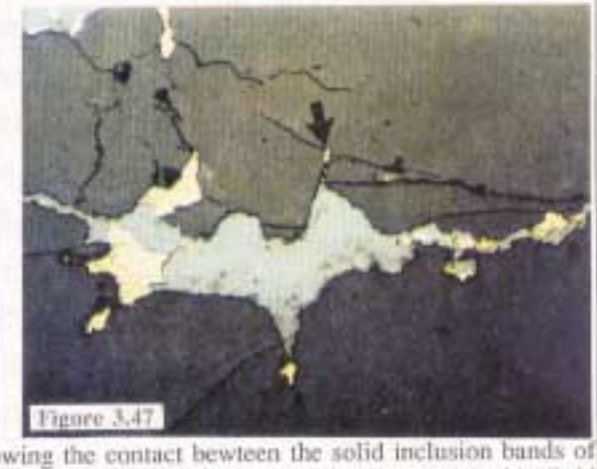
Figure 3.47

Figure 3.44 Crack-seal developed in quartz vein showing the contact bewteen the solid inclusion bands of tourmaline oriented subparallel to the crack (left). Note (on the right side) the crack healing enriched in fluid inclusions oriented as trails forming an high angle with the crack seals (PPL; TL; WOF = 500 µm; MG-R-229C, São Francisco mine).

Figure 3.45a Crack-seal showing a crack partially sealed with tourmaline (on the left side) oriented subparallel to the vein wall . Note on the right side the random enrichment of fluid inclusions (PLL; TL.; WOF = 500 µm; MG-R-224, Cachoeira de Minas mine).

Figure 3.45b Detail of the Fig. 3.45a displaying crustifed orbicular texture of tourmaline developed along the solid inclusion bands in quartz-tourmaline vein (PPL; TL; WOF = 400 µm; MG-R-204I Canafistula 'garimpo').

Figure 3.46 Crack healing (on the centre) showing the reorganization of planar cracks into arrays with formation and enrichment in secondary fluid inclusions (PPL; TL; WOF = 500 µm; MG-R-155, Itapetim Distric, Sertãozinho)

Figure 3.47 Quartz vein showing the enrichment in chlorite and opaque minerals developed along the crack healing. (XPL; TL; WOF= 750 µm; MG-T-114, Itapetim, Pimenteiras area).

Figure 3.48 Crack healing developed in quartz vein filled by iron oxide (grey colour); sulphides (white-yellow: pyrite and chalcopyrite) and gold (yellow; see the arrows). (XPL; RL.; WOF = 400 µm; MG-R-155A, Itapetim , Sertãozinho area).

in the subsidiary shears, and thus the latter will represent more favourable sites for gold precipitation.

As discussed earlier, the mineralized veins in Borborema Province are structurally controlled by high-angle reverse faults or high-angle strike-slip shear zones. According to Anderson's (1951) classic model these structures would be expected. In a compressive stress field the expectation from Coulomb failure theory is that faults should form along planes that contain the σ_2 axis and are orientated at 25°-30° to the maximum principle compression σ_1. Combined with the reasonable assumption that principal stress trajectories close to the Earth's surface will tend to be either subvertical or subhorizontal, thrust structures should dip at an angle below 45° in a region of compression. This suggests that high-angle thrusts in the area were either the result of the reactivation of pre-existing structures or the rotation of Anderson's-type thrusts to higher angles by increasing shortening.

Based on the 'fault-valve model' (Sibson *et al.*, 1988) these reactivated faults should ensure high fluid/rock ratios around the veins. Under supralithostatic fluid pressures, faulting will likely lead to nearly total relief of shear stress, and to a marked reduction in the component of normal stress acting across the faults. Thus, in the low deviatoric stress state following failure, geopressured fluids will tend to drain rapidly into the permeable rupture zones. As the faults may act as fluid-activated 'valves' they promote large cyclical fluctuations in fluid pressure from supralithostatic to hydrostatic values. Furthermore, abrupt reductions in the fluid pressure may have a strong effect on the aqueous solubility of the quartz (Walter and Helgeson, 1977) and are likely to play an important role in mineral precipitation (Helgeson and Lichtner, 1987).

It is suggested that high fluid pressure gradients were established at each crack-healing cycle resulting in intensive change in the physical properties of the rocks, such as pore geometry and also porosity (Walsh, 1965). The interruption of interconnected pore space at depth can have a dramatic impact on the effective state of stress through the pore fluid pressure providing enhanced permeability, and can result in the developement of sites in which material is deposited from solution to form vein-type ore deposits (Brace, 1972). The quartz vein textures suggests incremental deposition, the result of the fluid pervading the deformed zone and controlling the strain process, by moving the solution from highly stressed areas to the sites of deposition.

3.10 CONCLUSION

The Borborema Province is a medium to high-metamorphic-grade zone cut by transcurrent, predominantly plastic or plastic-brittle, shear zones. The E-W-trend shear zones, particularly those adjacent to synkinematic granitoids (Leterrier *et al.*, 1990), are

the first-order shear zones, while the N to NE-trending shears are second-order or subsidiary shear zones (see Vauchez *et al.*, 1989).

The first-order shear zones are largely unmineralized, whereas the second-order structures host the major gold deposits (see Fig. 3.1). Rarely, some deposits could occur at the contact between the first and second order shears (e.g. Itajubatibe deposit); similar situation occurs in Leonora area, Western Australia (Skwarnecki, 1987) and in the Norseman-Wiluna Belt, Australia (Eisenlohr *et al.*, 1989). This can be explained by the physico-chemical gradients between the the first- and second-order structures, which cause the migration (infiltration) of the fluid and/or selective transport (diffusion) of the gold within fluids into the second-order structures. In Borborema Province the subsidiaries shears are plastic to brittle-plastic, while the first order structures associated with granitoids are predominantly more plastic.

The secondary shear structures are characterised by:

(i) Shear deformation in a predominantly plastic regime, although evidence of plastic-semi-brittle deformation also occurs.

(ii) The metamorphic assemblage and the fabric of the minerals suggest temperature and pressure conditions at or below the amphibolite/sub-greenschist metamorphic boundary and subsequent retrogressive metamorphism.

(iii) Predominance of mylonitic rocks and schists, marked by anastomosing geometry with occasional development of conjugate shears.

(iv) Sense of shear movement has the same sense as the first-order shears (dextral sense; Seridó and Piancó/Alto Brígida fold belts) or opposite (sinistral; Pajeú/Paraíba Belt).

The gold-bearing quartz veins are characterised by the following structure and textural features:

(i) The mineralized quartz veins occur in all geotectonic units: fold belts, massifs or plutonic rocks of different compositions (acid to less acidic) and ages (Trans-Amazonian and Brasiliano granitoids).

(ii) The mineralization occurs in extensional veins either within the shear zones, on the limbs of folds commonly associated with thrust faults and strik-slip shear zones (fold belts), or in close association with major shear zones (granitoids).

(iii) The relationship between the mineralized quartz veins and the deformation indicates that the deposits that lie within the shears are syn-pre shearing. This suggests that the mineralization and the shear development overlapped in time; the deposits in close association with major shear are syn-post shearing, and may be associated with the end of the shearing process.

(iv) The form of the mineralization is laminated with quartz ribbons and crustiform textures filling the veins.

(v) The texture of the veins suggests that filling and deformation were synchronous under conditions of low mean stress, due to high fluid pressure. The association of the gold with the subsequent crack healing highlights the late nature of the gold mineralization in Borborema Province.

From the exploration viewpoint it is concluded that in Borborema Province the gold-bearing quartz veins are predominantly hosted by the subsidiary (N to NE-trending) shear zones and that economic concentrations commonly occur in thrust faults on the limbs of folds.

CHAPTER 4 PETROLOGY, GEOCHEMISTRY AND METAMORPHIC GRADE OF THE HOST ROCKS

4.1 INTRODUCTION

On a world and craton scale all lithologies in Archaean greenstone belts may be mineralized, and at the mine scale several different rock-types may host ecomonic gold mineralization (Groves and Foster, 1991). However, mafic volcanics associated with intrusive rocks are by far the most important host rocks to gold mineralization in various cratonic areas (e.g. Zimbabwe Craton; Foster, 1985; Yilgarn Block, Australia; Groves and Phillips, 1987; India; Hamilton and Hodgson, 1986; Quardilátero Ferrífero, Brazil; Ladeira, 1985; and Canadian Shield; Colvine *et al.*, 1988). Another important host rock of gold deposits is the banded iron formation (BIF) where the mafic rock is again Fe-rich. Intrusion-related vein gold deposits have been recently highlighted by several studies (Colvine *et al.*, 1988; Muller and Groves, 1993). Despite debate about the nature of the host lithologies of gold deposits, most discussion centres on the definition of their precise tectonic setting.

Gold-bearing quartz veins in Borborema Province are characterised by a diversity of host-rock lithologies. Gold mineralization is found in rock types ranging from meta-sedimentary to intermediate and mafic volcanic sequences, and plutons of different ages and compositions.

This chapter deals with the petrography and geochemistry of the rocks that are host to the gold. These comprise granites and supracrustal rocks (gneisses, schists and amphibolite) and Archaean amphibolite. Consideration of the likely geotectonic setting for these rocks is also presented. The last section addresses the P-T conditions of the pre-mineralization metamorphic events.

4.2 METHODS OF STUDY

The methods of study comprised geochemical analysis (XRF) of major and trace elements and petrographic studies under the reflected light microscope. Analysis of rock forming minerals was carried out using the electron microprobe. Details concerning the analytical tecniques are given in Appendices A4.1, 4.1a, 4.1b, 4.2, and A4.10.

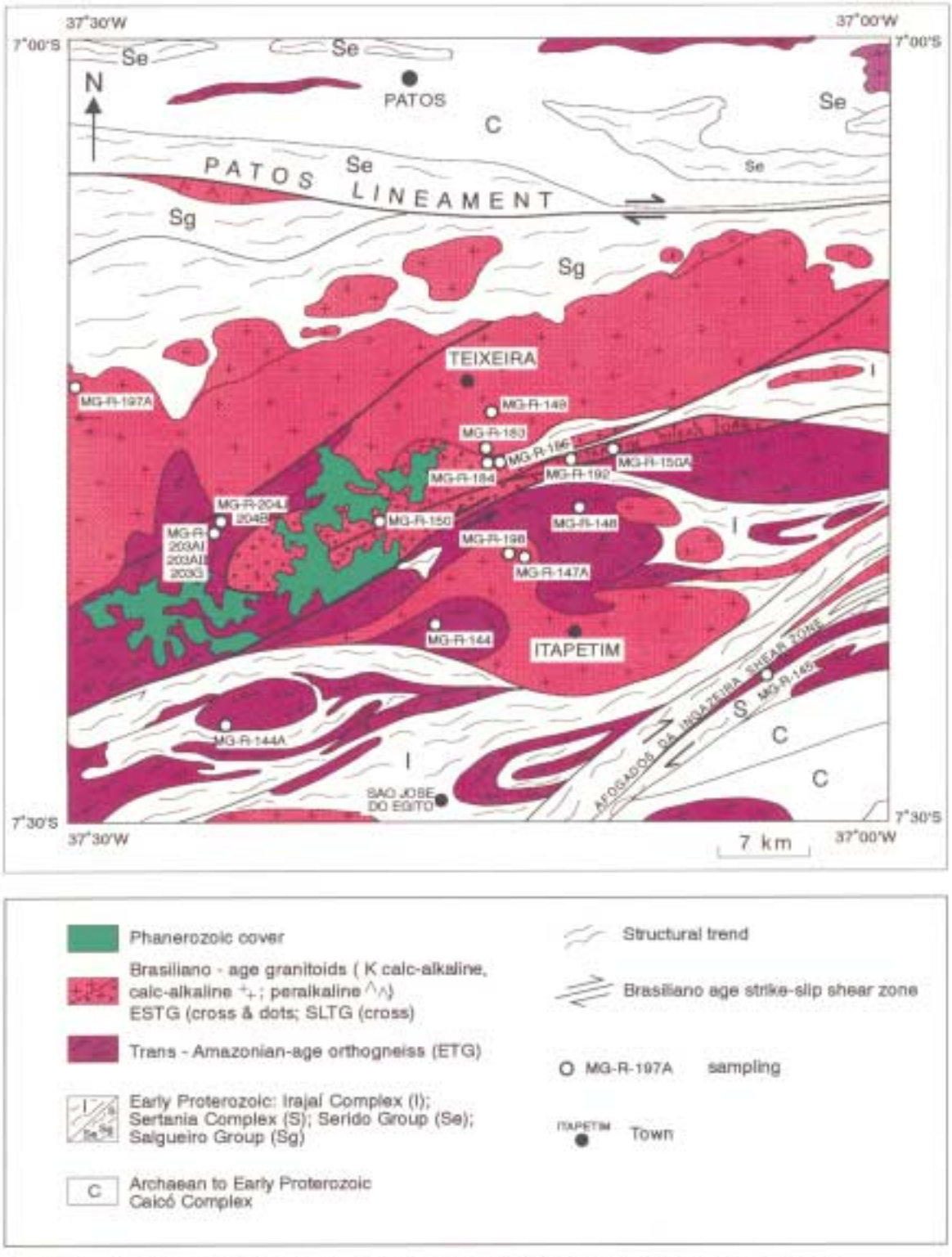

Figure 4.1 Geological map of the Itapetim area showing the location of the granite samples

4.3 GRANITOID ROCKS

4.3.1 Introduction

Granitoids, like all other rocks, represent the final product of many past physical and chemical processes. Granitic intrusions, throughout their emplacement and cooling history have tried to achieve mechanical and chemical equilibrium with their surroundings into which they were intruded. However, most granitoids failed to reach this equilibrium and as a result such features as disequilibrium textures and mineral assemblages, enclaves and fluid inclusions, provide constraints on the granite body's history. Granites play a important role in crustal evolution, either by recycling of material within the crust, or by production of new crust from the mantle (Clarke, 1992) and during these processes many granitoid rocks generate associated mineralization. The study of granitoids and their mechanisms of emplacement can be used to elucidate the source and the concentration of many metals, including the gold (see Sillitoe, 1991; Sawkins, 1990).

The structural relationships suggest a close association between the granites and gold-bearing quartz veins in Borborema Province. The mineralized veins occur either in supracrustals cross-cut by granitoids (Seridó and Piancó/Alto Brigída Fold Belts) or actually hosted by granites (Itapetim gold district). Quartz veins with gold were found in two types of granites: (i) Trans-Amazonian granites (ETG; early tectonic granites); and (ii) Brasiliano granites, comprising early-syn- tectonic granites (ESTG); and syn- and late-tectonic granites (SLTG).

Nineteen samples of granites which host mineralization in the Itapetim gold district were collected (see distribution in Fig. 4 1) and analysed. These comprised: nine ETG.; five ESTG; and five SLTG. The chemical data are shown in Appendix A4.3. Further information concerning the sample locations are given in Appendix A1.1.

Althought classifications of granitoid rocks have recently been challenged (Clarke,1992), an attempt was made to distinguish and classify the various types of granites hosting the gold mineralization in Borborema Province. A review of the main petrogenetic classifications of graniotids (Barbarin, 1990) indicates that most separate alkaline/peralkaline granitoids from calc-alkaline/aluminous and peraluminous granitoids. In addition, granite classification can be related to tectonics. Several authors (Streckeisen, 1974; Martin and Piwinski, 1972; Pearce *et al.*, 1984; Picher, 1983; 1987; Lameyre, 1988) have however commented that the source material for the melting process might have more effect on the final product than the tectonic setting. One clear example of this is the 'A'-type (anorogenic) granites. Clarke (1992) points out that A-type granites might just as well stand for ambiguous, since highly evolved I-type granite (implying source rocks of mafic to intermediate igneous composition or

infracrustal derivation) can have a very similar mineralogy and chemistry to anorogenic types. However, the one point common to most classifications is the recognition of three groups of granites based on the source: crustal, mantle derived or a mixture of the two.

During this study the term granitoid is used in the same context as by Clarke (1990) to refer to the whole family of granitic rocks from alkali feldspar granite to tonalite.

4.3.2 Mineralogical Composition

The CIPW normative feldspar proportions for the 19 samples (see Appendix A4.4) were plotted in the Ab-An-Or diagram, the distribution fixing these granitoids (ETG, ESTG and SLTG) in the granite field. However, some samples of the SLTG plot in the quartz-monzonite field, using the boundaries of O'Connor (1965; Fig. 4.2).

The distribution of the CIPW values in the QAP diagram (Streckeisen, 1976; see Fig. 4.3) plot predominantly in the field of alkali feldspar granite, although some samples of SLTG show a small scatter and plot in the syenite and granite field boundaries. The use of normative proportions in the QAP diagram will result in the plotted positions being displaced towards the alkali feldspar apex, because the normative contents of albite component were treated as modal alkali feldspar. According to Streckeisen (1976), the Itapetim plutons (ETG; ESTG ; and SLTG) are predominantly alkali felspar granites, althought syenogranites and quartz- monzonite occur in the SLTG suite.

4.3.3 Mineral Assemblage and Texture

Determination of the mineral assemblages using a petrographic microscope enabled the characterisation of the following mineral associations for each type of granitoid:

(i) The ETG contains alkali feldspar that occurs as porphyroclasts of microcline (4 to 5 cm length) disseminated in a matrix of quartz and plagioclase (oligoclase-andesine). The alkali feldspar sometimes has microperthitic texture and is altered to sericite and muscovite (see Fig. 4.4a). The rock has undergone a pronounced segregation into quartz-rich and biotite-rich layers, which form coarse bands. The fabric has been subsequently flattened to produce a new fabric. Hornblende is very rare although it is the only amphibole present. Biotite is altered to muscovite, chlorite, epidote and carbonate. Zircon, apatite, fluorite, garnet, tourmaline, magnetite, titanite and allanite occur as accessory minerals.

(ii) The ESTG shows intense deformation that has disrupted the original K-

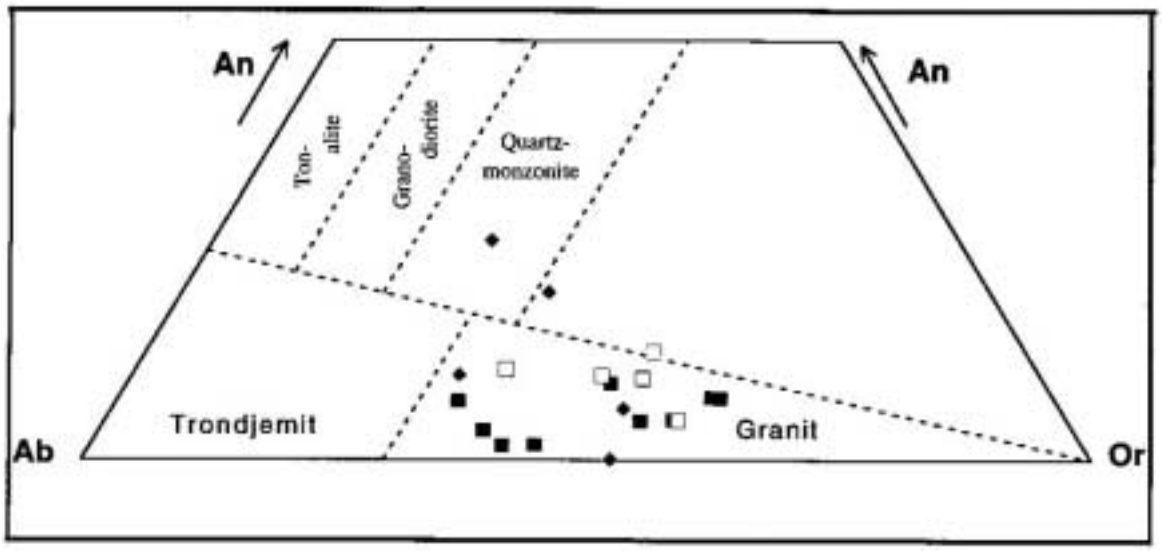

Figure 4.2 CIPW normative feldspar proportions for ETG (filled squares), ESTG (open squares) and SLTG. Boundaries follow the classification of O'Connor (1965).

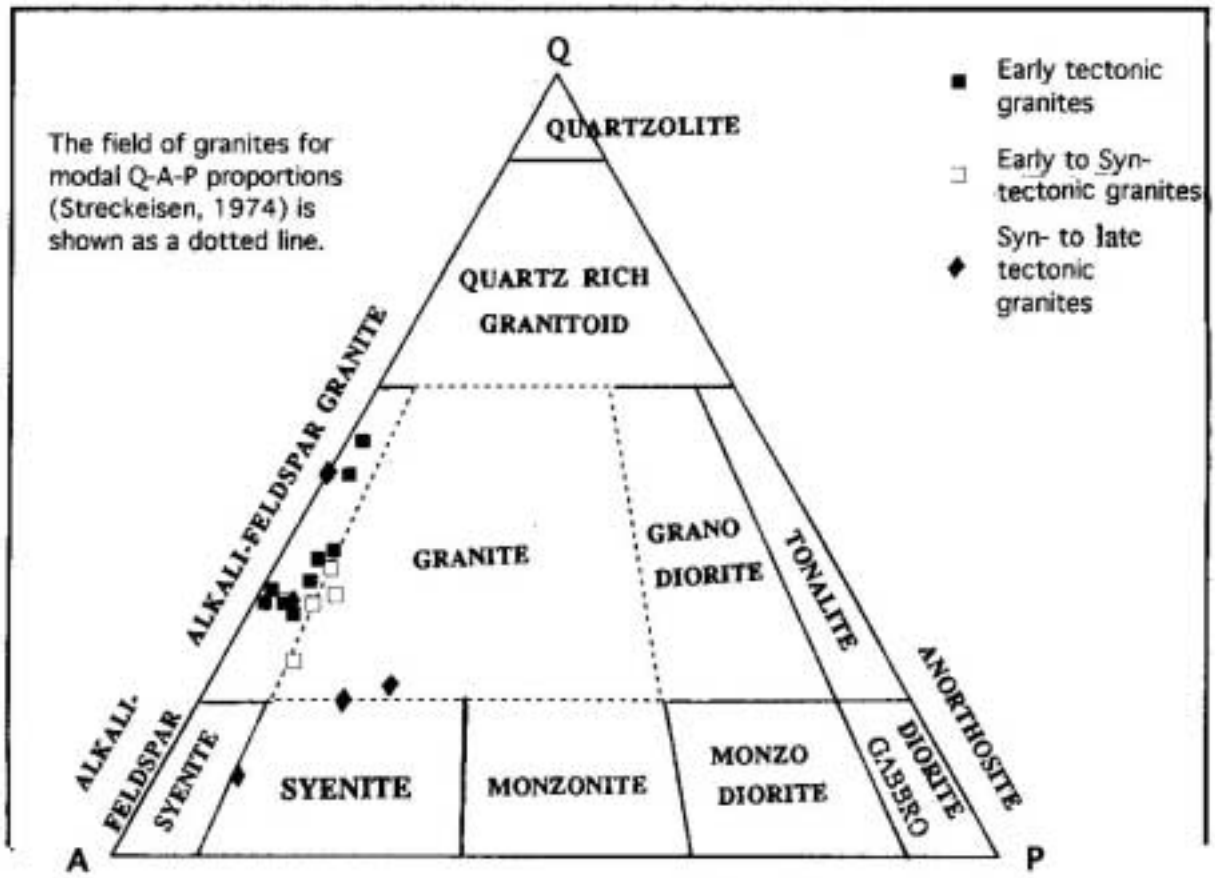

Figure 4.3 CIPW normative quartz-(orthoclase+albite)-anorthite proportions for granites. Note that the use of normative proportions will result in the plotted positions being displaced towards the alkali felpdspar apex relative to modal values due to the albite component being treated as alkali feldspar.
Symbols are: A = alkali feldspar (orthoclase + albite); Q = quartz; P = anorthite.

feldspar phenocrysts to produce porphyroclasts with patchy extinction and fracturing (Fig. 4.4b). The remaining texture of the granite has almost been destroyed. Quartz occurs as layers, and is surrounded by very fine segregations of biotite and muscovite. Plagioclase is rare and its association with muscovite suggests that the deformation may be associated with metasomatism, plagioclase breakdown and mica growth. Titanite, apatite, epidote, zircon, garnet, allanite and magnetite occur as accessory minerals. Chlorite and sericite indicate retrogressive metamorphic processes.

(iii) The SLTG shows a xenomorphic, granular texture (Fig. 4.4c). The rock contains plagioclase (oligoclase-andesine), microcline, quartz, biotite and hornblende (blue to dark green pleocroism; see Fig. 4.4d). Microcline occurs either as isolated grains or as reaction rims between plagioclase and K-feldspar. Inclusions of biotite, hornblende and myrmekitic intergrowths are common in microcline. The accessory minerals are: titanite (Fig. 4.4d), apatite, zircon, epidote, metamict allanite, carbonate and fluorite. Plagioclase is typically zoned, with myrmekitic intergrowths; it is also sassuritized.

The occurence of plagioclase divides the granites into two types (Clarke, 1992): (i) hypersolvus granites (ETG), where plagioclase is present as perthitic intergrowths within alkali feldpsar and suggesting crystallisation from a hot magma low in volatiles at ≈ 900 °C; and (ii) subslovus granites (ESTG and SLTG) where plagioclase is present as zoned grains, inferring higher water pressure and shallow depths of crystallisation.

A summary of petrographic information about the Borborema granitoids is shown in Table 4.1.

4.3.4 Chemical Composition

A close relationships between mineralogy and chemistry can be used to classify the granitoids based on the concept of alumina-saturation index (ASI; Shand, 1947). This classification is based on the range from < 1 to > 1 of the ratio A/CNK (molar $[Al_2O_3 / \{CaO + Na_2O + K_2O\}]$) and divides the granitoids into: peraluminous (A/CNK > 1); metaluminous (A/CNK < 1; A > NK); and peralkaline (A/CNK < 1; A < NK).

According to Shand's (1947; Fig. 4.6) classification peraluminous and very peralumionus granitoids were identified in all suites. The ETG are strongly peraluminous with some samples very peraluminous; the ESTG granitoids are dominantly peralumionus, whereas the SLTG are characterised by the dominance of metaluminous granitoids (see Table 4.2).

This classification has very precise chemical limits considering that the A/CNK

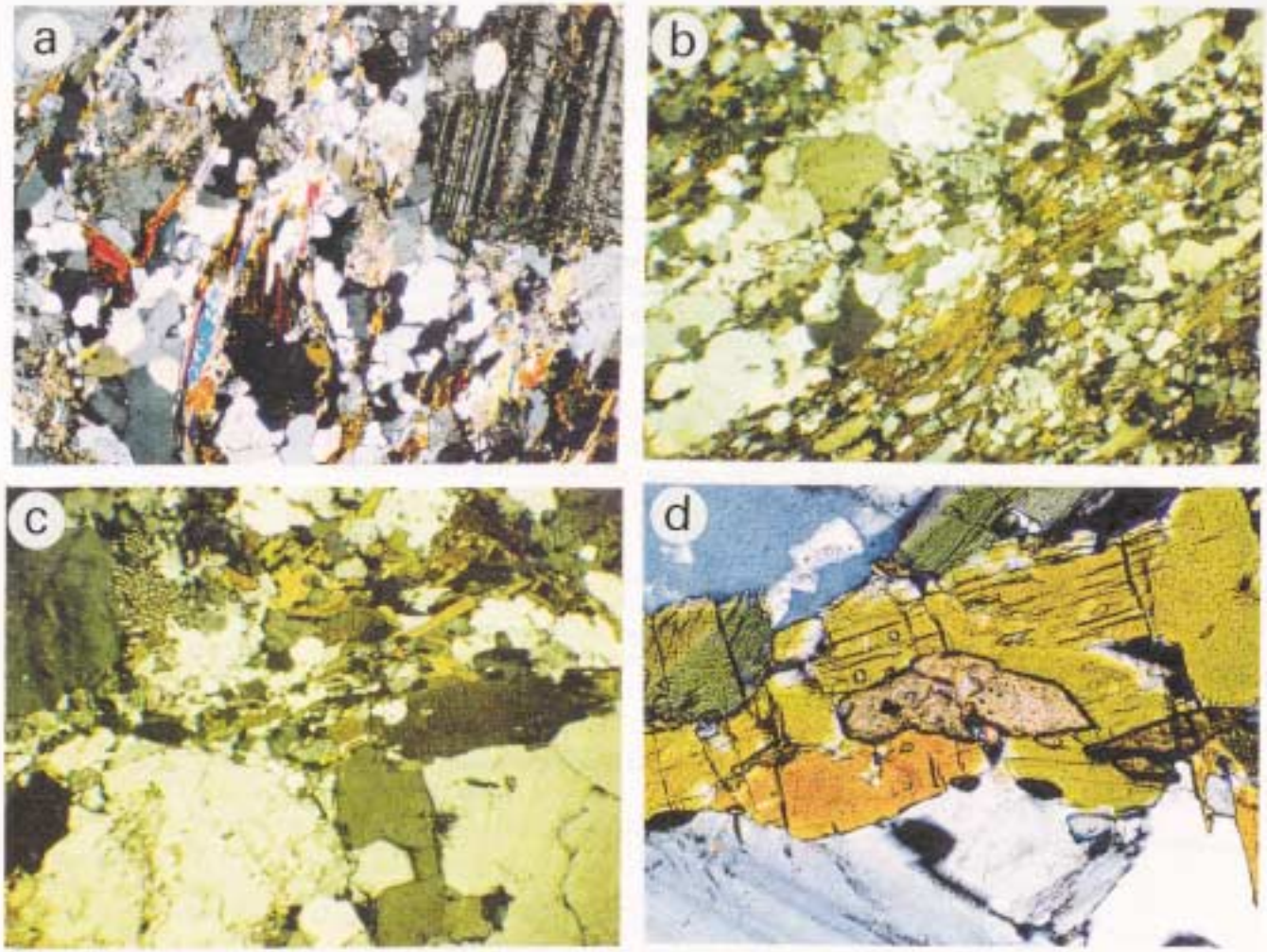

Figure 4.4 a Granitic biotitic orthogneiss (ETG) with medium to coarse texture. Feldspar (oligoclase-andesine) forms porhpyroclasts in a matrix consisting of quartz, muscovite and biotite. Note the saussuritization of the feldspar. The quartz has undergone extensive syntectonic recystallisation. The remaining texture of the granite is almost destroyed; a new fabric shows remarkable parallelism of the ribbons quartz and porhyroclast of feldspar surrounded by mica. Muscovite may be in part metasomatic in origin. (XPL.; TL; WOF = 2500 µm; MG-R-148, SE of Piedade dam, Itapetim District, central domain).

Figure 4.4b Granite mylonite (ESTG) showing intense deformation. The original texture was completely destroyed and a new mylonitic texture is developed. Quartz occurs in recrystallised layers with patchy extintion, separated by segregation of very fine mica (biotite and minor muscovite). Plagioclase is rare and with the presence of muscovite suggests that the deformation has been accompanied by metasomatism. (XPL.; TL; WOF = 4500 µm; MG-R-186, Riacho Verde area).

Figure 4.4c Granite protomylonite (SLTG), weakly mylonitized and formed mainly of quartz, feldspar and biotite. The rock is relatively undeformed and still retains a superficial igneous appearance. Most of the K-feldspar porphyroclast forms a myrmekitic intergrowth with quartz (XPL.; TL; WOF = 4500 µm; MG-R-198 Cacimba Salgada area).

Figure 4.4d Hornblende granite (SLTG) showing granular texture, formed mainly of quartz, feldspar, hornblende and biotite. Most of the feldspar is K-feldspar although it does not show microcline-type twinning in this figure. The rock shows the original igneous texture to be well preserved without evidence of deformation. In the center, a euhedral crystal of titanite occurs as an accessory phase (XPL.; TL; WOF = 1500 µm; MG-R-149, Taiuçu).

Table 4.1

Description of Granitoids from the Borborema Province: Central Domain

Age	Structural Relationship	Mineralogy Features	Petrographic Classification	Chemical Classification	Data Source
Trans-Amazonian	ETG	K-feldsp. phenocrysts with microperthitic texture and forms porphyroclasts; plag. (olig.-andes.); qz.; horn.; biot. Altered minerals: epid.; musc.; ser.; ch.; Acessory minerals: zr.; apat.; flu.; gar.; tu.; mg.; tit.; allan.	Augen gneiss; granitic orthogneiss; rare tonalite and granodiorite	Predominantly tholeiitic and peraluminous	Scheid and Ferreira, 1991; This study
Brasiliano	ESTG	Predominance of porphyroclasts of K-feldsp.; qz.; biot., plag., horn. Altered minerals: epid.; musc.; ser.; ch. Acessory minerals: zr.; apat.; flu.; gar.; tu.; mg.; tit.; allan.	Gabro-diorite; tonalite to qz.-monzonite Monzogranites and qz. monzonite Biot. granite and two-mica leucogranite	Shoshonitic affinity, K calc-alkaline and calc-alkaline Peraluminous and metaluminous	Leterrier et al., 1990 Scheid and Ferreira, 1991; This study
Brasiliano	SLTG	Microcl.; horn.; qz.; biot.; epid.; musc.; mg.; tit.; zr. Plag.; horn.; biot.; qz.; epid.; tit.; all.; ilm. Plag.; qz.; biot., horn.; zr.; all.; tit.; mg.; flu. Microcl.; aegir., qz., biot.; k-feldsp.;horn.; mg.	Tonalite to granodiorite ('Serrite-type'*) Granodiorite to tonalite ('Conceição-type'*) Porphyritic qz.-diorite ('Itaporanga-type'*) Syenite to qz. syenite ('Catingueira-type'*: saturated or 'Triunfo-type'*: oversaturated)	Trondhjemite; ilmenite series Calc-alkaline; ilmenite series K calc-alkaline; ilmenite series Peralkaline; magnetite series	Sial, 1986 Ferreira and Sial, 1986; Leterrier et al., 1990 Scheid and Ferreira, 1991 This study
Brasiliano	LTG	Mineralogy typical of the pegmatite veins (Li, Be, B mineralization)	Pegmatitic veins		

Observations:

* = local terminology

For further information see List of Abbreviations

composition is governed in part by the source rock composition (the primary magma). However, changes in the amount of alumina and alkalis lead to a spectrum of granites.

4.3.5 Geochemistry

The Harker variation diagrams (SiO_2 against some other elements; see Fig. 4.5) show that the ETG have a higher range in SiO_2 contents and lower values in Al_2O_3 (Fig. 4.5a) and CaO (Fig. 4.5d) than the other groups. The ESTG and the SLTG have low SiO_2 and high CaO values. No appreciable difference was found in the values of Fe_2O_3 (Fig. 4.5b); Na_2O (Fig. 4.5f) and TiO_2 (Fig. 4.5g) for the three granitoid types. The distributions of Al_2O_3, CaO, and MnO shows a large scatter and an inverse correlation between these elements and SiO_2 for all suites appears superficially consistent with differentiation processes. However, the trend for increasing Si correlates with increasing age, and the oldest granites appear to be the most evolved. Thus the gross chemistry of the granites must be controlled by processes other than differentiation, probably the nature of the source rocks.

Collins (1982) and White *et al.* (1990) point out that Ga/Al ratios > 3.0 are diagnostic of A-type (extension) granites. However, to use high Ga/Al ratios and also high Zr (about 2 x that of 'normal' S- and I-types) as an indicator of A-type granites, Ba and Sr contents must also be high and Rb relatively low, to screen out other highly evolved types. Zr contents are also high in A-type granites (> 400 ppm compared to an average of 240 and 38 ppm for 'normal' and 'fractionated' S-types), as with Nb, which is usually < 20 ppm in other types (White, 1990). Based on these concepts, the highest Ga/Al values in the Itapetim granitoids were found in the Brasiliano granites (SLTG and ESTG; Fig. 4.7), and two just plot in the A-type field.

The Rb against Sr diagrams (Figs. 4.8 and 4.9) show that some of the ETG and ESTG have Rb/Sr ratios of between 1 to 10, suggesting that they have undergone some fractionation. However, none of them are highly fractionated (fractionated granites have Rb/Sr ratios up to 3000). The SLTG shows the lowest ratios (1 to 0.01). The Cordilleran 'evolved' granites (Newberry *et al,* 1990) have Rb/Sr > 10. These are likely to be much more fractionated than the Itapetim plutons. The range in ASI (aluminium saturation index) suggests that the ESTG and ETG are fractionated, while the SLTG are less fractionated (Figs. 4.6 and 4.8). These results confirm the evidence from the Harker diagrams.

With an increasing amount of crystal-liquid or other fractionation processes acting on a magma, the Rb content of the magma will increase and Ba and Sr will decrease. Potassium contents will also increase in a residual melt with plagioclase crystallization, so the K/Rb and K/Ba ratios may provide some information about the evolution of the

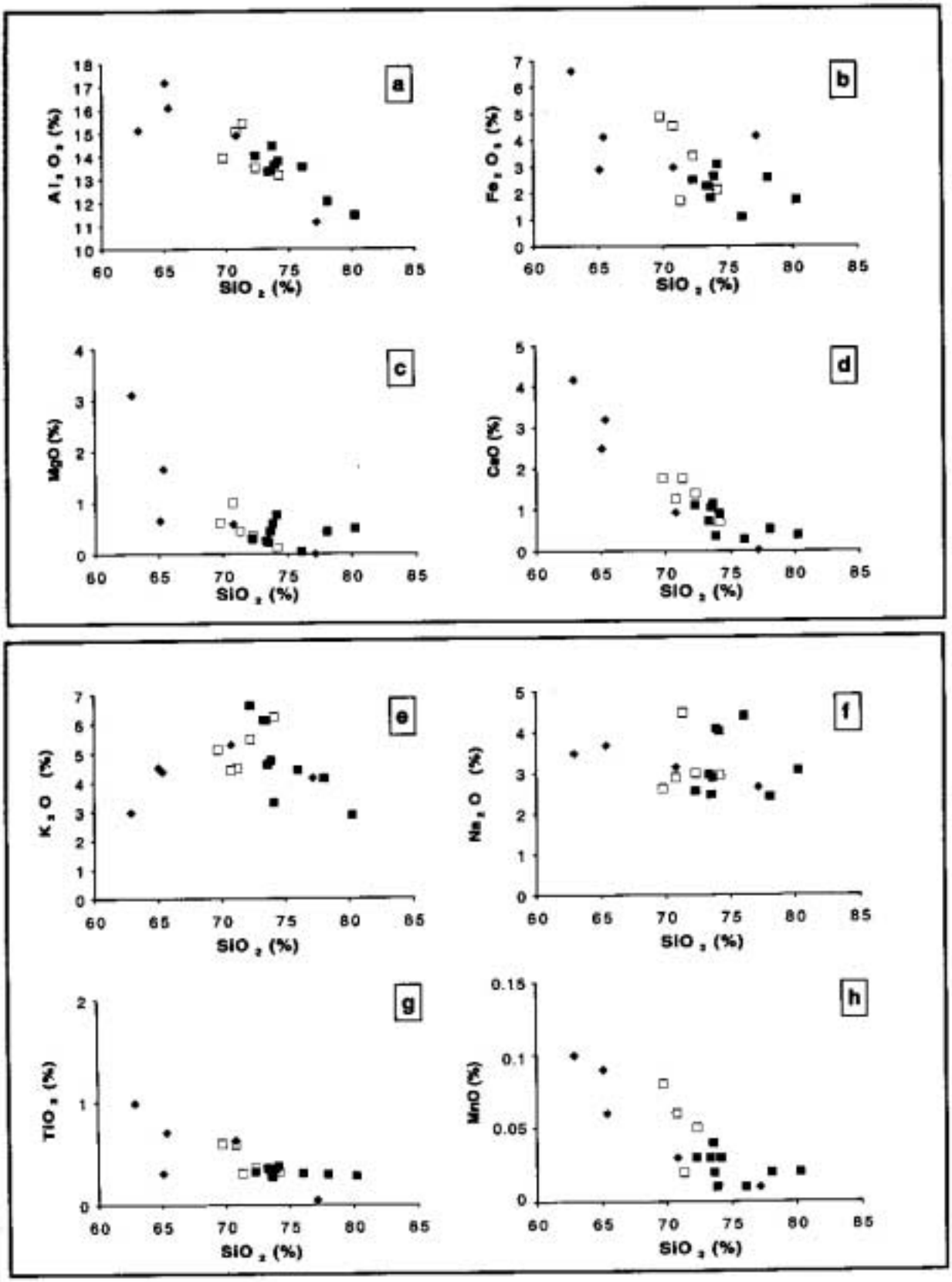

Figure 4.5 Major element contents of granites (ETG: filled squares; ESTG: open squares; and SLTG: filled diamonds) plotted as Harker-type diagrams (from a to h). Note the negative correlation between: in (a) SiO_2 and Al_2O_3; in (d) SiO_2 and CaO; and in (g) SiO_2 and TiO_2. These diagrams also show low values in (a) Al_2O_3 and in (d) CaO for the ETG (filled squares); and high values of K_2O (e) and Na_2O (f) for all granitic suites.

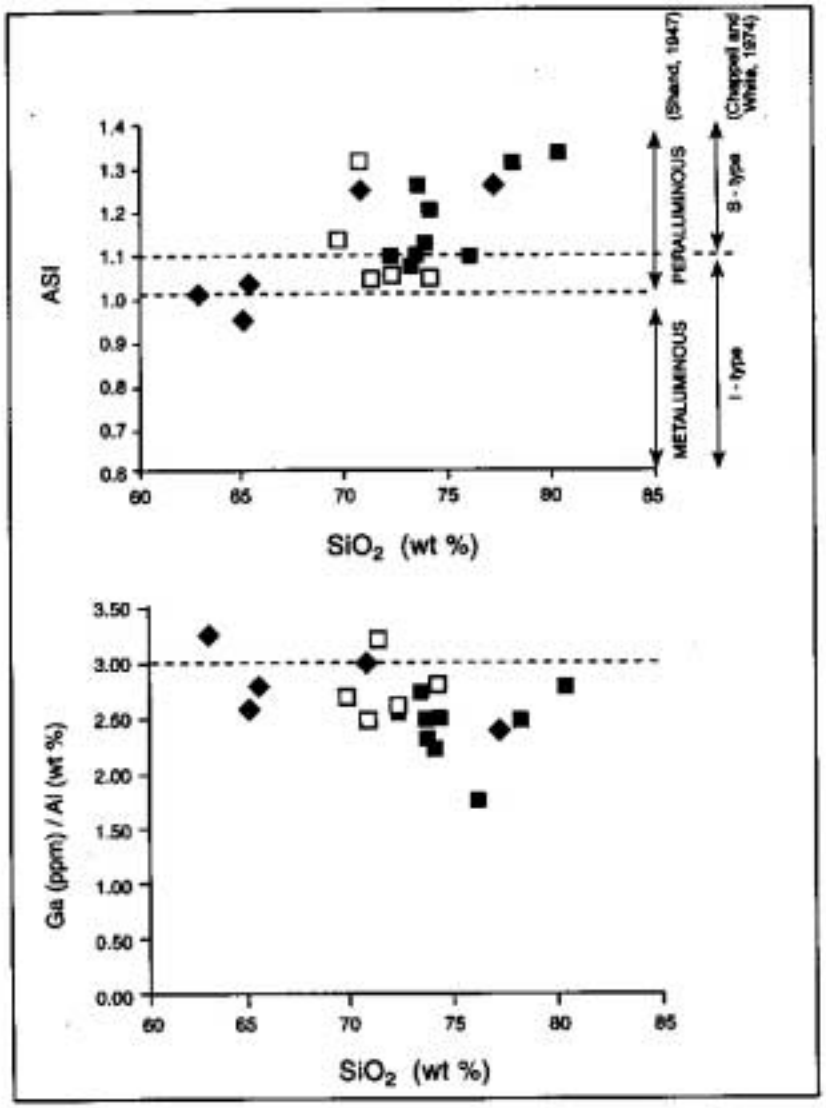

Figure 4.6 Diagram showing ASI (aluminium saturation index) against SiO_2. Symbols are: ETG (filled squares); ESTG (open squares) and SLTG (filled diamonds).

Figure 4.7 Ga/Al against SiO_2 diagram (Whalen *et al.*, 1987) for Itapetim granitoids. Symbols as in Fig. 4.6.

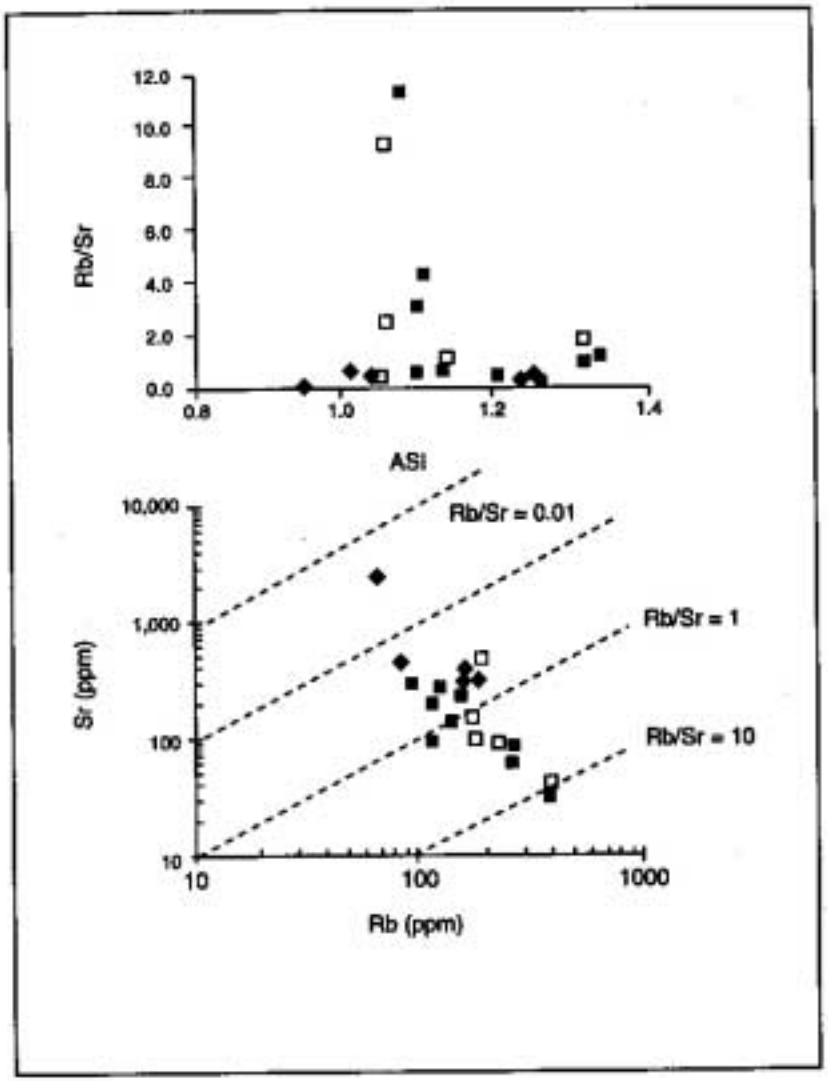

Figure 4.8 ASI against Rb/Sr diagram for Itapetim granitoids. Symbols as Fig. 4.6.

Figure 4.9 Diagram shows the distribution Sr against Rb is consistent with values between 0.1 to 10, but concentrated predominantly close to 1. Symbols are as in Fig. 4.6.

Figure 4.10 Chondrite-normalised incompatible element 'spidergrams' for the ETG (a) = MG-R-203AI, MG-R-203AII, MG-R-203G, MG-R-204B; (b) = MG-R-144, MG-R- 144A, MG-R-148 (highly fractionated); (c) = MG-R-145 and MG-R-204J (positive Ba anomalies and Y different to others).
Chondrite-normalised incompatible element 'spidergrams' for the ESTG: (d) = MG-R-150, MG-R-186 and MG-R-192; (e) = MG-R-150A and MG-R-184.
Chondrite-normalised incompatible element 'spidergrams' for the SLTG: (f) = MG-R-147A, MG-R-183 and MG-R-198; (g) = Mg-R-149 and MG-R-197A.
Normalising values used are as in Sun (1980).

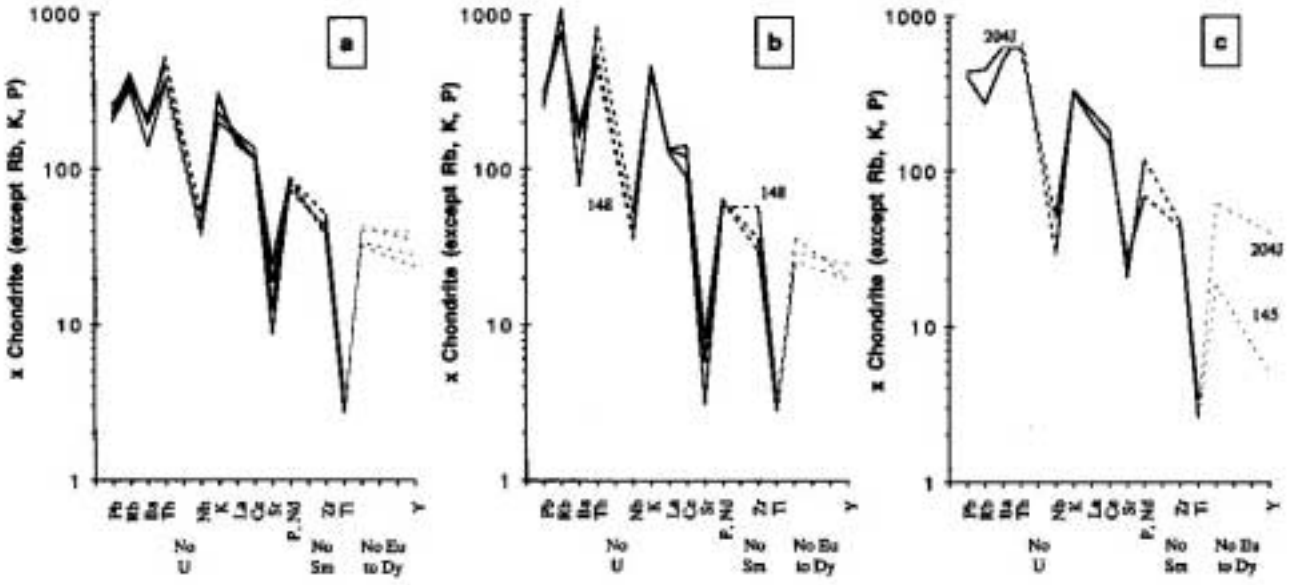
a
b
c
x Chondrite (except Rb, K, P)
1000
100
10
1
148
204J
145
No U
No Sm
No Eu to Dy

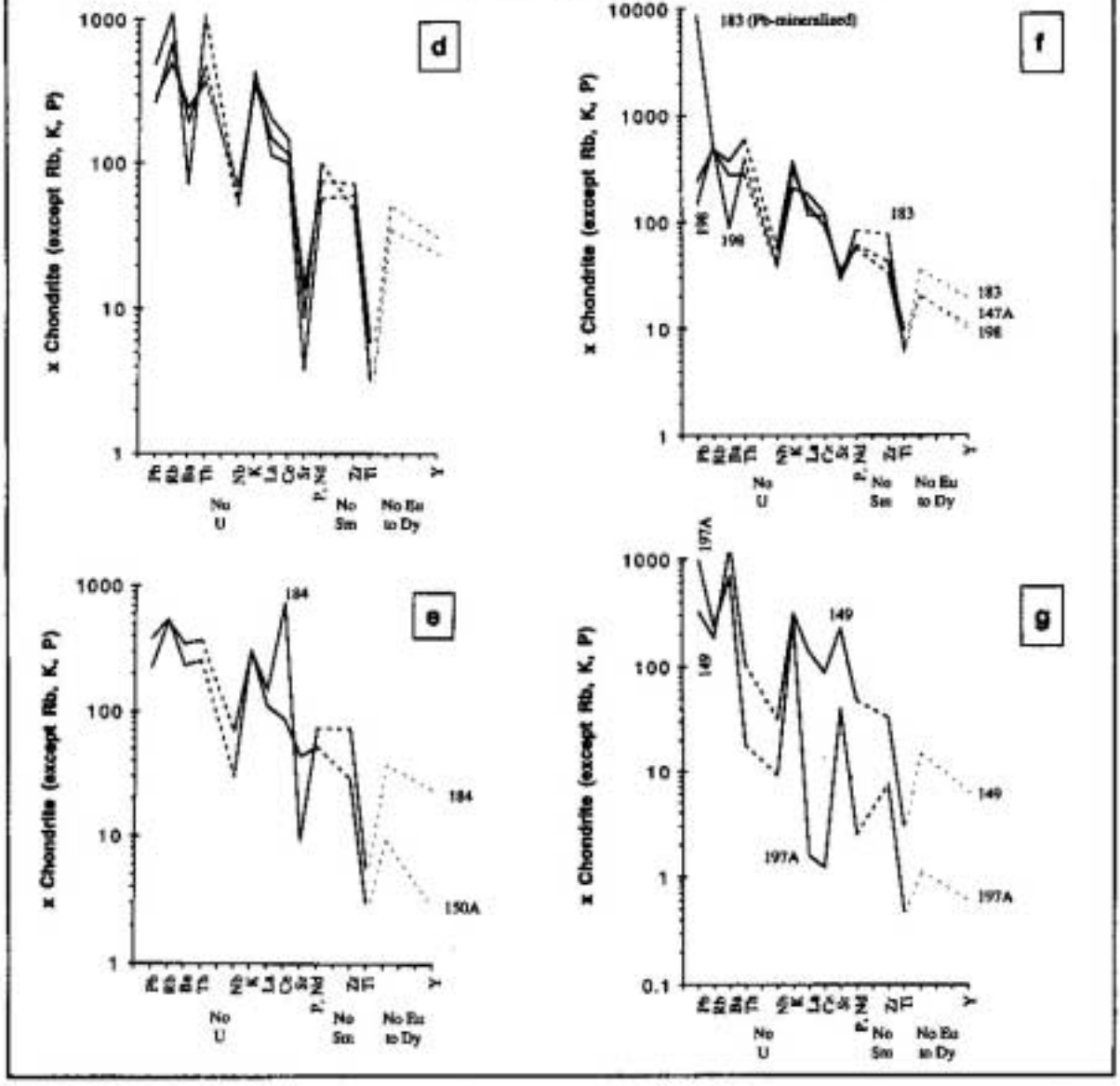
d
e
f
g
x Chondrite (except Rb, K, P)
10000
1000
100
10
1
183 (Pb-mineralised)
198
183
147A
184
150A
149
197A
0.1
No U
No Sm
No Eu to Dy

granitic magma. As a general principle, K/Ba is lowest in un-evolved granites, but high in fractionated granites; K/Rb is highest in the less-fractionated examples and rarely drops below 60. Neither ratio is especially dependant upon silica content of the pluton, at least in the case of subduction- or collision-related granites. There is a great range in ratios over the various types, so the use of these values for establishing tectonic setting will discussed later.

Spidergrams allow comparison of incompatible element contents, usually against hypothetical 'ocean-ridge granite', 'primitive-mantle' or chondrite-normalized composition. In this study the data set were normalised according to the values of Sun (1980) and results are dispalyed in Figs. 4.10a to 4.10f. These diagrams show the average for the three groups of granites ETG, ESTG and SLTG respectively, compared with the average continental crust. As expected, the LIL (large ion lithophile) elements show enrichments and the HFS (high field strength) elements show less enrichment or depletion relative to chrondrite. These diagrams are useful for sorting out which granites are highly evolved (fractionated), simply by the relative magnitude of the Rb, Sr and Ba anomalies, as continued plagioclase crystallization leads to enrichment in Rb and depletion in Ba and Sr, hence high Rb/Sr ratios, and with continued fractionation, the size of the negative Sr anomaly will far exceed that of Ba. The ETG shows a range of levels of fractionation (Figs. 4.10b and 4.10c), especially in the samples MG-R-144 and 144A.

The ESTG suite (Figs. 4.10d and 4.10e) represents the most- and least-evolved lithofacies and all gradations between the two. Note that the size of the positive Rb, and negative Ba and Sr anomalies increases, whereas the small positive K and nagative Nb anomalies become indistinct in the 'most fractionated' facies. The size of the negative Sr anomaly far exceeds that of Ba.

The SLTG suite spidergrams show that all the samples have a similar distribution, (Figs. 4.10f and 4.10g) that contrast with the ESTG values (Figs. 4.10d and 4.10e). This tectonic grouping has particularly strong positive K and Sr anomalies, negative Nb and slight negative Th and La-Ce anomalies. This pattern is similar to the Cordilleran suites that have a well documented crustal component (e.g. the Chemehuevi pluton; John and Wooden, 1990) that represents a syn- to late-orogenic (e.g. early facies are deformed, later are underformed), subduction-related suite. The spidergram for the Chemehuevi pluton is characterised by enrichement in K and Rb; decrease in positive Ba anomaly and lower La-Ce and Nb-Th contents. The sample MG-R-197A (Igarape Garapa; Fig. 4.10g) shows a similar pattern to that of Chemehuevi (calc-alkalic suite with probably a significant crust component). In the Chemehuevi plutons, the second-youngest facies are two-mica granites, suggesting that the amounts of sedimentary material that have been incorporated into these granites have increased (Sr_i increases with time).

4.3.6 Petrogenesis and Geotectonic Setting

Using mineralogy, chemistry and Sr-isotopes, Chappell and White (1974) defined two types of granites according to their probable source material: (i) I-type (intracrustal derivation from earlier igneous rocks) are predominantly metaluminous due to hornblende-biotite- or biotite-only mafic silicate content.; and (ii) S-type (source rocks of sedimentary or supracrustal protoliths), are more peraluminous due to their muscovite as well as biotite content and/or Al_2SiO_5 mineral phases. However, in this classification the alumina saturation index (A/CNK) does not have the same limit as Shand's (1947) classification. As a result sometimes I-type granites can be weakly peralumionus (e.g. biotite-only granites), and the approximate division is made at A/CNK = 1.1 (e.g. the 'crustal' granitoids of Barbarin, 1990). Due to isotopic fractionation during the weathering that produces source material for sedimentary rocks, granites derived from melting of 'fertile' lithologies such as greywackes will have higher $^{87}Sr/^{86}Sr$ isotopic ratios at the time of granite genesis. Again, there is some overlap between clearly I-type and S-type signatures. I-type will have $Sr_{(i)} \leq 0.709$ and S-type will have $Sr_{(i)} > 0.708$.

Based on this classification (see Table 4.2) the ETG are predominanlty S-type granites while the ESTG suite shows S- and I-type granites. The SLTG fit predominantly in the I-type field, but some samples are likely of S-type (Fig. 4.6).

According to Clarke (1992), although different tectonic environments have dominantly one type of granitioid (peraluminous granitoids are strongly related to continental collision; metalumious reflect zones of ocean-continental or ocean-ocean collision; and peralkaline granitoids suggest crustal extension) the chemical composition does not allow a definite conclusion to be reached on the relative amount of source material or tectonic environment of the granitoids emplacement. The primary magmas are smeared over the compositional range as a result of the infinite variety of sources. To place constraints on the petrogenetic history of the granitoids the field data must be combined with constraints from geochemical (McCarthy and Hasty, 1976) and isotope investigations (Faure, 1977; Doe, 1970; DePaolo, 1981).

The geochemical behaviour of elements (major and trace elements) in magmas has the potential to reveal information about tectonic environments (Clarke, 1992) assuming that: (i) these elements are immobile during the hydrothermal processes (Pearce and Cann, 1973; Pearce *et al.*, 1984); (ii) most of the trace elements do not form their own minerals; and (iii) major minerals have an ability to accommodate a trace element in their structures.

The ternary diagram Rb-Ba-Sr (Pearce *et al.*, 1984) relates the granitoids to three types of tectonic setting: (i) within-plate granites: WPG ; (ii) collision granites: COLG; and (iii) volcanic-arc graniotids: VAG. This classification divides the plutons from

Table 4.2

Geotectonic Characteristics of the Granitoids from Itapetim Area

Sample Lable	Structural	Harker Diagram	Spider Diagram	Rb-Ba-Sr (Pearce et al,1984)	Nb:Y (Pearce et al., 1984)	Rb:(Nb+Y) Pearce et al., (1984)	Rb/Sr	Ga/Al (White, 1990) (ppm/wt %)	A/CNK (Shand, 1947)	Miyashiro (1970)	Chappell & White (1974)
MG-R-144	ETG	ETG:	MF	WPG (MF)	VAG-SYN/WPG bdy	VAG/WPG bdy	4.3	2.51	peraluminous (1.06)	tholeiitic	S-type
MG-R-144A	ETG	High SiO2	MF	WPG (MF)	WPG	WPG	3.1	2.56	peraluminous (1.04)	tholeiitic	I-type
MG-R-145	ETG	Low Al2O3 and CaO	SF	WPG or COLG	VAG-SYN	VAG	<1		v. peraluminous	calc-alk.	S-type
MG-R-148	ETG		HF	WPG (HF)	WPG	SYN-COL/WPG bdy	11.3	2.77	peraluminous (1.04)	tholeiitic	I-type
MG-R-203AI	ETG		MF	COLG	WPG	WPG	>1		v. peraluminous	on boundary	S-type
MG-R-203AII	ETG		MF	COLG	WPG	WPG	>1		v. peraluminous	calc-alk.	S-type
MG-R-203G	ETG		MF	COLG	WPG	WPG	<1		v. peraluminous	calc-alk.	S-type
MG-R-204B	ETG		SF	COLG	n.d.	WPG	<1		peraluminous	tholeiitic	I-type
MG-R-204J	ETG		SF	WPG	WPG	WPG	<1		peraluminous	calc-alk.	S-type
MG-R-150	ESTG	ESTG:	MF	WPG	WPG	WPG	2.5	2.62	peraluminous (1.00)	tholeiitic	I-type
MG-R-150A	ESTG	High SiO2	SF	COLG	VAG-SYN	SYN-COL	<1	>3	peraluminous	calc-alk.	I-type
MG-R-184	ESTG	Low Al2O3 and CaO	Altered?	WPG?	WPG	WPG	>1		v. peraluminous	calc-alk.	I-type
MG-R-186	ESTG		MF	WPG or COLG	WPG	WPG	>1		peraluminous	tholeiitic	S-type
MG-R-192	ESTG		HF	WPG (HF)	WPG	SYN-COL/WPG bdy	9.2	2.79	peraluminous (1.02)	tholeiitic	I-type
MG-R-183	SLTG	SLTG:	SF	COLG	WPG	WPG	<1	>3	v. peraluminous	calc-alk.	S-type
MG-R-147A	SLTG	Low SiO2	SF	COLG	VAG-SYN	VAG	<1		metaluminous	calc-alk.	I-type
MG-R-149	SLTG	High Al2O3 and CaO	VAG*	VAG	VAG-SYN	VAG	<1		metaluminous	calc-alk.	I-type
MG-R-197A	SLTG		VAG*	COLG	VAG-SYN	VAG	<1		v. peraluminous	tholeiitic	I-type
MG-R-198	SLTG		SF	COLG	VAG-SYN	VAG	<1	>3	metaluminous	calc-alk.	S-type

Abbreviations:
HF= highly fractionated; MF= moderately fractionated; SF= slightly fractionated
ETG = early tectonic granites; ESTG = early and syn-tectonic granites; SLTG = syn- and late tectonic granites
WPG= within-plate granite; COLG= collision granite; VAG= volcanic-arc granite
A/CNK = {molar [Al2O3/(CaO+Na2+K2O)]}; CaO has the amount of CaO included in apatite subtracted; = CaO-3.3P2O5.
Note:
Ga /Al (ppm/wt %) > 3 as being diagnostic of A-type (extensional) granites
* denotes that these spidergrams have a distinct 'Cordilleran' signature.

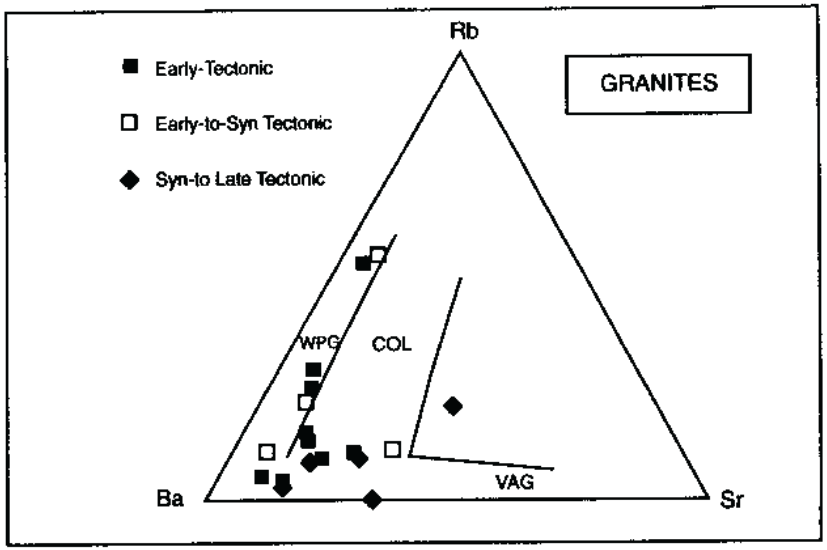

Figure 4.11 Rb-Ba-Sr diagram for ETG (filled squares); ESTG (open squares) and SLTG (filled diamonds). Boundaries for tectonic discrimination are after Pearce *et al.*, (1984): WPG = within plate granite; COL = collision granite; VAG = volcanic arc granite.

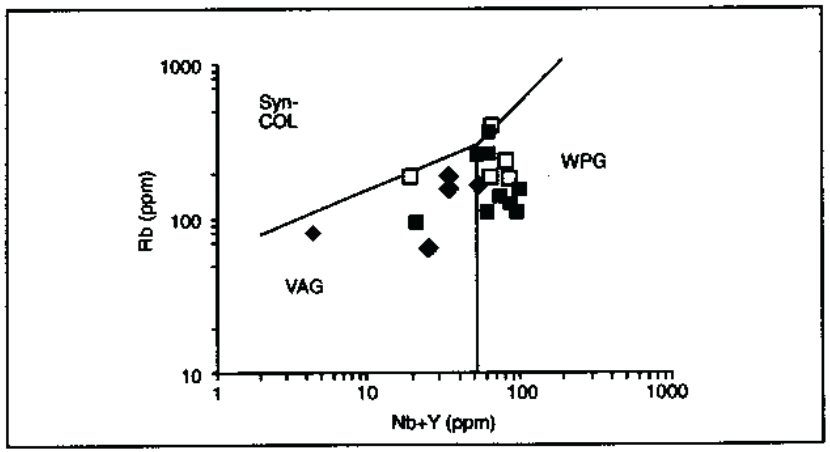

Figure 4.12 Rb against Nb + Y discriminant diagram for syn-collision granioitds (Syn-COL), within plate granitoids (WPG) and volcanic arc granitoids (VAG) after Pearce *et al.*, (1984).
Symbols are: ETG (filled squares); ESTG (open squares); and SLTG (filled diamonds).

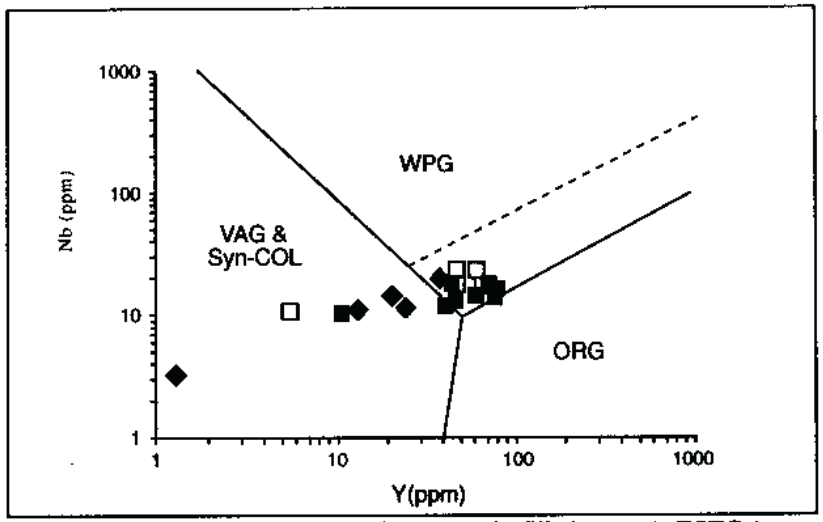

Figure 4.13 Nb versus Y diagram for the ETG (filled square); ESTG (open squares) and SLTG (filled diamonds).(WAG = within plate granitoids fields; VAG and Syn- COL = volcanic field; ORG = ocean ridge granitoids field, after Pearce *et al.*, 1984).

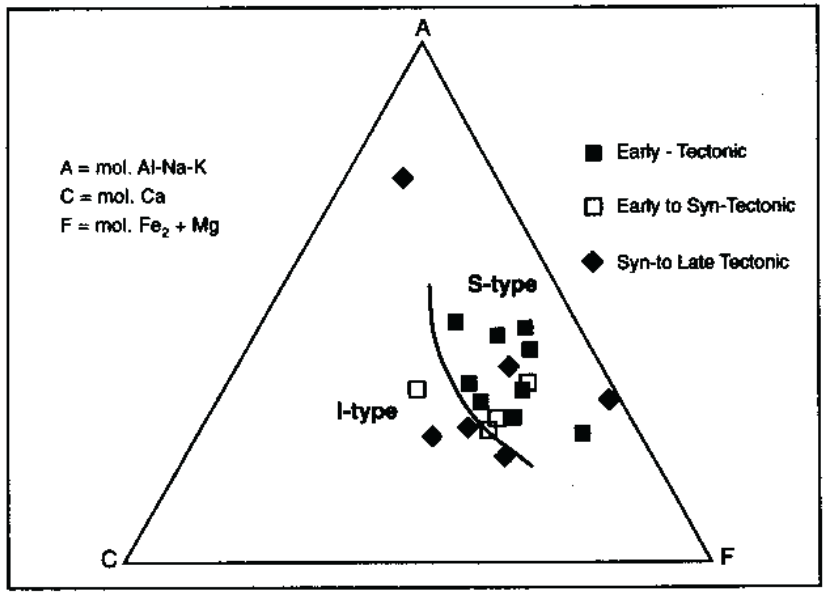

Figure 4.14 ACF diagram after Takahashi *et al.* (1980).

collision or anorogenic types, although there is still some possibility that metamorphism might produce mobility of Rb resulting in a shift of the plot position of Rb.

On this diagram those values that plot along the Rb-Ba edge, represent within-plate granites (e.g. A-type granites). The continent-collision granites have somewhat more Sr and plot to the left of the L-shaped boundary and right of the line. The volcanic-arc granites (e.g. subduction or Andean type) are most distinctive and they plot along the bottom (Ba to Sr) line.

Both suites ETG and ESTG display a similar distribution on the Rb-Ba-Sr diagram (Fig. 4.11). They fit close to the Ba corner, with five specimens plotting close to the WPG/COLG (within-plate granite/continental-collision-granite) boundary, but with relatively elevated Rb contents. On the basis of these criteria alone, most of the ETG and ESTG might be considered to be COLG, and five higher Rb specimens are close to WPG limit (ETG: MG-R-144, MG-R-144A, MG-R-148; ESTG: MG-150, MG-R-192). These five samples are peralumionus and they have moderately high Rb/Sr and K/Ba (hence they are fractionated plutons), but values of Ga/Al are too low to clearly identify them as anorogenic types; so it is suggested these five samples are COLG as well. (Table 4. 2).

The chemistry of these latter specimens is analagous to that of the moderately-evolved members of the low Ca, predominantly I-type granites of the Canadian Cordillera. Their tectonic setting is clearly subduction-related, but they plot along the WPG/COL boundary on the Rb-Ba-Sr diagram. Such granites are biotite granites with hornblende only in the least-evolved facies (e.g. they are metaluminous to weakly peralumionus), and have $Sr_{(i)}$ ratios from 0.7060 to 0.7074. Such anomalouns Cordilleran granites are considered to have been formed at the time of peak metamorphism (and, hence maximum crustal thickening) of the orogeny. They are chemically similar to the Caledonian granites rather than typical Cordilleran plutons (Liverton, 1992). The five 'evolved' Itapetim granites are here considered to be of similar mixed I-S source type.

The ESTG plots in the WPG field on the Rb against (Y+Nb) diagram (Pearce *et al.*,1984), except for the 'highly fractionated' facies that creeps over into the COLG field due to Rb enrichement (see Fig. 4.12). On the Nb against Y plot (Pearce *et al.*, 1984) these granites also fit on the field of the WPG (Fig. 4.13).

The use of the molar ACF criteria (as in Takahashi *et al.*, 1980) further reinforces the indication of a significant S-type component to the Itapetim magma (see Fig. 4.14).

The SLTG plutons are relatively Sr-rich and hence plot in the COLG field on the Rb-Ba-Sr diagram. These acid-intermediate plutons have much hornblende (see Fig. 4.4d). They plot in the Syn-COL and VAG fields of the Nb against Y diagram (Pearce *et al.*, 1984). In the Rb against Nb+Y diagram (Pearce *et al.*, 1984) these rocks fit on the field of VAG. A strong mantle-wedge (subduction) component for these magma is therefore possible. They are also marked by high K/Rb (low original Rb content).

Examination of the chrondrite-normalised spider diagrams for each of the Itapetim tectonic/age groupings shows that the ETG and ESTG groups mainly show negative Ba, large negative Nb, Sr, P and Ti and positive K anomalies (exceptions are samples MG-R- 204J and MG-R-145 of the ETG that lack the Ba and K anomalies; and MG-R-184 and MG-R-150A of the ESTG that have only slight Ba or K anomalies). The SLTG group show from prominent to very small negative Ba or positive K anomalies, while samples MG-R-149 and MG-R-197A exhibit slight positive Ba, prominent negative Th-Nb and positive Sr anomalies, with widely different La-Ce contents.

Comparison with similar diagrams from published analyses shows that the pattern shown by the first two groups is shown by both continental-collision granites (e.g. Cornubia; Stone, 1987) and the more evolved subduction-related mixed I-S types (Seagull-Thirtymile; Liverton, 1992). The patterns shown by the samples MG-R-149 and 197A are similar to those exhibited by Cordilleran granites of the gabbro-granodiorite association and also, in particular to some of the later granites of the Chemehuevi suite (i.e. from the 'mature magmatic arc') that are considerd by John and Wooden (1990) to have some crustal-derived component.

Examination of the K/Ba ratios of published analyses of granites from various tectonic settings (Fig.4.15) suggests that the minimum values of K/Ba found in continent-continent collision settings are significantly higher than those shown by suites from a subduction-related (Cordilleran) setting, irrespective of whether data such as Sr-isotopes indicate some crustal component to the magma (compare the collision granites to the Whipple, Chemehuevi and Bristol Mountains, California suites shown in Fig.4.15). A-type (extensional) granites have the lowest values for this ratio. Using this criterion (admittedly from a limited data base), it may be seen that the Itapetim ETG and ESTG might represent either a subduction or continent-continent collision setting, but that the SLTG fall mostly into the range of the extensional and Cordilleran (i.e. primarily I-type) plutons. The maximum value for the K/Rb ratio of the suites from the literature is somewhat higher for the clearly mantle-derived (African) extensional granites, but differences are too small to be readily diagnostic. This ratio does indicate that the Itapetim granites have not undergone a large amount of crystal-crystal fractionation, that is consistent with emplacement at a comparatively deep crustal level.

Extensional (A-type) granites have the lowest K/Ba ratios (≈ 6) in their least-evolved members, but the contrast is insufficient to use this criterion to distinguish them from Cordilleran (VAG) granites (Fig. 4.15). On the other hand, the lowest K/Ba ratios shown by the continent-collision types (i.e. ≈ 40) should serve to differentiate this tectonic group, provided the least-evolved members of a suite are sampled. The ESTG Itapetim granites, in having a higher minimum K/Ba ratio are consistent with the continent-continent collision type.

The Cordilleran granites are likely to be much more fractionated than the Itapetim

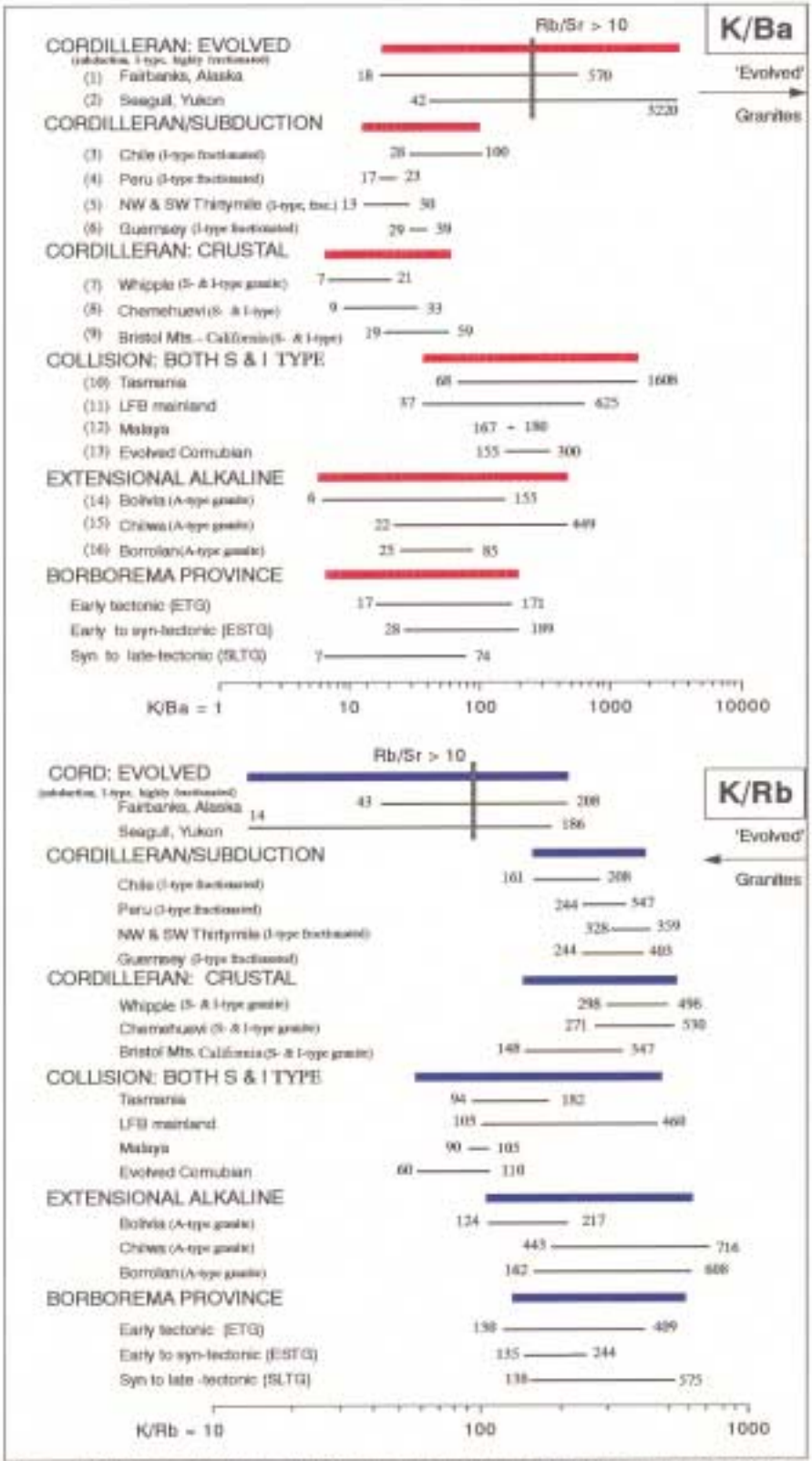

Figure 4.15 Range of K/Ba and K/Rb ratios selected from published analyses for diorite to granite plutons from varying tectonic settings compared to the Borborema Province plutons of this study. Data source is: (1) Newberry *et al.*, (1990); (2) Liverton (1992); (3) Mpodozis& Kay, 1992; (4) Bussell (1988); (5 Liverton (1992); (6) Bremond d'Ars *et al.*, (1992); (7) Anderson & Cullers (1990); (8) John and Wooden (1990); (9) Fox & Miller (1990); (10) Sawka *et al.*, (1990); (11) Chappell (1979); Chappell & White (1976) ; Hine *et al.*, (1978); White (1990); White & Chappell (1988); White *et al.*, (1977); White *et al.*, (1989); (12) Pitfield *et al.*, (1990); (13) Stone (1987); (14) Fletcher & Beddoe-Stephens (1987); (15)

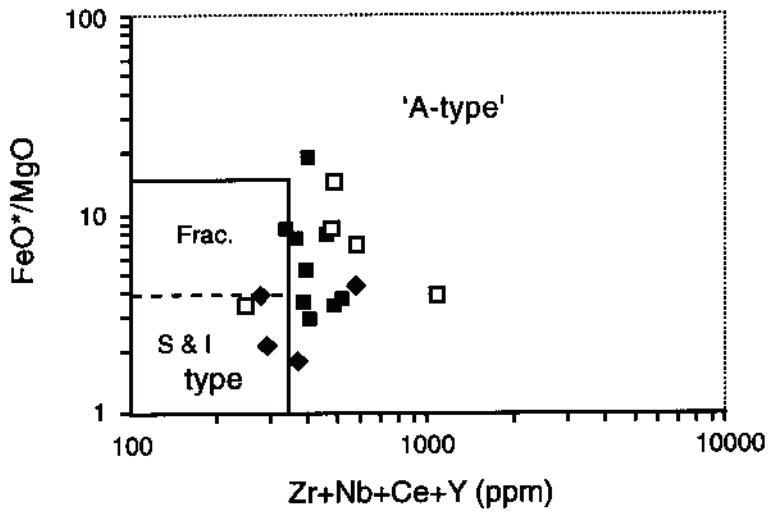

Figure 4.16 Diagram showing the variation of FeO*/MgO against (Zr+Nb+Ce+Y). Symbols are: ETG (filled squares); ESTG (open squares); and SLTG (filled diamonds).

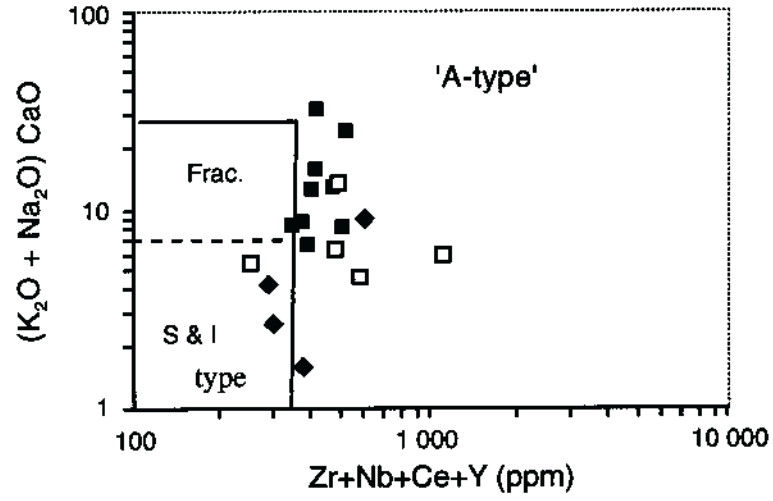

Figure 4.17 Diagram displaying the variation between (K_2O+Na_2O/CaO) and (Zr+Nb+Ce+Y) for Itapetim granitoids.
Symbols are: ETG (filled squares); ESTG (open squares); and SLTG (fillled diamonds).

plutons (e.g. Swanson *et al.*, 1988; Newberry *et al.*, 1990). However, as is shown by the FeO_{total}/MgO and (K_2O+Na_2O)/CaO against Zr+Nb+Ce+Y diagrams (Figs. 4.16 and 4.17) the ESTG are still well within what might be considered to be 'highly-fractionated'. They appear to anomalously similar to the anorogenic types, and the group might well include some very evolved I-type plutons. The SLTG tend to be less fractionated and fall predominantly in the field of normal S and I type granites.

Maniar and Piccoli (1989) recognised two types of continental anorogenic granites using major-element compositions and separated them from continental arc and collision granites. Their principal divisions comprise: (i) island arc-, continental arc- and continent collision- granitoids and, (ii) anorogenic: rift-related and continental epeirogenic uplift (hot-spot). In (ii) both types include alkali granites, quartz-alkali syenites and quartz syenites. Most of the Itapetim plutons (Fig. 4.18a) plotted on the Maniar and Piccoli FM diagram fit distinctly in the anorogenic field, but use of the FeO/(FeO+MgO) to SiO_2 plot shows the SLTG plutons (except one) to be in type (i), but of the remainder only one ESTG pluton falls clearly in the anorogenic field, the rest being evenly divided between the overlap region of (ii) and that of the post-orogenic granites, or are in the overlap field of type (i) and post-orogenic granites.

However, using the Muller and Groves (1993) tectonic discriminant diagrams TiO_2/10-P_2O_5/10-Lax10 and Zrx3-Ce/P_2O_5-Nbx50 all the Borborema granites plotted in the late oceanic arc and continental arc fields, respectively. (Figs. 4.19a and 4.19b).

To summarise, of the 19 Itapetim granite analyses presented here there is often conflicting chemical evidence for the tectonic setting of these plutons. It is not clear why this might be the case, but as these schemes use the contents of elements such as Rb, Sr, and Y, which are potentially mobile during metamorphism and hydrothermal activity, it could be that their initial concentrations in the granites have been altered.

Although the F-M diagram after Maniar and Piccoli suggests that many of the Itapetim plutons might be anorogenic, only three have Ga/Al ratios >3, and none are peralkaline. Clearly these granitoids cannot be anorogenic. The two SLTG granites with higher Ga/Al ratios (samples MG-R- 198 and MG-R-183) are metaluminous and peraluminous respectively and have Rb/Sr < 0.5, so they are not obviously evolved I-type granites.

Of the remainder, the ACF diagram (Fig.4.14) shows most fall within the S-type field and, indeed, 7 are clearly peraluminous and may be fairly confidently considered to have a large S-type component. The hornblende-rich mineralogy of the SLTG (MG-R-147, MG-R-149, MG-R-198) suggests a largely I-type nature, however, from the same suite the samples MG-R-149 and MG-R-197A have Th-Nb spidergram anomalies that are reminscent of mixed calc-alkaline granites, suggesting a high crustal component, and therefore close to S-type granite. These samples may represent the late magmatic suite and reflect crustal contribution increasing at the end of the magmatism.

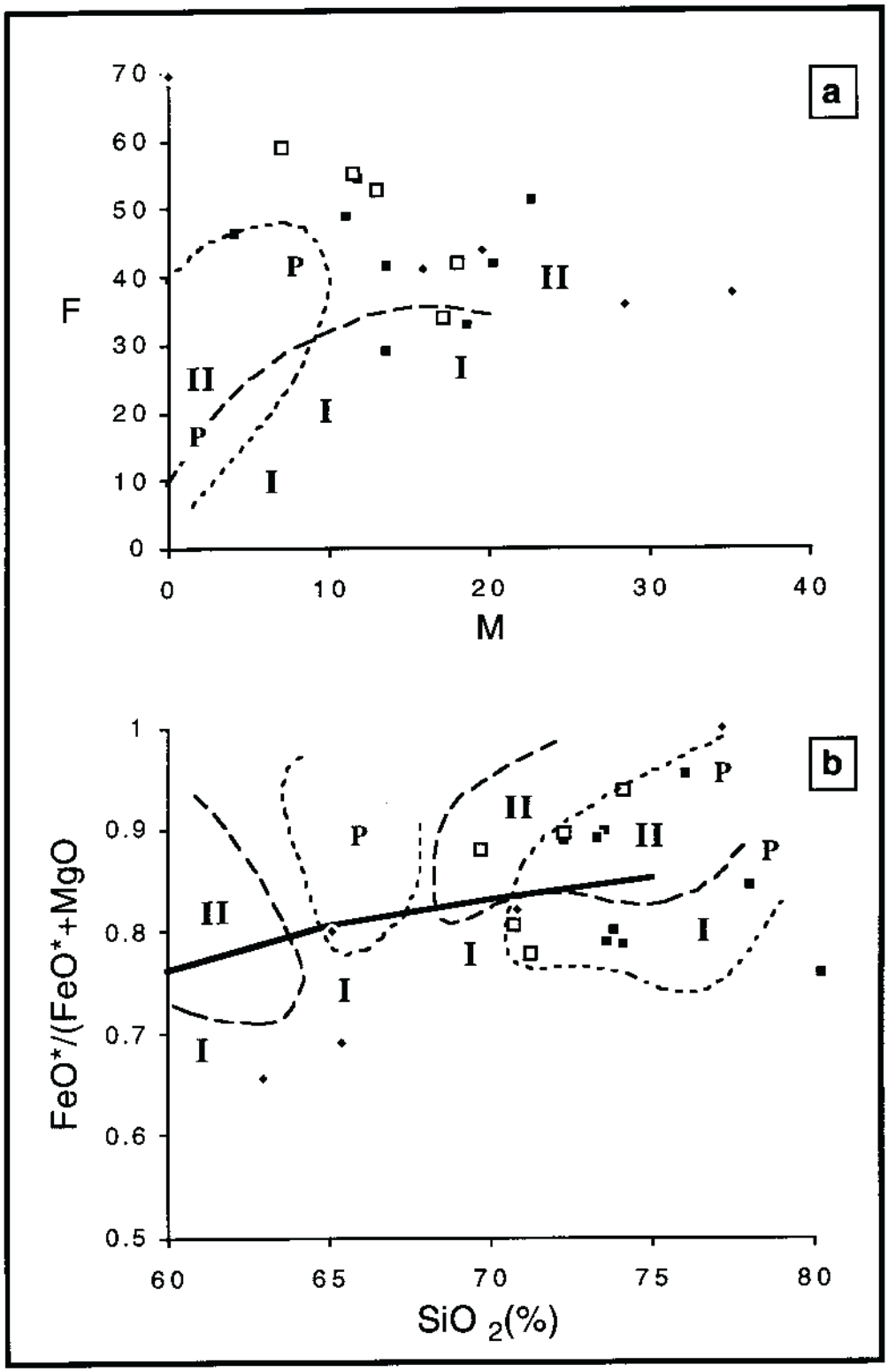

Figure 4. 18 Tectonic discrimination diagrams after Maniar & Piccoli (1989). Field II includes Rift-related & Continental epeirogenic granites; Field I includes Island-arc- Continental arc- & Continental collision- granitoids. The dotted field P covers the Post- orogenic granitoids. (**a**) Shows the F & M components of an AFM diagram and (**b**) shows FeO*/(FeO*+MgO) to silica. The heavy line is the discrimination line of the Miyashiro version of this diagram. Symbols depicting areas are as in Fig.4.12.

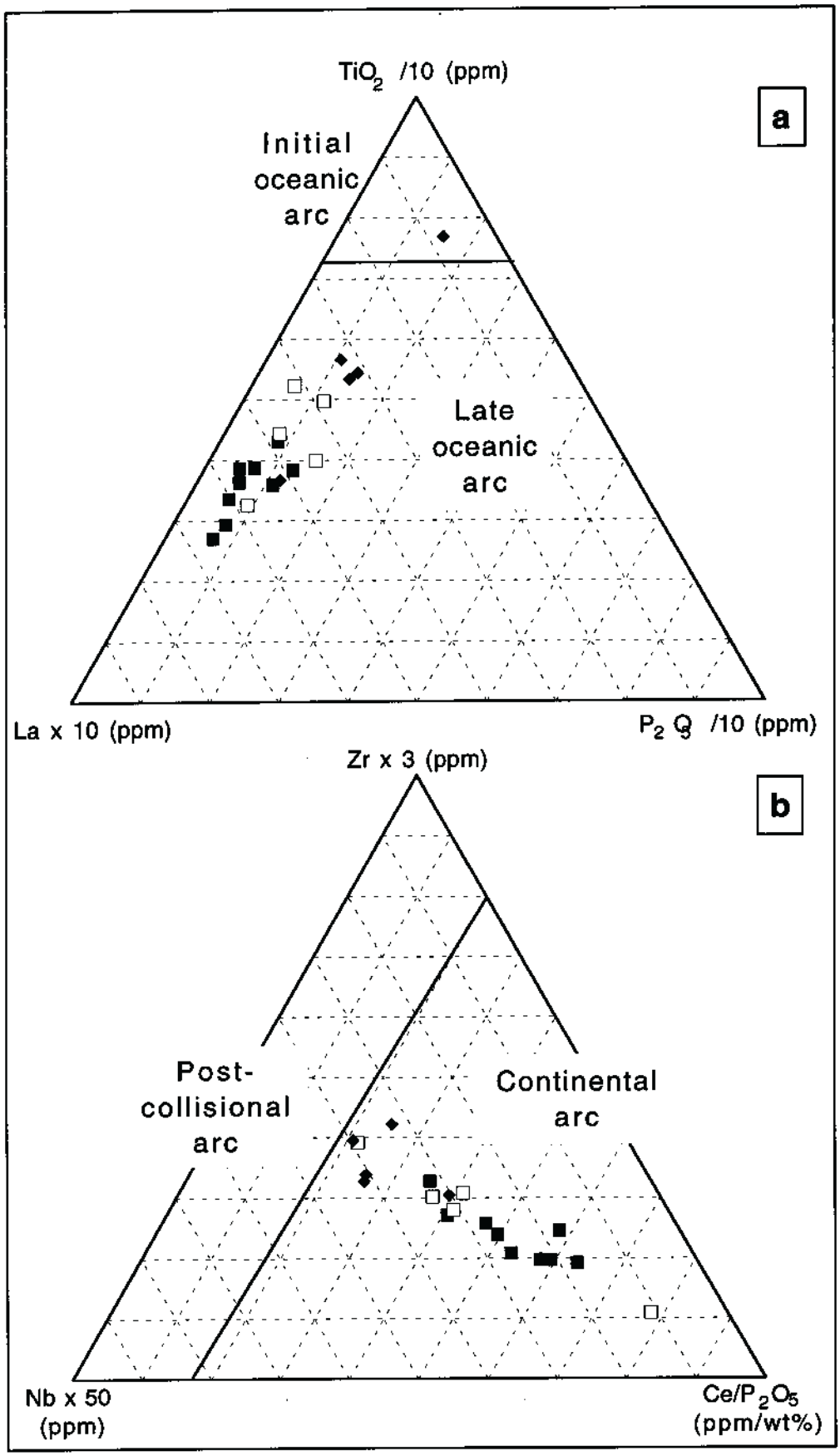

Figure 4.19 Borborema granites plotted on the tectonic discriminant diagrams of Muller and Groves (1993). Symbols are: ETG = filled squares; ESTG = open squares and SLTG - diamonds.

The ETG are predominantly S-type, but three samples (MG-R-144, MG-R-144A, MG-R-148) have the Rb-Ba-Sr relationships of evolved I-type plutons and suggest a mixed I- and S-type. The ESTG suite is characteristic of peraluminous and typical mixed S- and I-ype granites.

The bulk of these plutons therefore may be of hybrid S-I type origin and their chemistry is consistent with derivation in either a continent-continent collisional setting or in a mature Cordilleran arc, where melting of crustal material has generated a significant component of magma.

4.3.7 Isotopic and Rare-Earth Element Constraints

The different granitic suites exihibit a marked difference in their Pb isotopic composition (see Chapter 6 for data). The ETG (Trans-Amazonian granites) display highest $^{206}Pb/^{204}Pb$ and $^{208}Pb/^{204}Pb$ values (21.305 and 41.828, respectively) while the lowest and intermediate values are found in the Brasiliano granites. The lowest values (16.237 and 36.653) are found in the SLTG, and the ESTG has intermediated values ($^{206}Pb/^{204}Pb$ at 18.909 and 18.700 and $^{208}Pb/^{204}Pb$ at 39.598; and 38.463). These data suggest either the heterogeneous lead isotope composition of the original lithosphere or variable mixing of Pb isotopes from the crust.

Available isotope data ($^{87}Sr/^{86}Sr$ and δ^{18} O) and Σ REE (LREE and HREE) from the Brasiliano granitoids in Borborema Province of the Seridó and Piancó/Alto Brígida fold belts are used in this chapter to place constraints upon the magmatism and mechanism of emplacement, as will be discussed below. A summary of the petrogenetic features, isotope and REE data is given in Table 4.3.

It has been assumed (O'Neil and Chappell, 1974; O'Neil *et al.*, 1977) that granitic rocks with protoliths related to metasedimentary rock-types (S-type granites) are enriched in δ^{18} O (> 10 $^{0}/_{00}$), while granitoids originated from igneous rock-types (I-type granites) are depleted (δ^{18} O < 10 $^{0}/_{00}$). According to these authors S-type granites are also characterised by higher values of initial $^{87}Sr/^{86}Sr$ ratios (> 0.706), whereas I-types show lower values of $^{87}Sr/^{86}Sr$ (0.704 to 0.707).

Leterrier *et al.*, (1990) studies the Brasiliano granites of the Seridó Fold Belt and pointed out that the ESTG suite is characterised by a REE distribution equivalent to the highly fractionated patterns (La/Yb_N more than 10) and Eu present occasionally as a small anomaly. The SLTG granitoids display highly fractionated LREE patterns (La/Yb_N = 8.3 to 6.0) with an upward facing curvature for HREE and medium negative Eu anomaly, suggesting highly fractionated granites.

Macedo *et al.* (1990) defined for the granitoids of the Seridó Belt an initial $^{87}Sr/^{86}Sr$ of 0.708 and Σ Nd range from -13 to - 3.8 for the ESTG. In the SLTG those values

Table 4.3
Rare-Earth Element and Isotopic Characteristics of Granitoids from Borborema Province: Central Domain

Geological Setting	Structural Relationship	Stable and Radiogenic Isotope Data and Rare-Earth Elements	Data Source
Seridó Fold Belt	ESTG (K calc-alkaline or shoshonitic)	LREE : La/Yb >10; Eu occasionally and very small 87Sr/86Sr (i) = 0.708; Σ* Nd = - 13 to - 3.8	Leterrier et al., (1990) and Macedo et al., 1990
	SLTG (calc-alkaline)	LREE : La/Yb = 8.3 to 6.0; Eu negative anomaly 87Sr/86Sr (i) = 0.714; Σ* Nd = - 22 to -18	
Piancó/Alto Brígida Fold Belt	ESTG (K calc-alkaline, peraluminous and metaluminous)	δ18 O <10 per mil SMOW (from +7.0 to + 9.2) 87Sr/86Sr (i) = 0.7094±2	McMurry et al., 1978
	SLTG (trondjemitic)	δ18 O < 10 per mil SMOW (from +9.23 to + 9.94) and Relative enriched in LREE and depleted in HREE Eu/Eu* varies from 1.25 to 1.51; small positive Eu anomaly	Sial, 1986
	SLTG (K calc-alkaline, peraluminous and metaluminous)	δ 18 O < 10 per mil SMOW (from +6.93 to + 8.49) and 87Sr/86Sr (i) = 0.7058 LREE: Ce/Yb range from 28 to 217 (strong enrichment relative to chrondrite). HREE depleted relative to LREE; absence Eu anomaly Eu/Eu* varies from 0.89 to 1.00; Yb < 1 ppm Negative correlation between SiO2 and ΣREE	Sial, 1986
	SLTG (calc-alkaline, peraluminous)	δ18 O >10 per mil SMOW (from +11.57 to + 12.79) ΣREE varies from 116 to 166 ppm (less enrichment relative to chrondrite compared to the K calc-alkaline suite); La/Sm =1.90 to 2.67; HREE depleted relative to LREE; a variable negative Eu anomaly Eu/Eu* varies from 0.75 to 0.91; Yb < 1.45 ppm No correlation between SiO2 and ΣREE	Sial, 1986
	SLTG (peralkaline)	δ 18 O <10 per mil SMOW; sometimes values ∂ 18 0 > 10 occur Satured peralkaline granites have ΣREE varies: 89.2 to 296 ppm and have negative Eu anomaly (Eu/Eu* = 1.02 to 1.22 Negative correlation between SiO2 and ΣREE; K2O and CaO show a positive correlation with SiO2 Oversatured peralkaline granites have ΣREE from 67.07 to 309.79 ppm; Eu anomaly is either missing or slightly positive (Eu/Eu* ranges from 0.86 to 1.199)	Ferreira and Sial, 1986
Pajeú/Paraiba Fold Belt	ETG (tholeiitic, peraluminous)	206Pb/204Pb = 21.305±2; 208Pb/204Pb = 41.828±6 232Th/204Pb = 99.21	This study (see Chapter 6 for further information)
	ESTG (calc-alkaline, peraluminous)	206Pb/204Pb = 18.909±2; 208Pb/204Pb = 39.598±4 232Th/204Pb = 49.59 206Pb/204Pb = 18.700±3; 208Pb/204Pb = 38.463±4 232Th/204Pb = 18.41	
	SLTG (calc-alkaline, metaluminous)	206Pb/204Pb =16.237±2; 206Pb/204Pb = 36.653±4 232Th/204Pb = 8.28	
	SLTG (K calc-alkaline, shoshonitic affinity)	High ΣREE = 330 ppm and high ratio LREE/HREE Positive Eu anomalies show a variation in Eu* from 1.3 to 2.7 87Sr/86Sr (i) = 0.70709	Guimarães, 1989

Observations:
ETG = early tectonic granite; ESTG = early syn-tectonic granite; SLTG = syn- late tectonic granite
For more information see List of Abbreviations

are: initial ratio $^{87}Sr/^{86}Sr$ of 0.714 and Σ Nd range from - 22 to -18. The initial $^{87}Sr/^{86}Sr$ values for the ESTG rocks are very close to the Cordilleran crustal I- and S-types, e.g. the Chemehuevi plutons, whose $Sr_{(i)}$ range is 0.7083-0.7097 (John and Wooden, 1990). That result was interpreted to be due to melting derived from a basic to intermediate igneous component, whereas the SLTG data suggests increase in the crustal component.

A study of the δ^{18} O in porphyritic granites (ESTG) of the Seridó Belt carried out by McMurry *et al.* (1987) shows a range from + 7.0 to + 9.2 $^{0}/_{00}$, which is consistent with an I-type magma (δ^{18} O < 10 $^{0}/_{00}$). However, this information was combined with an initial ratio $^{87}Sr/^{86}Sr$ of 0.709 and low CaO and it was suggested that the source rocks may have had some metasedimentary (S-type) component.

Guimarães (1989) studied the Brasiliano granites in the Pajeú/Paraíba Belt and classified a potassic calc-alkaline suite with shoshonitic affinity with very high Σ REE content (330 ppm); Eu ranges from 1.3 to 2.7, and $^{87}Sr/^{86}Sr_{(i)}$ ratio = 0.70709. This suite was interpreted as S-type granites.

The Brasiliano granites in the Piancó/Alto Brígida Fold Belt have been intensively studied by Sial (1986) and Ferreira and Sial (1986), the data being shown in Table 4.3.

The potassic calc-alkaline granites (SLTG) are strongly enriched in LREE (LaN/YbN = 28 to 217) and show a *Eu negative anomaly, with values of Eu/Eu* from 0.89 to 1.0; they are depleted in HREE, suggesting transitional A-type granite. However, the $^{87}Sr/^{86}Sr_{(i)}$ ratio of 0.7058 indicates I-type granites. This is also supported by δ^{18} O < 10 $^{0}/_{00}$ (Sial, 1986).

The calc-alkaline granitoids (SLTG) are characterised by less enrichment in LREE relative to chondrite compared to the potassic calc-alkaline suite. The Yb content is low (< 1.45 ppm) and they show a Eu negative anomaly, with Eu/Eu* ranging from 0.75 to 0.91. LaN/SmN varies from 1.90 to 2.67. Σ Nd is - 22 to - 18; $^{87}Sr/^{86}Sr_{(i)}$ ratio = 0.714; and δ^{18} O > 10 $^{0}/_{00}$, and thus diagnostic of S-type granites (Sial, 1986).

The peralkaline granites show Σ REE from 89.2 to 296 ppm in the saturated group, while in the oversaturated group the Σ REE range from 67.07 to 309.79. Values of δ^{18} O are predominantly < 10 $^{0}/_{00}$. Eu/Eu* = 0.38 in the saturated group, and ranges from 0.86 to 1.19 in the oversatured group. These plutons have high K_2O, Ba and Sr. A more mafic magma is suggested as a source for these rocks (Ferreira and Sial, 1986).

4.3.8 Discussion

The petrogenetic study, and geochemical and isotopic signatures of the granites in the Itapetim district place constraints on the model for granitoid evolution and

emplacement. During this discussion this information will also combined with previous isotopic and REE data of granitoids from Borborema Province.

The ETG emplacement is probably related to the D_2 event that folded the supracrustal sequences. The deformation and the metamorphism provided conditions for the ascent and intrusion of subduction-related granites (ETG). This process resulted in crustal thickening and consequently increased heating provided conditions for the melting of the crustal material at depth, producing S-type, predominantly peraluminous granites.

The Brasiliano magmatism produced metalumionus and peraluminous granites (ESTG and SLTG) which originated from a mantle source (I-type, lower crustal derivation), whose emplacement mechanism resulted in mixed I- and S-type granites.

The ESTG marked by high K, Ba, Rb and Sr contents are indicative of a magmatic source. The distribution of the LREE (e.g. Nd and La/Yb) is equivalent to a highly fractionated pattern and indicates a mantle source origin (I-type, lower crustal derivation). δ^{18} O at < 10 $^{o}/_{oo}$ is also consistent with I-type granite. However, the $^{87}Sr/^{86}Sr_{(i)}$ ratios range from 0.709 to 0.708 and are more compatible with S-type granites. The presence of both types of granites in the same suite may reflect the mechanism of emplacement.

The metaluminous and peraluminous SLTG are calc-alkaline with a shoshonitic affinity (calc-alkaline and peralkaline suites) and show a high enrichment in K, Ba, Rb, Sr, Zr and in REE. The range of δ^{18} O displayed by these rocks indicates a magma which originated in the lower crust or upper mantle and which interacted with the crust during emplacement. This is also consistent with the range in the $^{87}Sr/^{86}Sr_{(i)}$ ratios. In the Itapetim district the SLTG suite consists predominantly of K calc-alkaline and calc-alkaline granites. Evidence of peralkaline granites is found along the Patos Lineament (see Fig. 3.21; Chapter 3).

The isotopic and REE data for the granitoids in Borborema Province indicate that the geochemical evolution cannot be related to a single crystal fractionation process (Tindle *et al.*, 1988; Brown and Becker, 1986), but it may have resulted from combined processes of wallrock assimilation and fractionation crystallization (DePaolo, 1981). An enriched mantle source and a crustal contribution to the granitic magma late during the granite fractionation sequence is proposed.

Several mechanisms of magma generation and evolution have been proposed for the granitoids of the Borborema Province: (i) crystal fractionation or wallrock assimilation (Leterrier *et al.*, 1990); (ii) crystal fractionation with multiple injection of basic magma (Sial *et al.*, 1992); (iii) immiscibility of magma (e.g. chemical equilibrium between ultrapotassic syenite and pyroxenite; Ferreira and Sial, 1992); and (iv) combination of immiscibility and crystal fractionation (Sial *et al.*, 1992), which resulted in the mixed I- and S-type granites with an increasing crustal component.

The emplacement was probably controlled by the dominant strike-slipe shear zones

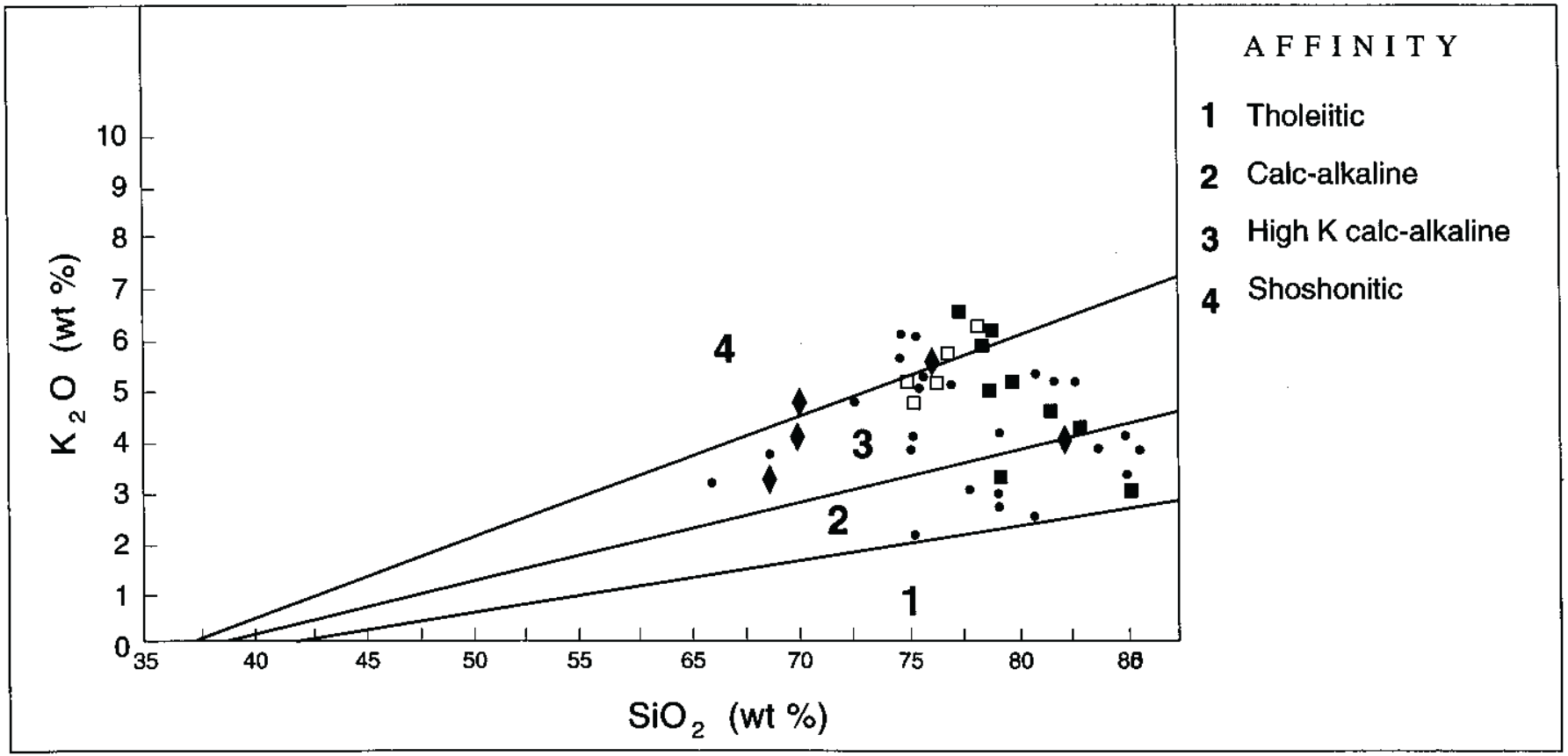

Figure 4.20 K_2O against SiO_2 diagram for Itapetim granitoids and gneisses hosting gold mineralization. Fields: tholeiitic, calc-alkaline, high-K calc-alkaline and shoshonitic igneous rocks (Peccerillo and Taylor; 1976).
Symbols are: ETG (filled square); ESTG (open square); SLTG (diamond); Gneisses (dot); For further information about sample labels see Appendix A4.3 for granites and A4.6 for gneisses.

(Leterrier *et al.*, 1990) producing the 'crustal shearing and thickening granitoids'.

With the continued orogeny one would expect considerable telescoping of the relationship between both Brasiliano type granites. A general progession from calc-alkaline or metaluminous hornblende-bearing suites to increasingly peraluminous (finally two-mica) granitoids is suggested. The maximum volume of Brasiliano (mixed I and S type) granite emplacement in the province may have occurred close to the time of transcurrent shearing. Subsequently, an extension regime followed the collision event with emplacement of late-tectonic peralkaline granites (not present in Itapetim).

There are general parallels between the evolution of Borborema Province and Mesozoic examples. In the northern North American Cordillera the maximum volume of Mesozoic (mixed I- and S-type) granite emplacement occurred close to the peak of metamorphism and approximately at the start of transcurrent motion on the Rocky Mountain-Tintina fault system. The greatest amount of dextral displacement of the (now) parautochthonous continental margin occurred well after consolidation of the batholiths. Late-orogenic highly fractionated granites of both mainly I-and A-(peralkaline) type followed closely after (5-8 Ma later). It took 70-80 Ma from earlier collision of the island-arc microcontinents to peak metamorphism.

The Itapetim petrogenetic data combined with the available isotope and REE information of the Borborema granitoids clearly suggests that the Brasiliano magmatism was generated by convergent plate margins above zones of active subduction marked by a high crustal component. This geotectonic setting played an important role in the gold mineralization, with a broad spectrum of intrusion-related gold vein deposits comparable to those found in the epizonal intrusive environment (Sillitoe, 1991). According to that author at least 85 % of Phanerozoic intrusion-related gold deposits were generated in association with a convergent plate tectonic regime.

In Itapetim area the gold mineralization hosted by K calc-alkaline, calc-alkaline and shoshonitic affinity igneous rocks (see Fig. 4.20) allows the possibility of a direct genetic link between potassic magmatism and the mineralization. Mesothermal gold deposits related to convergent plate margins above zones of active subduction and genetically associated with or hosted by potassic igneous rocks (e.g. Cripple Creek gold mining district, Colorado; N.S.W., Australia; Archaean lode-gold deposits in the Val d'Or and Timmins areas, Abitibi Subprovince, Canada; Norseman-Wiluna belt of the Yilgarn Block, Western Australia) have only recently been recognized, despite several occurrences (see Muller and Groves, 1993). In these deposits the relationships between the high-K igneous rocks and the subduction setting are also highlighted as a genetic association with the gold mineralization, which is an environment favorable to preservation of the gold deposits (Muller and Groves, 1993).

4.4 SUPRACRUSTAL ROCKS

4.4.1 Introduction

The supracrustal hosts for the gold mineralization in Borborema Province consist of schists, gneisses and amphibolites, albeit intensively mylonitised. Although, calc-silicate lithologies occur in the region, they are not present in these mineralized areas. In Itapetim District gneisses occur dominantly from the central domain to the Santo Aleixo area. A sequence consisting of schist, gneiss and amphibolite occurs from the central to the eastern domains. Schists are dominant in Cachoeira de Minas and São Francisco mines and also in the eastern side of the Itapetim District (Pimenteiras area). Amphibolite occurs intercalated in the supracrustal sequence in Itapetim District and also as lenses in the Archaean massif terrane (Boqueirão dos Cochos).

In this section of the Chapter, the petrography and geochemistry of the supracrustal hosts to the gold mineralization will be presented. This is followed by a discussion about the geotectonic setting for these rocks.

4.4.2 Petrography

a) Gneisses

Several varieties of gneiss occur, mainly in Itapetim District, but also associated with mafic rocks in Archaean massifs (Boqueirão dos Cochos). The following types have been identified: augen gneiss, garnet-biotite-muscovite gneiss, biotite gneiss, biotite-muscovite gneiss, and biotite-chlorite gneiss. Although not common, gneisses with fibrolitic sillimanite (São Francisco area) or prismatic sillimanite (Boquierão dos Cochos) were also found.

These rocks are mylonitized and intensely deformed (Fig. 4.21a). The original K-feldspar phenocrysts have produced porphyroclasts with evidence of deformation (e.g. fractures or recrystallized rims). Sometimes, porphyroblasts of feldspar represent likely poikiloblasts with inclusions of the matrix, as displayed in Fig. 4.21b. Ultramylonitic gneiss has undergone extreme plastic deformation. However, porphyroclasts of plagioclase feldspar or garnet respond in a rigid fashion and show brittle deformation with the grains completely fragmented (see Fig. 4.38d). Quartz has undergone extensive syntectonic recrystallisation and has reacted to strain by the development of subgrains which are oriented parallel to the deformation bands (Fig. 4.21c). A new fabric with a crenulation schistosity has been produced by refolding of an earlier deformation and forms segregation layers into phyllosilicate-rich and quartz-feldspar

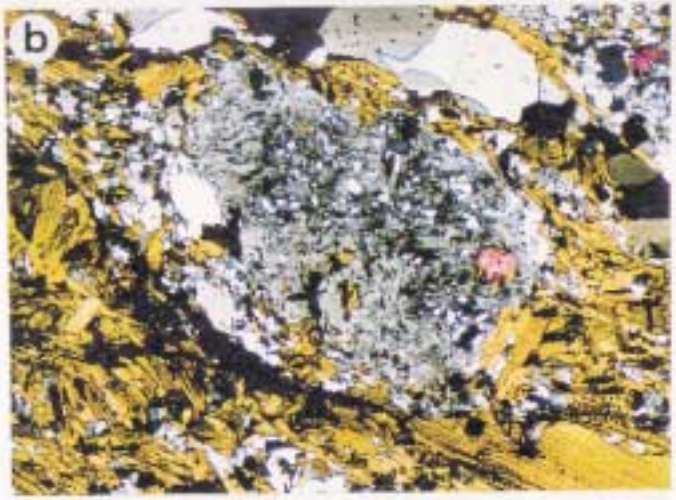

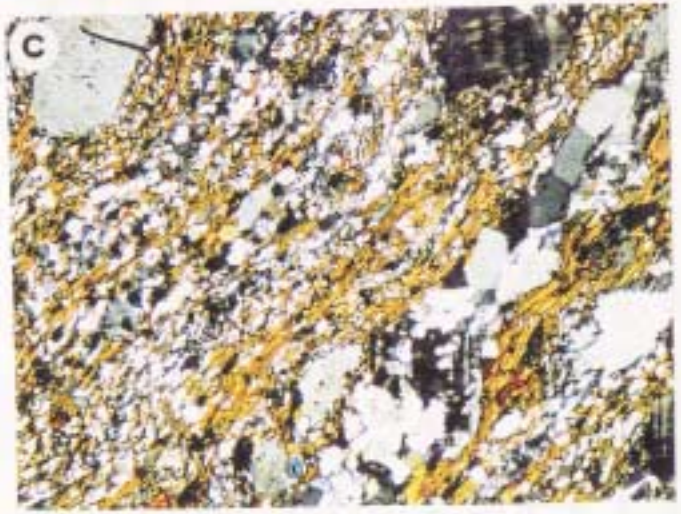

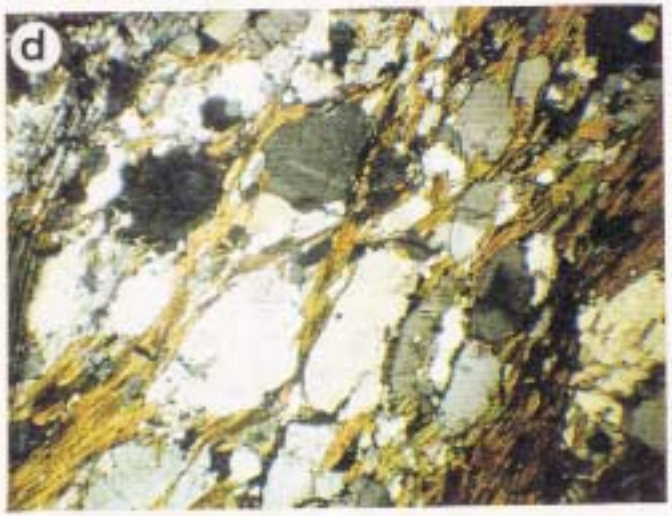

Figure 4.21a Ultramylonitic gneiss which has undergone extreme plastic deformation where a few porphyroclasts of plagioclase feldspar are dispersed in the matrix. Evidence of a new fabric is highlighted by iron oxide. Porphyroclasts of feldspar show fractures and develop trails where recrystallisation has occurred. (PPL.; TL; WOF = 2500 µm; MG-R-172B, Degredo, Itapetim District , west domain).

Figure 4.21b Poikiloblast of feldspar developed in biotite gneiss showing inclusions of quartz, biotite and epidote. (XPL.; TL; WOF = 750 µm; MG-T-033, Degredo, Itapetim District , west domain).

Figure 4.21c Biotite-muscovite gneiss where quartz has undergone extensive syntectonic recrystallisation with the development of subgrains. Segregation of quartz-feldspar and mica rich-layers produce a new fabric with remarkable parallelism (XPL.; TL; WOF = 2500 µm; MG-R-157, Sertãozinho, central domain, Itapetim District).

Figure 4.21d A pronounced segregation into quartz and plagioclase layers and thin layers of biotite developed in biotite gneiss. Note (in the middle) small quartz grains which have recrystallised and fill spaces at the end of the feldspar crystals (XPL.; TL; WOF = 750 µm; MG-R-157, Sertãozinho, central domain, Itapetim District).

bands (e.g. Boqueirão dos Cochos area); this probably developed by anatexis. Generally the gneisses show remarkable parallelism of the segregated quartz-feldspar and mica rich-layers (Figs. 4.21c and 4.21d) with a new superimposed fabric where ribbons of quartz are common.

Muscovite and biotite are common. Muscovite associated with plagioclase points to the breakdown of plagioclase to mica. This process may have formed by metasomatism, produced by fluid flow associated with the deformation. Biotite and chlorite are the only hydrous minerals present. Biotite and garnet altered to chlorite reflects retrogression.

The matrix consists of very fine grains of quartz and feldspar, and some mica. Sometimes, coarse poorly-sorted fragments of feldspar and quartz occur and may reflect a sedimentary origin. These fragments are embbed in a matrix enriched in mica and suggest an original volcanogenic or arkosic lithology (Fig. 4.21e). Opaque or 'heavy ' minerals (e.g. garnet and zircon) arranged in very fine layers are consistent with sedimentary banding (e.g. Pimenteiras area, Itapetim east domain). However, the breakdown of K-feldspar and plagioclase occurs in most of the gneisses and is interpreted as the result of metamorphism of acid plutonic rocks. This is consistent with an igneous texture retained by some less mylonitic specimens. The enrichment in allanite and titanite is in agreement with an igneous origin. (Fig. 4.21f). Kyanite is rare. Abundant albite, epidote, and titanite associated with crenulated chlorite reflect retrograde processes and may point to original mafic rocks.

b) Schists

Several varieties of schist have been identified. In Itapetim District they are predominantly mica-schists (biotite- and muscovite-schists) with garnet and rare kyanite. In São Francisco area mica-schists are usually associated with aluminum silicates and the following types occur: cordierite schist, andalusite schist, sillimanite-schist and garnet-mica schist. In Cachoeira de Minas area mica schists are very abundant, with a high content of chlorite. In this area the chlorite-muscovite-schist shows a crenulation fabric which is so intense and well developed that the early fabric is completely obliterated and a new fabric is formed in which kink bands are very common (see Fig. 4.38c). Generally the schists show a crenulation schistosity produced by refolding of an earlier fabric. The foliation tends to wrap around the porphyroblasts of cordierite, andalusite, (São Francisco area), K-feldspar or garnet (Itapetim District). Biotite porphyroblasts have been stretched by the shearing in one direction and form S and C fabrics in all areas (see Chapter 3).

General the groundmass of the schists consists of biotite, muscovite and quartz. However, in Cachoeira de Minas and Itapetim (central domain) areas graphite occurs as

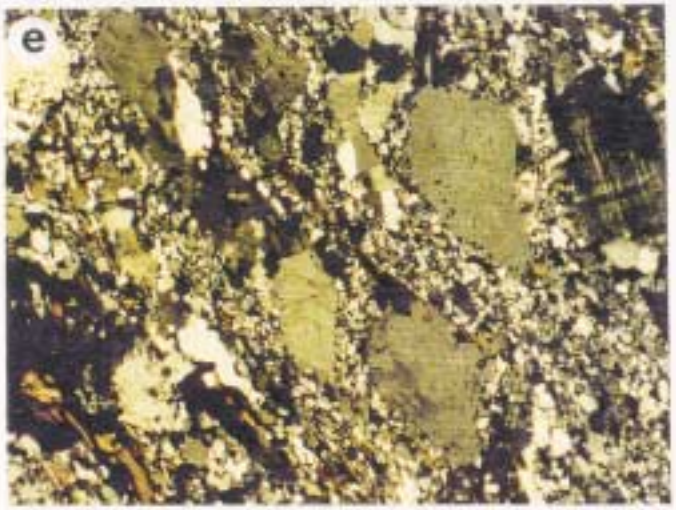

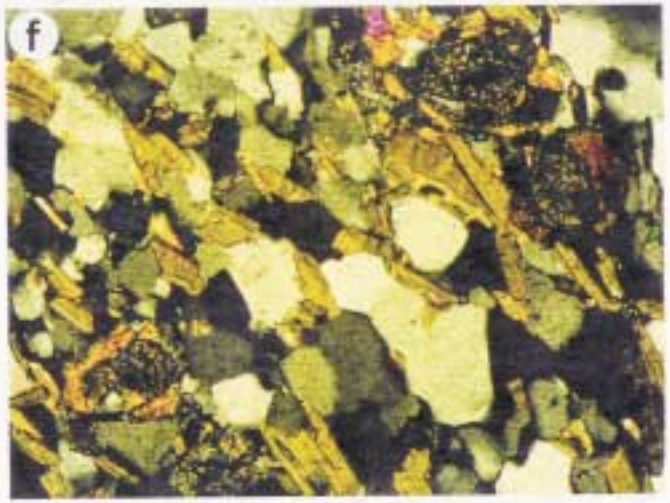

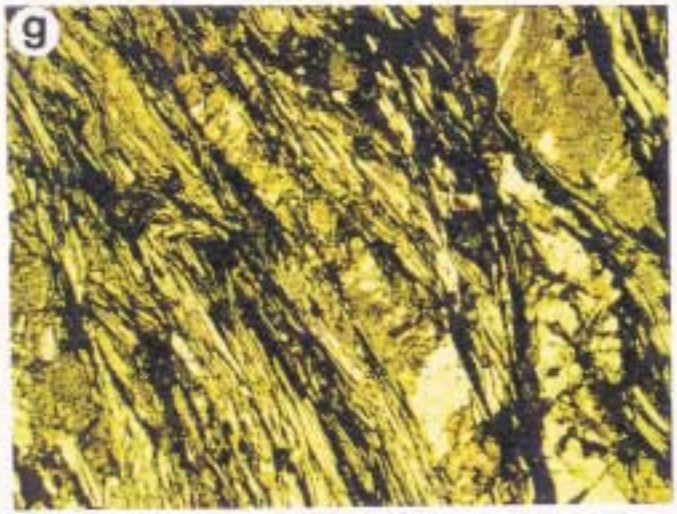

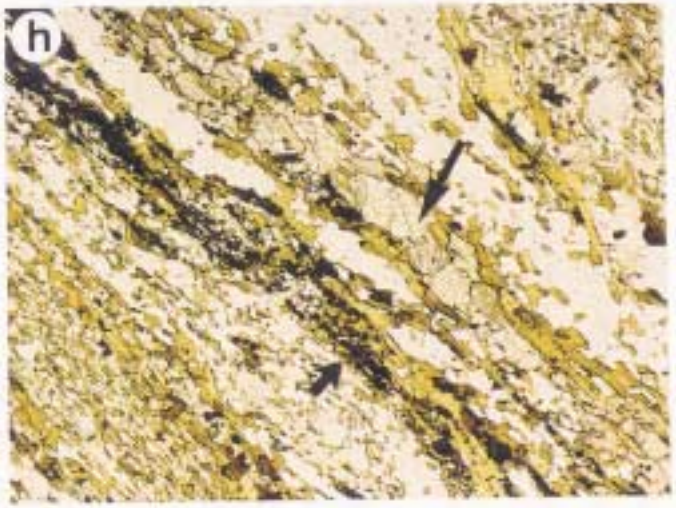

Figure 4.21e This gneiss contains abundant fragments of feldspar and quartz, which are poorly sorted and dispersed in the matrix. It could have a volcanogenic or graywacke origin. (PPL.; TL; WOF = 2500 µm; MG-T-037, Degredo, Itapetim District , west domain).

Figure 4.21f Gneiss characterised by a granular texture consisting of quartz, feldspar and biotite. The igneous texture and the enrichment in allanite (on the top right and on bottom left) suggest an igneous derivation (XPL.; TL; WOF = 750 µm; MG-T-115, Pimenteiras, Itapetim District , east domain).

Figure 4.21g Biotite-muscovite schist composed dominantly of segregated layers of muscovite and porphyroblastic albite, an association suggesting a metamorphosed volcanogenic sediment or a lava flow. (PPL.; TL; WOF = 4500 µm; MG-R-224, Cachoeira de Minas Mine area).

Figure 4.21h Penetrative foliation defined by layers of phyllosilicate (biotite, muscovite and chlorite) and quartz-feldspar in biotite-chlorite schist. Note (see large arrow) a layer of carbonate developed. An intense chloritization is produced and forms a layer enriched in opaque minerals (see small arrow). These assemblages indicate break-down of ferromagnesian minerals and suggests an original basic rock. (PPL.; TL; WOF = 2500 µm; MG-T-151A, Sertãozinho, Itapetim District, central domain).

part of the matrix. Fibrolitic sillimanite developed mainly at the expense of biotite (São Francisco mine); it also occurs in Boqueirão dos Cochos as prismatic sillimanite. Muscovite schists dominate in eastern Itapetim and Cachoeira de Minas mine areas, and are composed dominantly of segregated layers of light minerals consisting of muscovite and porphyoblastic albite and low contents of ferromagnesian minerals (Fig. 4.21g). This suggests that these rocks may have been derived from a metamorphosed volcanogenic sediment or a lava. The schists which are enriched in Al-silicates in São Farncisco mine may be pelite-derived or from a volcanogenic sediment. Biotite schists enriched in chlorite are common, but are dominant in central Itapetim and in Cachoeira de Minas. Usually these rocks show a relatively high content of ferromagnesian minerals (e.g relict hornblende; Fig. 4.21i) associated with titanite, apatite, epidote, and opaque minerals. An origin from basic rocks is probable for these schists. The tabular grains of carbonate (grain-flattening fabric) defined an L-fabric and reflect breakdown of ferromagesian minerals (Fig. 4.21h), probably also in original mafic rocks (Itapetim central area).

The schists have a mylonitic texture, and are usually characterised by a penetrative foliation, which produces the alignment of the individual phyllosilicate minerals. A marked parallelism results in a new fabric and this is interptered to be associated with the regional shearing direction. However, randomly orientated mica (biotite and muscovite) sometimes occurs and exhibits decussate texture (Figs. 4.16i and 4.16j), suggesting syntectonic development during late shearing related to retrograde metamorphic processes.

c) Amphibolites

The mineralogy of the amphibolite consists of altered hornblende (Fig.4.21k), greenish-brown biotite and epidote, with lesser amounts of plagioclase. Plagioclase is rare and hornblende shows corona texture with the rims surrounded by biotite (Fig. 4.21l). Titanite and epidote are common accessory minerals. Biotite gives a weak schistosity to the rock.

The classification of Leake (1978) was used to classify the amphiboles (see Appendix A4.1). Amphiboles from amphibolite samples from the fold belt (Itapetim area) and Archaean massif (Boqueirão dos Cochos) were analysed (see data in Appendix A4.9) . They meet the criteria for calcic amphiboles (Fig. 4.22). The 16 analyses for the Archaean amphibolite (MG-R-208A) cluster closely on the plot and fit in the field of ferro-tschermakite hornblende. The amphiboles are zoned, which is common for a metamorphic rock. The Itapetim samples fall in two fields: ferro-tschermakite hornblende (MG-R-163G, MG-T-056, MG-T-101); and tschermakite hornblende (MG-R-141, MG-R-137). The first group occurs intercalated in the mafic sequence of

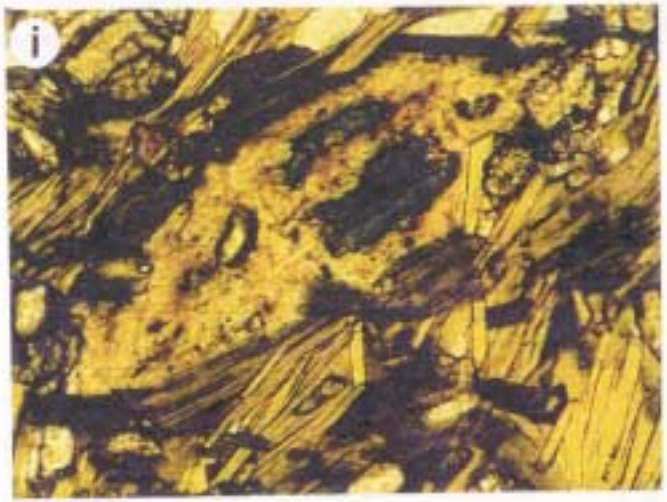

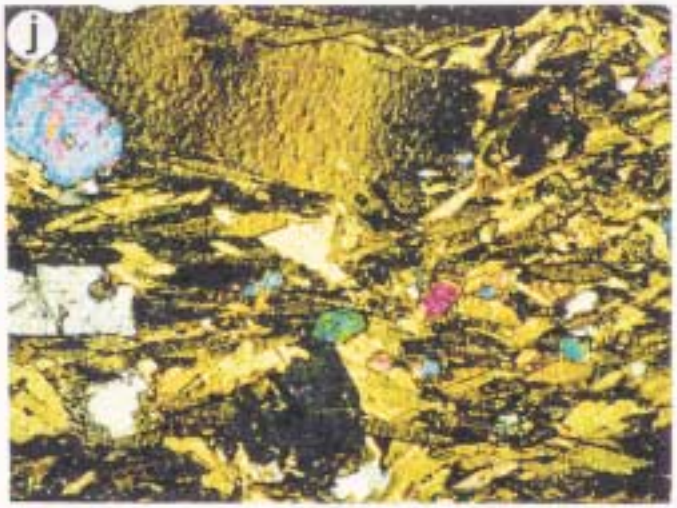

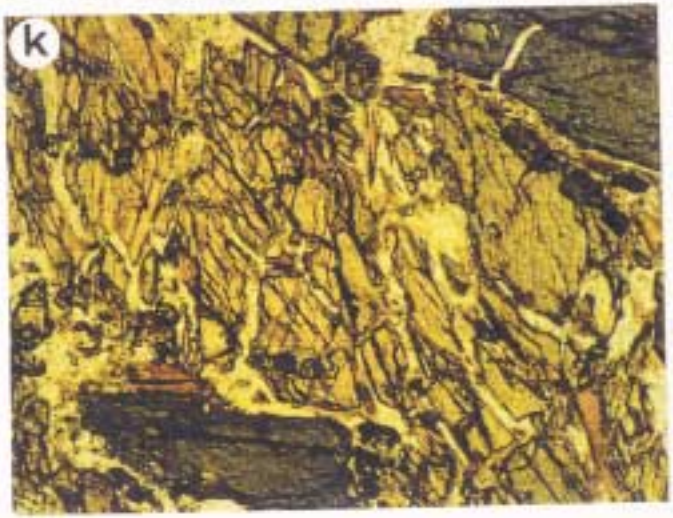

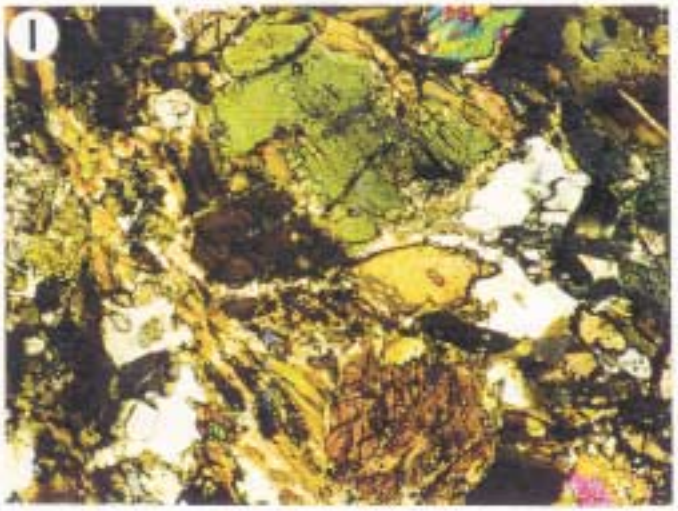

Figure 4.21i Biotite schist showing hornblende breakdown to produce chlorite and biotite. Relics of green hornblende occur in the middle of chlorite. Note the enrichment in titanite. The decussate texture suggests recrystallisation. A basic rock is suggested as a protolith for this rock. (XPL.; TL; WOF = 750 µm; MG-T-089, Sertãozinho, Itapetim District, central domain).

Figure 4.21j Biotite schist showing enrichment in epidote and titanite. The slight decussate texture suggests recrystallisation, and the high contents in titanium may be derived from mafic rocks. (XPL.; TL; WOF = 2500 µm; MG-T-050, Degredo, Itapetim District , west domain).

Figure 4.21k Amphibolite consisting mainly of bladed tschermakite hornblende, biotite, and lesser amounts of plagioclase. Titanite is an abundant accessory mineral. Biotite gives a weak schistosity to the rock. (XPL.; TL; WOF = 2500 µm; MG-R-141, São José do Egito to Brejinho road).

Figure 4.21l In this amphibolite the ferromagnesian minerals are destroyed and hornblende shows rims surrounded by biotite. (XPL.; TL; WOF = 2500 µm; MG-T-101, Sertãozinho, Itapetim District, central domain).

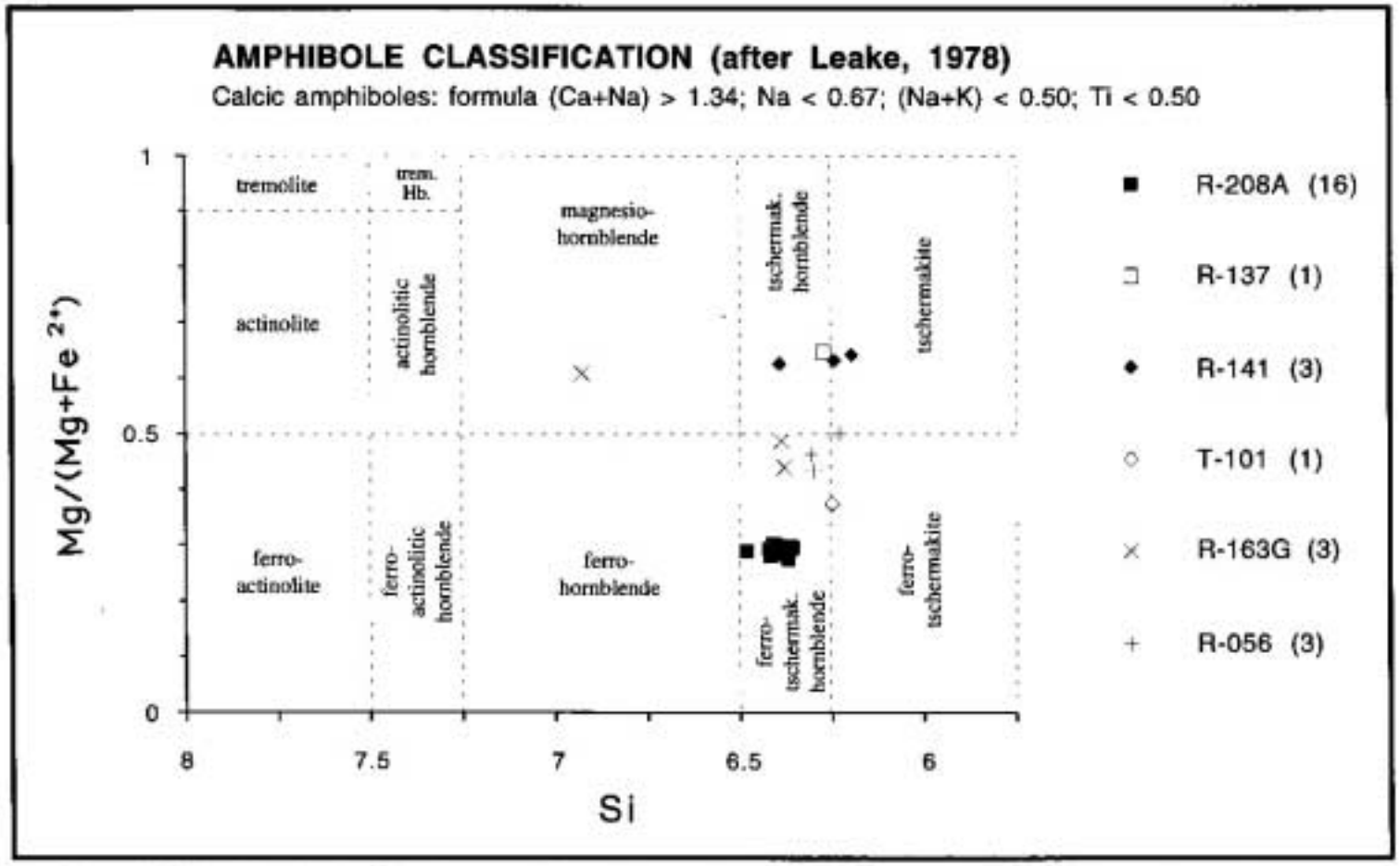

Figure 4.22 Amphibole classification according to (Leake, 1978), calculated from electron microprobe analyses. Ferrous/ferric iron contents have been estimated by varying oxide contents and maintaining constant total Fe, until the cation sum: (Si+Ti+Al+Fe+Mn+Mg) equals13. Bracket numbers give number of analyses; for further information see Appendix A4.9.

the Irajaí Complex, whereas the second group forms layers associated with paragneisses.

4.4.3 Geochemistry

The distribution of major elements in the supracrustal rocks (gneisses and schists) shows a general depletion in Fe, Mg and Ca, although the gneisses contain substantially less of these elements than the schists. Potassium and Na_2O have a marked enrichment in both rock-types, but K_2O is higher in schists and Na_2O slightly higher in gneisses. Aluminium and TiO_2 are relatively high and have a similar distribution in both lithologies, but TiO_2 is slight higher in the schists. The following discussion attempts to characterise the protoliths of the gneisses and schists using major and trace element classification schemes (Figs. 4.23 to 4.26). These schemes have been derived from both previous studies and from empirical observations during this study.

In the gneisses the range of K/Ba is from about 10 to 400 and K/Rb varies from about 100 to 400. These values would suggest a granitic protolith. The K/Ba range is within that covered by all granites types, but four gneisses do stand out as having the highest K/Ba (e.g. 250-400); these might be derived from quite fractionated granites. In the schists these ratios show a range of K/Ba from 25 to 150 and K/Rb from 70 to 300 (see Tables 4.4 and 4.5). These data are also consistent with a magmatic origin (Nesbitt and Sun, 1976).

However, some of these elements are extremely mobile during metamorphism, and it is likely that some original values have been modified. Govett (1985) has shown that decreased K/Rb ratios in conjunction with elevated K/Ba and Rb/Sr ratios, are typical of mineralised rocks in magmatic-related deposits. Ultramafic, mafic or felsic rocks possess intrinsically low primary abundances of lithophile elements and consequently the enhanced levels of K, Rb, and Ba in the host rocks could be related to enrichment by the hydrothermal fluids, such as occurs in Hollinger and Kerr Addison mines in Canada (Kerrich, 1989).

A distinctive negative correlation between the different lithologies and Sc was shown in schists (Fig. 4.27a). The contents in Sc defined two groups: < and > 30 ppm, approximately. The group with values < 30 ppm consists of São Francisco, eastern Itapetim and Cachoeira de Minas schists, whereas in the samples from Itapetim central domain, Santo Aleixo and Canafístula, the values are > 30 ppm. The distribution suggests a fractionation trend and it may reflect variations between mafic rocks with the high Sc values, and felsic rocks with lower Sc contents. For gneisses the correlation is not as distinctive but two groups are again suggested (< and > 11ppm). It is suggested that values < 11 ppm are felsic-derived, whereas the samples with values

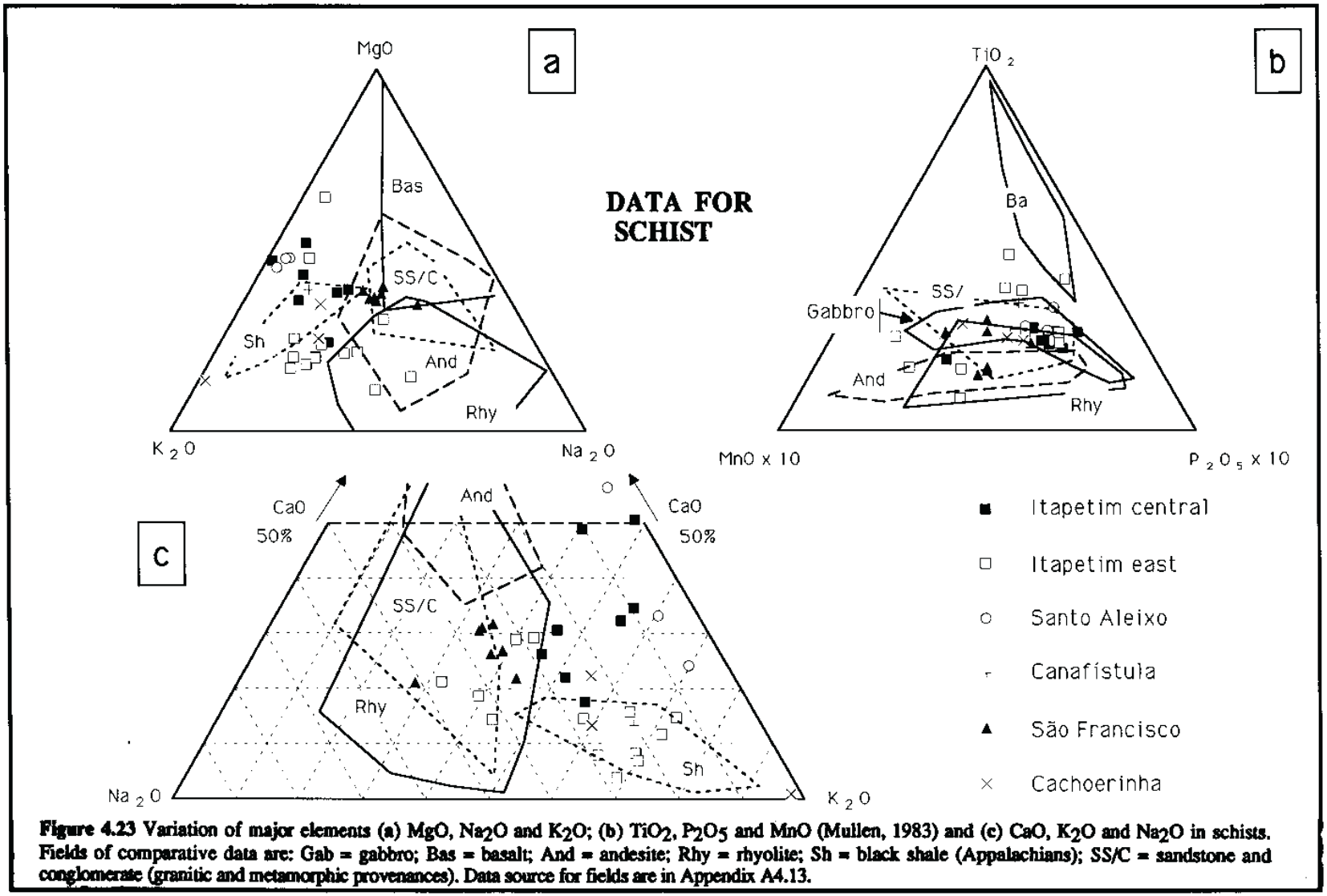

Figure 4.23 Variation of major elements (a) MgO, Na_2O and K_2O; (b) TiO_2, P_2O_5 and MnO (Mullen, 1983) and (c) CaO, K_2O and Na_2O in schists. Fields of comparative data are: Gab = gabbro; Bas = basalt; And = andesite; Rhy = rhyolite; Sh = black shale (Appalachians); SS/C = sandstone and conglomerate (granitic and metamorphic provenances). Data source for fields are in Appendix A4.13.

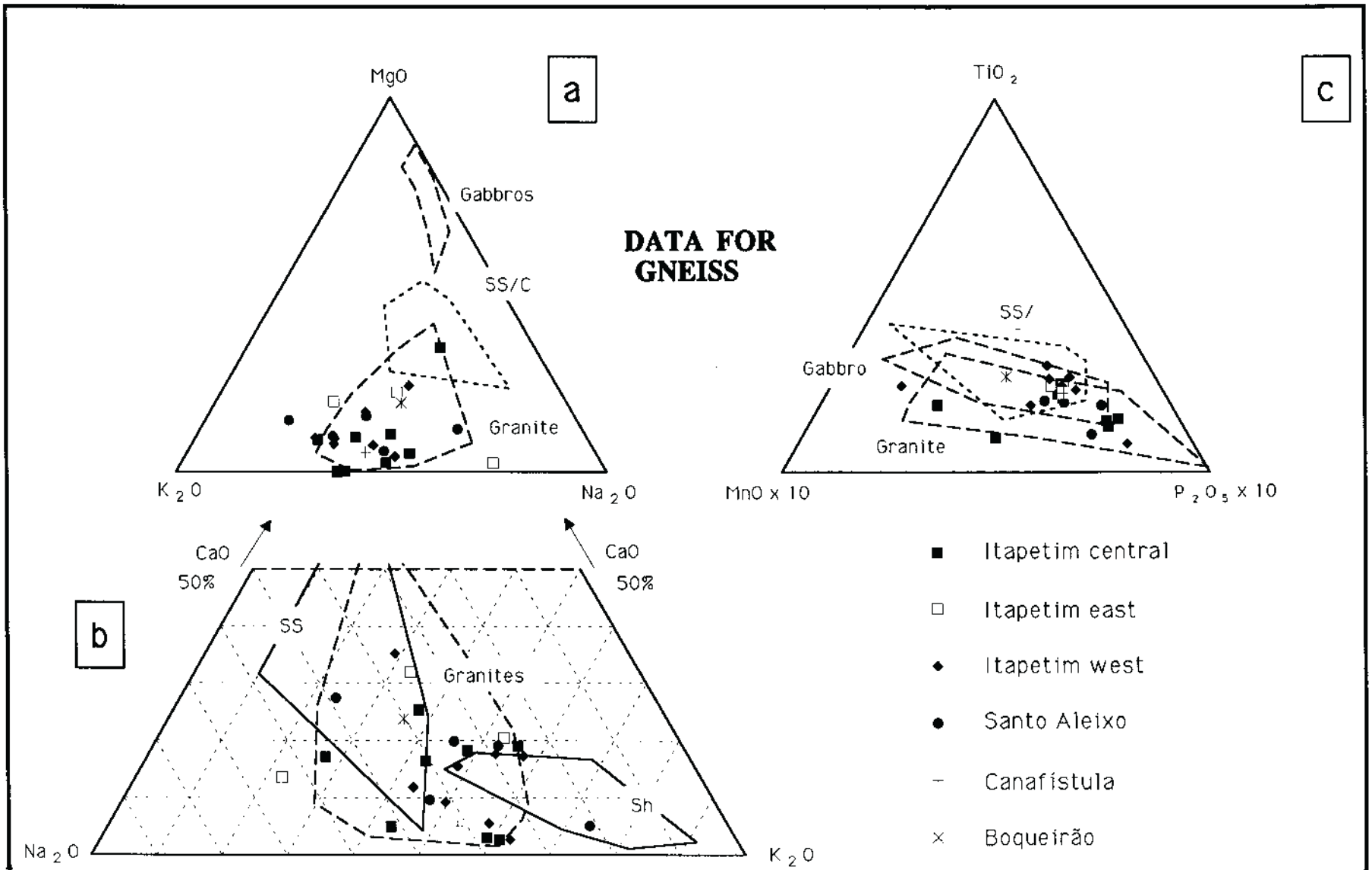

Figure 4.24 Variation of major elements (a) MgO, Na_2O and K_2O; (b) TiO_2, P_2O_5 and MnO (Mullen, 1983) and (c) CaO, K_2O and Na_2O in gneisses. Fields of comparative data are: Gabbro; Granite; Sh = black shale (Appalachians); SS/C = sandstone and conglomerate (granitic and metamorphic provenances). Data source for fields are in Appendix A4.13.

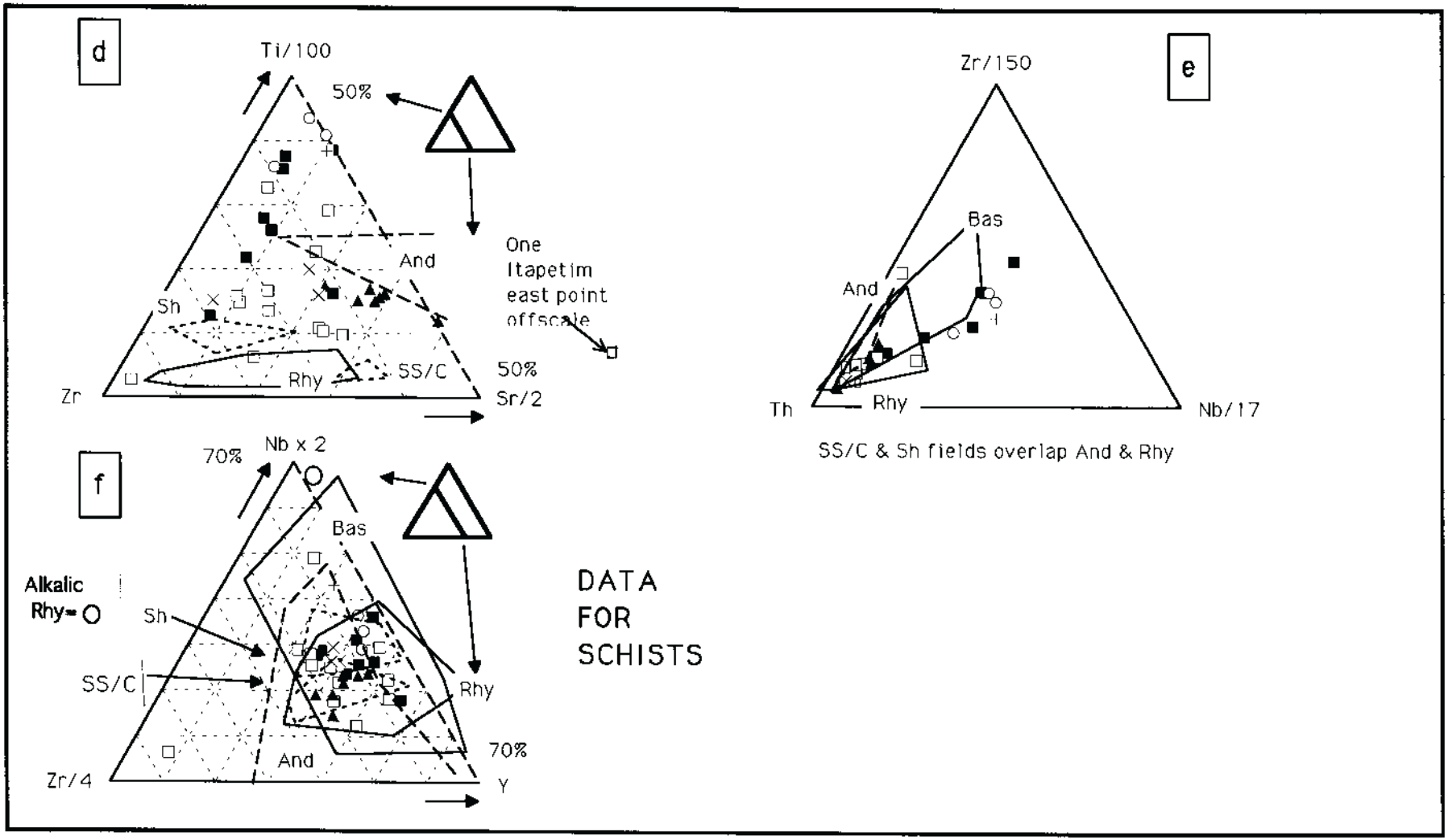

Figure 4.25 Variation of trace elements (d) Ti, Sr and Zr; (e) Zr, Nb and Th; (f) Nb, Y, and Zr in schists. The fields and the symbols are as mentioned in Fig. 4.23. Data source for fields are in Appendix A4.13.

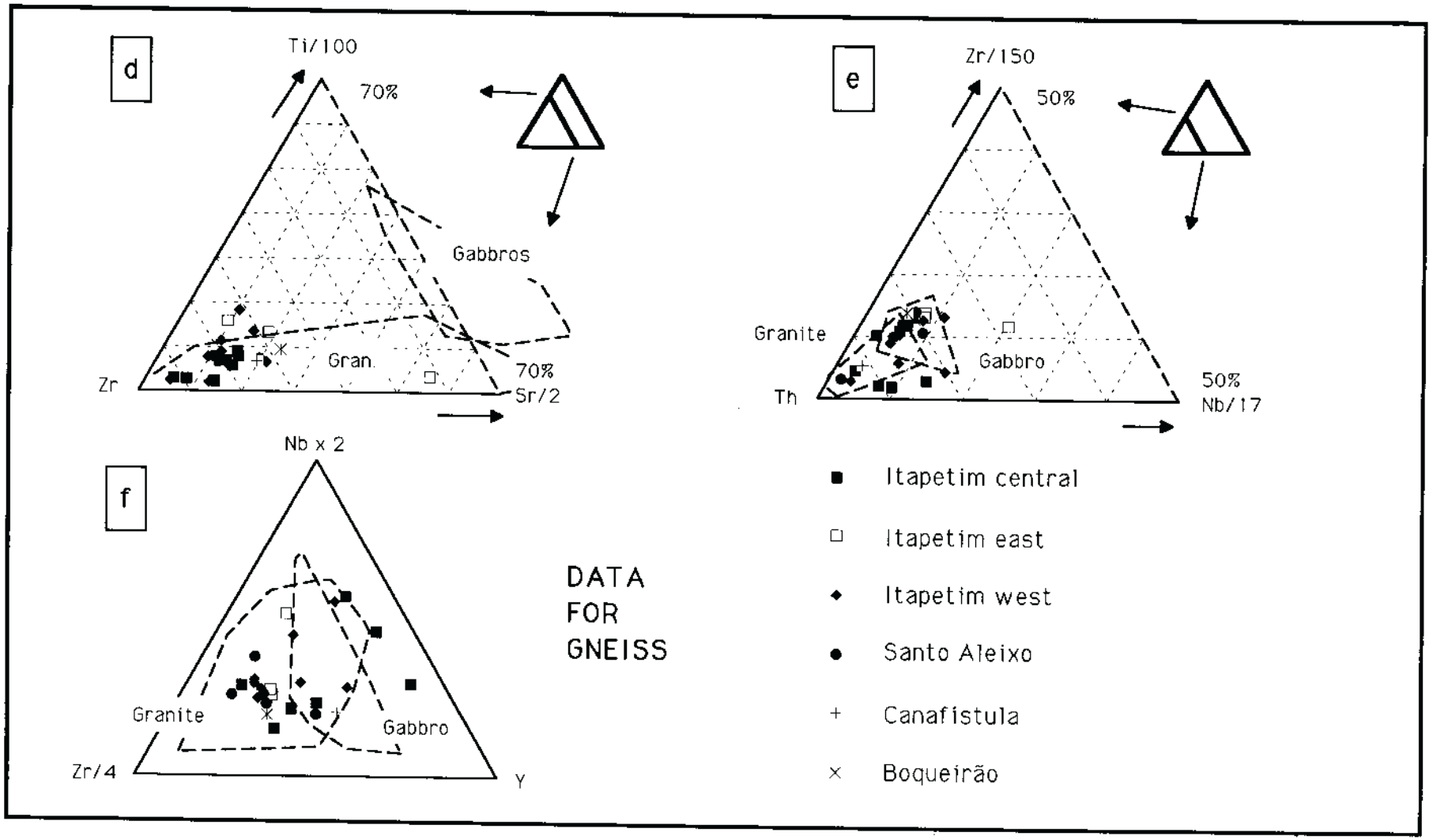

Figure 4.26 Variation of trace elements (d) Ti, Sr and Zr; (e) Zr, Nb and Th; (f) Nb, Y, and Zr in gneisses. The fields and the symbols are as mentioned in Fig. 4.24. Data source for fields are in Appendix A4.13.

> 11 ppm may be related to more intermediate rocks (Fig. 4.27b; see Turekian and Wedepohl, 1961).

The major and trace element contents suggest three group of schists are present:

(i) low values in Fe, Mg, Na, Y, Rb, Sc and high K, Zr, Th, Ba (Itapetim east and Cachoeira de Minas)

(ii) high Fe, Mg, Ca, Ba, Rb, Zr, Sc and low K (Itapetim central and Santo Aleixo)

(iii) high Mg, Ca, Th, Sr and Sc and low Fe, K, Rb, Ba (São Francisco).

Large variations shown in the distribution of major and trace elements by the schists and gneisses should reflect ranges in the original source composition. For example, the discrimination diagram for volcanic rocks (Winchester and Floyd, 1977) suggests a large variation in the source rocks for the schist: sub-alkaline basalt, andesite, rhyodacite/dacite and some alkali basalt (see Fig. 4.28a). The gneisses fall predominantly in the field of rhyolite and trachyandesite, and they could be related either to felsic volcanic rocks, or fractionated granitoids (see Fig. 4.28b).

Amphibolite samples from the fold belt (central Itapetim District) and the Archaean basement (Boqueirão dos Cochos area) were analysed. Although these two types of amphibolite occur in different geotectonic settings their geochemistry will be discussed together. The main petrochemical characteristics are given in Table 4.6

The Harker-type diagrams display a negative correlation of MgO, Al_2O_3 and CaO with SiO_2, which is typical for magmatic rocks (Fig. 4.29). Two groups are characterised based on the major element distribution: one group enriched in K, P and Ti (MG-T-101, MG-T-112) and the second one depleted in these elements (MG-R-141, MG-R-163G, MG-R-208A). Volcanic classification based on alkali and silica content (after LeMaitre, 1984) indicates that the Archaean amphibolite plots in the basaltic andesite field and the Itapetim samples are predominantly basalt (Fig. 4.30a). The AFM diagram indicates that the Itapetim amphibolites are calc-alkaline (MG-T-112, MG-T-101, MG-R-163G) and tholetiitic (MG-R-141), and the Archaean amphibolite (MG-R-208A) is tholeiitic (Fig. 4.30b).

The spidergrams for the Itapetim amphibolite show two distinct groups: the first one (MG-T-101, MG-T-112) characterised by large negative Sr, small negative Th and Ba anomalies, and strong positive K and Rb. The second group (MG-R-141, MG-R-163G) shows only small negative Sr anomalies and a hint of a positive Th anomaly. Potassium and Rb anomalies are less strong compared to the first group. The pattern of the Archaean amphibolite (MG-R-208A) is similar to the Itapetim second group. All samples show large positive K and Rb anomalies (Fig. 4.31). This data suggests an origin related to ocean floor basalts.

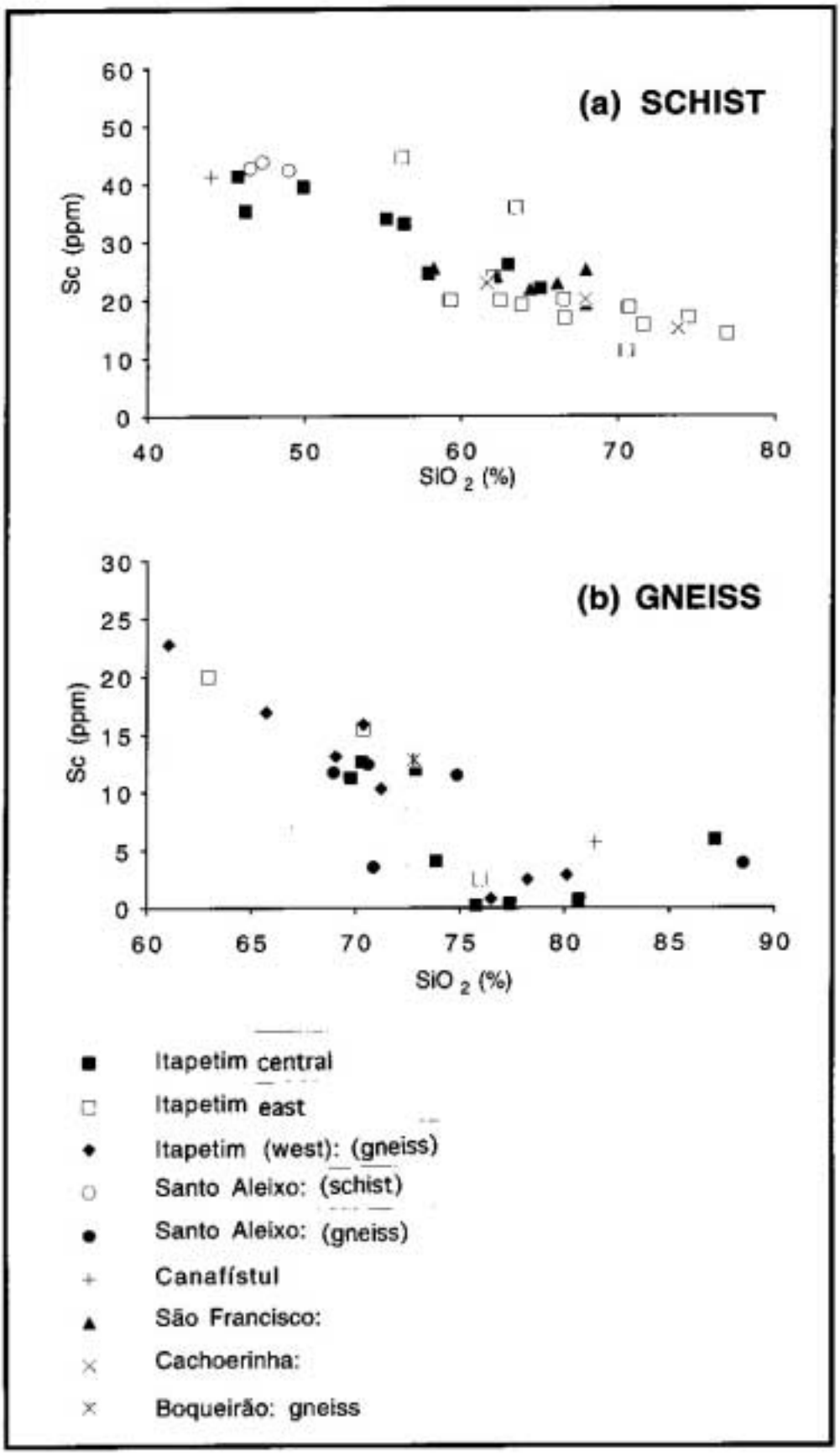

Figure 4.27 Scandium contents of (a) schist and (b) gneiss plotted against silica contents.

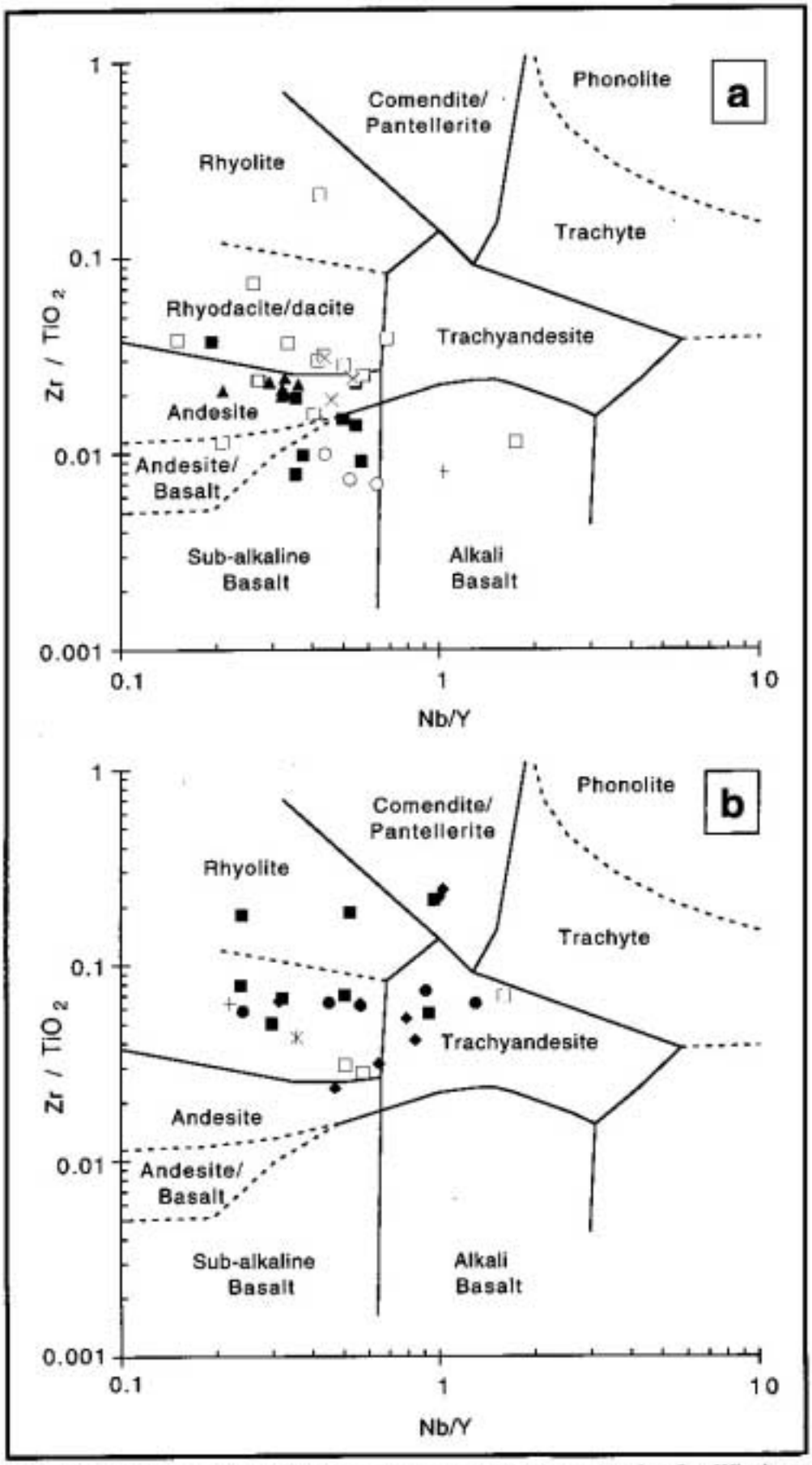

Figure 4.28 Trace element discrimination diagrams for volcanic rocks after Winchester and Floyd (1977): (**a**) schists and (**b**) gneisses. Symbols are the same as in **Fig. 4.27.**

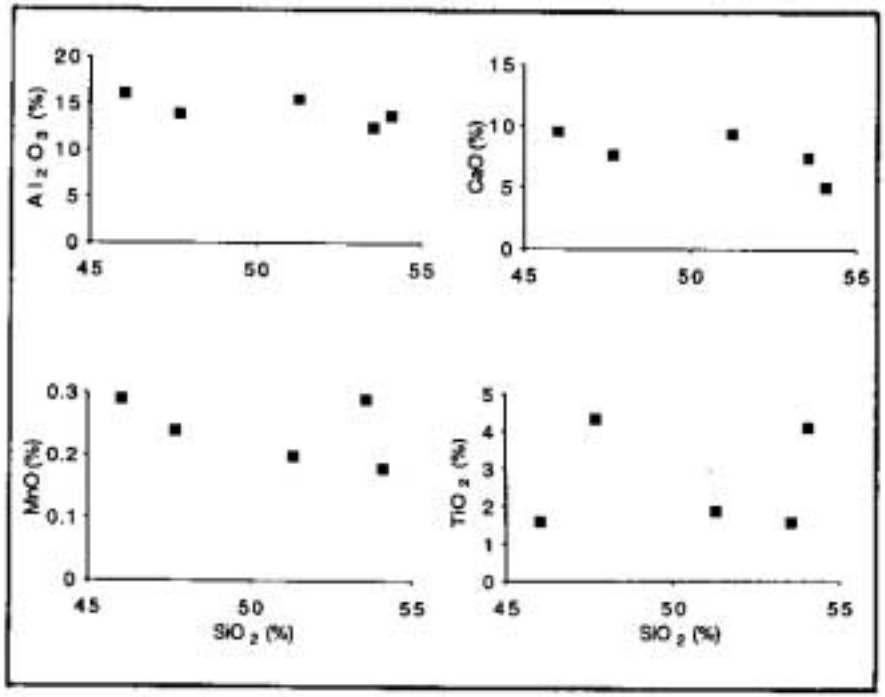

Figure 4.29 Major and minor element contents of amphibolites plotted as Harker-type diagrams.

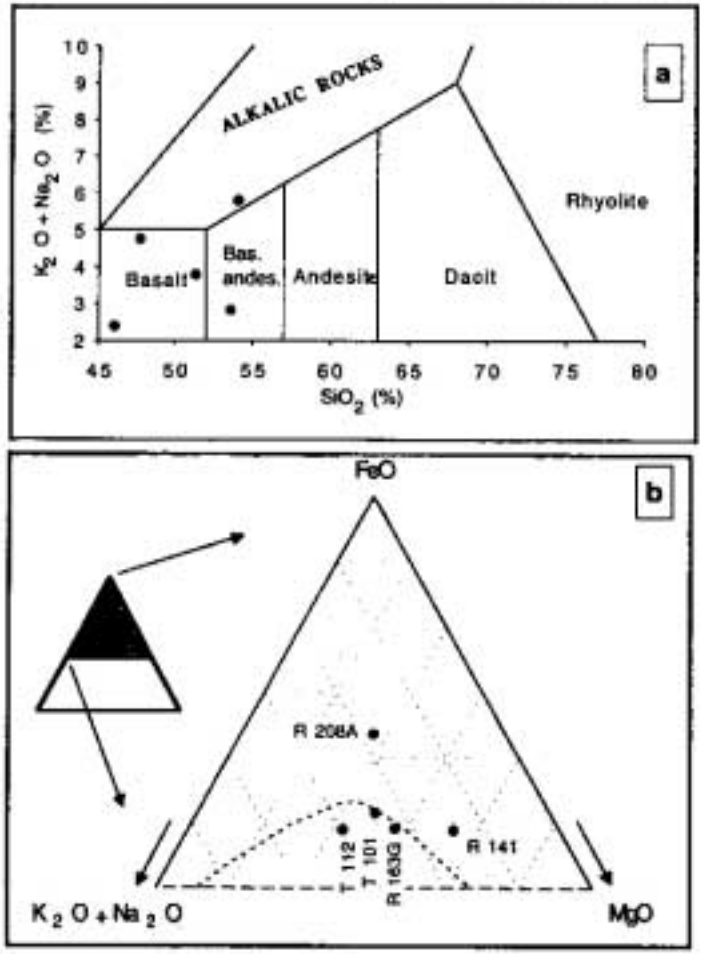

Figure 4.30 (a) Classification of the amphibolites by alkali and silica content (after LeMaitre, 1984). Note that the Archaean amphibolite plots in the basaltic andesite field and the Itapetim samples are predominantly basalt; one sample fits as an alkaline rock. **(b)** AFM diagram for amphibolites (Irvine and Baragar, 1971); the dotted curve is the tholeiitic (above)/calc-alkaline (below) boundary. The Archaean sample is tholeiitic and the Itapetim samples are predominantly calc-alkaline (except one MG-R-141).

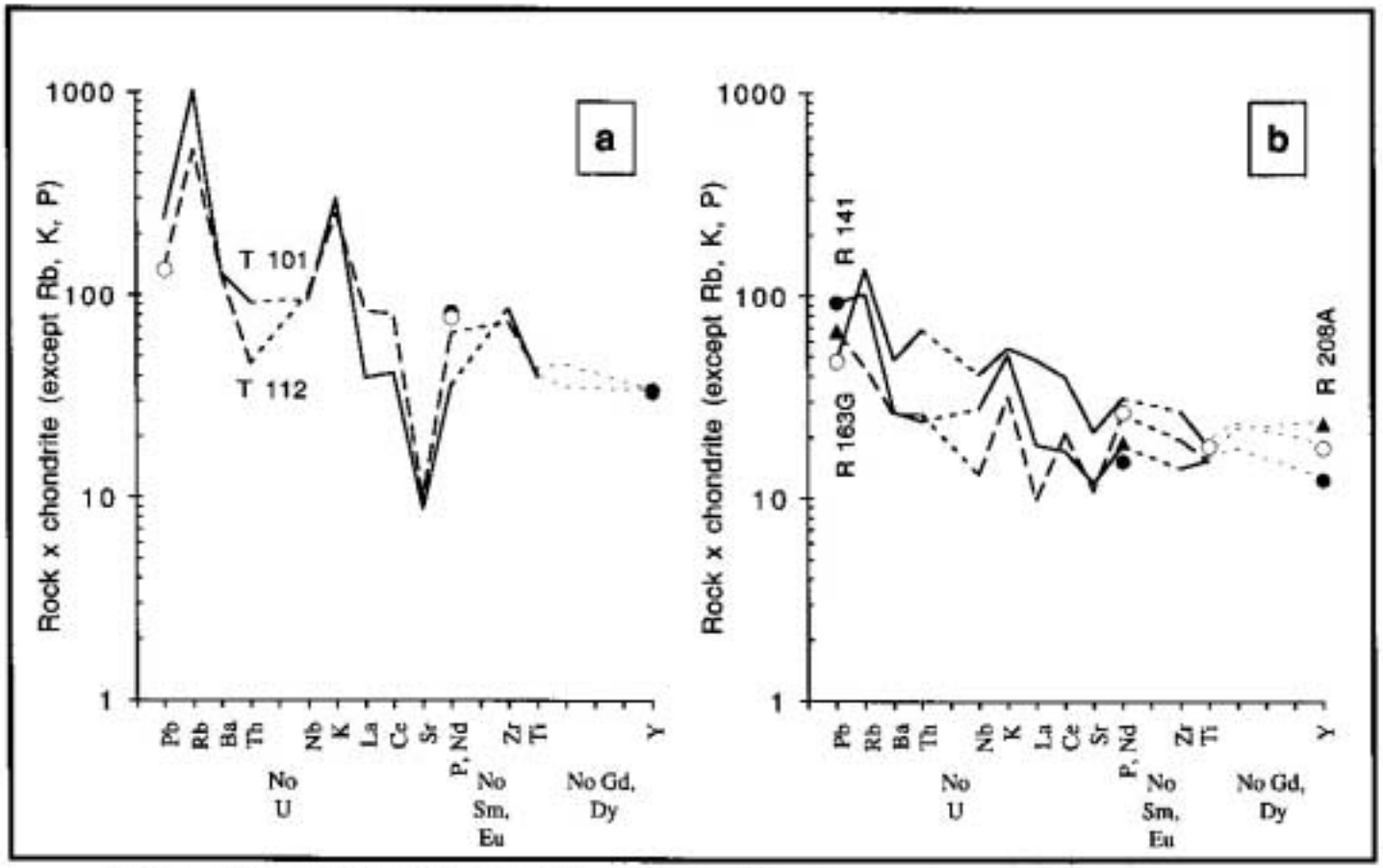

Figure 4.31 Chondrite-normalised incompatible trace element diagrams for amphibolites: (a) Samples MG-T-101and T-112; and (b) Samples MG-R-141; MG-R-163G and MG- R-208. See text for details.

4.4.4 Geotectonic Setting

The major and trace element data for schists and gneisses show conflicting evidence of the possible protoliths of these rocks. No doubt much of this can be related to mobility of some elements during metamorphism. Although an original derivation from mafic rocks is easier to identify, the difficulties increase when attempting to distinguish between protolith of an igneous acidic or sedimentary rock (e.g. greywackes). In this case the reconstruction of their protoliths is extremely difficult (e.g. Figs. 4.23 to 4.26). However, geochemical information combined with petrographic and field relationships makes the characterisation of the original rocks possible.

The Zr/TiO_2 against Nb/Y discrimination diagrams for volcanic rocks (Winchester and Floyd, 1977) show that the schists (Fig. 4.28a) fall within the fields of intermediate to basic rocks: (i) rhyodacite/dacite: eastern Itapetim and Cachoeira de Minas; (ii) andesite: São Francisco, Itapetim east domain and Cachoeira de Minas; and (iii) sub-alkaline basalt: Itapetim central domain and Santo Aleixo areas. The gneisses fit predominantly in the field of rhyodacite with a few samples falling in the trachyandesite field (Fig. 4.28b).

The chemistry of the schists (silica and alkali content; see Fig. 4.32a) is consistent with the Zr/TiO_2 against Nb/Y discrimination diagrams and similar protoliths are indicated: (i) rhyolite/dacite and andesite: Itapetim east domain, Cachoeira de Minas and São Francisco areas; and (ii) alkalic rocks: Itapetim central domain and Santo Aleixo areas. The alkalic and subalkaline divide (Irvine and Baragar; 1971) plotted in the LeMaitre (1984) diagram characterised the central Itapetim and Santo Aleixo schists as alkalic, whereas the samples from eastern Itapetim, São Francisco, and Cachoeira de Minas fall pedominantly in the subalkaline field.

According to Wilson (1989), alkaline to subalkaline magmatism is associated with convergent plate margins related to island arcs and active continental margins.

Using the Werner (1987) major elememt discrimination diagram, two types of schist were distinguished: (i) sedimentary rocks or paragneisses: Itapetim east domain, São Francisco and Cachoeira de Minas mines and Santo Aleixo area; and (ii) magmatic rocks or ortho-schists: Itapetim central and east domains and Santo Aleixo. Most (22) of the gneisses plot in the field of magmatic rocks, and just a few (four samples: MG-R-155, MG-R-162B, MG-R-176, MG-R-208B) plot in the field of the sedimentary rocks (Fig.4.33).

The Rb-Ba-Sr diagram (Pearce *et al.*, 1984) has previously been used to characterise the setting of granites, but here it is tentatively used on the schists and gneisses. The schists and gneisses are mostly concentrated in the corner close to the Ba apex, but some samples spread towards the Rb apex and very few fit along the Ba-Sr join. This distribution may be related to metamorphism and the mobility of Rb, Ba and Sr. The

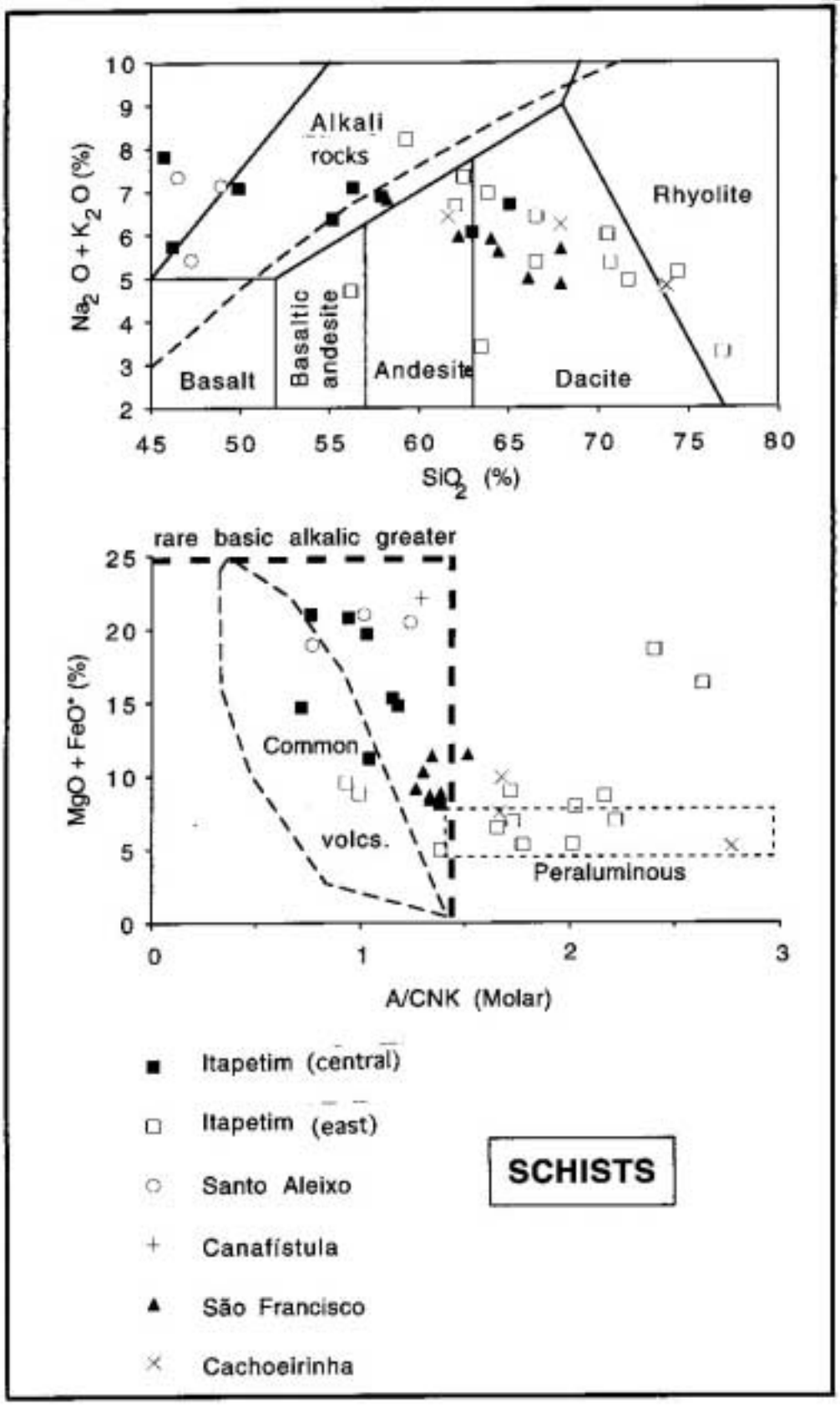

Figure 4.32 (a) Chemistry of schists (silica and alkali content) compared to volcanic rock classification (LeMaitre, 1984). The dashed line shows the alkalic/calc-alkaline divide of Irvine and Baragar (1971). (b) (FeO*+MgO) content compared to 'peraluminosity'. Note that although the schists do not exceed the limits of ferromagnesian contents of lavas, many are too peraluminous to have been derived by metamorphism of unaltered volcanics.

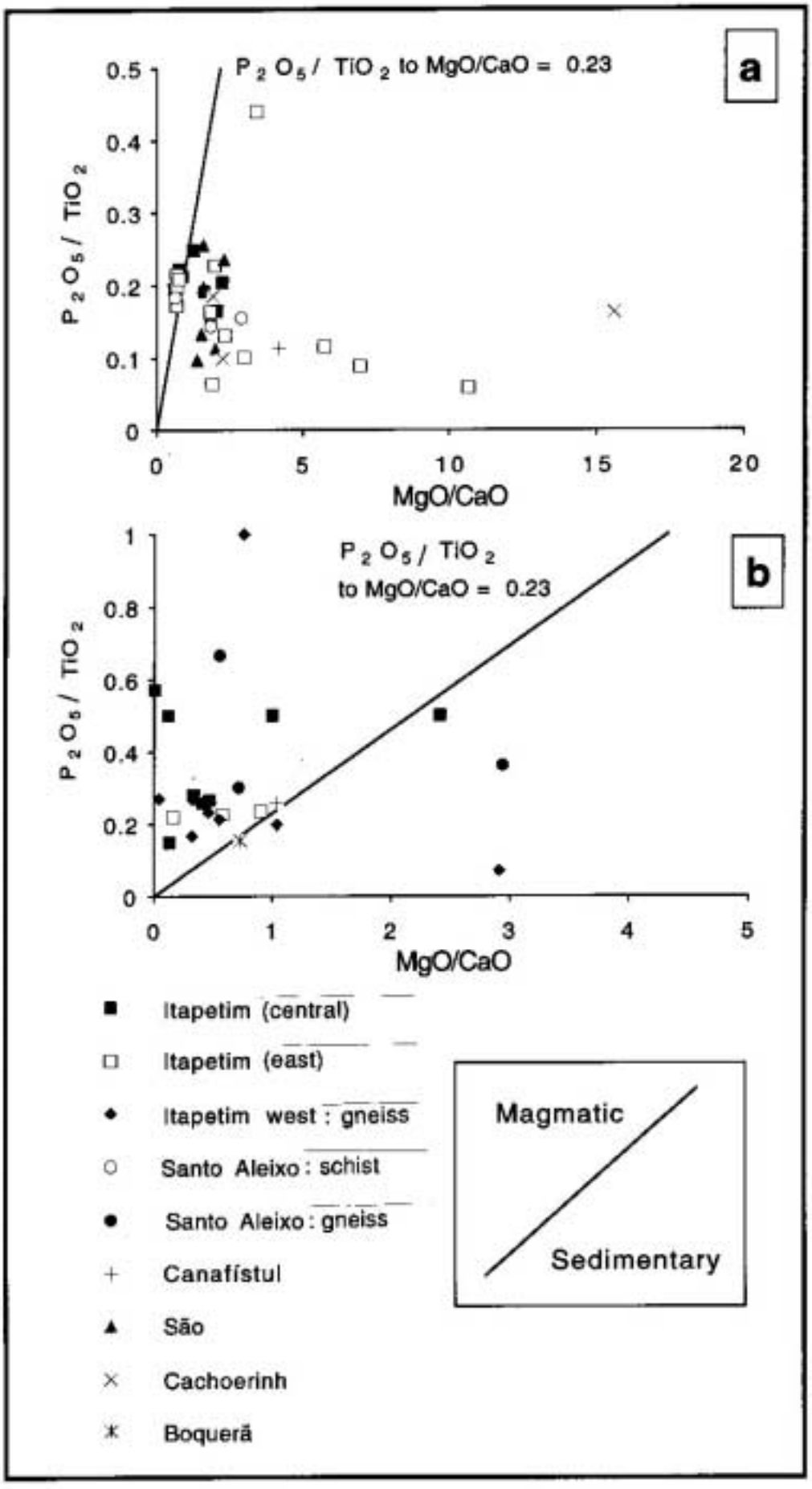

Figure 4.33 .Werner (1987) major element discrimination diagrams for (a) schist and (b) gneiss.

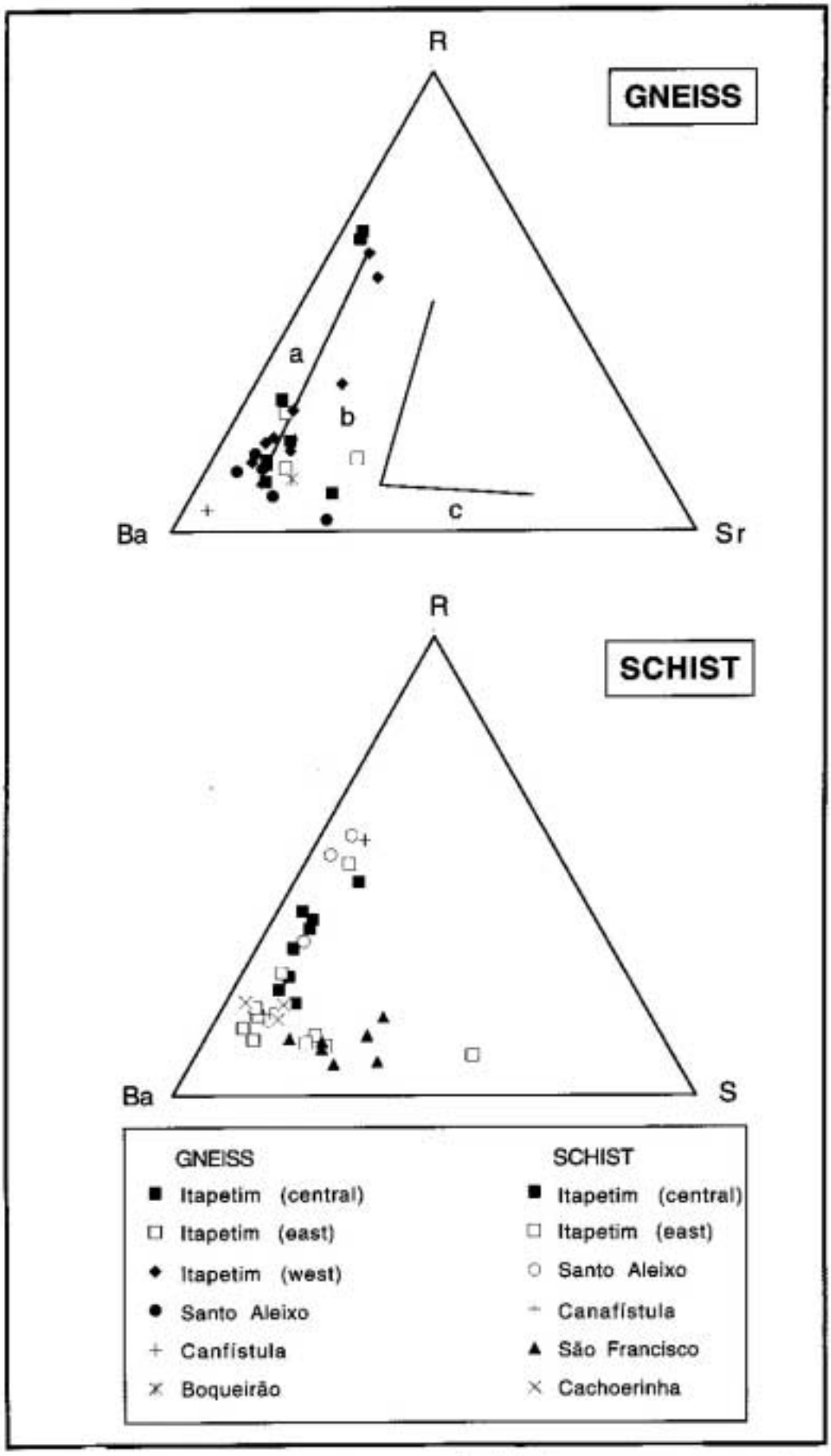

Figure 4.34 Rb-Ba-Sr ternary plots for gneiss and schist. Fields shown are for granites (Pearce *et al.*, 1984): (WP) within-plate; (COL) collision; and (VAC) volcanic-arc, for comparison.

distribution of these elements is broadly similar for both rock types, either because of the effects of metamorphism, or because the original source rocks (if felsic) came from similar tectonic settings. If the latter is correct, then the felsic source rocks came from within-plate and collision environments.

The MgO+FeO* against A/CNK plot (LeMaitre, 1984) shows that the schists do not exceed the limits of ferromagnesian contents of lava (basic rocks generally have A/CNK < 0.85), but many schists (Cachoeira de Minas, Itapetim east and some São Francisco areas) are too peralumionus to have been derived by metamorphism of unaltered volcanics (see Fig. 4.32). A schist derived from a pelitic source (originally related to felsic rocks) would however be quite peraluminous, and perhaps quite distinctive by this factor alone. This reasoning assumes that the schists are derived by metamorphism of a lava or ash-fall tuff. A tuff which has been reworked, with development of clays (and perhaps quartz), would be considerably modified compared to the original volcanic composition. The simple classification schemes do not distinguish these rocks. Addition of clay to a tuff should dramatically lower the (Mg+Fe) content, but on account of the Al content should make the resulting sediment highly peraluminous. In comparison to oceanic basalts many of the schists in this study are too peralumionus for their given (MgO+FeO) content to simply represent unaltered lavas. It is proposed that many of the schists from Itapetim east area, São Francisco, and Cachoaira de Minas were originally weathered lavas which were reworked as sediments.

The K/Ba and K/Rb ratios for mid-ocean ridge basalts (MORB) and rift-related volcanics from 129 published analyses are plotted for comparison to the Borborema schists in Fig. 4.35. This diagram illustrates that the schists could have been derived from volcanic rocks, particularly the calc-alkaline suites.

A plot of the K/Ba and K/Rb ratios from published analyses of 90 granites (see Fig. 4.36 for further data source) from different geotectonic settings (subduction, continent-collision and rift-related) was used to make comparison to the Itapetim District gneisses. This distribution indicated that the 26 analysed samples in this study fall totally into the field of subduction- or continent-collision types, except for three points which fall close to the rift-related field. It is concluded that the gneisses from Itapetim District and Santo Aleixo area are predominantly derived from subduction or continent-collision granites-types.

In the tectonomagmatic discrimination diagram (Ti/100-Zr-Yx3; Pearce and Cann, 1973), the Itapetim amphibolites overlap WPB/CAB (MG-R-112) or WPB/MORB (MG-R-141, MG-R-163G); and one sample falls in WPB (MG-T-101 (Fig.4.37a). In the Ti against Zr plot (Pearce and Cann, 1973), three samples (MG-R-141, MG-R-163G, MG-R-208) fall in the field of ocean-floor basalt (OFB), while two of them are well offscale (MG-T-101, MG-T-112; see Fig. 4.37b) due the high contents in TiO_2.

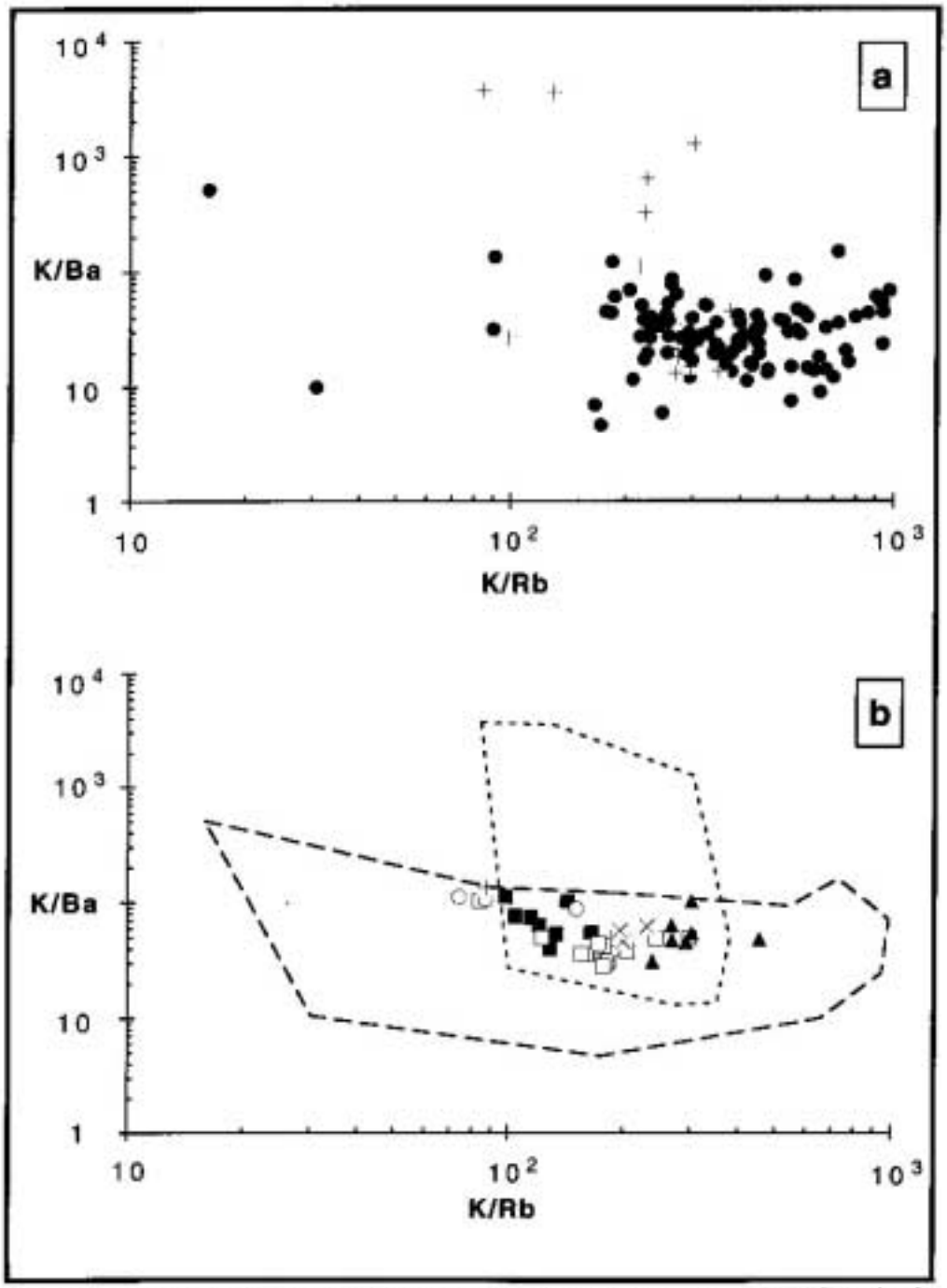

Figure 4.35 Range of K/Rb and K/Ba ratios (**a**) Shows these ratios in MORB and calc-alkaline volcanic suites (dots) and rift-related volcanics (crosses). Data from 129 analyses in Baker (1987); Blake *et al.*, (1992); Bevins *et al.*, (1991); Camp and Roobol (1989); Carlson and Moye (1990); Christe and Hannah (1990); Defant *et al.*, (1992); Ernst *et al.*, (1991); Fitton (1987); French *et al.*, (1979); Glazner (1990); Harmon *et al.*, (1984); Jones *et al.*, (1993); Kanaris-Sotiriou *et al.*, (1993); Kay *et al.*, (1988); Lipman (1988); López-Ruiz *et al.*,(1993); Lyle and Preston (1993); Macdonald *et al.*, (1984); Millward *et al.*, (1984); Petterson *et al.*, (1992); Pichvant and Montel (1988); Smith *et al.*, (1990); Sloan and Bennett (1990); Stone (1990); Thrilwall and Graham (1984); Thompson *et al.*, (1993); and Weaver *et al.*, (1987). (**b**) Shows the values for schists of this study, with envelopes surrounding the fields of diagrams (a). All are contained the range shown.
Symbols are the same as the **Fig. 4.32.**

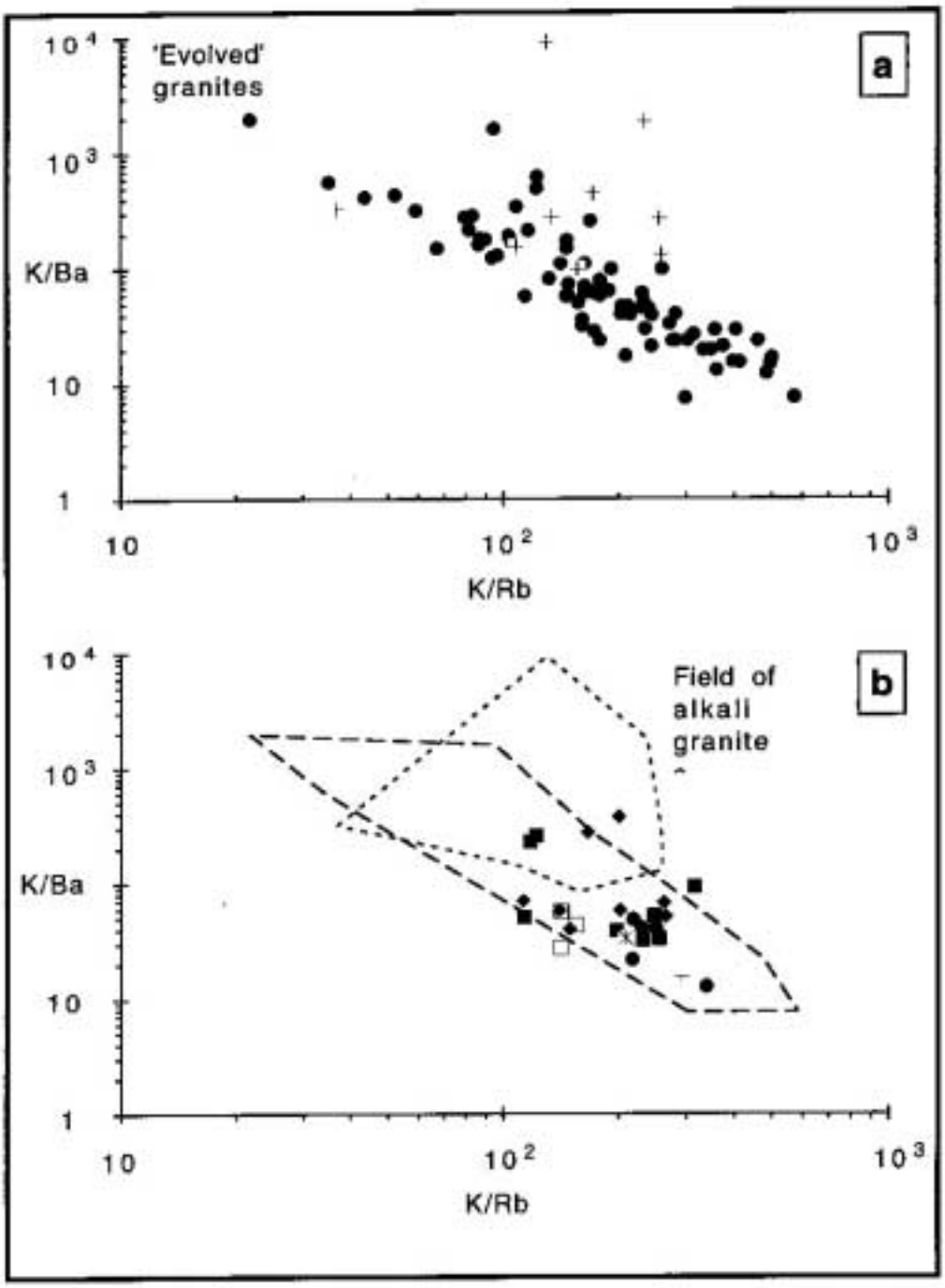

Figure 4.36 Gneisses compared to granite. (**a**) Plot of the ratios of K/Ba to K/Rb from published analyses of 90 granites from every tectonic setting. Crosses denote alkali (rift-related) types and dots all others. For data source see **Fig. 4. 15.**
(**b**) plot of the same ratios from analyses of gneisses in this study. Fields from (a) are shown. Note that only three points fall outside the field of subduction- or continent-collision types, and that one of these is within the range exhibited by the rift-related ('anorogenic') granites. Symbols for the gneisses are: (i) filled squares: Itapetim (central); (ii) open squares: Itapetim (east); (iii) diamonds; Itapetim (west); (iv) dots: Santo Aleixo; (v) cross: Canafístula; and (vi) X with bar: Boqueirão dos Cochos.

The MnOx10-TiO_2-P_2O_5 tectonomagmatic discrimination diagram for oceanic basaltic rocks according to Mullen (1983) fit the Itapetim amphibolites in two fields: OIA (ocean island alkalic); and IAT (island arc tholeiitic). The Archaean basalt fall in IAT field (Fig. 4.37c). As with the other classifications, metamorphism is likely to have affected some of these values.

Combining these results with the major element and spidergram data (see Table 4.6) it is suggested that there are two groups of amphibolite: (i) calc-alkaline, with high contents in LIL elements (Ti, K, P and Rb) and negative anomalies in Sr and Th and related to island arc tholeiite type (Itapetim area: MG-T-101, MG-T-112); (ii) tholeiitic, marked by low Ti, K and P, and a slight positive anomaly in Rb and negative in Sr. This type is related to ocean-floor basalt (Itapetim and the Archaean amphibolite: MG-R-141, MG-R-163G, MG-R-208A). In addition, althought some tectonomagmatic discrimination diagrams suggest MORB type, the high content in LIL elements is not compatible with this type of basalt. The IAT and OFB types are more consistent with the geotectonic environment associated with subduction mechanism as proposed for Borborema Province based on the granite study.

4.4.5 Discussion

Despite the mineralogical and chemical changes as a result of deformation and metamorphism, the following types of protoliths are suggested for the supracrustal hosts for the gold mineralization in Borborema Province: (i) granite and rhyolite for the gneisses predominantly; (ii) dacite-andesite-derived with minor sediment component for the schists; (iii) the amphibolite may be related to ocean-floor and island arc basalts (see Tables 4.4, 4.5 and 4.6).

The supracrustal sequences are dominated by felsic volcanics and greywackes, with depletion in Ni, Cr, Mg, Fe, and enriched in LIL (e.g. K, Rb, Ba, Th, Pb) and HFS elements (Ti, P, Zr, Y). The schists show a well-defined range of Sc contents, suggesting variation from more mafic to intermediate rock types (basalt to andesite-rhyodacite). The supracrustals are also characterised by elevated $^{206}Pb/^{204}Pb$ and $^{207}Pb/^{204}Pb$ ratios (see Chapter 6). The evolution of the rocks shows a pattern typical of the Early Proterozoic greenstone belts, characterised by the lack of komatiitic sequences, similar to provinces during the period 2.5-1.6 Ga. (see Beach, 1976; Condie, 1993). The mineralogy and composition of all rocks show evidence of considerable metasomatism (e.g. enrichment in K, Na, Rb, Y and H_2O). Generally, mafic or felsic rocks have intrinsically low primary abundances of LIL elements, consequently the enhanced levels of these elements in the host lithologies have been considered to be the result of enrichment by hydrothermal systems (Nesbitt and Sun,

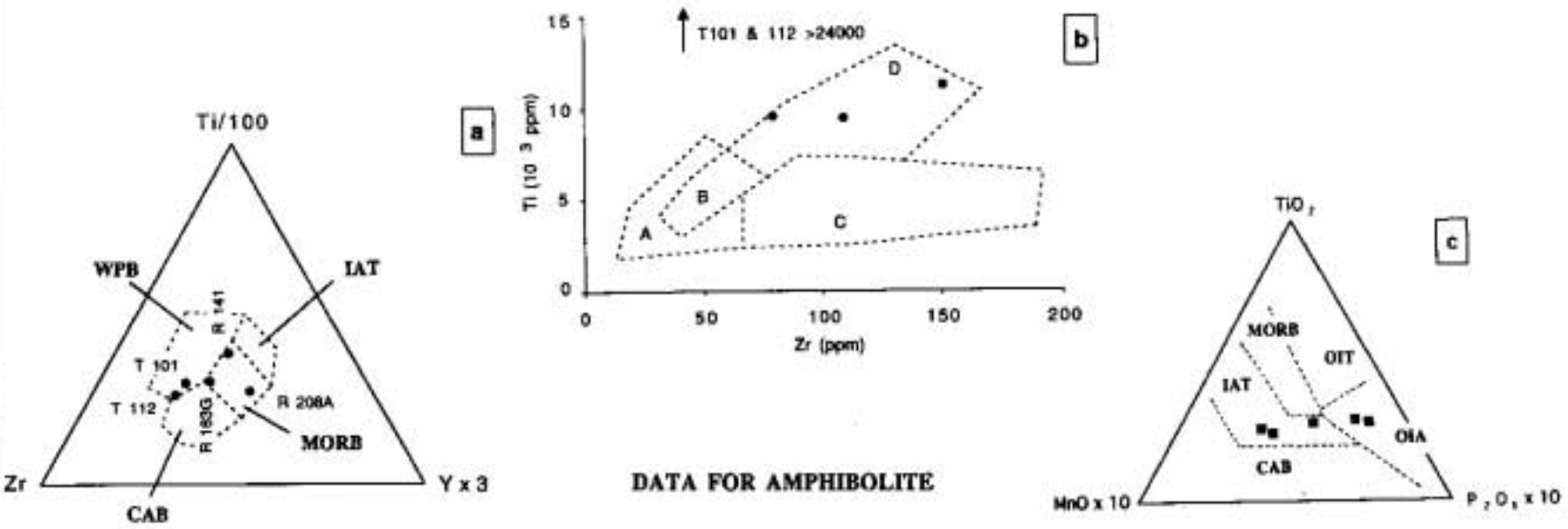

Figure 4.37a Zr-Ti/100-Yx3 diagram (Pearce and Cann, 1973) shown the fields: WPB = within-plate basalts; CAB = calc-alkaline basalts; MORB = mid-ocean ridge basalts ; IAT = island-arc tholeiite basalts. Note that the Itapetim samples overlap WPB/CAB (MG-R-112) or WPB/MORB (MG-R-141, MG-R-163G); one sample falls in WPB (MG-T-101) field ; the Archaean amphibolite (MG-R-208A) fits as MORB.

In **(b)** Ti to Zr diagram (Pearce and Cann, 1973) for amphibolites. Boundaries for magmatic types are: ocean-floor basalts plot in D and B; low-K tholeiites in A and B; and calc-alkali basalts in C and B. The Itapetim (MG-R-141, MG-R-163G) and Archaean samples fit in the ocean-floor basalt field; two Itapetim samples are offscale due the high content in TiO_2 (MG-T-101, MG-T-112).

In **(c)** tectonomagamtic discrimination diagram for basaltic rocks (Mullen, 1983) showing the variation of major elements MnO, TiO_2 and P_2O_5 ; Fields are: ocean island tholeiite (OIT); ocean island alkalic (OIA); mid-ocean ridge basalt (MORB); island arc tholeiite (IAT); island arc calc-alkaline basalt (CAB). The Itapetim samples, three fall on the IAT field and one on OIA with the Archaean amphibolite.

Table 4. 4
Schists and Their Possible Protoliths

Area	Sample	Irvine and Baragar, (1971)	Major Chemistry: Na2O + K2O/SiO2 (%) (LeMaitre, 1984)	Major Chemistry: FeO + MgO: A/CNK	Werner (1987)	K:Ba	K:Rb	A/CNK	Comments (Protolith)
Itapetim (central)	MG-T-052	Alkalic	>alkaline range	Very peraluminous	Sedimentary (para)	76	104	Ig	Sediment
Itapetim (central)	MG-T-089	Alkalic	alkaline: by andesite field	Very peraluminous	Sedimentary	39	128	Ig	Sediment
Itapetim (central)	MG-T-095	Alkalic	alkaline	Very peraluminous	Sedimentary	111	98	Ig	Igneous source
Itapetim (central)	MG-T-107	Alkalic	highly alkaline	Very peraluminous	Sedimentary	102	143	Ig	Sediment
Itapetim (central)	MG-R-148B	Alkalic	>alkaline range	Very peraluminous	Magmatic (orth)	64	120	Low	Igneous source
Itapetim (central)	MG-R-151A	On boundary	alkaline	In range	Magmatic	75	114	Low	Igneous source
Itapetim (central)	MG-R-151B	Subalkalic	on andesite/dacite bdy.	In range	Magmatic	53	133	Ig	Igneous source
Itapetim (central)	MG-R-156A	Subalkalic	dacite	Very peraluminous	Sedimentary	56	165	High	Sediment
Itapetim (east)	MG-R-165B	Subalkalic	basaltic andesite	Too peraluminous, too ferromagnesian	Sedimentary	50	122	High	Sediment
Itapetim (east)	MG-R-165C	Subalkalic	dacite	Too peraluminous, too ferromagnesian	Sedimentary	104	84	High	Sediment
Itapetim (east)	MG-R-169D	Subalkalic	andesite	In range	Magmatic	36	160	Ig	Igneous source
Itapetim (east)	MG-R-170B	Subalkalic	andesite	Too peraluminous for (MgO + FeO) content	Sedimentary	38	204	High	Sediment
Itapetim (east)	MG-R-190A	Subalkalic	dacite	In peraluminous dacite field	Sedimentary	42	178	High	Sediment
Itapetim (east)	MG-R-190B	Subalkalic	dacite	In range	Sedimentary	36	156	High	Sediment
Itapetim (east)	MG-T-117	Subalkalic	dacite	Offscale !	Magmatic	50	244	High	Igneous source
Itapetim (east)	MG-T-122	Subalkalic	dacite	In peraluminous dacite field	Sedimentary	47	201	High	Igneous source
Itapetim (east)	MG-R-126A	Subalkalic	dacite	In peraluminous dacite field	Magmatic	31	181	High	Igneous source
Itapetim (east)	MG-R-166B	Subalkalic	rhyolite	In peraluminous dacite field	Sedimentary	49	193	High	Sediment
Itapetim (east)	MG-R-167A	Subalkalic	rhyolite	In peraluminous dacite field	Sedimentary	50	297	High	Sediment
Itapetim (east)	MG-R-169B	Subalkalic	dacite	In peraluminous dacite field	Sedimentary	44	172	High	Sediment
Itapetim (east)	MG-T-111B	Alkalic	alkaline	Too peraluminous for (MgO+FeO) content	Sedimentary	28	177	High	Sediment
Santo Aleixo	MG-R-222A	Alkalic	>alkaline range	Highly (MgO + FeO): > basalts, = nephelinites	Sedimentary	88	151	Ig	Sediment
Santo Aleixo	MG-R-174A	Alkalic	alkaline	In range for slightly alkaline basalt	Magmatic	113	74	Ig	Igneous source
Santo Aleixo	MG-R-175A	Alkalic	>alkaline range	Highly ferromagnesian: > basalts, = nephelinites	Sedimentary	105	87	Ig	Sediment
Canaffstula	MG-R-181B	Subalkalic	Offscale!	At max ferromag. content, peraluminous	Sedimentary	137	87	Ig	Sediment
São Francisco	MG-R-225C	Subalkalic	dacite	Highly peralum., (Mg+Fe) high for Si content	Sedimentary	102	302	High	Sediment
São Francisco	MG-R-226	Subalkalic	dacite	Highly peralum., (Mg+Fe) high for Si content	Sedimentary	46	292	Ig	Sediment
São Francisco	MG-R-226C	Subalkalic	dacite	Highly peralum., (Mg+Fe) high for Si content	Sedimentary	63	268	High	Igneous source
São Francisco	MG-R-227	Subalkalic	dacite	Highly peralum., (Mg+Fe) high for Si content	Sedimentary	31	238	High	Sediment
São Francisco	MG-R-227C	Subalkalic	dacite	Highly peralum., (Mg+Fe) high for Si content	Sedimentary	49	454	High	Sediment
São Francisco	MG-R-228	Subalkalic	dacite	Highly peralum., (Mg+Fe) high for Si content	Sedimentary	47	269	High	Sediment
São Francisco	MG-R-228C	Subalkalic	andesite	Highly peralum., (Mg+Fe) high for Si content	Sedimentary	55	301	Ig	Igneous source
Cachoerinha de Minas	MG-R-224A	Subalkalic	andesite	Too peraluminous	Sedimentary	47	200	High	Sediment
Cachoerinha de Minas	MG-R-224D	Subalkalic	dacite	In peraluminous dacite field	Magmatic	62	231	High	Igneous source
Cachoerinha de Minas	MG-R-224E	Subalkalic	rhyolite	Too peraluminous	Sedimentary	57	196	High	Igneous source

Abbreviations:
Ig = in normal range of igneous rock; A/CNK = (molar) Al2O3/(CaO+Na2O+K2O)

Table 4. 5

Gneisses and Their Possible Protoliths

Area	Sample	Irvine and Baragar (1971)	Werner (1987)	K:Ba	K:Rb	Comments K/Ba, K/Rb	A/CNK	Comments (Protolith)
Itapetim (central)	MG-T-077	Subalkalic	Magmatic (ortho-)	230	117	High evolved granite	Ig	High evolved granite (A/NK=1.15)
Itapetim (central)	MG-T-086	Subalkalic	Magmatic	257	121	High evolved granite	Ig	High evolved granite (A/NK=1.13)
Itapetim (central)	MG-T-115	Subalkalic	Magmatic	52	247	Granite range	Ig	Granitic
Itapetim (central)	MG-R-142	Subalkalic	Sedimentary (para-)	50	113	Granite range	**High**	Sedimentary
Itapetim (central)	MG-R-153	Subalkalic	Magmatic	93	315	Off granite ?	Ig	Granitic (low A/CNK, A/NK)
Itapetim (central)	MG-R-148A	Subalkalic	Magmatic	33	231	Granite range	Ig	Granitic
Itapetim (central)	MG-R-155	Subalkalic	Sedimentary	33	254	Granite range	**High**	Sedimentary
Itapetim (central)	,MG-R-157	Subalkalic	Magmatic	39	197	Granite range	Ig	Granitic
Itapetim (east)	MG-T-110	Subalkalic	Magmatic	28	141	Off granite ?	Ig	Granitic
Itapetim (east)	MG-T-113	Subalkalic	Sedimentary (boundary)	56	142	Granite range	**High**	Sedimentary
Itapetim (east)	MG-R-135	Subalkalic	Magmatic	43	155	Granite range	Ig	Highly altered ?
Itapetim (west)	MG-T-005	Subalkalic	Magmatic	59	201	Granite range	Ig	Granitic
Itapetim (west)	MG-T-014	Subalkalic	Magmatic	378	200	High evolved granite	Ig	High evolved granite (A/NK=1.12)
Itapetim (west)	MG-T-028	Subalkalic	Magmatic	52	265	Granite range	Ig	Granitic
Itapetim (west)	MG-T-035	Subalkalic	Magmatic	70	112	Granite range	Ig	? evolved granitic
Itapetim (west)	MG-R-162B	Subalkalic	Sedimentary	58	139	Granite range	**High**	Sedimentary
Itapetim (west)	MG-R-163A	Subalkalic	Magmatic	277	166	High evolved granite	Ig	Granitic
Itapetim (west)	MG-R-171B	Subalkalic	Sedimentary	40	149	Granite range	Ig	? sedimentary
Itapetim (west)	MG-R-180B	Subalkalic	Magmatic	67	263	Granite range	Ig	Granitic
Santo Aleixo	MG-R-176	Subalkalic	Sedimentary	40	249	Granite range	**High**	Sedimentary
Santo Aleixo	MG-R-205A	Subalkalic	Magmatic	13	338	Granite range	Ig	Granitic (low A/CNK, A/NK
Santo Aleixo	MG-R-222B	Subalkalic	Magmatic	22	217	Granite range	Ig	Granitic
Santo Aleixo	MG-R-222C	Subalkalic	Magmatic	41	229	Granite range	Ig	Granitic
Santo Aleixo	MG-R-223	Subalkalic	Magmatic	49	218	Granite range	Ig	Granitic
Canafístula	MG-R-181A	Subalkalic	Magmatic	15	290	Granite range	Ig	Granitic
Boqueirão Cochos	MG-R-208B	Subalkalic	Sedimentary	33	208	Granite range	**High**	Sedimentary

Abbreviations:
Ig = in normal range of igneous rocks; A/CNK = (molar) Al2O3/(CaO+Na2O+K2O)

Table 4. 6

Amphibolite Petrochemistry

Sample	Harker Diagram	Alkali-silica diagram (LeMaitre, 1984)	AFM Diagram (Irvine & Baragar, 1971)	Spidergram	TiO2-Sr/2-Zr (Mullen, 1983)	Ti/100-Zr-Yx3 diagram (Pearce & Cann, 1973)	Ti-Zr diagram (Pearce and Cann, 1973)
MG-T-101	High K, Ti, P	Basalt	Calc-alkaline	Neg. Sr, Th; Posit. Rb, K	IAT filed	WPB field	High Ti
MG-T-112	High K, Ti, P	Alkaline	Calc-alkaline	Neg. Sr, Th; Posit. Rb, K	IAT filed	Overlap:WPB/CAB	High Ti
MG-R-141	Low K, Ti, P	Basalt	Tholeiitic	Weaker Sr, flat to posit. Th	OIA field	Overlap: WPB/MORB	OFB field
MG-R-163G	Low K, Ti, P	Basalt	Calc-alkaline	Weaker Sr, flat to posit. Th	IAT filed	Overlap: WPB/CAB/MORB	OFB field
MG-R-208A	Low K, Ti, P	Basaltic andesite	Tholeiitic	Weaker Sr, flat to posit. Th	OIA field	MORB field	OFB field

Abbreviations:
WPB = within-plate basalts; CAB = calc-alkaline basalts; OFB = ocean-floor basalts; IAT = island arc tholeiite; OIA = ocean island tholeiite; MORB = mid-ocean ridge basalt

1976). The rocks in this study are biotite-rich, suggesting an original hornblende-rich that was replaced during retrogressive metamorphism. The metasomatic fluid must therefore have been K-rich. The increase in biotite, muscovite and albite in the deformed rocks is associated with the shears. These zones channelled fluids and provided conditions for the metasomatic processes, resulting in the breakdown of the existing Fe-Mg phases and growth of new LIL-rich phases.

The schists are thought to be associated with alkaline to subalkaline volcanism, and probably related to convergent plate margins or island arcs in an active continental margin (Wilson, 1989). This is consistent with the ocean island alkalic or island arc tholeiitic basalt indicated as the geotectonic setting for the amphibolites. The gneisses were derived from subduction- or continent-collision granites-types, at an active continental margin.

4.5 METAMORPHIC GRADE OF THE HOST ROCKS

4.5.1 Introduction

The metamorphic P-T conditions that have affected the host lithologies in Borborema Province have been examined using an approach based on the chemical compositions of coexisting mineral phases which represent equilibrium conditions in the rock during metamorphism. The analytical data is shown in the Appendices A4.9, A4.11 and A4.12.

Temperature and pressure were calculated using the computer program 'Thermocalc' of Powell and Holland (1988). The chlorite temperature was estimated using the empirical equation derived by Cathelineau (1988) and was compared with that derived from the computer program of Walshe (1986). In an attempt to cross-check and compare the empirical results for the pressure calculations, the experimental calibrations of Johnson and Rutherford (1989) and Thomas and Ernst (1990), based on the aluminium content of amphiboles, were also used. The P-T results are given in Table 4.8. Further information concerning the analytical techniques is shown in Appendix A.10.

This study has employed the currently terminology used in metamorphic petrology. The term *metamorphic facies* applies to defined regions of P-T conditions distinguished by a mineral assemblage in any one rock type (Yardley, 1989). The boundaries to zones with a constant metamorphic grade are defined as *isograds*. *Peak metamorphic conditions* mean the maximum temperature and pressure to which the rock has been subjected (Passchier *et al.*, 1990). The P-T diagram showing the univariant curves for the reactions that control the appearence and breakdown of the metamorphic phases is

called the *petrogenetic grid* (Yardley, 1989).

4.5.2 Metamorphic Facies

The mineralized areas are polydeformed and polymetamorphosed, and they have been subjected to a polycyclic evolution (Jardim de Sá *et al.*, 1981). Three grades of metamorphism have been identified in the host lithologies. Their fields are depicted in Fig. 4.40. The use of P-T data combined with field evidence has enabled the characterisation of the following metamorphic facies (see Table 4.7):

a) Granulite-Upper Amphibolite Facies

A M_2 regional metamorphism associated with the D_2 deformation (Trans-Amazonian age) is well exposured in the Archaean terrane. It consists of migmatitic biotite-garnet-gneiss with or without sillimanite in the Boqueirão dos Cochos area. Quartz-feldspathic layers, probably formed by anatexis, and mica-sillimanite layering are oriented parallel to earlier bedding. The K-feldspar, plagioclase, and quartz may represent the leucosome and the mica-sillimanite-garnet is melanosome. Evidence of anatexis, probably of pelitic schists; also occurs in the mica gneisses. This produced quartz-eye phyllonite with fine leucosome layers (quartz, K-feldspar, biotite) which are completely folded (stromatic texture), suggesting that these layers are earlier structural features. Flatted quartz eyes and crystals of garnet are oriented along this new fabric. Locally the quartz-eye phllyonite exhibits a texture similar to migmatite, consisting of a mixture of schistose or gneissose portions. Garnet (Fig. 4.38a) and sillimanite (Fig. 4.38b) occur together and no staurolite was found. The mineral assemblage suggests a temperature sufficiently high for the mica to react with quartz to produce K-feldspar and an aluminium silicate mineral (sillimanite). The coexistence of garnet+K-feldspar+sillmanite is diagnostic of high temperature.

Using the Thermocalc program the temperature and the pressure were estimated in the garnet-biotite-sillimanite gneiss at P = 3.9 kb (1 sigma = ± 2) and T = 730° C (2 sigma = ± 110). In the garnet-biotite gneiss the results were: P = 4.7 kb (1 sigma = ± 1.6) and T = 703 °C (1 sigma = ± 101; Table 4.8). Two reactions are applicable to these mineral asssemblages:

(i) 3 an = gr + 2 sill + qz.

(ii) 3 alm + 3 east + 12 an = 2 pyro + 4 gr +3 ann + 12 sill.

The plot of these reactions on the petrogenetic P-T grid (Passchier *et al.*, 1990) define the field of high-grade metamorphic conditions of anatexis (see Fig. 4.39) :

plag + qz +K-feldsp + V = melt; (Holdaway and Lee, 1977).

Table 4.7
Mineral Assemblages Diagnostic of the Metamorphic Facies in Borborema Province: Central Domain

Facies	Meta Igneous Rocks	Pelitic Rocks (with quartz)	Calc-Silicate Rocks	Tectonic Setting	Rock Type	P-T (kb- °C)
Granulite- Upper Amphibolite	Hornblende + Plagioclase + Garnet+ Quartz	Garnet, Chlorite, Muscovite + Biotite, Sillimanite		Archaean massif Archaean massif	Gneiss migmatitic, amphibolite	5 kb 710 °C
Amphibolite	Hornblende + Plagioclase + Epidote + Garnet + Titanite + Calcite + Magnetite	Sillimanite + K-feldspar + Muscovite + Cordierite + Garnet ± Staurolite + Ilmenite	Tremolite + Zoisite + Biotite + Plagioclase + Calcite	Fold belt	Schist, gneiss amphilobite, calc-silicate,	5 to 7 kb 600 °C
Sub-greenschist	Epidote + Albite + Chlorite + Opaque Minerals	Chlorite + Muscovite + Albite + Sericite + Opaque Minerals	Chlorite ± Muscovite	Fold belt, Plutonic rocks and Archaean massif	Schist, gneiss amphilobite, calc-silicate, granite	2 Kb 339 °C

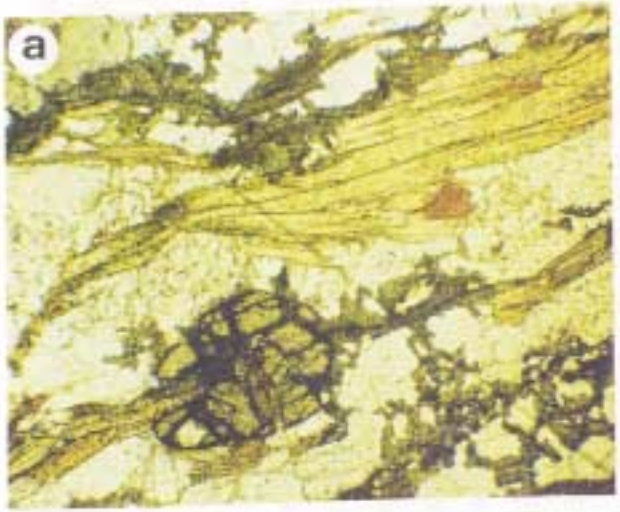

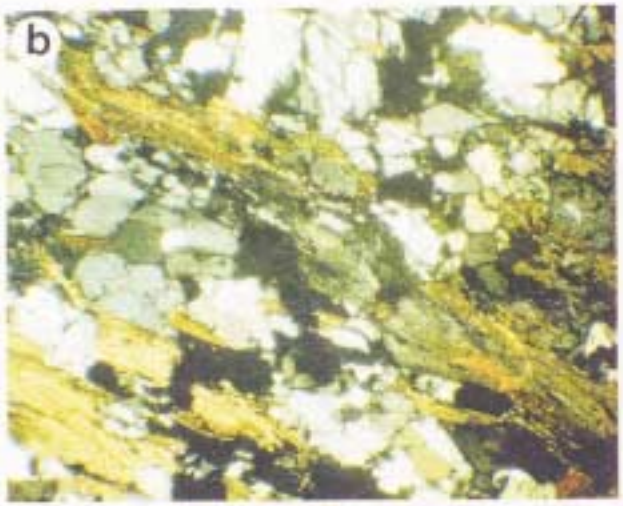

Figure 4.38a Garnet partially replaced by biotite and muscovite in migmatitic gneiss. Micas have grown along the fractures in garnet and continue thought the matrix suggesting that they are not inclusions in garnet crystal. The rock shows strong segregation into micaceous portions (in the middle) and quartz-feldspar bands (in both sides) as a result of anatexis, indicating high-grade metamorphic conditions (XPL.; TL; WOF = 2500 µm; MG-R-208B, Boqueirão dos Cochos area).

Figure 4.38b Same rock (migmatitic gneiss) as in Fig. 4.38a showing fibrolitic form of sillimanite developing mainly at the expense of biotite, notably in the centre of the field of view, where garnet (black) also occurs. The sillimanite and garnet were formed as a result of the peak metamorphism. The needles of sillimanite are easily seen intergrown with quartz and biotite. (XPL.; TL; WOF = 2500 µm; MG-R-208B, Boqueirão dos Cochos area).

Figure 4.38c Diagnostic assemblage of coexisting quartz, biotite, muscovite, K-feldspar and contorted fibrolite developed in sillimanite pelitic schist, under the isograd of sillimanite conditions. (XPL.; TL; WOF = 2500 µm; MG-R-228, São Francisco mine area).

Figure 4.38d Garnet zone pelitic schist developed under amphibolite facies conditions. The relationships (clear in the bottomleft) suggest that the garnet stopped growing before the schistosy was fully developed. (XPL.; TL; WOF = 1500 µm; MG-R-169B, Itapetim district, eastern domain, Pimenteiras area).

The pressure estimated from the Al content of amphiboles in garnet-amphibolite from the same area (see Appendix A4.9), using the experimental calibration (Johnson and Rutherford, 1989; Thomas and Ernst, 1990), indicates a value of 5 kb (1 sigma). This result is in close agreement with the previous estimates for pressure.

The P-T data for the Archaean gneisses indicate conditions consistent with a transition between the granulite and upper amphibolite facies (see Fig. 4 .40).

b) Amphibolite facies

Two events (D_3 and D_4) can be recognised in the polydeformed supracrustal rocks. These deformations produced different mineral assemblages reflecting different metamorphic grades: amphibolite and retrogressive facies. The host lithologies (gneiss, schist and amphibolite) were extensively tectonised and mostly transformed into mylonitic rocks. Although in the three fold belts (Seridó, Pajeú/Paraíba and Piancó/Alto Brigída) the main lithologies have similar compositions, they each contain different D_3 mineral assemblages.

A diagnostic assemblage of coexisting quartz, biotite, muscovite, K-feldspar and aluminosilicate minerals (sillimanite + cordierite + garnet + staurolite) occurs in the São Francisco area. The breakdown of muscovite + quartz produced K-feldspar + aluminosilicate minerals (Figs. 4.38c and 4.38e). The enrichment in aluminous minerals suggests melting as a result of metamorphism of pelitic rocks, and the mineral assemblage indicates conditions close to the cordierite-garnet-K-feldspar isograd (Yardley, 1998). According to this author this zone is characterised by high temperatures, and the assemblages result from continuous reactions such as:

(i) biotite + sillimanite + quartz ----> K-feldspar + cordierite + melt

(ii) biotite + sillimanite + quartz ----> K-feldspar + garnet + melt

However, in the São Francisco area sillimanite occurs in the form of very fine needles (fibrolite; see Fig. 4.38c), which is diagnostic for the sillimanite isograd, and usually associated with biotite. Staurolite is very rare and it may disappear from muscovite-quartz pelites as a result of the discontinous reaction (Yardly, 1989):

staurolite + muscovite + quartz -----> garnet + biotite + sillimanite + H_2O

This mineral assemblage reflects the staurolite isograd. It is suggested that in the São Francisco area the metamorphic conditions are consistent with a transition between the cordierite and sillimanite isograds .

For the rocks in the Itapetim area two mineral assemblages were characterised under amphibolite metamorphic conditions: (i) related to igneous mafic rocks (Fig.4.38e); and (ii) related to pelitic sediments or igneous felsic rocks (Fig. 4.38d). The first one occurs

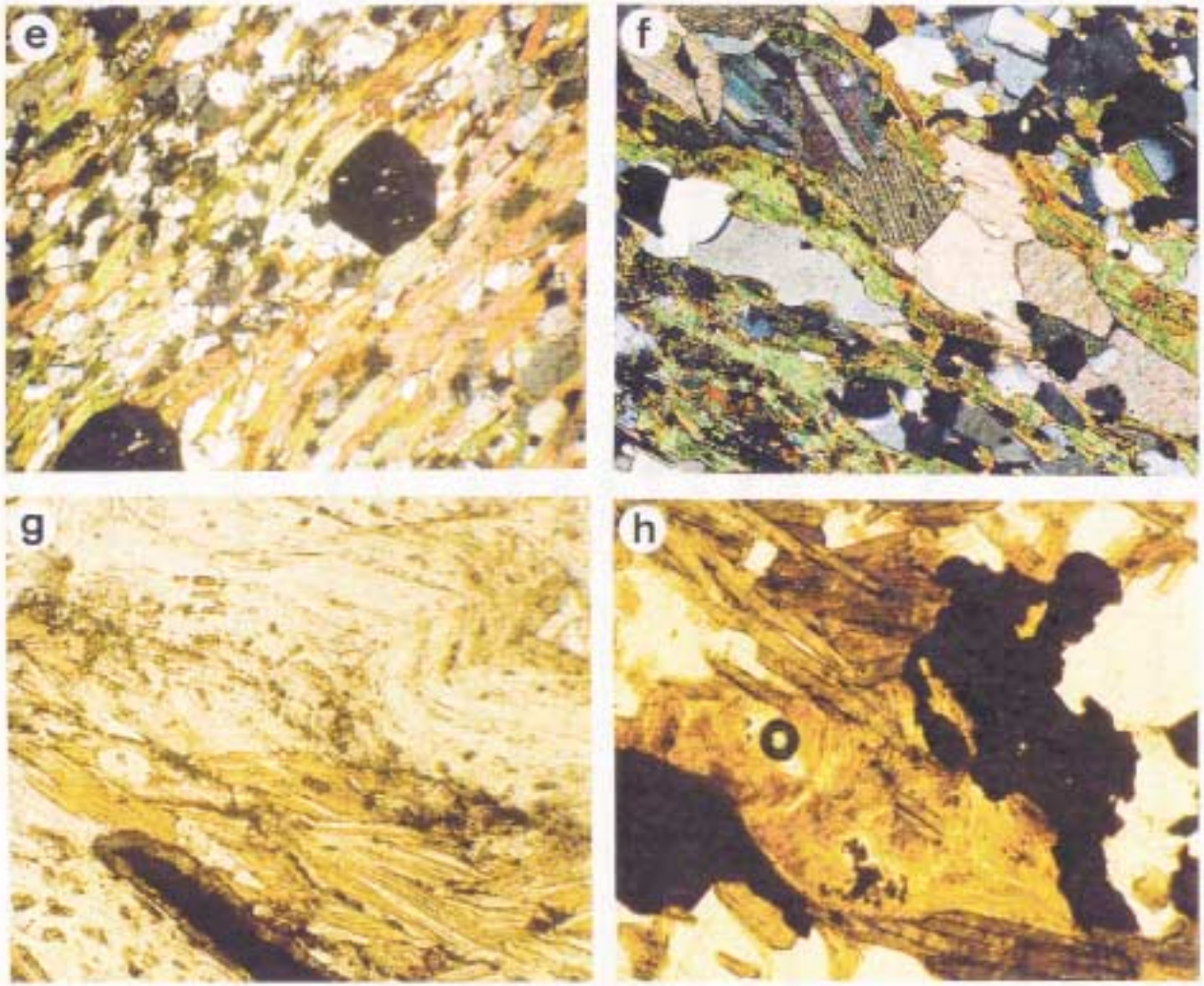

Figure 4. 38e Porphyroblast of garnet wrapped around by foliation developed in garnet zone pelitic schist under amphibolite facies conditions. Inclusion trails of quartz in the centre of the garnet porphyroblast may suggest an early syn-foliation. The external foliation has the same orientation as the regional shear (NE-SW). Note the K-feldspar at the top right. (XPL.; TL; WOF = 2500 μm; MG-R-228, São Francisco mine area).

Figure 4.38f Retrograde metamorphism developed in basic igneous rock showing biotite replaced by chlorite (on the middle) and carbonate developed from the breakdown of the amphibole (on the top right).(XPL.; TL; WOF = 1500 μm; MG-R-151A, Itapetim District, central domain, Sertãozinho area).

Figure 4. 38g Diagnostic features shown by sub-greenschist facies. Folds in chlorite schist showing kink bands (S4; top right). Biotite has grown along pre-existing foliation (middle). Note the enrichment in titanite (small crystals) oriented along an earlier foliation (S3). In the bottom left a coarse grain of ilmenite is surrounded by leucoxene. (PPL.; TL; WOF = 2500 μm; MG-R-224, Cachoeira de Minas mine area).

Figure 4.38h Decussate aggregate of chlorite (on the top left) sugesting post-tectonic texture developed under sub-greenschist conditions, where relics of biotite occur. Note the enrichment in opaque minerals (black areas). (PPL.; TL; WOF = 750 μm; MG-T-035, Itapetim District, western domain, Degredo area).

predominantly in the central domain (Sertãozinho area) and consists of amphibole (ferro-tschermakitic to tschermakitic hornblende; see Fig. 4.22), K-feldspar, biotite, garnet, epidote, quartz, sphene and magnetite. It refletcs conditions consistent with the garnet-biotite isograd. The second type occurs in the eastern domain (Pimenteiras area) and is characterised by garnet, biotite, muscovite and rare sillimanite, cordierite, and rare kyanite probably close to the sillimanite isograd.

According to Deer *et al.* (1985) K-feldspar is a stable product of both high grade thermal and regional metamorphism and it is a typical mineral of the sillimanite zone of metamorphism. The formation of K-feldspar in high grade rocks is due largely to the instability of the micas in this P-T environment. The following reaction is suggested:

$$K\,Al_3Si_3O_{10}(OH)_2 + SiO_2 \text{ ----> } KAlSi_3O_8 + Al_2SiO_5 + H_2O$$

muscovite orthoclase sillimanite

In the biotite-sillimanite-cordierite schist in the São Francisco area the pressure and temperature (see Table 4.8) were estimated at: P = 4.2 (± 0.5) kb and T = 600 °C (± 15). The following reactions are applicable to these mineral asssemblages at these conditions:

(i) 3 an = gr + 2 sill + qz

(ii) pyro + musc + pa = phl + ab + 3 sill + H_2O

(iii) ann + 2 sill + qz = alm + musc

These reactions occur in the kyanite stability field, close to the limit of the sillimanite field (see Fig. 4.39). This position is diferent to the higher metamorphic conditions suggested by the mineral assemblages, (e.g. sillimanite stability). This may be explained by the presence of the fibrolitic form of sillimanite. Althought the stability of the Al_2SiO_5 minerals is of great importance for determining pressure at which metamorphism has taken place, it has been shown that a considerable uncertainty remains concerning the stability field of prismatic and fibrolitic sillimanite (Yardley, 1990). Usually fibrolite enlarges the Al_2SiO_5 stability field to higher pressures (Yardley, 1990).

For the rocks in the Pimenteiras area, the average estimated pressure and temperature in the muscovite-biotite-garnet schist and muscovite-garnet schist (Table 4.8) were P = 6.0 (± 0.5) and T = 600 °C (± 25).

The following reactions are suggested and plot in the field of the kyanite stability (Fig. 4.39).

(i) gr + alm + musc = ann + 3 an

(ii) 6 an + 3 cel = pyro + 2 gr + 3 musc + 6 qz

The pressure estimated from the Al content of five amphibole samples (see Appendix

4.9) from the central domain (Sertãozinho area) indicated an average of 6.8 kb, which is in close agreement with the earlier results (Table 4.8).

In summary, the P-T data is estimated at P = 4 kb and T = 600 °C for the rocks of São Francisco area and indicate that these rocks were formed at depths around 25 km. These conditions are consistent with amphibolite facies conditions at the garnet and cordierite-sillimante isograds. In the Itapetim area two types of metamorphic mineral assemblages (associated with igneous and pelitic sediments) indicate that both rock types were formed under similar conditions.

c) Retrogressive Metamorphism

The D_4 deformation event and associated metamorphism (M_4) can be recognised by a mineral assemblage consisting of albite, epidote, muscovite, biotite altered to chlorite, sericite, and locally carbonate. Chlorite-muscovite intergrowths are common. It is possible that the pale green colour exhibited by muscovite suggests a phengite content. Opaque minerals are also common (e.g. corona texture of ilmenite surrounded by leucoxene; Fig. 4.38g) and occur associated with tourmaline and gold (Fig. 4.38h). Sericite and chlorite occur along the axial plane S_4 suggesting that they have recrystallised during or after the development of D_4. Chlorite commonly occurs as veins cutting the original fabric, resulting from retrograde alteration along cracks.

The general formula for the chorites is $(Fe_{3.54}\ Mg_{3.49}\ Al_{3.81}Mn_{0.06}\ Ti_{0.01})\ [(Al_{5.03}\ Si_{5.50})O_{20}](OH)_{16}$. Chlorite with a close association with sulphides and gold exhibits Fe/Fe+Mg ratios in the range of 0.47 to 0.53. Silica contents ranging from 5.48 to 5.51 ions per formula unit and variation in $Al^{(IV)}$ (2.45-2.51 ions per unit formula) indicates the chlorite to be the ripidolite variety. This mineral is a typical mineral of the lowest zone of metamorphism and it generally decreases in amount at sucessively higher grades of metamorphism. Thus the increase in chlorite in the amphibolite facies host lithologies (M_3) is a result of retrogressive metamorphic processes (M_4), suggesting that the rocks were subsequently subjected to greenschists facies conditions. Evidence of retrograde metamorphism is very common in all the host lithologies indicating that it may be a regional scale process. The predominance of chlorite and muscovite in schists from Cachoeira de Minas mine area reflects retrogressive processes developed under the isograd of the chlorite zone, whereas in the Itapetim and São Francisco areas the metamorphic conditions are more consistent with the isograd of the biotite zone. This is reflected by the mineral assemblage, where biotite and chlorite occur associated with microcline, quartz, epidote (São Franciasco area) and also carbonate (Itapetim; see Fig. 4.38f). Chlorite is commonly found also in the host granites as a product of biotite alteration. Chlorite also occurs in the quartz veins generally associated with tourmaline and opaque minerals as a product of hydrothermal alteration (Fig. 4.38h).

The abundance of chlorite, epidote, and locally carbonate and rutile in the retrograde metamorphic assemblages, is indicative that in Borborema Province the fluids that entered the rock at that time were low temperature and contained appreciable CO_2 (Yardley, 1989).

Thermometry was carried out on chlorite samples of the supracrustal rocks from Itapetim and Cachoeira de Minas areas in an attempt to determine if a temperature difference could be found between the D_3 and D_4 events. For this purpose samples that occur along the axial plane S_4 were analysed (see Appendix 4.12). The temperatures were derived using the empirical equation of Cathelineu (1988; see Appendix A4.10) . For the amphibolite in Itapetim area, the chlorite has a mean tetrahedral site $Al^{(iv)}$ occupancy of 2.50 (2 sigma = ± 0.01), corresponding to a mean temperature of 341°C (1 sigma = ± 4°C). In schist from Cachoeira de Minas mine, chlorite has a mean tetrahedral site $Al^{(iv)}$ occupancy of 2.48 (2 sigma ± 0.06), with an average temperature of 337°C (2 sigma = ± 18°C). The data are displayed in the Table 4.8.

The chlorite temperature for the Cachoeira de Minas area was also calculated using the Walshe (1988) computer program; it yielded an average temperature of 337 °C ± 60. This data is very similar to the previous results (see Table 4.8).

It is concluded that the chlorite temperatures determined from both areas are similar and it is thought that chlorite grains grew during the regional D_4 and their compositions represent D_4 conditions. The average temperature given by the total chlorite population at 339°C (2 sigma = ± 36°C) is consistent with sub-greenschist facies metamorphic conditions (greenschist facies has a lower limit around 400°C; Yardley, 1989; Fig. 4.40).

4.5.3 Discussion

Three stages of metamorphism were identified in Borborema Province:

(i) Granulite-upper amphibolite facies with temperature and pressure estimated at 720°C and 4.0 kb respectively; rock-types are predominantly migmatitic gneiss and amphibolite.

(ii) Amphibolite facies; rock-types are schist, gneiss, amphibolite and calc-silicate, mostly transformed to mylonitic rocks; indicated temperature and pressure are 600°C and 5.0 kb, respectively.

(iii) Sub-greenschist facies, consisting of a large variety of rocks (schists, gneisses, amphibolites, calc-silicates and granites); temperature of 339°C.

The basement terrane is characterised by a transition from granulite to upper amphibolite facies. The supracrustal rocks are marked by amphibolite facies and

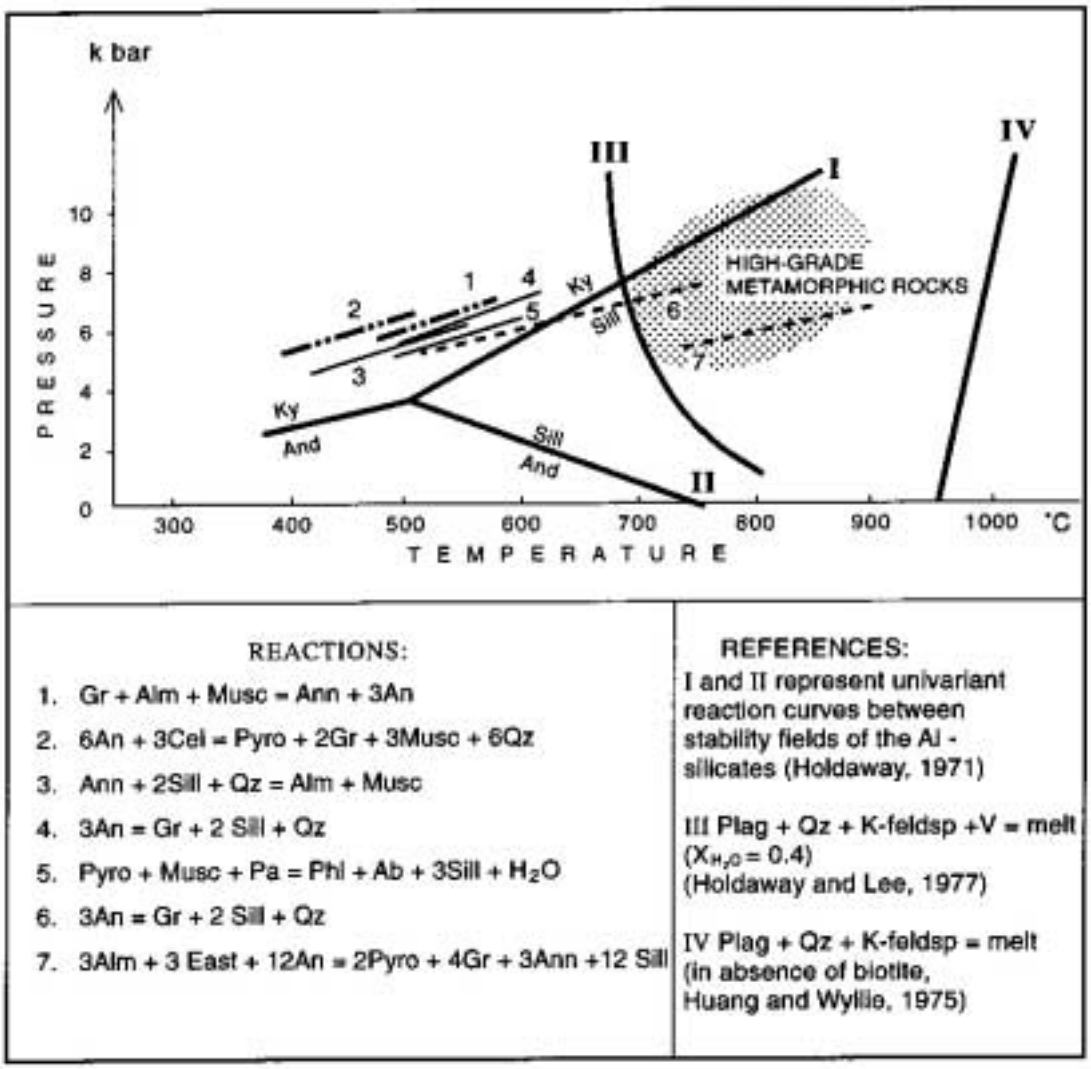

Figure 4.39 Petrogenetic P-T grid showing common reactions in Itapetim District-Pimenteiras area (dots and lines 1 and 2); São Francisco mine (thin lines 3 to 5); and Boqueirão dos Cochos (dashed lines 6 and 7). The reactions have been calculated from the data set of Powell and Holland (1988). Shaded area represents the most commonly encountered conditions in high-grade metamorphic rocks (Passchier *et al*, 1990).

The following abbreviations are used: And-andalusite; Ab-equilibrium albite, An-anorthite; Ann-annite; Alm-almandine; Cel-celadonite; East-eastonite; Gr-grossular; Musc-muscovite; Pa-paragonite; Phl-phlogopite; Pyro-pyrope; Sill-sillimanite; Ky-kyanite; Qz-quartz; Plag-plagioclase; Kfeldsp K-feldspar; V-vapour

Table 4.8

Rock Pressure - Temperature Data

Sample	Locality	Rock-Type	Equilibrium Mineral Assemblage and/ or Mineral Used as Geother. or Geobar.	Data Source	Calculation Method	Parameters and/or Formula	P (kbar)	T (°C)
MG-R-196BI	Itapetim District, E domain (Pimenteiras area)	Garnet-muscovite-biotite schist	Garnet, plagioclase, biotite, muscovite	Microprobe Analyses (see Appendix A4.11)	Powell and Holland, 1988	For 95% confidence, fit less than 1.54: Temperature fit=0.99; sd=0.60; avP=6.18 Pressure fit=1.04; sd=19; avT=609	6.8 ± 0.5	625 ± 25
MG-R-196BII	Itapetim District, E domain (Pimenteiras area)	Garnet-muscovite schist	Garnet, plagioclase,muscovite	Microprobe Analyses (see Appendix A4.11)	Powell and Holland, 1988	For 95% confidence, fit less than 1.96: Temperature fit=1.16; sd=0.72; avP=5.98 Pressure fit=1.21; sd=26; avT=577	5.3 ± 0.5	575 ± 25
MG-R-228	São Francisco Mine	Garnet-biotite-sillimanite schist	Garnet, plagioclase, biotite muscovite, sillimanite	Microprobe Analyses (see Appendix A4.11)	Powell and Holland, 1988	For 95% confidence, fit less than 1.54: Temperature fit=0.59; sd=0.49; avP=4.17 Pressure fit=0.62; sd=14; avT=600	4.2 ± 0.5	600 ± 15
MG-R-208BI	Boqueirão dos Cochos	Garnet-biotite-sillimanite gneiss	Garnet, plagioclase, biotite, sillimanite	Microprobe Analyses (see Appendix A4.11)	Powell and Holland, 1988	For 95% confidence, fit less than 1.73: Temperature fit=0.73; sd=1.59; avP=4.84 Pressure fit=0.79; sd=101; avT=703	3.9 ± 2.0	730 ± 110
MG-R-208BI	Boqueirão dos Cochos	Garnet-biotite gneiss	Garnet, plagioclase, biotite,	Microprobe Analyses (see Appendix A4.11)	Powell and Holland, 1988	For 95% confidence, fit less than 1.96: Temperature fit=0.17; sd=1.94; avP=3.72 Pressure fit=0.01; sd=110; avT=736	4.7 ± 1.6	703 ± 101
MG-T-056I	Itapetim District, central Domain (Sertãozinho area)	Amphibolite	Chlorite	Microprobe Analyses (see Appendix A4.12)	Cathelineau, 1988	T(°C) = -61.92+321.98 (Al IV) Al IV= 1.249 for 14 oxygens	-	340
MG-T-056II	Itapetim District, central Domain (Sertãozinho area)	Amphibolite	Chlorite	Microprobe Analyses (see Appendix A4.12)	Cathelineau, 1988	T(°C) = -61.92+321.98 (Al IV) Al IV= 1.256 for 14 oxygens	-	342
MG-R-224AI	Cachoeira de Minas Mine	Chlorite-muscovite schist	Chlorite	Microprobe Analyses (see Appendix A4.12)	Cathelineau, 1988	T(°C) = -61.92+321.98 (Al IV) Al IV= 1.245 for 14 oxygens	-	339
					Walshe, 1986		-	342 ± 10
MG-R-224AII	Cachoeira de Minas Mine	Chlorite-muscovite schist	Chlorite	Microprobe Analyses (see Appendix A4.12)	Cathelineau, 1988	T(°C) = -61.92+321.98 (Al IV) Al IV= 1.251 for 14 oxygens	-	341
					Walshe, 1986		-	355 ± 10
MG-R-224AIII	Cachoeira de Minas Mine	Chlorite-muscovite schist	Chlorite	Microprobe Analyses (see Appendix A4.12)	Cathelineau, 1988	T(°C) = -61.92+321.98 (Al IV) Al IV= 1.225 for 14 oxygens	-	332
					Walshe, 1986		-	315 ± 10
MG-T-056	Itapetim, Sertãozinho	Amphibolite	Total aluminium of amphiboles	Micropb. (see Ap.A.9)	Thomas & Ernst, 1990	P = - 6.23 + 5.34 (Al total)	7.5 ± 1	-
MG-T-101	Itapetim, Sertãozinho	Amphibolite	Total aluminium of amphiboles	Micropb. (see Ap.A.9)	John & Rutherford, 1989	P = 4.32 (Al total) - 3.46	6.0 ± 1.0	-
MG-T-137	Itapetim, Sertãozinho	Amphibolite	Total aluminium of amphiboles	Micropb. (see Ap.A.9)	John & Rutherford, 1989	P = 4.32 (Al total) - 3.46	7.0 ± 1	-
MG-R-141	Itapetim, Sertãozinho	Amphibolite	Total aluminium of amphiboles	Micropb. (see Ap.A.9)	John & Rutherford, 1989	P = 4.32 (Al total) - 3.46	7.0 ± 1	-
MG-T-163G	Itapetim, Sertãozinho	Amphibolite	Total aluminium of amphiboles	Micropb. (see Ap.A.9)	John & Rutherford, 1989	P = 4.32 (Al total) - 3.46	6.0 ± 1.0	-
MG-R-208A	Boqueirão dos Cochos	Amphibolite	Total aluminium of amphiboles	Micropb. (see Ap.A.9)	John & Rutherford, 1989	P = 4.32 (Al total) - 3.46	5.0 ± 1	-

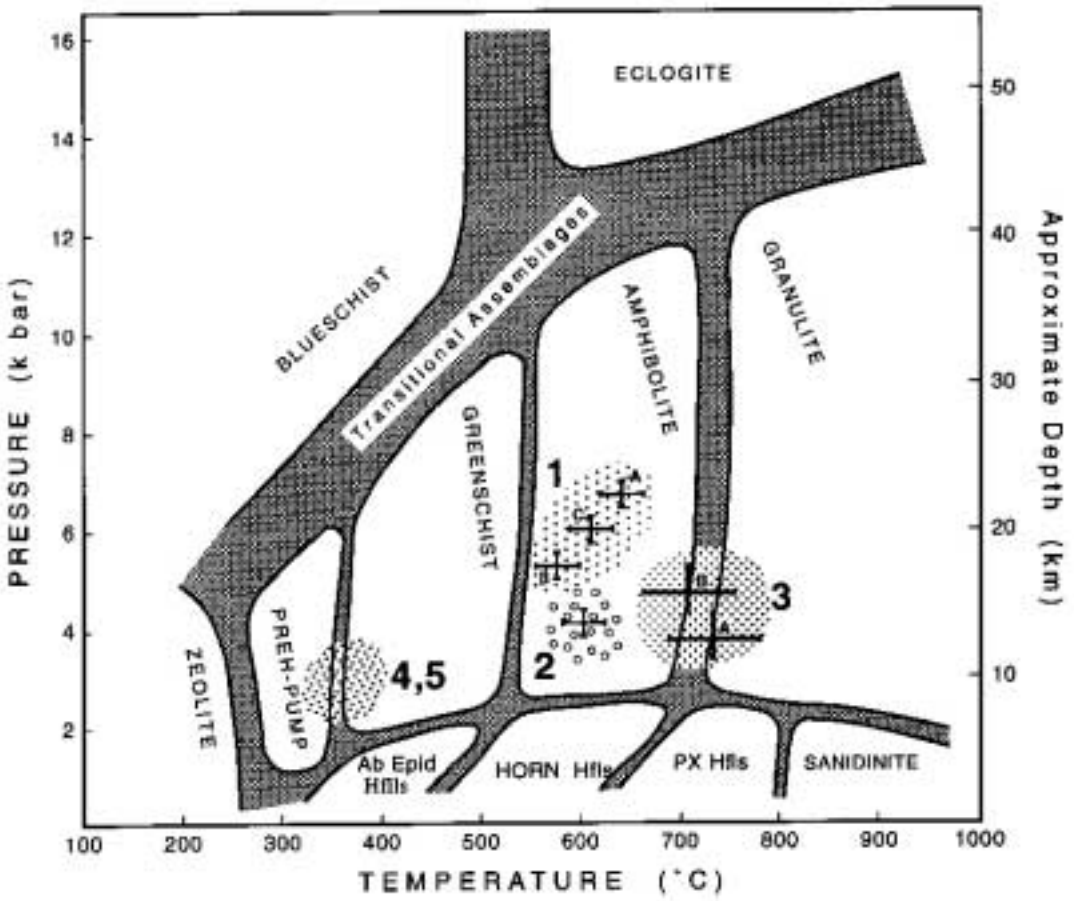

Figure 4.40 Pressure-temperature diagram showing the fields of metamorphic facies (Yardley, 1989) and the distribution of the rocks calculated from microprobe analyses using the data set of Powell and Holland (1988) for the following areas: 1 - Itapetim District, Pimenteiras area (A: plagioclase, garnet, muscovite and biotite; B: plagioclase, garnet and muscovite; C: average); 2 - São Francisco mine; 3 - Boqueirão dos Cochos (A: plagioclase, muscovite, garnet and biotite; B: plagioclase, muscovite, garnet, biotite and sillimanite). For 4 and 5 - Cachoeira de Minas mine and Itapetim, Sertãozinho areas, the temperature was calculated according to Cathelineau (1988) and Walshe (1986) and the pressure was estimated from fluid inclusions (see Chapter 7).
Abbreviations used are: Hfls - hornfels, Ab Epid - albite, epidote; HORN - hornblende, PX - pyroxene; PREH-PUMP - prehnite-pumpellyite.

subsequently subjected to retrograde metamorphism, the origin of which is due to later reworking and infiltration of fluids enriched in CO_2, as indicated by the mineral assemblage. Temperature data indicate that the retrograde metamorphic conditions took place under sub-greenschist facies conditions. These rocks may be the end-products of retrogressive metamorphism of igneous rocks and pelitic sediments. Calc-silicate rocks are present on the regional scale; althought not relevant in the context of the gold mineralization, they were probably derived from metamorphism of calcareous sediments.

Regional metamorphism was most likely a result of the decompressive melting of crustal rock. The heat generated from this melting provided conditions for granite magmatism (see Brown, 1993).

4.6 CONCLUSIONS

The petrogenetic and geochemical studies of granitoids in the Borborema Province enable constraints to be placed on the evolutionary model for granitoid emplacement, and thus associated gold mineralisation:

(i) The Brasiliano magmatism was generated at convergent plate margins, above zones of active subduction, and the resulting batholiths were derived from a combination of subduction slab, mantle wedge, and continental crust.

(ii) The emplacement mechanism mixed I- and S-type granites with an increasing crustal component in the younger granites

(iii) The granite emplacement might be controlled by the dominant strike-slip shear zones, which also provided the channels for the hydrothermal fluids.

(iv) The gold mineralization is genetically associated with the K calc-alkaline magmatism.

(v) The magmatism and associated gold mineralization may have been triggered by thickening as a result of collision tectonics.

(vi) The host gneisses were derived from lithologies dominated by felsic rocks. The schist were derived from volcanics (intermediated predomiantly) and greywackes. It is suggested that these rocks were formed in an environment related to a continental margin arc-trench system (see Dickinson, 1974), marked by the development of island arc basins as a result of subduction mechanism.

(vii) The Proterozoic supracrustal sequences are similar to other post-Archaean greenstone belt sequences, and reflect a different mode of crustal formation after 2.5 Ga (see Condie, 1993).

CHAPTER 5 MINERALIZATION AND WALLROCK ALTERATION

5.1 INTRODUCTION

Gold is widespread in Borborema Province and its most common occurrence is in quartz veins. However, despite its abundance, the mineralogical and petrological characteristics of the gold mineralization in this area have received little attention, and previous studies are restricted (e.g. Cassedanne *et al.*, 1973). No systematic investigations have been carried out on the ore and gangue minerals, or the wallrock alteration, in these deposits. The aim of this chapter is to describe the ore, gangue, and alteration assemblages in the gold deposits, and to use the resulting information to elucidate the evolution of the gold mineralization. It is hoped that this study will be of relevance not only for determining a genetic model for the mineralization, but also for developing a more efficient basis for exploration and exploitation.

Mineral exploration in Borborema Province has in the past been carried out mainly for three commodities:

(i) *Skarn-related tungsten* in the Seridó Belt. Several scheelite-producing mines resulted from these surveys: Brejuí, Barra Verde, Boca de Lage, and Zangarellhas are all now in production. In these tungsten deposits small amounts of copper, molybdenum and gold are recoved as by-products.

(ii) *Niobium-tantalum minerals* associated with pegmatites.

(iii) *Gold*. This metal was first discovered in the region in the early 1940's, and over the past 50 years extensive small-scale exploration and exploitation have been carried out by 'garimpeiros' (local prospectors). These operations tend to use simple, rudimentary processes ('garimpo') and mainly work placer deposits and superficial lode gold veins. Since the end of the 1970's gold exploration and exploitation have gradually decreased as a result of the decrease in the metal price.

Following a period of declining gold exploration, mining companies are now showing more interest in the region. Two gold mines have been developed. Since 1975 the São Francisco mine, located near Currais Novos (Rio Grande do Norte State), has been worked by Xapetuba Mineração, a subsidiary of the Companhia de Mineração e Participações (CMP). Cachoeiras de Minas mine, situated near Princesa Isabel (Paraíba State), has been worked by the Companhia Odebrech de Engenharia since 1981. Both are small deposits (metal reserve $\leq$ 10 tonnes Au) with a grade ranging from 2.3 to 3.7

g/tonne of gold in São Francisco and Cachoeira de Minas respectively (Ferran, 1988; Brito, 1986). The ore consists of gold-bearing quartz veins which are mined by open cast methods, the gold being recovered by cyanide heap-leaching.

5.2 METHODS OF STUDY

Eighty six polished blocks of ore minerals and host rock samples have been studied by reflected light microscopy (see Chapter 1, Appendix A1.1 for sample details). This study was combined with scanning electron microscopy (SEM) and X-ray elemental mapping investigations (Appendices A5.1 to A5.3). Many of the ore minerals have also been analysed quantitatively by electron microprobe (Appendices A5.4 to A5.6). Details of the analytical techniques and information about the detection limits are given in the Appendix A4.1.

Selected polished blocks of pyrite were etched with warm 20% HNO_3 to study textures and growth features (e.g. grain boundaries and overgrowths).

Samples of the wallrock alteration adjacent to the veins have been analysed by X-ray fluorescence (XRF) for major and trace elements (see Apppendix A5.8), using the analytical procedures described in Chapter 4 (Appendix A4.1). Some gangue minerals were also analysed quantitatively by microprobe (Appendix A5.7).

5.3 ORE-MINERALS

The mineralized veins are invariably dominated by quartz and locally tourmaline, and these make up at least 95 vol.% of the vein. The overall 'ore'-mineral assemblage and paragenesis identified in all deposits consist of the following: oxides; sulphides; intergrown native bismuth, selenium/tellurium minerals and alloys of gold-silver and gold-bismuth; tellurides and native gold. The detailed paragenesis for each deposit is displayed in Table 5.1. Usually the oxides occur disseminated in the host rocks, and the other mineral groups are mainly present in the quartz veins. The relationships between the ore-minerals and their textural features will be discussed below.

5.3.1 Mineral Assemblages

a) Oxides

Magnetite ($Fe^{II}\ Fe_2^{III}\ O_4$) occurs as euhedral grains disseminated in the host rocks, and

Table 5.1
Mineral Assemblages in the Gold-Bearing Quartz Veins in Borborema Province

Itapetim-Sertãozinho (Supracrustal Rocks)	São Francisco Mine (Supracrustal Rocks)	Cachoeira de Minas Mine (Supracrustal Rocks)	Itapetim-Santo Aleixo (Granitoids)	Cacimba Salgada (Granitoids)	Canaffstula (Granitoids)	Igarape Garapa (Granitoids)	Boqueirão dos Cochos (Basement)
Magnetite	Magnetite	Ilmenite	Ilmenite	Ilmenite	Hematite	Hematite	Ilmenite
Ilmenite	Ilmenite	Leucoxene	Hematite	Hematite	Rutile	Pyrite III	Hematite
Hematite	Hematite	Rutile	Rutile	Rutile	Pyrite III	Pyrrhotite	Rutile
Maghemite	Rutile	Pyrite II	Pyrite III	Pyrite III	Pyrrhotite	Chalcopyrite	Pyrite III
Rutile	Molybdenite	Pyrite III	Pyrrhotite	Pyrrhotite	Marcasite II	Galena II	Marcasite II
Pyrite I	Pyrite II	Marcasite II	Marcasite II	Marcasite II	Gold II	Hessite	Pyrrhotite
Pyrite III	Pyrite III	Pyrrhotite	Chalcopyrite	Galena I	Tourmaline	Greenockite	Gold II
Marcasite I	Pyrrhotite	Chalcopyrite	Covellite	Gold II	K-feldspar	Gold II	Tourmaline
Marcasite II	Marcasite II	Covellite	Chalcocite	Tourmaline	Jarosite	Tourmaline	Jarosite
Marcasite III	Marcasite III	Chalcocite	Galena I	Jarosite	Chlorite	Jarosite	Chlorite
Pyrrhotite I	Native Bismuth	Sphalerite	Gold II	Chlorite	Goethite	Chlorite	Goethite
Chalcopyrite	Bismuthinite	Galena I	Tourmaline	Goethite	Quartz	Goethite	Quartz
Sphalerite	Maldonite	Cerussite	Jarosite	Quartz		Fluorite	
Galena I	Unch. Se /Te minerals	Gold II	Chlorite			Quartz	
Cerussite	Gold II	Tourmaline	Goethite				
Covellite	Chalcopyrite	Jarosite	Quartz				
Chalcocite	Covellite	Pyromorphite					
Ag (+Au) Te-bearing phase	Chalcocite	Chlorite					
Gold I	Galena I	Goethite					
Gold II	Sphalerite	Quartz					
Tourmaline	Tourmaline						
Jarosite	Jarosite						
Chlorite	Pyromorphite						
Goethite	Chlorite						
Quartz	Goethite						
Sericite	Quartz						
	Sericite						

Abbreviations:
Unch.= uncharacterised
Roman numbers refer to successive generations of a mineral

in reflected light it displays a grey/brownish/pink color (Figs. 5.1a and 5.1b). Magnetite is replaced by hematite (Fe_2O_3) which has a grey/blue colour, and occurs as exsolution lamellae with two different orientations, corresponding to the (111) planes of magnetite. The magnetite is also converted to maghemite (f-Fe_2O_3), which has a characteristic greyish-blue colour, and goethite (FeO.OH), both common products of the weathering of Fe-rich minerals (Ramdohr, 1969). The transformation to maghemite has proceeded from the inside outward (as noted by Basta, in Ramdohr, 1969) but the goethite occurs as rims to the magnetite.

Rutile (TiO_2) occurs in an idiomorphic form (Fig. 5.2a), usually disseminated and oriented parallel to the rock foliation. X-ray mapping of the distribution of Ti, Fe and Mn (Fig. 5.2b) shows a distinct zoned pattern (Fig. 5.2c). In polished section this zoning correlates well with a distinct range of colour from brownish pink in the centre to faint bluish at the rims, with an intermediate white-gray region. Based on this correlation it is interpreted that the rutile came originally from a primary ilmenite ($FeTiO_3$) rich in Mn that was subsequently transformed by hydrothermal processes which removed Fe and Mn.

Rutile also occurs as columnar crystals elongated parallel to the c axis (Fig. 5.3a) which originated from hematite as indicated by the X-ray elemental distribution of Ti and Fe (Fig. 5.3b) and characterised by polished section study.

Ilmenite was found as crystals marginally transformed to leucoxene and displaying corona texture or surrounded by hematite.

Usually all the oxides described above occur in the wallrocks (see Chapter 4), except the hematite, which is commonly also associated with the sulphides and gold. In this case hematite, either as crystals or radial aggregates, is very typical (Figs. 5.4a and 5.4b). These often have chalcopyrite inclusions (Fig. 5.5). No trace of lamellae can be seen in the hematite associated with the mineralization, possibly indicating that they disappeared as a result of recrystallisation (Ramdohr, 1969). Hematite, rhythmically replaced by goethite during the weathering, can also be seen (Fig. 5.6).

b) Sulphides

The main sulphides in the ore are: pyrite, pyrrhotite and chalcopyrite and, as minor constituents, marcasite, galena, covellite, chalcocite, cerussite molybdenite, sphalerite, bismuthinite, and greenockite.

Pyrite (FeS_2) is the predominant sulphide and shows a tendency towards forming relatively coarse crystals, either idiomorphic (Fig. 5.7) or xenomorphic (Fig. 5.8), but colloform shapes also occur. The grains often exhibit poikilitic development with inclusions of other sulphides or gold. Porphyroblasts of pyrite with numerous inclusions of chalcopyrite commonly occur (Fig. 5.15). Residual forms of the earliest

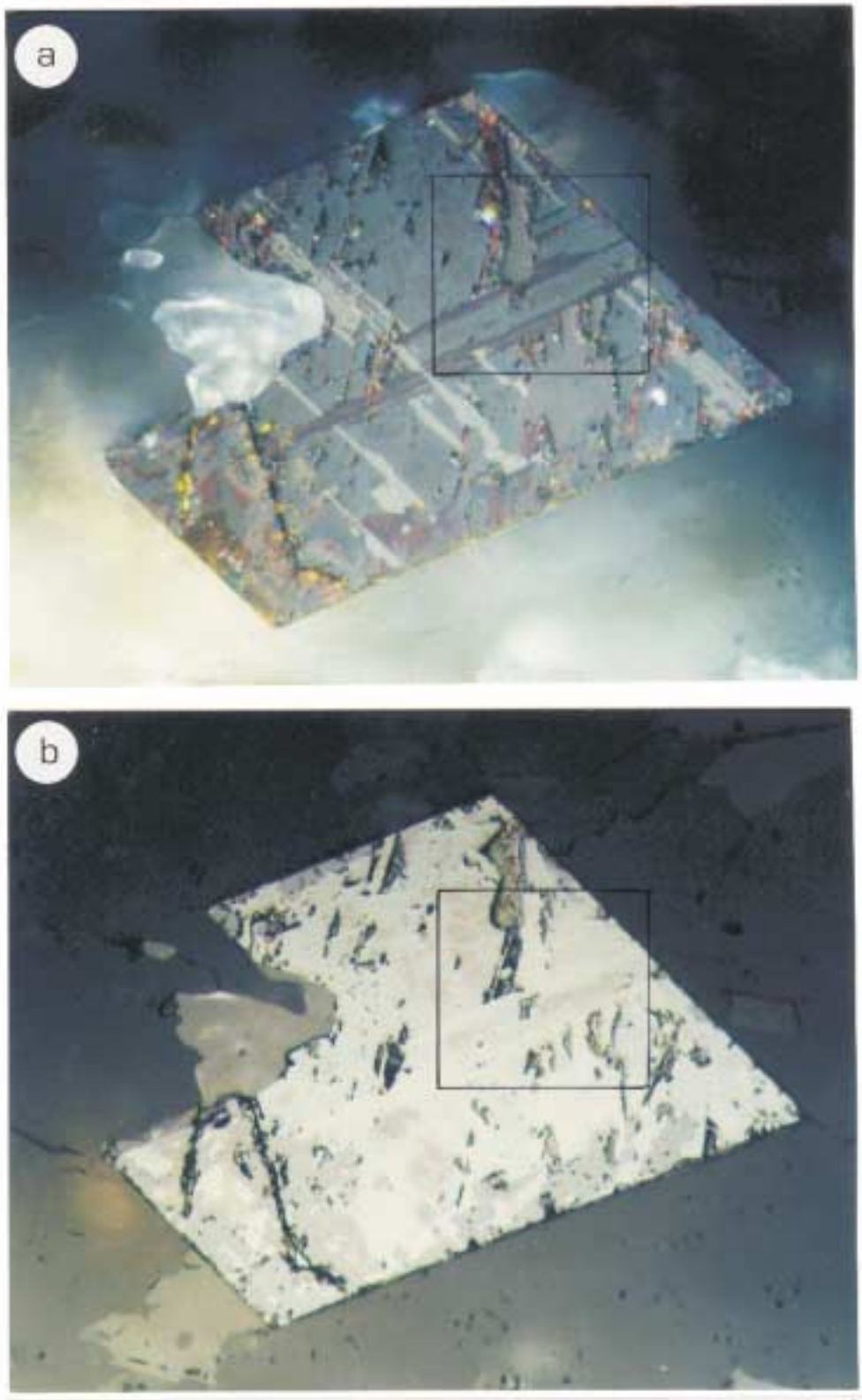

Figure 5.1a Photomicrograph of a polished block displaying a euhedral grain of magnetite with exsolution lamellae of hematite (greyish-blue colour). The lamellae show two different orientations corresponding to (111) plane of magnetite. Note that the photo was taken with the analyser slightly uncrossed to highlight the lamellae. (b) a view in plane polarised light showing the magnetite converted to an intergrowth of interstitial greyish-blue maghemite. Surrounding the grain (left and right bottom) goethite occurs (grey-deep colour) where red internal reflection can be seen (RL; WOF = 400 µm; MG-T-031, Itapetim District, Sertãozinho).

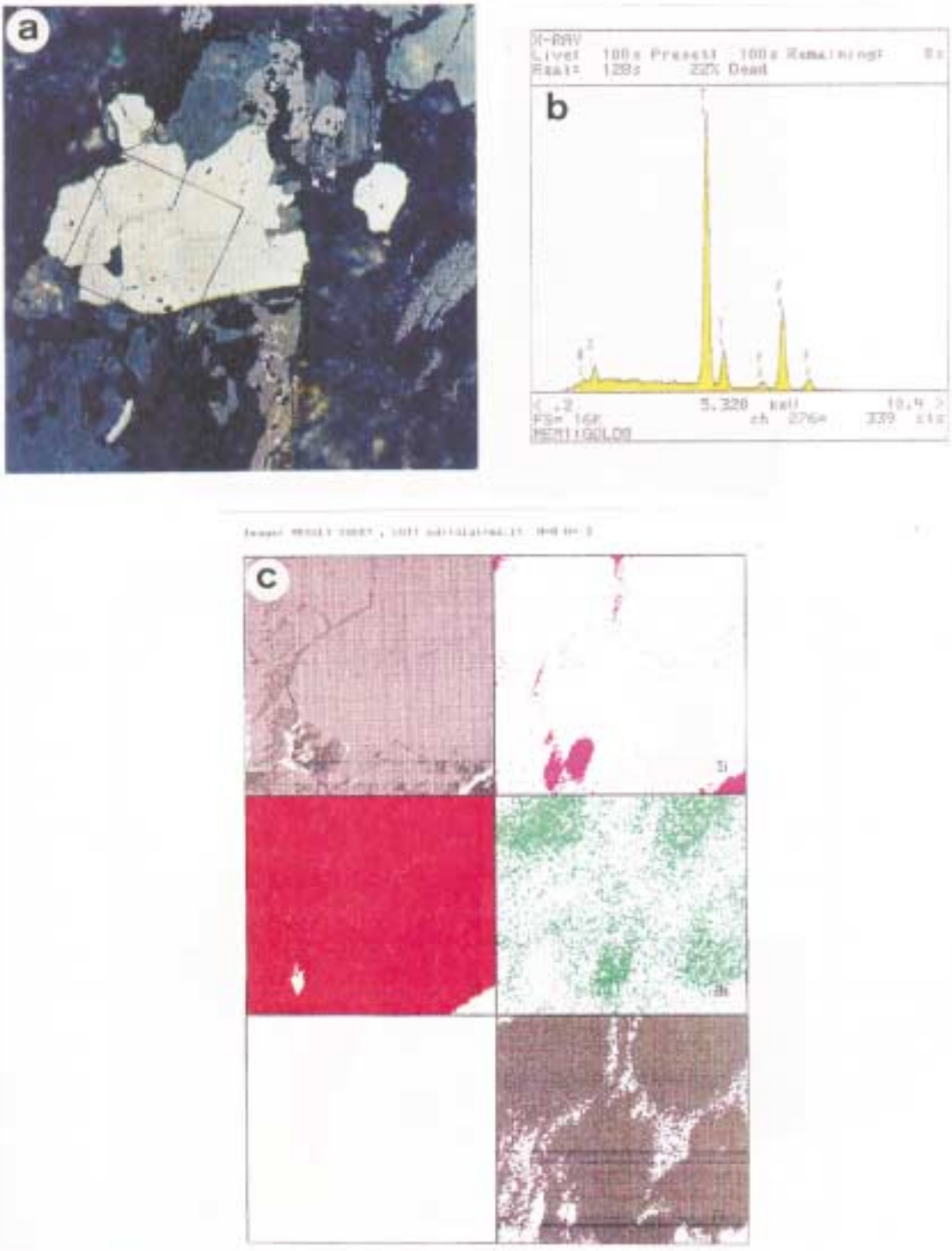

Figure 5.2a Photomicrograph of polished block displaying rutile and ilmenite with a distinct range in visible colour, from brownish pink in the center to faint bluish at the rims with an intermediate white-gray area. Note that the scanning area is marked. (PPL; RL; WOF = 750 µm; MG-T-134, Itapetim District, Sertãozinho). (**b**) X-ray spectrum showing the presence of iron (Fe), manganese (Mn) and titanium (Ti) in the sample Fig. 5.2a. (**c**) X-ray mapping of the elements shows from left to right: the SEM image and the distribution of silica (Si); titanium (Ti); manganese (Mn); and iron (Fe). Note the correlation between the colours displayed in the polished block and the elemental distribution. (MG-T-134, Itapetim District, Sertãozinho).

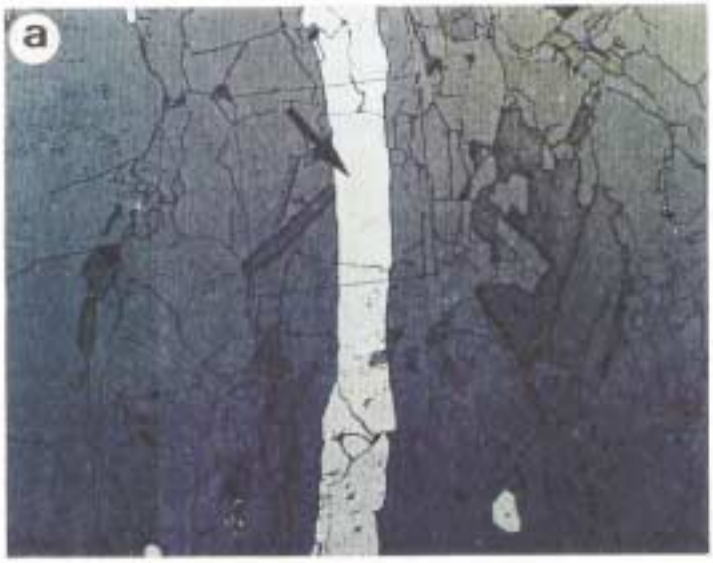

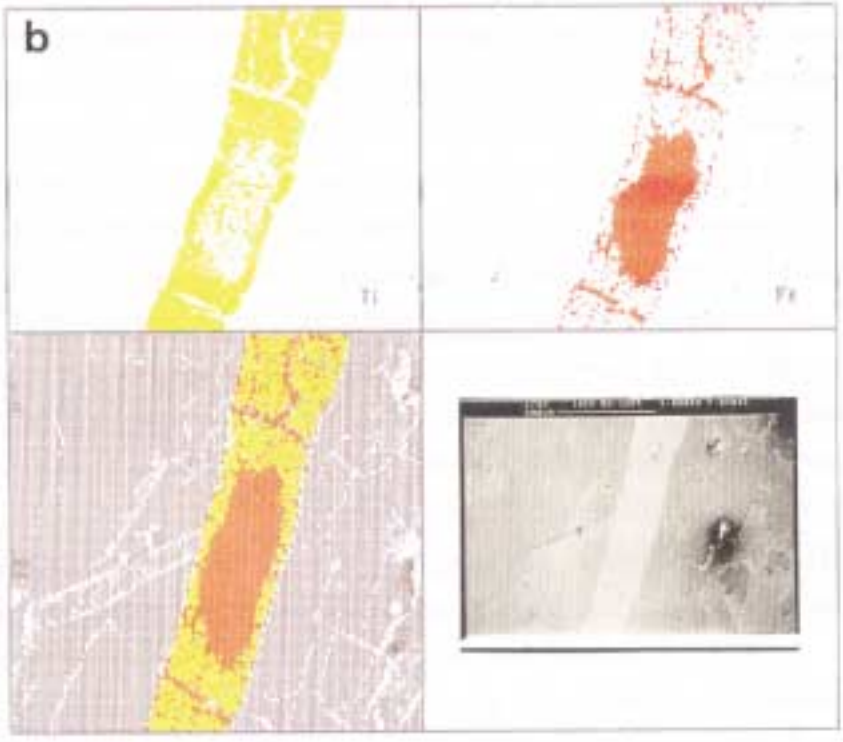

Figure 5.3a Photomicrograph of polished block (PPL; RL; WOF= 750 µm) showing a columnar crystal of rutile elongated along its c axis, displaying a faint bluish tint. In the central area of the crystal there is an area with slight pink colour which indicates hematite (MG-T-143A, Itapetim District, Sertãozinho). The X-ray distribution of the elements is shown in (**b**) which contains the following: titanium (Ti); iron (Fe); Ti plus Fe; and the SEM photomicrograph. Scanning area is indicated in (**a**).

pyrite, with apparent replacement textures, can also be seen. Pyrite is replaced by chalcopyrite and is commonly associated with pyrrhotite and marcasite. Under the microscope three types of texture are distinct: *colloform*, *zoning* and *annealed*. The relationship between these textures and the deformation, their association with pyrrhotite and marcasite, and their significance in terms of the mineralization will be described in detail in 5.3.2.

Pyrrhotite (FeS), characterised in polished section by light yellow to brown pink colour and fairly high reflectivity, occurs as anhedral grains intergrown with pyrite or chalcopyrite (Fig. 5.9). Pyrrhotite occurs in association with pyrite-marcasite and these form 'birds-eye' textures (Ramdohr, 1969) where later chalcopyrite can be seen filling microcracks (Fig. 5.35). The colloform texture shown by the association of pyrite, pyrrhotite and marcasite suggests primary deposition (Fig. 5.28).

Marcasite (FeS_2) occurs in several forms, including idiomorphic crystals (Figs. 5.16a and 5.16b), fine aggregates forming 'birds-eye' texture with primary pyrite (Fig. 5.35), and fractured crystal aggregates with a 'filament-structure' of marcasite-pyrite (Fig. 5.32). However, idiomorphic crystals showing strong blue, green and yellowish green anisotropy and displaying coarse twin lamellae, are the most abundant and are always associated with recrystallised pyrite. In the 'birds-eye' texture the grainsize is generally extremely fine and the distinction between marcasite and pyrite is very difficult in polished section. However, a slighly more yellowish tint may indicate pyrite. From the textural relationship between recrystallised pyrite and the marcasite it appears that polysynthetic twin lamellae and 'filament-structures' (Bonnemaison and Marcoux, 1990) are caused by both tectonic and crystal growth processes.

Chalcopyrite ($CuFeS_2$) is quite abundant in all deposits and occurs predominantly associated with sulphides (pyrite; Fig. 5.8 and pyrrhotite; Fig. 5.9) or hematite (Fig. 5.5). It is entirely allotriomorphic and tends to fill wedge-shaped spaces between adjacent grains, or is found along cracks. Inclusions of chalcopyrite in hematite are very common. The textural evidence suggests that it replaces pyrite (Fig. 5.15a to 5.15c) and pyrrhotite. However, sometimes it is difficult to decide whether a given texture is due to replacement or to filling of an open fracture.

Galena (PbS) is quite easy to distinguish by the presence of coarser grains with triangular cleavage. It shows granular recrystallisation (granoblastic texture) displaying twin laminae caused by deformation (Fig. 5.10). Galena without any deformation (Fig. 5.11) also occurs; in this case it is associated with tellurides and represents the latest phase of galena deposition. However, both phases of galena deposition are interpreted to be late in the paragenesis. Galena and cerussite forming a zonal weathering texture were also found (Fig. 5.12).

Covellite (CuS) is quite easily recognised. It is characterised by a deep blue colour with a slight violet tone, pleochroism, and strong anisotropy (bright orange to copper

Figure 5.4a Hematite (gray-bluish tint) with pyrite, yellow colour.(PPL; RL; WOF = 400 µm; MG-R-155, Itapetim District, Sertãozinho).

Figure 5.4b Same view as Fig.5.4a but in XPL showing the botryoidal hematite texture and deep red brown internal reflections. (XPL; RL; WOF = 400 µm; MG-R-155, Itapetim District, Sertãozinho).

Figure 5.5 Pyrite (yellowish-white) surrounded by hematite (gray-bluish). Chalcopyrite (brassy-yellow) occurs as inclusions in both minerals (PPL; RL; WOF = 400 µm; MG-T-034, Pimenteiras).

Figure 5.6 Photomicrograph of polished block showing hematite (white) rhythmically replaced by goethite (grey) during weathering. (PPL; RL; WOF = 750 µm; MG-R-204I; Canafístula).

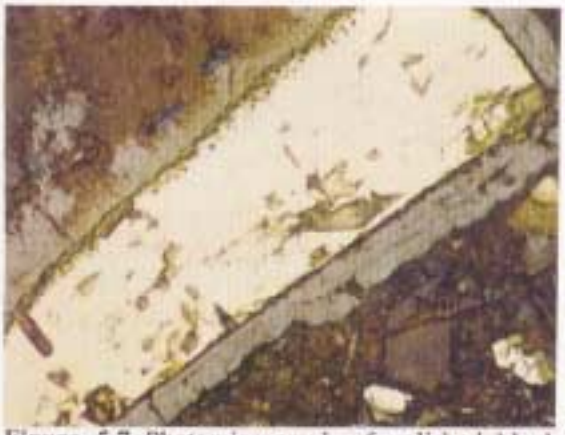

Figure 5.7 Photomicrograph of polished block showing pyrite (yellowish-white) crystal surrounded by hematite (grey) associated with small grains of covellite (blue) at the top left. (PPL; RL; WOF = 2500 µm; MG-R-207, Santo Aleixo).

Figure 5.8 Allotriomorphic chalcopyrite (brassy-yellow) along cracks in pyrite (yellowish-white). (PPL; RL; WOF = 750 µm; MG-R-229C, São Francisco mine).

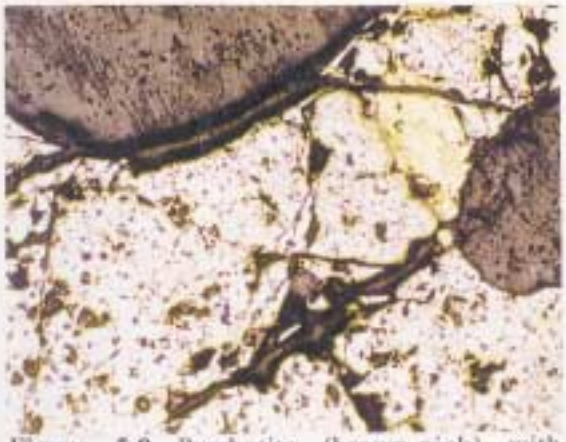

Figure 5.9 Pyrrhotite (brown-pink) with chalcopyrite (brassy-yellow) filling cracks; Black area is quartz gangue. (PPL; RL; WOF = 2500 µm; MG-R-229B, São Francisco mine).

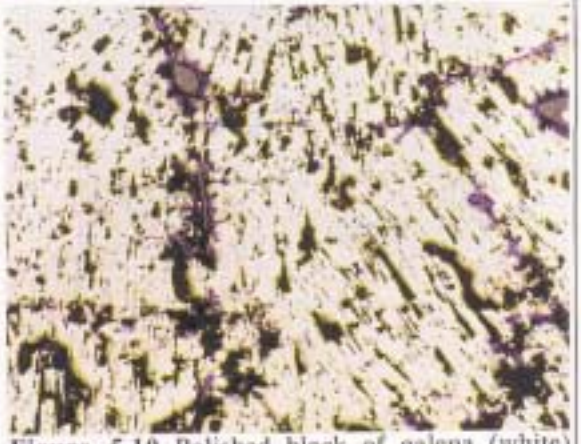

Figure 5.10 Polished block of galena (white) displaying curved cleavage pits developed as a result of post deposition deformation (PPL; RL; WOF = 1500 µm; MG-R-205, Santo Aleixo).

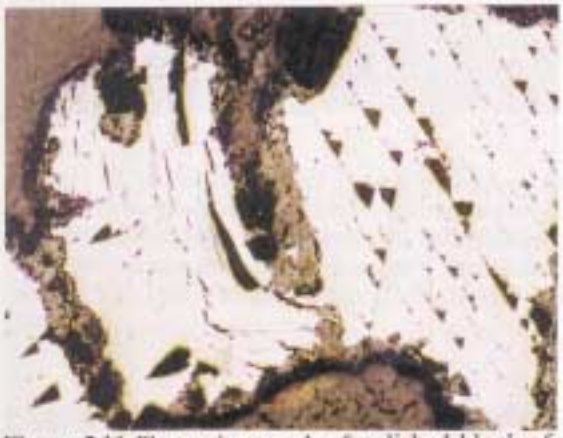

Figure 5.11 Photomicrograph of polished block of galena (white); cleavage pits do not show any evidence of deformation (PPL; RL; WOF = 1500 µm; MG-R-197, Igarape Garapa).

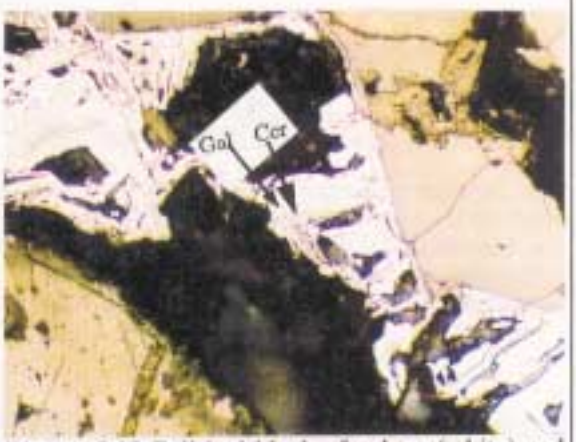

Figure 5.12 Polished block of galena (white) and cerussite (grey-white) forming zonal weathering texture. Black area is quartz gangue. (PPL; RL; WOF = 2500 µm; MG-T-111, Sertãozinho).

Figure 5.13 Disintegration of chalcopyrite (yellow-brownish) to a network of covellite (blue). Note the incipient decomposition of covellite to chalcocite (white lamellae).(PPL; RL; WOF = 400 µm; MG-R-210, Santo Aleixo).

Figure 5.14 Chalcopyrite (yellow) replaced along fractures by covellite (blue), on the right side; on the left magnetite replaced by maghemite. (PPL; RL; WOF = 400 µm; MG-T-031, Sertãozinho, Itapetim District).

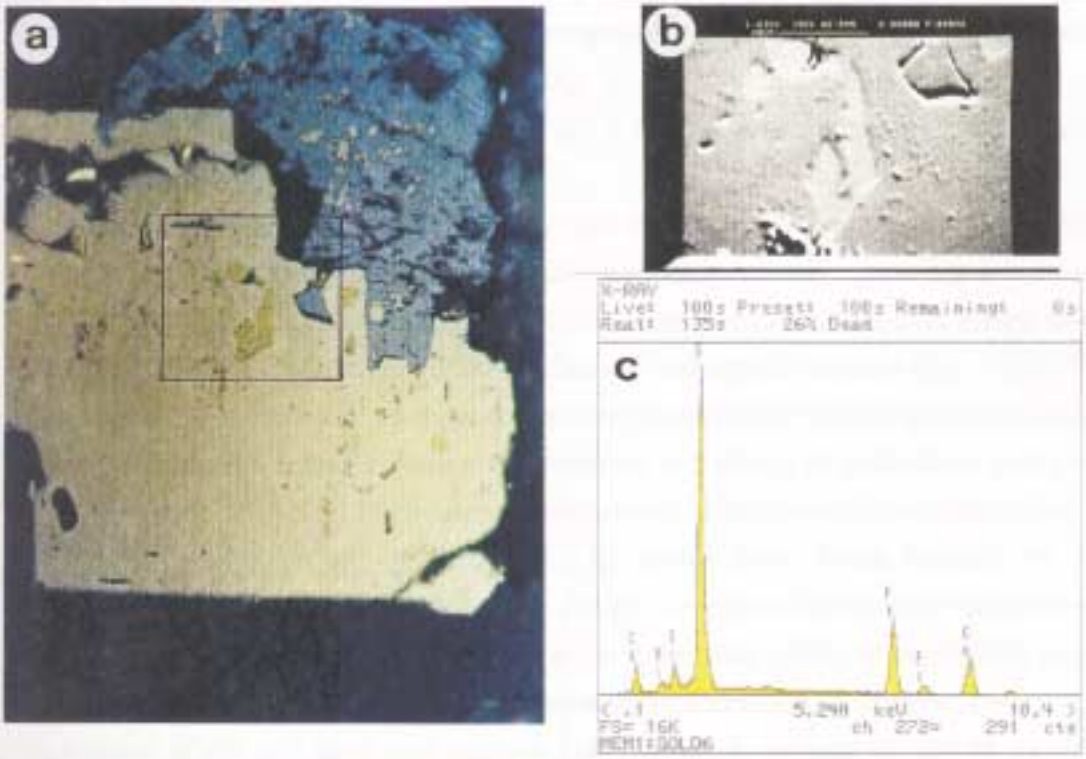

Figure 5.15a Polished block showing an idiomorphic pyrite crystal (white-yellow) partly replaced by xenomorphic chalcopyrite (brassy-yellow) in part along cleavage (PPL; RL; WOF = 400 µm). At the top left chalcopyrite also occurs enclosed in hematite (grey-bluish). Note that the scanning area is marked in the microphotograph.The SEM image is shown in (**b**); (**c**) shows the X-ray spectrum where the peaks of sulphur (S), iron (Fe) and copper (Cu) are well represented. (MG-T-113, Itapetim District, Sertãozinho area).

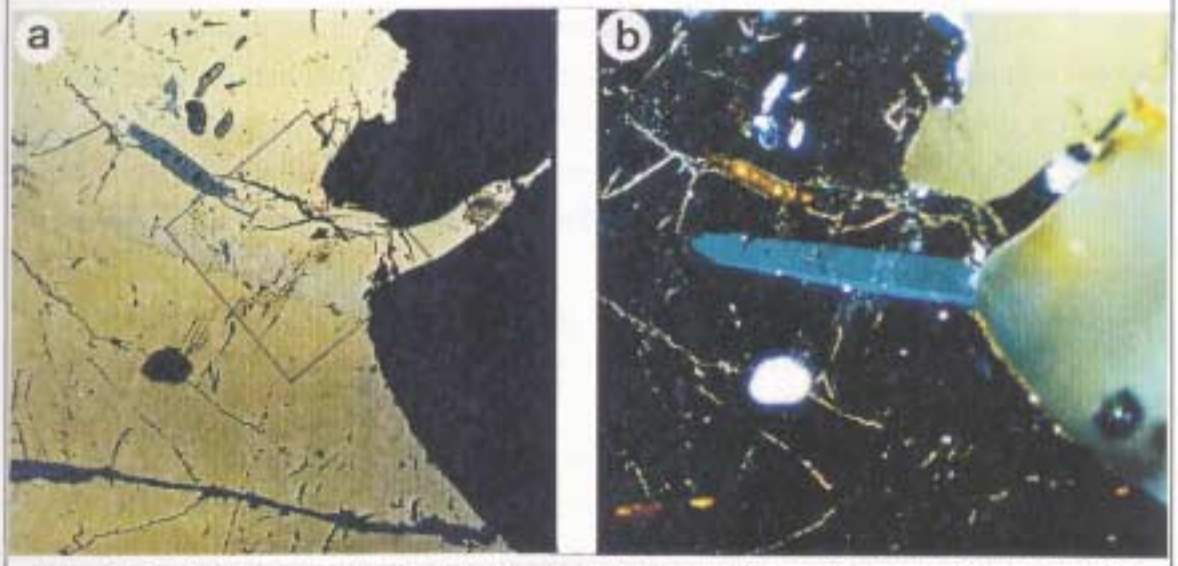

Figure 5.16a Photomicrograph of polished block displaying an idiomorphic marcasite crystal (white-yellow to greenish tint) enclosed in pyrite (white-yellow); Scanning area is marked; (**b**) represents a XPL view characterised by the isotropic pyrite and the strong blue-green anisotropy of the marcasite. (RL; a: PPL; b: XPL.; WOF = 750 µm; MG-R-155, Itapetim District, Sertãozinho area).

bronze). It occurs as idioblastic crystals displaying abundant lamellae which replace chalcopyrite. Sometimes this process has progressed much further, so that only sparse relicts of chalcopyrite have survived (Fig. 5.13). Covellite is derived from the decomposition of copper sulphides (Fig. 5.14), most commonly chalcopyrite (Ramdohr, 1969).

Chalcocite (Cu_2S) can be seen as very thin and lighter lamellae associated with covellite (Fig. 5.13), and is also a product of weathering.

Bismuthinite (Bi_2S_3) occurs intergrown with native bismuth. It displays a very slight blue tint and shows a distinct tendency to form xenomorphic clusters (Fig. 5.24). The X-ray investigations indicate a very characteristic but complex mineralogical association with native bismuth, selenium/tellurium minerals, and alloys of gold-silver and gold-bismuth. Native bismuth in symplectic intergrowth with bismuthinite (identified by microprobe analyses; see Appendix A5.6) could have been formed by the decomposition of lead-bismuth sulphosalts during a regime of decreasing temperature, and quite late in the crystallisation sequence (see Ramdohr, 1969). Bismuthinite seems to be characteristic of deposits of high temperature of formation (Ramdohr, 1969).

Sphalerite (ZnS) is a very rare mineral and when it is present occurs as rounded grains only a few μm in diameter. It is characterised by low reflectivity, numerous internal reflections and isotropy. It occurs in association with other sulphides such as pyrrhotite, pyrite and chalcopyrite.

Molybdenite (MoS_2) is readily recognised but very rare (see Table 5.1).

Greenockite (CdS) was indentifed in polished section and occurs as small rounded grains (less than 1 μm in size) as exsolutions in tellurides (Fig. 5.18a). It has developed a tabular habit (Figs. 5.18b and 5.18c) and shows a grey reflection colour similar to sphalerite. The greenockite is a component of the telluride, which occurs as inclusions associated with the latest phase of galena. According to Ramdohr (1969) greenockite has been found sporadically in hydrothermal sphalerite deposits.

c) Intergrowths of Native Bismuth, Uncharacterised Selenium/Tellurium Minerals and Alloys of Gold-silver and Gold-bismuth.

Small aggregates of native bismuth (Bi) occur intergrown with native gold and some very small and uncharacterised selenium/tellurium minerals (Fig. 5.17). Evidence of exsolution appears in the lamellar texture (Fig. 5.17b). This mineral assemblage is mutually intergrown with bismuthinite, developing a symplectic texture (Fig. 5.24) and occurs in, or close to, pyrite. The microprobe analyses (see Appendix A5.6) indicate the presence of: native bismuth, bismuthinite, native gold, and one or more phases containing selenium, sulphur, tellurium, lead and bismuth. The extremely fine grain size of these minerals did not allow the full identity of these phases to be established,

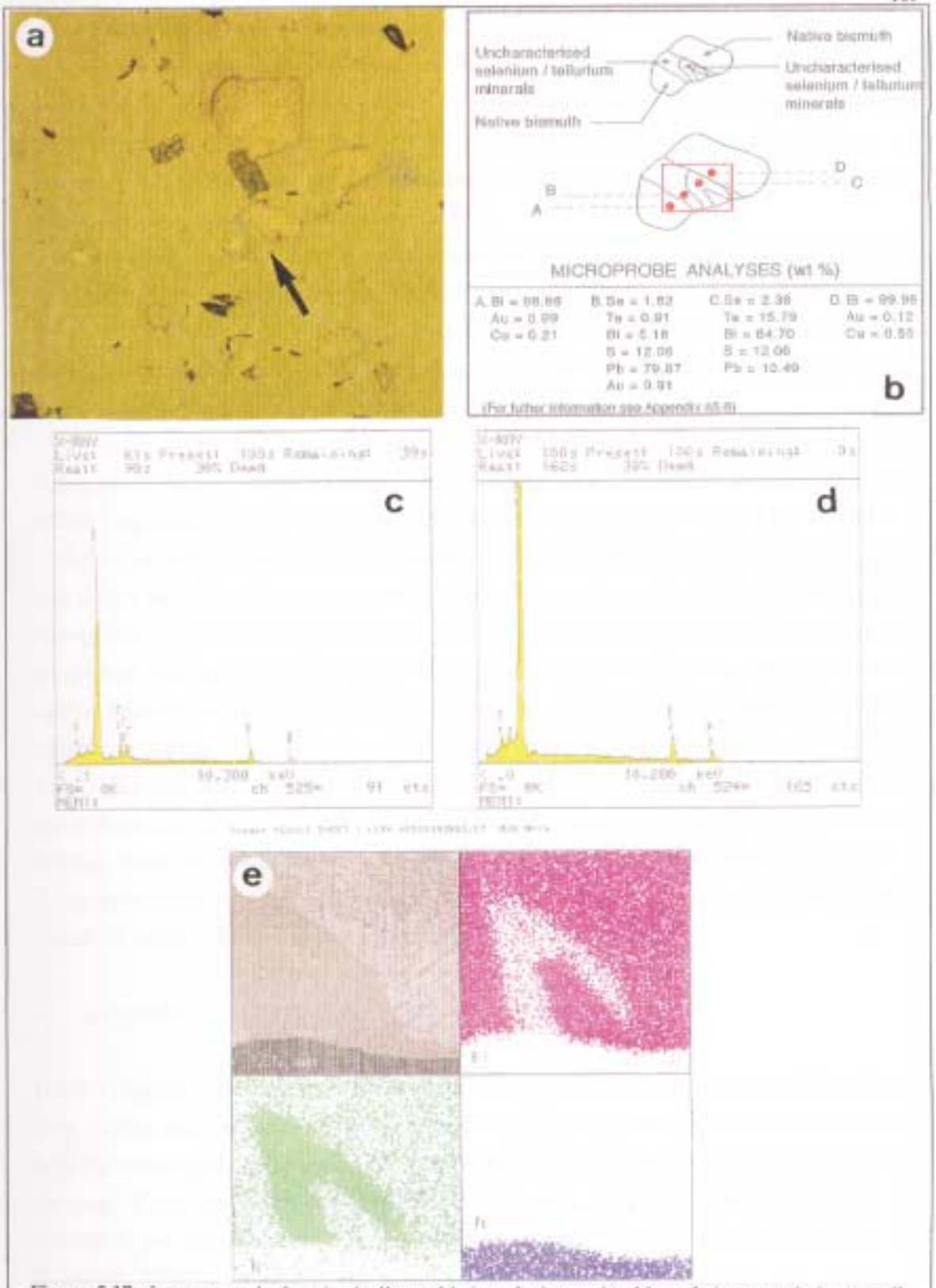

Figure 5.17a Large crystal of pyrite (yellow-white) enclosing native bismuth (creamy tint) as small rounded grains intergrown with uncharacterised selenium/tellurium minerals (slight blue tint) with exsolution laths of selenium/tellurium and bismuth (very slight blue-grey lamellae). On the bottom right is a small grain of gold (PPL; RL; WOF = 400 µm; MG-R-229C, São Francisco mine); (b) shows a sketch of (a) depicting this relationship and the microprobe points (in red) with resulting analyses (see Appendix A5.6); Note the scanning area (red); (c) and (d) display the X-ray spectra for these minerals.The X-ray maps with the distribution of Bi and Te in the area of the uncharacterised selenium/tellurium minerals are shown in (e).

although the appearance under the microscope, and the element ratios, do not suggest that a mixture of minerals is present.

Selenium-bearing minerals tend to be very rare, but are most common in hydrothermal gold deposits. Anthony *et al.* (1990) mention several rare minerals which have compositions close to those found here, although none are exact matches: (i) *junoite* [$Pb_3Cu_2Bi_8(S,Se)_{16}$]; (ii) *nordstromite* [$Pb_3CuBi_7(S,Se)_{14}$]; (iii) *kawazulite* (Bi_2Te_2Se); (iv) *poubaite* [$PbBi_2Se_2(Te,S)_2$].

Native gold associated with native bismuth and selenides has previously been described in some Brazilian metal deposits (e.g.Ibiajara deposit, Bahia State; Mello, 1992; or in Cabaçal gold-copper deposit, Mato Grosso State; Marchetto, 1989). However, as in this study, their very fine grain size and intergrowths did not allow their characterization.

The gold-bismuth alloy (maldonite) was observed in this study among the intergrowths of uncharacterised selenium/tellurium minerals. The Bi content is 10.7 wt % (see Appendix A5. 3). It is characterised by a more greenish tint and it is isotropic.

Native bismuth replaces both pyrrhotite and chalcopyrite (Fig. 5.24) which suggests that it was introduced later in the paragenesis. According to Ramdohr (1969), native bismuth is often the youngest mineral in a paragenetic sequence, and it occurs as symplectic intergrowths with bismuthinite. Edwards (1974) pointed out that where native bismuth is associated with bismuthinite, the sulphide is normally earlier. Maldonite occurs in a particularly high temperature gold-quartz vein in the Maldon Mine, Victoria, Australia (Ramdohr, 1969). Boyle (1976) reports maldonite as a fine myrmekitic intergrowth in gold that contains small amounts of bismuth (up to 3 % Bi), derived from the breakdown of Au_2Bi which is stable only at high temperatures. Bismuth-bearing minerals are widespread in gold deposits throughout the world, but mainly in skarn gold-quartz and polymetallic types (Boyle, 1976).

d) Tellurides

Hessite (Ag_2Te) occurs as inclusions of very small grains (30 μm in size) within galena (Fig. 5.18a) and is related to the latest phase of mineralization. It is characterised under high-power magnification by a pinkish tone and distinct pleochroism (dull brownish to greyish). X-ray investigations (Figs. 5.18b to 4.18f) clearly show the distribution of tellurium and silver. Hessite is widespread in gold deposits (Stillwell, 1931; In Ramdohr, 1969).

A telluride of silver is also associated with chalcopyrite, and X-ray mapping reveals a clear concentration of Ag and Te at the edgs of the chalcopyrite grain (Fig. 5.19a and 5.19b). The BSE image shows distinctive spongiform aggregates along these areas (Fig. 5.19c). Microprobe analyses of these areas (see Fig. 5.19d) indicate very low

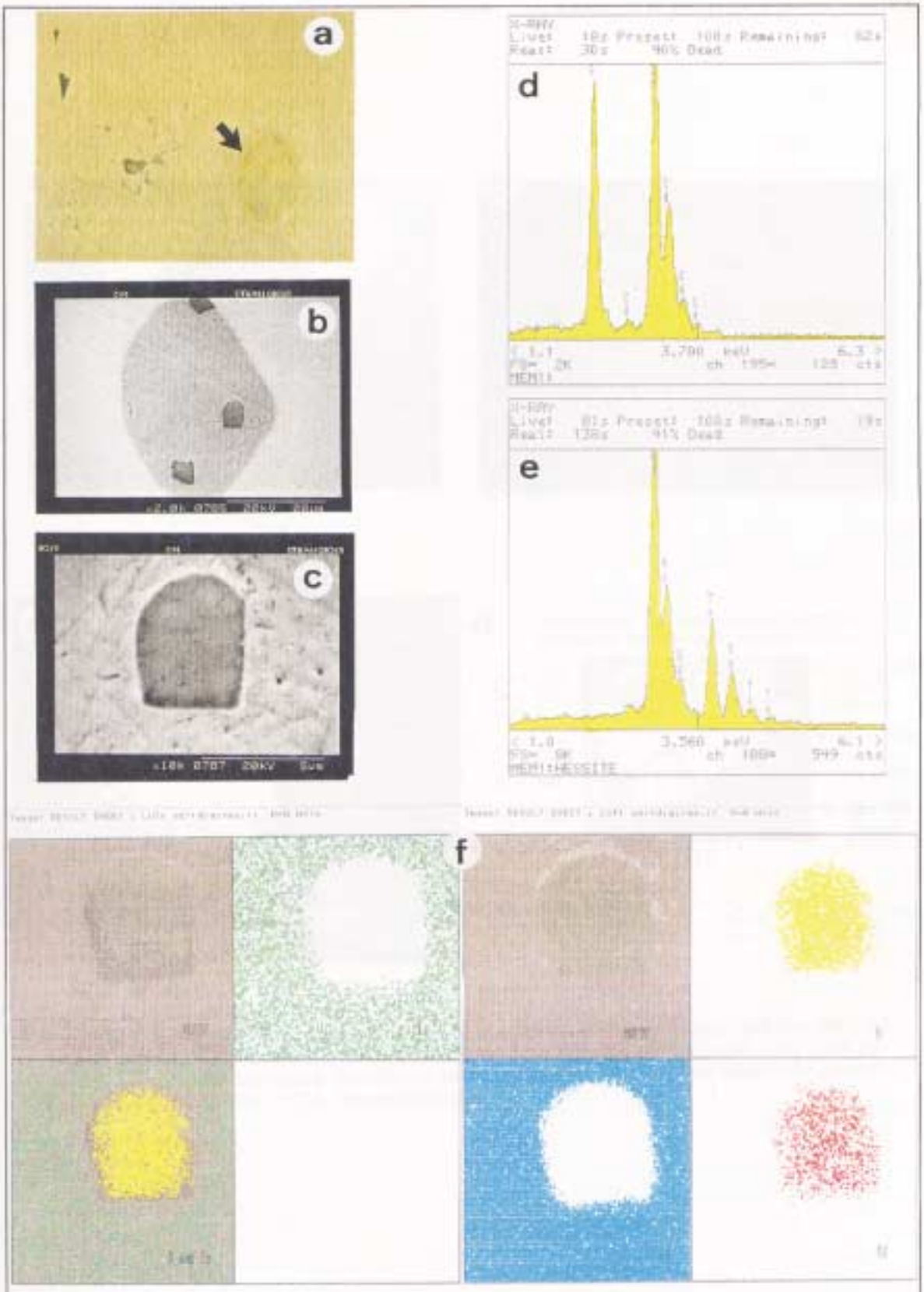

Figure 5.18a Photomicrograph of polished block of a large crystal of galena (see the cleavage pits) enclosing a small rounded grain of hessite intergrown with greenockite. (PPL; RL; WOF = 400 μm; MG-R-197, Igarape Garapa). The SEM images of hessite and greenockite are shown in (b) and (c), respectively. The X-ray spectra of these minerals are displayed in (d) (greenockite) and (e) (hessite); (f) shows the X-ray maps of Ag and Te for hessite, and Cd and S for greenockite.

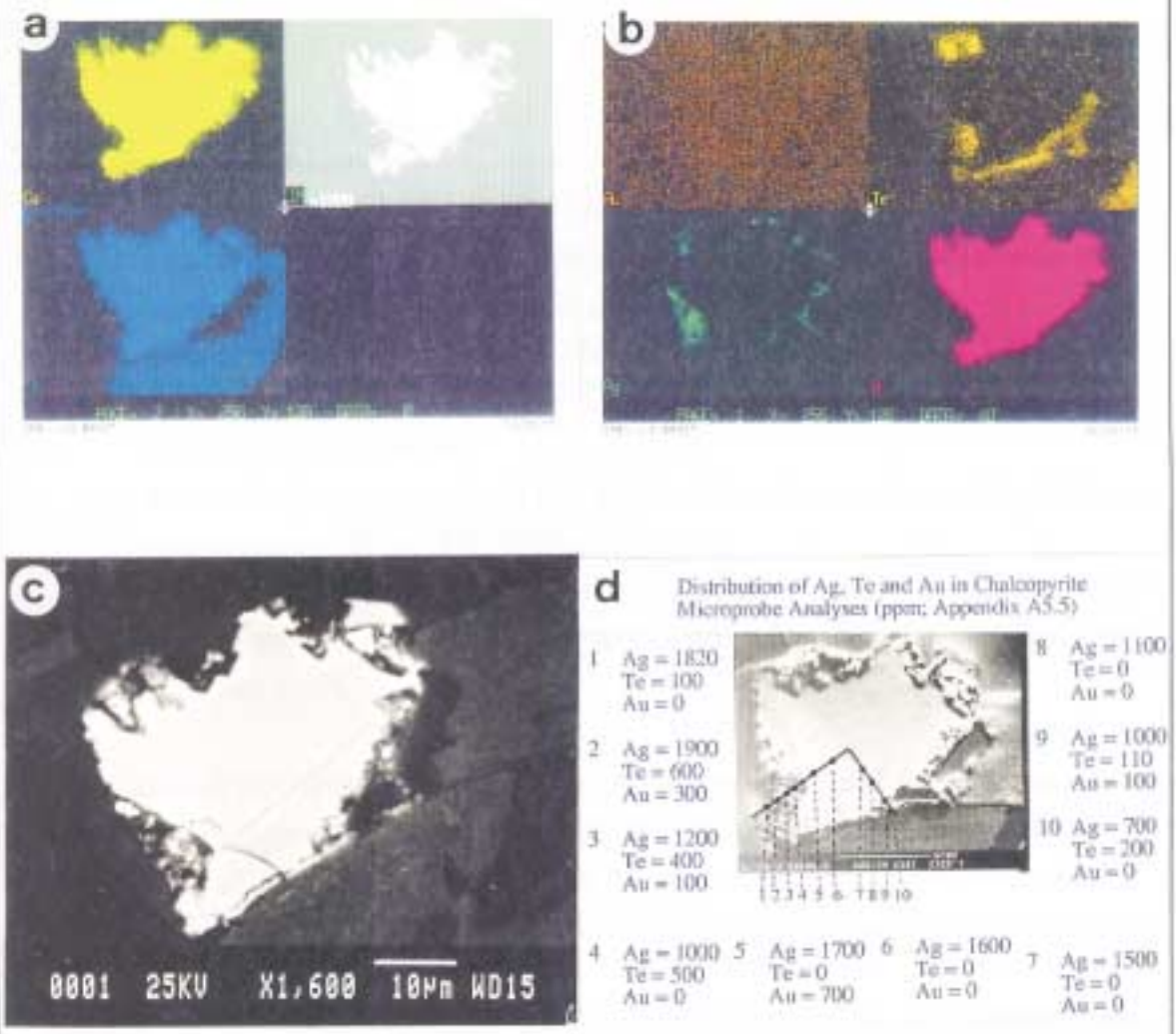

Figure 5.19 X-ray maps of chalcopyrite showing the distribution of (**a**) copper (Cu) and iron (Fe); (**b**) gold (Au); tellurium (Te); silver (Ag); and sulphur (S). In (**c**) the BSE image displays the areas of the Ag-(+Au) telluride phase concentrated at the edges of grain.; (**d**) shows the points of the microprobe analyses and the resulting data (MG-R-1551A, Itapetim District).

contents of gold (Appendix A5.5). These features, which are not consistent with the hessite associated with galena, could be indicative of a separate silver-gold-telluride phase. However, the lower contents of gold detected by microprobe analyses do not characterise this mineral as a silver-gold tellluride (e.g. muthmannite, petzite or sylvanite).

e) Native Gold

Gold occurs in several forms:

(i) Very small particles associated with sulphides such as pyrite (Fig. 5.20) or chalcopyrite (Fig. 5.19) where the grain-size is extremely fine (around a few μm or less-grading into 'invisible gold').

(ii) Disseminated randomly (Fig. 5.21a) or filling microcracks (Fig. 5.21b) in the quartz veins, where it occurs as visible native gold; the grain size is predominantly ≈ 100 μm;

(iii) Disseminated within pyrite as free grains of fine (size ≈ 100 μm; Fig. 5.22) or coarse (size ≈ 10 mm; Fig. 5.23) visible gold.

(iv) As coarse grains of gold intergrown with native bismuth, bismuthinite and selenium/tellurium minerals, and associated with pyrite (size 10 mm; Fig. 5.24 and 5.25).

Chemical analysis by electron microscopy (Appendices A5.2 and A5.3) indicates that the native gold disseminated in quartz veins (Fig. 5.26 and 5.27) contains ≈ 95.9 to 73.4 wt % Au; 20.1 to 4.1 wt % Ag; 0.4 to 0.2 wt % Cu, and 0.1 to 0.3 wt % Bi (see Table 5.2). The gold content in sulphides ('invisible gold') ranges up to 0.72 wt % (Appendix A5.1).

Quantitative chemical analysis in pyrite shows that the gold distribution is not homogeneous. In the same crystal of pyrite (≈ 100 μm in size) the gold content varies from below detection limit (≈ 0.10 %) to 0.72 wt % Au. Thus the gold content varies widely both within small grains and in adjacent grains. It is concluded that the gold occurs as submicron particles of native metal. In contrast, the gold distribution pattern revealed by X-ray mapping on the surface of chalcopyrite is more uniform and it does not show the same pattern as for Te and Ag, the distribution of which suggests random concentration areas in these elements (Fig. 5.19b).

On the other hand, this silver-gold-tellurium-bearing enrichments are concentrated in fractured grain boundaries and display a spongiform texture. This pattern of distribution is very similar to that of gold within sulphides detected by Starling *et al.* (1989). It could indicate the destabilization of aqueous Te-Ag-bearing complexes on the surface of the sulphides. These observations confirm the importance of sulphide

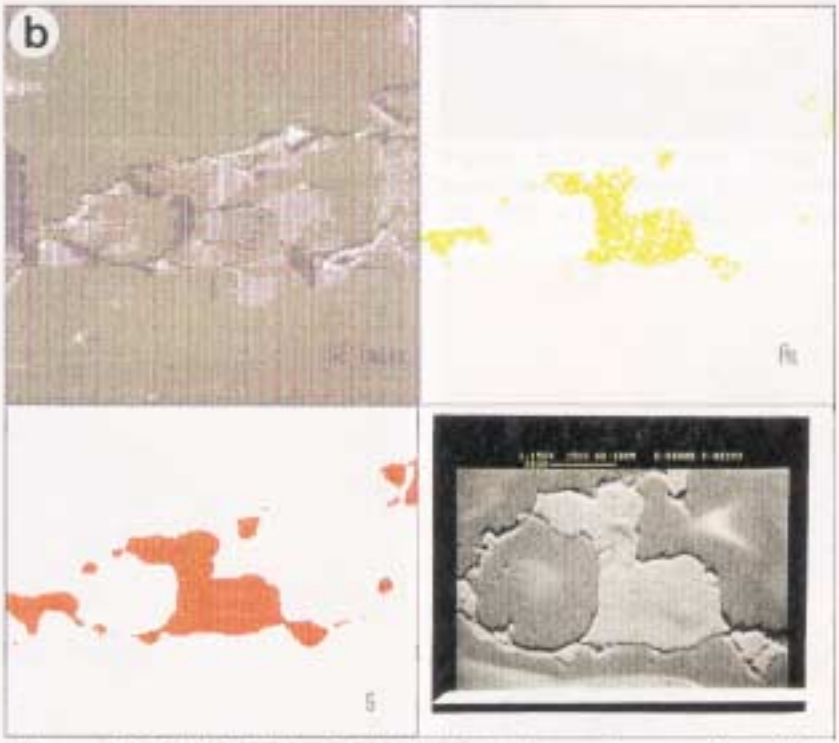

Figure 5.20 Gold within sulphide (a) (pyrite; see the arrow); pyrite (white-yellow); chalcopyrite (brassy-yellow), and hematite (grey) filling crack developed in quartz vein (dark area). (PPL; RL; WOF = 750 µm; MG-R-155, Sertãozinho shaft, level N-35, Itapetim). In (b) the X-ray mapping shows from left to right: the SEM and the distribution of: gold (Au) and sulphur (S), and the SEM photomicrograph.

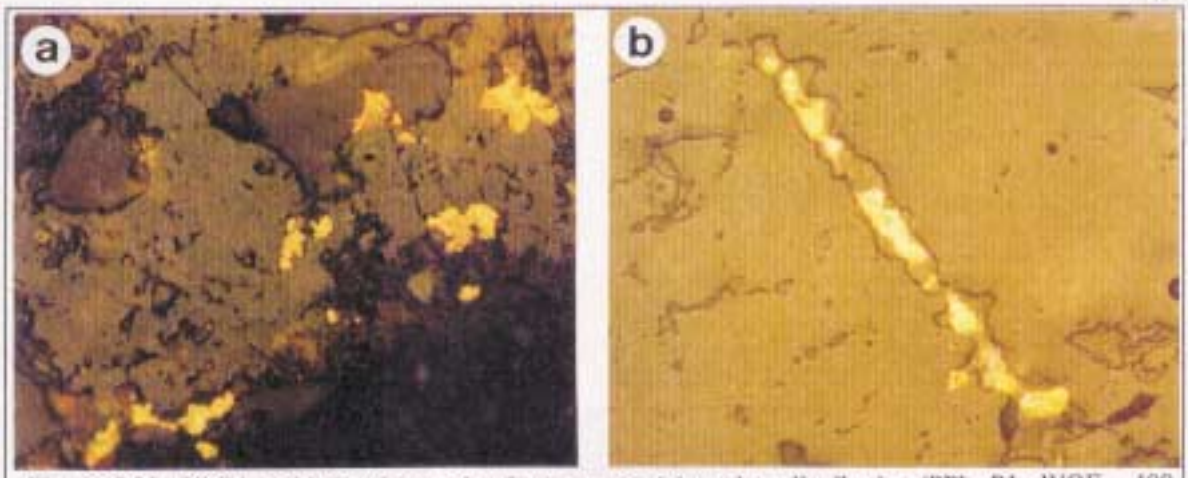

Figure 5.21a Visible gold showing mode of occurrence: (a) random distribution (PPL; RL; WOF = 400 µm; MG-R-159, Sertãozinho) and (b) filling crack healing microfractures (PPL; RL; WOF = 750 µm; MG-R-224B, Cachoeira de Minas mine).

Figure 5.22 Gold (see arrow) filling tiny holes in pyrite (white-yellow) associated with chalcopyrite (brassy-yellow). The dark area is quartz gangue. (PLL; RL; WOF = 750 µm; MG-R-203I, Canafístula.

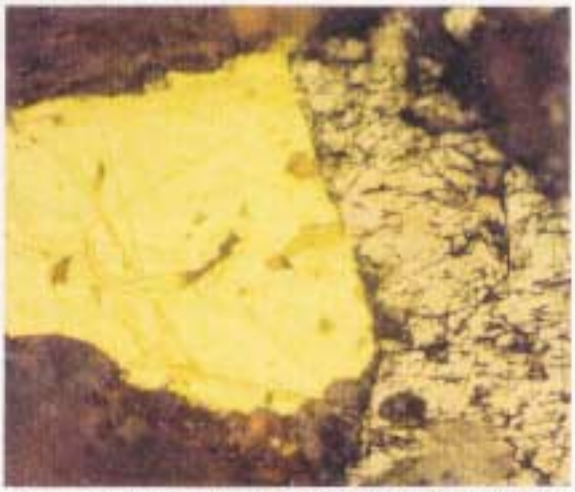

Figure 5.23 Coarse gold (bright golden yellow) associated with fractured pyrite (white-yellow) (PPL; RL; WOF = 1500 µm; MG-R 197, Igarape Garapa).

Figure 5.24 Coarse grain of gold (see the arrow) enclosed in coarse pyrite (white-yellow 'matrix') and associated with native bismuth (creamy tint). Uncharacterised selenium/tellurium minerals and bismuthinite are the very slight blue tinted areas; the dark area is quartz gangue. (PPL; RL; WOF = 750 µm; MG-R-229C, São Francisco mine).

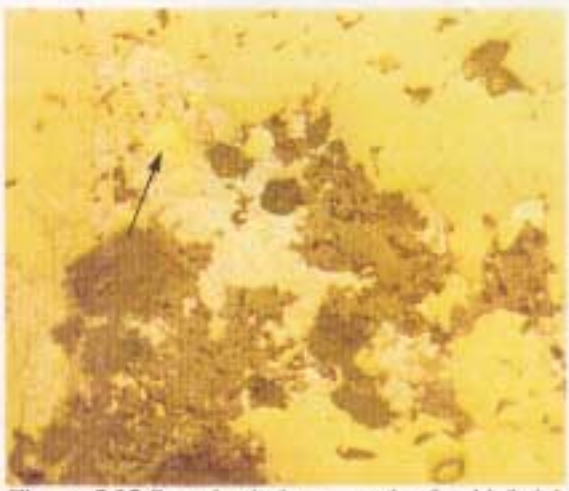

Figure 5.25 Symplectic intergrowth of gold (bright golden yellow; arrowed), native bismuth (creamy tint) and uncharacterised selenium/tellurium minerals and bismuthinite (pale blue) enclosed in pyrite (white-yellow 'matrix'). The dark area is quartz gangue. (PPL; RL; WOF = 750 µm; MG-R-229C, São Francisco mine).

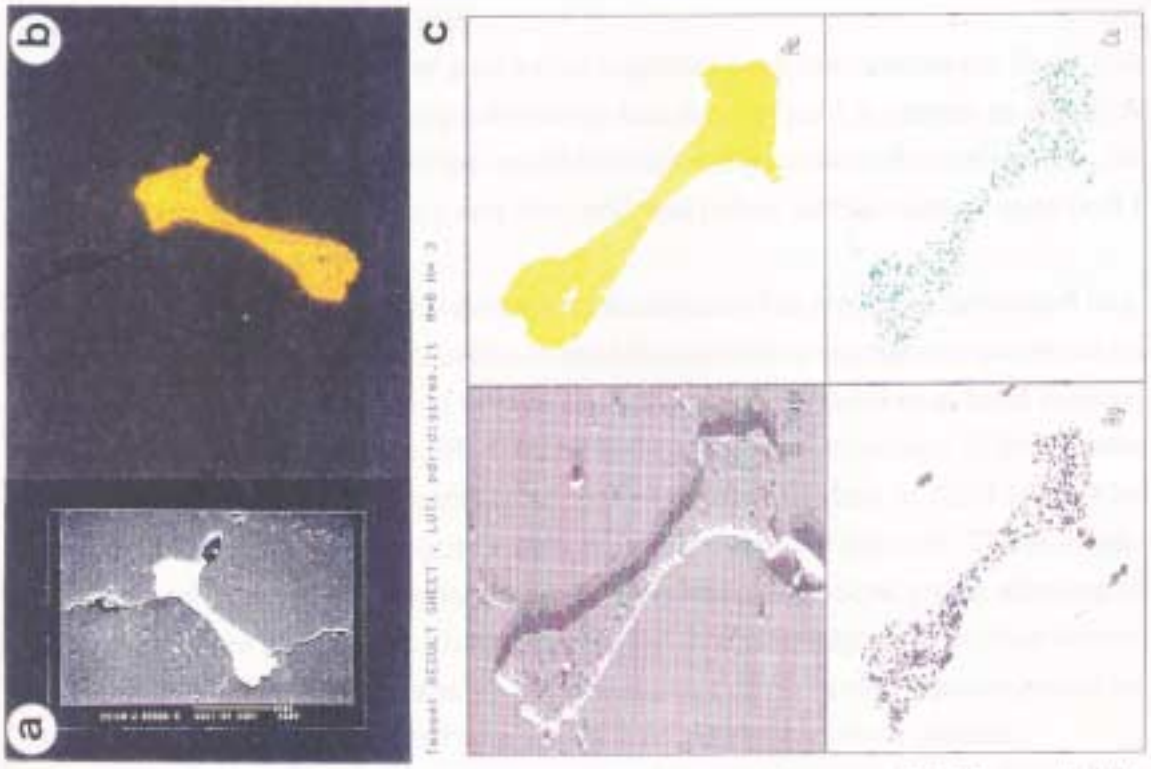

Figure 5. 26 Native gold associated with silver and copper disseminated in quartz. (a) SEM image; (b) PPL view; RL; WOF = 400 µm); (c) shows the X-ray distribution of the chemical elements: gold (Au) ; silver (Ag), and copper (Cu). (MG-T-159, Sertãozinho shaft, level N-13, Itapetim District).

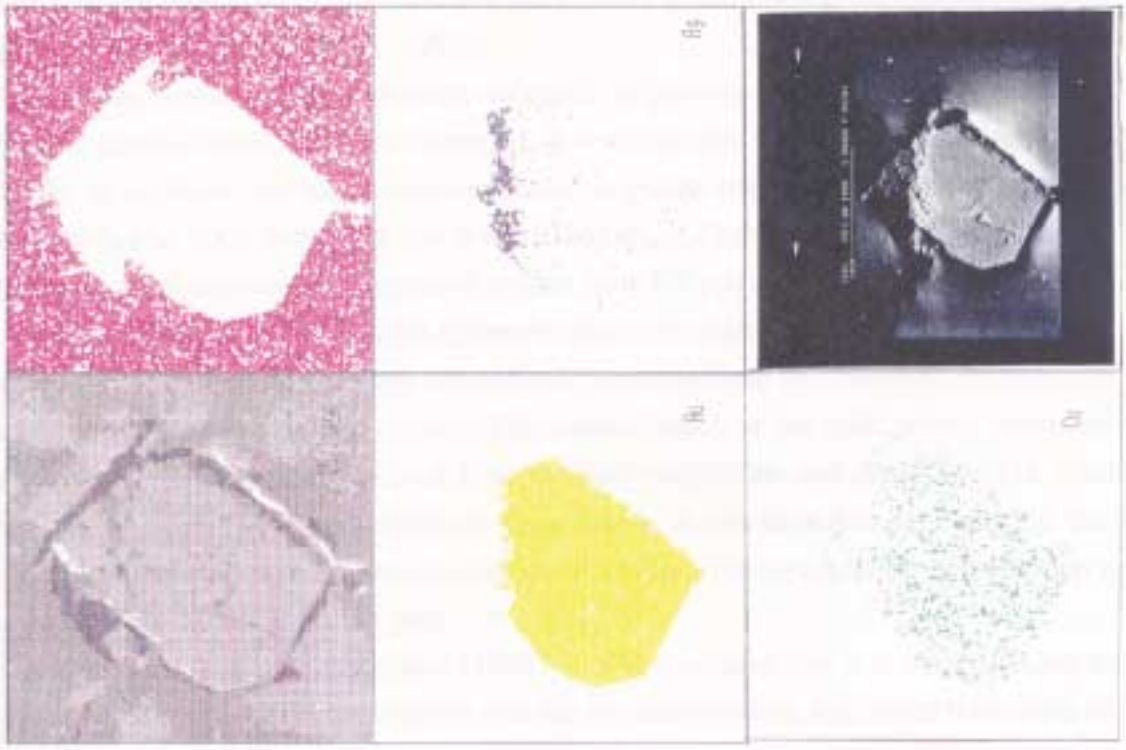

Figure 5.27 X-ray distribution of elements associated with native gold disseminated in quartz: silicon (Si); gold (Au); silver (Ag); copper (Cu); and the SEM photomicrograph. (MG-R-224, Cachoeira de Minas mine). Note the distribution of silver at the edge of the grain.

surfaces and the conducting properties of sulphides to metal precipitation as previously mentioned by Starling *et al.* (1989).

Investigations on the nature of gold within sulphides have been carried out in the past by several authors. Two views predominate: one that the gold is present in chemical combination (solid solution) in the sulphides (especially pyrite and arsenopyrite), the other that the gold is present in a very fine (colloidal) often submicroscopic state (< 0.1 μm).

The presence of gold as solid solution within sulphides has long been advocated (e.g. Clark, 1960). An extensive discussion of gold distribution in sulphides is presented by Boyle (1976) with description of several examples of gold and silver as solid solution within pyrite and arsenopyrite. More recently the textural relationships of gold on the surface of pyrite as submicroscopy state have been investigated in SEM studies by Starling *et al.* (1989), using pyrite grains from different gold deposits. These results show that gold occurs as extremely fine sub-spherical to subhedral grains adhering to the surface of the pyrite grain. Gold concentrates on crystal edges and surface defects from partially destroyed cleavage, by hydrothermal processes and it is accompanied by native tellurium, native silver and tellurides of lead (altaite) and silver (hessite).

Several microbeam analytical techniques have been used to elucidate the form of the trace amounts of gold in minerals. These include the ion microprobe (Cabri *et al.*, 1984; 1985; Cabri *et al* 1989); the electron microscope (Starling, *et al.*, 1989) and the electron and proton microprobe (Cabri *et al.*, 1985). However, despite these studies, the available analytical techniques are not yet capable of measuring the concentration of gold at very low levels (Cabri , 1992).

Gold may occur invisibly in many sulphide, sulpharsenide, and arsenide minerals, but the greatest concentration is attained in arsenopyrite (Cabri, 1992; Arehart *et al.*, 1993). In addition, the highest concentration in pyrite was reported for a Columbian sample (up to 3000 ppm) and one from Villeranges, France (up to 600 ppm). In the literature there are very few reports of greater than 200 ppm of Au in sulphides.

According to Cabri (1992) some epigenetic deposits originally contained gold-bearing arsenopyrite and pyrite but were subsequently recrystallized as a result of deformation and continued hydrothermal activity. This caused much of the gold, silver, antimony and other elements to be exsolved from the early sulphides, and redeposited in local tension fractures, and small faults in shear zones. It can therefore be expected that auriferous deposits which have been subjected to less recrystallization may contain a greater porportion of invisible gold.

It is important to note that Cabri (1992) is of the opinion that it is very difficult to distinguish between precious metals that are in solid solution and those that occur as minute colloidal-size particles.

According to these approaches, notwithstanding the very low contents of gold (close

to the detection limit of the analytical methods) the random distribution pattern and scattered values of gold contents detected during this study appear to be more consistent with gold occurring as submicron particles within the sulphides rather than as solid solution, which is usually suggested in references. A similar intrepretation has been given by Wells and Mullens (1973) concerning the gold deposits of Nevada.

Electron microcopy and microprobe analyses carried out on native gold grains shows that the values of the Au/Ag weight ratios were within the range from 3.7 to 23.1 (see Table 5.2). The higher values (16.5 to 23.1) were detected in Itapetim deposits while the lower values were found in São Francisco mine. The purity ('fineness') of the native gold in quartz ranges from 797 to 959 (Table 5.2). This result is close to values found in mesothermal lode gold deposits, typically ranging from 750 to 900 (Boyle, 1976). According to that author, gold of very high fineness (990 or more), is generally the result of oxidation under conditions favourable for the complete removal of silver. In some auriferous deposits there is an indication that the early deposited gold is more silver-rich (lower in finess) than that deposited later in the paragenetic sequence.

5.3.2 Microstructure of Pyrite and Marcasite

Although metamorphism is commonly responsible for the obliteration of primary textures in minerals, the refractory nature of pyrite offers the opportunity for preservation of some evidence of pre- or syn-metamorphic development (Scott, 1976; 1983). The mechanism of pyrite deformation during metamorphism has been investigated and the results have shown that pyrite may behave either as a brittle substance (Graf and Skinner, 1970) or have plastic behaviour (Mookherjee, 1971; Cox *et al.*, 1981) under all conditions of deformation. The modification in the texture of pyrite produced by pressure solution has also been the subject of many studies (McClay and Ellis, 1984; Cox, 1987; Marshall and Gilligan, 1987).

Recent studies of pre-metamorphic textures preserved in pyrite from several types of deposit, including metamorphosed massive sulphides, show that some pre-metamorphic textures persist through a metamorphic episode and retain very useful information for the understanding of genetic processes (Lianxing and McClay, 1992; Craig and Vokes, 1993; Brown and McClay, 1993).

Etching of the pyrite grains in polished blocks during this study has revealed primary and growth structures that are not visible, or are only poorly visible, after normal polishing. This study carried out on the ore samples has allowed recognition of three types of pyrite:

Table 5.2
Gold/Silver Ratios and True Fineness

Wt% Elem. Normalized (*)	MG-R-1591	MG-R-1591I	MG-R-1591II	MG-R-1591IV	MG-R-1591V	MG-R-1591VI	MG-R-1591VII	MG-R-1591VIII	MG-R-1591IX	MG-R-229IX	MG-R-229X	MG-R-229II	MG-R-229III
Au	94.30	94.28	94.28	95.86	95.85	95.00	95.08	94.99	95.48	79.02	78.82	78.27	78.56
Ag	5.70	5.52	5.52	4.14	4.15	5.00	4.92	5.01	4.53	20.15	21.15	17.76	17.83
Cu	0.00	0.20	0.20	0.00	0.00	0.00	0.00	0.00	0.00	0.41	0.32	-	-
Bi	0.00	0.00	0.00	0.00	0.00	0.00	0.00	0.00	0.00	0.00	0.00	0.13	0.25
Total	100.00	100.00	100.00	100.00	100.00	100.00	100.00	100.00	100.00	99.57	100.30	96.16	96.65
Au/Ag Ratio (Au ppm/ Ag ppm)	16.53	16.98	17.07	23.14	23.11	19.00	19.31	18.98	21.10	3.92	3.73	4.41	4.40
True Fineness (Au / Au+Ag) x 1000	943	945	945	959	959	950	951	950	955	797	788	815	815

Observations:
(*) For further information see Appendix 5.2 for samples MG-R-1591 to MG-R-1591X ; Appendix A5.6 for samples MG-R-229IX to MG-R-229X and Appendix A5.3 for samples MG-R-229II to MG-R-229III.
Not analysed:-

(i) *Pyrite type I* is characterised by relict primary depositional textures such as spheroidal, rhythmic texture formed by fine aggregates of pyrite and marcasite (Fig. 5.28) and overgrowth zoning features (Figs. 5.30 and 5.31). Brittle deformation textures (e.g. brecciation) are also found associated with this type of pyrite (Fig. 5.29), revealing that a phase of deformation followed the first stage of pyrite formation.

(ii) *Pyrite type II* is marked by ductile deformation textures such as stylolitic indentation of porphyroblastic euhedral pyrite due to pressure solution (Fig. 5.33); fractures and cleavage filling with remobilised marcasite ('Filament-structure' of marcasite-pyrite; Bonnemaison and Marcoux (1990; Fig. 5.32); and slip lines suggesting folding (Fig. 5.34).

(iii) *Pyrite type III* is defined by post deformation textures, e.g. annealing deformation (Fig. 5.36), which has produced grain growth with boundaries at 120° triple junctions (Fig. 5.35) and a marked tendency towards large idioblastic pyrite porphyroblasts (Fig. 5.36). Annealing pyrite crystal enclose coarse grain of gold (Fig. 5.37). Locally, formation of 'birds eyes' - a fine-grained pyrite-marcasite aggregate, is associated with pyrrhotite (Fig. 5.35) suggests recrystallization.

Pyrite type I is closely associated with pyrrhotite and marcasite, but the textural evidence suggests that it is actually replaced pyrrhotite. It is marked by a clear zonal growth pattern with cores of the earliest-formed pyrrhotite (Fig. 5.30).

An open system in which the decomposition of pyrite by loss of sulphur has resulted in the formation of pyrrhotite has been indicated by Plimer and Finlow-Bates (1978); Stose and Stose (1957); Vokes (1963); and Nilsen (1978). However, pyrite and pyrrhotite coexisting as primary phases have been recently observed by Craig and Vokes (1993) in many massive sulphide deposits. These authors point out that if only one or the other of those minerals was decomposed, any ore body or sulphide-bearing rock could move off the pyrite-pyrrhotite buffer during the metamorphic cycle. At low temperatures, reaction kinetics may not be sufficient to maintain equilibrium, but at temperatures above 300°C it is almost certain that pyrite and pyrrhotite would remain in equilibrium. The constant re-equilibration of a pyrite-pyrrhotite assemblage during retrograde cooling would result in a drop in the activity of S_2, a decrease in the sulphur content of the pyrrhotite, and growth of pyrite (Craig and Vokes, 1993).

Pyrite type II is marked by clear deformation textures. It occurs intergrown with marcasite, and sometimes occurs in the shape of fractured prisms, due to brittle deformation (Fig. 5.32). Although marcasite has no field of true stability (Gronvold and Westrum, 1976) it appears that annealing, even at relatively low temperature, results in transformation of the marcasite to pyrite (Craig and Vokes, 1993). Inclusions

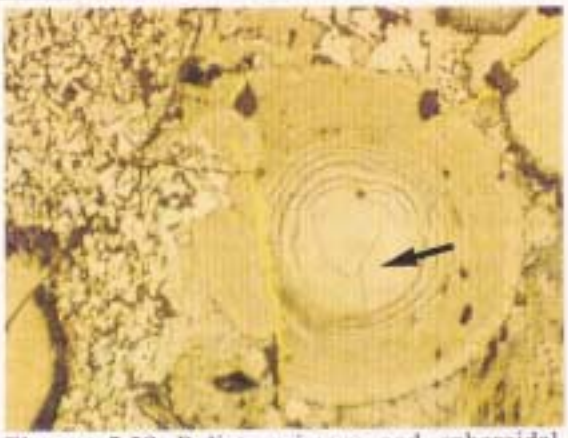

Figure 5.28 Relict, primary and spheroidal, rhythmic texture in pyrite-marcasite and pyrrhotite (Type I). The cracks (see the arrow) are characteristic of former gel precipitation. Note chalcopyrite filling microfractures. (PPL; RL; WOF = 750 µm; MG-R-210; Itapetim central)

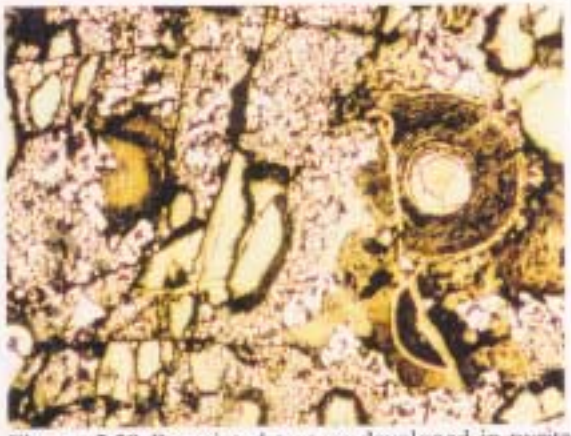

Figure 5.29 Brecciated texture developed in pyrite and marcasite suggesting brittle deformation. (Type I). (PPL; RL; WOF = 750 µm; MG-R-210; Itapetim District, central area).

Figure 5.30 Zoned euhedral overgrowths of pyrite on cores of pyrrhotite (Type I). Cores of earliest formed pyrrhotite occur on the left (see the arrow; PPL; RL; WOF = 750 µm; MG-R-229A; São Francisco mine).

Figure 5.31 Overgrowth texture on pyrite (Type I) is indicated by the zoned texture (PPL; RL; WOF = 750 µm; MG-R-229A; São Francisco mine).

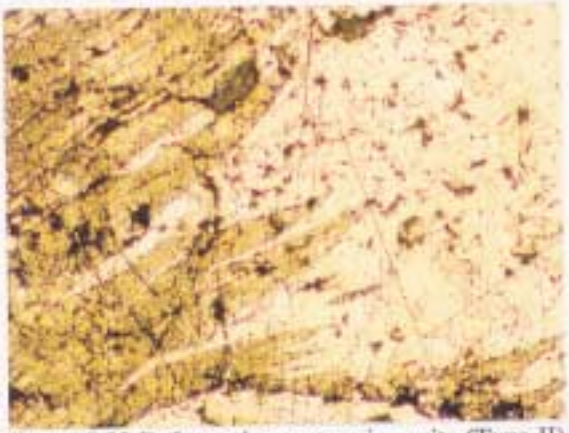

Figure 5.32 Deformation texture in pyrite (Type II) showing fractures and cleavage filled by marcasite (filament structure) (PPL; RL; WOF = 750 µm; MG-R-229A; São Francisco mine).

Figure 5.33 Deformation texture shows stylolitic indentation of porphyroblastic euhedal pyrite (Type II) due to pressure solution with a seam of pyrrhotite. (PPL; RL; WOF = 2500 µm; MG-R-207; Santo Aleixo area).

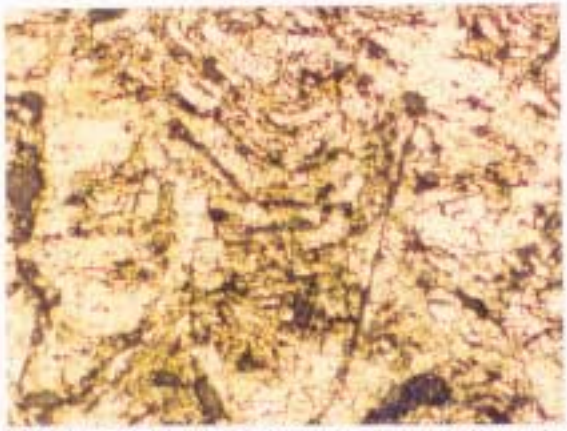

Figure 5.34 Plastic deformation texture in pyrite (Type II) forming dislocation microstructures where slip lines suggest folding (PPL; RL; WOF = 750 μm; MG-R-229A; São Francisco mine).

Figure 5.35 Recrystallised pyrite (Type III) showing truncated grain boundaries forming 120° dihedral angle. At the top left 'birds eye' texture is an aggregate of very fine pyrite-marcasite grains associated with pyrrhotite. Chalcopyrite is enclosed in pyrite (see the arrow). (PPL; RL; WOF = 750 μm; MG-R-210; Santo Aleixo).

Figure 5.36 Recrystallisation product of pyrite (yellow; Type III) forming idiomorphic crystals. (PPL; RL; WOF = 750 μm; MG-R-197; Igarape Garapa).

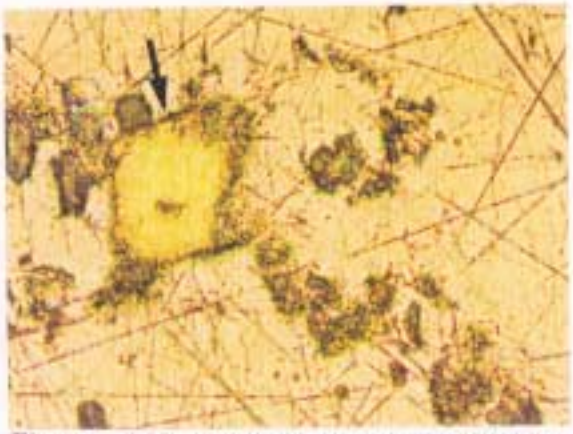

Figure 5.37 Detail of Fig. 5.36 showing a recrystallised pyrite crystal (Type III) enclosing a coarse grain of gold (see the arrow) (PPL; RL; WOF = 400 μm; MG-R-197; Igarape Garapa).

commonly occur in this type of pyrite and display a concentric distribution pattern which could be attributed to rotation during the growth of the crystal. The largest porphyroblasts of pyrite exhibit an arrangement of folding (Fig. 5.34) suggesting brittle-plastic deformation.

Pyrite type III (Fig. 5.36) is marked by recrystallisation to yield typical annealed textures with 120° dihedral angles (as described by Stanton, 1972). According to Craig and Vokes (1993) the degree to which rocks or ore bodies remain as isochemical units or an open system during metamorphism varies from one place to another, and also depends on of the scale of observation. However, these authors suggest that the recrystallisation of pyrite with typical annealed textures may be related to an isochemical system relative to iron and sulphur, even if some fluids were expelled from or passed through the rocks.

5.2.3 Mineralization Evolution

The combined action of deformation and the migration of fluids through the different lithologies has produced an important transformation of the mineral assemblages and the geochemistry of the host rocks in the region. These processes are associated with dissolution and subsequent redistribution of the chemical components and also with the influx of 'new' elements towards the shear zone.

Research in other gold-bearing areas has shown that the economic concentration of gold in shear zones is the end-product of a complex evolution, often comprising several, successive stages (Colvine *et al.*, 1984; Colvine *et al.*, 1988; Bonnemaison and Marcoux, 1990). A 'three-stage model of metallogenesis' based on the progressive increase of gold concentration related to the evolution of the shear zone has been proposed by Bonnemaison and Marcoux (1990):

(i) At the earliest stage, stress and deformation are focussed on restricted zones, resulting in the development of mylonitic rocks and stuctures which provide conduits for fluid flow. An influx of fluid helps to aid mineralization and rock alteration, and these increase in intensity towards the cores of the structures. Silicification and sulphidation are common. Gold is generally invisible and at first fixed in pyrrhotite.

(ii) In the second stage, the shear zone shows several phases of opening and closing; the hydrothermal activity increases and a highly silicified zone results. The hydrothermal fluids are rich in Fe, Cu, Pb, and Zn, and these lead to the breakdown and replacement of the original Fe-sulphides. Gold is liberated and forms fine-grained free gold (often Ag-poor), which is precipitated in the quartz veins. P-T conditions are around 250-350°C and

0.5-2 kb.

(iii) The latest stage corresponds to a stage of opening of the shear zone, and the formation of quartz stockworks. Gold is remobilized and precipitated as coarse visible gold, often rich in silver. Temperatures of the fluids are lower (150-200°C).

This model also seems to fit the gold mineralisation in Borborema Province, and the following paragenetic sequence for the mineralization is proposed (see Table 5.3) with the various stages described below.

a) The First Stage of Mineralization

A first stage of gold mineralization in the second-order shear zones is common in Borborema Province. Magnesium and iron, mainly in the mafic rocks, wee leached and partially fixed by the formation of opaque minerals (e.g. oxides and sulphides). Chloritization was common (see Chapter 4) and caused release of titanium from primary Ti-bearing minerals. The enrichment in titanium is very clear, with significant amounts of titanite being produced. Ilmenite breakdown resulted in the formation of rutile and/or leucoxene along the foliation of the mylonitic rocks. The titanium is thus mobile within the shear zone and indicative of intense hydrothermal activity in this structure during the first stage of evolution. Subsequent hydrothermal processes are accompanied by crystallisation of pyrrhotite and pyrite disseminated in the mylonitic rocks.

Deposition of pyrite I is associated with pyrrhotite and marcasite (marcasite I). Spheroidal textures and overgrowth structures are preserved in porphyroblasts of pyrite, thus suggesting the first stage of mineralization.

The increase in the hydrothermal processes produced highly silicified zones where the quartz veins were developed. During this process the fluid flow provided conditions for mass transfer or fluid/rock interaction which caused change in the pyrite-pyrrhotite ratios. These ratios vary with the metamorphism since prograde heating results in sulphur release from pyrrhotite and retrograde cooling permits re-growth of pyrite as pyrrhotite releases sulphur (Craig and Volkes, 1993). During this process the 'invisible' gold in the pyrrhotite (see Bonnemaison and Marcoux, 1990) is liberated and located at the surface of pyrite (in edges and surface defects), and as submicron particles in pyrite (I) and chalcopyrite as demonstrated in this study. Invisible gold associated with sulphides (pyrite and chalcopyrite) is therefore interpreted as gold formed during the first stage of the mineralization (gold I) .

Examples of gold related to this first stage of mineralization and incorporated in the lattice of sulphides such that it cannot be expressed mineralogically occur at: (i) the Obuasi and Prestea gold mines in Ghana, West Africa where gold deposits are hosted

Table 5.3 Paragenetic Sequences for the Mineralization in Borborema Province

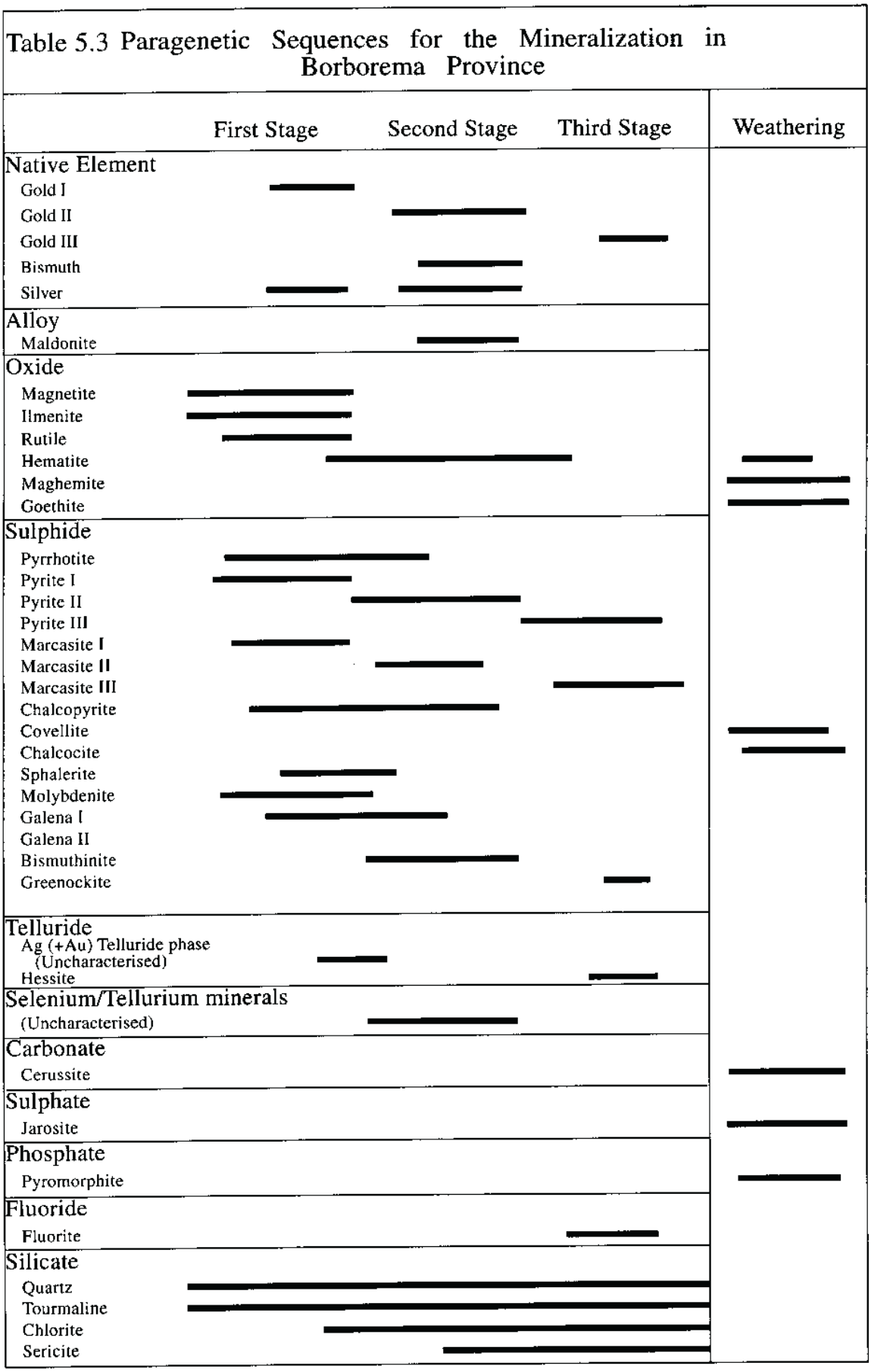

by Early Proterozoic sequences that have been intruded by granitoids (Kesse, 1985; Milesi *et al*, 1989); and (ii) Massif Central, France, where arsenopyrite is contemporaneous with pyrrhotite and enriched in gold (Marcoux *et al.*, 1989).

b) The Second Stage of Mineralization

During the second stage of mineralization rock/fluid mass transfer is more effective as a result of opening and shearing processes. The mineralized fluids rich in elements leached from the host rocks (e.g. Fe, Cu, Zn, Pb) cause destabilisation of the gold-bearing pyrrhotite-pyrite. The first mineralization is strongly obliterated. The presence of 'filament-structures' in marcasite-pyrite is characteristic of the transformation of pyrrhotite-pyrite, representing a relitc of the first stage (marcasite II; Fig. 5.32).

The second stage is marked by an Au-Pb correlation, with minerals such as sphalerite and galena (which are not associated with tellurides: galena I), chalcopyrite, and the first deposition of visible gold (gold II). Gold occurs disseminated randomly (Fig. 5.21a) or filling microcracks (Fig. 5.21b) in the quartz vein where the grainsize is predominantly ≈ 100 μm. Chalcopyrite commonly occurs replacing pyrite and/or pyrrhotite. This generation of pyrite is defined by a typical deformation texture and displays evidence of brittle-plastic deformation (pyrite II; see Figs. 5.32 to 5.33).

The mineral assemblage consists of intergrowths of native bismuth, bismuthinite, uncharacterised selenium/tellurium minerals and alloys of gold-silver and gold-bismuth, and marks a second stage of precipitation. Molybdenite also occurs in this stage. This paragenesis is characterised by enrichments in Cu, Zn, Bi, and Mo, elements which possibly reflect a plutonic influence.

Native gold is associated with native bismuth and selenides in other gold-bearing quartz veins hosted by Proterozoic metavolcanic-sedimentary sequences in Brazil (e.g. Ibiajara deposit, Bahia State; Mello, 1992; or in Cabaçal gold-copper deposit, Mato Grosso State; Marchetto, 1989). In these deposits gold was also precipitated in two stages. The finer gold is included in sulphides (indicating that it has been formed slightly earlier) and the coarse gold is associated with native bismuth and selenides, and are interpreted to have formed later.

c) The Third Stage of the Mineralization

The third stage of the mineralization is marked by the introduction of lead and tellurides, as can be seen in the Igarape Garapa occurrence.

The gold (gold III) occurs as coarse grains which are disseminated in sulphides (pyrite; see Fig. 5.37) and associated with galena and hessite (galena III; see Fig. 5.18a).

The pyrite is usually characterised by annealing texture and coarse grains (pyrite III; Fig. 5.36). It is often associated with idiomorphic marcasite (marcasite III) which displays coarse twin lamellae (Figs. 5.16a and 5.16b).

5.4 GEOTHERMOMETRY

5.4.1 Introduction

In recent years several calibrations of the pressure-temperature response of sulphide minerals in hydrothermal systems and metamorphic terranes have been derived. These studies incorporated both an empirical approach (e.g. Hutchison and Scott, 1981) and a more rigorous thermodynamic approach (e.g. Bryndzia *et al.*, 1990). The importance of sulphide minerals to geothermometry has long been recognised by several researchers (e.g. Edwards, 1974).

On the other hand, because of their non-refractory nature, the modification of sulphide textures has also been used to understand the conditions of deformation and metamorphism (Moorkherjee, 1971; Cox *et al.*, 1981; Brown and McClay, 1993).

5.4.2 Evidence from the Ore-Minerals

The mineral parageneses and textures suggest that the oxide phases in the first stage of mineralization (magnetite, ilmenite and rutile) were formed at comparatively high temperatures (see Ramdohr, 1969). Brecciation textures in pyrite and marcasite found in this stage were probably affected by brittle deformation under conditions of high-grade metamorphism.

The textural relationships of the second mineralized stage suggest the replacement of both pyrrhotite and chalcopyrite by the selenium/tellurium minerals and native bismuth, indicating that they were introduced later. The melting point of bismuth (271.5°C) places an upper limit to this phase of mineralization. The mineral assemblage bismuthinite and native bismuth is also consistent with a temperature of 270°C (Hansen and Anderko, 1985; In Barnes, 1979)

Temperatures of < 450° C are consistent with the plastic deformation textures found in pyrite, which occurs well below the threshold of 450°C at 300 MPa confining pressure, determined experimentally in the laboratoty (Cox *et al.*, 1981).

The ore-gold mineralogical study has therefore suggested that two main phases of mineralization have occurred in the Borborema Province:

(i) An oxide phase containing magnetite, ilmenite, and rutile. This assemblage is

primarily the result of modifications to the original host rocks. It took place under high temperatures (around 500°C), and a brittle regime.

(ii) A sulphide/selenide/telluride stage containing base and precious/rare metals (Au, Bi, Ag). This assemblage was formed at a temperature < 275°C under plastic-brittle conditions. The mineral assemblage bismuthinite and native bismuth is also consistent with a temperature of 270°C.

5.5 GANGUE MINERAL ASSEMBLAGES

The gangue consists of two types of mineral assemblages: supergene and hypogene. The hypogene minerals are dominated by quartz and tourmaline, and more rarely by: K-feldspar, albite, biotite, muscovite/sericite, fluorite, and chlorite. The supergene assemblage is related to weathering, and consists of jarosite, goethite, maghemite and pyromorphite. Some of these minerals serve as a constraint on the genesis of the ore deposits (e.g. tourmaline) and some help to characterise the weathering conditions (e.g. jarosite).

Tourmaline is predominantly associated with the quartz veins and typically has a polyphase occurrence, suggesting several superimposed hydrothermal generations. It occurs as 'hair' tourmaline displaying plastic deformation; needles of tourmaline included in porphyroclasts of K-feldspar; and coarse crystals of tourmaline as epitaxial growths and as kinked crystals. In thin section, tourmaline has a strong blue-green colour and it shows zoning, particularly in basal section. Usually the blue-green variety is associated with a yellow-coloured type. In the doubly-polished sections of quartz veins, yellow tourmaline commonly occurs in 'sun-bursts' where fluid inclusions are abundant (see Chapter 3).

Tourmalinization is a typical product of magmatic-hydrothermal activity (see Alderton, 1979; Deer *et al.*, 1985; Charoy, 1982). In granitic rocks, biotite is attacked first to give yellow tourmaline, and subsequently the feldspar is replaced by a blue or blue-green tourmaline. Some yellow tourmaline may be primary (magmatic) in origin but, after a period of corrosion, serves as a nucleus for radially-disposed acicular secondary tourmaline forming the sun-bursts.

During this study, epitaxial crystals of tourmaline were analysed by microprobe giving a formula of $Na_{0.8}(Mg_{1.2}Fe_{1.9}Ti_{0.1}Al_{0.6})Al_6[Si_{6.6}O_{18}][(BO_3)_3(OH,F)_4$ indicative of a ≈ 50 : 50 schorl-dravite mixture. The atomic ratio Fe/(Mg+Ti) was calculated at = 1.48. (Appendix A5.7).

The atomic ratio Fe/(Mg+Ti) is closest to the values for hydrothermal tourmaline, the ratios of which range from 2 to 6; tourmaline from other environments has values higher than 6 (Charoy, 1979). The iron content is compatible with the analyses of

tourmaline from granites, aplites, pegmatites, greisens and lodes (Power, 1968). The blue-green pleochroism is also consistent with that of hydrothermal tourmaline (Charoy, 1979). In contrast, tourmaline from metamorphic terranes is usually dravitic in composition (Deer *et al.* 1985).

Fluorite (CaF_2) is very rarely seen in the mineral assemblages. It occurs as disseminated grains associated with quartz hosted by the less-deformed syn- and post-tectonic granites (e.g. Igarape Garapa).

Jarosite [$KFe_3^{+3}(SO_4)_2(OH)_6$] has been identifed by its optical features and confirmed by microprobe analysis (see Appendices A5.7), as a very persistent but not predominant mineral in all of the gold mineralized quartz veins. Usually jarosite occurs together with goethite and hematite. The mass ratio of goethite/(goethite+hematite+jarosite) is smaller for weathered rocks which initially had larger total sulphide abundances (e.g. less pyrite has been oxidised) and/or larger mole ratios of pyrite/(pyrite+chalcopyrite) (Bladh, 1982). Peterson *et al.* (1951) described goethite replacing jarosite in porphyry copper deposits, after weathering had oxidised all pyrite. During the chemical weathering of sulphide-bearing felsic rocks, in the presence of excess free oxygen, jarosite and alunite are precipitated according to the reactions (Bladh, 1982):

$$K^+ + 3Fe^{+3} + 2SO_4^{2-} + 6H_2O \text{ --------> } KFe_3(SO_4)_2(OH)_6 + 6H^+$$

$$K^+ + 3Al^{+3} + 2SO_4^{2-} + 6H_2O \text{ ----------> } KAl_3(SO_4)_2(OH)_6 + 6H^+$$

Because jarosite and alunite have different stability fields, they cannot co-exist together. When the solutions contain a molar ratio of Fe/Al less than 0.5, these generate alunite, while with a ratio greater than 1.0, jarosite forms after goethite.

Jarosite is interpreted to be a product of reaction between pyrite and chalcopyrite, and oxygenated ground water in a near-surface environment (Bladh, 1982). It is very common in most porphyry copper deposits where sulphide oxidation is not complete. Its presence seems to be controlled by climate, and it subsequently breaks down to hematite and goethite (Ramdohr, 1969). The persistence of jarosite in all lode gold quartz veins of this study, indicates that sulphide oxidation is not complete.

5.5 WALLROCK ALTERATION

5.5.1 Introduction

Wallrock alteration is a process of irreversible chemical exchange between a hydrous solution and adjacent wallrock. Certain components are selectively leached from the wallrock and are added to the fluid, and other components (including the ore metals) are

selectively taken up by wallrock and are removed from the hydrothermal fluid. The net result depends on the physical conditions at the wall rock/fluid reaction interface on the composition of wallrock and fluid, and on the relative amounts of fluid and wallrock involved in the exchange process. The fluids are the agents that perform the changes and, since they are beyond the scope of this chapter, will be discussed in Chapter 7. In this Chapter, discussion will focus on the change in mineralogy, chemistry and texture of the rocks to more stable conditions in response to flow fluid through the rocks. The study of wallrock alteration is important because it provides information on the physico-chemical characteristics of the hydrothermal fluid and the nature of the fluid-rock interaction.

In the Borborema Province gold occurs predominantly in quartz veins without extensive development of alteration zones. However, in some of the deposits, the wallrocks show that the gold mineralization is associated with wallrock alteration and a characteristic mineral assemblage is present.

Four alteration zones were selected with varying host rock lithologies: mafic igneous, schist, and granitoid (Table 5.4). Although the host lithologies show differences they were all subjected to the same metamorphic processes. The areas are characterized by amphibolite facies domain which have been subjected to metamorphic retrogression (see Chapter 4).

Two of these zones are developed in supracrustal rock types and they are located in the São Francisco Mine and Itapetim District, and the other two are related to granitoid rocks, both in the Canafístula 'garimpo'. In the supracrustal environment the alteration is slight and only a small volume of rocks may have been affected. In the granitoid environment the wallrock alteration is more extensive.

Sketches depicting the correlation between the lithologies and the sampling for geochemical analysis in the four altered zones are shown in Figs. 5.38 to 5.41.

Enrichment/depletion diagrams from the alteration zones, normalised to the unaltered host rock, can be seen in Figs. 5.44, 5.45, 5.48 and 5.49. These diagrams all have a logarithmic scale.

5.5.2 Wallrock Alteration in the Granitoids

Two types of wallrock alteration types have been identified at Canafístula 'garimpo':

(i) Potassic-silicic alteration.

(ii) Tourmaline-potassic-silicic.

The first type of the wallrock alteration (Fig. 5.42a) exhibits a zone of alteration penetrating the host rock from a few centimetres to 1 m, which is developed along a fault (S 60° E). It is characterised by a pervasive style of alteration where brown biotite

Table 5.4

Wallrock Alteration: Enrichment/Depletion

Locality	Original Host Rock	Type of Alteration	Mineralogy	Geochemistry Major Element (wt %)	Geochemistry Trace Element (ppm)
Canafístula (MG-R-203)	Granite	Potassic-silicified-tourmaline	Biotite, K-feldspar, quartz, tourmaline and sericite	Enrichment: K, Mg, Fe, Mn, Ti and B Depletion: Ca and Na	Enrichment: Ba, Pb, Cr, Ni, V, Zn, Sc, Ga, Rb, Nb and Nd Depletion: Th, Ce, La and Zr
Canafístula (MG-R-204)	Granite	Tourmaline-Potassic-silicified	Tourmaline, K-feldspar, quartz and sericite	Enrichment: K, Mg, Fe, Mn, Ti and B Depletion: Ca and Na	Enrichment: Ba, Cr, Ni, V, Sc, Cu, Zn, Pb and Ga Depletion: Nb, Zr, Rb and Th
São Francisco (MG-R-225)	Schist	Silicified-tourmaline-potassic (+iron oxide)	Quartz, tourmaline, iron oxide, jarosite, pyromorphite and sericite	Enrichment: K, Fe, Si, Ti and B Depletion: Ca and Na	Enrichment: Pb, Th, Ba, Cu, Ga, V, Sc, Ga, La, Nd and Y Depletion: Cr, Sr, Zr and Nb
Itapetim (MG-R-163)	Amphibolite/ Gneiss	Silicified-potassic-tourmaline	Quartz, K-feldspar, tourmaline, biotite and sericite	Enrichment: K, Ti, Si and B Depletion: Fe, Mg and Ca (in contact with amphibolite)	Enrichment: Ba, Pb, Th, Zn, Ga, Rb, Nb, La and Y Enrichment: Ce and Nd (in the contact with gneiss) Depletion: Cu, Sr,

Observation:

Boron (B) was assumed based on tourmaline presence;

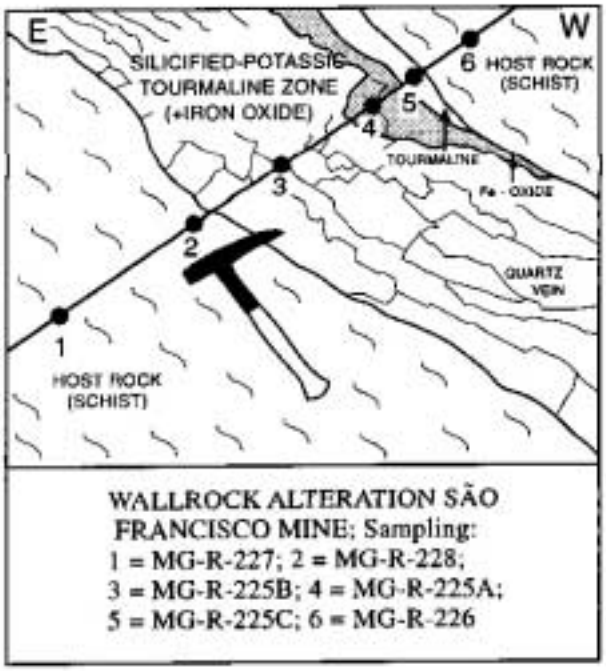

Figure 5.38 Sketch of Fig. 5.46a showing the correlation between the wallrock alteration samples and the lithologies in São Francisco mine.

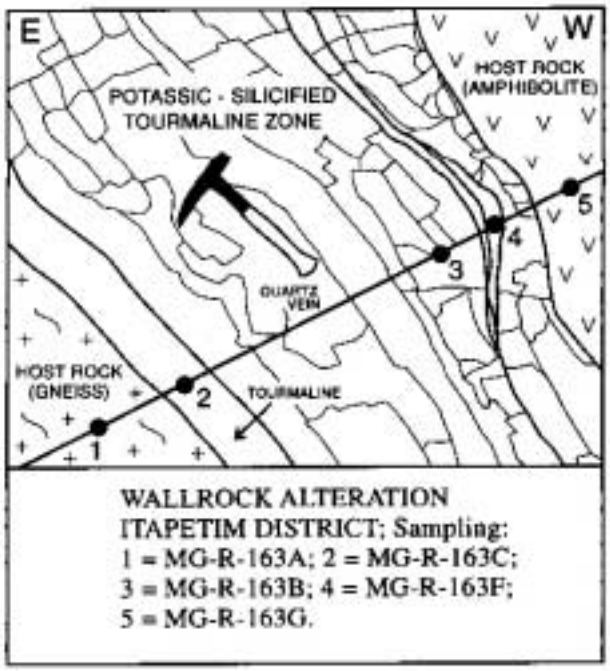

Figure 5.39 Sketch of Fig. 5.47a showing the correlation between the wallrock alteration samples and the lithologies in Itapetim District.

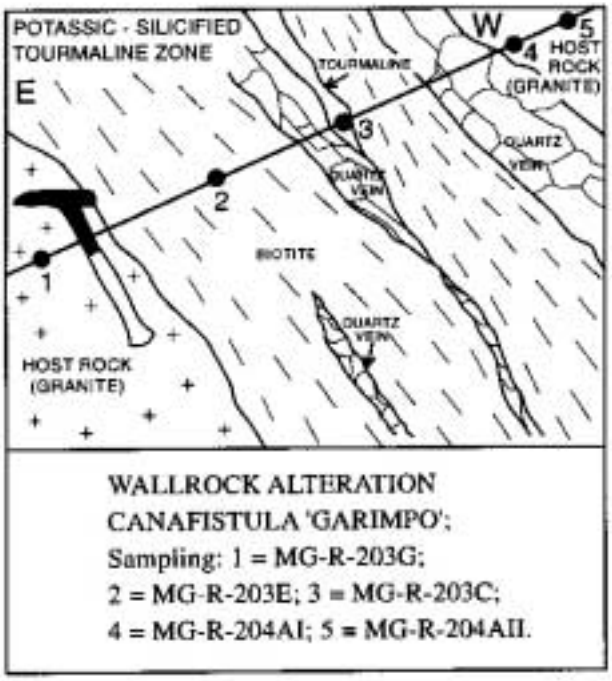

Figure 5.40 Illustration of Fig. 5.42a depicting the correlation between the wallrock alteration samples and the lithologies in Canafístula 'garimpo'.

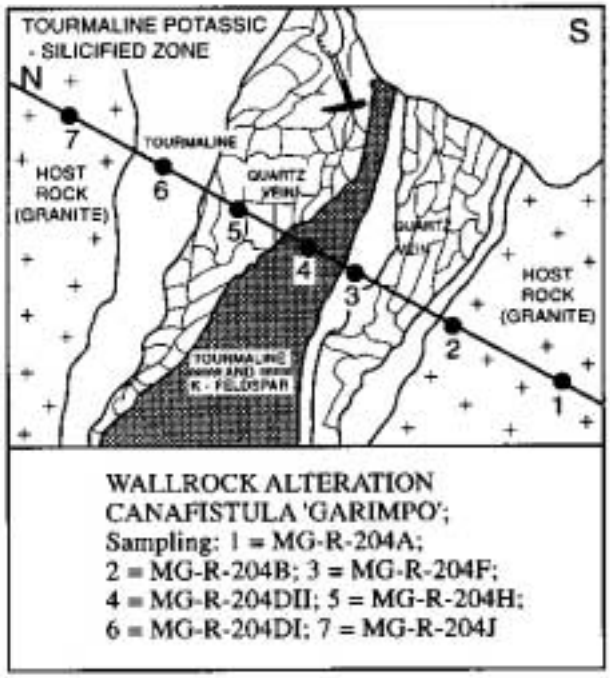

Figure 5.41 Illustration of Fig. 5.43a depicting the correlation between the wallrock alteration samples and the lithologies in Canafístula 'garimpo'.

is the dominant mineral (Fig. 5.42b), although K-feldspar (Fig. 5.42c) forms thin pink layers. Intercalated in the alteration zone are several very thin quartz veins which are mineralized with gold and sulphide. Their thickness is commonly 10 to 20 cm.

The second type (see Fig. 5.43a) extends to ≈ 4 m width, and is dominated by a rhythmic alternation of zones ranging from 10 cm to 60 cm in width. It consists of a wide transition zone of: (i) dark tourmaline; (ii) pink K-feldspar (orthoclase) whose grain size ranges from fine to coarse (5 cm length); and (iii) silicified areas (see Fig. 5.43b). The relationship between these wallrock alteration zones produces an alternation of: (i) pink orthoclase-rich layers associated with radiating aggregates consisting predominantly of schorl (sun-bursts); and (ii) pink orthoclase megacrysts set in a matrix of schorl-dravite (tourmaline hair), and quartz. It forms a mixture of tourmaline-quartz or tourmaline-potassium feldspar zones as a result of early potassium silicate alteration and a later overprinting tourmaline alteration. The alteration style is vein-controlled and may be expressed by the reaction:

$$4KAlSi_3O_8 + 2Al^{3} + 3(Fe,Mg)^{2+} + 3B^{3} + Na^{+} + 5H^{+} \text{--------} > Na(Fe,Mg)_3(Al_6Si_6)O_{18}(BO_3)_3(OH)_4 + 4K^{+} + 6Si^{4+} + H_2O$$

(K- feldspar) (tourmaline)

Although there are multiple phases, they probably represent a fluid continuum within an evolving semi-brittle-plastic shear zone rather than temporally discrete pulses of hydrothermal activity. Gold associated with pyrite occurs disseminated in very large silicified zones formed by ribbon quartz, which are oriented parallel to the regional foliation. Kinked tourmaline crystals in quartz veins suggest that the tourmalinization is pre-syn shear (D_4 event; see Fig. 43c).

In both types of wallrock alteration the host rock is a biotite-granite consisting of K-feldspar = 40%; plagioclase (albite) = 20%; quartz = 20%; and biotite = 20% (Fig. 5.42c) . The rock has a mylonitic to protomylonitic texture which shows evidence of plastic deformation e.g., a sigmoidal arrangement of the mineral fabric. The mylonitic banding is parallel to the regional foliation (S_3). Older folded foliation (S_2) cut by planar (S_3) foliation can be seen in the flakes of biotite. Crenulated biotite (S_4) altered to muscovite, and sericite also occurs. Biotite seems to have replaced plagioclase and other mafic minerals. Small amounts of sericite commonly accompany alteration of plagioclase to orthoclase, indicating that K/H is on the sericite-K-feldspar boundary. Porphyroblasts of K-feldspar and ribbons of quartz are very common. Epidote, titanite, ilmenite and rutile occur as accessory minerals. The mineral assemblage suggests a transition from amphibolite to greenschist facies.

Evidence of deformation in the wallrocks is shown by a new mineral fabric oriented parallel to the regional shearing. Deformation in the gold-bearing quartz-tourmaline veins that occur intercalated in the wallrock alteration, for example kinked tourmaline

Figure 5.42a Potassic-silicified zone consisting predominantly of biotite with mineralized quartz veins. Thickness ranges from 10 to 20 cm. (MG-R-203; Canafístula 'garimpo').

Figure 5.43a Tourmaline-silicified-potassic zone ≈ 4m wide, parallel to the main foliation of the wallrock. (MG-R-204; Canafístula 'garimpo').

Figure 5.42b Photomicrograph of the potassic-silicified zone consisting of biotite and mineralized quartz ribbons, intensely recrystallised and oriented parallel to the foliation of the wallrock. (XPL; TL; WOF = 4500 µm; MG-R-203E; Canafístula 'garimpo').

Figure 5.43b Detail of the tourmaline-silicified-potassic zone showing the rhythmic alternation of: tourmaline (dark); K-feldspar (pink-brownish); and silicified (white) zones. (MG-R-204-III; Canafístula 'garimpo').

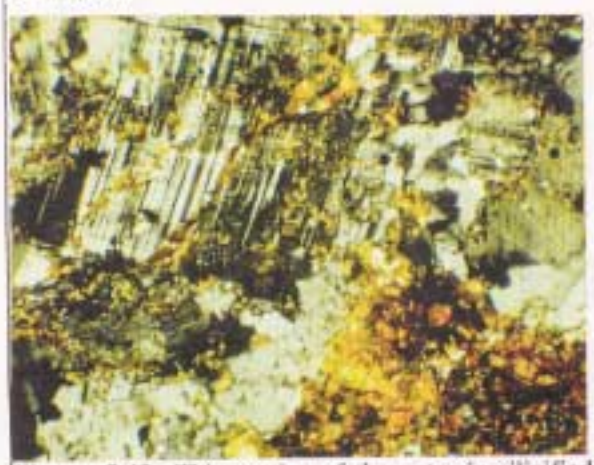

Figure 5.42c Thin section of the potassic silicified zone showing the enrichment in K-feldspar and biotite (XPL; TL; WOF = 2500 µm; Sample MG-R-203; Canafístula 'garimpo').

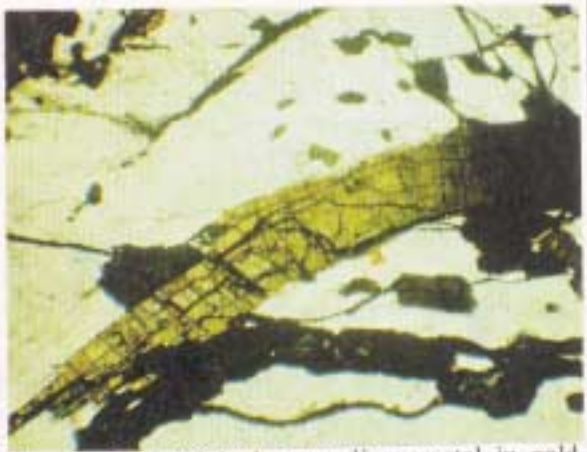

Figure 5.43c Kinked tourmaline crystal in gold-bearing quartz vein intercalated in the tourmaline-silicified-potassic zone (XPL; TL; WOF = 4500 µm; MG-R-204-D; Canafístula 'garimpo').

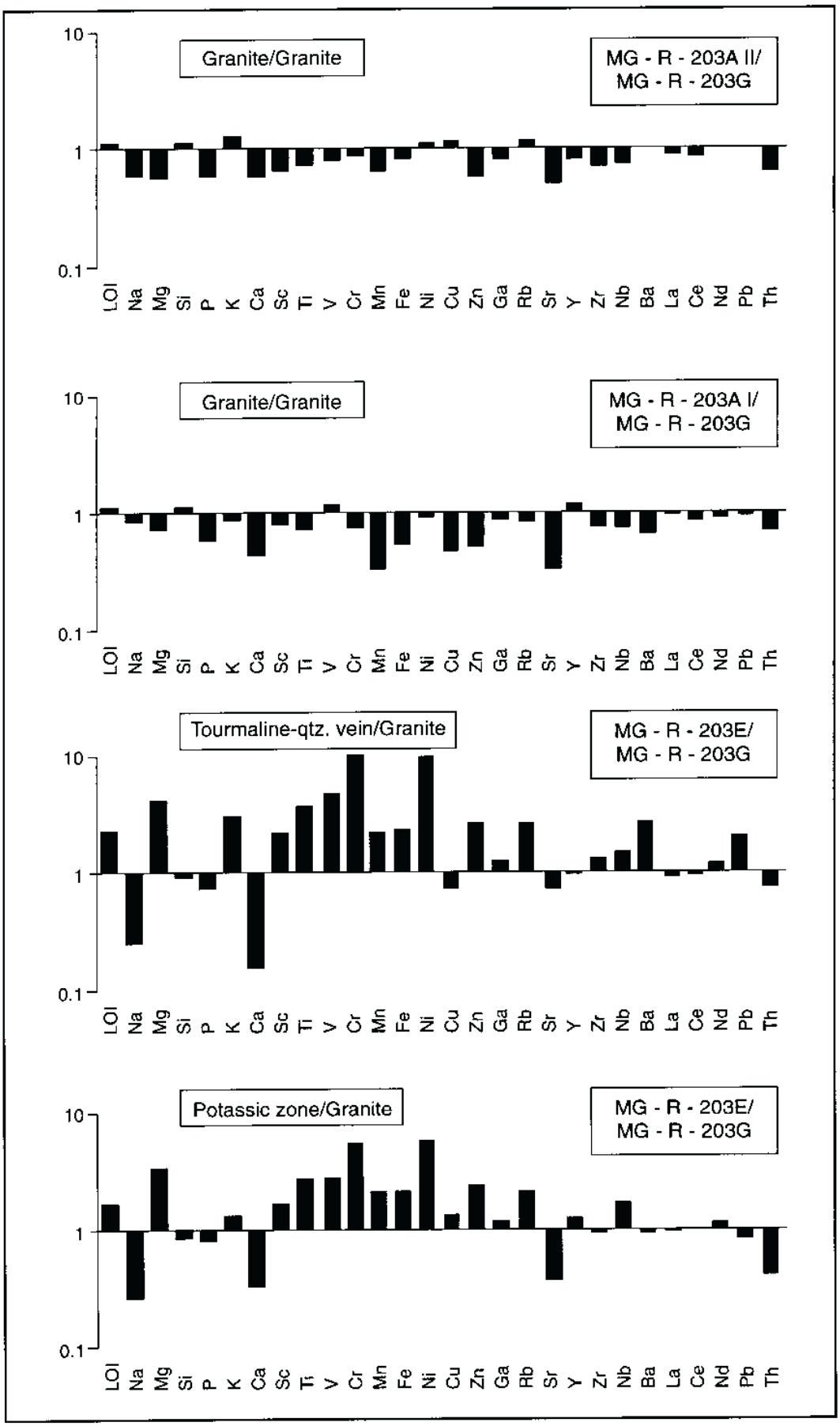

Figure 5.44 Enrichment/depletion diagrams for Canafístula (potassic-silicified-tourmaline zone). Alteration zone chemistry compared to granitic country rock (MG-R-230G); (see Fig. 5.40).

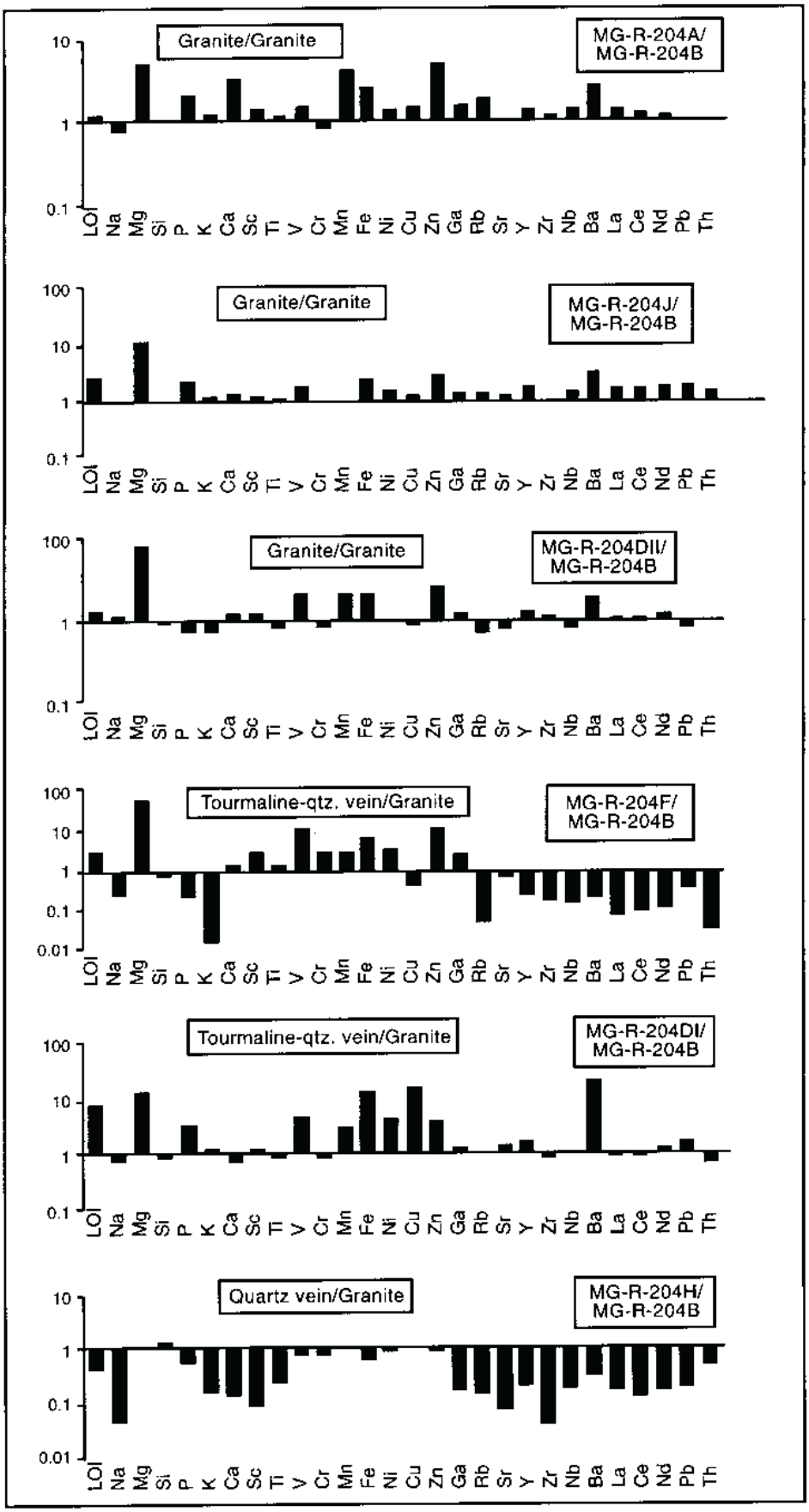

Figure 5.45 Enrichment/depletion diagrams for Canafístula (tourmaline-silicified-potassic zone). Alteration zone chemistry compared to granitic country rock (MG-R-204B); (see Fig. 5.41).

crystals (Fig.5.43c) and very fine grains of quartz surrounding porphyroblasts of K-feldspar or ribbons of quartz (see Fig.3.33, Chapter 3), is indicative that the alteration is earlier than the deformation produced during the retrogressive processes.

The major element geochemistry data (Appendix A5.8) indicates that the wallrock alteration involved massive additions of K, Mg and Ti, and less Fe and Mn (Figs. 5.44 and 5.45). The trace element data defines the mineralized areas as a region of high mass transfer marked by an enrichment of a distinctive suite of elements such as: Ba, Pb, Cr, Ni, V, Zn, Sc, Ga, Rb, Nb and Nd in the potassic zone. In the tourmaline zone significant enrichment was shown in a similar suite of trace elements: Ba, Ni, V, Sc, Cu, Zn and Ga. In both zones depletion in Ca and Na was found (see Table 5.4).

5.5.3 Wallrock Alteration in the Supracrustal Rocks

In the supracrustals, although the alteration products do not extend as far as in the granitoid environment, two types of wallrock alteration were recognised :

(i) Wallrock alteration in schist (São Francisco Mine area; Morro Pelado shear zone).

(ii) Wallrock alteration in the contact meta-mafic/gneiss rocks (Itapetim District: Pimenteiras-Desterro area).

In the metasediments (Morro Pelado shear; see Fig. 5.46a) a mixed zone occurs from the unaltered rock (Fig. 5.46b) inward towards the vein, involving alteration consisting of silicifed-hematitic and silicified-potassic-tourmaline zones, with a predominance of the first type. Both types are marked by a high degree of silicification. The hematitic-silicifed type consists of quartz, hematite, goethite and jarosite (Fig. 5.46c). It usually has a rusty-red colour and pervasive, finely disseminated alteration, while the second type can be recognised by its black colour, which is formed by tourmaline and quartz. The alteration products extend from a few centimetres to 1m away from the vein and are vein-controlled (Fig. 5.46a).

The host rock consists predominantly of schist, enriched in aluminium silicates such as sillimanite (fibrolite), andalusite and cordierite, with biotite, microcline and garnet (Fig. 5.46b). Accessory minerals are epidote, apatite, iron oxide, rutile, chlorite and muscovite. Since the mylonitic texture is parallel to the regional shearing, this suggests that the original texture was completely obliterated during deformation. A higher content of opaque minerals is common (Fig. 5.46b).

Geochemical data (Appendix A5.8) indicates a large addition in the wallrock alteration (Table 5.4), in both either the silicifed-hematitic (K, Al, P, V, Sc, Cu, Ga, Ba, La, Th and Pb) or the silicified-potassic-tourmaline zones (Fe, Si, Cu, Th and Pb; see Fig. 5.

Figure 5.46a Silicified-potassic-tourmaline zone, ≈ 1m wide, consisting of quartz, hematite, goethite, tourmaline and jarosite (yellow). Note the orientation of the quartz veins parallel to the foliation of the wallrock. (MG-R-229, Morro Pelado, São Francisco mine).

Figure 5.47a Silicified-potassic-tourmaline zone developed parallel to the regional shearing direction N65°E ,where wallrocks are: gneiss (on the left) and amphibolite (on the right). (MG-R-163; Itapetim; Pimenteiras-Desterro).

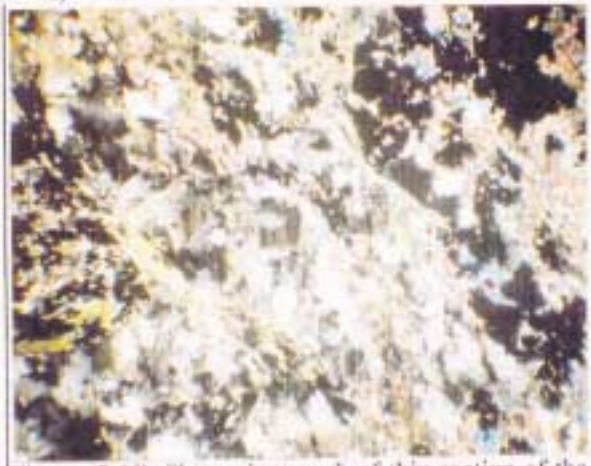

Figure 5.46b Photomicrograph of thin section of the wallrock consisting of schist enriched in opaque minerals. The fabric is oriented parallel to the shear direction (N 65° NE). (XPL; TL; WOF =2.5 µm; MG-R-229, Morro Pelado, São Francisco mine).

Figure 5.47b Photomicrograph of gneiss (wallrock of the Fig. 5.47a) consisting of layers of quartz-feldspar and mafic minerals associated with tourmaline. Note the alteration and recrystallisation of the minerals and the fabric orientation.(XPL; TL; WOF = 2.5 µm; MG-R-163A).

Figure 5.46c Photomicrograph of the mineralized quartz vein rich in jarosite (yellow) and iron oxide (hematite and goethite). Note the recrystallisation of the quartz vein. (XPL; TL; WOF =2.5 µm; MG-R-229, Morro Pelado, São Francisco mine).

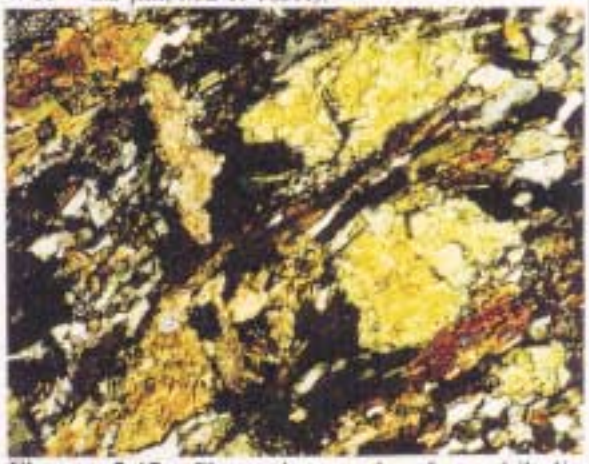

Figure 5.47c Photomicrograph of amphibolite (wallrock of Fig. 5.47a) showing the breakdown of the amphibole to produce opaque minerals and biotite replacing chlorite. (XPL; TL; WOF = 9 µm; MG-R-163G; Itapetim; Pimenteiras-Desterro).

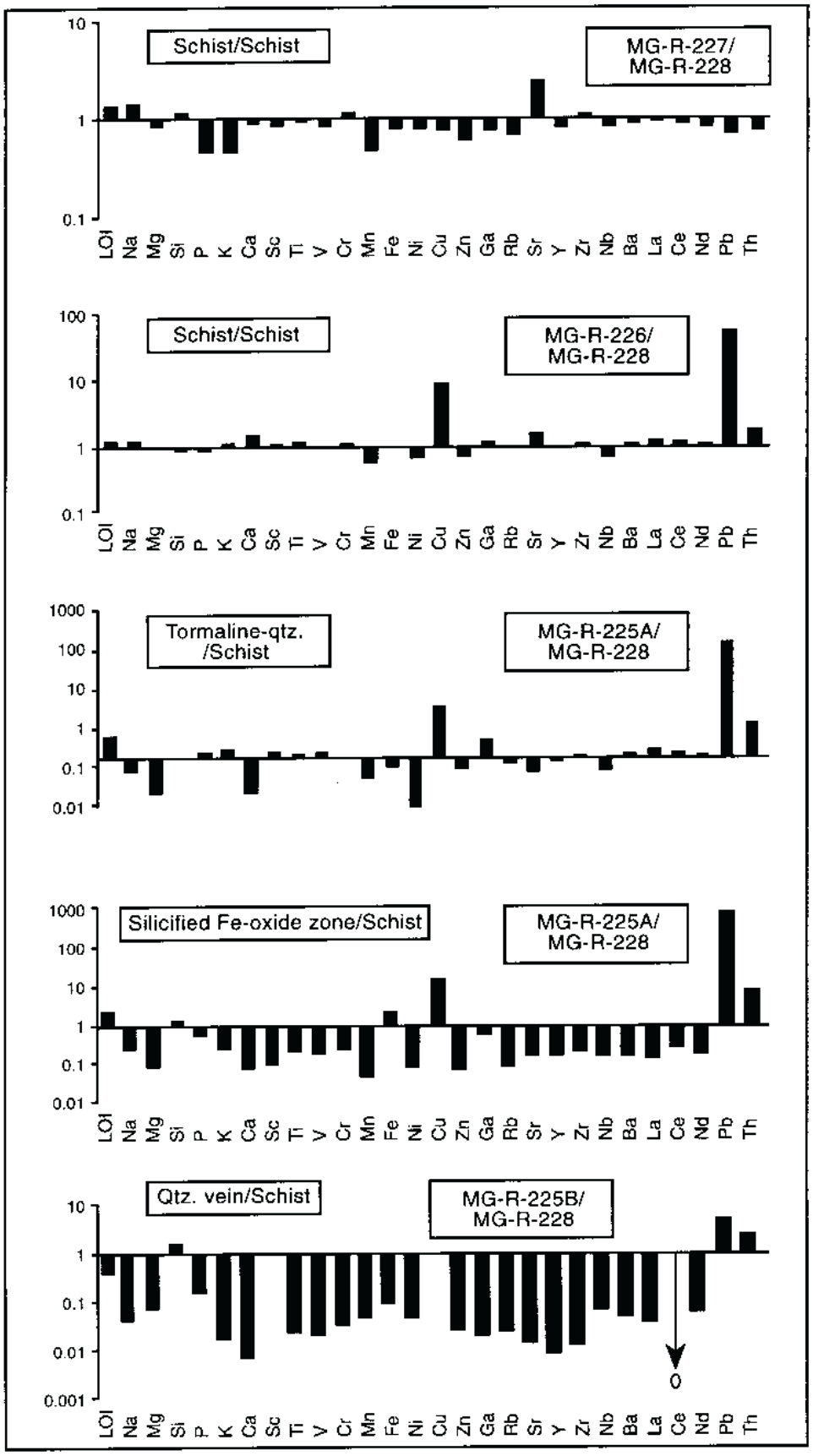

Figure 5.48 Enrichment/depletion diagrams for São Francisco mine. Alteration zone chemistry compared to schist country rock (MG-R-228); (see Fig. 5.38).

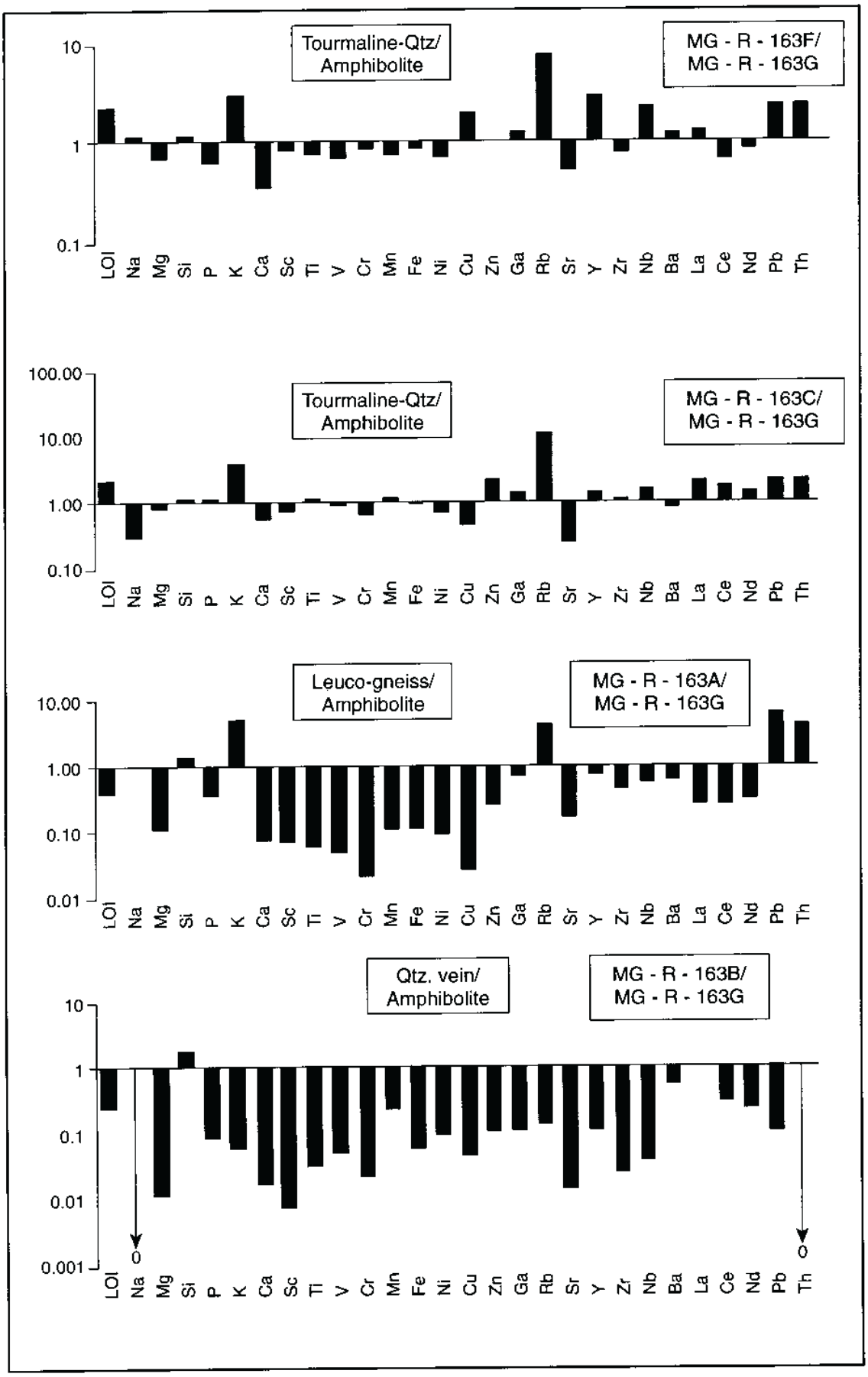

Figure 5.49 Enrichment/depletion diagrams Itapetim area. Alteration zone chemistry compared to amphibolite country rock (MG-R-163G); (see Fig. 5.39).

48).

The silicified-potassic-tourmaline zones within the shear zone in the Itapetim District (Pimenteiras/Desterro areas) provide a second example of wallrock alteration in the supracrustal domain. In this case the alteration is pervasive and vein-controlled and consists of quartz veins with an intense silicification-feldspathisation zone where tourmaline may be locally abundant. The wallrock exhibits a white colour and extends from a few centimetres to 1.5 m into the host rock (Fig. 5.47a).

The footwall host rock is a leuco-gneiss consisting mainly of quartz, K-feldspar, plagioclase (albite) and biotite. Chlorite, sericite, muscovite, apatite, rutile, tourmaline and opaque minerals occur as accessory minerals. The rock shows a gneissic texture with alternation of felsic (quartz-feldspar) and mafic (chlorite and biotite) layers with a predominance of the first. The fabric is completely stretched and oriented parallel to the regional shearing (Fig. 5.47b). The hangwall is amphibolite (Fig. 5.47c) and it consists of amphibole (ferro-tschermakitic hornblende), biotite, chlorite and quartz; plagioclase (labradorite) is rare. Titanite, epidote, rutile, apatite are accessories minerals.

The geochemical data (see Appendix 5A.8) indicate that the wallrock alteration in the mineralized areas involves a large addition of a distinctive suite of elements : K, Ti, Si, Ba, Rb, Pb, Th, Ga, Nb, La, Y, Ce and Nd (Fig. 5.49). Depletions in Fe, Mg, and Ca were found in the amphibolite wallrock and in Cu and Sr when the wallrock is gneiss (see Table 5.4).

5.5.4 Relationships Between Wallrock Alteration, Deformation and Gold Mineralization

Although different lithologies have been subjected to wallrock alteration, they exhibit a similar pattern of wallrock alteration, and the resulting mineral assemblages reflect the fact that these rocks were all subjected to the same metasomatic processes.

The geochemical study demonstrates that there has been a major introduction of K, Ti and Mg and locally Fe, and other elements (Pb, Th, Rb, Zr, B, Ba, Nb, Y, Sc, Ga) into all rock types. Depletions in Ca and Na are common. So, the petrographic and geochemical data reveal that the nature of the local host rock has not been an important influence on the resulting alteration assemblage, and therefore has not controlled the hydrothermal fluid composition.

Major and trace element analyses also suggest a genetic link between the gold mineralization and the granitic magmatism. The high values of K, Ba and Rb, and the high contents in B (assumed by the presence of tourmaline), suggest that the hydrothermal fluid was associated with a K-silicate phase of a typically hydrothermal-metasomatic paragenesis (Nesbitt and Sun, 1976; Kerrich, 1989). Similar wallrock

assemblages associated with gold deposits have been noted at other localities where the host rocks consist of granitic rocks (e.g. GoldenMile, Kalgoorlie, Yilgarn, W. Australia; Mueller and Groves, 1991).

Gold occurs in the tourmaline-rich veins. However, there is evidence of deformation taking place in these veins prior to gold mineralization. For example, kinked tourmaline crystals and very fine-grained quartz surrounding porphyroblasts of K-feldspar, or recrystallised ribbons of quartz, all indicate that the tourmalinization is pre-syn shear event (D_4) and pre the gold mineralization. Thus the wallrock alteration seems to have taken place before the gold mineralization, possibly at the same time as some of the early sulphide-rich stages of mineralization. A similar syn-deformation phase of alteration and later gold mineralization has also been proposed for other Precambrian gold deposits (Mueller and Groves, 1991; Colvine *et al.*, 1988; Foster, 1989).

5.6 CONCLUSIONS

The study of ore-mineral and gangue assemblages, wallrock alteration and the sulphide textures has placed several constraints on the evolution of the mineralization in Borborema Province:

(i) The ore development and its concentration is characterised by three stages of mineralization. The first stage results predominantly from brittle deformation and hydrothermal alteration. The mineral assemblage is characterised by early, high temperature formation of titanium minerals and iron oxides from the destabilisation of mafic minerals. The Fe and Mg leached and removed from the host rocks provided conditions for the precipitation of the sulphides and some metals (e.g. gold and silver) on the surface of the sulphides as submicron particles. An increase in the hydrothermal processes produced the quartz veins. During this stage the fluid/rock interaction placed constraints on the mass transfer, causing a change in the pyrite-pyrrhotite ratio (prograde heating released sulphur to form pyrrhotite and retrograde cooling allowed re-growth of pyrite).

(ii) During the second stage, the mineral assemblage is enriched in elements that indicate a plutonic influence, in particularly K, F, and B, but also Pb, Bi, Te, Mo and B. This stage was marked by a Au-Pb correlation and deposition of sulphides, oxides and tellurides. The visible gold liberated from the sulphides is associated with recrystallised sulphides (pyrite and chalcopyrite) or intergrown with bismuth and selenium/tellurium minerals, suggesting

deposition at a temperature of ≈ 270°C. The paragenetic sequence indicates that the mineralization postdated the amphibolite facies metamorphism (major regional metamorphism) and took place mainly between 270-300°C. The association of mineralization with early potassic alteration and tourmaline suggests primarily acidic magmatic-hydrothermal fluid.

(iii) The third stage is marked by the enrichment in lead, tellurides, gold and fluorite. Gold occurs disseminated in the annealed sulphides with a fine to medium grain size.

(iv) Weathering provided the conditions for the formation of: maghemite, cerussite, pyromorphite, jarosite and goethite.

(v) Tourmaline, one of the dominante gangue mineral after quartz, is indicative of hydrothermal activity. The anomalous boron contents appear as several generations of tourmaline.

(vi) Although alteration haloes are not always well developed, the major and trace element distribution appears to be consistent for all deposits. The geochemical data for the major elements indicate that the wallrock alteration involves massive additions of K and less Ti, Fe and Mn. The trace element data defines the mineralized areas as a region of a distinctive suite of elements: Ba, Pb, Th, Rb, Cr, Ni, V, Zn, Sc, Ga, Y, Zr, Nb and Nd. Removal of Ca and Na is typical. The high values of K, Ba and Rb and the high contents in B and F (assumed by the presence of tourmaline and fluorite) suggest that the addition of these elements was effected by a K-silicate phase of a typically hydrothermal-metasomatic paragenetic association (Nesbitt and Sun, 1976; Kerrich, 1989).

(vii) Petrographic and geochemical data reveal that the nature of the local host rock has not been an important influence on the resulting alteration assemblage, and therefore has not controlled the hydrothermal fluid composition.

(viii) The wallrock alteration seems to have taken place before the gold mineralization, possibly at the same time as the early sulphide-rich stages of mineralization.

CHAPTER 6 LEAD ISOTOPE STUDIES

6.1 INTRODUCTION

Shear zones in Pre-Cambrian greenstone belts provide important sites for the hydrothermal transport and precipitation of gold (Allison and Kerrich, 1980; Eisenlohr *et al* ., 1989; Fyfe and Kerrich, 1985; Hodgson, 1989; Park, 1981; Bursnall *et al* ., 1989; Groves *et al.*, 1991). However, despite the abundance of such shear-zone hosted gold deposits, and their economic importance, the source of the hydrothermal fluids and their dissolved constituents remain a matter of debate. Similarly, there is still a great deal of uncertainty regarding the reationship between the mineralization process and magmatic and metamorphic events.

In principle, lead isotopic analysis could be used to elucidate such problems as the source of the metals, and the age relationships between sulphide mineralization and deformation; rather surprisingly however, such studies have been relatively few (Reynolds, 1971; Richards, 1981; Doe and Stacey, 1974; Rye *et al.*, 1974; Kramers and Foster, 1982; Fletcher and Farquhar, 1982; Fletcher *et al.*, 1993).

This Chapter present the results of a Pb-isotopic study of the lode gold deposits in the Borborema Province. The study utilises the lead isotopic compositions of sulphides and host rocks to the mineralization, with the aim of providing an insight into the timing of mineralization and metamorphism, and the source of the ore components.

6.2 PRINCIPLES

The decay of uranium and thorium to stable isotopes of lead forms the basis of lead isotope studies. There are three isotopes of relevance to such studies:

(i) ^{238}U (99.27% of all U) which decays to ^{206}Pb.

(ii) ^{235}U (0.72% of all U) which decays to ^{207}Pb.

(iii) ^{232}Th (100% of all Th) which decays to ^{208}Pb.

In addition there is a fourth naturally-occurring isotope of lead, ^{204}Pb; as the abundance of this isotope has not been affected by radioactive decay of U or Th, it is commonly used as a stable reference.

Thus it is possible to date a mineral or rock using the concentrations of the relevant isotopes of U, Th, and Pb. For example the equation for the decay of Th is:

$$^{208}Pb/^{204}Pb = (^{208}Pb/^{204}Pb)_i + (^{232}Th/^{204}Pb)\ (e^{\lambda t}-1)$$

where $^{208}Pb/^{204}Pb$ represents the isotopic ratio of the mineral at the time of analysis, and the subscript i represents the ratio at the time of its formation; λ is the decay constant for ^{232}Th, and t is the time elapsed since closure of the mineral to U, Th, and Pb. Assumptions are that the mineral has remained closed to U, Th, and Pb and all intermediate daughters throughout its history; the decay constants are accurately known; and that the correct initial Pb isotope ratios are used (Faure, 1986). In this study no U contents were determined. Only thorium concentrations were measured, and these were derived by the slightly less precise method of X-ray fluorescence. However, by combining the equations for the decay of the uranium isotopes and assuming a constant U isotopic ratio, a $^{207}Pb/^{206}Pb$ date can then be derived without knowing the concentration of uranium; the effects of lead loss are also minimised using this approach (Faure, 1986).

The *model-age* of a sample ('the time when a sample had an isotopic composition identical to that of its source'; Nicholas and Goldstein, 1987) can be derived from the Pb isotopic compositions, and for rocks it represents the 'crustal-residence age' as proposed by O'Nions *et al.*, (1983). It reflects the age of a specific crust-formation event, for example metamorphism, when the U/Pb system of the rocks is reset and their isotopic compositions are changed. As a result, the variation in isotopic compositions can be used to date this event. On the other hand, the disturbances to the U/Th/Pb system of the rocks by geological events do not allow the use of the Pb-Pb method to date the 'crust-formation age' (Nelson and DePaolo, 1985), that is the 'time of differentiation of the crust from the mantle'. In this case, other radiogenic methods must be used.

The isotope geology of Pb has been used to unravel the evolutionary history of Precambrian terranes where the lithology and structure cannot be used, such as in the Narryer gneiss complex in NW part of the Yilgarn block of W Australia (Nutman *et al.*, 1991); in the Svecokarelian terrane of Southern Finland (Pachett and Kouvo, 1986); and in Scandinavia and Greenland (Pachett and Bridgwater, 1984; Bridgwater *et al.*, 1974).

6.3 METHODS OF STUDY

6.3.1 Sampling

Representative samples of the main lithologies hosting the gold deposits were collected for Pb-isotopic analysis. These consisted of sixteen samples: two amphibolites, two gneisses, eight schists and four granites (one ETG, two ESTG and one SLTG). In addition, five samples of sulphides from four widely-separated deposits, and closely

Table 6.1
Samples: Location and Geological Setting

Sample	Northing & Easting (km)	Locality	Description	Geological Unit
Rock				
MG-T-077	9192060 N; 692913 E	Drill core: 03-IT-36-PE; depth: 3.45-3.69 m. (Sertãozinho, Itapetim-Central Domain)	Leuco-gneiss with predominance of coarse bands of quartz-feldspathic minerals.	Pajeú/Paraíba Fold Belt Irajaí Complex: Early Proterozoic
MG-T-086	9192060 N; 692613 E	Drill core: 03-IT-36-PE; depth: 16.90-21.60m. (Sertãozinho, Itapetim-Central Domain)	Gneiss light-pink colour, medium-coarse grained	Pajeú/Paraíba Fold Belt Irajaí Complex: Early Proterozoic
MG-T-095	9192060 N; 692613 E	Drill core: 03-IT-36-PE; depth: 30.65-31.15 m) (Sertãozinho, Itapetim-Central Domain)	Quartz-feldspathic rock intercalated in mafic rock (schist)	Pajeú/Paraíba Fold Belt Irajaí Complex: Early Proterozoic
MG-T-122	9193350 N; 695950 E	Drill core: 03-IT-13-PE; depth: 11.01-12.65 m. (Pimenteiras, Itapetim-East Domain)	Mica schist, fine grained, light-grey colour	Pajeú/Paraíba Fold Belt Irajaí Complex: Early Proterozoic
MG-R-148	9193000 N; 697580 E	Along the road Mulungu-Mãe D'Agua, SE of Piedade dam, Itapetim-East Domain	Biotite orthogneiss ('Brejinho granite')	Early tectonic granite (ETG): Early Proterozoic
MG-R-149	9199000 N; 693500 E	Along the road Teixeira-Desterro, close to Santa Maria, Itapetim	Biotite granite with enclaves of mafic rock ('Teixeira batholith')	Syn-late tectonic granite (SLTG): Late Proterozoic
MG-R-150	9191200 N; 685900 E	Vaca Morta farm, NW of Desterro, Itapetim-East Domain	Biotite syenogranite (protomylonite)	Early-syn tectonic granite (ESTG): Late Proterozoic
MG-R-150A	9191780 N; 706900 E	NW of Serraria dam, Itapetim-Central Domain	Biotite monzo-granite; occurs as sheet; mylonitic foliation	Early-syn tectonic granite (ESTG): Late Proterozoic
MG-R-157	9191520 N; 692800 E	Level N-13 in Sertãozinho shaft (depth: 13.00m) Itapetim-Central Domain	Biotite schist, host rock of the gold-bearing quartz vein (level N-13, Sertãozinho shaft)	Pajeú/Paraíba Fold Belt Irajaí Complex: Early Proterozoic
MG-R-163G	9196400 N; 702000 E	Desterro area, Itapetim-East Domain	Amphibolitic rock intercalated in paragneisses of Irajaí Complex	Pajeú/Paraíba Fold Belt Irajaí Complex: Early Proterozoic
MG-R-225C	9339200 N; 806200 E	São Francisco mine; Morro Pelado shear zone	Mica schist, host rock in altered zone in Morro Pelado shear zone	Seridó Fold Belt: Early Proterozoic Seridó Formation
MG-R-226	9339200 N; 806200 E	São Francisco mine; Morro Pelado shear zone	Mica schist, host rock in altered zone, mylonitic foliation N40°E; 40°SE	Seridó Fold Belt: Early Proterozoic Seridó Formation
MG-R-227	9338150 N; 815700 E	São Francisco mine; Santa Monica shear zone	Mica schist with garnet; mylonitic foliation N40°E	Seridó Fold Belt: Early Proterozoic Seridó Formation
MR-R-208A	9206000 N; 593000 E	Boqueirão dos Cochos occurrence	Amphibolite with garnet; schistosity N120°E; 40°SW	Amphibolite intercal. in Archaean Basem. Piancó/Alto Brígida Belt: Early-Middle Prot.
MG-R-224A	9160100 N; 600100 E	Cachoeira de Minas mine, Covico area	Chlorite schist associated with the host rock of the mineralization	Piancó/Alto Brígida Belt: Early-Middle Prot. Salgueiro Group
MG-R-224D	9160100 N; 600100 E	Cachoeira de Minas mine, Covico area	Muscovite-quartz schist, host rock of the mineralization, highly deformed and orientated N 70° E, dipps 70°SE	Piancó/Alto Brígida Belt: Early-Middle Prot. Salgueiro Group
Sulphide				
MG-R-197C	9197000 N; 673000 E	Garapá 'garimpo', Itapetim-Teixeira	Galena associated with mg.+ py.+ chp., disseminated in quartz vein (N70°E) cross-cut undeformed granite	Syn-late tectonic granite: Late Proterozoic (SLTG)
MG-R-205B	9187200 N; 677700 E	'Zé Ferreira 'garimpo', Itapetim-West Domain	Galena disseminated in quartz vein (N65°E) concordant with the foliation of the host rock which consists of biotite gneiss	Pajeú/Paraíba Fold Belt Irajaí Complex: Early Proterozoic
MG-R-224	9160100 N; 600100 E	Cachoeira de Minas mine, Covico area	Galena disseminated in qz. vein (N60°E) discordant with the host rock consists of biotite-muscovite schist	Piancó/Alto Brígida Fold Belt: Early Prot. Salgueiro Group
MG-R-229A	9339200 N; 806200 E	São Francisco mine, Morro Pelado thrust fault	Py. associated with gold, chp., pyrr., marcs., molyb. disseminated in quartz vein discordant w/ the host rock consists of biot. musc. schist	Seridó Fold Belt: Early Prot. Seridó Formation
MG-R-229B	9339200 N; 806200 E	São Francisco mine, Morro Pelado thrust fault	Py. associated with gold, chp., pyrr., marcs., molyb., disseminated in qz. vein discordant w/ the host rock consists of biot. musc. schist	Seridó Fold Belt: Early Prot. Seridó Formation

Abservations:
Chp. = chalcopyrite; mg. = magnetite; marcs. = marcasite; musc. muscovite; molyb. molybdenite; py = pyrite; pyrr = pyrrhotite; qz = quartz;
For further informations see Abbreviations List;
Grid reference in UTM Projection (central meridien = 39°)

associated with gold, were collected for analysis. These consisted of three samples of galena, and two of pyrite. Sampling localities are presented in Table 6.1.

Visible galena is rare or non-existent in most of the deposits and consequently few samples could be analysed. However, the nearly constant isotopic composition of lead within many ore deposits has been noted by several authors, and Doe and Stacey (1974) have concluded that one anlaysis can usually characterise the lead isotopic composition of a mineral deposit. Based on this approach, the sulphide data are presumed to be representative of the lead isotopic composition of the ore bodies.

6.3.2 Analytical Procedure and Error.

Lead was extracted from the samples and prepared for isotopic analysis using the method employed in the Radiogenic Isotope Laboratory, Royal Holloway Geology Department (see Appendix A6.1). Lead was extracted from the samples using standard ion exchange procedures and loaded on single Re filaments with H_3PO_4 and silica gel. Pb isotope measurements were obtained on a 30 cm radius, 90° sector, VG Micromass 354 thermal ionization mass spectrometer.

All analyses were corrected for a procedural blank and for mass fractionation using repeated measurements of the SRM 981 isotope standard. Errors in the isotopic analyses are < 0.005% /amu (2se), and reproducibility, based on the SRM 981 data, is estimated at better than 0.05% /amu (2sd). Thorium and lead contents in the rocks were determined by X-ray fluorescence on pressed powder pellets.

Pb-Pb and Th-Pb isochrons and the ratio Th/U were calculated by a VAX program used in the Radiogenic Isotope Laboratory at Royal Holloway .

6.4 DISCUSSION OF LEAD ISOTOPE DATA

6.4.1 Lead Isotopic Characteristics of the Host Lithologies

The results of the Pb-isotopic analyses of the rocks are presented in Table 6.2 and in standard ^{207}Pb / ^{204}Pb - ^{206}Pb / ^{204}Pb - ^{208}Pb / ^{204}Pb plots in Figs. 6.1a and 6.1b.

The rocks exhibit a large amount of Pb-isotopic heterogeneity. For example, the variation in ^{206}Pb / ^{204}Pb ratios is from 15.30 to 22.03. The higher values (18.70 to 22.03) occur in the early to syn-tectonic granites and granitic gneisses, while in the rocks with pelitic composition the variation is from 17.80 to 18.81. In the schists the highest value (sample MG-R-122) occurs in the schist related to acid volcanic rocks, while the lowest values occur in schists whose protolith is sedimentary rocks. Overall,

Table 6.2
Rock and Sulphide Lead Isotope Ratios

Sample	206Pb/204Pb	207Pb/204Pb	208Pb/204Pb	232Th/204Pb
Rock				
MG-T-077	20.706 ± 2	15.848 ± 2	40.417 ± 4	68.08
MG-T-086	22.028 ± 2	15.940 ± 1	41.743 ± 4	107.57
MG-R-148	21.305 ± 2	15.897 ± 2	41.828 ± 6	99.21
MG-R-150	18.909 ± 2	15.749 ± 1	39.598 ± 4	49.59
MG-R-150A	18.700 ± 2	15.702 ± 2	38.463 ± 4	18.41
MG-R-149	16.237 ± 2	15.338 ± 2	36.653 ± 4	8.28
MG-T-095	19.377 ± 2	15.759 ± 2	38.731 ± 4	27.69
MG-T-122	18.810 ± 2	15.751 ± 2	39.391 ± 4	45.37
MG-R-157	18.115 ± 1	15.641 ± 1	38.093 ± 3	35.34
MG-R-224A	17.804 ± 3	15.633 ± 3	37.986 ± 8	34.88
MG-R-227	18.645 ± 4	15.648 ± 3	38.645 ± 9	27.72
MG-R-224D	18.532 ± 2	15.743 ± 2	38.907 ± 5	5.78
MG-R-163G	19.355 ± 3	15.777 ± 2	39.223 ± 6	40.64
MG-R-208A	15.300 ± 3	15.181 ± 3	34.918 ± 6	9.8
MG-R-225C	18.455 ± 3	15.670 ± 2	37.824 ± 6	-
MG-R-226	18.655 ± 2	15.704 ± 2	38.205 ± 3	-
Sulphide				
MG-R-197C	17.844 ± 4	15.616 ± 3	36.840 ± 8	33.244
MG-R-205B	17.294 ± 3	15.527 ± 3	37.188 ±7	36.882
MG-R-224	17.595 ± 3	15.604 ± 3	37.810 ± 8	39.506
MG-R-229B	17.543 ± 3	15.572 ± 3	37.177 ± 7	36.667
MG-R-229A	17.571 ± 5	15.585 ± 4	37.343 ±1	37.439

Observation:
Values for thorium were determined by XRF.

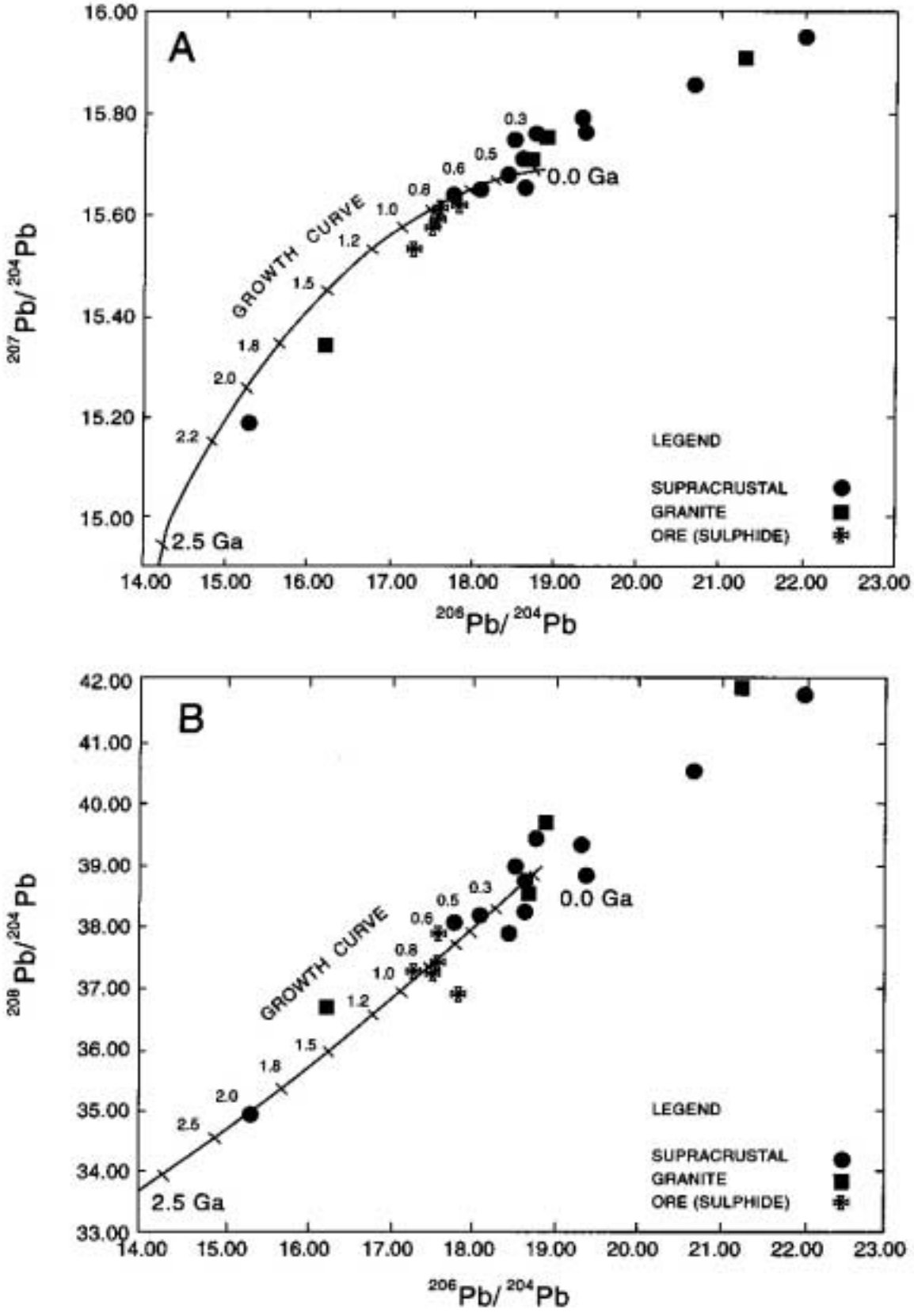

Figure 6.1 Diagrams showing the lead isotopic ratios (**A**; $^{207}Pb/^{204}Pb$ against $^{207}Pb/^{204}Pb$ and **B**; $^{206}Pb/^{204}Pb$ against $^{208}Pb/^{204}Pb$) at the present time in rocks and in sulphides. Symbols: square = granite; circle = supracrustal rock, and cross = sulphides. Note the Pb isotope growth curve from Doe and Stacey (1974).

the fact that the schists plot close to the average terrestial Pb evolution curve suggests that they were derived from a well-mixed source, such as multicycled sediments.

On a ^{207}Pb / ^{204}Pb against ^{206}Pb / ^{204}Pb plot (Fig. 6.1a) the data points for the rocks form a rough linear trend, which can be interpreted in several ways:

(i) A primary crystallization event (e.g. magmatic crystallization),

(ii) Mixing of lead (e.g. supracrustal with basement), or

(iii) A major post-depositional remobilization event (e.g. metamorphism)

In the case of (ii) the trend would have no age significance, whereas in (i) and (iii) it would represent an isochron.

The lowest Pb-isotopic value (15.30) was found in the amphibolite intruded into the Archaean basement (MG-R-208A). Presumably the intrusion and subsequent metamorphism of this amphibolite led to a mobilization and incorporation of old, unradiogenic lead from the surrounding Archaean basement rocks. In contrast, the amphibolite from the supracrustal sequence (MG-R-163G) has a ratio of 19.36. The amphibolite in the Archaean basement, and the syn-late tectonic granite, seem to have particularly low ratios which set them apart from the other rocks, perhaps suggesting that in these rocks at least some mixing has been important.

The lead isotope ratios and Th contents of the granitoids seem to exhibit a distinct trend which can be correlated with the different grades of deformation: the early tectonic granite (sample MG-R-148) has the most radiogenic lead and most Th (41.5 ppm), the early- syntectonic granites have intermediate amounts (Th = 12.8; 23.5 ppm), and the syn-late tectonic granite has the least radiogenic lead and least Th (5.2 ppm). This might suggest that whilst the genesis and metamorphism of the early to syn-tectonic granites was from younger crustal rocks with high μ ($^{238}U/^{204}Pb$) values (e.g. the early Proterozoic schists), the source of the latest granites contained a greater component of older material with a low μ value (e.g. Archaean basement). In any case, the scatter in Pb isotopic data for the granitoids points to a heterogeneous source, and possibly indicates a derivation from differeent crustal levels.

Overall, the metamorphosed supracrustals are characterised by quite radiogenic lead, and enrichments in large ion lithophile elements (LIL elements), K, Ba, Pb, and Th (see Chapter 4). These features are characteristic of high-grade metamorphic units which have suffered tectonic transportation to higher crustal levels where they have subsequently suffered retrogressive metasomatic enrichment in LIL elements (e.g. Moorbath and Taylor, 1986).

For the remaining 11 supracrustal rocks the trend in isotopic values could approximate to an isochron (Fig. 6.2) and have an age significance. The slope of the correlation on this plot for these 11 rocks corresponds to an age of 1.028 Ga (+ 0.377 / - 0.491; MSWD = 28, enhanced errors). This age of $\approx$ 1.0 $\pm$ 0.3 Ga presumably represents a time of major lead mobilisation, and subsequent fixation. This could be a

magmatic crystallization event (e.g. of the precursor metavolcanic rocks and volcaniclastics) but, considering the diverse range of rock types analysed, it seems more reasonable to conclude that the 'isochron' represents a major, regional metamorphic event. The scatter of the Pb-isotopic data in this study severely limits an assumptions of the age significant of this data; no doubt points to variable mobility of Pb during metamorphism (e.g. Reynolds, 1971), and possibly to some mixing of lead from different sources.

An independent 'age' can be derived using Th concentrations of the rocks (from XRF). However, it was apparent that Th mobility had been more severe, and the scatter in the data was more marked. For this reason only 7 sample were used in the age calculations; three samples were removed, although the inclusion of these does not alter the age substantially, only the scatter in the data (the MSWD). For these 7 supracrustals (see Table 6.2) a ^{232}Th-^{208}Pb 'age' of 0.792 Ga (± 0.014; MSWD = 14) was derived (see Fig. 6.3). The scatter in this diagram (particularly for the schists) could be related to some isotopic heterogeneity in these lithologies.

Considering the errors in the Pb-Pb age, the difference between the Pb-Pb age and Th-Pb age are probably not be significant. However, it might be expected that U and Th would behave differently during retrogressive metamorphism, and the difference in age may be related to this. The retrogressed rocks tend to have higher Pb contents than their equivalent non-retrogressed amphibolite facies rocks, with consequent variation in Th/Pb ratios (Friend *et al.*, 1988). Probably, 0.80 Ga represents the time when the metamorphic conditions changed from amphibolite facies metamorphism to retrogressive greenschist facies metamorphism.

Thus, the age 1.0 Ga is tentatively interpreted as the time of regional, high-grade metamorphism, and this probably represents a major phase of Pre-Brasiliano deformation and metamorphism in Borborema Province. Such an early event has not previously been recognised in the region, but it would be consistent with the recently-determined Rb-Sr age of 0.95 Ga for the rocks in the Piancó/Alto Brígida Belt (Brito Neves *et al.*, 1990).

Based on their geological and geotectonic setting, the supracrustal rocks of the area are thought to be Early Proterozoic in age, and so could have been deformed by a thermal-tectonic event during the 2.1-1.8 Ga Trans-Amazonian Orogeny (Santos *et al.*, 1984; Brito Neves and Cordanni, 1991). The total distribution of the data points in the Pb-isotopic plots suggests a model-age of around 2.2 to 2.0 Ga for the age of the supracrustal rock sources; if correct this age would correlate well with the age of the Trans-Amazonian Orogeny, and represent the crustal-formation age for the region. O'Nions *et al.*, (1983) suggest that when the model-age coincides with any specific orogenic event it can be interpreted as the time of crust-mantle differentiation. This concept has been widely used, and at other localities the 2.0-2.2 Ga model-age is

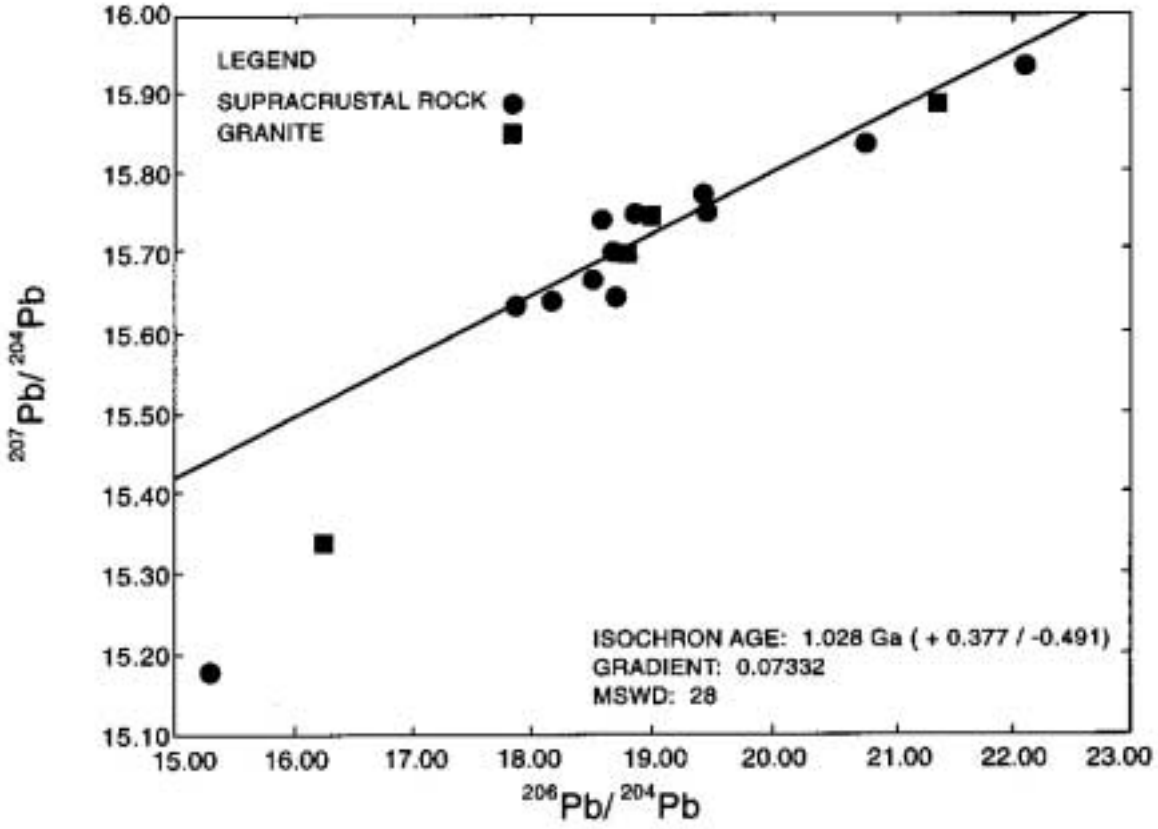

Figure 6.2 $^{207}Pb/^{204}Pb$ against $^{206}Pb/^{204}Pb$ diagram showing the **Pb-Pb isochron** in rocks (amphibolite, schist, gneiss and granite) calculated for 12 points. See text for detail.

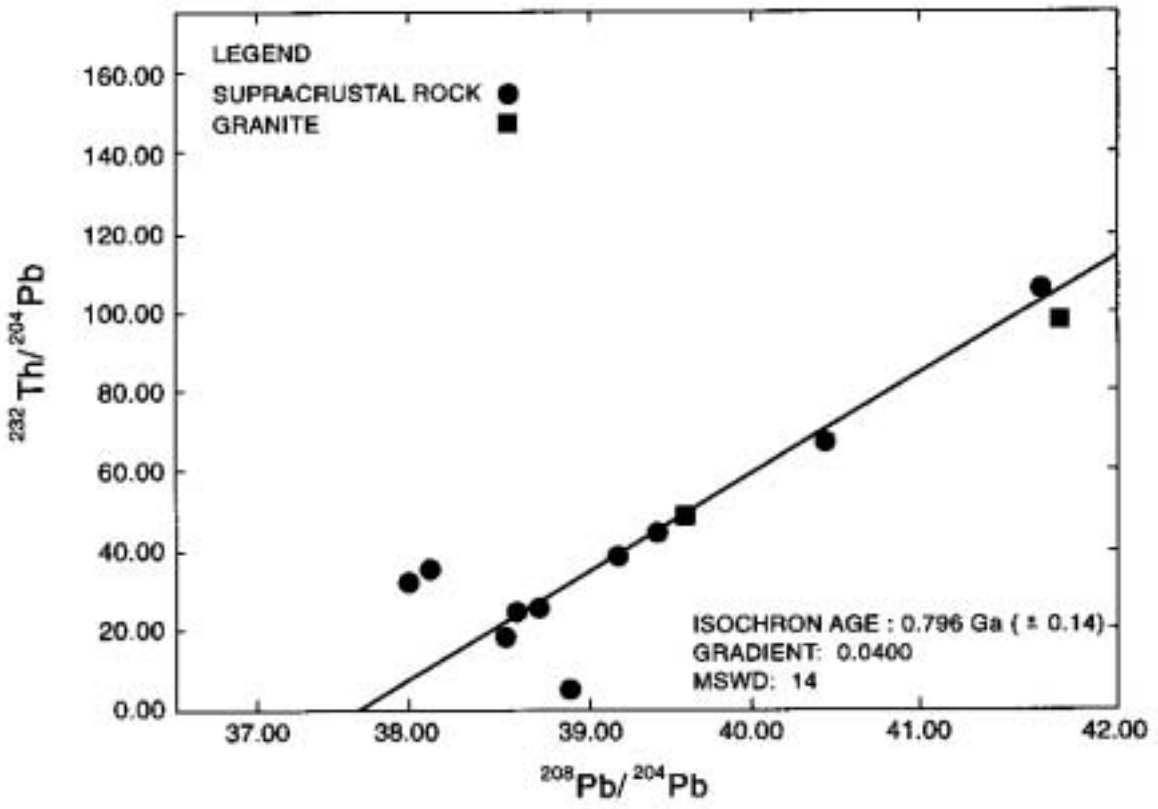

Figure 6.3 $^{232}Th/^{204}Pb$ against $^{208}Pb/^{204}Pb$ diagram showing the **Th-Pb isochron** in rocks (schist, gneiss and granite) calculated for 7 points. See text for detail.

recognised as a time of major crustal formation (e.g. Australia, McCulloch, 1987; Penokean terrane, Nelson and DePaolo, 1984).

6.4.2 Lead Isotopic Characteristics of the Mineralization

Lead does not only occur as the radiogenic daughter product of U and Th, but also forms its own minerals from which U and Th are exclued. Thus, the isotopic composition of Pb varies between wide limits from the highly radiogenic Pb in very old U and Th-bearing minerals, to the common Pb in galena. Because galena is frequently associated with other sulphides and usually occurs in gold-bearing veins it enables us to study the origin (both as regards time and source) of gold deposits using the isotopic composition of Pb in the ore minerals. If it is assumed that the Pb in these deposits is derived from the same source as the gold (Kramers and Foster, 1982) conclusions from the isotopic data regarding the early crustal history of the lead may have a bearing on the source of the gold. It has also been recognised that the lead isotope composition of any ore is characteristic of the source from which the lead was derived, and that it is independent of the mode of ore deposition (Richards, 1971).

When the lead evolved in closed source the radiogenic Pb in the U/Pb system evolved under *single-stage* model conditions. The Pb in this case was thought to have been derived from sources in the lower crust and mantle and was emplaced by volcanic activity without contamination by radiogenic Pb from the crust. Single-stage model Pb evolution provides valuable information on the crust-formation age (model-age) and the source of the lead in some ores. However, the number of ore deposits that meets the stringent requirements of the single-stage model is quite small (Faure, 1977). According to Doe and Stacey (1974) many major ore deposits contain lead that evolved under conditions of a *two-stage* Pb evolution model, where lead first evolved under single-stage conditions, and then subsequently mixed with varying amounts of radiogenic Pb derived from U and Th-bearing minerals in the crust.

The results of the Pb-isotopic analyses of the sulphides are presented in Table 6.3 , and in standard $^{207}Pb/^{204}Pb$ - $^{206}Pb/^{204}Pb$ - $^{208}Pb/^{204}Pb$ plots, in Figs. 6.1a and 6.1b. Overall, the five samples analysed in this study only exhibit a small degree of isotopic variation when compared with that seen in the host rocks. The sulphide data plot on or just below the Pb isotopic growth curve (see Fig. 6.1a). In common with the lead from many other ore deposits (e.g. Franklin *et al.*, 1983) the Borborema ore leads are reasonably homogeneous and approximate to single-stage leads.

However, the geological environment of the region makes it unlikely that the lead was derived from the lower crust and mantle and emplaced without contamination with crustal lead. It is much more likely that the lead in the mineral deposits of the

Table 6.3

Sulphide Lead Isotopic Ratios and Model-age Data

Sample	206Pb/204Pb	207Pb/204Pb	208Pb/204Pb	238U/204Pb	232Th/204Pb	232Th/238U	206Pb/238U	207Pb/235U	208Pb/232Th	Slope (m)	Model-age (Ga)
MG-R-197C	17.844 ± 4	15.616 ± 3	36.840 ± 8	9.227	33.244	3.603	0.100	0.834	0.031	0.391	0.616 ± 0.01
MG-R-205B	17.294 ± 3	15.527 ± 3	37.188 ±7	9.044	36.882	4.079	0.142	1.328	0.043	0.412	0.858 ± 0.01
MG-R-224	17.595 ± 3	15.604 ± 3	37.810 ± 8	9.318	39.506	4.24	0.136	1.247	0.502	0.404	0.822 ± 0.01
MG-R-229B	17.543 ± 3	15.572 ± 3	37.177 ± 7	9.292	36.667	3.946	0.139	1.287	0.042	0.403	0.840 ± 0.01
MG-R-229A	17.571 ± 5	15.585 ± 4	37.343 ±1	9.32	37.439	4.017	0.139	1.283	0.042	0.403	0.838 ± 0.01
Parameters for Two-Stage Pb Evolution Model of Stacey and Kramers (1975)											
Start, stage 1:	9.307	10.294	29.476	7.192	32.208						
Start, stage 2:	11.152	12.998	31.230	9.735	36.837						
Present time:	18.700	15.628	38.630	9.735	36.837						

Decay Constants:
238U = 1.55125 x 10-10 y -1
235U = 9.8485 x 10-10 y -1
232Th = 4.9475 x 10-11 y -1

Earth's Age: 4.55 x 10 9

Observation:
Model-age for sulphides calculated according to the Two-Stage Pb Evolution Model of Stacey and Kramers (1975).

region evolved under two or more stages such that there is a component of 'anomalous Pb' attributed to mixing.

The sulphide data points do not directly overlap those for the major rock types. For instance, the sulphides from occurrences hosted by schists have lower ^{207}Pb / ^{204}Pb and ^{206}Pb / ^{204}Pb ratios than the schists themselves. In addition, the sulphides from the latest granite have ratios which are much higher those for that granite (see Tables 6.2 and 6.3). This indicates that the Pb in the sulphides has not been derived directly from the associated lithologies. However, these diagrams are slightly misleading as they only show present-day ratios, and not those at the time of formation (i.e. radiogenic decay has continued in rocks since then; sulphides are not affected because of their low contents of U and Th). Figures 6.5a and 6.5b display the lead isotopic ratios for rocks and sulphides after correction for post-formation, in situ, radiogenic decay in the rocks, and assuming an approximate age of 0.8 Ga. However, the grouping for the sulphides in these plots futher emphasises that lead in the mineralization has not been derived from the full range of lithologies in the region, and in fact must be derived from a source with a fairly uniform Pb isotopic composition.

The sulphide data seems to exhibit a linear trend which is similar (although less extensive) to that proposed for the host rocks. This trend for the sulphide data could therefore also be explained either by mixing or by remobilization; a third possibility is that the sulphides initial ratios have not been preserved and values reflect post-formation Pb growth. The proximity of the sulphide data points to the Pb evolution curve (see Fig. 6.1a) signifies that the majority of the Pb in the sulphides was derived from a well-mixed source, such as that suggested for the schists (e.g. see Fletcher *et al.*, 1993). However, it is not immediately apparent which model is correct for the source of the lead in the mineralization. However, it is clear that the predominant and most likely source for the Pb in the veins is a mixing from the schist with minor contributions possible from the basement or the granites (Table 6.4).

Using the two-stage Pb evolution model of Stacey and Kramers (1975) and the lead isotope ratios for the sulphides, model ages of 0.86-0.62 Ga are obtained (Table 6.3). For the veins hosted by the supracrustal rocks the age range is 0.86-0.82 Ga, and it is 0.62 Ga for the vein hosted by the syn- and late tectonic granites. The analytical error on these analyses is approximately 0.01 Ga, so it seems that the differences are significant. The model ages of 0.8 and 0.6 Ga can be explained in two ways: (i) first there were two periods of mineralization that were sourced from a common homogeneous parent; and (ii) second, that the time of mineralization was the same for the two groups, but the group with the younger model age was contaminated with a more radiogenic component of lead (for example the granites). It is not at present clear which mechanism is important here. However, the geotectonic setting of the gold-bearing veins, and the date of 0.55 Ga as the end of the Brasiliano Orogeny in the area

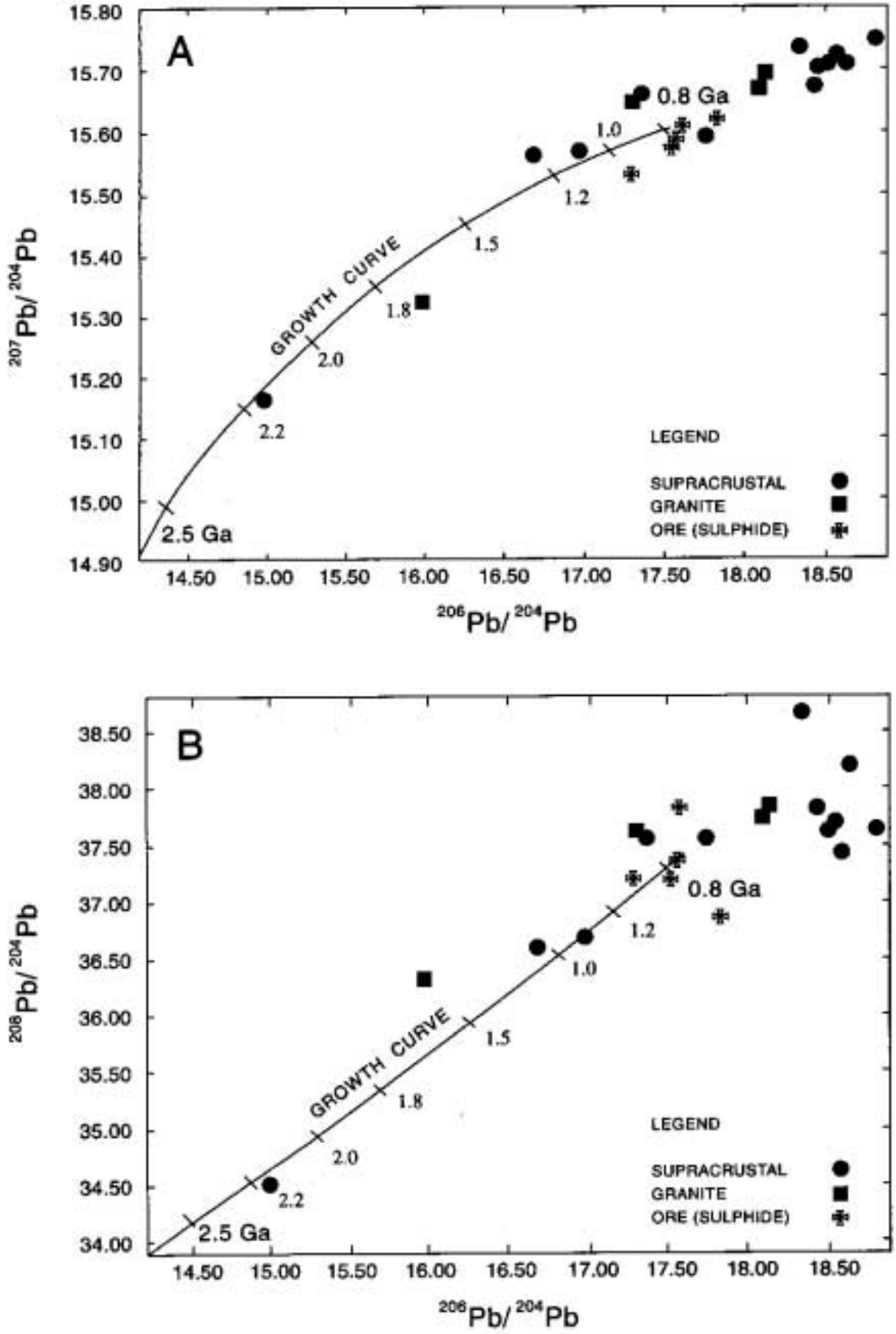

Figure 6.4 Diagrams showing the lead isotopic ratios (**A**: $^{207}Pb/^{204}Pb$ against $^{206}Pb/^{204}Pb$ and **B**: $^{208}Pb/^{204}Pb$ against $^{206}Pb/^{204}Pb$) at 0.8 Ga in rocks and in sulphides. Symbols: square = granite; circle = supracrustal rock and cross = sulphides. Note the growth curve from Doe and Stacey (1974).

Table 6.4

Lead Isotopic Ratios of Rocks at 0.8 Ga calculated from the Th/U Ratios

Sample	Th (ppm; XRF)	Pb (ppm; XRF)	U (ppm; Th/U=4)	Initial Ratios 206Pb/204Pb	207Pb/204Pb	208Pb/204Pb
MG-T-077	40.20	41.10	10.05	18.529	15.705	37.668
MG-T-086	52.10	34.90	13.03	18.587	15.714	37.400
MG-R-148	41.50	29.90	10.38	18.133	15.688	37.824
MG-R-150	23.50	31.80	5.88	17.320	15.644	37.593
MG-R-150A	12.80	46.00	3.20	18.113	15.663	37.722
MG-R-149	5.20	39.10	1.30	15.974	15.321	36.321
MG-T-095	6.50	15.70	1.63	18.489	15.701	37.614
MG-T-122	15.40	22.70	3.85	17.358	15.655	37.558
MG-R-157	16.80	30.80	4.20	16.981	15.566	36.660
MG-R-224A	15.90	29.50	3.98	16.688	15.560	36.579
MG-R-227	5.30	12.70	1.33	17.761	15.590	37.533
MG-R-224D	12.60	144.90	3.15	18.348	15.731	38.674
MG-R-163G	3.40	5.70	0.85	18.827	15.742	37.603
MG-R-208A	1.30	8.10	0.33	14.991	15.161	34.534
MG-R-225C	40.40	4440.60	10.10	18.436	15.669	37.800
MG-R-226	14.00	1173.60	3.50	18.630	15.702	38.173

Observations:

Th and Pb values analysed by XRF (X-Ray Fluorescence); Th/U assumed = 4.

Initial ratios calculated on VAX program in use by the Radiogenic Laboratory at RHBNC.

(Galindo, 1984), would support the concept of multiple stages of mineralization. In particular it is interesting to note that the order of increasing $^{207}Pb/^{204}Pb$ and $^{206}Pb/^{204}Pb$ ratios for the sulphides seems to correlate with the nature of the host rocks. It is thus possible that the different sulphides had the same lead isotopic source, but this lead was trapped at different times. On the other hand, the similarity between the Pb-isotopic trend for sulphides and the rocks suggests that some mixing between crustal Pb and magmatic Pb may also have been important for the mineralization. The well-documented Late Proterozoic Brasiliano magmatism in the Borborema Province is characterised by intense fractional crystallisation of magma, and this activity could have provided the fluids and the heat necessary to form the quartz-gold-sulphide veins in the province (as also proposed by De Ronde *et al.*, 1991, for the Barberton). This is consistent with the ore-mineral assemblage, study of which indicate enrichment in elements that sugest a plutonic influence (see Chapter 5). Thus the separation in time of peak metamorphism and sulphide mineralization would have important implication for the genesis of the gold deposits. It would imply that the regressive metamorphism and/or the later magmatic activity generated the gold deposits in the shear zones of the region.

6.5 ECONOMIC IMPLICATIONS

The application of lead isotope studies to mineral exploration has been discussed by several authors (Doe and Stacey, 1974; Cannon and Buck , 1961; Delevaux *et al* ., 1967). Notwithstanding the main controls on the economic viability of a particular deposit, Delevaux *et al.* (1967) propose that a mineral prospect with the same lead isotopic composition as a deposit that is already a producer in a district will have the greatest economic potential.

Clearly, in Borborema Province, the effect of the host rock lithologies on the lead isotopic ratios and the economic concentration of gold mineralization was subordinate to regional geologic and structural setting. However, the sulphide with the highest $^{206}Pb/^{204}Pb$ and $^{207}Pb/^{204}Pb$ ratios occurs in quartz veins emplaced in granitic rocks (MG-R-197). Areas dominated by schist-type lithologies associated with supracrustal rocks (e. g. São Francisco and Cachoeira de Minas mines) show lower lead isotopic ratios. In the latter two deposits the lead isotope ratios suggest some mixing with an older component of lead, whilst the granite-hosted vein seems to contain a greater proportion of younger crustal material.

No economic gold deposits are known in Itapetim District, where granitic rocks predominate, but the two deposits hosted by schists (São Francisco and Cachoeira de Minas) do contain producing mines. In Itapetim District, in the areas where granite and

orthogneiss are predominant, the gold forms small occurrences, for example on the west side, between Santo Aleixo and Sertãozinho. The majority of gold production in this district was from the east side (Pimenteiras area) where the rocks are essentially schist and paragneiss.

As previously noted, the amphibolite in the basement, and the latest (syn and late tectonic) granite contain Pb-isotope ratios which are indicative of the incorporation of a substantial proportion of 'old lead'. The absence of economic gold deposits hosted by either of these two lithologies points to the importance of the supracrustals as a source for the lead (and therefore possibly the gold as well, as suggested by Kramers and Foster, 1982).

6.6 CONCLUSIONS

The lead isotope study has placed several constraints on the metamorphism and mineralization in the Borborema Province of N.E. Brazil. Several assumptions have been used, and there are limitations to the models adopted, but in combination with other geological observations, the following scenario for the geological evolution of the area is proposed:

(i) The predominant crustal lithologies in the region were initially generated by the thermotectonic Trans-Amazonian event at around 2.1-1.8 Ga. Conditions of metamorphism were typical for mid to lower crustal levels, and it is likely that these rocks were a component for source for the gold.

(ii) The region then underwent an extended period of sedimentation and volcanism, until around 1.0 Ga a major regional high-grade metamorphism event took place. This amphibolite facies metamorphism most likely mobilized the lead and the gold from the early Proterozoic lithologies.

(iii) By 0.90-0.50 Ga the Brasiliano thermal-tectonic event was dominant. It was associated with intense granite emplacement and by polyphase folding and northeast-trending ductile shear zones. The developement of large-scale shear zones allowed the migration of metal-bearing hydrothermal fluids and provided sites for mineralization.

(iv) Multiple stages of mineralization are suggested during the time interval 0.8-0.6 Ga. It is presumed that the mineralization event was related to granite intrusion and associated retrogressive metamorphism. Hydrothermal fluids

leached the lead (and presumably other metals) from a well-mixed source characteristic of upper crustal rocks (e.g. schist). Whereas the heat and the fluids may well have originated in the granite (or been associated with melt generation) the majority of the lead was immediately derived from this source. However, there is some evidence that early (Archaean-early Proterozoic) lead may form a small component of the ores.

There is currently a major debate concerning the genesis of the Pre-Cambrian 'lode' gold deposits (e.g. Groves and Foster, 1991). Until fairly recently the concensus view was that the hydrothermal fluids were generated by dehydration of silicates during peak metamorphism; the gold and the other metals were presumed to be derived by leaching of associated lithologies (particularly basic igneous rocks). However, some recent studies have advocated a different mechanism for mineralization, one that involves granite-related fluids some time after peak metamorphism (e.g. Spooner, 1991; see also Wilkins, 1993). The results of this study confirm that magmatic activity plays an important role in the genesis of shear-zone related gold mineralization. Furthermore, such an interpretation could have important implications for exploration philosophy in such terranes.

CHAPTER 7 HYDROTHERMAL FLUIDS

7.1 INTRODUCTION

In virtually every geological environment, fluids play important roles in mineralizing processes and have thus been the subject of numerous studies (e.g. Fyfe 1987; Foster *et al* ., 1989; Groves *et al.*, 1991). One of the important reasons for this intense interest is that changes in the physico-chemical character of these fluids, for example P, T, fO_2, fCO_2, fH_2S, and pH, may lead to the destabilization of metal-bearing complexes, and result in the deposition of 'ore' metals.

Fluid inclusion studies combined with stable isotopic analyses can provide insights into the nature of this fluid. They can contribute useful data on: (i) the P-T conditions of mineralization and alteration; and (ii) the nature of the fluid and its source.

Fluids generated during low to medium grade metamorphism have been relatively well documented in the past few years (Roedder, 1984; Crawford and Hollister, 1986; Mullis, 1979; 1987). However, very little data exists on the geometry of fluid migration linked to time-space relationships between deformational events and regional metamorphism. In particular, the relationships between fluid migration during brittle to plastic deformation are relatively poorly known. Recently it has been demonstrated (Cathelineau *et al.*, 1993) that one of the most sensitive markers of fluid migration is the microfracture network of the rock, which may be fossilized when the percolating fluid is trapped as fluid inclusions through microfissure healing. Lespinasse *et al.* (1991) have emphasized the use of fluid inclusion planes for relating the different stages of fluid percolation to a regional succession of deformational events.

The use of fluid inclusions in genetic studies of Archaean lode-gold deposits has been highlighted by many researchers from several countries (Colvine *et al.*, 1988; Groves *et al.*, 1989), particularly for the larger mesothermal deposits in greenschist to lower amphibolite facies greenstone host rocks. Recently, controversy concerning the source of the ore fluids of the higher metamorphic grade Pre-Cambrian lode gold deposits has been stimulated by the work of Groves *et al.* (1991). Less attention has been paid to the study of fluids related to the gold deposits formed in metamorphic terranes where the deposition processes are controlled by crustal-scale shear zone systems. Such minor emphasis is surprising considering that gold deposits in either sub-greenschist or amphibolite-granulite terranes are present in most Pre-Cambrian regions as, for example, in the Yilgarn Block of Australia and in the Superior Province of Canada.

The shear-zone hosted gold deposits of the Borborema Province of N.E. Brazil provide interesting examples where fluids have percolated along such crustal-scale

shear zones and which have subsequently caused metal deposition. The fluid inclusions trapped in the quartz veins provide the best example of the composition of the fluid phase likely to have existed at the P and T conditions prevalent during mineralization.

This chapter focuses on the modelling of the P-V-T-X properties and composition of the mineralizing fluids. It comprises firstly the fluid inclusion study and then the stable isotope investigations.

7.2 FLUID INCLUSION STUDY

7.2.1 Introduction

The original hydrothermal solution from which a mineral precipitated can often be found trapped as tiny inclusions within that mineral. Studies of such fluid inclusions have revealed much about the composition of the hydrothermal fluids (Roedder, 1979).

The trapping of the fluid inclusion is a process that often takes place at a comparatively high temperature and pressure. At the moment of trapping the fluid may be an homogeneous (one phase) or a heterogeneous system, and on cooling it may unmix to give immiscible liquids or become saturated with respect to one or more solute components to form daughter minerals. Differential contraction between the fluid and the host mineral may result in the appearance of a vapour bubble. It is assumed that no loss or addition of material happens after trapping and, as consequence, the fluid inclusion has behaved as constant volume-constant composition system (isochoric-isopleth behaviour).

Microthermometric analysis of the fluid inclusions is based on the careful observation and recognition of phase changes involving solid-, liquid- and vapour-phase transformations in the fluid inclusions during heating and cooling. It allows us to place constraints on the chemical composition and original temperature of the mineralizing fluid, and thus indicate the most likely environment of mineralization.

7.2.2 Method of Study

The fluid inclusions study was restricted to samples of gold-bearing quartz veins that formed in different fold belts and geotectonic settings: occcurrences associated with supracrustal rocks, and several occurrences hosted by granites (ETG, ESTG, and SLTG) (see Table 7.1). Doubly-polished wafers of $\approx$ 100 μm thickness were prepared and studied by transmitted light microscopy for characterization and classification of the different types of fluid inclusion. Eleven samples were found to be suitable for

Table 7.1
Gold-bearing Quartz Veins Sampling and Relationship with the Geological Setting

Sample	Northing & Easting (km)	Locality	Description	Geological Unit
MG-R-197B	9197000N; 673000E	Garapá 'garimpo', close to NE Teixeira' batholith	Qz vein with gold, gal, mg, py, cpy, disseminated, oriented N70°E cross-cutting underformed granite	SLTG.; Late Proterozoic cross-cutting supracrustal in Pajeú/Paraíba Fold Belt
MG-R-147B	91899880N; 696000E	Cacimba Salgada 'garimpo'	Qz vein with gold cross-cutting monzogranite with diorite-granite xenoliths orient. by shearing N60°E (parallel to regional shear)	SLTG.; Late Proterozoic cross-cutting supracrustal in Pajeú/Paraíba Fold Belt
MG-R-222C	9189200N; 679500E	Guilhermina 'garimpo', Santo Aleixo area	Qz vein with gold N135°E, assoc. with py, hosted by gneiss mylonitic with foliation N80°E. (discordant vein)	ESTG; Late Proterozoic cross-cutting supracrustal in Pajeú/Paraíba Fold Belt
MG-R-174B	9188000N; 679640E	Santo Aleixo 'garimpo' Santo Aleixo area	Qt. vein with gold discordant with gneiss mylonitic	ESTG; Late Proterozoic cross-cutting supracrustal
MG-R-203D	9189200N; 674000E	Canafistula 'garimpo';	Qz vein with gold intercalated in tourmaline alterated zone, concordant with hosted mylonitic granitic rock with foliat. N150°E,70°NW	ETG.; Early Proterozoic occurs as sheet in supracrustal in Pajeú/Paraíba Fold Belt
MG-R-159	9191520N; 692800E	Sertãozinho, Itapetim-Central Domain	Qz -tourmaline vein mineralized in gold , occurs in the level N-13 (underground) concordant with biotite schist (host rock of mineralization)	ESTG.; Late Proterozoic Early proterozoic, Pajeú/Paraíba Fold Belt Irajaí Formation,
MG-R-166A	9193680N; 6933400E	Shaft in Queiroz Galvão, Itapetim-East Domain	Qz vein concordant with hosted rock muscovite-biotite gneiss, foliated N70°E	Early proterozoic, Pajeú/Paraíba Fold Belt Cachoeirinha Formation,
MG-R-224C	9160100N; 600100E	Cachoeira de Minas mine	Qz vein with gold and gal, N60°E, discordant, with hosted rock biotite-muscovite schist	Early Proterozoic, Piancó/Alto Brídida Fold Belt Seridó Group, Seridó Form.,
MG-R-229C	9339200N; 806200E	São Francisco mine, Morro Pelado shear zone	Qz vein with gold, py, chp, and molyb interc. in the wallrock of silicified-hematitic zone with mylonitic foliation N60°E, 40° SE	Early Proterozoic, Seridó Fold Belt Archaean basement in
MG-R-230	9339200N; 806200E	São Francisco mine, Morro Pelado shear zone	Qz vein with gold, py, chp, and molyb interc. in the wallrock of silicified-hematitic zone with mylonitic foliation N60°E, 40° SE	Early Proterozoic, Seridó Fold Belt Archaean basement in
MG-R-208C	9206000N; 593000E	Boqueirão dos Cochos	Qz vein with gold and py hosted by garnet-amphibolite, schistosity N20°E, 40°SW	Piancó/Alto Brídida Fold Belt

Abbreviations:
Chp = chalcopyrite; gal = galena; mg = magnetite; molyb = molybdenite; py = pyrite; qz = quartz
Grid reference based on UTM Projection (central meridian = 39° W of Gr.); For further information concerning the sample labels see Appendix A1.1.

microthermometric analysis.

Microthermometric measurements were carried out using a Linkam TH600 microscope stage. Calibration of the microthermometric stage was performed using synthetic fluid inclusion standards: the triple point of pure CO_2 (- 56.6 °C); the melting point of ice (0°C); and the critical temperature of homogenization of pure H_2O (+ 374.5°C). All the analyses were performed within a period of five months and the calibration was monitored every week during the development of this work (see Appendix A7.1). All the phase changes were measured during this study on one heating and cooling cycle to minimize nucleation problems. Estimated accuracy between -100 and -20°C is ± 0.5°C, whereas above - 20 °C it is ± 1°- 5°C. During the freezing and warming stages the heating rates were reduced to less then 0.5 °C per minute and 5 degrees per minute respectively to allow measurements to within ± 1°C.

Salinity, density, and CH_4 and CO_2 content, were all calculated using the approach of Shepherd *et al.* (1985; see Apppendix A7.2). The salinity of the aqueous phase was calculated from the temperature of clathrate melting for the carbonic inclusions or the ice melting temperature for the aqueous inclusions. The density of CO_2 was calculated from the temperature of homogenization of the solid CO_2 phase for the CO_2 or H_2O-CO_2 inclusions. The CH_4 content (expressed as mole % of CO_2) was determined from the final melting temperature of solid CO_2. The CO_2 contents (wt %) were calculated using the density information combined with visual estimates of the phase ratios at room temperature. The bulk compostion of the inclusions was calculated using the approach of Ramboz *et al.* (1985).

The P-T conditions were further defined using the graphical technique developed by Schwartz (1989) which allows the theoretical homogenization temperature of CO_2-rich inclusions to be determined. The method can also be employed to predict the homogenization pressure if the values of molar fraction and volume fraction of CO_2 are known. Details concerning the use of this technique (see Appendix A7.3) and the results will be discussed later. In order to cross-check data, P-T conditions were also calculated from a combination of chlorite geothermometry and the fluid inclusion isochores.

7.2.3 Fluid Inclusions Types and Mode of Occurrence

The relationships between the fluid inclusions in the quartz veins are complex and sometimes not easy to characterise. The mechanisms of fluid trapping (Roedder, 1972) and the textural relationship between the fluid inclusions and the host crystal suggest the presence of three types of fluid inclusion distribution (Fig. 7.1):

(i) Type I: fluid inclusions associated with crystal growth during the initial

formation of the enclosing mineral.

(ii) Type II: fluid inclusions associated with sealed cracks by a *crack-seal* mechanism during the growth of the quartz vein.

(iii) Type III: fluid inclusions related to *crack healing* or microfractures formed during some later event.

The first two types are primary fluid inclusions with respect to the growth of the quartz *vein*, but Type II is secondary with respect to the individual quartz *crystals*. Both types represent the hydrothermal fluid trapped during the growth of the quartz vein. Type I relates to crystal growth zones and is characterized by a concentrated spatial distribution parallel to the boundary of the crystal (see Fig. 7.2). Type II is related to vein growth by a crack-seal mechanism (Ramsay, 1980) and is marked by a random distribution of inclusions and a high content of solid inclusions, consisting predominantly of tourmaline (Fig. 7.3). This process is characterised by transport in one direction by infiltration and subsequently precipitation along the fractures (Batzle and Simmons, 1976). It is envisaged that Type II inclusions follow Type I in a cyclical, multistage process (as illustrated in Fig. 3.42).

Type III represents secondary inclusions, which were formed when the fluid was trapped in hydraulic extension-fractures, which are associated with high fluid pressure and consequently low effective stresses (see Chapter 3). This process developed at some unspecified time after crystal growth when the fluid pressure equalled the tensile strength of the rock (Ramsay, 1980). They form planar and very thin straight trails. Type III is marked by conjugate-sets and occur: (i) within a single quartz grain; (ii) cross-cutting grain boundaries; and (iii) cross-cutting type I and II fluid inclusions (Fig. 7.4).

The following types of fluid inclusion have been observed according to their different proportions of liquid and vapour (see Fig.7.5):

(i) Aqueous inclusions, with a regular, spheroidal shape (Fig. 7.5b). These inclusions have the largest size (mostly 15 to 45 μm, mean about 26 μm). The degree of fill (DF; the volume % of liquid relative to the total volume of the fluid cavity) was estimated visually and varies from 0.40 to 0.90, with a mean around 0.70 (Fig. 7.11).

(ii) CO_2 monophase inclusions. This type shows a rounded shape (Fig. 7.5d). The CO_2 monophase inclusions actually have a small amount of H_2O that tends to wet the wall of the inclusion cavity. Thus 10 to 20 mole % H_2O may not be detected optically because of the high refractive index contrast between the inclusion and the host crystal (Crawford and Hollister, 1986). Consequently, a small amount of H_2O may be expected in most CO_2-rich inclusions. These inclusions vary in size from 15 to 45 μm with a mean value of 25 μm (Fig. 7.10).

Figure 7.1 Photomicrograph and accompanying sketches of doubly-polished section of gold-bearing quartz vein. (A) Different fluid inclusion trapping mechanisms: diffusion intra grains (type I); crack-seal (type II); and crack healing (type III); (B) detail of the crack-seal process showing the concentration of the inclusion bands, consisting of solid inclusions (mainly tourmaline) and fluid inclusions; (C) Diffusion inter grains showing the fluid moving along the grain boundaries; (D) Fluid inclusions concentrated along conjugate trails.

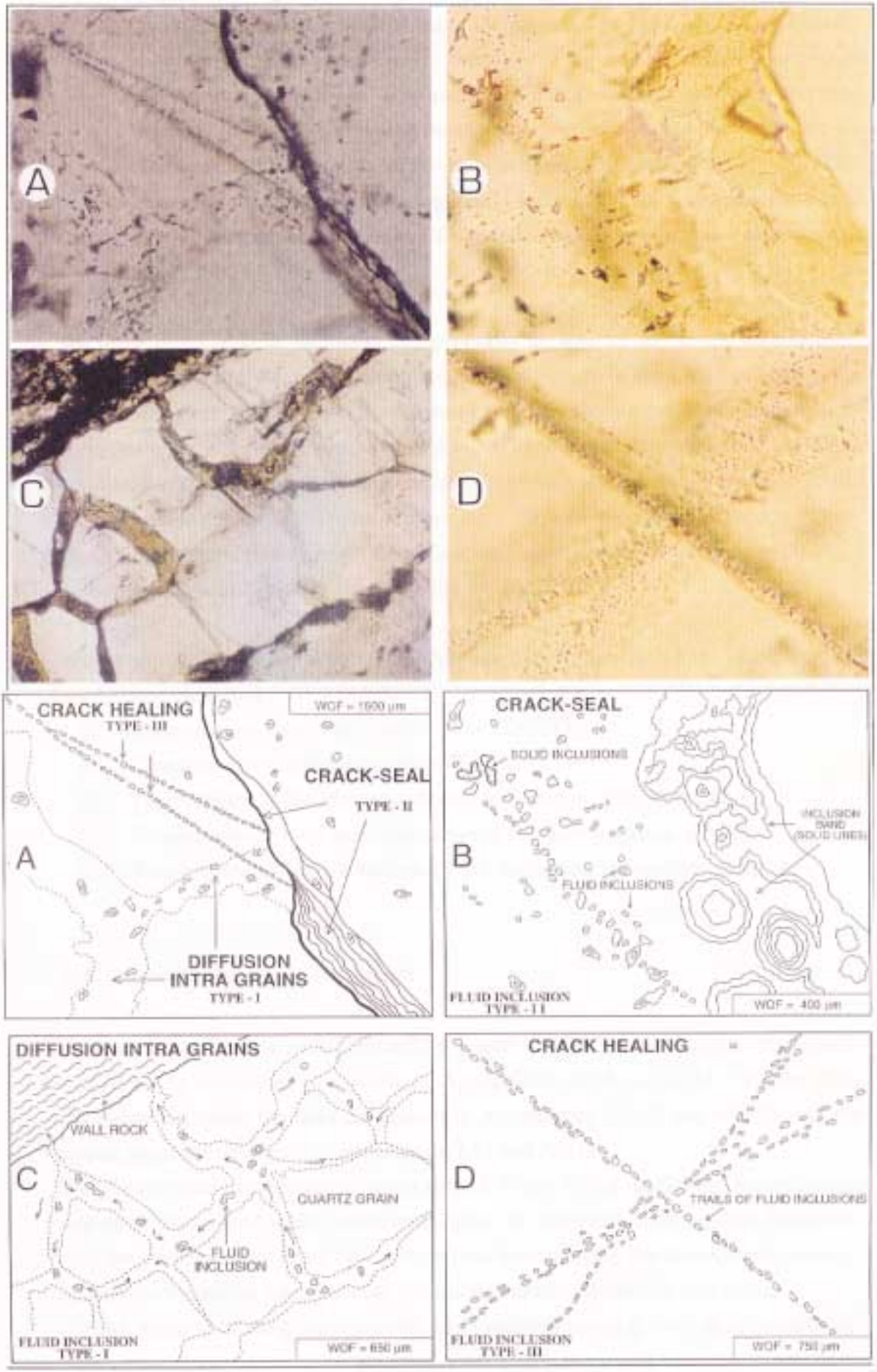
A
B
C
D
CRACK HEALING
TYPE - III
WOF = 1500 µm
CRACK-SEAL
TYPE - II
A
DIFFUSION
INTRA GRAINS
TYPE - I
CRACK-SEAL
SOLID INCLUSIONS
INCLUSION
BAND
(SOLID LINES)
B
FLUID INCLUSIONS
FLUID INCLUSION
TYPE - II
WOF = 400 µm
DIFFUSION INTRA GRAINS
WALL ROCK
C
QUARTZ GRAIN
FLUID
INCLUSION
FLUID INCLUSION
TYPE - I
WOF = 650 µm
CRACK HEALING
D
TRAILS OF FLUID INCLUSIONS
FLUID INCLUSION
TYPE - III
WOF = 750 µm

(iii) H_2O-CO_2 inclusions, characterized by the presence of two immiscible liquids, one aqueous and the other CO_2-rich (Figs. 7.5a and 7.5b). Usually they are two-phase, but rarely, three-phase H_2O-CO_2 inclusion occurs at room temperature (Figs. 7.5e and 7.5f). The inclusions show a size range between 10 and 34 μm with a mean value around 25 μm. The degree of fill (DF) has a large scatter with a range from 0.50 to 0.95 (Fig. 7.7). This variation suggests that trapping could have occurred when the fluid was already heterogeneous and the CO_2 and H_2O fluids were immiscible (Ramboz *et al.*, 1982).

All three types of fluid inclusion can generally be seen in any given gold-bearing quartz vein, and can be found along crack-seals, crack healing or between grain contacts. However, the healing microfractures typically show a predominance of CO_2-rich inclusion of very small size. The H_2O-CO_2 type is the dominant fluid inclusion type overall with ≈ 68% of the inclusions; the CO_2-rich variety is less common (usually ≈ 10 %), while the aqueous type represents ≈ 22% of the total inclusions. There appears to be no significant difference in fluid inclusion populations within the different lithologies (supracrustal rocks or granitoids; see Fig. 7.6).

Where possible, during heating and freezing the following phase changes were observed and measured:

(i) *Temperature of melting of solid* CO_2 (Tm CO_2).
(ii) *Temperature of clathrate melting* (Tm Cl).
(iii) *Temperature of liquid-vapour homogenization of* CO_2 (Th-CO_2).
(iv) *Temperature of total homogenization of the fluid inclusion* (T-Th).
(v) *Temperature of first ice melting* (T-fm Aq) or *last ice melting* (T-lm Aq)

7.2.4 Microthermometric Results

Microthermometric data were obtained for a total of 290 fluid inclusions. The results for H_2O-CO_2 inclusions are given in Appendices A7.4 to A7.11.; for the CO_2 monophase inclusion the data are shown in Appendices A7.12 and A7.13; and the aqueous inclusion data are in Appendices A7.14 and A7.15.

The present study comprised all types (type I, II and III) of inclusions, located along crack-seals, distributed within grain boundaries, or related to crack healing. However, due to the small size displayed by the inclusions located along the trails (crack healing), the microthermometric measurements were concentrated on the two first types.

Quartz grains showing evidence of recrystallization (e.g. undulose extinction,

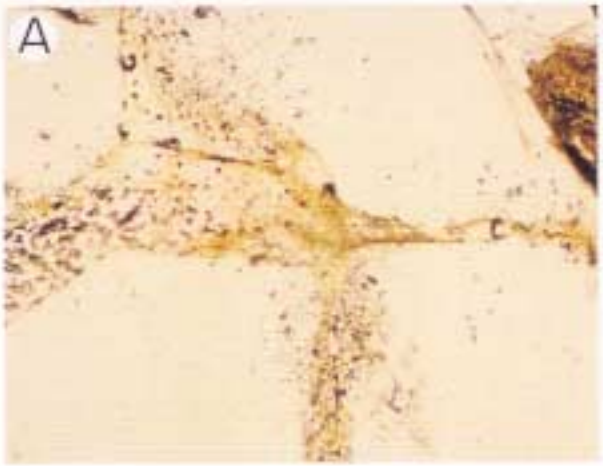

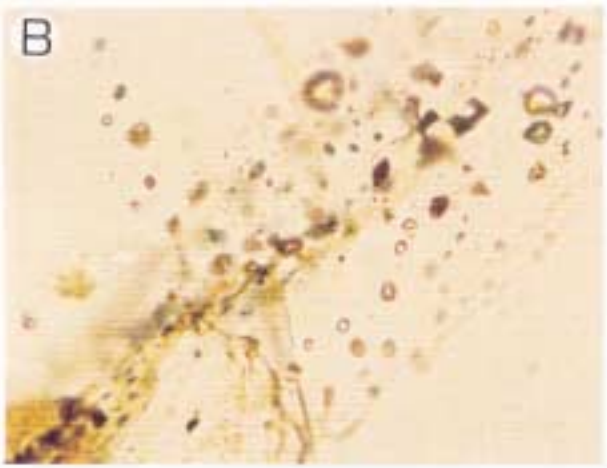

FLUID INCLUSION TYPE I

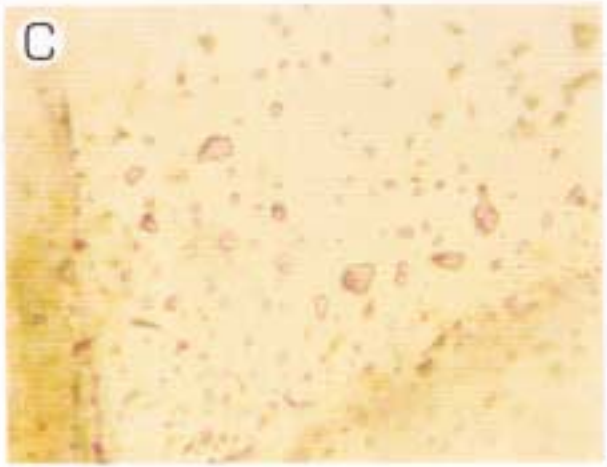

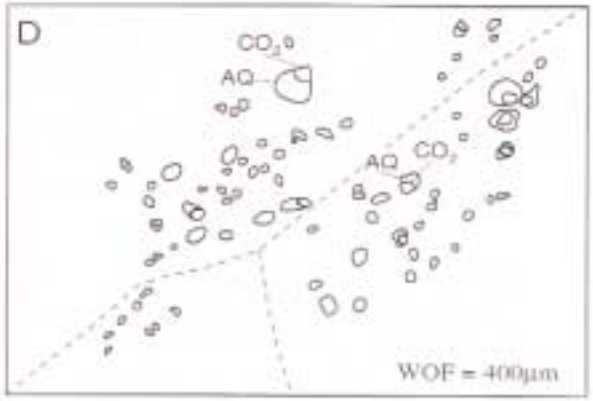

Figure 7.2 Photomicrograph of doubly-polished section of gold-bearing quartz vein showing the mode of occurrence of (**type I**) fluid inclusions. Note (**A**) the random distribution of fluid inclusions along the triple-point between the grains (WOF = 750 µm). Detail (**B**) of A showing the random distribution of the fluid inclusions (WOF = 400 µm) ; and (**C**) the predominance of CO_2-rich two phase fluid inclusions (WOF = 400 µm). In (**D**) a sketch of (B) shows the fluid inclusions concentrated along the grain boundary (dashed line). (Microphotographs: TL ; MG-R-197; Igarape Garapa).

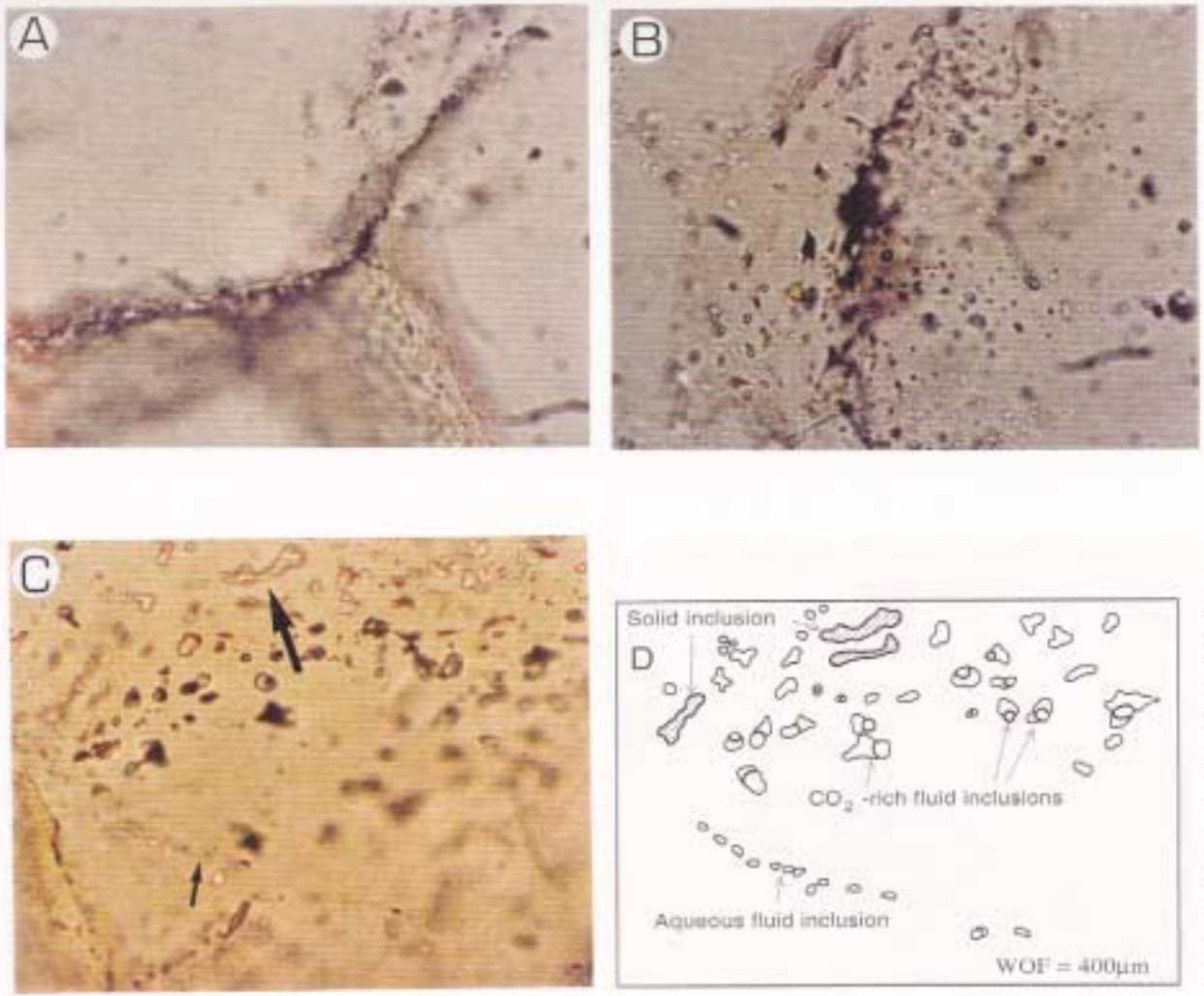

FLUID INCLUSION TYPE II

Figure 7.3 Photomicrograph of doubly-polished section of gold-bearing quartz vein showing (**A**) the mode of occurrence of (**type II**) fluid inclusions (TL; WOF = 750 µm; MG-R-166A; Itapetim, Pimenteiras). Note (**B**) the random distribution of solid and fluid inclusions (TL; WOF = 400 µm; MG-R-208A; Boqueirão dos Cochos). Detail (**C**) of B showing the types of inclusions: solid inclusions displaying very irregular shape (middle-top; see large arrow); CO_2-rich inclusions and aqueous phase inclusions (very small and well rounded shape; see small arrow) (TL; WOF = 400; MG-R--208A; Boqueirão dos Cochos). In (**D**) a sketch of (C) shows the different types of inclusions present: solid inclusions; CO_2-rich fluid inclusions and aqueous inclusions.

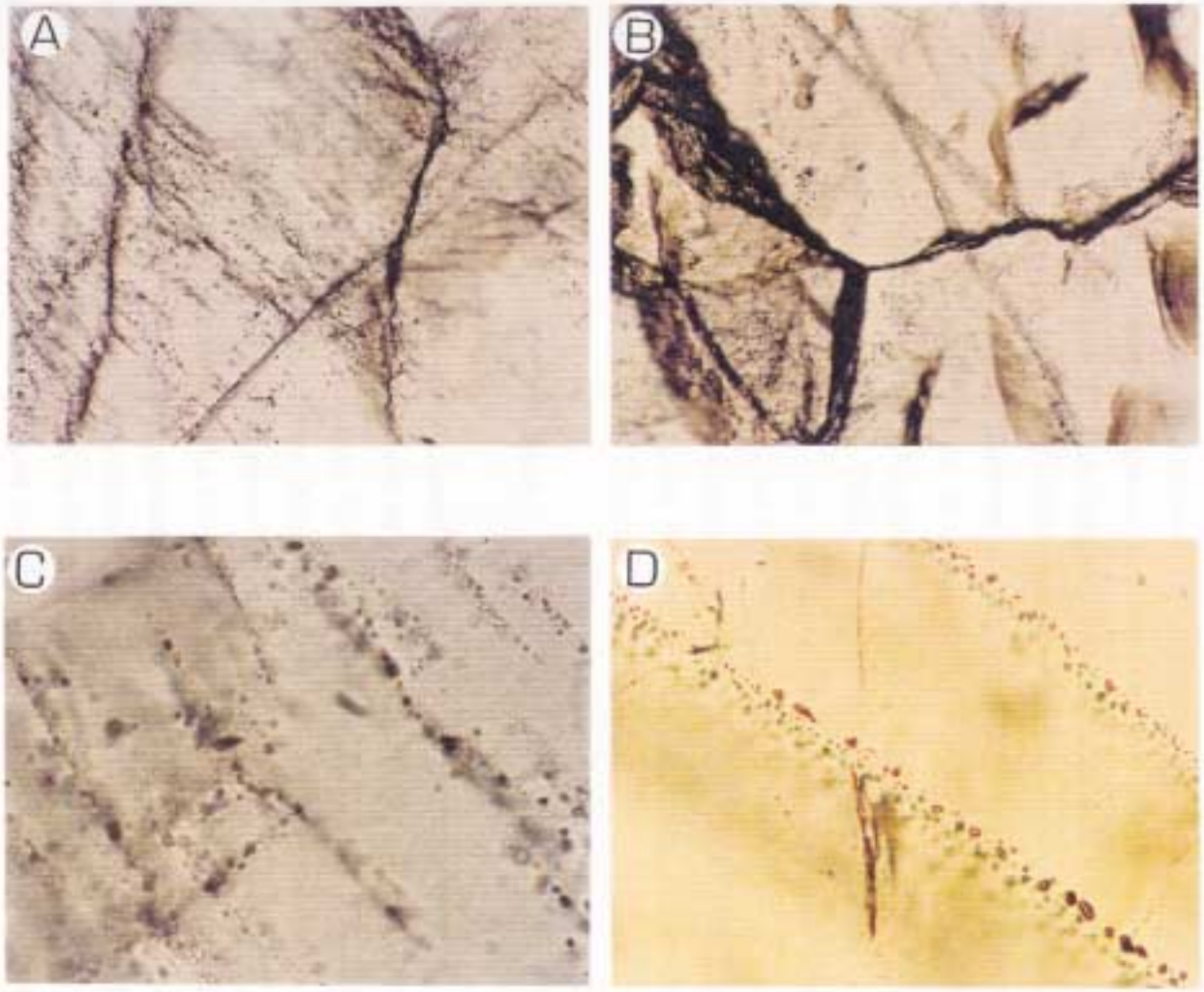

FLUID INCLUSION TYPE III

Figure 7.4 Photomicrograph of doubly-polished section of gold-bearing quartz vein showing the mode of occurrence of (**type III**) fluid inclusions. Note (A) that the trails cross-cut the crack-seal (TL; WOF = 4500 µm; MG-R-166A; Itapetim, Pimenteiras) and also (B) the contact between grains (TL; WOF = 2500 µm; MG-R-159; Itapetim, Sertãozinho). The trails (C) form a linear structures defining closely-spaced sets of microfractures (WOF = 400 µm) or a reticulate system in D; WOF = 750 µm) where CO_2-rich monophase fluid inclusion predominate (C and D: TL; MG-R-229C; São Francisco mine).

deformation lamellae) were avoided during the microthermometric analyses due the possibility of anomalously high homogenization temperatures (see Kerrich, 1976). Necked inclusions, although very rare, were also avoided.

During this study, the H_2O-CO_2 inclusions invariably showed partial homogeniztion to the liquid phase, with the disappearence of the CO_2 vapour phase. Decrepitation was not common in these inclusions. The CO_2 'monophase' inclusions also homogenize into the liquid state, but here decrepitation did occur before total homogenization. No daughter crystals were found in this study.

a) H_2O-CO_2 Fluid Inclusions

At room temperature the H_2O-CO_2 inclusions contain an aqueous phase (H_2O) and a CO_2-rich liquid phase, although sometimes two CO_2 phases can be seen (L-CO_2 and V-CO_2) with the vapour phase in constant motion. These inclusions contain ≈ 9.7 to 25.0 CO_2 wt %. The solid CO_2 melting temperatures scatter between - 56.6 and - 59.6 °C with the greatest peak at - 57.4 °C. This indicates that the inclusions contain minor amounts of other gases besides CO_2 and would equate to a CH_4 concentration of 1.5 to 6.9 mole % of CO_2. Temperatures of clathrate melting range from 6 to 8 °C, indicating that salinity varies from 4.6 to 7.3 wt % (mean of 6.0 wt %) NaCl equivalent. Homogenization of the liquid-vapour CO_2 occurred over a temperature range from 19 to 24 °C with multi-peaks at 9 to 27 °C. These values indicate a variation from 0.76 to 0.85 g cm^{-3} for CO_2 density. The total homogenization of the inclusions is characterised by a conspicuous scatter of the T-Th values, from 255 to 387 °C.

The microthermometric measurements are expressed as mean values in Table 7.2 and the complete data are given in Appendices A7.4 to A7.11. The scatter in the data is portrayed in the histograms depicted in Figures 7.7 to 7.9.

b) CO_2 Monophase Fluid Inclusions

The phase transition seen in the monophase/CO_2-rich inclusions during freezing and heating place them in the H-type category of van der Kerkhof (1988). This inclusion type has high CO_2 contents and very little H_2O (Crawford and Hollister, 1986) and its phase behaviour is similar to that of pure CO_2.

The CO_2 melting temperatures are clustered around - 57.9 °C, ranging from - 57.6 to - 58.7 °C. These values indicate that the CO_2 phase contains only small amounts of other gases (e.g. CH_4, N_2). Mean homogenization of CO_2 (Th CO_2) in these inclusions was observed around + 14 to + 10 °C with a total range from - 2 to + 16 °C. The mode of total homogenization in this type of inclusion is not easy to identify, because it is hindered by the lack of visible H_2O and also by decrepitation. However, this type

Figure 7.5 Photographs and accompanying sketches of CO_2-rich and H_2O fluid inclusions showing different degrees of fill: (A) H_2O-CO_2 two phase inclusion (see arrow) with 0.95 DF (WOF = 400 μm); (B) H_2O inclusion (see arrow) with 0.70 DF (WOF = 400 μm); (C) H_2O-CO_2 two phase inclusion with 0.50 DF (WOF = 400 μm); and (D) CO_2 monophase fluid inclusion (see arrow); (E) and (F) show H_2O-CO_2 three phase.

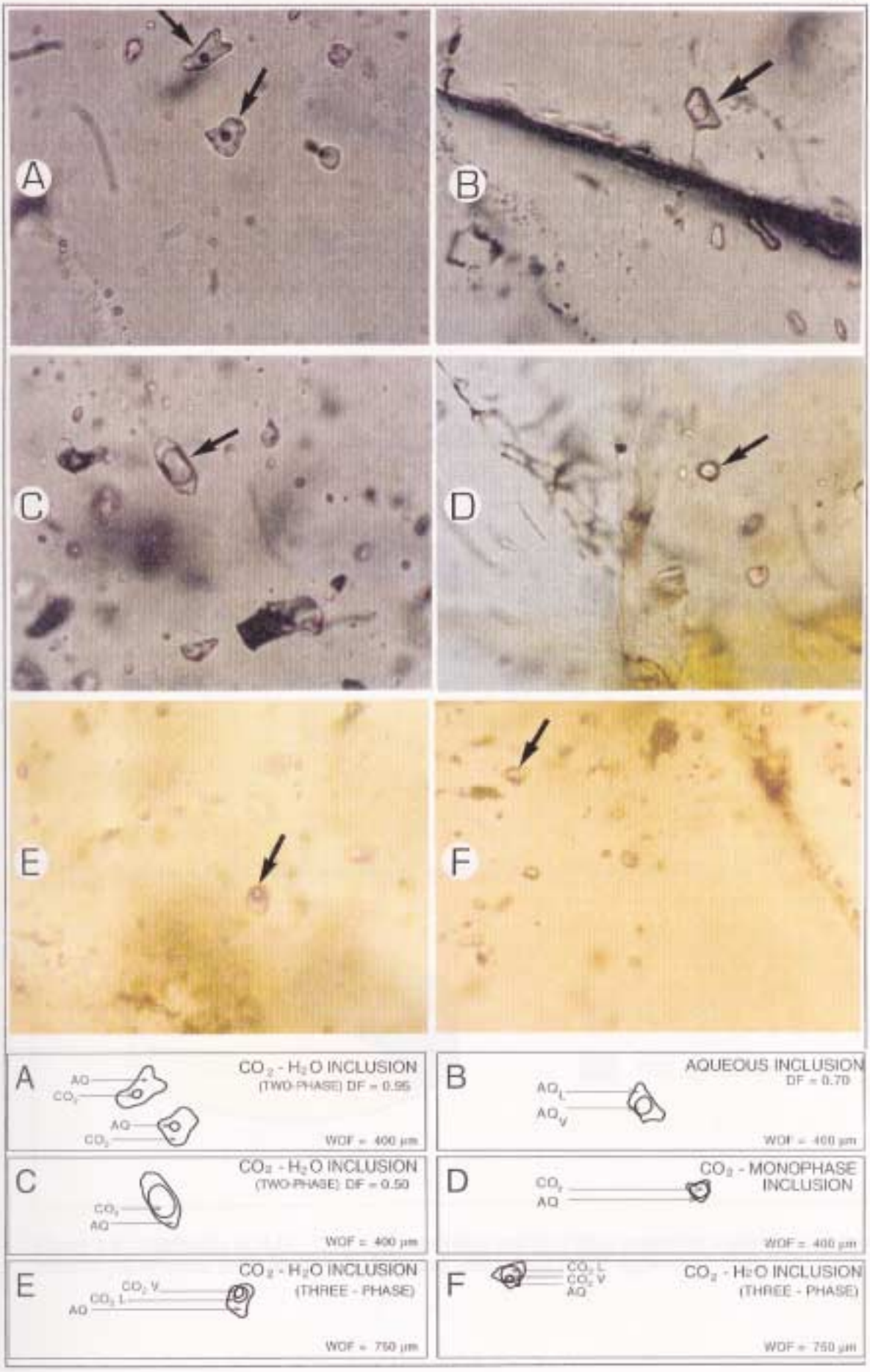
A
B
C
D
E
F
A
AQ
CO_2
AQ
CO_2
CO_2 - H_2O INCLUSION
(TWO-PHASE) DF = 0.95
WOF = 400 µm
B
AQ_L
AQ_V
AQUEOUS INCLUSION
DF = 0.70
WOF = 400 µm
C
CO_2
AQ
CO_2 - H_2O INCLUSION
(TWO-PHASE) DF = 0.50
WOF = 400 µm
D
CO_2
AQ
CO_2 - MONOPHASE
INCLUSION
WOF = 400 µm
E
CO_2 V
CO_2 L
AQ
CO_2 - H_2O INCLUSION
(THREE - PHASE)
WOF = 750 µm
F
CO_2 L
CO_2 V
AQ
CO_2 - H_2O INCLUSION
(THREE - PHASE)
WOF = 750 µm

(A) Fluid inclusion distribution in gold-bearing quartz veins (all samples)

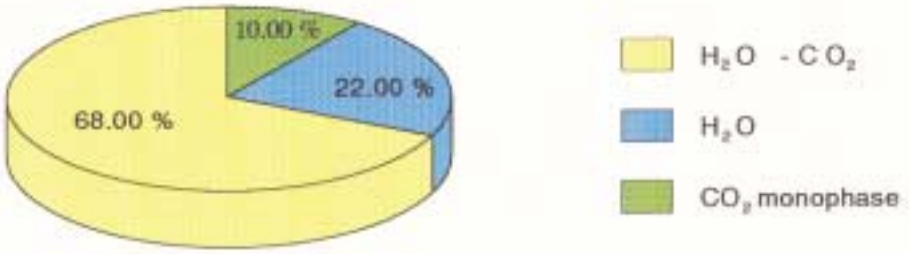

(B) Fluid inclusion distribution in gold-bearing quartz veins hosted by granite

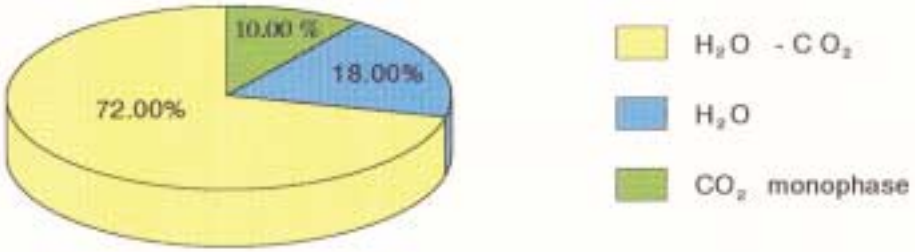

(C) Fluid inclusion distribution in gold-bearing quartz veins hosted by supracrustal rocks

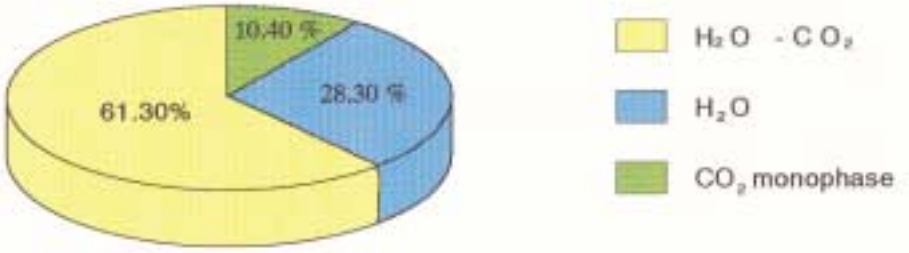

Figure 7. 6 Distribution of H_2O - CO_2, CO_2 monophase and H_2O fluid inclusions in gold-bearing quartz veins; in (A) all rocks; in (B) quartz veins hosted by granites and (C) by supracrustal rocks.

Table 7.2
Microthermometric Data for H2O-CO2 Fluid Inclusions in Quartz Veins Hosted by Granitoids, Supracrustals and Amphibolite

Rock-type	Locality	NFI	Size (μm)	DF	Tm CO2 (°C)	Tm Cl (°C)	Th CO2 (°C)	T-Th (°C)	D (*) (g cm-3)	CO2 (*) (wt % of total fluid)	CH4 (*) (mole % CO2)	S (*) (NaCl wt % eq.)
SLTG	Igarape Garapa	N = 33	10 to 45	0.50 to 0.95	(-56.6 to -59.2)	4.4 to 9.6	10.1 to 26.1	193 to 467	0.72 to 0.88	3.9 to 45.7	0.5 to 13.0	2.0 to 8.0
Mean value	(MG-R-197B)		**26**	**0.79**	**-57.7**	**7**	**19**	**293**	**0.80**	**17.4**	**6.9**	**6.3**
SLTG	Cacimba Salgada	N = 26	25 to 45	0.70 to 0.95	(-56.6 to - 58.9)	5.3 to 9.5	9.0 to 24.0	220 to 385	0.77 to 0.89	4.4 to 27.6	0.2 to 11.5	2.0 to 9.0
Mean value	(MG-R-147B)		**34**	**0.85**	**-57.6**	**6**	**14**	**255**	**0.85**	**12.6**	**5.0**	**7.3**
ESTG	Santo Aleixo	N = 44	15 to 50	0.70 to 0.90	(-56.6 to -59.2)	4.1 to 9.1	11.3 to 25.0	200 to 395	0.73 to 0.87	8.3 to 26.5	0.5 to 15.0	2.0 to 11.0
Mean value	(MG-R-174B & 222C)		**31**	**0.75**	**-57.5**	**7**	**17**	**287**	**0.82**	**21.0**	**4.8**	**6.7**
ETG	Canafístula	N = 25	15 to 50	0.70	(-56.6 to -58.5)	4.5 to 9.0	12.3 to 26.6	201 to 376	0.72 to 0.85	23.6 to 26.7	0.5 to 14.5	2.0 to 9.0
Mean value	(MG-R-203D)		**23**	**0.70**	**-57.6**	**7**	**19**	**319**	**0.80**	**25.4**	**4.8**	**6.0**
Supracrustal rock	Cachoeira de Minas	N = 18	15 to 25	0.70 to 0.90	(-56.9 to -59.6)	5.2 to 9.0	15.5 to 26.0	226 to 320	0.60 to 0.85	7.0 to 26.7	1.5 to 17.0	0.5 to 9.0
Mean value	mine (MG-R-224C)		**19**	**0.88**	**-57.5**	**7**	**22**	**270**	**0.76**	**9.7**	**4.8**	**6.0**
Supracrustal rock	São Francisco mine	N = 25	15 to 50	0.50 to 0.95	(-57.0 to -58.6)	6.7 to 9.9	21.4 to 26.7	200 to 313	0.66 to 0.78	4.1 to 43.5	2.5 to 10.5	2.0 to 6.4
Mean value	(MG-R-229C & 230)		**26**	**0.70**	**-57.7**	**8**	**24**	**273**	**0.77**	**23.4**	**5.8**	**4.6**
Supracrustal rock	Itapetim (Central &East)	N = 22	15 to 25	0.70 to 0.90	(-56.6 to 57.1)	5.0 to 8.3	13.6 to 25.0	233 to 408	0.73 to 0.85	8.4 to 26.7	1.0 to 3.0	4.0 to 9.0
Mean value	(MG-R-159 & 166A)		**20**	**0.70**	**-56.9**	7	**18**	**336**	**0.80**	**25.1**	**1.5**	**7.0**
Amphibolite	Boqueirão dos	N = 6	20 to 25	0.70 to 0.90	(-56.8 to -57.5)	6.0 to 9.5	19.4 to 22.0	369 to 394	0.80 to 0.82	8.2 to 26.0	1.5 to 4.5	1.5 to 8.0
Mean value	Cochos (MG-R-208C)		**24**	**0.77**	**-57.0**	**7**	**21**	**387**	**0.81**	**20.2**	**2.3**	**5.6**

Observations:
SLTG = Syn-and late tectonic granite; ESTG = Early-syn tectonic granite; ETG = Early tectonic granite.
NFI = number of fluid inclusion measurements;For further information see Appendices A7.4 to A7.11.
DF = degree of fill; Tm CO2 = temperature of CO2 melting; Tm Cl = temperature of clathrate melting; Th CO2 = temperature of homogenization of CO2; T-Th = temperature of total homogenization of fluid inclusion;
D = density; CH4 = methane; S (NaCl equiv.) = salinity (halite equivalent); CO2 = carbon dioxide.
(*) The density, the salinity, the wt % of CO2 and mole % CH4 were calculated according to the approach of Shepherd et al.,1985 (see Appendix A7. 2 for details).

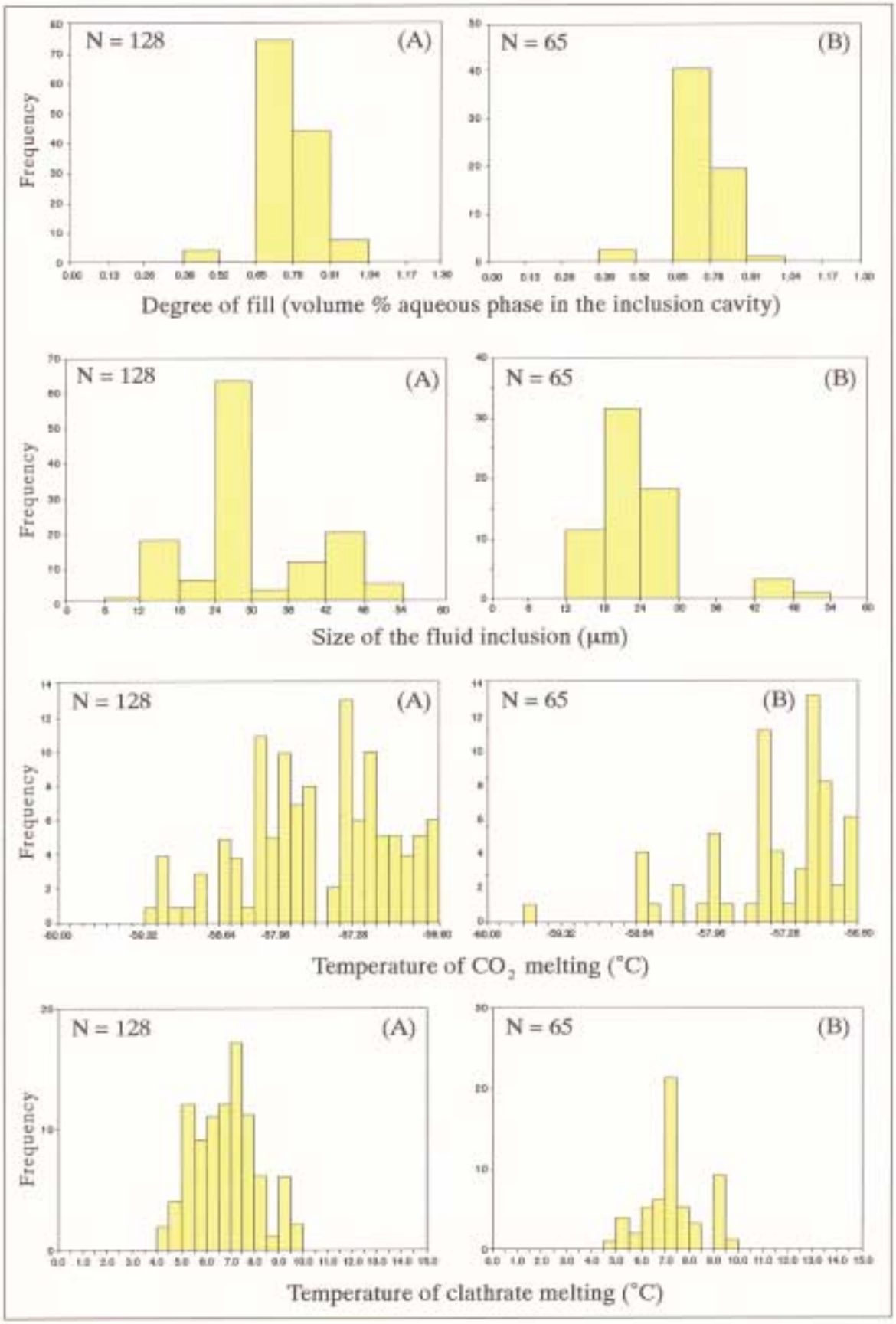

Figure 7. 7 Histograms for H_2O - CO_2 fluid inclusions in gold-bearing quartz veins hosted by (A) granites and (B) supracrustal rocks showing: degree of fill (volume % of aqueous phase in the inclusion cavity); size of the fluid inclusions (μm); the temperature of CO_2 melting (°C) and temperature of clathrate melting (°C). N = number of inclusion measurements.

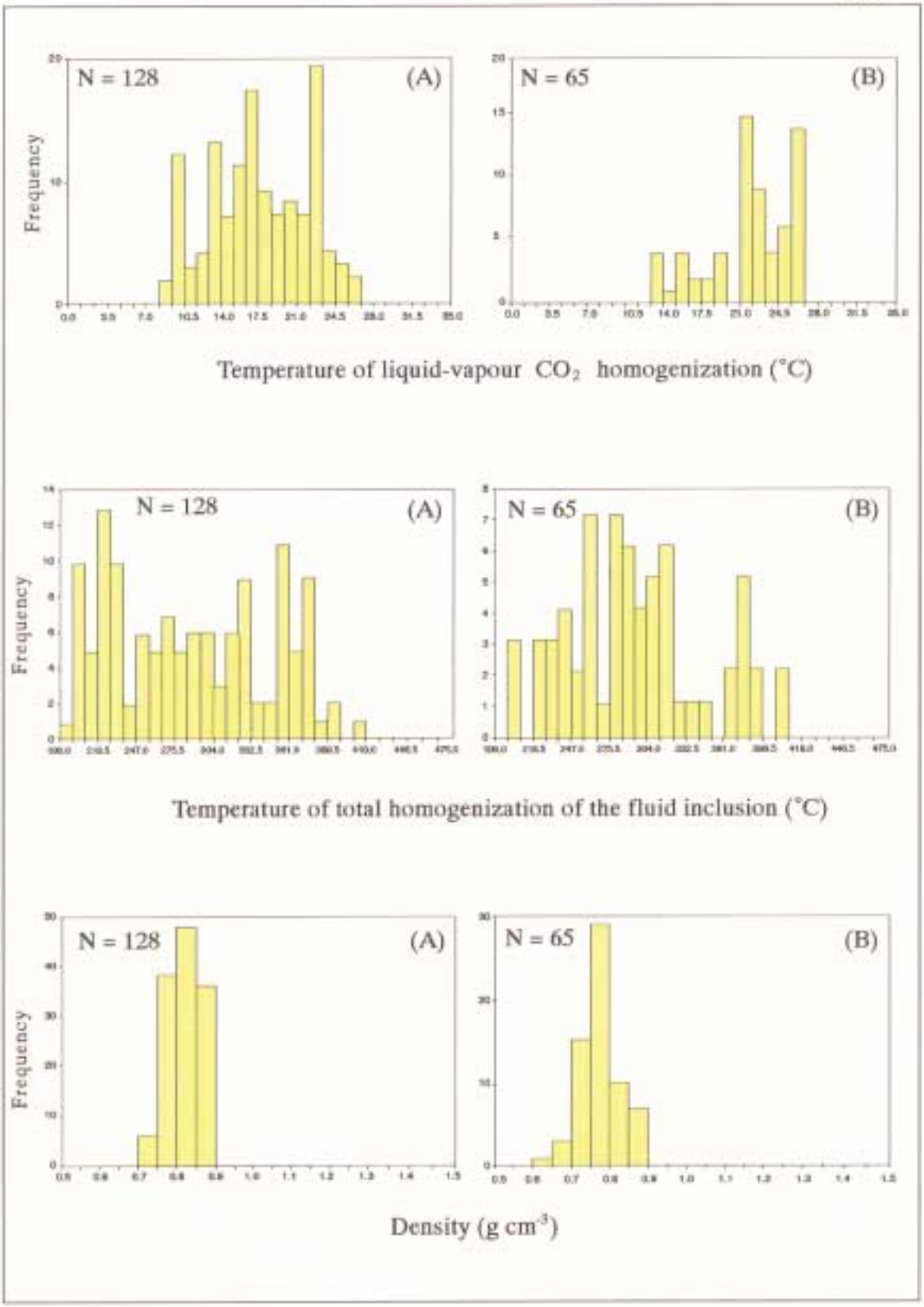

Figure 7.8 Histograms for H_2O - CO_2 fluid inclusions in gold-bearing quartz veins hosted by (A) granites and (B) supracrustal rocks showing: temperature of liquid-vapour CO_2 homogenization (°C); temperature of total homogenization of the fluid inclusion (°C); and density of the fluid inclusion (g cm^{-3}). N= number of inclusion measurements.

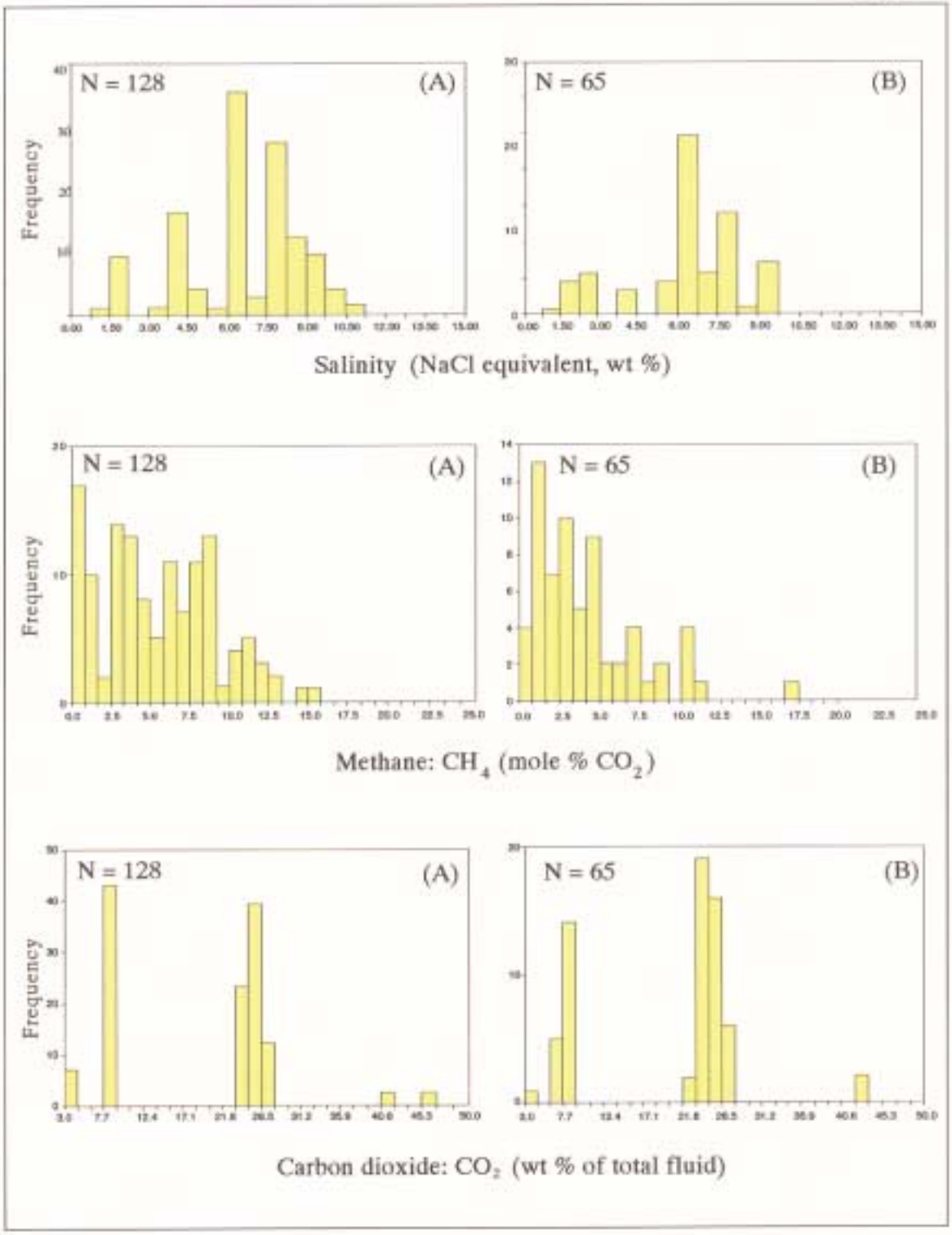

Figure 7. 9 Histograms for H_2O - CO_2 fluid inclusions in gold-bearing quartz veins hosted by (A) granites and (B) supracrustal rocks showing the salinity of the fluid (NaCl equivalent wt %); and the amounts of methane (mole % CO_2) and carbon dioxide (wt % of total fluid). N = number of fluid inclusion measurements.

homogenize into the liquid state by expansion of the CO_2 phase.

The compositional data for the monophase/carbonic-rich inclusions obtained from the microthermometric analysis (Tm CO_2 and Th CO_2) indicate that the amount of CH_4 disssolved in the carbonic phase ranges from 4.5 to 9.8 mole %. The CO_2 homogenization (Th CO_2) data are equivalent to a mean density variation around 0.85 to 0.93 g cm $^{-3}$ with a total range from 0.84 to 1.20 g cm $^{-3}$.

The microthermometric mean values are presented in Table 7.3 and as histograms in Figure 7. 10; the data is given in Appendices A7.12 to 7.13.

c) H_2O-rich Fluid Inclusions

The temperature of first melting in the aqueous inclusions (T-fm Aq) could not be measured, but the movement in the inclusion around - 23.0 °C may represent a eutectic, and thus indicate that the fluid is dominated by the cations NaCl and KCl. The data suggests that below this point only solids are present, whilst above this temperature solids and liquid coexist. Values between - 47.7 to - 42.4 °C were also found in one sample from quartz vein hosted by supracrustal rock (MG-R-166A), indicating that Ca salts may be present. Higher temperatures (up to - 12.0 °C) are not consistent with the eutectic temperature for the system H_2O-NaCl (20.8 °C) and thus other components (e.g. $NaHCO_3$, Na_2SO_4 or Na_2CO_3) could be present.

The mean temperature of melting of the aqueous phase ranges from - 1.3 to + 1.4 °C, the higher temperatures perhaps being indicative of a mixed ice and salt hydrate. The salinity ranges from 1.0 to 14.0 wt % (NaCl equivalent). The aqueous inclusions homogenize over a temperature range of 250 to 352 °C, corresponding to a low-moderate fluid density of 0.76 g cm $^{-3}$ (mean value).

The microthermometric data are given in Table 7.4 and in Appendices A7.14 and A7.15 The scatter in this data is depicted in the histograms (Fig. 7.11).

7.2.5 Bulk Composition of the Fluid Inclusions

Bulk compositions of the H_2O-CO_2 inclusions were derived using the approach of Ramboz *et al.* (1985). The results for the H_2O-CO_2 inclusions are displayed in Appendix A7.16 and the bulk composition is given in Table 7.5.

The bulk compositions obtained for a total of 199 H_2O-CO_2 inclusions show a range from ≈ 3.0 to 23.0 mole % CO_2. The amount of CH_4 varies from 0.1 to 3.0 mole %. The salinity has a range from 0.5 to 8.7 mole % of NaCl. The amount of H_2O ranges from 72.0 to 94.0 mole % and the fluid density varies from 0.72 to 0.86 g cm $^{-3}$ (Table 7.5).

Table 7.3

Microthermometric Data for CO2 Monophase Fluid Inclusions in Quartz Veins Hosted by Granitoids and Supracrustals Rocks

Rock-type	Locality	NFI	Size (μm)	Tm CO2 (°C)	Th CO2 (°C)	D (*) (g cm-3)	CH4 (*) (mole % of CO2)	CO2 (**) (wt % of total fluid)
SLTG	Cacimba Salgada (MG-R-147B)	N = 13	45	-58.7	10	0.93	9.8	90.2
ESTG	Santo Aleixo (MG-R-174B & 222C)	N = 03	25	-57.6	10	0.85	4.8	95.2
ETG	Canafístula (MG-R-203D)	N = 02	15	-57.8	10	0.86	4.5	95.5
Supracrustal rock	Cachoeira de Minas mine (MG-R-224C)	N = 04	15	-57.7	12	0.87	5.4	94.6
Supracrustal rock	São Francisco mine (MG-R-229 &230)	N = 03	25	-57.8	14	0.85	5.5	94.5
Supracrustal rock	Itapetim, east domain (MG-R-166A)	N = 04	26	-57.7	10	0.88	4.8	95.1

Observations:
SLTG = Syn-and post tectonic granite; ESTG = Early-syn tectonic granite; ETG = Early tectonic granite.
NFI = number of fluid inclusion measurements.
DF= degree of fill; Tm CO2 = temperature of CO2 melting; Th CO2 = temperature of liquid-vapour homogenization of CO2; D = density; CH4 = methane; CO2 = Carbon dioxide.
(*) The density and the mole % of CH4 were calculated according to Shepherd et al., (1985; see Appendix A7.2).
(**) The CO2 wt % total of the fluid was calculated: CO2 = 100 - CH4, assumed that H2O = 0 wt %, based on the approach of Van der Kerkhof (1988; see text for details).
Numbers are expressed in mean values; See Appendices A7.12 and A7.13 for further information.

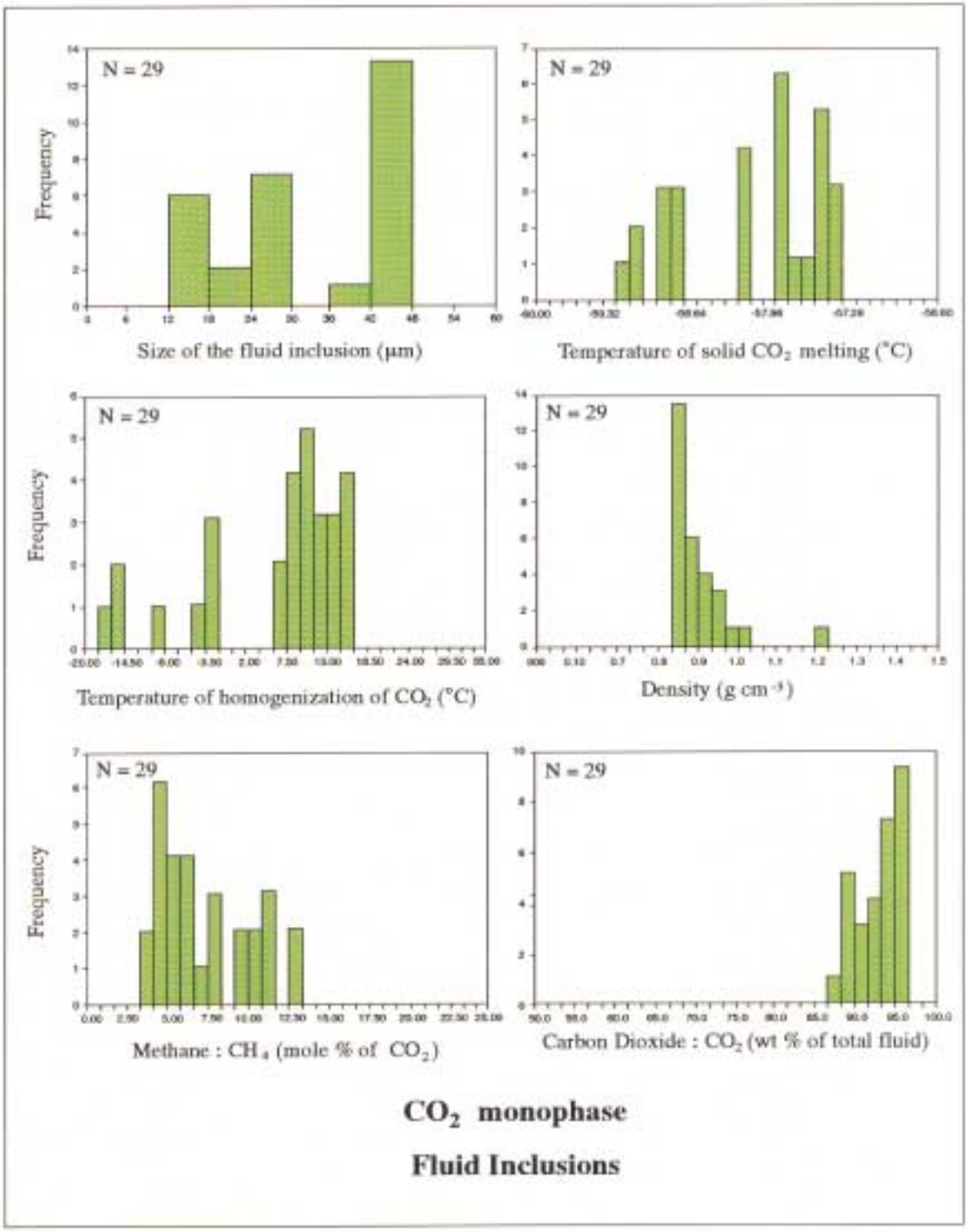

Figure 7. 10 Histograms for CO_2- monophase fluid inclusions in gold-bearing quartz veins hosted by granites and supracrustal rocks showing: size of the fluid inclusions (μm); the temperature of solid CO_2 melting (°C); the temperature of liquid-vapour homogenization of CO_2(°C); the density of the fluid (gcm^{-3}); the amount of methane (mole % CO_2) and the amount of carbon dioxide (CO_2; wt % of total fluid). N = number of fluid inclusion measurements.

Table 7.4

Microthermometric Data for H2O Fluid Inclusions in Quartz Veins Hosted by Granitoids and Supracrustals Rocks

Rock-type	Locality	NFI	Size (μm)	DF	T Im Aq (°C)	T-Th (°C)	S (*) (NaCl eq. % wt)	D (*) (g cm -3)
SLTG	Cacimba Salgada (MG-R-147B)	N = 06	45	0.70	-1.2	275	3.0	0.78
SLTG	Igarape Garapa (MG-R-197B)	N = 08	27	0.80	1.4	282	3.9	0.76
ESTG	Santo Aleixo (MG-R-174B & 222C)	N = 09	25	0.70	1.4	257	6.0	0.83
ETG	Canafístula (MG-R-203D)	N = 07	23	0.70	-1.3	300	1.6	0.72
Supracrustal rock	Cachoeira de Minas mine (MG-R-224C)	N = 10	20	0.90	1.1	280	6.7	0.80
Supracrustal rock	São Francisco mine (MG-R-229 & 230)	N = 10	27	0.70	0.8	250	2.9	0.80
Supracrustal rock	Itapetim, east domain (MG-R-166A)	N = 12	15	0.70	-1.1	352	2.3	0.62

Observations:
SLTG = Syn-and post tectonic granite; ESTG = Early-syn tectonic granite; ETG = Early tectonic granite.
NFI = number of fluid inclusion measurements; DF = degree of fill; D = density;
T Im Aq = temperature of last melting of aqueous phase; T-Th = temperature of total homogenization of the fluid inclusion.
(*) Salinity and density were calculated according to the approach of Shepherd et al., (1985); (see Appendix A7.2)
Numbers are expressed in mean values; See Appendices A7.12 and A7.13 for further information.

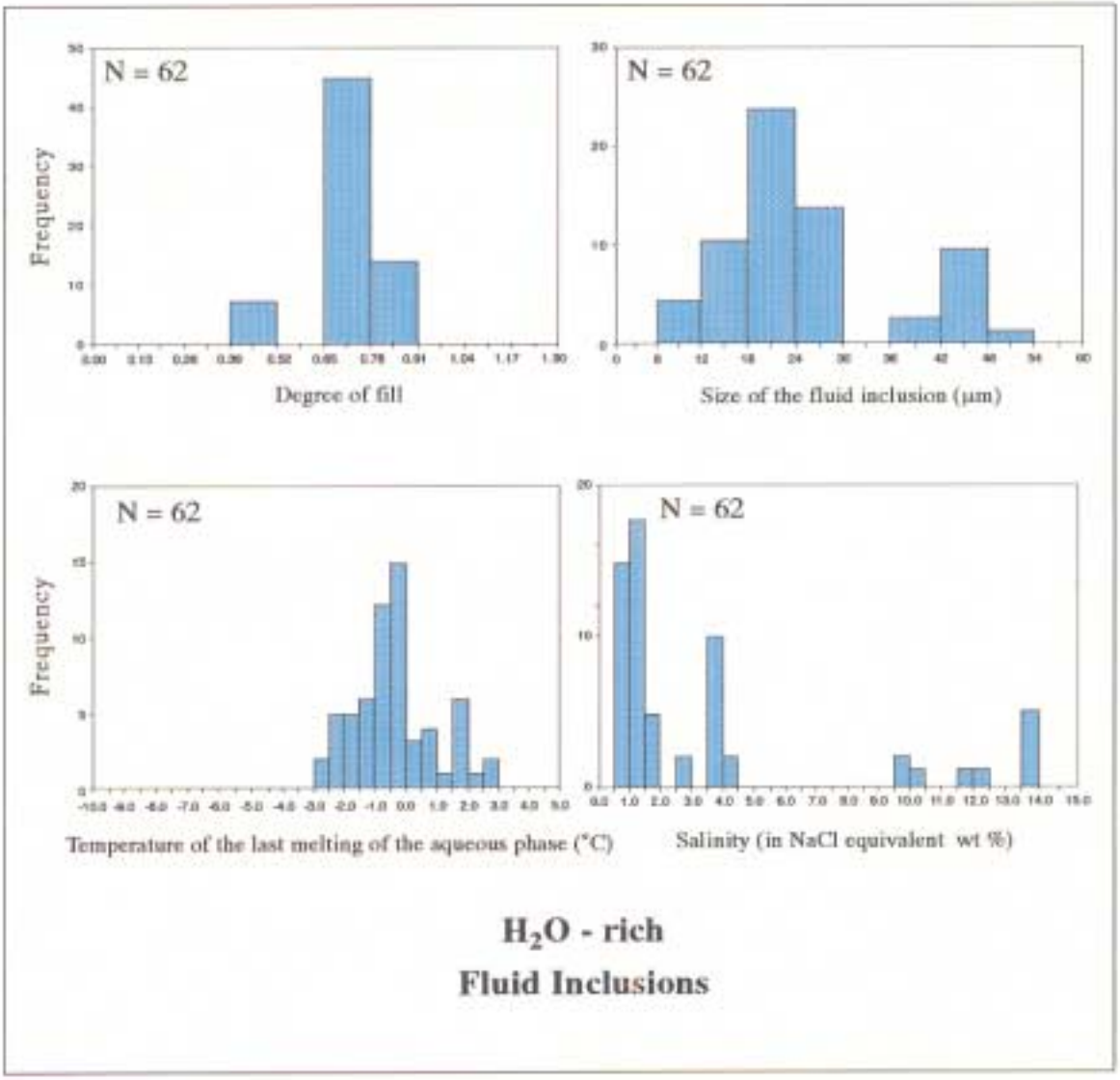

Figure 7. 11 Histograms for H_2O - rich fluid inclusions in gold-bearing quartz veins hosted by granites and supracrustal rocks showing: degree of fill (volume % of aqueous phase in the inclusion cavity); size of the fluid inclusions (μm); the temperature of the last melting of the aqueous phase (°C); and the salinity of the fluid (in NaCl equivalent wt %). N = number of fluid inclusion measurements.

The spatial evidence of contemporaneity shown by the occurrence of the H_2O-CO_2 and CO_2-rich inclusions suggests that both inclusions have been formed from the same CO_2-bearing fluids (Ho *et al.*, 1985; Robert and Kelly, 1987; Xavier, 1991). If they are part of the same system the bulk composition of the CO_2 inclusion can be calculated using the same expression as adopted for the H_2O-CO_2 inclusions. However, to do this it was necessary to assume that for the 'monophase' inclusions:

(i) contain 10 % wt H_2O (as suggested by Crawford and Hollister, 1986).

(ii) the salinity = 0, assuming that the CO_2 phase has negligible solute contents due to strong partitioning of the solutes into the residual liquid phase.

For 29 inclusions a bulk composition is characterised by high values of CO_2 range from ≈ 77.0 to 80.0 mole%. The amount of CH_4 ranges from 3.5 to 10.0 mole %. The content of H_2O is less then 20.0 mole % with a variation from 13.0 to 19.6 mole %. The fluid density ranges from 0.85 to 0.91 g cm $^{-3}$ (Table 7.6).

7.2.6 Fluid Inclusion Pressure and Temperature

Mean values of the CO_2 composition, temperatures of homogenization of the CO_2 phase (Th CO_2), and density of the fluid (plotted on the system H_2O-CO_2-NaCl; Bowers and Helgeson, 1983) allow a minimum pressure of entrapment to be derived from mixed CO_2-H_2O inclusions.

During this study the graphical method developed by Schwartz (1989) was used to predict the pressure of homogenization for the H_2O-CO_2 and the CO_2 monophase inclusions. The technique consists of using only two values of microthermometric measurements (e.g. T-Th; wt % of CO_2; mole % of CO_2; or density of CO_2); the values of the other two variables can be taken from a diagram depicting the relationship between all four variables (see Appendices A7.3 a,b, c and d).

For the CO_2 monophase inclusions, first the predicted temperature of homogenization was determined using the diagram (Appendix A7.3a) showing the relationship between mole % CO_2, the density of the CO_2 phase, and the T-Th CO_2 isotherms for nonsaline CO_2-H_2O inclusions. The values of mole % CO_2 and density were plotted in this diagram and the values of vol. % CO_2 were derived. Secondly, the intersection of the mole % and vol. % CO_2 values plotted in the diagram (Appendix A7.3b) showing the relationship between mole % and vol. % of CO_2 indicate the internal pressure of the inclusion at total homogenization (i.e. the minimum trapping pressure). The data are given in Table 7.6 and were calculated using mean values from all analysed samples grouped into three populations according to the CO_2 content. The minimum pressures derived are: 1.4 kb (< 77.0 mole % CO_2), 0.9 kb (77 to 79 mole % CO_2), and 0.8 kb (> 79 mole % CO_2).

A similar procedure was adopted to calculate the pressures for the system H_2O-CO_2. The values of wt % of CO_2, density, and temperature of homogenization (T-Th) derived from the microthermometric data were plotted in the diagram for CO_2-H_2O-NaCl inclusions at 6 % wt eq. NaCl (Schwartz, 1989; see Appendix A7.3c). The mean values assumed for three populations based on mole % CO_2 (see Table 7.5) indicate the following values for the minimum trapping pressure: 1.4 kb (5 to 10 mole % of CO_2), 1.8 kb (10 to 20 mole % CO_2), and 1.9 kb (> 20 mole % CO_2).

As pointed out by Schwartz (1989) this method works well where the miscibility-gap isotherms intersect the density contours at relatively large angles. In order to minimize errors, where this is not the case, the pressure values were not used (see the blank space in Tables 7.5 and 7.6). To cross-check the values for vol. % CO_2, these values were also calculated using the graph of Roedder (1984). Where the two sets of values show a large difference they were not used (see Tables 7.5 and 7.6).

According to Robert and Kelly (1987), for aqueous and CO_2-rich inclusions interpreted to be contemporaneous and trapped as immiscible fluids (see below), the homogenization temperature of the aqueous inclusions may not represent the temperature of entrapment. These fluids were trapped in different fractures and they were not in equilibrium with one another. According to Kerrich (1989) the homogenization temperature of aqueous fluid inclusions can be significantly lowered by CO_2 effervescence resulting from pressure fluctuations (see Fig. 7.12). Under such conditions, the temperature of homogenization does not represent the temperature of trapping, it is the minimum temperature of the hydrothermal system; thus, an independent geothermometer has to be used. In this case, it was assumed that the formation temperature was in the range 315 to 355 °C from the analyses of chlorite (see Chapter 4). The temperature calculated from the chlorite (mean value 339° C) is in close agreement with the homogenization temperature of the H_2O-CO_2 inclusions (mean value 303 °C; see Table 7.2).

The predicted pressure for both the H_2O-CO_2 and CO_2 monophase systems indicate a minimum entrapment pressure for the fluid inclusions ranging from 0.8 to 2.0 kb. This range of pressure is consistent with the range of 1.0 to 3.0 kb estimated for Archaean gold deposits (Ho *et al.*, 1985). This result is also consistent with the P - T conditions indicated from a combination of chlorite geothermometry and the fluid inclusion isochores (see Fig. 7.14): the suggested range in pressure and temperature is 315 °C - 350°C and 2.0 - 3.4 kb. Based on these data and assuming lithostatic overload, it is suggested that mineralization took place at a depth around 7 to 10 km.

Table 7.5

Bulk Composition, Density, Temperature of Homogenization and Pressure for H2O-CO2 Fluid Inclusions in Gold-Bearing Quartz Veins

Rock-type	Locality (Sample)	NFI	CO2 (mole %)	NaCl (mole %)	H2O (mole %)	CH4 (mole %)	D (**) (g cm -3)	T-Th (*) (°C)	CO2 (***) (vol %)	CO2 (****) (vol %)	P CO2 *** (kb)
SLTG	Igarape Garapa	N = 33	2.9	6.2	90.7	0.2	0.82	289	30.0	10.0	-
	(MG-R-197B)		9.5	3.1	86.8	0.7	0.76	267	26.0	22.0	1.6
			13.6	5.2	80.5	0.8	0.80	291	30.0	32.0	1.8
			23.2	2.2	71.6	3.0	0.84	333	45.0	50.0	2.0
SLTG	Cacimba Salgada	N = 26	3.1	7.0	89.8	0.1	0.86	258	21.0	10.0	-
	(MG-R-147B)		9.8	8.7	80.8	0.7	0.75	260	21.0	22.0	1.6
			11.5	7.7	80.0	0.8	0.82	241	-	30.0	1.6
			-	-	-	-	-	-	-	-	-
ESTG	Santo Aleixo	N = 44	3.4	5.4	91.0	0.3	0.86	324	40.0	10.0	-
	(MG-R-174B & 222C)		9.4	5.3	84.5	0.8	0.73	257	21.0	22.0	1.6
			11.1	5.2	83.3	0.4	0.81	274	25.0	30.0	1.8
			-	-	-	-	-	-	-	-	-
ETG	Canafístnla	N = 25	-	-	-	-	-	-	-	-	-
	(MG-R-203D)		9.5	4.3	85.8	0.4	0.76	305	32.0	22.0	1.6
			11.0	4.8	83.6	0.6	0.81	323	40.0	30.0	1.4
			-	-	-	-	-	-	-	-	-
Supracrustal rock	Cachoeira de Minas mine	N = 18	2.8	5.8	91.4	0.1	0.76	265	21.0	10.0	-
	(MG-R224C)		8.4	0.5	90.9	0.2	0.72	320	38.0	21.0	1.0
			12.2	6.6	81.0	0.2	0.85	312	31.0	32.0	1.4
			-	-	-	-	-	-	-	-	-
Supracrustal rock	São Francisco mine	N = 25	2.2	4.2	93.5	0.1	0.76	285	26.0	10.0	-
	(MG-R-229C & 230)		9.0	0.6	87.3	0.5	0.73	279	26.0	21.0	1.2
			-	-	-	-	-	-	-	-	-
			20.7	4.0	73.0	2.3	0.77	203	-	48.0	2.0
Supracrustal rock	Itapetim (central & east)	N = 22	3.2	8.3	88.5	0.1	0.81	246	-	10.0	-
	(MG-R-159 & 166A)		9.4	4.1	86.7	0.2	0.75	279	27.0	22.0	1.4
			11.3	5.2	83.3	0.2	0.82	345	47.0	30.0	1.4
			-	-	-	-	-	-	-	-	-

Observations:

NFI = number of fluid inclusion measurements

Data are mean values expressed as four populations based on the CO2 mole %: < 5%; 5-10 %; 10-20 %; >20 % (for further information see Appendix A7.16)

(-) interval of mole % CO2 not present; (*) Microthermometric measurements;

Calculated according to the approach of (**) Shepherd et al., 1985; and (***) Schwartz (1989)

(****) data calculated according to the approach of Roedder (1984) used for comparison.

Table 7.6

Bulk Composition, Density, Predicted Temperature of Homogenization and Pressure for CO2 Monophase Fluid Inclusion in Gold-Bearing Quartz Veins

Rock-type	Locality (Sample)	NFI	CO2 (mole %)	CH4 (mole %)	H2O (mole %)	D (*) (g cm -3)	T-Th (**) (kb)	CO2 (**) (vol %)	CO2 (***) (vol %)	P CO2 (**) (kb)
SLTG	Cacimba Salgada	N = 13	76.0	7.4	16.7	0.86	235	90.0	95.0	1.5
	(MG-R-147B)		77.5	9.9	14.2	0.94	220	90.0	96.0	1.5
			80.0	8.4	13.0	1.10	220	92.0	96.5	0.8
ETG	Canafístula	N = 02	-	-	-	-	-	-	-	-
	(MG-R-203D)		77.1	3.5	19.5	0.86	230	93.0	95.0	0.8
			-	-	-	-	-	-	-	-
ESTG	Santo Aleixo	N = 03	76.8	3.6	19.6	0.85	240	91.0	95.0	1.2
	(MG-R-174B &222C)		-	-	-	-	-	-	-	-
			-	-	-	-	-	-	-	-
Supracrustal rock	Itapetim Central & East	N = 04	-	-	-	-	-	-	-	-
	(MG-R-166A & 159)		77.5	3.8	18.8	0.88	230	92.0	96.0	0.8
			-	-	-	-	-	-	-	-
Supracrustal rock	São Francisco	N = 03	76.7	4.3	18.9	0.85	240	90.0	95.0	1.4
	(MG-R-229C & 230)		-	-	-	-	-	-	-	-
			-	-	-	-	-	-	-	-
Supracrustal rock	Cachoeira de Minas	N = 04	-	-	-	-	-	-	-	-
	(MG-R-224C)		77.1	4.2	18.8	0.87	235	93.0	95.5	0.8
			-	-	-	-	-	-	-	-

Observations:

NFI = number of fluid inclusion measurements

Data are mean values expressed as three populations based on the CO2 mole %: <77 %; 77-79 %; >79 % (for further information see Appendix A7.17)

(-) interval of mole % CO2 not present;

Calculated according to the approach of (*) Shepherd et al., 1985; and (**) Schwartz (1989)

(***) data calculated according to the approach of Roedder (1984) used for comparison

7.2.7 Discussion of the Fluid Inclusions Data

Three types of fluid were associated with the development of the quartz veins (see Tables 7.4, 7.5 and 7.6):

(i) A dominant H_2O-CO_2 fluid characterised by low salinity (≈ 6.0 wt % NaCl equivalent) containing varying proportions of H_2O (96.0 to 72.0 mole %) and CO_2 (3.0 to 24.0 mole %), and small amounts of CH_4 (< 3.0 mole %).

(ii) A nonsaline CO_2-rich phase (> 77.0 mole % CO_2) containing small amounts of CH_4 (3.5 to 10.0 mole %) and H_2O (13.0 to 20.0 mole %).

(iii) An aqueous phase of low to moderate salinity (2.0 to 7.0 wt % NaCl).

Coexistence of all the fluid inclusions types (H_2O-CO_2, CO_2 and H_2O) along crack-seal and grain boundaries, as irregular clusters cutting across grain rims, and in healed microfractures suggests some contemporaneity (Fig. 7.1). Several generations of each type of fluid inclusion are present in every sample, as indicated by the multiple cross-cutting healed cracks. Furthermore, the thermometric analyses indicate no significant temperature or compositional differences between the various generations, either in the quartz veins hosted by granites, supracrustal rocks or amphibolite (see Fig. 7.6).

Monophase carbonic inclusions or CO_2-rich inclusions in coexistence with H_2O-rich fluids have been described several times in fluid inclusion studies of quartz veins from Archaean to Phanerozoic mesothermal gold deposits and they are often attributed to immiscibility in the H_2O-CO_2-salt fluid system (Ramboz *et al.*, 1982; Ho *et al.*, 1985; Robert and Kelly, 1987; Walsh *et al.*, 1984). The contemporaneity between the CO_2-rich and H_2O-CO_2 inclusions detected in the present study (see Fig. 7.12) is consistent with the basic criterion to support immiscibility according to Ramboz *et al.* (1982).

Another important criterion for immiscibility, based on the opposing modes of total homogenization of the CO_2 phases (to liquid and vapour for the H_2O-CO_2 and CO_2 monophase respectively; Ramboz *et al.*, 1982) is not present; during this study both inclusions homogenized invariably to liquid. However, for both systems total homogenization of these inclusions took place within the same P-T range, as required for immiscibility.

Experimental data and thermodynamic calculations have also been used to test if the monophase carbonic inclusions are part of an immiscible H_2O-CO_2 fluid system. The system H_2O-CO_2-NaCl has been intensely investigated to test the causes that affect the system equilibria and the relationships between miscibility, temperature and salinity (Takenouchi and Kennedy, 1965; Bowers and Helgeson, 1983). The H_2O-CO_2 fluid system characterised in this study was compared with the solvus determined experimentally for the system H_2O-CO_2-6 wt % eq. NaCl. The value of 6 wt % eq. NaCl is consistent with the salinity range of the H_2O-CO_2 fluids (see Table 7.2). The

values used to make this comparison take into account the ranges of total homogenization temperature (T-Th) of 270 to 387 °C, and 3.0 to 24.0 mole % CO_2 contents from the microthermometric measurements for the H_2O-CO_2 inclusions (Table 7.5). For the CO_2 monophase system the total homogenization temperatures were predicted according to the graphical technique of Schwartz (1989; see Appendix A7.3a). These values vary from 220 to 240 °C. The contents of CO_2 show a variation from 76.0 to 80.0 mole %. As shown in Figure 7.13, these data plot in the T against CO_2 diagram at 2.0 kb in such a fashion as to indicate that these two fluids coexisted at these P-T conditions. Thus, based on the compositional data, it is interpreted that the monophase CO_2 phase in the gold-bearing quartz veins in Borborema Province resulted from vapour separation during immiscibility, and the H_2O-CO_2 phase represents the liquid-rich fluids generated from the same process.

According to this phase separation model, the predominance of the H_2O-CO_2 inclusions (≈ 70 %) in comparison with the rarer CO_2 monophase inclusions (≈ 10 %) is a result of the migration and loss of considerable amounts of vapour during the cyclic crack-seal and crack healing processes of vein growth (Xavier, 1991). During the stages of gradual pressure build-up, due to the progressive sealing of the fluid conduit via the crystallization of the quartz vein, the CO_2-rich vapour phase may undergo condensation and get trapped as monophase carbonic inclusions. The range in the fluid inclusion density values (see Tables 7.5 and 7.6) is probably related to progressive boiling of the fluids. The unmixing of these fluids could have been produced by progressive cooling or by a pressure decrease (Robert and Kelly, 1987).

Xavier's (1991) study of the fluid inclusions in quartz from lode gold deposits in the Itapicuru greenstone belt (Brazil) showed that during continuous deformation under fluctuating P-T conditions, a fluid undergoing immiscibility would trap the carbonic and aqueous phases separately. The fluctuations in pressure may also result in ranges in the density and the temperature of homogenization of the inclusions. The liquid-rich phase tends to be trapped early as H_2O-CO_2 inclusions. On the other hand, the vapour-rich phase tends to separate continuously and migrate within the hydrothermal system. As a result of this phase separation model, inclusions can exhibit different modes of occurrence and do not have to be trapped in cavities at exactly the same time and place (Ramboz *et al.*, 1982). Thus the different modes of occurrence shown by the fluid inclusions in this study appear to be consistent with a fluid undergoing simultaneous immiscibility.

Many of the CO_2-rich inclusions in the gold-bearing quartz veins in the present study appear to contain methane. However, the amount of CH_4 shows a distinct range for both CO_2-rich and CO_2-poor systems (see Tables 7.5 and 7.6). In the H_2O-CO_2 inclusions the amount of CH_4 is lower (0.1 to 3.0 mole %) compared with the values obtained for the CO_2 monophase inclusions (3.5 to 10.0 mole %). The variability in

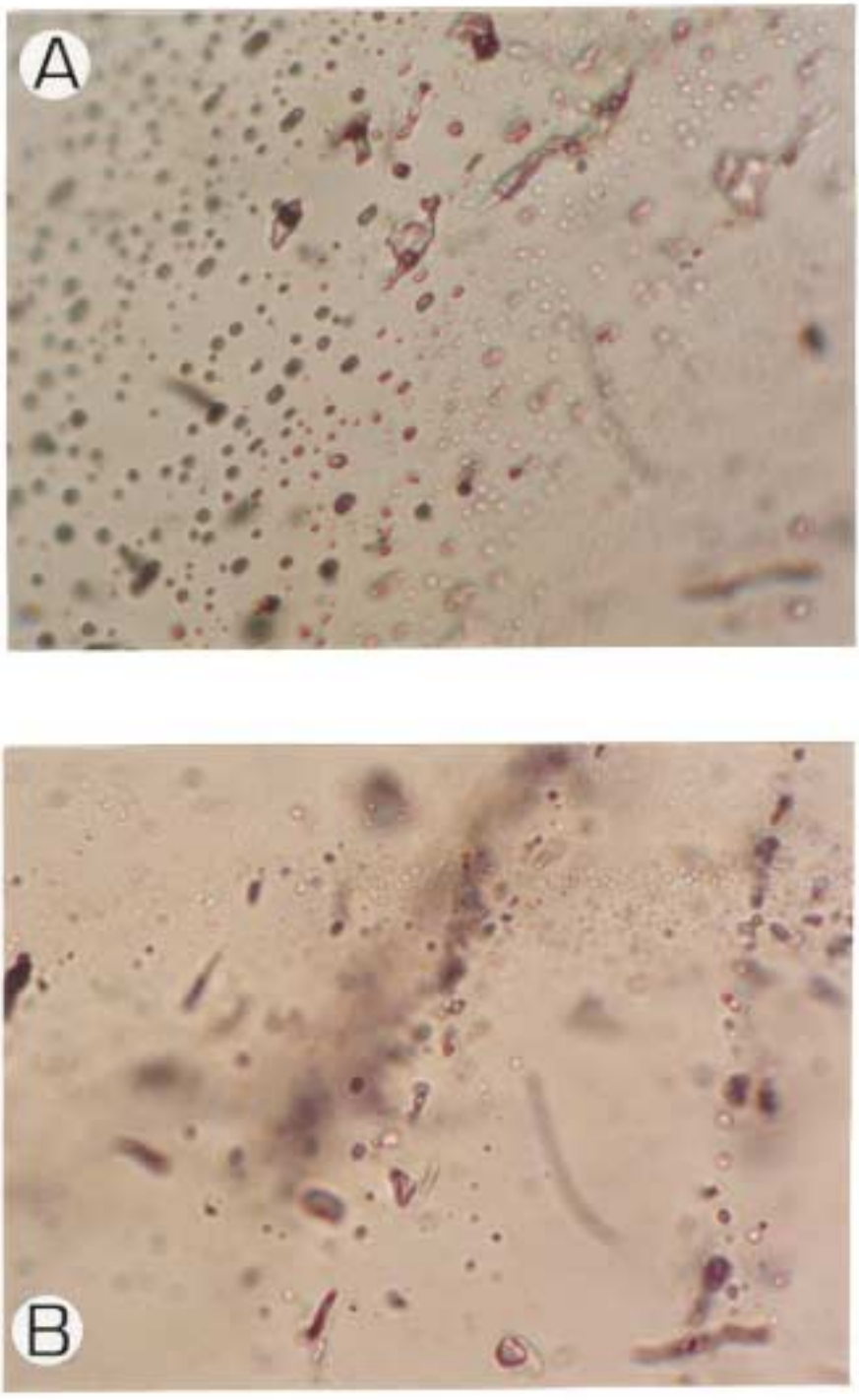

Figure 7.12 (A) Evidence of CO_2 effervescence with coeval CO_2-rich (the smallest) and H_2O-CO_2 inclusions (the largest) showing different CO_2 contents; (TL; WOF = 750 μm; MG-R-174, Santo Aleixo); (B) Evidence of CO_2 effervescence coeval CO_2-rich and H_2O-CO_2 inclusions along trails. (TL; WOF = 500 μm; MG-R-197, Igarape Garapa).

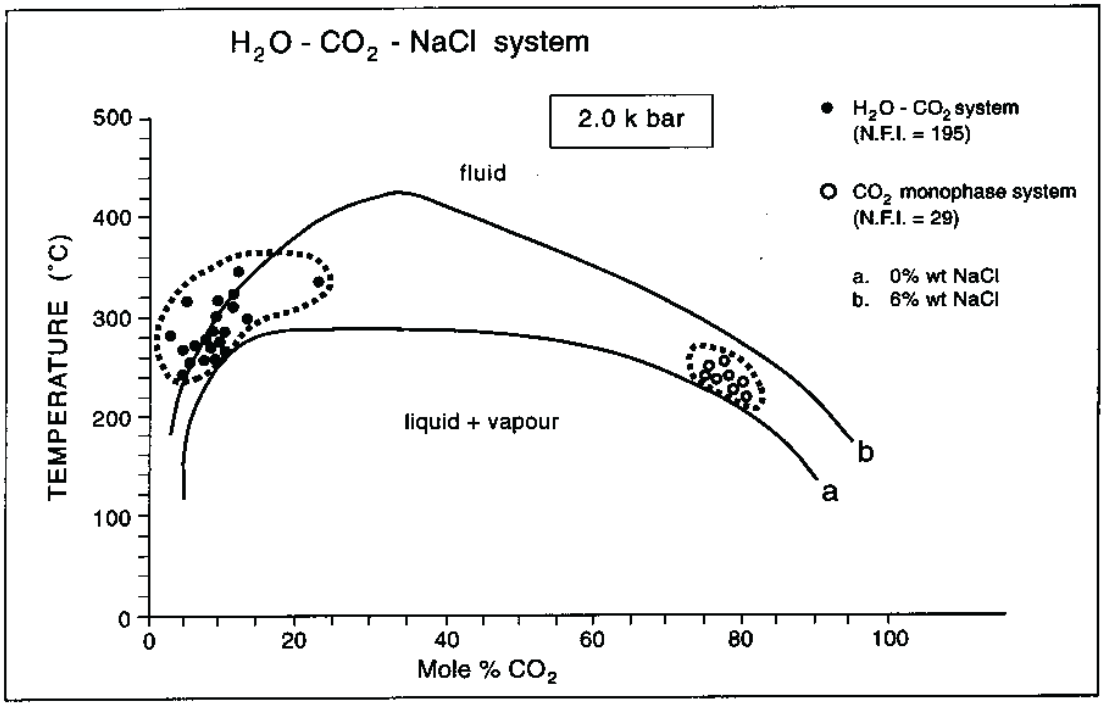

Figure 7.13 Compositions of H_2O - CO_2 and monophase CO_2 - rich fluid inclusions in relation to the solvus for the H_2O - CO_2 - NaCl system at 2.0 k bars and 0 and 6 wt % NaCl (Bowers and Hegelson, 1983) within the predicted range of temperature of total homogenization for the CO_2 - rich inclusions (Schwartz, 1989). For further information see Tables 7.5 and 7.6.

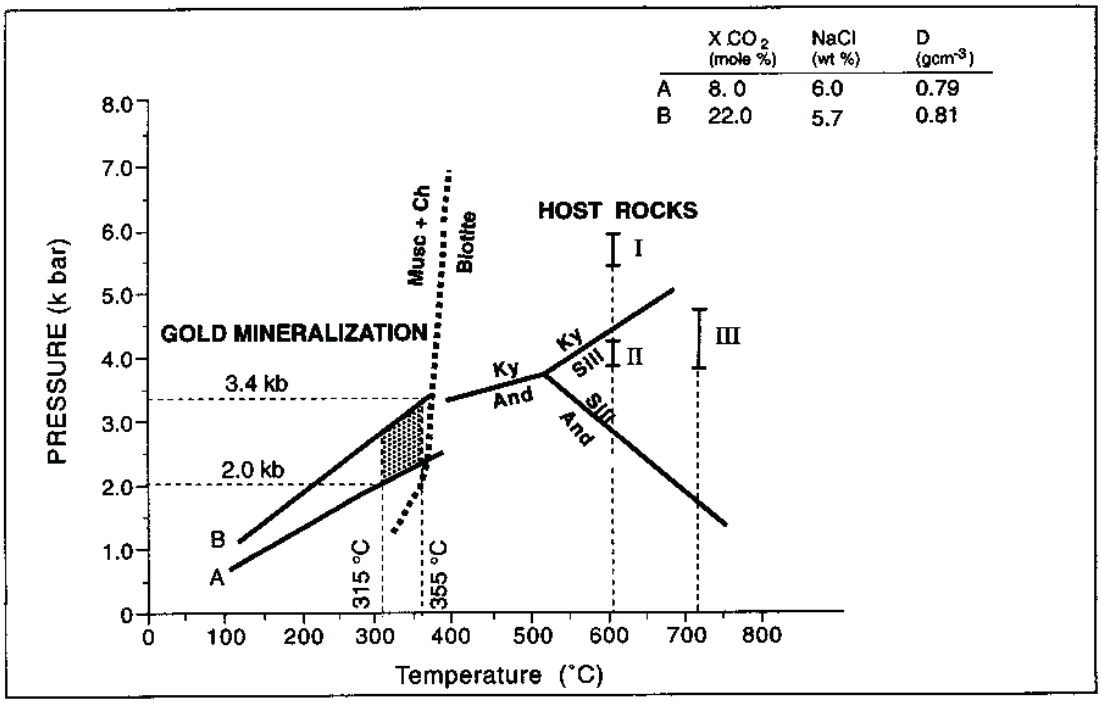

Figure 7.14 P - T conditions for hydrothermal fluids inclusions (stippled area). The temperature was calculated from chlorite analyses (Cathelineau, 1988). Pressure was calculated using the isochore plot. For further information see Tables 7.6 and 7.7. The univariant stability fields of the Al - silicates (Holdaway, 1971) and the curve that marks the first appearence of biotite as determined experimentally (Nitsch, 1970) are used as reference. Pressure and temperature of metamorphic facies in the host rocks (I = Itapetim area; II = São Francisco mine and III = Boqueirão dos Cochos area) are indicated.

CH_4 mole % suggests fluctuating fO_2 during entrapment of theses fluids. Separation of immiscible fluid phases and changing oxygen fugacities are important for the mobilisation of gold as the Au $(HS)_2^-$ complex, and for subsequent gold precitipation (see Robert and Kelly, 1987; Xavier, 1991; Xavier *et al.*, 1994).

Although some assumptions are involved, the fluid inclusion study can be combined with structural and mineralogical observations to place constraints on the P-T conditions of the gold-bearing fluids. These Au-bearing fluids were associated with crack healing (type III) and were trapped at a late stage, after recrystallization. This is supported by the association of gold with sulphides and chlorite that occur along the cracks marked by later fluid enrichment (see Figs. 3.47 and 3.48, Chapter 3).

This fluid immiscibility may have occurred in response to cooling and pressure reduction caused by regional uplift and consequent retrogressive metamorphic activity (see Hollister and Burruss, 1976).

7.3 STABLE ISOTOPES

7.3.1 Introduction

The source of the hydrothermal fluids in mineral deposits has been an extensively debated and is still an unsolved problem in the genesis of Precambriam gold deposits, although the amount of data available is significant (Colvine *et al*, 1988; Kerrich, 1989). The fluid and its dissolved components have variously been attributed to:

(i) *Mantle source* (Fyon *et al.*, 1984; Colvine *et al*, 1984; Colvine *et al*, 1988; Cameron, 1988).

(ii) *Magmatic fluids* (Burrows *et al.*, 1986; Wood *et al.*, 1986; Burrows and Spooner, 1986; Spooner , 1991; Cameron and Hattori, 1987; Hattori, 1987).

(iii) *Metamorphic processes (e.g. dewatering during retrogressive metamorphism* ; Kerrich and Fryer, 1979; Kerrich and Fyfe, 1981; Kerrich, 1983; Kerrich, 1987; Golding *et al.*, 1987; Groves and Phillips, 1987).

(iv) *Highly -evolved meteoric waters* (Nesbitt *et al.*, 1986).

The analysis of minerals and fluid inclusions for oxygen, hydrogen, and carbon isotopes provides an effective means of studying the origin and the history of fluids in crustal hydrothermal systems and mineral deposits (Clayton *et al.*, 1968; Taylor, 1979). A study of the δ^{18} O values of quartz and δ^{13} C in fluid inclusions in gold-bearing quartz veins was carried out to elucidate the source of the hydrothermal fluids. Unfortunately, due to logistical problems, it was not possible to complete a H isotope study of the fluid inclusions.

7.3.2 Methody of study

Eight samples of gold-bearing quartz veins hosted by granites, supracrustal rocks, and amphibolite were analysed for fluid inclusion δ^{13} C at RHBNC. The results are given in Table 7.7 and further information concerning the sample locations are given in Table 7.1.

Quartz vein samples were crushed in a jaw-crusher, sieved to remove the > 0.5 and < 2.0 mm fraction, and then a pure quartz concentrate was separated by hand under a binocular microscope. Around 0.5 g of quartz were boiled in concentrated HNO_3 for several hours, repeatedly washed in doubly distilled and deionized water, and dried at 50 °C. Fluid was released from a sample by decrepitation in a vacuum. A step-heating procedure was utilised to monitor the pattern of fluid release. This was carried out at nine 100 °C temperature intervals, from 300 to 1200 °C. H_2O and non-condensible gases were removed using a variable temperature liquid-nitrogen trap, and CO_2 was collected for mass-spectrometric analysis.

The isotope ratios were measured on a Micromass 602C mass-spectrometer, equipped with an inlet system suitable for handling small samples. 45/44 ratios were corrected for coincidence of ^{12}C, ^{16}O, and ^{17}O ions, and 46/(44+45) ratios for the contribution of mass 45 to the major peak. The analytical precision is 0.1 ‰ (per mil).

The δ^{18} O analyses were performed by NIGL personnel at the British Geological Survey, Keyworth. Approximately 50 mg of quartz grains from ten samples (see Table 7.7) were reacted with ClF_3 in a nickel bomb at 600° C. The recovered oxygen was converted to CO_2 by reaction with a hot carbon rod and the CO_2 was analysed using a mass spectrometer.

The isotopic data reported as δ (delta) are expressed in $^0/_{00}$ (per mil). The standards used were standard mean ocean water (SMOW) for oxygen, and Pee Dee Belemnite (PDB) for the carbon.

7.3.3 Discussion of the δ^{13} C Analyses of Fluid Inclusions

Archaean gold deposits are often characterised by the presence of abundant hydrothermal carbonate, either in the quartz veins (Kerrich, 1989) or as part of the wallrock assemblage (Kerrich and Fyfe, 1981). However, in Borborema Province, this mineral appears to be very rare. Locally, in the wallrock alteration assemblages which envelop the vein system, predominantly in mafic rocks (Itapetim District, central domain), carbonate (calcite and magnesite) sometimes occur associated with chlorite, epidote and albite. On the other hand, the fluid inclusions in the gold-bearing quartz veins are dominantly rich in CO_2 and thus were utilised for C-isotopic analysis.

The analyses of the fluid inclusions for all quartz veins show a total range of mean values of δ^{13} C from - 7.60 to - 2.11 $^{0}/_{00}$ (per mil, PDB; see Table 7.7). The distribution of δ^{13} C mean values with temperature is given in the Figure 7.15a and the full data in the Appendix A7.18. There appears to be no consistent pattern of fluid composition and temperature of fluid release, and so only mean values have been utilised. Furthermore, in some samples a large amount of C with anomalous composition is released at the highest temperature; this could perhaps represent a small amount of mineral (e.g. carbonate) contamination. The variation in δ^{13} C values in quartz veins hosted by different rock-type appears to be almost identical.

The difference in δ^{13} C values between populations of veins can be explained either by: (i) the different δ^{13} C values from the host lithologies encountered along the plumbing system (Kerrich, 1989); or (ii) the CO_2 immiscibility, similar to that in the McIntry mine, Timmins, Canada, where a small range (≈ 2.0 %) in δ^{13} C data is attributed to immiscible separation of CO_2 + CH_4 (Smith *et al.*, 1984). However, (ii) is more likely as it is in agreement with the fluid inclusion study, which suggests immiscibiliy of fluids. Differential effects of mixing between fluids and host rocks is also not indicated from the wallrock alteration study.

The range of δ^{13} C from - 7.60 to - 2.11 $^{0}/_{00}$ is consistent with the range for fluids from Precambrian gold deposits (see Fig. 7.15b), typically from - 9.00 to - 0.40 $^{0}/_{00}$ (Kerrich, 1989). In the Norseman-Wiluma greenstone belt (Western Australia), magnesite developed along early thrust faults has values of δ^{13} C from - 7.0 to - 2.5 $^{0}/_{00}$, and these data have been interpreted as C derived from a deep magmatic (possibly mantle) source (Kerrich, 1989). The close agreement with this result, and taking in account the range in the δ^{13} C values for the Precambrian gold deposits, suggests that the C in gold-bearing quartz veins in Borborema Province may be mantle-derived (Fig. 7.17), but modified by immiscibility. It is consistent with the structural environment, related to crustal-scale shear zones which act as conduits for fluids with a 'deep' source (Kerrich, 1986).

7.3.4 Discussion of the δ^{18} O Isotope Results in Quartz

The δ^{18} O values of gold-bearing quartz veins in Borborema Province show a range from 4.5 to 14.50 $^{0}/_{00}$ (Table 7.7). The large range embraces deposits distributed over a huge area (450.000 km^2), in different geological and geotectonic settings, and variously hosted lithologies (granites, supracrustal and amphibolite rocks). The highest values were found in the granitoid SLTG (MG-R-197B), while the lowest occur in the supracrustal rocks (Itapetim central area, MG-R-159).

Although variations in δ^{18} O values of minerals are related to a number of

Table 7.7

Oxygen and Carbon Isotope Data for Quartz and Fluid Inclusions in Gold-Bearing Quartz Veins

Sample	Rock-type	Locality	δ 18 O (quartz) (per mil SMOW)	δ18 O (H2O) (per mil SMOW)	δ13 C (range) (per mil PDB)	δ13 C (mean value) (per mil PDB)
MG-R-197B	SLTG	Garapá 'garimpo'	12.80 12.79	7.19 7.18	(-1.92 to - 4.51)	-3.17
MG-R-147B	SLTG	Cacimba Salgada 'garimpo'	11.10	5.49	-	-
MG-R-222C	ESTG	Guilhermina 'garimpo', Santo Aleixo area	7.95 7.94	2.34 2.33	(- 5.90 to - 9.24)	-7.60
MG-R-203D	ETG	Canafistula 'garimpo'	7.02 7.06	1.41 1.45	(- 0.33 to -12.43)	-2.54
MG-R-205B	Supracrustal	Ze Ferreira 'garimpo', Itapetim-West Domain	10.00	4.39	-	-
MG-R-159	Supracrustal	Sertãozinho, Itapetim-Central Domain	4.45 4.60	-1.16 -1.01	(- 1.77 to - 6.56)	-2.99
MG-R-166A	Supracrustal	Pimenteiras 'garimpo', Itapetim-East Domain	12.50	6.89	(- 0.53 to - 4.28)	-2.36
MG-R-224C	Supracrustal	Cachoeira de Minas mine	14.50	8.89	(- 0.43 to - 3.70)	-2.11
MG-R-229C	Supracrustal	São Francisco mine, Morro Pelado shear zone	13.20	7.59	(- 5.45 to - 9.33)	-7.14
MG-R-208C	Amphibolite	Boqueirão dos Cochos	11.10	5.49	(- 1.00 to - 5.69)	-3.41

Observations:

δ 18 O quartz by fluorination; analysed in the Isotope Geosciences Laboratory, British Geological Survey, Nottingham.

δ 18 O (H2O) compositions calculated based on the quartz-H2O isotope fractionation of Matsuhisa et al. (1979).

δ 13 C of fluid inclusions analysed 300°C to 1200°C in the Stable Isotope Laboratory at Royal Holloway College.

Temperature based on the composition of chlorite (339° C) using microprobe analyses.

SMOW = standard mean ocean water; PDB = Pee Dee belemnite; Numbers are expressed as mean values.

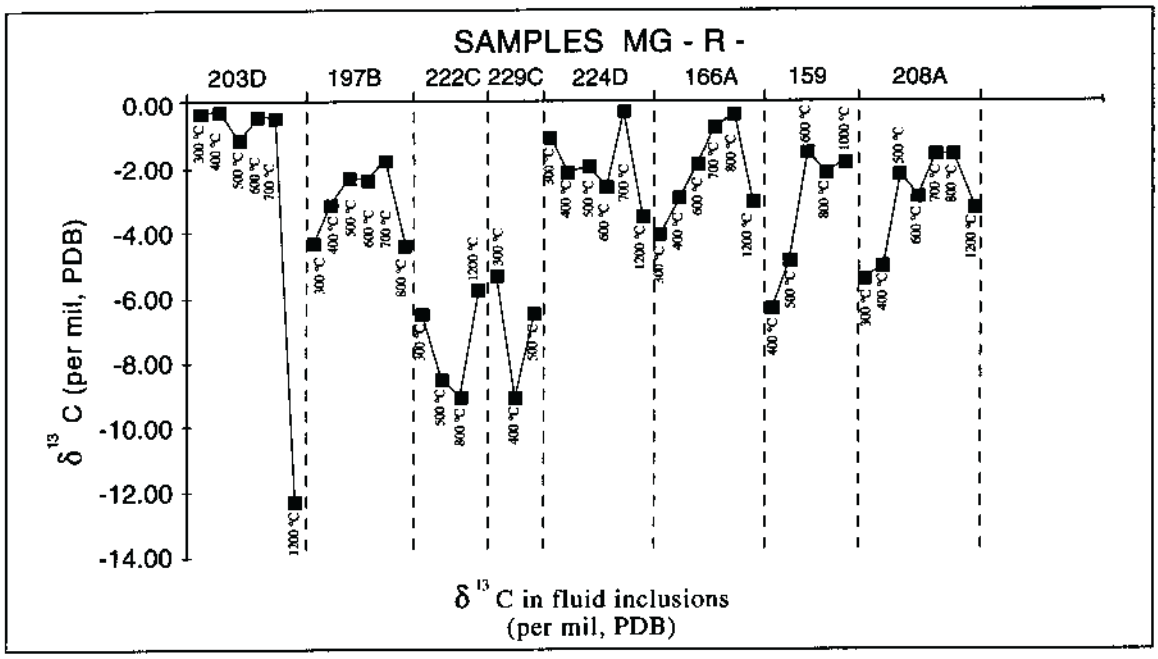

Figure 7.15a $\delta^{13}C$ data for fluid inclusions from gold-bearing quartz veins in Borborema Province, N.E. Brazil. Note the range and the distribution of the data for each analysed sample (see Appendix A7.18).

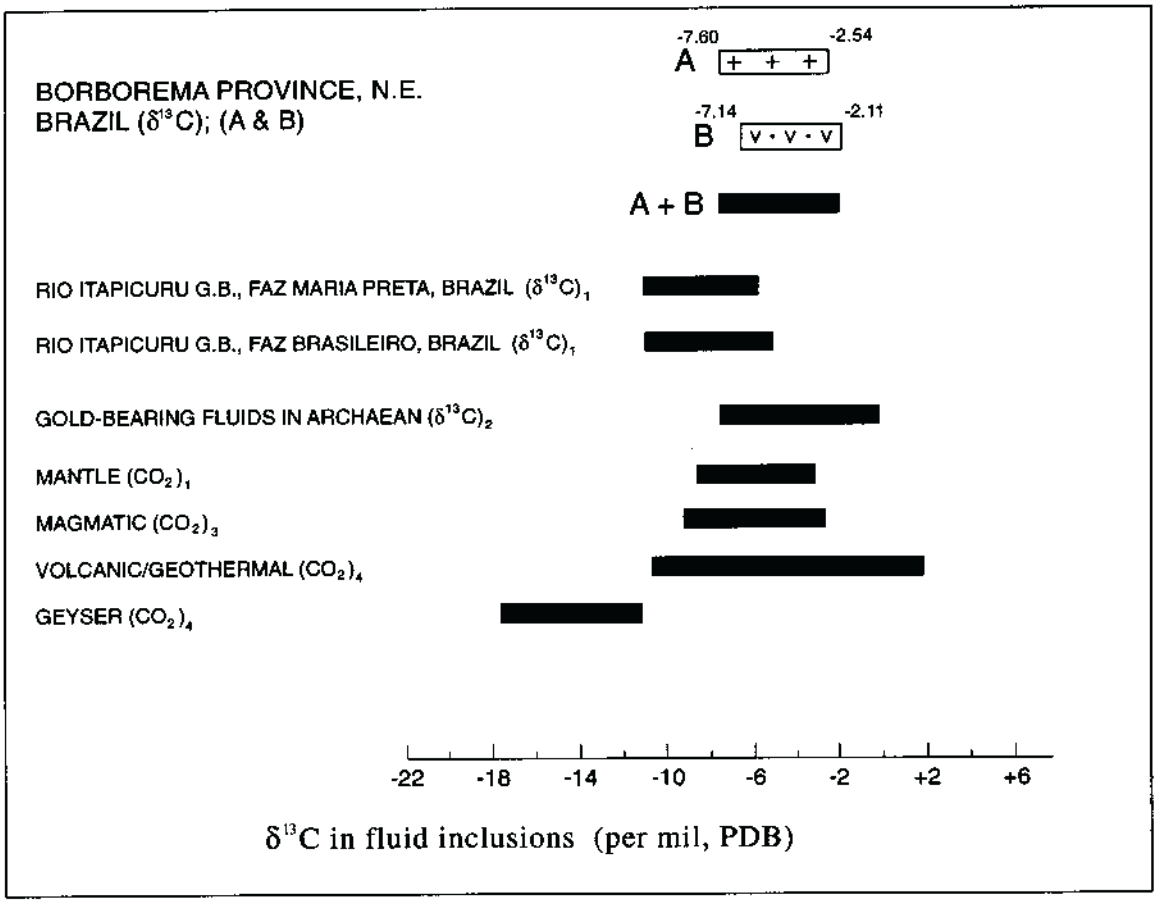

Figure 7.15b $\delta^{13}C$ mean values from fluid inclusions in gold-bearing quartz veins (A = quartz veins hosted by Early and Late Proterozoic granitoids and B = quartz veins hosted by Early Proterozoic supracrustal sequences and Archaean amphibolite) in Borborema Province, N.E. Brazil. For comparison note the range of $\delta^{13}C$ of fluids from other environments: (1) Xavier, 1991; (2) Colvine *et al*, 1988; (3) Giggenbach, 1982; Taylor, 1977; Chivas *et al*, 1987; (4) Field and Fifrek, 1985.

independent parameters (Kerrrich, 1989), the two primary variables involved are temperature of deposition and the δ^{18} O value of the water. The δ^{18} O value of the water is strongly dependent on how much the initial water input has been modified by isotopic exchange with previously unaltered rock along the pathway through the crust or by mixing of different fluids.

Accordingly, the large scatter in δ^{18} O values (see Fig. 7.16a) can be explained by either: (i) a variation in the temperature of mineralization; or (ii) heterogeneity of the hydrothermal fluids. However, the chlorite geothermometry and fluid inclusion studies do not indicate a large range in the temperature of ore-formation in the analysed deposits. Thus, δ^{18} O variation is more likely due to variation in isotopic composition of the fluid.

7.3.5 Discussion of the δ^{18} O Values of Water

Isotopic exchange between the oxygen in the fluid inclusions and that in the host quartz do not allow the derivation of δ^{18} O fluid compositions directly from the fluid inclusions. The δ^{18} O compositions of the hydrothermal fluids coexisting with quartz must be calculated indirectly from the analyses of quartz, given an appropriate quartz-H_2O fractionation equation valid for the range of temperature of formation of the quartz vein. The quartz-H_2O fractionation equation of Matsuhisa *et al.* (1979) was used, as this is applicable over the range 250-500°C :

$$\delta_A - \delta_{H2O} = X + (Y \times 10^6 \times T^{-2})$$

where: $\delta_A = \delta\ ^{18}O$ quartz

T = temperature in ° K

X = - 3.34 (constant)

Y= 3.31 (constant)

The temperature was assumed from chlorite geothrmometry (339 °C; see Chapter 4). Thus, since the δ^{18} O of quartz is known, the δ^{18} O of H_2O can be calculated.

The δ^{18} O_{H2O} results thus derived show a range approximately from - 1.00 to + 9.00 $^0/_{00}$ (Table 7.7), and there is little correlation between host rock and fluid composition. The lowest value (- 1.01 $^0/_{00}$) was found in the supracrustal rocks from Itapetim central area (MG-R-159), whereas the highest (+ 8.89 $^0/_{00}$) also occurs also in supracrustals, in Cachoeira de Minas mine. This range of values is mostly outside the range for magmatic fluids (typically 6 to 9 $^0/_{00}$; Taylor, 1979). The fluids may have a component of magmatic fluid in them, but must also contain a substantial amount derived from another source, such as convection meteoric water or metamorphic fluids. Possibly, the aqueous fluid inclusions observed in the fluid inclusion study may represent one additional fluid entrained into the system. Thus, the variation in O-

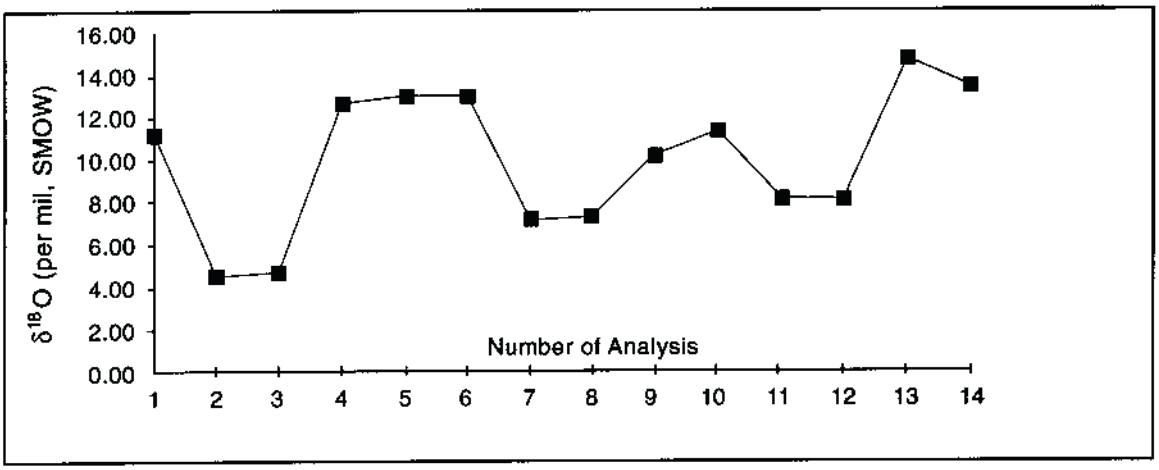

Figure 7. 16a $\delta^{18}O$ values for gold-bearing quartz veins of Borborema Province, N.E. Brazil (see Appendix A7. 18)

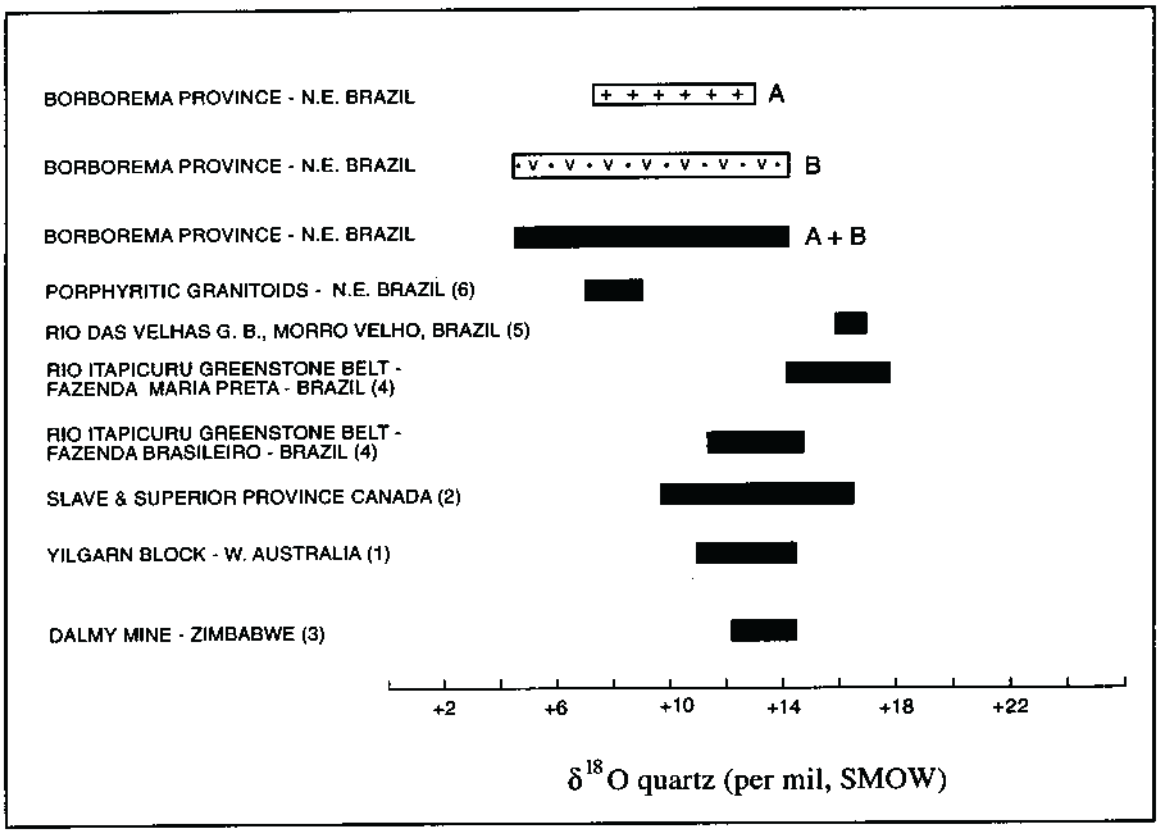

Figure 7.16b $\delta^{18}O$ values for gold-bearing quartz veins (A = quartz veins hosted by Early and Late Proterozoic granitoids and B = quartz veins hosted by Early - Middle Proterozoic supracrustal sequences and Archaean amphibolite) of the Borborema Province, N.E. Brazil. For comparison note the range of $\delta^{18}O$ observed in other Archaean gold deposits, based on the data from (1) Golding and Wilson (1987); (2) Colvine *et al.* (1988); (3) Carter (1991); (4) Xavier (1991); and (5) Ladeira (1988). Data source from Borborema porphyritic granitoids is also used (6) McMurry *et al.*, (1987).

isotopic composition is most likely related to different amounts of fluid mixing and/or water/rock interaction. Immiscibility and the presence of graphite in the supracrustal rocks may alter the δ^{18} O isotopic composition of the fluid, although it is unclear at present whether such effects can be significant (e.g. Bottinga, 1968; Smith and Kesler, 1984). However, there appears to be no correlation between the δ^{18} O and δ^{13} C values, so the causes of the variations must be different for each component.

The variation in the δ^{18} O data for the gold-bearing quartz veins compares well with the range of values for other Precambrian gold deposits (Figs. 7.16b and 7.17). Thus, it is interpreted that the variations in the δ^{18} O values of the hydrothermal system in Borborema Province reflect the change in the isotopic compositions related to mixing of the fluid rather than variation in the isotopic composition of the initial fluid reservoir. Unfortunately, the lack of H-isotopic data does not allow a more accurate constraining of the possible fluid sources.

7.4 CONCLUSIONS

The fluid inclusion and stable isotpe studies have placed several constraints on the nature and source of the gold-bearing fluids in Borborema Province. Although some assumptions have been adopted, the following interpretation is proposed:

(i) The hydrothermal fluid from which the gold-bearing quartz veins crystallised is characterised by moderate temperatures range from 270-350 °C, a pressure varies from 2.0 to 3.4 kb, low salinity (≈ 6.0 wt % NaCl) and small amounts of CH_4. This fluid was originally homogeneous and rich in CO_2 but unmixing caused separation of CO_2-rich and CO_2-poor or H_2O-CO_2 phases. This unmixing is believed to be related to the abrupt pressure drops during the development of large-scale vein increments under fluid pressure. The P - T conditions suggests a depth of mineralization close to lithostatic conditions estimated around 7 to 10 km.

(ii) Three stages are proposed for the hydrothermal system evolution:
I An initial CO_2-rich fluid.
II The amount of water increases as CO_2 drops because of immiscibility
III The production of volatile-rich fluids stops and the fluid becomes essentially aqueous.

(iii) The progressive and rapid variations in the volatile-bearing phase contents (e.g. CH_4, H_2, H_2S), and the separation of the CO_2 as a consequence of the

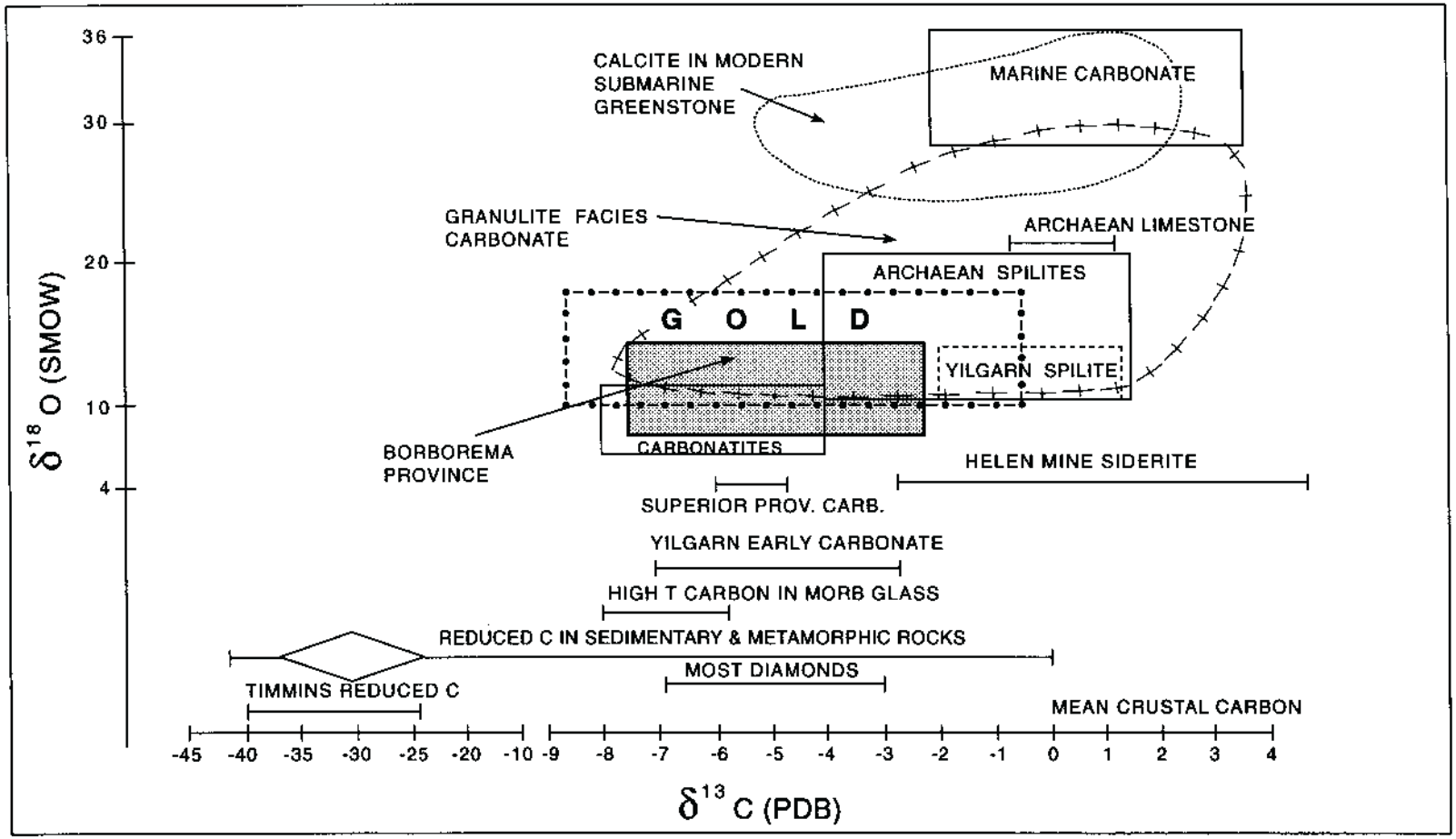

Figure 7.17 The $\delta^{18}O$ and $\delta^{13}C$ isotope fields of various $\delta^{13}C$ reservoirs used for comparison with Borborema data (Kerrich, 1989). The fields and the equivalent data sources are: Carbonatite and granulite facies carbonates: Valley (1986); Calcite in modern submarine greenstone: Muehlenbachs and Clayton (1972); High temperature $\delta^{13}C$ in MORB glass: Taylor (1986); Marine carbonate; most diamonds and reduced $\delta^{13}C$ in metamorphic and sedimentary rocks: Ohmoto and Rye (1979). Estimate of average crustal $\delta^{13}C$: Hoefs (1978) and Ohmoto and Rye (1979); Reduced $\delta^{13}C$ in Superior Province: Schoell and Wellmer (1981); Superior Province carbonate (SPC): Strauss (1986); Archaean organic $\delta^{13}C$: Schidlowski (1988); Yilgarn spilites and early carbonates: Groves *et al.*, (1988); Helen mine siderite: Thode and Goodwin (1983). Note that the Borborema data overlap the fields of the gold Precambrian deposits (Kerrich, 1989); the carbonatite field and part of the Archaean spilites.

pressure fluctuations, increase the pH. This results in the oxidation of the fluid (Bowers, 1991). It is inferred that the gold was precipitated from cooling hydrothermal fluid, as a result of immiscibility. The cooling was a result of boiling of the fluid, in direct response to episodic hydraulic fracturing providing conditions for pressure fluctuations (hydrostatic pressure exceeding lithostatic pressure). During the boiling of the fluid, the concentration of the H_2S in the residual fluid drops, thus resulting in a change of pH and the destabilization of gold-bearing complexes.

(iv) The range of the δ^{18} O data (7.0 to 14.5 $^0/_{00}$) in the gold-bearing quartz veins is similar to that of other Precambrian gold deposits (Kerrich, 1989). The hydrothermal fluids contained a large component derived from a non-magmatic source, although mixing with magmatic fluids cannot be ruled out. Such non-magmatic fluids could include convection meteoric waters.

(v) The δ^{13} C data are consistent with magmatic, possibly mantle-derived values (Groves *et al.*, 1988), the source regions of which were isotopically uniform with respect to δ^{13} C. Isotopic changes occurred after the fluid left its source, either by fluid, mixing, by fluid/rock interaction, or as a result of immiscibility.

(vi) This study confirms the complex nature of the gold-mineralizing process in Pre-Cambrian terranes, and in particular the presence of several sources for vein components.

CHAPTER 8 A MODEL FOR GOLD MINERALIZATION IN BORBOREMA PROVINCE

8.1 GEOLOGICAL SETTING AND EVOLUTION OF THE AREA

An understanding of the geological evolution of the Borborema Province is crucial as a basis for determining the source and genesis of the gold mineralization. Although the province shows a complex crustal evolution, the general structural features consist of a mosaic of Archaean-Early Proterozic massif terranes surrounded by Proterozoic fold belts. An evolutionary model comprising three stages and involving tectonism, fluid mobilization, and mantle heat flow, is proposed for this accreted terrane (Fig. 8.1):

(i) A rifting phase produced break-up of the original continental crust which consisted of migmatite/gneiss terranes (basement) derived from tonalite-trondjemite-granite (TTG), supracrustals, and plutonic rocks, during the Archaean-Early Proterozoic (> 2.5-1.8 Ga). This rifting phase was followed by sedimentation and magmatism.

(ii) Subduction associated with convergent plates produced a magmatic arc, back arc basins, and a convergent-margin orogenic belt, where sedimentation, plutonism and bi-modal volcanism took place, during the Middle Proterozoic (1.8-0.9 Ga).

(iii) Continent-continent collision produced crustal shortening and consequent tectonic thickening associated with uplift, resulting in crust-scale shear zones and synkinematic plutonism, during the Late Proterozoic (0.9-0.57 Ga). The gold mineralization is related to this stage (≈ 0.8 Ga).

8.1.1 The Extensional Regime: Rifting (Archaean-Early Proterozoic)

During *stage I*, a thickened continental crust comprising the São Francisco (Brazil) and Western Africa cratons, was broken up. Terranes such as the Pernanbuco-Alagoas and Rio Piranhas massifs in Brazil and some relict massifs in Western Africa are the products of the rifting of an original supercontinent during this time (Caby, 1989; Brito Neves and Cordani, 1991). As a consequence of the lack of geological information, these massif terranes are poorly understood. However, they consist of migmatite/gneiss TTG plutonics with mafic and ultramafic rocks, granite and granodiorite batholiths, and folded cover with minor mafic rocks (metasediment-volcanic sequences). Mg-rich

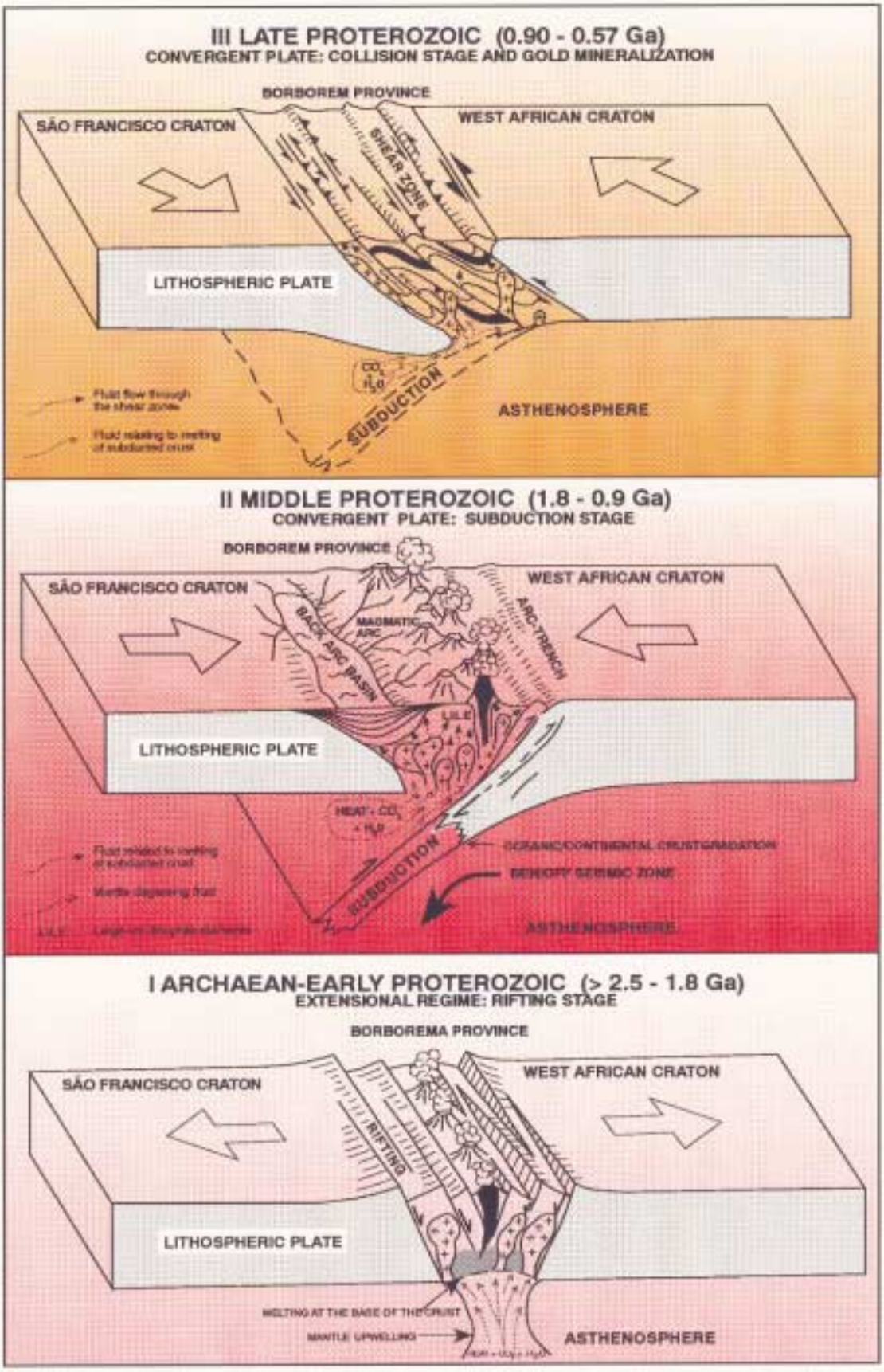

Figure 8.1 Borborema Province Evolution

amphibolite, associated with volcanic breccias, tremolite schist, calc-silicate rocks and Al-rich metapelitic schists, and local banded iron formation, form the folded cover. These sequences have been interpreted as an Archaean greenstone belt precursor (Brito Neves, 1975). Gold-bearing quartz veins occur intercalated in the mafic lenses in the migmatite/gneiss terranes, although they are rare and small. An age of 3.5-2.9 Ga is proposed for the massif terranes and their consolidation occurred at the end of the Trans-Amazonian Orogeny (2.1-1.8 Ga; Brito Neves and Cordani, 1991).

Evidence of the early rifting in Borborema Province, for example a suture zone, could be the eclogites (Beurlen, 1988; Beurlen *et al.*, 1991) formed at the contact between the Pajeú/Paraíba Fold Belt and the Pernambuco Massif. Anorthosites associated with Fe-Ti mineralization are interpreted also as the early products of rifting of original crust. A cryptic suture existing along the boundary of the Western African and São Luiz cratons (south-western of Borborema Province) was suggested by Burke and Dewey (1973) based on a tectonic model.

In response to deformation during the Early Proterozoic (< 2.5-1.8 Ga) a period of continental sedimentation associated with alkaline volcanism took place (e.g. Jucurutu and Equador formations). Partial melting at the base of the crust, and decarbonatization of the upwelling mantle resulted in the emplacement of granitic rocks and alkaline volcanism (e.g. 'Oros' volcanism dated at 1.7 Ga; Sá *et al.*, 1991). Geochemical data indicate that these (ETG) granites are peraluminous and relatively highly fractionated granites with a high amount of crustal material (S-type).

8.1.2 Convergent Plates: The Subduction Stage (Middle Proterozoic)

Stage II covered the Middle Proterozic and extended from 1.8 to 0.9 Ga. This period saw an increase in thermal and tectonic underplating activity. As a consequence of the melting of the lower crust, the heat provided conditions for initiation of subduction. Changes in the tectonic setting, from an extensional to convergent regime, resulted in the development of a magmatic arc and back arc basins. Evolutionary changes in the supracrustal environment resulted in the deposition of metavolcanic-sedimentary sequences (e.g. Irajaí, Seridó, Salgueiro formations) surrounding the massif terranes.

The lithologies dominantly consist of supracrustals (intermediate and minor mafic volcanics and metasediments) intruded by granitoids. Commonly the supracrustals have been transformed into mylonitic schists or gneisses. Granite or rhyolite appear to be possible protoliths for the gneisses. Most of the schists probably originated from volcanic rocks (andesite-basalt to rhyodacite-dacite) with a predominance of the felsic type, although a contribution from sediments or tuffs is also possible. The main feature of the supracrustal rocks is their deformed and recrystallised nature under amphibolite

facies metamorphic conditions. Pressure and temperature are estimated at 5.5 kb and 600 °C respectively, indicating a depth of ≈ 25 km, and consistent with a brittle-pastic regime.

The amphibolite metamorphism dated at ≈ 1.0 Ga during this study is interpreted to be related to a main phase of regional deformation that produced recumbent folds or metamorphic nappes. This interpretation is consistent with the dates for the acid to intermediate Salgueiro volcanism (1.10 Ga), meta-volcanic rocks (0.95 Ga) and orthogneisses (Serra do Machado and Afeição granitoid types) dated at 1.1 Ga. On the basis of these data a Pre-Brasiliano thermal-tectonic event is proposed during the Middle Proterozoic in the Borborema Province.

The supracrustals have been subjected to intense metasomatism and high levels of K, Ba, and H_2O have been introduced. Enrichment in HFS elements such as Ti, Zr, Y, and P may indicate a magmatic derivation for the fluids. Depletions in Ni, Cr, Fe and Mg are typical features in the supracrustal host lithologies. The enhanced level of LIL elements, such as K, Rb, Ba, Pb and Th in the host lithologies is interpreted to be the result of enrichment by the hydrothermal fluid system , similar to that envisaged for the Kerr Addison and Hollinger gold mines, Canada (Kerrich, 1989). High ratios of $^{206}Pb/^{204}Pb$ and $^{207}Pb/^{204}Pb$ suggest that these rocks were formed from continental crust, at a depth close to the lower/upper crust boundary (Fig. 8.2), at ≈ 25 km depth, consistent with amphibolite metamorphism.

The supracrustal sequences are chracterised by high components of felsic volcanics and greywackes. On the basis of the geochemical data, the evolution of these sequences shows a pattern similar to that for Early Proterozoic greenstone belts, where tholeiite-komatiite and banded iron formation sequences are rare, and the proportion of intermediate volcanics rocks is high (see Condie, 1993).

An alkaline to subalkaline volcanism as indicated by the chemistry of the schists is consistent with a convergent plate margin or island arc at an active continental margin (Wilson, 1989). The gneisses were probably derived from subduction or continental collision granite types (Pearce *et al.*, 1984) and are also consistent with a subduction environment.

8.1.3 Convergent Plates: The Continent-Continent Collision Stage (Late Proterozoic)

The major tectonic features during *stage III* are related to the Brasiliano Orogeny (0.9-057 Ga). The major features of the resulting crustal shortening and consequent tectonic thickening are:

(i) The developemnt of crustal-scale shear zones, and ;

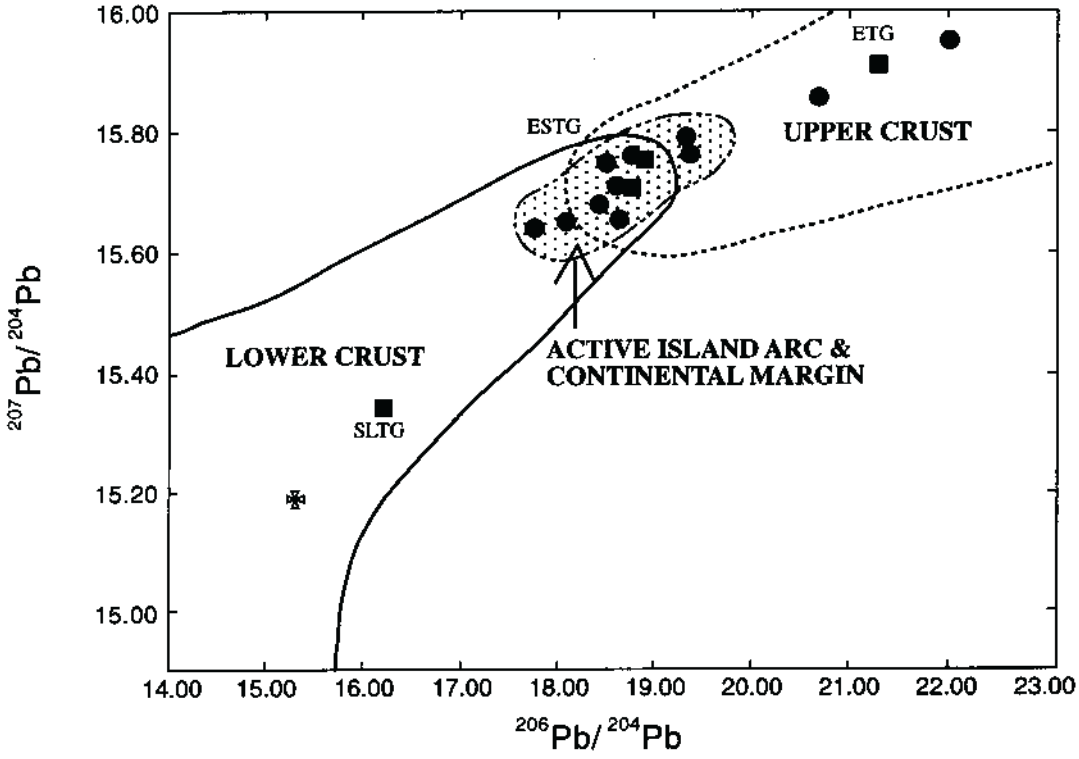

Figure 8.2 Diagram showing the variation of lead isotopic ratios ($^{206}Pb/^{204}Pb$ against $^{207}Pb/^{204}Pb$) in supracrustal rocks and granites in Borborema Province. The fields for rocks from the upper and lower continental crust are plotted from Zartman and Doe (1981). Shown for comparison are the fields for island arc and active continental margin (subduction setting) volcanic rocks from Wilson (1989).
Symbols: square = granite; circle = supracrustal rock; cross = Archaean amphibolite; ETG = early tectonic granite; ESTG = early -syn tectonic granite; SLTG = syn- late tectonic granite.

(ii) The widespread emplacement of batholiths and stocks of granitoid.

The shear zones are an integral part of the tectonic evolution of Borborema Province, primarily through providing a structural control for the fluid pathways. Gold deposits are commonly hosted by subsidiary NE-SW shear zones adjacent to the E-W, first-order shears. The mineralized structures consist of strike-slip and thrust faults within the shears, or extension fractures in close association with the shear zones. Multi-increment crack-seal deformation, particularly when accompanied by antitaxial vein-growth maximised fluid-rock interaction resulted in the enhance of chemistry changes. The different structural styles reflect the movement on the shear zones in lithologies of different competences. The major gold deposits (São Francisco and Cachoeira de Minas mines) occur in the fold belts (Piancó/Alto Brígida and Seridó belts) where anastomosing sets of thrust faults have developed, predominantly in supracrustal rocks. In the Pajeú/Paraíba fold belt (Itapetim District) the gold-bearing quartz veins occur in strike-slip structures close to the contact between regional granitoids and supracrustal sequences, where igneous rocks are predominant.

The mineralization occurs parallel to the shear zones in laminated and boudinaged quartz veins, suggesting a structural relationship bewteen stretching and the development of the channelways for the fluid-flow (see Groves and Foster, 1991).

Within the shear zones, the shear fabric exhibits complex folding patterns, mineral stretching, crenulation cleavage and S-C structures reflecting the intensity of the deformation. As kinematic indicators these planar fabrics reveal that the shears underwent sinistral (Itapetim area) or dextral displacement (Seridó and Cachoeira de Minas mines) and attest to their evolution under a transition from a semi-brittle to a plastic regime.

Despite widespread magmatism, Brasiliano supracrustal rocks are not extensive and consist of metapsammite and phyllonite with rare acid volcanics and conglomerate (e.g. Cachoeirinha Formation). However, mineralogical and chemical changes in the earlier lithologies indicate that the Early and Middle Proterozoic supracrustals were intensively reworked under retrogressive metamorphic conditions during the Brasiliano event. A temperature around 350 °C and pressure of 2-3.4 kb are indicative of a sub-greenschist grade, at 7-10 km depth.

The geochemical and petrographic data indicate that the granites may be of hybrid S-I type origin. The isotopic and REE element data from the Itapetim plutons show that their geochemical evolution cannot be related to a single crystal fractionation process, but may result from contamination during emplacement. The mechanism of emplacement was probably controlled by the strike-slip faults, and it may have occured during the transcurrent shearing. A considerable telescoping of the relationships between the Brasiliano granites is to be expected as the orogeny developed. Thus, the

ESTG appear to represent continent-continent collision or subduction-related granites, where melting of crustal material has become a component of the magma. The chemistry of these granites is analogous to that of the moderately-evolved members of the low Ca, predominantly I-type granites of the Canadian Cordillera, which are clearly subduction-related. However, the SLTG granites fall mostly into the range of extension-related plutons. The peralkaline granites may also be related to the extensional phase of the convergent regime.

8.2 A MODEL FOR GOLD MINERALIZATION

8.2.1 Source of the Gold

A debate concerning the source of the gold basically comprises two divergent points of view:

(i) The source of gold is restricted to some petrogenetic types of rocks that concentrated the gold in anomalous amounts (Viljoen *et al.*, 1970; Keays, 1984).

(ii) The gold is derived from enormous volumes of ('average') rock through the interaction with fluids in the deep crust (Kerrick, 1983; Groves and Phillips, 1987; Colvine *et al.*, 1988).

Assuming that the gold was derived from the same source as the lead (see Kramers and Foster, 1982), the Pb isotope study indicates that the Pb in the sulphides has not been derived directly from the host lithologies, but must be from a well-mixed source. The distribution of lead isotopic ratios of the sulphides is quite different from most of the other lithologies in the area. The geological evolution of the area makes it likely that some lead (and thus the gold also) could have originated from the primitive crust that was broken-up during the Archaean-Early Proterozoic (e.g. in old greenstone belts). This 'old' gold would have been incorporated into the supracrustals and the S-type granites, the latter by assimilation of crustal material.

A genetic association between gold mineralization and calc-alkaline magmatism (see Sillitoe, 1991; Muller and Groves, 1993) is invoked to explain the source for the gold, supported by the Pb isotope study, geochemistry of the granites and evolution of the area. The widespread gold-bearing quartz veins hosted by granites reflect a genetic link between the magmatism and the gold, at deep crustal levels. Granites related to this type of magmatism in subduction environments are produced both from the upper mantle and derived from melting of the lower crust (Sillitoe, 1991; Muller and Groves, 1993). Fluids enriched in CO_2 and H_2O were probably generated during mantle-degassing and

during the melting (Groves and Foster, 1991). Chlorine derived either from the dehydration of subducted lithospheric slabs (Sillitoe, 1991), or enriched together with F, B, and K_2O in the residual melts as a result of crystal-liquid differentiation (Muller and Groves, 1993), were incorporated into the hydrothermal system. It is assumed that the Cl-rich hydrothermal fluids which exsolved during magma crystallization should have been an efective transport for the gold from the magma to upper levels.

Thus, it is interpreted that the source of the gold is most likely related to the calc-alkaline magmatism. It is not clear where this magmatic gold was ultimately derived from, but it could have been derived from melting of the lower crust or upper mantle. Some additional, 'old' gold could have been leached from the immediate host lithologies and incorporated into the hydrothermal system by the mineralizing fluids.

8.2.2 Hydrothermal Fluids

a) Nature and Composition of the Fluid

On the basis of fluid inclusion studies, three types of fluid seem to have been associated with the development of the quartz veins:

(i) A dominant H_2O-CO_2 fluid characterised by low salinity (≈ 6.0 wt % NaCl equivalent) containing varying proportions of H_2O (96.0 to 72.0 mole %) and CO_2 (3.0 to 24.0 mole %), small amounts of CH_4 (< 3.0 mole %) and with temperatures of homogenization (T-Th) ranging from 270 to 387 °C.

(ii) A nonsaline CO_2-rich phase (> 77.0 mole % CO_2) containing small amounts of CH_4 (3.5 to 10.0 mole %) and H_2O (13.0 to 20.0 mole %), and with the predicted temperature of homogenization between 220 and 240°C.

(iii) An aqueous phase of low to moderate salinity (2.0 to 7.0 wt % NaCl).

These fluids occur along grain boundaries, crack-seals and crack healing in any given gold-bearing quartz vein. The first two types are primary inclusions formed with respect to the growth of the quartz vein, but the second type is secondary with respect to the individual quartz crystal. Fluid inclusions along crack healing occur later where gold occurs associated with chlorite and sulphides. The coexistence of all three types of fluid inclusion in any mode of occurrence (grain boundaries, crack-seal or crack healing) is indicative of contemporaneity. This fact is in agreement with the thermometric analyses, the data of which do not show significant difference in the temperatures of homogenization of the fluids.

The coexistence of CO_2-rich inclusions with H_2O-rich fluids is interpreted evidence of immiscibility in the H_2O-CO_2-salt fluid system. Immiscibility of fluids has been

invoked during fluid inclusion studies in several gold deposits and it is suggested as an important mechanism in gold precipitation (Ramboz *et al.*, 1982; Ho *et al.*, 1985; Robert and Kelly, 1987). Similarly, in this study it is interpreted that the monophase CO_2-rich phase, is the result of vapour separation during immiscibility, and the H_2O-CO_2 phase represents the liquid-rich fluid genetated from the same process.

Thus, three stages are proposed for the hydrothermal system evolution:

(i) An initial CO_2-rich fluid.

(ii) Increase in amount of water as the CO_2 drops as a result of fluid immiscibility.

(iii) A decrease in the volatile-rich phase until the fluid becomes predominantly aqueous.

b) Source of the Fluid and P-T Constraints

The δ^{13} C isotope signature (- 7.60 to - 2.11 $^0/_{00}$) indicates an ultimate 'deep-seated' source. However, as magmatic and mantle fluids are closely interrelated, particularly in subduction settings, it is possible that the hydrothermal system may contain carbon that is a mixture of magmatic and mantle-derived fluids. These fluids could have been generated directly from the mantle or from partial melting at the base of the lower crust. The δ^{13} C values could have been also resulted from the interaction of the fluid with carbon or graphite-rich lithologies during the metamorphic conditions. However, it seems unlikely, since metamorphism of such host lithologies would produce aqueous fluids with $CH_4 > CO_2$ (Xavier *et al.*, 1994); this is inconsistent with the CO_2/CH_4 ratios chracterised in the fluid inclusion investigations.

The depletion of the δ^{18} O values of the fluid (- 1.0 to + 9.0 $^0/_{00}$) compared with the range for a magmatic source (typically + 6 to + 9 $^0/_{00}$) suggests that a substantial amount of the water was probably derived from meteoric water. The δ^{18} O values are also not consistent with metamorphic fluids, the latter typically having values higher than + 10 $^0/_{00}$. (Kerrich and Fryer, 1979).

Another piece of evidence suggesting a component of 'shallow' hydrothermal fluid could be also suggested from the presence of selenium and tellurium-bearing phases. Selenium, and to a lesser extent tellurium, tend to be restricted to epithermal deposits (Saunders, 1990) which are generally accepted to have formed from the convection of local meteoric waters (Nesbitt, 1988) .

Thus, the gold-bearing hydrothermal fluids in Borborema Province must have had a complex evolution. It is proposed that the fluids were derived from large-scale convection of lower crust or mantle-derived fluids in hydrothermal systems which were driven by synmetamorphic plutons. These fluids subsequently mixed with convecting,

shallow meteoric waters.

Several lines of evidence have been able constraints on the P-T conditions of the gold deposition in Borborema Province (fluid inclusions, ore mineral assemblages and pyrite textures, chlorite geothermometry, temperature of fluid inclusion homogenization, and fluid inclusion isochores). On basis of these it is suggested that the P-T conditions of the fluid from which gold precipitated were 270-350 °C and 1.0-3.4 kb. This temperature range is also in agreement with the muscovite and chlorite stability fields and also with the absence of biotite in the mineralized quartz veins, despite the fact that this mineral is very common in all the host rocks.

8.2.3 Gold Transport and Deposition

Gold solubilization and transport are predominantly related to two types of complex:

(i) Chloride-gold complex $AuCl^-_2$ at higher temperatures (350-550°C; Seward, 1984).

(ii) Bisulphide-gold complex $Au(HS)^-_2$ at moderate temperatures (Seward, 1973).

A genetic link between the hydrothermal fluids and Brasiliano magmatism in Borborema Province has already been demonstrated. It would be reasonable to assume that high temperature, Cl-rich, hydrothermal fluids would be exsolved from the magma, and that this fluid would effectively transport the gold (and/or base metals) as a chloride-gold complex (Sillitoe, 1991; Muller and Groves, 1993).

However, the fluid inclusion study indicates that the hydrothermal fluids were of moderate temperature and low salinity. Similarly the ore-mineral studies have shown the close association of gold with sulphides. Thus the gold could also have been transported as a bisulphide complex. This is also consistent with the suggestion that in mesothermal gold deposits the concentration of $Au(HS)^-_2$ is approximately six orders of magnitude larger than that of $AuCl^-_2$ (Krupp and Seward, 1987).

In a hydrothermal system any reduction in gold solubility (resulting in its deposition) can be brought about by several mechanisms: (i) immiscibility of fluids; (ii) solution mixing; (iii) cooling; and (iv) fluid-rock interaction (Xavier *et al.*, 1994).

In Borborema Province, immiscibility of fluids is indicated by the fluid inclusion study and it could thus be a significant mechanism of gold precipitation. During boiling the volatile-bearing phases (e.g. CH_4, H_2, H_2S) tend to escape, with consequent changes in the chemistry of the residual liquid. The loss of volatiles causes a significant increase in fluid pH resulting in oxidation of the fluid (Seward, 1991). As

a result, the decrease in reduced sulphur concentration and the lowering of the oxidation potential lead to the loss of hydrogen from the residual aqueous phase (see Bowers, 1991).

This process is shown by the reaction (Phillips *et al.*, 1983):

$$2Au\,(HS)^{-}_{2} + 2H^{+} + FeO \text{ -------> } 2Au^{0} + 2\,H_2S + FeS_2 + H_2O$$

Incorporation of meteoric water into the hydrothermal system, as indicated by the δ^{18} O data, would have added cool, oxygenated fluids (Nesbitt, 1988). This mixing would further decrease the activity of reduced sulphur, as a result of the oxidation of H_2S and HS^- to sulphur and sulphate, leading to gold deposition (as demonstrated by Krupp and Seward, 1987). Cooling could also have been a significant factor in reducing the solubility of the gold-bearing complexes.

Fluid/rock interaction was probably not very relevant in gold deposition, as wallrock alteration is not very well-developed at all sites of mineralization. However, this process may have been active during the first phase of mineralization. Infiltration of the mineralizing fluid into the shear zones may have triggered a reaction with Fe^{2+}-bearing minerals in the host rocks (chlorite, Fe sulphides, magnetite, ilmenite) (see reaction given above). The decrease of fS_2 as a result of the desulphidation could have lowered the solubility of gold-bearing thio-complexes and thus caused the eventual precitipation of gold and sulphides synchronously with chlorite.

8.2.4 The Model for Gold Mineralization

The genesis of the gold deposits in Borborema Province is a result of the complex interaction of tectonic evolution, structure, igneous activity, and fluid mobilization. A genetic model for the gold deposits is proposed to account for the sources of the metals and fluid, and the mechanisms for their mobilization, transport and deposition. This model is depicted in Figure 8.3.

Continent-continent collision during the Late Proterozoic Brasiliano/Pan African Orogeny (0.9-0.5 Ga) involved a wide spectrum of geological processes, including the generation of major shear zones and granitoid emplacement. The calc-alkaline plutonism associated with this collision and subduction was generated from melting in the lower crust. Crustal-scale lineament systems developed a complex anastomosing network of thrust faults and subsidiary strike-slip shear zones. The melting would have produced lubrification of the shears in the lower crust (e.g. Hollister and Crawford, 1986) providing conduits for the fluid and emplacement of synkinematic plutons. A hydrothermal system enriched in CO_2 and H_2O was generated as a result of mantle-degassing and melting (Groves and Foster, 1991). These subduction-related

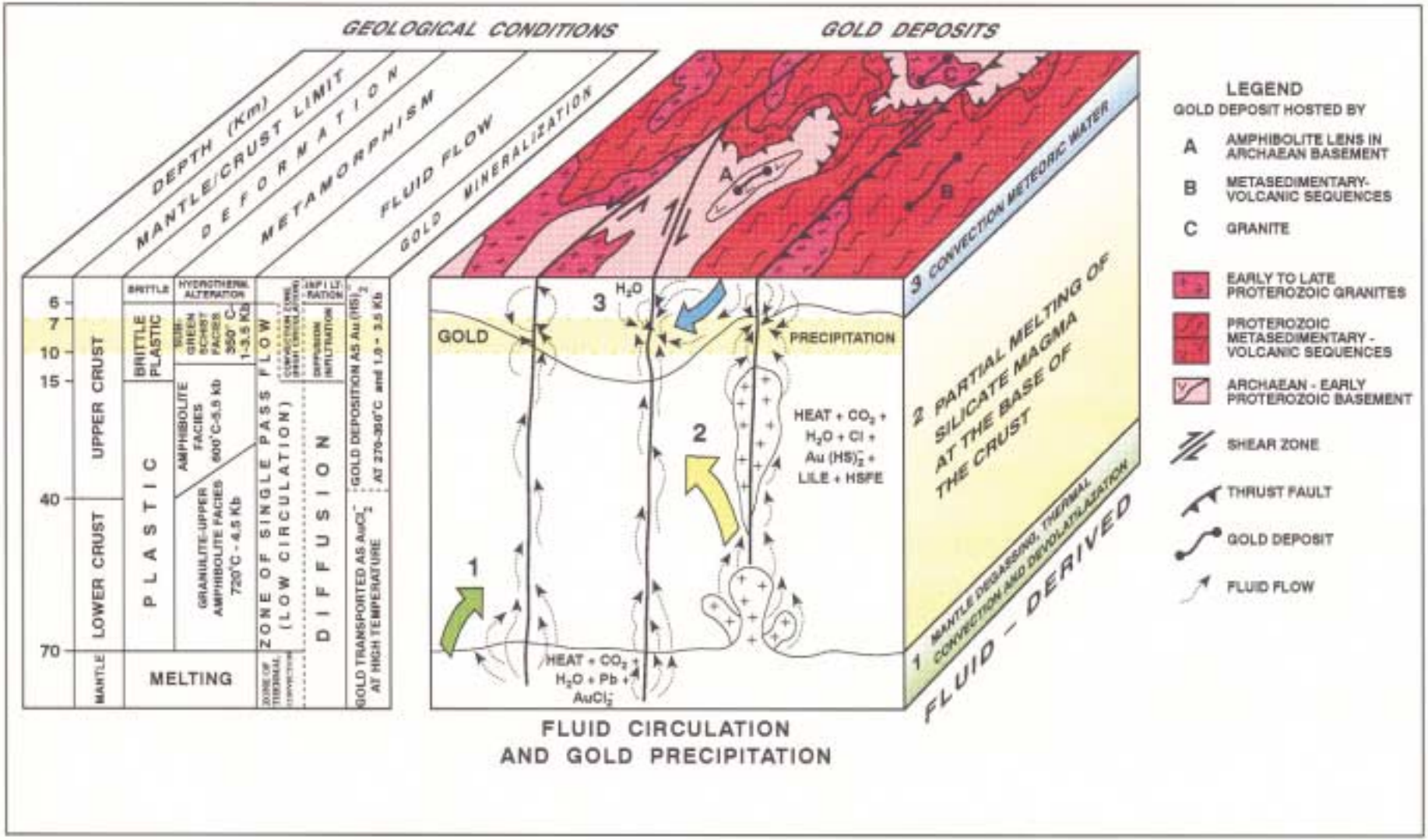

Figure 8.3 Schematic diagram showing a model for the gold mineralization in Borborema Province.

magmas were likely to be Cl-rich from either the dehydration of subduction lithospheric slabs (Sillitoe, 1991), or as a result of crystal-liquid differentiation of vapor-poor magmas (Muller and Groves, 1993). Cl-rich fluids could thus have been liberated from these magmas and transported available metals, including gold, from the magma to higher crustal levels through the shear pathways. During the ascent of the fluid to higherer levels additional 'old' gold could also have been leached from the supracrustal lithologies and incorporeted into the mineralizing fluids.

At ≈ 0.8 Ga, crustal shortening and consequent tectonic thickening associated with uplift provided conditions for retrogressive metamorphic processes, under sub-greenschist facies conditions (around 350°C). Shear faults and vein fractures which developed under a brittle-plastic regime at 7-10 km depth provided fluid pathways. Shear bands underwent dilation, giving rise to microstructural conduits for fluid percolation through the host rocks, and producing enrichment of LIL elements. Reverse shear zones with faults acted as valves and anabled pressure fluctuations in the fluid to vary from supralithostatic to hydrostatic (Sibson *et al.*, 1988). Development of the gold-bearing quartz veins by multi-increment crack-seal and crack healing deformations and structurally controlled by high-angle reverse faults or strike-slip shear zones ensured high fluid/rock ratios around the veins.

Wallrock alteration resulted from the early rock/fluid interaction. This early alteration/mineralization produced phases such as ilmenite, magnetite and sulphides from the destabilisation of mafic minerals. The sulphides were important as the elements Ag, Te, and Au were precipitated on their surfaces. The alteration also involved massive additions of K and B and less Ti, Fe and Mn. Enrichments in Ba, Pb, Th, Cr, Ni, V, Zn, Sc, Ga, Zr, Rb, Nb and Nd are also characteristic, whilst removal of Ca and Na was common. The chemical changes suggest the involvement of a typical granite-related hydrothermal fluid, rather than one derived from metamorphic dewatering.

Although very different lithologies were subjected to wallrock alteration, the mineral asssemblages and the patterns of alteration have shown that all rock types were subjected to the same metasomatic changes. Thus the host lithologies to the mineralization have not controlled the fluid composition. The textures in the veins and wallrocks show that the alteration took place before the shearing processes and the gold mineralization.

Following a phase of uplift, the hydrothermal fluids cooled and mixed with convecting meteoric water. Pressure decreases led to immiscibility, and resulted in the increase of the oxidation of the hydrothermal system; chemical changes were further brought about by equilibration with greenschist facies assemblages. Oxidation of pyrrhotite to pyrite liberated the *'invisible* ' gold. The second stage of mineralization consists of *'visible' gold*, and elements such as Pb, Zn, Bi, Te and Mo, all indicating a

plutonic influence. The P-T conditions at that time of gold precipitation ranged from 1.0-3.4 kb and 270-350 °C respectively, under a semi-brittle-plastic regime.

Subsequently, the production of volatle-rich fluid stopped and the hydrothermal fluid became essentially aqueous. The third stage, and the last phase of mineralization, consists of *coarse gold*, telluride, galena and fluorite, dated at 0.6 Ga. This is associated with an extensional phase of the convergent regime and suggests the end of Brasiliano magmatism in the area.

Within the shear zones the timing of mineralization overlaps that of the shearing, and the gold mineralization was emplaced towards the later stage of the shearing process. It is suggested that gold deposition occured under greenschist conditions at ≈ 0.8 Ga, post-peak regional metamorphism.

This proposed model therefore has many similarities to others put forward for similar gold deposits, in particular those in the Archaean (see below). As with these previous models a complex evolution and mixture of sources and components are envisaged. The main point which emerges from the present study, and which is different, is the importance of granitic magmatism and convecting meteoric fluids, such as is invoked for classical porphyry Cu or granite-hosted Sn-W mineralization.

8.3 COMPARISONS WORLD-WIDE

Gold-bearing quartz veins with geological characteristics rather similar to those in the Borborema Province are widespread in several Precambrian shield areas, including Australia, Brazil, Canada, India, Zimbabwe and South Africa. Some relevant geological features of Archaean lode gold deposits are given in Table 8.1 for comparison.

The Borborema Province gold mineralization belongs to a broad class of vein-type gold deposit that are strikingly similar to the Archaean lode gold deposits in terms of tectonic setting, structural control, and chemical composition of the hydrothermal fluid. Magmatic activity coeval with the mineralization and some aspects of the ore mineralogy are also a common feature.

However, differences are displayed in certain aspects of their host rocks, wallrock alteration and ore mineral assemblages. In addition, the mixed fluid source does not seem to be typical for Archaean lode deposits.

Mesothermal lode gold deposits are particularly common at old convergent plate boundaries, and in association with subduction-related magmatism. Such an environment seems be strikingly similar to the tectonic setting proposed for the Borborema Province. In the Itapetim District the presence of gold-bearing quartz veins in calc-alkaline plutonic rocks indicates a direct genetic link between this magmatism

Table 8.1
Comparison of Geological Features of Archaean Lode Gold Deposits

(a) Region/Deposit	(b) Structural	(c) Host Rocks	(d) Wallrock Alteration	(e) Ore Minerals	(f) Metamorphism/Timing of Mineralization	(g) Fluid Inclusions and Stable Isotope	Data Source (s)
Golden Mile, Kalgoorlie Norseman-Wiluna GSB Yilgarn, W Australia	Transcurrent shear zones Steeply dipping brittle-plastic shear zones	Tholeiitic basalts and dolerite sill	Muscovite, ankerite, siderite, albite, sericite; Chlorite-carbonate very intense; Intense K metasomatism	Gold, pyrite, pyrrhotite, tetrahedrite, sphalerite, chalcopyrite, scheelite, arsenopyrite, Au-Ag-Pb-Hg tellurides titanomagnetite, hematite, barite	Greenschist facies. Mineralization is syn or postdates the regional peak metamorphism and post dates the last folding event in the greenstone	(a) CO2-L & CO2 -V; (b) CO2-rich & CH4; (c) H2O-rich. S = 0.1-9.0 eq wt % NaCl; Th = 250-370 °C	(b, c, e) Groves & Foster, 1991; (d, f) Travis et al., 1971; (d, e, f) Mueller & Groves, 1991; (d) Woodall, 1979; (g) Ho et al., 1985
Sons of Gwalia, Leonora Norseman-Wiluna GSB Yilgarn, W Australia	Transcurrent shear zones Steeply dipping plastic shear zones Strike-slip and thrust faults	Tholeiitic to high Mg basalts and dolerite sill at the base. Meta-sediment (schists) associated	Biotite, ankerite, dolomite, chlorite, sericite, phlogopite phlogopite; (trace of Bi, Mo, W)	Gold, pyrite, arsenopyrite, pyrrhotite, scheelite; minor chalcopyrite, galena, magnetite, sphalerite, rutile	Greenschist facies. Mineralization is syn or postdates the regional peak metamorphism and post dates the last folding event in the greenstone		(b, c, d, e) Groves & Foster, 1991 (b, c, e, f) Sargeant, 1983 (d, e) Mueller & Groves, 1991
Mt Charlotte, Kalgoolie Norseman-Wiluna GSB Yilgarn, W Australia	Transcurrent shear zones. Steeply dipping brittle-plastic shear zones Quartz vein stockworks	Granophyric unit in tholeiitic dolerite sill	Muscovite, paragonite, ankerite, albite, chlorite, calcite	Gold, pyrite, pyrrhotite, tetrahedrite, Pb tellurides, rutile, scheelite	Greenschist facies. Mineralization postdates the regional peak metamorphism and post dates the last folding event in the greenstone	H2O-CO2 (20-30 mole % CO2) T-h = 350-440° C; P = 1.2-2.0 kb Low salinity (< 4 eq wt% NaCl)	(b, c, d, e) Groves & Foster, 1991 (g) Clark, 1980; (g, f) Phillips et al., 1984; (e) Mueller & Groves, 1991
Hunt mine, Kambalda Norseman-Wiluna GSB Yilgarn, W Australia	Shear zones dipping brittle-plastic deformation. Stockwork and brecciated qz. veins: hydraulic fract.	Metabasalt (tholeiitic) at the top of schist zone	Alteration postpeak metamorphism consists of: calcite, ankerite, albite, sericite, biotite, chlorite	Gold, pyrite, pyrrhotite, chalcopyrite, Fe-Ni-Au-Ag-Pb-Bi tellurides, magnetite, rutile, scheelite	Amphibolite-greenschist facies	H2O-CO2 (25 mole % CO2) T-h = 285-340° C; P = 0.8-1.4 kb Low salinity (< 3 eq wt% NaCl)	(b, c, f) Sawkins, 1990; (d, e) Mueller & Groves 1991; (d) Edward & Atkinson, 1986; (e) Phillips et al., 1984; (g) Neall & Phillips, 1987
Big Bell, Murchison Province, GSB Yilgarn, W Australia	Steeply dipping plastic shear zones	Tholeiitic basalt or dolerite (schist), qz-feldspar porphyry, quartz-magnetite gneiss	Muscovite, andalusite, sillimanite, K-feldspar, sericite,	Gold, pyrite, arsenopyrite, pyrrhotite, stibnite, chalcopyrite, sphalerite, berthierite, scheelite, molybdenite, wolframite, bornite, tetrahedrite, rutile	Amphibolite facies. Mineralization postdates the regional peak metamorphism and post dates the last folding event in the greenstone	The δ32 S rich pyrite & arsenopyrite data in schist do not suggest oxidation of S species during the ore deposition. It is consistent w/ isotopic fractional.	(c) Phillips, 1985a; (b, d, e) Mueller & Groves, 1991; (c, f) Colin, 1993; (e) Woodall et al., 1979; (g) Phillips & DeNooy, 1988;
Water Tank Hill Norseman-Wiluna GSB Yilgarn, W Australia	Deformed narrow zones along fold axes that show intense fracturing and brecciation	Oxide facies BIF dominated by quartz+magnetite+hematite	Zonation from the vein: quartz+ magnetite±hematite; minor carbonate+sericite+ quartz	Gold, pyrrhotite, magnetite	Amphibolite facies. Mineralization postdate the regional peak metamorphism and post dates the last folding event in the greenstone	H2O-CO2; other gas indicated T-h = 370-600° C; P = 1.8-3.5 kb Low salinity. Heterogeneous fluids	(b, c, e, g) Phillips & Groves, 1984 (f) Woodall, 1979
Nevoria Southern Cross Province Yilgarn, W Australia	Sub-horizontal fractures cut the BIF; the contacts amphibolite/ schist are sheared+plastic deformed	Oxide facies BIF dominated by quartz+pyrrhotite	Pyralspite, hedenbergite, fe-actinolite, ferro-hornblende, biotite, calcite, stilpnomelane, chlorite, muscovite	Gold, pyrrhotite, magnetite, scheelite, chalcopyrite, pyrite, arsenopyrite, Bi-tellurides	Amphibolite facies. Mineralization is early-syn- peak metamorphism		Phillips & Groves, 1984 (d, e) Mueller & Groves, 1991
Morro Velho Rio das Velhas GSB Minas Gerais, SE Brazil	Shear zones developed thrust faults	Carbonate BIF	Ankerite, ferroan-dolomite, siderite, calcite, chlorite,white mica, albite, stilpnomelane, tourmaline	Gold, pyrrhotite, arsenopyrite; minor chalcopyrite, cubanite, galena, tetrahedrite, sphalerite	Amphibolite facies and subsequent retrograde processes	δ18 O in quartz veins range from 16.00 to 17.4 o/oo	Ladeira 1980; 1985
Fazenda Brasileiro Itapicuru GSB Bahia, SE Brazil	Steeply dipping brittle-plastic shear zones	Mafic sill in the contact of tholeiitic basalts/felsic volcanics. The host rock has low TiO2 & high Fe2O3	Carbonate, chlorite, albite	Gold, arsenopyrite, pyrite, pyrrhotite, magnetite, hematite	Greenschist facies and locally amphibolite facies.	a) H2O-CO2 (15.0-45.0 mole % CO2) b) CO2-rich; c) H2O. T = 250-300° C Low S (< 6 eq wt % NaCl)	(c) Kishida & Riccio, 1980 (g) Xavier, 1987

Fazenda Maria Preta Itapicuru GSB Bahia, SE Brazil	Steeply dipping brittle-plastic shear zones	Mafic sill (dolerite) in the contact tholeiitic basalts/felsic volcanics. (tuff, dacite, andesite)	Carbonate, chlorite,	Gold, pyrite, pyrrhotite, arsenopyrite, Minor galena, chalcopyrite	Greenschist facies The mineralization is syn-post shearing	a) H2O-CO2 (11.5-40.5 mole % CO2) b) CO2-rich; c) H2O. T = 360-420° C; P = 2.0-4.0 kb Low S (< 4 eq wt % NaCl); δ18O = 14.3 to 17.2 o/oo δ18O H2O = 9.8 to 13.0 o/oo δ13C = - 6.5 to -10.2	(b, f) Coelho et al., 1991 (g) Xavier, 1989; 1994
Sigma, Val d' Or Abitibi GSB Quebec, Canada	Steeply dipping brittle-plastic shear zones	Massive and pillowed andesite and dolerite intruded and folding by porphyritic diorite	Calcite and white mica Tourmaline	Gold, pyrite, pyrrhotite; minor chalcopyrite, sphalerite, galena tellurides, scheelite	Regional greenschist facies with evidence of amphibolite facies Mineralization is late event	a) H2O-CO2 (15-30 mole % CO2) & Th = 285-395 °C; S< 10 eq wt % NaCl b) H2O-rich 25-34 eq wt % salt; Th = 60-295 °C; c) CO2-rich inclusions	(b,e) Groves & Foster, 1991; (c) Robert & Brown, 1986a,b; (d, e, f, g) Sawkins,1990 (g) Robert & Kelley, 1987; Colvine et al., 1988; Robert & Brown, 1984; Stone; 1990
Hollinger Tinamins; Abitibi GSB Canada	Steeply dipping shear zones	Mafic and minor felsic flows; pyroclastics; qz-feldspar porphyries	Sericite, ankerite, chlorite, calcite, quartz, albite	Gold, pyrite, pyrrohotite, galena, sphalerite	Greenschist facies	a) H2O-CO2 (6 mole % CO2) Th = 225-355 °C b) CH4-rich (> 26 mole % CH4)	(b, c, d, e) Groves & Foster, 1991; Colvine et al., 1988; (g) Wood et al., 1986; (g) Robert & Kelly, 1987; (g) Fyon et al., 1983
Kerr Addison, Larder Lake Abitibi GSB Canada	Steeply dipping shear zones	High-Mg basalts, tholeiitic bsalts; flesic porphyry to syenite dykes; clastic sediments	Ankerite/dolerite, albite, muscovite	Gold, pyrite, scheelite, arsenopyrite	Greenschist facies		(b, d,e, f) Groves & Foster, 1991 Colvine et al., 1988
Hemlo Hemlo Heron Bay GSB Ontario, Canada	Steeply dipping brittle-plastic shear zones	Andesitic to rhyolitic volcanics or pyroclastics; some clastic metasediments	Quartz, muscovite, (some V-rich), biotite, phlogopite, microcline barite, titanite. Strong K-enrichment and depletion of Na, Ca, Mg, Mn	Gold, pyrite, molybdenite, barite, sphalerite, arsenopyrite, stibnite; a large variety of minor Pb-, Cu-, Sb-, Hg-, Tl- and Te-bearing phase. Tu+fluor. occur as gangue minerals	Amphibolite facies. Mineralization later post peak metamorphism and post shearing. The ore exhibits retrograde metamorphism. Strong metasomatism		(b, c, d, f, g) Groves and Foster, 1991 (d, e, g) Kuhns et al.,1986 (f) Burk et al., 1986;
Giant, Yellowknife, Canada	Steeply dipping brittle-plastic shear zones	Pillowed and massive basalt	Sericite, ankerite, chlorite, albite	Gold, pyrite, stibnite, sulphosalts, sphalerite, galena	Amphibolite facies	a) H2O-CO2 (10-30 vol% CO2) Low S (5 eq wt % NaCl); Th = 200-320 °C b) CO2-rich (95 vol CO2); Th = 280-322 °C c) H2O (11 eq wt % NaCl); Th = 120-150°C	Padgham, 1979; Groves & Foster, 1991 (g) Robert & Kelly, 1987
Cam and Motor Kadoma Zimbabwe	Steeply dipping shear zones	Tholeiitic basalt/andesite, high Mg basalts, dolerite intrusions; minor clastics sediments	Quartz, ankerite, serpentine in high- Mg rocks	Gold, pyrite, arsenopyrite, stibinite, sphalerite, scheelite	Greenschist facies		Groves & Foster, 1991
Phoenix Kwekwe Zimbabwe	Steeply dipping brittle-plastic shear zones	Dunite-peridotite intrusive complex and granite gneiss	Magnesite, fuchsite, talc	Gold, pyrite, stibnite,arsenopyrite	Greenschist facies		Groves & Foster, 1991
Daisy Kadoma Zimbabwe	Folded plastic shear zones with later brittle deformation	Tholeiitic basalt flows Andesite	Ankerite, white mica, chlorite, albite magnesite, siderite. Significant enrichment in K2O, CaO, Ba, Rb	Gold, pyrite, pyrrhotite, arsenopyrite, chalcopyrite, galena, tetrahedrite, scheelite, sphalerite, bornite	Greenschist facies. Carbonatization post dated peak metamorphism	H2-CO2 (5-10 mole % CO2). Low S (6.7 eq wt % NaCl); Th = 200-320 °C P-T conditions : 3.6 kb; 390 °C	Groves & Foster, 1991 (g) Carter, 1991
Renco, Limpopo mobile belt Zimbabwe	Shear zones with low-angle fractures; brittle and plastic deformations	Hyperthene-quartz-feldspar granulite (enderbite)	Serpentine, biotite, sericite, epidote Negligible carbonate alteration	Gold, pyrrhotite, chalcopyrite, pyrite, bismuth, bismuth telluride, maldonite	Granulite facies. Retrograde processes locally modified the mineral assemblage and caused the late gold deposition		(b, c, d, e) Groves & Foster, 1991 (b) Tabeart, 1987; (f) Phillips & De Nooy, 1988
Redwing gold mine Umtali GSB Penhalonga, Zimbabwe	Shear zones with brittle and plastic deformations	Granitoid batholith (felsite and diorite) in contact with ultramafic rocks and BIF		Gold, pyrite, pyrrhotite, galena, arsenopyrite, chalcopyrite, sphalerite	Gold mineralization related to the last phase of regional metamorphism Metasomatism		(b, c, f,) Harrison, 1979

Kolar Kolar GSB Banbalore, Karnataka, India	First and second order shear zones	Mainly basaltic rocks; subsidairy ultramafic rocks and minor chemical sediments (BIF)	Quartz, diopside, hornblende, biotite, minor sericite and chlorite; calcite and tourmaline. Metasomatic process	Gold, pyrite, pyrrhotite, galena, arsenopyrite, sphalerite, chalcopyrite Minor ilmenite and magnetite	Amphibolite facies. The mineralization is syn-post metamorphism associated with the late stage of deformation	Gold transported as thiocomplexes at a temperature of 350°C; $fO2 = 10 (-31)$; $f S2 = 10 (-10)$	Hamilton & Hodgson, 1986) (g) Anil et al.,1991
Sheila mine Barbeton GSB Transvaal, South Africa	Steeply dipping, anastomosing shear zones with strike-slip faults	Greywackes and shales related to ultramafic-komatiitic sequences, BIF	Ankerite, dolomite, sericite, chlorite, K-feldspar. From the veins to the wallrock the contents in Na increase and Cu, Sb, K decrease.	Gold, pyrite, arsenopyrite; minor chalcopyrite, sphalerite, pyrrhotite, tetrahedrite, iron-rich NiAsS (gersdorffite)	Greenschist facies	P-T conditions for the gold deposition calculated using sphalerite geothermometry: P = 4.2 kb; T = 300-425 °C	(b, d) Phillips & Groves, 1984 (e, c, g) Schouwstra & Villiers, 1988
Homestake S Dakota, USA	Dilatant zones formed by superposition of two phases of deformation	Cherty carbonate BIF	Ankerite	Gold, arsenopyrite, pyrite, pyrrhotite, magnetite, hematite, scheelite	Amphibolite		Rye & Rye, 1974 (b) Sawkins, 1990

and the gold mineralization. Mesothermal gold deposits related to convergent plate margins above zones of active subduction and genetically associated with or hosted by similar igneous rocks have been recognized in Archaean lode-gold deposits in the Val d'Or and Timmins areas, Abitibi Subprovince, Canada and in the Norseman-Wiluna belt of the Yilgarn Block, W. Australia (see Muller and Groves, 1993). Gold mineralization related genetically to peralkaline magmatism with affinity to magnetite-series magmas is also well documented (Sillitoe, 1991; Cameron and Hattori, 1987; Burnham and Ohmoto, 1980). However, although peralkaline magmatism is well exposed in Borborema Province gold deposits hosted by these type of granitoids were not found. Thus, the gold mineralization appears more closely related to the calc-alkaline magmatism.

One of the most obvious similarities between the Archaean and Borborema gold deposits is the structural control of the gold distribution. On a regional scale the majority of mesothermal gold deposits are predominantly sited adjacent to crust-scale shear zones (e.g. Yilgarn Block, W. Australia; Abitibi, Superior Province, Canada; Rio Itapicuru deposits, Brazil; Zimbabwe). On the deposit scale they differ in their structural styles, ranging from strike-slip to thrust-faults, but usually in steeply dipping semi-brittle-plastic shears. In addition, most of the deposits do not actually occur in crustal-scale shears but in subsidiary structures (Eisenlohr *et al.*, 1989). The same relationships were also found in this study.

Fluid inclusion data from this study show the same characteristics as in other Archaean gold deposits: in particular a low salinity and high amounts of CO_2. Homogenization temperatures of H_2O-CO_2 inclusions fall within the range of 200 to 400°C, similar to that of inclusions in other Archaean mesothermal gold deposits (Roedder, 1984). Immiscibility of fluids (H_2O-CO_2, CO_2-rich and H_2O inclusions) is another common characteristic of these deposits, as for example in the Sigma mine, Canada (Robert and Kelly, 1987), and the Fazenda Maria Preta and the Fazenda Brasileiro gold mines (Xavier, 1991; Xavier *et al.*, 1994).

The isotope δ^{13} C values of the fluid show the same range as for most of the Archaean lodes deposits (Kerrich, 1989), and have indicated a 'deep' source for the carbon.

Borborema gold mineralization seems to differ from most of the Archaean gold deposits in the host lithologies and wallrock alteration. The host rocks consist of volcanic-metasediment sequences, predominantly mylonitic, and intruded by granitoids. Felsic rocks are predominant. Strong K enrichment produced a mineral assemblage dominated by tourmaline, K-feldspar, albite and minor fluorite. Absence of tholeiite-komatiite sequences and banded iron formations appears relevant as they are both typical in Archaean deposits. Extensive, metre-thick envelopes of wallrock alteration is also lacking, with a notable paucity of carbonates.

The hosts rocks for the Borborema mineralization were high to medium metamorphic grade unlike the situation with most Archaean lode gold deposits. Exceptions include Big Bell (Australia), Hemlo (Canada), Kolar (India) and Renco (Zimbabwe), all deposits in high-grade metamorphic terranes. It is interesting to note that these deposits show other similarities with the Borborema gold mineralization, for example a paucity of carbonate wallrock alteration, moderate to high-strain environments, and a proximity to granitoid margins (Phillips and De Nooy, 1988). However, all of these Archaean examples were subsequently subjected to retrogressive processes under sub-greenschist facies conditions. Thus, mineralization which post-dates regional peak metamorphism seems to be a factor common to the majority of Archaean lode deposits and also to the Borborema Province (see Table 8.1). Conditions of mineralization also appear similar, with P-T conditions of gold deposition in the range of 270-350°C and 1.0 to 3.4 kb, respectively.

Mineral assemblages tend to be similar: gold, tellurides and bismuth minerals identified in Borborema and in some Archaean lode gold deposits (e.g. Hunt mine, Kambalda and Nevoria; W. Australia; Renco, Zimbabwe). Molybdenite, although not common occurs at Big Bell, Hemlo, and Renco. Of critical importance is the absence of Hg, Sb, W, and As minerals in the Borborema mineralization. These elements form a common mineral assemblage in many Archaean gold deposits, as for a example, Hemlo, several deposits in the Yilgarn Block (e.g. Golden Mile, Mt. Charlotte, Big Bell), Morro Velho (Brazil), Dalmy mine (Zimbabwe), and the Sheba mine (South Africa). In contrast, selenium-bearing phases have not as yet been found in Archaean deposits.

Comparisons between the Borborema gold deposits and Phanerozoic mesothermal gold-bearing quartz veins are given in Table 8.2. As pointed out by Nesbitt (1991) there are also a number of genetic similarities between Archaean and Phanerozoic mesothermal gold deposits. The main similarities between Borborema mineralization and the Phanerozoic gold deposits are in tectonic setting and the host lithologies. The regional tectonic evolution suggests that both types occur in accreted terranes, with metasedimentary and volcanic sequences intruded by plutonics rocks, similar to that of greenstone terranes (e.g. deposits in Nova Scotia, Canada). Magmatism and gold mineralization seem to be linked in both types of deposit. These deposits are hosted by a variety of igneous and sedimentary rock types, and usually they are related to shear zones and closely associated with (predominantly S-type) granitic plutons (Nesbitt, 1991; e.g. Mother Lode, California; New South Wales and Victoria, Eastern Australia; North China craton; and Urals, Russia). However, the metamorphic grade of the host rocks is typically greenschist facies, even in regions of high grade metamorphism (e.g. Nova Scotia, where the Meguma terrane around the mine area is restricted to low grade metamorhpic facies). The Mother Lode deposit is the only exception, where the host

Table 2
Comparison of Geological Features of Phanerozoic Lode Gold Deposits

a) Region/Deposit	b) Structural	c) Host Rocks	d)Wallrock Alteration	e) Ore Mineral Assemblage	f) Metamorphism/Timing of Mineralization	g) Fluid Inclusions and Stable Isotope	Data Source
Victoria Walhalla Group, Australia	Shear zones (strike-slip) High-angle reverse faults Compressional regime	Marine sediments (slates, siltstone and greywackes) intruded by dykes	Biotite, sericite,	Gold, arsenopyrite, pyrite, galena, chalcopyrite, sphalerite,	Mineralization post dates metamorphism	Th = 160-330 °C; ≈ 5 mole % CO2 S = 1-9 wt % NaCl δ18 O : + 14 to +21 (quartz) δ13 C : -20 to -3 (carbonate)	Nesbitt, 1991
Monte Rosa Tertiary, Alps Italy	Alpine nappes	Tertiary metasediments associated with metamorphosed felsic intrusives	Chlorite, white mica, sericite; minor carbonate	Gold, pyrite, arsenopyrite, pyrrhotite, chalcopyrite, galena, sphalerite, native bisbuth, bismuthinite, tetrahedrite, covellite, scheelite	Greenschist facies Mineralization post dates the metamorphism	a) CO2-H2O; S < 10 eq.wt % NaCl; Th = 220-340 °C b) H2O; S ~ 0; Th = 150-200 °C P = 0.8-1.6 kb and T = 350-47 °C (from ore geothermometry) δ18 O range: 11.4 to 13.3 per mil	Curti (1987)
Codosera area Iberian Peninsula SW Spain	Shear zone involving early transpressive plastic deformation to late-kinematic transpressive brittle strucures	Cambrian to Devoniana black slates and quartzites	Carbonaceous	Gold, arsenopyrite, pyrite, goethite, lepidocrocite, scorodite	Up to greenschist facies Mineralization post dates the main plastic shearing	CO2-rich fluids; N2 present; High CH4 content (> 20 mole %) P = 2.8-3.3 kb; T = 350-400°C	Roberts et al.,1991 Dee & Roberts, 1993
Ratagain Complex NW Scotland	Fault associated with Ratagain complex intrusion	Quartz monzonite intruded in Lewisian and Moinian paragneisses and schists and minor limestone	K-feldspar, fluorite, calcite, muscovite, celestite	Gold, pyrite, chalcopyrite, galena, sphalerite, marcasite, molybdenite, hessite, aikinite gersdorffite, tennantite, rutile,	Greenschist facies	CO2-rich varieties; minor CH4, N2, H2 ; Low salinity (4-16 eq. wt % NaCl)	Alderton, 1988
Avoca District, **Croagh Patrick,** **South Mayo,** Ireland	Shear zones	Rocks of Caledonian age Acid volcanic rocks, tuffs with felsic intrusions or Dalradian metasediments	Sericite, chlorite, locally phyllic alteration	Gold, chalcopyrite, sphalerite, galena, pyrite, arsenopyrite, stibnite, tetrahedrite-tennantite	Greenschist facies		McArdle, 1989
Mother Lode Jurassic; Sierra Nevada, California, USA	Steeply dipping shear zone	Accreted Paleozoic and Mesozoic units. Greenstone and slates. Locally serpentinite	Sericite, carbonate	Gold, telluride (petzite), pyrite, arsenopyrite, sphalerite, galena, chalcopyrite, tetrahedrite, scheelite	Greenschist facies Mineralization later than the prograde metamorphism	CO2-rich; δ18O: + 14.0 to + 23.0 Temperature range from 250-350 °C and pressure 0.67-2.5 kb	Sawkins, 1990 (g) Nesbitt, 1991
Nova Scotia Meguma Group Canada	Strike-parallel, ductile shear shear zones	Turbidite (middle Devonian) Flyschoid sequence of shales & grey wackes. Accreted terrane Peraluminous granite intruded	Carbonate, tourmaline, phyllic alteration	Gold, pyrite, pyrrhotite, galena, sphalerite, arsenopyrite, chalcopyrite, scheelite, stibnite molybdenite, complex mix of Bi-Te-Ag-S	High-grade metamorphic and retrogessive processes Mineralization later	H2O-CO2 rich; 10-15 mole % CO2 S = < 10 wt % NaCl; Th = 280-300°C δ 18 O : + 12 to +18 (carbonate) δ 13 C : -25 to -14 (carbonate) δ 34S = 9.0 to 25.0 per mil	Nesbitt, 1991 Kontak et al., 1990

rocks were metamorphosed at high grade before the mineralization, similar to the Borborema deposits. Coincidentally, the Mother Lode contains gold-bearing quartz veins which are tourmaline-enrich.

Thus, it appears that the Borborema Province gold deposits could represent Proterozoic equivalents of the Archaean high-grade metamorphic lode gold deposits (see Table 8.3).

8.4 EXPLORATION SIGNIFICANCE

This study of the geology and gold mineralization of the Borborema Province will be of great assistance to exploration programmes in the region. However, because of the complex geology of accreted magmatic-volcanic terranes, mineral deposits associated with this type of environment are not easy to locate (Sawkins, 1990). The demarcation of the boundary between principal arc and back arc regimes is very difficult. Furthermore, migration of the principal arc has occurred in response to repeated changes in both the position and angle of subduction, and the whole tectonic assemblage has usually been telescoped by accretion. On the other hand, more information concerning the characteristics and setting of such deposits is constantly being obtained and new examples will no doubt be found, as for example in the young island arc systems of the western Pacific or in the Andes.

Although gold-bearing quartz veins are common in the Precambrian terranes of the province, gold is very heterogeneously distributed: 2 mines, 8 deposits, 205 occurrences (CPRM, Comitê do Ouro, 1983) and several hundred 'garimpos'. These deposits or prospects are widespread and the majority do have no information concerning either production or reserves.

Archaean greenstone belts appear to have an important control on the abundance of gold mineralization. However, economic gold deposits occur both in Late Archaean (ca. 2.7 Ga) greenstone belts (e.g. Western Australia) and in late Paleozoic to Quarternary convergent plate boundaries (North American Cordillera, e.g. Mother Lode). Thus an initial review of the literature might suggest that the Proterozoic does not represent a good target for gold exploration. However, in Borborema Province, the Early Proterozoic fold belts (2.4-2.0 Ga) contain abundant examples of gold occurrence, despite the lack of the tholeiitic-komateiitic volcanic sequence and banded iron formation (see Saager *et al.*, 1982).

Variations in gold production do occur in Archaean terranes. For example, in the 'older' Pilbara terrane (c. 3.5 Ga) have lower gold production compared with the Murchison Province (Yilgarn Block; 2.8-3.0 Ga) where BIF- and tholeitic-hosted deposits are abundant. Possible causes of much lower gold production from the older

Table 8.3
Comparison of Archaean, Phanerozoic and Borborema Province Mesothermal Gold Deposits.

Features	Archaean (> 2.5 Ga)	Phanerozoic (< 0.57 Ga)	Borborema Province (< 2.5 and > 0.57 Ga)
Host Rocks	Tholeiitic-komatiitic sequences Banded iron formation	Mafic to felsic volcanics Minor serpentine. Metasediments Banded iron formation	Granitoids and felsic porphyries Mafic to felsic volcanics Metsasediments
Structure	Crust-scale shear zones with development of subsidiary reverse faults	Controlled by fold or fault Faults related to second-order faults	Crust-scale shear zones with development of subsidiary reverse faults
Tectonic Setting	Convergent plate: post collisional arc	Late oceanic arc predominantly and minor post collisional-arc	Convergent plate: continental arc
Wallrock Alteration	Quartz-carbonate veining Mica V-or Cr-rich Dolomite-magnesite-talc Ankerite-magnesite-siderite	Quartz-carbonate veining Carbonate, albite, sericite, chlorite	Intense K metasomatism Quartz-tourmaline veining
Ore Minerals	Gold, Fe sulphide, arsenopyrite, scheelite, stibnite Au-Ag-As-Sb-W-Bi-bearing phase	Gold, Fe sulphide, arsenopyrite, scheelite, stibnite, Au-Ag-As-Sb-W-Bi-bearing phase Ca-Mg-Fe carbonate	Gold; Fe, Cu, Pb, Zn, Mo sulphides; Se /Te bearing mineral phase; Bi minerals; Au-Ag-Te-bearing phase
Geochemistry	Addition of SiO2, K2O, CO2, H2O, Au Au associated with As, Ag, W, Sb, Te, Bi Very low Cu, Pb, Zn, Mo High LILE; Low LREE; Low HFSE	High LILE; Low LREE; Low HFSE Au:Ag typically > 1	Addition of SiO2, K2O, CO2, H2O, Au; Au associated with Pb, Ag, Te, Bi, Se and minor Mo. Very low Zn, Cu High LILE;
Metamorphism Timing of Mineralization	Predominantly greenschist facies with rare examples of amphibolite facies (Bib Bell & Hemlo) subjected to retrogressive processes. Gold was deposited post peak metamorphism	Greenschist facies (except Mother Lode deposit where the host rocks were first subjected to amphibolite metamorphic grades and subsequently to retrograde processes) Mineralization later	Amphibolite facies subjected to retrograde processes at sub-greenschist facies conditions Gold was deposited post peak metamorphism and wallrock alteration was pre shearing
Fluid Inclusions	H2O-CO2 rich; Low salinity	H2O-CO2 rich; Low salinity	H2O-CO2 rich; Low salinity
Stable Isotopes in Fluids & range of P-T Conditions	δ18 O range from + 2.5 to + 10.0 per mil δ13 C range from 0 to - 10.0 per mil 1-2 kb; 300-400°C	δ18 O range from + 2.0 to + 4.0 per mil δ13 C range from- 8.0 to - 17.0 per mil > 0.2 kb; 200-350°C	δ 18 O range from - 1.0 to + 9.0 per mil δ13 C range from - 2.1 to - 7.6 per mil 1-3.4 kb; 270-350 °C
Source of Fluid	Metamorphic, magmatic, mantle	Metamorphic, meteoric	Magmatic, mantle, meteoric

Observation: Table prepared from the following sources: Barley et al., 1989; Mueller & Graoves, 1993; Phillips & DeNooy, 1988; Nesbitt, 1991; This study.

terrane include the likelihood of sulphide- and gold-depleted source-rocks (Groves *at al.*, 1984; Groves and Foster, 1991).

On the basis of these suggestions, the different gold productivities in Borborema Province compared with the Archaean lode gold deposits could be explained by:

(i) The gold source was a more differentiated, more gold-depleted upper mantle
(ii) Lack of the tholeiite-komateiitic volcanic sequence and banded-iron formation
(ii) Lack of geological studies, such as geochemical, geophysical and isotopic analyses for understanding the evolution of accreted terranes, followed by an exploration program specifically targed toward this tectonic setting.

Based on this concept about the evolution of the accreted belt, a number of first-order exploration targets can be selected. Priority must be given to the areas with a high density of anastomosing shear zones where the subsidiary shear zones are concentrated. Fold belts with a predominance of supracrustals are the best targets. The supracrustal lithologies are favorable to the development of S-C fabric and have thus ensured the most efficient circulation of the mineralised fluids. Although granites appear to be both the source of the gold and the hydrothermal fluids, a proximity to granites does not appear to be important.

Petrographic and geochemical data have indicated a predominance of calc-alkaline and minor tholeiitic volcanism associated with metasediments in the fold belts located in the west (Seridó and Pinacó/Alto Brígida belts). In contrast, in the eastern part (Pajeú/Paraíba fold belt), although calc-alkaline volcanism is present, it is associated with minor metasediments and abundant plutonic rocks. This could reflect a different tectonic setting for these belts - a volcanic arc enviroment for the eastern belt, and a back arc basin evolved to a marginal basin in the west. This model suggests west-dipping subduction. As a result of the tectonic settings the major gold deposits should be confined to rift-style basins, rather than the magmatic arc. Thus exploration should be concentrated in fold belts to the west of the region.

The presence of a clear increase in K, Ba, Rb during wallrock alteration could be of great value during prospecting. Decreased K/Rb ratios, in conjunction with elevated K/Ba and Rb/Sr ratios, are pronounced in mineralized rocks relative to their granitic hosts. Analyses for Pb, Bi, Te, and Se during a surface exploration programme might also be advantageous. Lower values of base metal such as Zn and Cu, and the absence of an Sb-Hg and As-bearing phases, do not recommend these elements as pathfinders for gold prospecting in the province.

REFERENCES

Alderton, D.H.M. (1979) 'Luxullianite in situ within the St. Austell granite, Cornwall: a discussion'. *Mineral. Mag.* **43**, 441-442.

Alderton, D.H.M. (1988) Ag-Au-Te mineralization in the Ratagain complex, northwest Scotland. *Inst. Minning Metall.* **97**, B171-B180.

Allison, I. and Kerrick, R. (1980) History of deformation and fluid transport in shear zones at Yellowknife. In *Proceedings of Gold Workshop, Yellowknife, Northwest Territories*, ed. Morton, R. D., 201-222.

Almeida, F.F.M. de, Leonardos, O.H. and Valença, J. (1967) Review on granitic rocks of Northeast South America. In IUGS/UNESCO Symposium, Recife, Brazil, Special Pub., 41 pp.

Almeida, F.F.M. de, Hasui,Y., Brito Neves, B.B.de and Fuck, R. (1981) Brazilian structural provinces. *Earth Sci. Rev* .**17**, 1-29.

Anderson, J.L. and Cullers, R.L. (1990) Middle to upper crustal plutonic construction of magmatic arc: An example from the Whipple Mountains metamorphic core complex. *Geol. Soc. Amer. Memoir* **174**, 47-69.

Anderson, E.M. (1951) The Dynaimcs of Faulting and Dyke Formation with Application to Britain, Oliver and Boyd.

Angel, M. and Riera, F. (1959) Report de la mission au Pernambuco. S. I. Bureau Minier Guyanais, Service Français de Cooperation Technique.

Anil, G.S., Menon, A.G. and Anantha Iyer, G.V. (1991) Thermodynamic characteristic of the physico-chemical conditions attending gold mineralisation in the sulphide-rich Oriental type lodes, Kolar Gold Fields, India. In *Brazil Gold'91 The Economics Geology Geochemisrty and Genesis of Gold Deposits*, ed. Ladeira, Balkema, Rotterdam.

Anthony, J.W., Bideaux, R.A., Bladh, K.W. and Nichols, M.C. (1990) *Handbook of Mineralogy, Vol. I Elements, Sulfides, Sulfosalts*, Mineral Data Pub., Tucson, Arizona.

Arehart, G.B., Chryssoulis, S.L., Kesler, SE. (1993) Gold and arsenic in iron sulphides from sediment-hosted disseminated gold deposits: Implications for depositional processes. *Econ. Geol.* **88**, 171-185

Arndt, N.T. and Goldstein (1987) Use and abuse of crust-formation ages. *Geol.* **15**, 893-895.

Baker, B.H. (1987) Outline of the petrology of the Kenya rift alkaline province. *Geol. Soc. London Spec. Pub.* **30**, 293-311

Barbarin, B. (1990) Granitoids: main petrogenetic classifications in relation to origin and tectonic setting. *Geol. J.* **25**, 227-238.

Barbosa, O. et al., (1970) Geologia economica de parte da região do médio São Francisco, Nordeste do Brasil, Rio de Janeiro, DNPM/DFPM, **140**.

Barley, M.E., Eisenlohr, B.N., Groves, D.I., Perring, C.S., and Vearncombe, J.R. (1989) Late Archaean convergent margin tectonics and gold mineralization: A new look at the Norseman-Wiluna Belt, Western Australia. *Geol.* **17**, 826-829.

Barnes, H.L. (1979) *Geochemistry of Hydrothermal Ore Deposits*. Wiley, 2nd edition, New York, 789 pp.

Batzle, M.L. and Simmons, G. (1976) Microfractures in rocks from two geothermal areas. *Earth Planet. Sci. Lett.*, **30**, 71-93.

Beach, A. (1976) The interrelations of fluids transport, deformation, geochmistry and heat flow in early Proterozoic shear zones in the Lewisian complex. *Phil. Trans. Royal Soc. London* **280**, 569-604.

Beach, A. (1979) Pressure solution as a metamorphic process in deformed terrigenous sedimentary rocks. *Lithos*, **12**, 51-58.

Beurlen, H. (1988) Fazenda Esperança e Riacho da Posse: duas ocorrencias atípicas de Fe-Ti no estado de Pernambuco. Prof. Titular Thesis, Univ. of Recife, PE, Brazil (unpub.).

Beurlen, H., Da Silva Filho A.F. and Guimães, I do P., (1991) Evolução metamórfica dos eclogitos da ocorrencia de Fe-Ti da Fazenda Esperança, Bodocó, Brasil. *37th Congress Bras. Geol., São Paulo, SP*, vol. **4**, *Soc. Bras. Geol.*, 2025-2039.

Bevins, R.E., Lees, G.L. and Roach, R.A. (1991) Ordivician bimodal volcanism in SW Wales: gechemical evidence for petrogenesis of the silicic rocks. *J. Geol. Soc. London* **148**, 719-729.

Bladh, K.W.(1982) The Formation of goethite, jarosite, and alunite during the weathering of sulfide-bearing felsic rocks. *Econ. Geol.* **77**, 176-184.

Blake, S., Wilson, C.J.N., Smith, I.E.M. and Walker, G.P.L. (1992) Petrogolgy and dynamics of the Waimihia mixed magma eruption, Taupo Volcano, New Zealand. *J. Geol. Soc. London* **149**, 193-207.

Bonnemaison, M. and Marcoux, E. (1990) Auriferous mineralization in some shear-zones: A three-stage model of metallogenesis. *Mineral. Depos.* **25**, 96-104.

Bottinga,Y. (1968) Calculation of fractionation factors for carbon and oxygen isotope exchange in the

system calcite-carbon dioxide-water. *J. Phys. Chem.* **72.**, 800-808.

Bouiller, A.M. and Robert, F. (1992) Paleoseismic events recorded in Archaean gold-quartz vein networks, Val d'Or, Abitibi, Quebec, Canada. *J. Struct. Geol.*, **14**, 161-179.

Bowers, T. S. and Helgeson, H. (1983) Calculation of the thermodinamic and geochemical consequences of nondideal mixing in the system H_2O-CO_2-NaCl on phase relations in geologic systems: Equation of state for H_2O-CO_2-NaCl fluids at high pressure and temperature. *Geochim. Cosmchim. Acta* **47**, 1247-1275.

Bowers, T.S. (1991) The deposition of gold and other metals: pressure-induced fluid immiscibility and associated stable isotope signatures. *Geochim. Cosmochim. Acta* **55**, 2471-2434.

Boyle, R.W. (1979) The Geochemistry of Gold and its Deposits. *Can. Geol. Surv. Bull.* **280,** 584 pp.

Brace, W. F. (1972) Pore pressure in geophysics. In *Flow and Fracture of Rocks, Geophys. Monogr. Ser.*, **6**, eds. Heard, H.C., Borg, I.Y., Carter, N.L. and Rayleigh, C.B., 265-273, Washington, D.C.

Brantley, S.L., Evans, B., Hickman, S.H. and Crerar, D.A. (1990) Healing of microcracks in quartz: Implications for fluid flow. *Geol.* **18**, 136-139.

Bremond d'Ars, J. de, Martin, H., Auvray, B. and Lecuyer, C. (1992) Petrology of a magma chambre: the plutonic complex of Guernsey (Channel Islands, U.K.) *J. Geol. Soc. London*, **149**, 701-708.

Bridgwater, D., McGregor, V.R. and Myers, J.S. (1974) A horizontal tectonic regime in the Archaean of Greenland and its implications for early crustal thickening. *Precam. Res.* **1**, 179-197.

Brito Neves, B.B. de (1975) Regionalização geotectônica do Pre-Cambriano nordestino. Ph.D. thesis, Earth Science Inst., Univ. of São Paulo, Brazil (unpub.).

Brito Neves, B.B. de (1978) Estudo da geocronologia da faixa costeira Pre-cambriana do nordeste. Relatório para CNPq, Recife.

Brito Neves, B.B. de (1983) O mapa geológico do Nordeste Oriental do Brasil, scale 1:1.000.000, MSc thesis, Earth Sciences Inst., Univ. of São Paulo, Sp, Brazil (unpub.).

Brito Neves, B.B. de (1986) Tectonic regimes in the Proterozoic of Brazil. *12 th Simp. Geol. Nordeste,* João Pessoa, Soc. Bras. Geol., 135-251.

Brito Neves, B.B. de, Sial, A.N., Patrocinio, J.P. (1977) Vergencia centrífuga residual no sistema de dobramentos Sergipano. *Rev. Bras. Geoc.* **7**, 102-114.

Brito Neves, B.B. de , Sial, A.N., Rand, H. and Manso, V.A.V. (1982) The Pernambuco-Alagoas massif, *Rev. Bras. Geol.* **12**, 240-250.

Brito Neves, B.B.de, Schmus, W.R.V., and Basei, M.A.S. (1990) Contribuição ao estudo da evolução geocronológica do sistema de dobramento Piancó-Alto Brígida. *36 th Cong. Bras. Geol.*, Natal, RN, **6**, Soc. Bras. Geol., Núcleo Nordeste, 2698-2712.

Brito Neves, B.B. de and Cordani, U.G. (1991) Tectonic evolution of South America during the Late Proterozoic. *Precamb. Res* . **53**, 23-40.

Brito, A. de L. F. (1986) Projeto Ouro Princesa Isabel, Relatório final, Convênio SUDENE-CDRM/PB.

Brown, D. and McClay, K.R. (1993) Deformation textures in pyrite from the Vangorda Pb-Zn-Ag deposit, Yukon, Canada. *Mineral. Mag.* **57**, 55-66.

Brown, G.C., Thorpe, R.S. and Webb, P.C. (1984) Geochemical characteristcs of granitoids in contrasting arcs and comments on magma sources. *J. Geol. Soc. London* **141**, 413-426.

Brown, M. (1993) P-T-t evolution of orogenetic belts and causes of regional metamorphism. *J. Geol. Soc. London* **150**, 227-241.

Brown, P.E. and Becker, S.M. (1986) Fractionation, hybridisation and magma-mixing in the Kialieneg Centre, east Greenland. *Contrib. Min. Petrol.* **92**, 57-70.

Bryndzia, L.T., Scott, S.D., Spry, P.G. (1990) Sphalerite and hexagonal pyrrhotite geobarometer: experimental calibration and application to the metamorphosed sulphides ores of Broken Hill, Australia. *Econ. Geol.* **83**, 1193-1204.

Burk, R., Quartermain, R. A. and Hodgson, C.J. (1986) Geological setting of the Teck-Corona Au-Mo-Ba deposit, Hemlo, Ontario. In *Gold'86 Canadian Precambrian Gold Deposits Re-Interpreted*, ed. Macdonald, A.J., Konsult Internation, Toronto.

Burke, K. and Dewey, J.F. (1973) An outline of Precambrian plate development. In *Implications of Continental Drift to the Earth Sciences*; eds.Tarling, D.H. and Runcorn, S.K., Academic Press., 1035-1044.

Burnham, C.W. and Ohmoto, H. (1980) Late-stage processes of felsic magmatism. In *Granitic Magmatism and Related Mineralization*, eds. Ishihara, S. and Takenouchi, S., Mining Geol. (Japan), Spec. Issue, **8**, 1-11.

Burrows, D.R. and Spooner, E.T.C. (1986) The McIntyre Cu-Au deposit, Timmins, Ontario, Canada. In In *Gold' 86: Geologic Characteristics, Fluid Properties and Light Isotope Geochemistry*, ed. Macdonald, A. J., Konsult Internation, Toronto, 23-39.

Burrows, D.R., Wood, P. C. and Spooner, E.T.C. (1986) Carbon isotope evidence for a magmatic

origin for Archaean gold-quartz vein ore deposits. *Nat.* **321**, 851-854.

Bursnall, J.T., Hodgson, C.J., Hubert, C., Kerrich, R.W., Marquis, P., Murphy, J.B., Osmani, I., Poulsen, H., Robert, F., Sanborn-Barrie, M., Stott, G., and Williams, H.R. (1989) Mineralization in Shear Zones. *Geol. Assoc. Can., Short Course Notes* **6**, Montréal, Québec, 299 pp.

Bussell, M. A. (1988) Structure and petrogenesis of a mixed ring dyke in the Peruvian Coastal batholith: eruptions from a zoned magma chamber. *Trans. Royal Soc. Edinburgh* **79**, 87-104.

Cabri, L.J., Blank, H., El Goresy, A., Laflamme, J.H.G., Nobiling, R., Sizgoric, M.B., and Traxel, K. (1984) Quantitative trace-element analyses of sulphides from Sudbury and Stillwater by proton micropobe. *Can. Mineral.* **22**, 521-542.

Cabri, L.J., Campbell, J.L., Laflamme, J.H.G., Leigh, R.E., Maxwell, J.A. and Scott, J.D. (1985) Proton microprobe analyses of trace elements in sulfides from some massive-sulfide deposits. *Ibid.* **23**, 133-148.

Cabri, L.J. (1992) The distribution of trace precious metals in minerals and mineral products. *Mineral. Mag.* **56**, 289-308.

Cabri, L.J., Chryssoulis, S.L., Villiers, J.P.R., Laflamme, J.H.G. and Buseck, P.R. (1989) The nature of 'invisible' gold in arsenopyrite. *Can. Mineralog.* **27**, 353-362.

Caby, R. (1989) Precambrian terranes of Benin-Nigeria and northeast Brazil and the Late Proterozoic south Atlantic fit. *Geol. Soc. Amer., Spec. Paper* **230**, 145-153.

Caby, R. and Arthaud, M. (1986) Major Precambrian nappes of the Brasilian belt, Ceará, Northeastern Brazil. *Geol.* **14** , 871-874.

Caby, R., Bertrand, J.M. and Black, R. (1981) Pan-African closure and continental collision in the Hoggar-Iforas segment, central Sahara. In *Precambrian Plate Tectonics*, ed. Kroner, A., Elsevier, Amsterdam, 407-434.

Caby, R., Rahaman, M.A. and Boesse, J.M. (1987) Archaean and Proterozoic of southwest Nigeria: lithostratigraphy and petrostructural evolution compared with the Saharian and Brasilian segments, Abstr. *14 th Col. African Geol.*, Berlin.

Caby, R., Sial, A.N., Arthaud, M. and Vouchez, A. (1990) Crustal evolution and the Brasiliano Orogeny in Northeast Brazil. In *The West African Orogenes and Circum-Atlantic Correlatives*, eds. Dallmeyer, R.D. and Lecorché, J.P., Springer-Verlag, (in press).

Caldasso, A.L.S., Costa, A.C. and Horikava, Y. (1973) Projeto Sudeste Piauí II, Relatorio Final, DNPM/CPRM, Recife.

Cameron, E. M. and Hattori, K. (1987) Archean gold mineralization and oxidized hydrothermal fluids. *Econ. Geol.* **82**, 1177-1191.

Cameron, E.M. (1988) Archean gold: relation to granulite formation and redox zoning in the crust. *Geol.* **16**, 109-112.

Camp, V.E. and Roobol, M.J. (1989) The Arabian continental alkali basalt province: Part 1. Evolution of Harrat Rahat, Kindom of Saudi Arabia. *Geol. Soc. Amer. Bull.* **101**, 71-95.

Cannon, R. S. and Buck, K.L. (1961) The data of lead isotope geology related to problems of ore genesis. *Econ. Geol.* **56**, 1-36.

Carlson, D.H. and Moye, F.J. (1990) The Colville Igneous Complex; Paleogene volcanism, plutonism, and extension in northeastern Washington. *Geol. Soc. Amer. Memoir* **174**, 375-394.

Carter, A.H.C. (1991) Fluid-rock interaction and gold deposition within a late Archaean shear zone, Dalny mine, Zimbabwe. In *Brazil Gold'91 The Economics Geology Geochemisrty and Genesis of Gold Deposits*, ed. Ladeira, Balkema, Rotterdam.

Cassedanne, J.P (1973) et al. A paragenese da mina de ouro de São Francisco. *Rev. Eng. Min. Met.* **37** (**343**), 6-13.

Cathelineau, M. (1988) Cation site occupancy in chlorites and illites as a function of temperature. *Clay Miner.* **23**, 471-485.

Cathelineau, M., Boiron, M.C., Essarraj, S., El Jarray, A., Marignac, C. and Lespinasse, M. (1993) Reconstruction of paleofluid migration in microfissured rocks. In *Geofluids'93 Contributions to an International Conference on fluid evolution, migration and interaction in rocks*, eds. Parnell, J., Ruffell, A.H. and Moles, N.R., Torquay, England.

Chappell, B.W. and White, A.J.R. (1974) Two contrasting granite types. *Pacif. Geol.* **8**, 173-174.

Chappell, B.W and White, A.J. (1976) *25 th International Geological Congress* Excursion Guide 13C.

Chappell, B.W. (1979) Granitoids from the Moonbi district, New England batholith, eastern Australia. *J. Geol. Soc. Aust.*. **25**, 267-283.

Charoy, B. (1979) Definition et importance des phénomenes deutériques et des fluids associés dans les granites. Conséquences métallogeniques. *Mém. Sci. de la Terre* **37**, Nance.

Charoy, B. (1982) Tourmalinization in Cornwall, England. In *Mineralization Associated with Acid Magmatism*, ed. Evans, A.M., Wiley, New York.

Chivas, A.R., Barnes, I., Evans, W.C., Luptore, J.E. and Stone, J.O (1987) Liquid carbon-dioxide of magmatic origin and its role in volcanic-eruptions. *Nat.* 326, 587-589.

Christe, G. and Hannah, J.L. (1990) High-K, continental-arc volcanism in the Kettle Rock sequence of

the eastern Mesozoic belt, northern Sierra Nevada, California; Implications for lower Mesozoic Cordilleran tectonics. *Geol. Soc. Amer. Memoir* **174**, 315-329.

Clark, L.A. (1960) The Fe-As-S system: phase relations and applications. *Econ. Geol.* **55**, 1345-1381, 1631-1652.

Clark, M.E. (1980) Localization of gold, Mt. Charlotte, Kalgoorlie, Western Australia. BSc. thesis, Univ. W. Australia, (unpub.).

Clarke, D.B. (1992) *Granitoid Rocks*.. Chapman and Hall, London, 280 pp.

CPRM (1983) Avaliação dos recursos auríferos do Brasil

CPRM (1984) Itapetim Prospect, Final Prospect, Rio de Janeiro, RJ.

Clayton, R.M., Muffler, L.J.P. and White, D.E. (1968). Oxygen isotope study of calcite and silicates of the River Rand No. 1 well, Salton Sea geothermal field, California. *Amer. J. Sci* **266**, 968-979.

Coelho, C.E.S., Beny, C., Ramboz, C., Touray, J.C. and Giuliani, G. (1991) Quartz fabrics and fluid inclusion volaties at Fazenda Brasileiro gold mine: A petrographical microthermometrical and Raman microprobe study. *Depart. des Sciences de la Terra, Univ. d'Orleans/CNRS*, France, (unpub.).

Colin, W. (1993) A post-deformational, post-peak metamorphic timing for mineralization at the Archaean Bib Bell gold deposit, Western Australia. *Ore Geol. Rev.* **7**, 439-483.

Collins, W.J., Beams, S. D., White, A.J.R. and Chappell, B.W. (1982) Nature and origin of A-type granites with particular reference to southeastern Australia. *Contrib. Mineral. Petrol.* **80**, 189-200.

Colvine, A.C., Andrews, A.J., Cherry, M.E., Durocher, M.E., Fyon, A.J., Lavigne, M.J., Macdonal, A.J., Marmont, S., Poulsen, K.H., Springer, J.S. and Troop, D.G. (1984) An integrated model for the origin of Archean lode gold deposits. *Ontario Geol. Surv., Open File Report* **5524**, 98 pp.

Colvine, A.C., J.A. Fyon, Heather, K.B., Marmont, S, Smith, P.M. and Troop, D.G. (1988) Archaean lode gold deposits in Ontario. Part I. A depositionnal model. Part II. A genetic model. *Ontario Geol. Sur., Miscellaneous Paper* **139**, 136 pp.

Condie, K.C. (1982) Early and Middle Proterozoic supracrustal succession and their tectonic settings. *Amer. J. Sci.* **282**, 341-357.

Condie, K.C. (1993) Chemical composition and evolution of the upper continental crust: Contrasting results from surface samples and shales. *Chem. Geol.* **104**, 1-37.

Corsini, M.,Vauchez, A., Jardim de Sá, E.F and Archanjo, C. (1991) Strain transfer at continental scale from a transcurrent shear zone to a transpressional fold belt: The Patos-Seridó system, northeastern Brazil. *Geol.* **19**, 586-589.

Costa, A.C., Mendes, V.A., Rocha, D.E.G.A. and Andrade, D.A. (1979) Projeto Extremo Nordeste do Brasil, Relatório I, DNPM/CPRM.

Cowie, J.D. and Basset, M.G. (1989) International Union of Geological Sciences: 1989 global stratigraphic chart with geochronometric and magnetostratigraphic calibration. *Epis.* **12**, 2, (suppl.).

Cox, S.F. (1987) Flow mechanism in sulphide minerals. In *Ore Geol. Reviews*, Marshall, B. and Gilligan, L.B. (eds), Elsevier, Amsterdam, 133-171.

Cox, K.G. (1991) Tectonics and volcanism of the Karoo period in southern Africa and adjacent areas. *Geol. Society London, International Multidisciplinary Tectonic Studies Group Meeting*, October, Programm with abstracts.

Cox, S.F., Etheridge, M.A. and Hobbs, B.E. (1981) The experimental ductile deformation of polycrystalline and single crystal pyrite. *Econ. Geol.* **76**, 2015-2118.

Cox, S.F. and Etheridge, M.A. (1982) Fibre development in deformed hydrothermally altered acid volcanic rock. In *Atlas of Deformational and Metamorphic Rock Fabric*, eds. Borradaile, G.J., Bayly, M.B. and Powell, C.McA, Springer, Berlin, 304-306.

Cox, S.F. and Etheridge, M.A. (1983) Crack-seal fibre growth mechanism and their significance in the developmnet of oriented layer silicate microstructures. *Tectonoph.* **92**, 147-170.

Cox, S.F., Etheridge, M.A. and Wall, V.J. (1986) The role of fluids in syntectonic mass transport, and the localization of metamorphic vein-type ore deposits. *Ore Geol. Rev.* **2**, 65-86.

Craig, R.J. and Vokes, F.M. (1993) The metamorphism of pyrite and pyritic ores: an overview. *Mineral. Mag.* **57**, 55-66.

Crawford, M.L. and Hollister, L.S. (1986) Metamorphic fluids: the evidence from fluid inclusions. In *Fluid-Rock Interactions During Metamorphism*, eds. Walter, J.V. and Wood, B.J., Spring-Verlag, New York.

Curti, E. (1987) Lead and oxigen isotope evidence for the origin of the Monte-Rosa gold lode deposit (Western Apls, Italy): A comparison with Archaean lode deposits. *Econ Geol.* **82**, 2115-2140.

Da Silva Filho, A.F. and Guimarães, I.P. (1989) Shoshonitic and ultrapotassic Proterozoic intrusive suites in the Piancó-Alto Brigída belt, NE Brazil; A transition from collision to post collision-related magmatism. *J. Volc. Geother. Res.* (in press).

Dantas, J.R.A. (1971) Levantamento dos estudos geológicos do curso de geologia da UFPE (1961-

1970), Recife, DNPM, (unpub.).
Dantas, J.R.A. and Brito Neves, B.B. (1980) Mapa geológico do Estado de Pernambuco-Texto explicativo. DNPM/Minerios de Pernambuco, Recife.
Debon, F. and LeFort, P. (1983) A chemical mineralogical classification of common plutonic rocks and association. *Trans. Royal Soc. Edinburgh, Earth Sci.* **73**, 135-149.
Dee, S.J. and Roberts., S. (1993) Late-kinematic gold mineralization during regional uplift and the role of nitrogen: an example from the La Codosera area, W. Spain. *Mineral. Mag.* **57**, 437-450.
Deer, W.A, Howie, R.A. and Zussman, J. (1985) An Introduction to the Rock-Forming Minerals, Longman, Essex, England, *15 th edition*, 528 pp.
Defant, M.J., Jackson, T.E., Drummonds, M.S., De Boer, J.Z., Bellon, H., Feigenson, M.D., Maury, R.C. and Stewart, R.H. (1992) The geochemistry of young volcanism throughout western Panama and southeastern Costa Rica: an overview. *J. Geol. Soc. London* **149**, 569-579.
Delevaux, M.H., Doe, B. R. and Brown, G.F. (1967) Preliminary lead isotope investigations of brine from the Red Sea, galena from the Kingdom of Saudi Arabia, and galena from United Arab Republic (Egypt). *Earth Planet. Sci. Lett.* , **3**, 139-144.
DePaolo, D.J. (1981) Trace element and isotopic effects of combined wallrock assimilation and fractionational crystallization. *Earth Plan. Sci. Lett.* **53**, 189-202.
DeRonde, C.E.J.de, Wit, M.J., Spooner, E.T.C. and Bray, C.J. (1991). Mafic-ultramafic hosted, shear zone related, Au-quartz vein deposits in the Barberton greenstone belt, South Africa: Structural style, fluid properties and light sable isotope geochemistry. In *Proc. of Brazil Gold'91, The Economics geology Geochemistry and Genesis of Gold Deposits* , ed. Ladeira, E.A., Balkema, Rotterdam, 279-285.
Dickinson, W.R. (1974) Plate tectonics and sedimentation. In *Tectonics and Sedimentation*, ed. Dickinson, W.R., *Econ. Paleont. and Miner. Soc., Spc. Pub.* **22**, 1-27.
Doe, B.R.(1970) *Lead Isotopes*, Spring-Verlag, New York, 137 pp.
Doe, B.R. and Stacey, J.S.(1974) The application of lead isotope to the problems of ore genesis and ore prospect evaluation: A review. *Econ. Geol.* **69**, 757-776.
Ebert, H. (1970) The Precambrian Geology of the Borborema Belt; State of Paraíba and Rio Grande do Norte, Northeastern Brazil. *Geol. Rundsch.*, 59 (3), 1299-1326.
Edward, R. and Atkinson, K. (1986) Ore Deposit Geology, Great Britain Univ. Press., Cambrige, 466 pp.
Edwards, A.B. (1974) Textures of the ore minerals and their significance. *Australas. Inst. Min. Metall.*, Melbourne, 242 p.
Eisenlohr, B.N., Groves, D. and Partington, G.A. (1989) Crustal-scale shear zones and their significance to Archaean gold mineralization in Western Australia. *Mineral. Depos.* **24**, 1-8.
Ernst, W.G., Hacker, B.R., Barton, M.D. and Sen, G. (1991) Igneous petrogenesis of magnesian metavolcanic rocks from the central Klamath Mountains, northern California. *Geol. Soc. Amer. Bull.* **103**, 56-72.
Etheridge, M.A., Wall, V.J. and Vernon, R.H. (1983) The role of the fluids phase during regional metamorphism and deformation. *J. Metamor. Geol.* **1**, 205-226.
Faure, G. (1977) *Principles of Isotope Geology* , ed. Wiley, New York, 282-340.
Ferran, A. (1988) Mina de Ouro de São Francisco, Currais Novos, Rio Grande do Norte. In *Principais Depositos Minerais do Brasil*, ed. Schobbenhaus, C. and Coelho, C.E.S., Vol. **III**, DNPM, Brasília.
Ferreira, J.A.M. (1967) Considerações sobre uma nova estratigrafia do Seridó. *Rev. Eng. Min. Met.* **45** (265), 25-28, Rio de Janeiro, RJ.
Ferreira, V.P and Sial, A.N. (1986) The peralkalic magmatism in the Precambrian Cachoeirinha-Salgueiro Fold Belt, Notheast Brazil: Geochemical aspects. *Rev Bras. Geoc.* **16 (1)**, 73-85.
Ferreira, V.P and Sial, A.N. (1992) Liquid immscibility in the Triunfo pluton, Northeastern Brazil: mineral chemistry approch *37 th Cong. Bras. Geol.*, São Paulo, SP, **1**, *Soc. Bras. Geol.*, 363-364.
Field, C.W. and Fifarek, R.H. (1985) Light stable isotope systematics in the epithermal enviroment. In Geology and Geochemistry of Epithermal Systems, Econ. Geol. Rev. 2, Berger, B.R. and Bethke, P.M. (eds), 99-128.
Fitton, J.G. (1987) The Cameroon line, West Africa: a comparison between oceanic and continental alkaline volcanism. *Geol. Soc. London Spec. Pub.* **30**, 273-291
Fletcher, I.R and Farquhar, R.M. (1982) Lead isotopic composition of Balmat ores and their genetic implications. *Econ. Geol.* **77**, 464-473.
Fletcher, C.J.N. and Beddoe, S. and Stephens, B.(1987) The petrology, chemistry and crystallisation history of the Velasco alkaline province, eastern Bolivia. *Geol. Soc. London Spec. Pub.* **30**, 403-413.
Fletcher, C.J.N., Swainbank, I.G. and Colman, T.B. (1993). Metallgenetic evolution in Wales: constrainsts from lead isotope modelling. *J. Geol. Soc. London* , **150**, 77-82.

Foster, R.P. (1985) Major controls of Archaean gold mineralization in Zimbabwe. *Trans. Geol. Soc. S. Af.* **88**, 109-133.

Foster, R.B. (1988) Archaean gold deposits mineralization in Zimbabwe: implications for metallogenesis and exploration. In *Bicentennial Gold' 88*, 62-72, Melbourne, Australia.

Fox, L.K. and Miller, D.M. (1990) Jurassic granitoids and related rocks of the southern Bristol Mountains, southern Providence Mountains and Colton Hills, Mojave desert, California. *Geol. Soc. Amer. Memoir* **174**, 111-132.

Franklin, J.M., Roscoe, S.M., Loveridge, W.D. and Sangster, D.F. (1983) Lead isotope studies in Superior and Southern provinces. *Geol. Sur. Can. Bull.* **351**, 60 pp.

French, W.J., Hassan, M.D. and Westcott, J. (1979) The petrogenesis of Old Red Sandstone volcanic rocks of the western Ochils, Stirlingshire. *Geol. Soc. London Sepc. Pub.* **8**, 635-642.

Friend, C.R.L., Nutman, A.P. and McGregor, V.R. (1988) Late Archaean terrane accretion in the Godthab region, southern West Greenland. *Nat.* **335**, 535-538.

Fyfe, W.S. (1986) Fluids in deep continental crust. In *Refletion Seismology: The Continental Crust. Amer. Geophy. Geophys Un. Geodyn.* **14**, 33-40.

Fyfe W.S. (1987) Tectonic, fluids and ore deposits: mobilization and remobilization. *Ore Geol. Rev.* **2**, 21-36.

Fyfe, W.S. and Kerrich, R. (1985) Fluids and thrusting. *Chem. Geol.* **49**, 353-362.

Fyfe, W.S., Price, N.J. and Thompson, A.B. (1978) *Fluids in the Earth's Crust.* Elsevier, Amsterdam, 383 pp.

Fyon, J.A., Crocket, J.H. and Schwarcz, H.P. (1983) Application of stable isotope studies to gold metallogeny in the Timmins-Porcupine camp: *Ontario Geol. Surv.*, Open File Report 5464:182.

Fyon, J.A., Schwarcz, H. P. and Crocket, J. H. (1984) Carbonatization and gold mineralization in the Timmins area Abitibi grenstone belt: genetic links with Archaean mantle CO_2-degassing and lower crust granulitization. *Geol. Assoc. Canada Progm. with Abstracts* **9**, 65 p.

Galindo, A.C. (1984) Geocronologia do Precambriano do Rio Grande do Norte. *Bol. Dep. Geol., CCE-*Univer. of Rio Grande do Norte, Natal, RN, Brazil, 20-35.

Giggenbach, W.F. (1982) The chemical and isotopic composition of gas discharges from New Zealand andesite volcanos. Bull. *Volc.* **45** (3), 253-255.

Glazner, A.F. (1990) Recycling of continental crust in Miocene volcanic rocks from the Mojave block, southern California. *Geol. Soc. Amer. Memoir* **174**, 147-168.

Golding, S.D. and Wilson, A.F. (1987). Oxygen and hydrogen isotope relations in Archaean gold deposits of Eastern Goldfields Province, Western Australia: constraints on the source of Archean gold-bearing fluids. In Recents advances in understanding Precambriam gold deposits, eds. Ho, S.E. and Groves, D.I., Geol. Depart. and Univ. Extension, *Univ. W.Aust. Pub.* **11**, 703-713.

Gomes, F.E.M. (1990) Relações litoestratigráfico-estruturais e evolução tectônica na faixa Riacho do Pontal-região de Paulistana (PI), *36 th Congress Bras. Geol.*, Natal, RN, vol. **6**, *Soc. Bras. Geol.*, 2843-2857.

Govett, G.J.S. (1985) Rock geochemistry in mineral exploration. In *Handbook of Exploration Geochemistry* vol. **3**, Elsevier, Amsyterdam, 462 pp.

Graf, J.L. and Skinner, B.J. (1970) Strength and deformation of pyrite and pyrrhotite. *Econ. Geol.* **65**, 206-215.

Gronvold, F. and Westrum, E.F. (1976) Heat capacities of iron disulfides. Thermodynamics of marcasite from 5 to 700 K, pyrite from 350 to 700 K, and the transformation of marcasite to pyrite. *J. Chem. Thermody.* **8**, 1039-1048.

Groves, D.I., Phillips, G.N., Ho, S.E., Henderson, C.A., Clark, M.E. and Wood, G.M. (1984) Controls on distribution of Archaean hydrothermal gold deposits in Western Australia. In *Gold'82*, ed. Foster, R.P., Balkema, Rotterndam, 689-712.

Groves, D.I., Golding, S.D., Rock, N.M.S., Barley, M.E. and McNaughton, N.J. (1988) Archaean carbon reservoirs and their relevance to the fluid source for gold deposits. *Nat.* **331**, 254-257.

Groves, D. I. and Phillips, G.N. (1987) The genesis and tectonic control on Archean gold deposits of the Western Australian Shield- a metamorphic replacement model. *Ore Geol. Rev* . **2**, 287-322.

Groves, D. I., Barley, M.E. and Ho, S.E. (1989). The nature, genesis and tectonic setting of mesothermal gold mineralization in the Yilgarn Block, Western Australia. *Econ. Geol. Monograph* , **6**, 71-85.

Groves, D. I. and Foster, R. P. (1991) Archaean lode gold deposits. In *Gold Metallogeny and Exploration*, ed. Foster, R. P., Blackie, London, 63-103.

Groves, D.I., Barley, M.E., Cassidy, K.C., Hagemann, S.E.Ho, S.E., Hronsky, J.M.A., Mikucki, E.J., Mueller, A.G., McNaughton, N.J., Perring, C.S. and Ridley, J.R. (1991). Archaean lode-gold deposits: The products of crustal-scale hydrothermal systems. *In Brazil Gold'91:Petrology and geochemistry of gold deposits*, ed. Ladeira, E.A., Balkema, Rotterdam, 299-305.

Guimarães, I.P. (1989) The petrological evolution and tectonic association of the Bom Jardim Complex, Pernambuco State, NE Brazil. Ph.D. Thesis, Imperial College, Univer. of London,

(unpubl.), 324 pp.
Hackspacher, P.C., Schums, W.R.V. and Dantas, E.L. (1987) Um embasamento Tansamazonico na Província Borborema. *36 th Congress Bras. Geol.*, Natal, RN, vol.**6**, *Soc. Bras. Geol.*, 2683-2696.
Hamilton, J.V. and Hodgson, C.J. (1986) Mineralization and structure of the Kolar Gold Field, India. In *Proc. of Gold'86, an International Symposium on the Geology of Gold*, ed. Macdonald, A. J. Konsult International Symposium Inc. Toronto, 270-283.
Harmon, R.S., Barreiro, B.A., Moorbath, S., Hoefs, J., Francis, P.W., Thorpe, R.S., Deruelle, B., McHugh, J. and Viglino, J.A. (1984) Regional O-, Sr- and Pb-isotope relationships in late Cenozoic calc-alkaline lavas of the Andean Cordillera. *J. Geol. Soc. London* **141**, 803-822.
Harris, N.B.W., Pearce, J.A. and Tindle, A.G. (1986) Geochemical characteristics of collision-zone magmatism. In *Collision Tectonics*, eds Coward, M.P. and Ries, A.C., *Geol. Soc. London Spec. Public.* **19**, 67-81.
Harrison, N.M. (1979) The geology of the Rewing gold mine Penhalonga, Umtali district, Rhodesia. *Sepc. Pub. Geol. Soc. Africa* **5**, 55-60.
Hasui, Y., Costa, J.B.S. and Abreu, F.A.M. (1984) Província Tocantins, Setor Setentrional. In *O Pre-Cambriano do Brasil* , eds. Almeida, F.F.M. and Hasui, Y., Blucher, São Paulo, 187-204.
Hattori, K. (1987) Magnetic felsic intrusions associated with Canadian Archaean gold deposits. *Geol.* **15**, 1107-1111.
Helgeson, H.C. and Lichtner, P.C. (1987) Fluid flow and mineral reactions at high temperature and pressure. *Geol. Soc. London J.* **144**, 313-326.
Helmstaedt, H., Padgham, W.A. and Brophy, J.A. (1986) Multiple dikes in the Lower Cam Group, Yellowknife greenstone belt: evidence for Archaean seafloor spreading?. *Geol.* **14**, 562-566.
Hine, R.H., Williams, L.S., Chappell, B.W. and White, A.J.R. (1978) Geochemical contrasts between I- and S-type granites. *J. Geol. Soc. Aust.* **25**, 219-234.
Ho, S.E, Groves, D.I. and Phillips, G.N. (1985) Fluid inclusions as indicators of the nature and source of fluids and ore depositional conditions for Archaean gold deposits of the Yilgarn Block, Western Australia. *Geol. Soc. S. Africa Trans.* **88**, 149-158.
Hodgson, C.J. (1989) The structure of the shear-related vein-type gold deposits: A review. *Ore Geol. Rev.* **4**, 231-273.
Hoffman, P.F. (1988) United plates of America, the birth of a craton: early Proterozoic assembly and growth of Laurentia. *Ann Rev.Earth Planet Sci* .**16**, 543-603.
Holdaway, M.J. (1971) Stability of andalusite and the aluminum silicate phase diagram. *Amer. J. Sci.* **272**, 91-131.
Holdaway, M.J. and Lee, S.M. (1977) Fe-Mg cordierite stability in high-grade pelitic rocks based on experimental, theoretical and natural observations. *Contrib. Mineral. Petrol.* **63**, 175-198.
Hollister, L.S. (1981) Information intrinsically available from fluid inclusions. In *Fluid inclusions: Applications to Petrology*, Short Course Handbook, vol. 6, eds. Ghent, E.D., Hollister, L.S. and Crawford, M.L., *Mineral Assoc. of Canada*, Calgary.
Hollister, L.S and Burruss, R. (1976) Phase equilibria in fluid inclusions from the Khtada Lake metamorphic complex. *Geochim. Cosmochim. Acta* **40**, 163-175.
Hollister, L.S. and Crawford, M.L. (1986) Melt enhanced deformation: a major tectonic process. *Geol.* **14**, 558-561.
Hurley, P.M., Almeida, F.F.M. de, Melcher, G.C., Cordani, U.G., Rand, J.R., Kawashita, K., Vandoros, P., Pinson, Jr., W.H. and Fairbairn, H.W. (1967) Test of continental drift by comparison of radiometric ages. *Sci.* **157**, number 3788, 496-500.
Hutchison, M.N. and Scott, S.D.(1981) Sphalerite geobarometry in Cu-Fe-Zn-S system. *Econ. Geol.* **76**, 143-153.
Irvine, T.N. and Baragar, W.R.A. (1971) A guide to the chemical classification of the common rocks. *Can. J. Earth Sci.* **8**, 523-548.
Jardim de Sá, E.F. (1987a) Evolução orogenica monocíclica vs policíclica: (I) Argumentos estratigráficos e geocronológicos no Proterozoico da Província Borborema. *Primeiro Simposio Nacional de Estudos Tectonicos, Bol. de Resumos*, 9-14.
Jardim de Sá, E. F. (1987b) Relatório de Consultoria-Mineração Xapetuba LTDA., Currais Novos, RN.
Jardim de Sá, E.F. (1984) A evolução Proterozoica da Província Borborema. *Symposium Geol. Nordeste*, Natal, RN, *Soc. Bras. Geol.*, 297-316.
Jardim de Sá, E.F. (1988) An update of the Precambrian geology of northeast Brazil. In *International Meeting on Proterozoic Geology and Tectonics of High-Grade Terranins: Ile-Ife, Nigeria*, Programme and Lecture Series.
Jardim de Sá, E.F. and Hackspacher, P.C. (1980) Reconhecimento estrutural na borda Nordeste do Craton São Francisco. *31 th Congress Bras. Geol.*, **5**, *Soc. Bras. Geol.*, 2719-2731.
Jardim de Sá, E.F. and Sá, J.M. (1987) In *International Symposium Granites and Association*

Mineralization, (I.S.G.A.M.), Salvador, BA, Brazil, Abstr., 103-109.

Jardim de Sá, E.F., Legrand, J.M. and McReath, I. (1981) 'Estratigrafia' de rochas granitoides na região do Seridó (RN-PB) com base em criterios estruturais. *Rev. Bras. Geoc.* **11**, 50-55.

Jardim de Sá, E.F., Macedo, M.H.F., Legrand, J.M., McReath, I., Galindo, A.C. and Sá, J.M. (1987) Proterozoic granitoids in polycyclic setting. The Seridó region, NE Brazil. In *International Symposium Granites and Association Mineralization, (I.S.G.A.M.)* Salvador, BA, Brazil.

Jardim de Sá, E.F., Macedo, M.H.F., Torres, H.H.F. and Kawashita, K. (1988) Geochronology of metaplutonics and the evolution of supracrustal belts in the Borborema Province, NE Brazil. *7 th Congress Latino Americano de Geologia*, Belém, PA, vol. **1**, 49-62.

John, B.E. and Wooden, J. (1990) Petrology and Geochemistry of the metaluminous to peraluminous Chemehuevi Mountains Plutonic Suite, southeastern California. *Geol. Soc. Amer. Memoir* **174**, 71-98.

Johnson, M.C. and Rutherford, M.J. (1989) Experimental calibration of the aluminium-in-hornblende geobarometer with application to Long Vally caldera (California) volcanic rocks. *Geol.*. **17**, 837-841.

Jones, G., Sano, H. and Valsami-Jone, E. (1993) Nature and tectonic setting of accreted basalts from the Mino terrane, central Japan. *J. Geol. Soc. London* **150**, 1167-1181.

Kanaris-Sotiriou, R., Morton, A.C. and Taylor, P.N. (1993) Paleogene peraluminous magmatism, crustal melting and continental break-up: the Erlend complex, Faeroe-Shetland Basin, NE Atlantic. *J. Geol. Soc. London* **150**, 903-914.

Kay, S.M., Maksaev, V., Moscoso, R., Mpodozis, C., Nasi, C. and Gordillo, C.E. (1988) Tertiary Andean magmatism in Chile and Argentina between 28°S and 33°S: Correlation of magmatism chemistry with a changing Benioff zone. J. South Amer. *Earth Sci.* **1**, 21-38.

Keays, R.R. (1984) Archaean gold deposits and their source rocks: The upper mantle connection. *In Gold'82: The Geology, Geochemistry and Genesis of Gold Deposits*, ed. Foster, R.P., Balkema, Rotterdam, 17-52.

Kerrich, R. (1976) Some effects of tectonic recrystallisation on fluid inclusions in vein quartz. *Contrib. Mineral. Petrol.* **59**, 195-202.

Kerrich, R. (1983) Geochemistry of gold deposits in the Abitibi Greenstone Belt. *Can. Inst. Mining Metall. Sepc. Paper* **27**, 75 pp.

Kerrich, R. (1986) Fluid infiltration into fault zones: chemical, isotopic and mechanical effects. *J. Pure Appl. Geophys.* **124**, 225-268.

Kerrich, R. (1989) Geochemical evidence on the sources of fluids and solutes for shear zone hosted mesothermal Au deposits. In *Mineralization and Shear Zones*, ed. Bursnall, J.T., *Geol. Assoc. Can. , Short Course Notes* **6**, 129-198.

Kerrich, R. and Fryer, B.J. (1979) Archaean precious-metal hydrothermal systems, Dome Mine, Abitibi greenstone belt: Part II. REE and oxygen isotope relations. *Can. J. Earth Sci.* **16**, 440-458.

Kerrich, R. and Fyfe, W.S. (1981) The gold-carbonate association: source of CO_2 and CO_2-fixation reactions in Archaean lode gold deposits. *Chem. Geol.* **33**, 265-294.

Kerrich, R. (1978) An historical review and synthesis of research on pressure solution, *Z. Geol. Paleont.*, 1977, 512-550.

Kesse, G.O. (1985) *The Mineral and Rock Resources of Ghana*, Balkema, 610 pp.

Kishida, A. and Riccio, L. (1980) Chronostratigraphy of lava sequence from Itapicuru belt, Bahia state, Brazil. *Precamb. Res.* **11**, 161-178.

Kleeman, J.D. (1985) Origin of disseminated wolframite-bearing quartz-topaz rock at Torrington, New South Wales, Australia. In *High Heat Production (HHP) Granites, Hydrothermal Circulation and Ore Genesis. Inst. Minning Metall.*, 197-210.

Kontak, D.J., Smith, P.K., Kerrich, R. and Williams, P.F. (1990) Integrated model for Meguma Group lode gold deposits, Nova Scotia, Canada. *Geol.* **18**, 238-242.

Kramers, D.J. and Foster R.P. (1982) A reappraisal of lead isotope investigations of gold deposits in Zimbabwe. In *Gold'82: The geology, Geochemistry and Genesis of Gold Deposits*, ed. Foster R.P., Balkema, Rotterdam, 569-582.

Krupp, R.E. and Seward, T.M. (1987) The Rotokawa geothermal system, New Zealand: an active eipthermal gold-depositing environment. Bull. Soc. Econ. Geolog. 82-5, 1109-1129.

Kuhns, R.J., Kennedy, P., Cooper, P., Brown, P., Mackie, B., Kusins, R. and Friesen, R. (1986) Geology and mineralization associated with the Golden Giant deposit, Hemlo, Ontario, Canada. In *Gold'86, An International Symposium on the Geology of Gold Deposits*, ed., Macdonald, J., Toronto.

Ladeira, E.A (1980) Genese do ouro na mina Morro Velho no distrito de Nova Lima, Minas Gerais, Brasil. *31 th Cong. Bras. Geol.* **2**, Camburiu, 371 pp.

Ladeira, E.A. (1985) Gold in Archaean iron formation at the Nova Lima District and in Quadrilátero

Ferrífero, Minas gerais. *Geol. Soc. Amer.* , *98 th Annual Meeting Abstract* **17**, 1310 pp.
Ladeira, E.A. (1988) Metalogenia dos depositos de ouro do Quadrilátero Ferrífero, Minas Gerais. In *Depositos Minearis do Brasil*, eds. Schobbenhaus, C. and Coelho, C.E.S, Vol. **III**, DNPM, Brasília.
Lameyre, J. (1988) Granite setting and tectonics. *Rendiconti della Societa Italiana di Miner. e Petrolog.* **43**, 215-236
Leake, B.E. (1978) Nomenclature of amphiboles. *J. Min. Assoc. Can.* **16**, 501-520.
Legrand, J.M. and Sá, J.M. (1986) Geotermometria, geobarometria e a zonação metamórfica do sinforme de Cruzeta-RN/Brasil. *34 th Cong.Bras.Geol.* 34, Goiania, GO, **4**, *Soc. Bras. Geol.*, 1407-1419.
LeMaitre, R.W. (1984) A proposal by the IUGS Subcommision on the systematics of igneous rocks for a chemical classification of volcanic rocks based on the total alkali silica (TAS) diagram. *Aust. J. Earth Sci.* **31**, 243-255.
Lespinasse, M., Cathelineau, M and Poty, B. (1991) Time/space reconstruction of fluid percolation in fault system: The use of fluid inclusion planes (FIP). Proceedings *25 th* SGA aniversary, Nancy, A. A., Balkema Pub., 468-495.
Leterrier, J., Jardim de Sá, E.F., Macedo, M.H. de F., Amaro, V.E. (1990) Magmatic and geodynamic signature of the Brasiliano cycle plutonism in the Seridó belt, NE Brazil. *36 th Congr. Bras. Geol.*, Natal, RN, **4**, *Soc. Bras. Geol.*, 1640-1654.
Lianxing, G. and McClay, K.R. (1992) Pyrite deformation in stratiform lead-zinc deposits of the Canadian Cordillera. *Mineral. Depos.* **27**, 1-13.
Lipman, P.W (1988) Evolution of silicic magma in the upper crust: the mid-Tertiary Latir volcanic field its cogenetic granitic batholith, northern New Mexico, USA. *Trans. of the Royal Soc. Edinburgh* **79**, 265-288.
Liverton, T. (1992) Tectonics and metallogeny of the Thirmymile Range, Yuko Territory, Canada. PhD thesis, Univ. London, (unpub.)
López-Ruiz, J., Cebriá, J. M., Doblas, M., Oyarzun, R., Hoyos, M. and Martin, C. (1993) Cenozoic intra-plate volcanism related to extensional tectonics at Calatrava, central Iberia. *J. Geol. Soc. London* **150**, 915-922.
Lyle, P. and Preston, J. (1993) Geochemistry and volcanology of the Tertiary basalts of the Giant's Causeway area, Northern Ireland. *J. Geol. Soc. London* **150**, 109-120.
Macdonald, R., Gass, K.N., Thrope, R.S. and Gass, I.G. (1984) Geochemistry and petrogenesis of the Derbyshire Carboniferous basalts. *J. Geol. Soc. London* **141**, 147-159.
Macedo, M.H. de F., Jardim de Sá , E.F. and Sá, J.M. (1984) Datações Rb-Sr em ortogneisses e a idade do Grupo Seridó. *21 th Symposyum of NE Geology* , João Pessoa, PB, Soc. Bras. Geol. **9**, 253-262.
Macedo, M.H.F., Jardim de Sá, E.F., Sato, K. and Kawashita, K. (1990) Dados isotópicos preliminares de Nd e Sr na região do Seridó (RN-PB),e suas implicações tectonicas. *36 th Cong. Bras.Geol.*, **4**, Natal, RN, *Soc. Bras. Geol.*
MacGeehan, P.J. and Hodgson, C.J. (1982) Environments of gold mineralization in the Campbell and Dickenson mines, Red Lake District, Ontario. *Can. Inst. Min. Metall.*, Sep. Vol.**24**, 184-210.
Maniar, P.D. and Piccoli, P.M. (1989) Tectonic discrimination of granitoids.*Geol. Soc. Amer. Bull.* **5**, 635-643.
Marchetto, C.M.L. (1989) Petrography of Cabaçal-1 gold-copper deposit, Mato Grosso State, Brazil. *Inst. Min. Metall.* **98,** B13-16.
Marcoux, E., Bonnemaison, M., Braux, C. and Joran, Z. (1989) Distribution de Au, Sb, Fe dans l'arsenopyrite aurifère du Châtelet et de Villeranges (Creuse, Massif Central Fançais). *C.R. Acad. Sci. Fr.* **II 308**, 293-300.
Marshall, R.L. and Gilligan, L. B. (1987) An introduction to remobilisation: Information from ore-body geometry and experimental considerations. *Ore Geol. Rev.* **2**, 87-131.
Martin, R.F. and Piwinski, A.J. (1972) Magmatism and tectonic setting. *J. Geophys. Reser.* **77**, 4966-4975.
Mason, R. and Melnik, N. (1986) The anatomy of an Archean gold system-The McIntyre-Hollinger complex at Timmins, Ontario, Canada. In *Gold'86 Canadian Precambrian Gold Deposits Re-Interpreted* , ed. Macdonald, A.J., Konsult Internation, Toronto, 40-55.
Matsuhisa, Y., Goldsmith, J.R. and Clayton, R.N. (1979) Oxygen isotope fractionation in the system quartz-albite-anorthite-water. *Geochim. Cosmochim. Acta* **42**, 1131-1140.
McArdle, P. (1989) Geological setting of gold mineralization in the Republic of Ireland. *Inst. Mining Metall.* **98**, B7-B12.
McCaig, A.M. (1987) Deformation and fluid-rock interaction in metasomatic dilatant shear bands. *Tectonophy.* **135**, 121-132.
McCarthy, T.S. and Hasty, R.A. (1976) Trace elements distribution patterns and their relationship to

the crystallisation of granitic melts. *Geochem. Cosm. Acta* **40**, 1351-1358.
McClay, K.R. and Ellis, P.G. (1984) Deformation of pyrite. *Econ. Geol.* **79**, 400-403.
McCulloch, M.T. and Wasserburg, G.J. (1987) Sm-Nd and Rb-Sr chronology of continental crust formation. *Sci.* **200**, 1003-1011.
McMurry, J., Long, L.E. and Sial, A.N. (1987) Petrology and isotope systematics of magma mushes: some porphyritic granitoids of northeastern Brazil. *Rev. Bras. Geoc.* **17 (4)**, 473-480.
McNaugton, N.J., de Laeter, J.R. and Groves, D.I. (1987) Constraints on the source of strontium and alkalies in auriferous alteration zones at Hunt mine, Kambalda, Norseman-Wiluna belt. In *Recent Advances in Understanding Precanbriam Gold Deposits*, eds. Ho, S.E. and Groves, D.I., *Univ. W. Aust. Pub.* **12**, 209-216.
Mello, E.F. (1992) Mineralogia e sucessão paragenética do minério aurífero de Ibiajara, BA. *37 th Congress Bras. Geol., São Paulo, SP*, vol. **1**, *Soc. Bras. Geol.*, 232-233.
Meunier, A.R. (1964) Sucession stratigraphique et passages lateraux dus au metamorphisme dans la Serie Ceará, Antecambrien du Nort-Est Brésilien. *Comp. Rendus Acad. Sci.*. **259**, 3796-3799, Paris.
Milesi, J.P., Feybesse, J.L., Ledru, P., Dommanget, A. Ouedraogo, M.F., Marcoux, E., Prost, A., Vinchon, C., Sylvain, J.P.(1989) West African gold deposits in their lower Proterozoic lithostructural setting. *Chron. Res. Min.* **497**, 3-98.
Millward, D., Merriner, G.F. and Saunders, A.D. (1984) Cretaceous tholeiitic volcanic rocks from the Western Cordillera of Columbia. *J. Geol. Soc. London* **141**, 847-860.
Miyashiro, A., Shido, F. and Ewing, M. (1970) Crystallisation and differentiation in abyssal tholeiites and gabbros from mid-oceanic ridges. *Earth Planet. Sci. Lett.* **7**, 311-365.
Mookherjee, A. (1971) Deformation of pyrite. *Ibid.* **66**, 200.
Moorbath, S. and Taylor, P.N. (1986) Geochronology and related isotope geochemistry of high-grade metamorphic rochs from the lower continental crust. In *The Nature of the Lower Continental Crust,* ed. Dawson, J.B., Carswell, D.A., Hall, J.and Wedepohl, K.H., *Geol. Soc. Spec. Pub.*, **24**, 211-220.
Moreira, J.A. de M., Medeiros, W.E. de, Ling, F.A.P., and Archanjo, C. J. (1989) Uma anomalia magnetica de caracter regional no Seridó (RN/PB) e discussão de sua origem., *1 st Congress, Braz. Soc. Geophysics, Rev. Bras. Geof.* **7**, 81.
Mpodozis, C. and Kay, S.M. (1992) Late Paleozoic to Triassic evolution of the Gondwana margin: evidence from Chilean frontal Cordilleran batholiths (28°S to 32°S). *Geol. Soc. Amer. Bull.* **104**, 999-1014.
Mueller, A.G. and Groves, D.I. (1991) The classification of Western Australian greenstone-hosted gold deposits according to wallrock-alteration mineral assemblages. *Ore Geol. Rev.* **6**, 291-331.
Mullen, E.D. (1983) $MnO/TiO_2/P_2O_5$: a minor element discriminant for basaltic rocks of ocean environments and its implication for petrogenesis. *Earth Planet. Sci. Lett.* **62**, 53-62.
Muller, D. and Groves, D.I. (1993) Direct and indirect association between potassic igneous rocks, shoshonites and gold-copper deposits. *Ore Geol. Rev.* **8**, 383-406
Mullis, J. (1979) The system methane-water as a geologic thermometer and barometer from the external part of the Central Alps. *Bull. Mineral.* **102**, 526-536
Mullis, J. (1987) Fluid inclusion studies during very low-grade metamorphism. In *Low-temperature metamorphism,* ed. Frey, M., Blackie, 162-199
Munis, M.de B. and Santos, E.J. dos (1980) Prospecto cobre, chumbo e zinco na faixa Cachoeirinha-Salgueiro. Intern Report CPRM- Recife, PE, Brazil.
Murphy, J.B. and Nance, R.D. (1990) Supercontinent model for the contrasting character of Late Proterozoic orogenic belts. *Geol.* **9**, 469-472.
Myers, J.S. (1978) Formation of banded gneisses by deformation of igneous rocks. *Precam. Res.* **6**, 43-64.
Nance, R.D., Worsley, T.R. and Moody, J.B. (1988) The supercontinent cycle. In Moors, E.M. ed., Shaping the Earth: reading from the *Sci. Amer. Mag.*, 177-187.
Neall, F.B. and Phillips, G.N. (1987) Fluid-wall rock interaction in an Archaean hydrothermal gold deposit: A thermodynamic model for the Hunt mine, Kambalda. *Econ. Geol.* **82**, 1679-1694.
Nelson, B.K. and DePaolo, D.J. (1984) 1700 Myr greenstone volcanic successions in southwestern North America and isotopic evolution of the Proterozoic mantle. *Nat.* **312**, 143-146.
Nelson, B.K. and DePaolo, D.J. (1985) Rapid production of continental crust 1.7 to 1.9 b.y. ago: Nd isotopic evidence from the basemnet of the North America mid-continent. *Geol. Soc. Amer. Bull.* **96**, 746-754.
Nesbitt , B.E., Murowchick, J.B. and Muehlenbachs, K. (1986) Dual origin of gold deposits in the Canadian Cordillera. *Geol.* **14**, 506-509.
Nesbitt, B.E. (1988) Gold deposit continum: A genetic model for lode Au mineralization in the continental crust. *Geol.* **16**, 1044-1048.
Nesbitt, B.E. (1991) Phanerozoic gold deposits in tectonically active continental margins. In *Gold*

Metallogeny and Exploration, ed. Foster, R.P., Blackie and Son Ltd., London, 432 pp.
Newberry, R.J., Burns, L.E., Swanson., S.E. and Smith, T.E. (1990) Comparative petrologic evolution of the Sn and W granites of the Fairbanks-Circle area, interior Alaska. *Geol. Soc. Amer. Sep. Paper* **246**, 121-142.
Nilsen, O. (1978) Caledonian sulphide deposits and iron-formations from the southern Trondheim region, central Norwegian Caledonides. *Norges Geol. Unders.*, **340**, 35-85.
Nitsch, K.H. (1970) Experimental determinetion of the upper stability of stilplomelane. Fortsch. Mineral. **47**, 48-49.
Novais, F., Brito Neves, B.B. de and Kawashita, K. (1979) Reconhecimento cronoestratigráfico na região Nordeste do Ceará. *33 th Symposyum Geol. NE*, Natal, RN.
O'Connor, J.T. (1965) A classification for quartz-rich igneous rocks based on feldspar ratios. *USGS Prof. Paper* **525B**, 79-84
O'Neil, J.R. and Chappell, B. (1977) Oxygen and hydrogen isotope compositions of granite genesis, in the New England batholih, Australia. *Contrib. Mineral. Petrol* . **62**, 313-325.
O'Neil, J.R., Shaw, S.E., Flood, R.H. (1977) Oxygen and hydrogen isotope compositions as indicators of granite genesis in the New England batholith, Australia. *Contrib. Mineral. Petrol.* **62**, 313-325.
O'Nions, R.K., Hamilton, P.J. and Hooker, P.J. (1983) A Nd isotope investigation of sediments related to crustal development in the Brithish Isles. *Earth Planet. Sci. Lett.* , **63**, 229-240.
Padgham, W.A. (1979) Gold deposits of the Northwest Territories. In *Proc. Gold Workshop, Yellowknife, NW.T.*, ed. Morton, R.D., 174-201.
Park, R.G. (1981) Shear-zone deformation and bulk strain in granite-greenstone terrain of the western Superior Province, Canada. *Precamb. Res.* **14**, 31-47.
Patchett, P.J. and Bridgwater, D. (1984) Origin of continental crust of 1.9-1.7 Ga age as defined by Nd isotopes in the Ketilidian terrain of South Greenland. *Contrib. Mineral. Petrol.* **87**, 311-318.
Patchett, P.J. and Kouvo, O. (1986) Origin of continental crust of 1.9-1.7 Ga ages: Nd isotopes and U-Pb zircon ages in the Svecokarelian terrain of south Finland. *Contrib. Mineral. Petrol.* 92, 1-12.
Passchier, C.W., Myers, J.S. and A. Kroner (1990) *Field Geology of High-Grade Gneiss Terrains*. Intern. Union of Geol.Sciences, Commmission on Tectonics, Springer-Verlag, 150 pp.
Pearce, J.A. and Cann, J.R. (1973) Tectonic setting of basic volcanic rocks determination using trace element analyses. *Earth Planet. Sci. Lett.* **19**, 290-300.
Pearce, J. A., Harris, N.B.W. and Tindle, A. G. (1984) Trace element discrimination diagrams for the tectonic interpretation of granitic rocks. *J. Petrol.*, 25, 956-983.
Peccerillo, A. and Taylor, S.R. (1976) Geochemistry of Eoceno calc-alkaline volcanic rocks from the Kastamonon area, Northern Turkey. *Contrib. Mineral. Petrol.* **58**, 63-81.
Peterson, N.P., Guilbert, C.M. and Quick, G.L. (1951) Geology and ore deposits of the Castle Dome Area, Gila Country, Arizona. *U.S. Geol. Surv. Bull.* **971**, 134 pp.
Petterson, M.G., Beddoe-Stephens, B., Millward, D. and Johnson, E.W. (1992) A pre-caldera plateau-andesite field in the Borrowdale Volcanic Group of the English Lake District. *J. Geol. Soc. London* **149**, 889-906.
Phillips, G.N. (1985a) Interpretation of Big Bell/Hemlo-type gold deposits: Precursors, metamorphism, melting and genetic constrains. *Trans. Geol. Soc. S. Africa* **88**, 159-173.
Phillips, G.N. (1985b) Archaean gold deposits of Australia. *Econ. Geol. Reser. Witwatersrand Univ. Pub.*, Johannesburg.
Phillips, G.N. and De Nooy, D. (1988) High-grade metamorphic processes which influence Archean gold deposits, with particular reference to Big Bell, Australia. *J. Metamorph. Geol.* **6**, 95-114.
Phillips, G.N., Groves, D.I. and Clark, M.E. (1983) The importance of host-rock mineralogy in the location of Archaean epigenetic gold deposits. *Geol. Soc. S. Africa Spec. Pub.* **7**, 79-86.
Phillips, G.N., Groves, D.I. and Martyn, J.G. (1984) An epigenetic origin for Archaean banded iron-formation hosted gold deposits. *Econ. Geol.* **79**, 162-171.
Phillips, G.N.and Groves, D.I. (1984) Fluid access and fluid-wall interaction in the genesis of the Archaean gol-quartz vein deposit at Hunt mine, Kambalda, Western Australia. In *Gold' 82: The Geology, Geochemistry and Genesis of Gold Deposits*, ed. Foster, R.P., Balkema, Rotterdam, 389-416.
Phillips, W.J. (1972) Hydraulic fracturing and mineralization. *J.Geol. Soc. London*, **128**, 337-359.
Pichavant, M. and Montel, J.M. (1988) Petrogenesis of two-mica ignimbrite suite: the Macusani Volcanics, SE Peru. *Trans. Royal Soc. Edinburgh* **79**, 197-207.
Piper J.D.A. (1976) Paleomagnetic evidence for a Proterozoic supercontinent. *Phil. Trans. Royal Society London* **A-280**, 469-490.
Piper, J.D.A. (1987) *Paleomagnetism and continental crust*. Open University Press., U.K., 434 pp.
Pires, A.C.R., Oliveira, J.L. de, Brito, A.de L.F. and Moura, F.A.P. (1984) Projeto Ouro Cachoeira de Minas, Convênio SUDENE-CDRM/PB, Relatório Final, CDRM/PB.
Pitcher, W.S. (1983) Granite: typology, geological environment and melting relationships. In

Migmatites, Melting and Metamorphism, eds. Atherton, M.P. and Gribble, C.D., Shiva, Cheshire, 277-287.

Pichter, W.S. (1987) Granites and yet more granites, forty years on. *Geol. Rundschau* **76**, 51-79.

Pitfield, P.E.J., Teoh, L.H. and Cobbing, E.J. (1990) Textural variation and tin mineralization in granites from the Main Range Province of the Southeast Asian Tin Belt. *Geol. J.* **25**, 419-429.

Plimer, I.R. and Finlow-Bates, T. (1978) Relationship between primary iron sulphides, sulphur source, depth of formation and age of submarine exhalative deposits. *Mineral. Depos.* **13**, 399-410.

Porada, H. (1989) Pan-African rifting and orogenesis in southern to equatorial Africa and eastern Brazil. *Precamb. Res.* **44**, 103-136.

Powell, R. and Holland, T.J.B.(1988) Thermocalc. *J. Metamorph. Geol.* **6**, 173-204.

Power, G.M. (1968) Chemical variation in tourmaline from southwest England. *Mineralog. Mag. London* **36**, 1078-1089

Ramboz, C., Pichavant, M. and Weisbrod, A. (1982) Fluid immiscibility in natural processes: use and miuse of fluid inclusion data. *Chem. Geol.* **37**, 29-48.

Ramboz, C., Schnapper, D. and Dubbessy, J. (1985) The P-V-T-X-fO_2 evolution of H_2O-CO_2-CH_4-bearing fluid in a wolframite vein: reconstraction from fluid inclusion studies *Geochim. Cosmochim. Acta* **49**, 205-219.

Ramdohr, P. (1969) *The Ore Minerals and Their Intergrowths*, 2 nd edition, Pergamon Press, New York, 1207 pp.

Ramsay, J.G.(1967) *Folding and Fracturing of Rocks*. New York, McGraw-Hill, 567 pp.

Ramsay, J.G. (1980) Shear zone geometry: a review. *J. Struct. Geol.* **2**, 83-99.

Ramsay, J.G. and Huber, M.I. (1983) *The Techniques of Modern Structural Geology*, Vol. 1: Strain Analysis, London, Academic Press, Toronto, 307 pp.

Reynolds, P.H.(1971) A U-Th-Pb lead isotope study of rocks and ores from Broken Hill, Australia. *Earth Planet. Sci. Lett.* **12**, 215-223.

Richards, J.R. (1971) Major lead orebodies, mantle origin ? *Econ. Geol.* **66**, 425-434.

Richards, J.R., Fletcher, I.R. and Blockley, J.G. (1981) Pilbara galenas: Precise isotopic Assay of the oldest australian leads; Model ages and growth-curve implications. *Mineral. Depos.* **16**, 7-30.

Robert, F. and Brown, A. (1986a) Achaean gold-bearing quartz veins at the Sigma mine Abitibi greenstone belt, Quebec: Part I Geology relations and formation of the vein system. *Econ. Geol.* **81**, 578-592.

Robert, F. and Brown, A. (1986b) Achaean gold-bearing quartz veins at the Sigma mine Abitibi greenstone belt, Quebec: Part II Vein paragenesis and hydrothermal alteration *Econ. Geol.* **81**, 593-616.

Robert, F. and Brown, A.C. (1984) Progressive alteration with gold-quartz-tourmaline veins at the Sigma Mine, Albitibi Greenstone Belt, Quebec. *Econ. Geol.* **79**, 393-399.

Robert, F. and Kelly, W. (1987) Ore forming fluids in Archaean gold-bearing quartz veins at the Sigma mine, Abitibi greenstone belt, Quebec, Canada. *Econ. Geol.* **82**, 1464-1482.

Roberts, S., Sanderson, D.J., Dee, S. and Gumiel P. (1991) Tectonic setting and fluid evolution of auriferous quartz veins from the La Codosera area, Western Spain. *Econ. Geol.* **86**, 1012-1022.

Roedder, E. (1972) Composition of fluid inclusions. *USGS Prof. Paper 440-JJ*, 164 p

Roedder, E. (1979) Fluid inclusions as samples of ore fluids. In *Geochemistry of Hydrothermal Ore Deposits*, ed. Barnes, H.L., 2 nd edition, John Wiley & Sons, New York, 798 pp.

Roedder, E. (1981) Origin of fluid inclusions and changes that occur after trapping. In *Fluid Inclusions: Applications to Petrology*, Short Course Handbook, vol. 6, eds. Ghent, E.D., Hollister, L.S. and Crawford, M.L., *Mineral Assoc. of Canada*, Calgary.

Roedder, E. (1984) Fuild Inclusions. *Reviews in Mineralogy* **12**, *Mineral. Soc. Amer.*, ed. Ribbe, P., 644 pp.

Rutter, E.H. and Brodie, K.H. (1985) The permeation of water into hydrating shear zones. In *Metamorphic Reactions, Kinetics, Textures, Deformation*, eds. Thompson, A.B. and Rubie, D.C., Springer-Verlag, Berlin, 242-250.

Rye, D.M. and Rye, R.O. (1974) Homestake gold mine, South Dakota, I: stable isotope studies. *Econ. Geol.* **69**, 293-317.

Rye, D.M., Doe, B.R. and Delevaux, M. H.(1974) Homestake gold mine, South Dakota: II.Lead isotopes, mineralization ages, and source of lead in ore of Northern Black Hills. *Econ. Geol.* **69**, 814-822.

Sá, F.T. and Tinoco Sobrinho, J. (1979) Estratigrafia da região sudeste de São Raimundo Nonato-PI e norte de Remanso-BA, 9 th *Symposium N.E Geol.*, Natal, RN, vol. **9**, 1-12.

Sá, J.M., Bertrand, J.M. and Leterrier, J. (1991) Evolution géodynamique et géochronologie (U-Pb, Rb-Sr et K-Ar) de la ceinture plissée d'Orós, NE du Brésil. *Comptes-Rendus de l'Académie des Sciences Paris*, Tome 313, Série II, 231-237.

Saager, R., Meyer, M. and Muff (1982) Gold distribution in supracrustal rocks from Archaean

greenstone belts of Southern Africa and from Paleozoic ultramafic complexes of the European Alpes: Metallogenetic and chemical implications. *Econ. Geol.* **77**, 1-16.

Santos, E.J. dos and Brito Neves, B.B. de (1984) Província Borborema. In *O Pre Cambriano do Brasil*, eds. Almeida, F.F.M. and Hasui, Y., Blucher, São Paulo, 123-186.

Santos, E.J. dos, Coutinho, M.G.N., Costa, M.P.A. and Ramalho, R. (1984a) A região de dobramento do nordeste e a bacia do Parnaíba, incluindo o craton de São Luis a as bacias marginais. In *Geologia do Brasil*, eds., Schobbenhaus, C., Almeida Campos, D., Derze, G.R. and Asmus, H.E., DNPM, Brasília, 131-189.

Santos, J.E. dos, Rocha, D.E.G.A., Costa, F.S.F. da and Maranhão, R.J.L. (1985) Projeto Itapetim: Pesquisa de ouro. Relatório Final , CPRM.

Sargeant, D.W. (1983) Geological setting of Sons of Gwalia gold mine, Leonora, West Australia (unpub).

Saunders, J. A. (1990) Colloidal transport of gold and silica in epithermal precious-metal system: evidence from the Sleeper deposit, Nevada. *Geol.* **18**, 757-760.

Sawka, W.N., Heizler, M.T., Kistler, R.W. and Chappell, B.W. (1990) Geochemistry of highly fractinated I- and S-type granites from the tin-tungsten province of western Tasmania. *Geol. Soc. Amer. Sp. Paper* **246**, 161-179.

Sawkins, F.J. (1990) Metal Deposits in Relation to Plate Tectonics. Serie: Mineral and rocks, Spring Verlag, USA, *2 nd edition*, 461 pp

Scheid, C. and Ferreira, C.A. (1991) Patos Folha SB.24-Z-D-I-Estados de Pernambuco e Paraíba, Programa Levantamentos Geológicos Básicos do Brasil, DNPM/CPRM, Brasília.

Schobbenhaus, C., Campos, D. de A., Derze, R.G. and Asmus, H.E. (1984) Mapa Geológico do Brasil e das Areas Oceanicas Adjacentes Incluindo Depositos Minerais, scale 1:2.500 000, DNPM, Brasília.

Schouwstra, R.P. and Villiers, J.P.R. de (1988) Gold mineralization and associated wallrock alteration in Main Rut Complex at Sheba mine, South Africa. *Inst. Mining Metall.* **97**, London, B158-170.

Schwartz, M.O. (1989) Determining phase volumes of mixed CO_2-H_2O inclusions using microthermometric measurements. *Mineral. Depos.* **24**, 43-47.

Scott, S. D. (1976) Application of the sphalerite geobarometer to regionally metamorphosed terrains. *Amer. Mineral.* **61**, 661-670.

Scott, S. D. (1983) Chemical behaviour of sphalerite and arsenopyrite in hydrothermal and metamorphic enviroments. *Mineral. Mag.* **47**, 427-435.

Secor, D.T. (1965) Role of fluid pressure in jointing. *Amer. J. Sci.*, **263**, 633-646.

Secor, D.T. (1968) Mechanics of natural extension fracturing at depth in the Earth's crust. *Geol. Surv. Canada*, Paper, 68-52, 3-48.

Seward, T.M. (1973) Thio-complexs of gold and transport of gold in hydrothermal ore solutions. *Geochim. Cosmochim. Acta* **17**, 379-399.

Seward, T.M. (1984) The transport and deposition of gold in hydrothermal systems. In *Gold' 82 The Geology, Geochemistry and Genesis of Gold Deposits*, ed. Foster, R.P., Balkema, Rotterdam, 165-182.

Seward, T.M. (1991) The hydrothermal geochemistry of gold. In *Gold Metalogeny and Exploration*, ed. Foster, R.P., Blackie, 432 pp.

Shand, S.J. (1947) *Eruptive Rocks. Their Genesis, Composition, Classification, and their Relation to Ore-Deposits, 1fs.* edition, J. Wiley and Sons, New York, 488 pp. J. Wiley, New York.

Shaw, D.M. (1968) A review of K-Rb fractionation trends by covariance analysis. *Geochim. Cosmochim. Acta* **32**, 573-601.

Shepherd, T., Rankin, A.H. and Alderton, D.H.M.(1985). *A Practical Guide to fluid Inclusion Studies*, ed. Blackie, New York.

Sial, A.N. (1984) Padrão regional de isótopos de oxigenio em granitoides do espaço Cachoeirinha, Nordeste do Brasil. *33 th Congress Bras. Geol.*, Rio de Janeiro, vol. **6**, *Soc. Bras. Geol.*, 2710-2722.

Sial, A.N. (1986) Granite-types in Northeast Brazil: Current Knowledge. *Rev. Bras. Geoc.* **16 (1)**, 54-72.

Sial, A.N. (1987) Granitic rocks of Northeast Brazil. Int. Symp. Granites Assoc. Mineraliz., ISGAM., Salvador, Brazil, 61-69.

Sial, A.N. and Menor, E. (1969) Geologia de meia quadrícula sul de Taquaritinga do Norte. Intern Report Inst. Geoc. Univ. of Recife.

Sial, A.N. and Ferreira, V.P. (1988) Brasiliano-age peralkaline plutonic rocks of the central srtuctural domain, Northeast Brazil. *R.C. Soc. Ital. Mineral Petrol.*, **43** (2), 307-342.

Sial, A.N., Ferreira, V.P. and Mariano, G. (1992) Coexistence of two magmas and igneous processes in some Brasiliano age granitoids in Northeastern Brazil. *37h Cong. Bras. Geol.*, São Paulo, SP, **1**, Soc. Bras. Geol., 362-363.

Sibson, R.H. (1980) Transient discontinuities in ductile shear zones. *J. Struct. Geol.* **2**, 165-171.
Sibson, R.H. (1977) Fault rocks and fault mechanisms. *J. Geol. Soc. London* **133**,191-213.
Sibson, R.H. (1981) Fluid flow accompanying faulting: Field evidence and models. In *Earthquake Prediction: An Internation Review*, eds. Simpson, D.W. and Richards, P.G., *Amer. Geophys. Union*, Maurice Ewing series, **4**, 593-603.
Sibson, R.H., Robert, F. and Poulsen, K.H. (1988) High-angle reverse faults, fluid-pressure cycling, and mesothermal gold-quartz deposits. *Geol.* **16**, 551-555.
Sillitoe, H.R. (1991) Intrusion-related gold deposits. In *Gold Metalogeny and Exploration*, ed. Foster, R.P., Blackie, 432.
Silva Filho, M.A. da, Bonfim, L.F.C., Santos, R.A., Rodrigues, T.N. and Braz Filho, P.A. (1981) Projeto Canindé do São Francisco: Mapa geológico integrado 1: 100.000, DNPM/CPRM, Salvador, (unpub.).
Silva Filho, M.A. da, Nesi, J. de R. and Mendes, V.A. (1985) *Projeto Cachoeirinha* , Relatório Final, Recife, DNPM/CPRM.
Skawarnecki, M.S.(1987) Controls on Archaean gold mineralization in the Leonora area, Western Australia. In Recent advances in understanding Precambrian gold deposits, eds. Ho, S.E., Groves, D.I., Geol. Dept. and Univ. Extension, *Univ. W. Aust. Publ.*, 109-135.
Sloan, R.J. and Bennett, M.C. (1990) Geochemical character of Silurian volcanism in SW Ireland. *J. Geol. Soc. London* **147**, 1051-1060.
Smith, D.L. and Evans, B. (1984) Diffusional crack healing in quartz. *J. Geophys. Res.* **89**, B6, 4125-4135.
Smith, E.I., Feurbach, D.L., Naumann, T.R.and Millis, J.G. (1990) Mid-miocene volcanic and plutonic rocks in the Lake Mead area of Nevada and Arizona; Production of intermediate igneous rocks in an extensional environment. *Geol. Soc. London Memoir* **174**, 169-194.
Smith, T.J., Cloke, P.L. and Kesler, S.E. (1984) Geochemistry of fluid inclusions from the McIntyre Hollinger gold deposit, Timmins, Ontario, Canada. *Econ. Geol.* **79**, 1265-1285
Spooner, E.T.C. and Fyfe, W.S. (1973) Sub-sea floor metamorphism, heat and mass transfer. *Contrib. Mineral. Petrol.* **42**, 287-304.
Spooner, E.T.C. (1991) The magmatic model for the originof Archean Au-quartz vein ore systems: An assessment of the evidence. In *Proc.of Brazil Gold'91, The Economics geology Geochemistry and Genesis of Gold Deposits* , ed. Ladeira, E.A., Balkema, Rotterdam, 313-318.
Stacey, J.S. and Kramers, J.D.(1975) Aproximation of terrestrial lead isotope evolution by a two-stage model. *Earth Planet. Sci. Lett.* **26**, 207-221.
Stanton, R.L. (1972) *Ore Petrogoly*. McGraw-Hill, New York, 713 pp.
Starling, A., Galligan, J.M., Carter, A.H.C., Foster, R.P. and Saunders, R.A. (1989) High-temperature hydrothermal precipitation of precious metals on the surface of pyrite. *Nat.* **340**, no.6231, 298-300.
Stone, M. (1987) Geochemistry and origin of the Carnmenellis pluton Cornwall; further considerations. *Proceeding of the Ussher Soc.* **6**, 454-460.
Stone, M. and Exley, C.S. (1985) High heat production granites of southwest England and their associated mineralization: a review. In *High Heat Production (HHP) Granites, Hydrothermal Circulation and Ore Genesis, Inst. Mining Metall. London*, 571-593.
Stone, W.E. (1990) Archaean volcanism and sedimentation in the Bousquet gold district, Abitibi greenstone belt, Quebec: Implications for stratigraphy and gold concentration. *Geol. Soc. Amer. Bull.* **102**, 147-158.
Stose, A.J. and Stose, G.W. (1957) Geology and mineral resources of the Gossan Lead District and adjacent areas in Virginia. *Virginia Div. Min. Res.*, Bull. **72**, 233 pp.
Strauss, H. (1986) Carbon and sulfur isotopes in Precambrian sediments from the Canadian Shield. *Geochim. Coschim. Acta* **50**, 2653-2662.
Streckeisen, A.L. (1974) Classification and nomenclature of igneous rocks. Recomendations of the IUGS subcommission on the systematics of igneous rocks. *Geol. Rundsch.* **63**, 773-786.
Streckeisen, A.L. (1976) To each plutonic rocks its proper name. *Earth Sci. Rev.* **12**, 1-33.
Sun, S.S (1980) Lead isotopic study of young volcanic rocks from mid-ocean ridges, ocean islands and island arcs. *Phil. Trans. Roy Soc.London* A **297**, 409-445.
Swanson, S.E., Bord, J.F. and Newberry, R.L. (1988) Petrogenesis of the Ear Mountain tin granite, Sewerd Peninsula, Alaska. *Econ. Geol.* **83**, 46-61.
Tabeart, C.F. (1987) Controls to deposition of gold, copper and bismuth at Renco Mine, Zimbabwe. *African Inst. Min. Metall.*, 347-363.
Takahashi, M., Armaki, S. and Ishihara, S. (1980) Magnetite-series/Ilmenite-series vs I-type/S-type granitoids. *Mining Geol. Spec. Issue* **8**, 13-28.
Takenouchi, S. and Kennedy, G.C. (1965) The solubility of carbon dioxide in NaCl solution at high temperature and pressure. *Amer. J. Sci.* **263**, 445-454.
Taylor, H.P.(1979) Oxygen and hydrogen isotope relationships in hydrothermal mineral deposits. In

Geochemistry of Hydrothermal Mineral Deposits, ed. Barnes, H.L., John Wiley and Sons, New York.

Taylor, B.E. and O'Neil, J.R. (1977) Stable isotope studies of metasomatic Ca-Fe-Al-Si skarns and associated metamorphic and igneous rocks, Osgood Mountains, Nevada. *Contrib. Mineral. Petrol.* **63**, 1-49.

Thirlwall, M.F. and Burnard, P. (1990) Pb-Sr-Nd isotope and chemical study of the origin of undersaturated and oversaturated shoshonitic magmas from the Borrolan pluton, Assynt, NW Scotland. *J. Geol. Soc. London* **147**, 259-269.

Thirlwall, M.F. and Graham, A.M. (1984) Evolution of high-Ca, high-Sr C-series basalts from Grenada, Lasser Antilles: the effects of intra-crustal contamination. *J. Geol. Soc. London* **141**, 427-445.

Thomas, W.M. and Ernst, W.G. (1990) The aluminium content of hornblende in calc-alkaline granitic rocks: a mineralogic barometer calibrated experimentally to 12 Kbars. In *Fluid-Mineral Interactions: A Tribute to H.P. Eugster*, Spencer, R.J. and Chou, I-Ming, eds. *The Geochem. Soc.*, Spec. Pub. No.2

Thompson, R.N., Gibson, S.A., Leat, P.T., Mitchell, J.G., Morrison, M.A., Hendry, G.L. and Dickin, A.P. (1993) Early Miocene continental extension-related basaltic magmatism at Walton Peak, northeast Colorado: further evidence on continental basalt genesis. *J. Geol. Soc. London* **150**, 277-292.

Tindle, A.G., McGravie, D.W. and Webb, P.C. (1988) The role of hybridization and crustal fractionation in the evolution of the Cairnsmore of Carphairn Intrusion, Southern Uplands of Scotland. *J. Geol. Soc. London* **145,** 11-21.

Torquato, J.R. and Cordani, U.G. (1981) Brazil-Africa geological links. *Earth Sci. Rev.* **17**, 155-176.

Torquato, J.R. and McReath, I. (1983) Precambriano Médio-idade provável para a Formação Jucurutu do Grupo Seridó-RN. *Ciencias da Terra* **7**, 16-17

Travis, G.A., Woodall, R. and Bartram, G.D. (1971) The geology of the Kalgoorlie Goldfield. *Spec. Pub. Soc. Aust.* **3**, 175-190.

Turekian, K.K. and Wedwpohl, K.H. (1961) Distribution of the elements in some major units of the Earth's crust. *Geol. Soc. Amer. Bull.* **72**, 175-192.

Van den Kerkhof, A.M. (1988) The system CO_2-CH_4-N_2 in fluid inclusions: Theoretical modelling and geological Applications. Thesis, Free Univ. Amsterdam, (unpub.) 206 pp.

Vauchez A., Amaro, V., Arcanjo, C., Arthaud, M., Bouchez, J.L., Caby, R., Corsini, M., Egydio Silva, M., Jardim de Sá, E.F., Neves, S.P., Sá, J.M. and Sial, A.N. (1992) The Borborema shear zone system: a tectonic model. *37 th Cong. Bras. Geol.*, São Paulo, SP, **1**, *Soc. Bras. Geol.*, 371-373.

Viljoen, M.J. (1984) Archaean gold mineralization and komatiites in southern Africa. In *Gold' 82 The geology, geochemistry and genesis of gold deposits*, ed. Foster, R.P., Balkema, Rotterdam, 595-627.

Vokes, F.M. (1963) Geological studies on the Caledonian pyritic lead-zinc ore-body at Bleikvassli, Nordland, Norway. *Norges Geol.Unders.* **222**, 126 pp.

Voll, G.(1976) Recrystallization of quartz, biotite and feldspar from Erstfeld to the Levantina Nappe, Swiss Alps and its geological significance. *Schweiz. Mineral. Petrogr. Mitt.*, **56**, 641-647.

Walsh, J.B. (1965) The effect of crakcs on the compressibility of rock. *J. Geohpys. Res.*, **70**, 381-389.

Walsh, J.F., Cloke, P.L. and Kesler, S.E. (1984) Fluid (CO_2-H_2O) immiscibility and fO_2 as factors in gold deposition: Pamour No. 1 mine, Timmins, Ontario. *Annual Meeting, Reno, Nevada, 581*, Abstract with Programms.

Walshe, J.L. (1986) A six-component chlorite solid solution model and the conditions of chorite formation in hydrothermal and geothermal systems. *Econ.Geol.* **81**, 681-703.

Walther, J.V. and Helgeson, H. C. (1977) Calculation of the thermodynamic properties of aqueous silica and the solubility of quartz and its polymorphs at high pressure and temperature. *Amer. J. Sci.*, **277**, 1315-1351.

Walther, J.V. and Orville, P.M. (1982) Volatile production and transport in regional metamorphism. *Contrib. Mineral. Petrol.* **79**, 252-257.

Wanderley, A.A. (1983) Projeto mapas metalogenéticos e de previsão de recursos minerais: Patos, Folha SB. 24-Z-D, scale 1:250.000, Recife, DNPM/CPRM.

Wanderley, A.A. (1990) Monteiro, Folha SB. 24-Z-C-IV, texto explicativo, Recife, DNPM/CPRM.

Wanderley, A.A., Veiga Junior, J.P., Santos, E.J. dos (1992) O complex Irajaí no contexto evolutivo da Provincia da Borborema. *37 th CongressBrasi. Geol., Bol. Resumos, Soc. Bras. Geol., São Paulo, SP* **3**, 302-303.

Weaver, B.L., Wood, D.A., Tarney, J. and Joron, J.L. (1987) Geochemistry of ocean island basalts from the South Atlantic: Ascension, Bouvet, St. Helena, Gough and Tristan da Cunha. *Geol. Soc.*

London Spec. Pub. **30**, 253-267.
Weissberg, B. C. (1970) Solubility of gold in hydrothermal alkaline sulfide solutions. *Econ. Geol.* **65**, 551-556.
Wells, J.D. and Mullens, T.E. (1973) Gold-bearing arsenian pyrite determined by microprobe analysis, Cortez and Carlin gold mines. *Ecom. Geol.* **68**, 187-201.
Werner, C.D. (1987) Saxonian granulites - igneous or lithogenous. A contribution to the geochemical diagnosis of the original rocks in high-metamorphic complexes. In Contributions to the Geology of the Saxonian Granulite Massif (Sachsisches Granulitgebirge), ed. Gerstenberger H, Zfl-Mitteilungen Nr 133, 221-250.
Whalen, J.B., Currie, K.L. and Chappell, B.W. (1987) A-type granites: geochemical characteristic, discrimination and petrogenesis. *Contrib. Mineral. Petrol.* **95**, 407-419.
White , S.H. and Johnston, D.C. (1981) A microstructural and microchemical study of cleavage lamellae in a slate. *J. Struct. Geol.* , **3**, 279-290.
White, A.J.R. (1990) A workshop on crustal protoliths of granites. Note for January 1990 short course, Univ. St. Andrews.
White, A.J.R., Williams, I.S. and Chappell, B.W. (1977) Geology of the Beridale Sheet 8625 NSW . Geol. Surv. NSW, 138 pp.
White, A.J.R. and Chappell, B.W. (1988) Some supracrustal (S-type) granites of the Lachlan Fold Belt. *Trans. Royal Soc. Edinburgh* **79**, 169-181.
White, A.J.R. and Chappell, B.W. (1989) Geology of the Numbla 1:100000 sheet 8624 N.S.W. *Geol. Surv.*, 160 pp.
Wilkins, C. (1993) A post-deformational, post-peak metamorphic timing for mineralization at the Archaean Bib Bel gold deposit, Western Australia. *Ore Geol. Rev.* **7**, 439-483.
Wilson, M. (1989) *Igneous Petrogenesis*. Oxford University Press, 466 pp.
Winchester, J.A. and Floyd, P.A. (1977) Geochemical discrimination of different magma series and their differentiation products using immobile elements. *Chem. Geol.* **20**, 325-343.
Windley, B.F. (1978) *The Evolving Continents*. John Wiley and Sons, New York, 385pp.
Wood, P.C., Burrows, D.R., Thomas, A. V. and Spooner, E.T.C. (1986) The Hollinger-McIntyre Au-quartz veins system, Timmins, Ontario, Canada; geologic characteristics fluid properties and light stable isotope geochemistry. In *Gold'86 Canadian Precambrian Gold Deposits Re-Interpreted*, ed. Macdonald, A.J., Konsult Internation, Toronto, 56-80.
Woodall, R. (1979) Gold Australia and the world. *Geol. Dep. Univ. W. Aust. Pub.* **3**, 1-34.
Woodall, R.(1988) Gold in 1988. In *Bicentennial Gold 88*, Extended Abstracts Oral Programme, eds. Goode, A., D.T. Smyth, E.L., Birch, W.D. and Bosma, L.I.*Geol. Soc. Aust. Inc. Abstr.* **22**, 1-12.
Wooley, A.R. and Jones, G.C. (1987) The petrochemistry of the northen part of the Chilwa alkaline province, Malawi. *Geol. Soc. London Spec. Pub.* **30**, 335-355.
Wormald, R.J. and Price, R.C. (1988) Peralkaline granites near Temora, southern New South Wales: tectonic and petrological implications. *Aust. J. Earth Sci.* **35**, 209-221.
Xavier, R.P. (1987) Estudo de inclusões fluidas na mina de ouro Fazenda Brasileiro, greenstone belt do Rio Itapicuru. MSc thesis, Univ. of São Paulo, Brazil, (unpub.)
Xavier, R.P. (1991) The role of microstructural and fluid processes in the genesis of gold-bearing shear zones: Fazenda Maria Preta mine, Rio Itapicuru greenstone belt, Bahia, Brazil. PhD thesis, Southampton Univ., 241 pp.
Xavier, R.P., Foster, R.P., Fallick, A.E. and Alderton, D.H.M. (1994) Microstructural and chemical evolution of gold-bearing brittle-ductile shear zones: Fazenda Maria Preta mine, Rio Itapicuru greenstone belt, Bahia, Brazil. (in press).
Yardley, B.J.D. (1989) An Introduction to Metamorphic Petrology. Longman, Essex. 248 pp.
Zartman, R.E. and Doe, B.R. (1981) Plumbotectonics - the model. *Tectonophy.* **75**, 135-162.

Appendix A1.1
Sample Descriptions

Sample	Northing km	Easting km	Depth (m)	Drill Core	Locality	Main Lithology
MG-T-005	9193350	690153	6.47-7.53	03-BJ-05-PE	Degredo, Itapetim-West Domain	Biotite gneiss
MG-T-006	9193350	690153	7.53-7.73	03-BJ-05-PE	Degredo, Itapetim-West Domain	Granitic biotite gneiss
MG-T-014	9193350	690153	12.74-13.30	03-BJ-05-PE	Degredo, Itapetim-West Domain	Quartz-feldspathic rock
MG-T-019	9193350	690153	17.07-20.20	03-BJ-05-PE	Degredo, Itapetim-West Domain	Granitic biotite gneiss
MG-T-025	9193350	690153	32.90-33.50	03-BJ-05-PE	Degredo, Itapetim-West Domain	Biotite gneiss, mafic-rock + intercalated quartz vein
MG-T-027	9193350	690153	35.50-36.80	03-BJ-05-PE	Degredo, Itapetim-West Domain	Biotite gneiss, mafic-rock + intercalated quartz vein
MG-T-028	9193350	690153	36.80-37.55	03-BJ-05-PE	Degredo, Itapetim-West Domain	Biotite gneiss, mafic-rock + intercalated quartz vein
MG-T-030	9193350	690153	41.80-43.75	03-BJ-05-PE	Degredo, Itapetim-West Domain	Biotite gneiss, mafic-rock + intercalated quartz vein
MG-T-031	9193350	690153	43.75-45.05	03-BJ-05-PE	Degredo, Itapetim-West Domain	Gneiss, mafic-rock intercalated
MG-T-032	9193350	690153	45.05-46.00	03-BJ-05-PE	Degredo, Itapetim-West Domain	Gneiss, mafic-rock intercalated
MG-T-033	9193350	690153	46.00-47.80	03-BJ-05-PE	Degredo, Itapetim-West Domain	Gneiss, mafic-rock + mineralized quartz vein intercalations
MG-T-034	9193350	690153	47.80-48.40	03-BJ-05-PE	Degredo, Itapetim-West Domain	Gneiss, mafic-rock + mineralized quartz vein intercalations
MG-T-035	9193350	690153	48.40-49.80	03-BJ-05-PE	Degredo, Itapetim-West Domain	Biotite gneiss, mafic-rock intercalated
MG-T-037	9193350	690153	54.80-56.70	03-BJ-05-PE	Degredo, Itapetim-West Domain	Gneiss, mafic-rock intercalated
MG-T-050	9193350	690153	77.95-79.25	03-BJ-05-PE	Degredo, Itapetim-West Domain	Gneiss, mafic-rock intercalated
MG-T-052	9193350	690153	80.35-81.95	03-BJ-05-PE	Degredo, Itapetim-West Domain	Biotite schist, well silicified
MG-T-056	9193350	690153	88.45-90.65	03-BJ-05-PE	Degredo, Itapetim-West Domain	Mafic rock (amphibolite) intercalated in gneisses
MG-T-058	9193350	690153	91.90-92.70	03-BJ-05-PE	Degredo, Itapetim-West Domain	Mafic-rock with leuco-gneiss and gneiss intercalations
MG-T-059	9193350	690153	92.70-94.95	03-BJ-05-PE	Degredo, Itapetim-West Domain	Mafic-rock with leuco-gneiss and gneiss intercalations
MG-T-064	9193350	690153	101.10-102.25	03-BJ-05-PE	Degredo, Itapetim-West Domain	Biot. gneiss, mafic-rock+qz. vein intercalated
MG-T-073	9193350	690153	112.74-114.08	03-BJ-05-PE	Degredo, Itapetim-West Domain	Mafic-rock with leuco-gneiss and gneiss intercalations
MG-T-077	9192060	692913	3.45-3.69	03-IT-36-PE	Sertãozinho, Itapetim-Central Domain	Leuco-gneiss, quartz-feldspathic bands
MG-T-086	9192060	692613	16.90-21.60	03-IT-36-PE	Sertãozinho, Itapetim-Central Domain	Gneiss light-pink, medium-coarse grained
MG-T-087	9192060	692613	21.60-22.43	03-IT-36-PE	Sertãozinho, Itapetim-Central Domain	Gneiss porphyritic, ultramafic-rock intercalations
MG-T-089	9192060	692913	23.50-23.85	03-IT-36-PE	Sertãozinho, Itapetim-Central Domain	Mafic-rock (schist), gneiss intercalation
MG-T-090	9192060	692613	23.85-25.18	03-IT-36-PE	Sertãozinho, Itapetim-Central Domain	Mafic-rock (schist), gneiss intercalation
MG-T-095	9192060	692613	30.65-31.15	03-IT-36-PE	Sertãozinho, Itapetim-Central Domain	Quartz-feldspahtic rock intercalated in mafic-rock (schist)
MG-T-101	9192060	692613	37.85-39.20	03-IT-36-PE	Sertãozinho, Itapetim-Central Domain	Mafic-rock, fractures filled by calcite and quartz
MG-T-103	9192060	692613	42.26-44.22	03-IT-36-PE	Sertãozinho, Itapetim-Central Domain	Gneiss with ultramafic intercalations with tu. + py. + ch.
MG-T-104	9192060	692613	44.22-47.96	03-IT-36-PE	Sertãozinho, Itapetim-Central Domain	Gneiss with intercalations of ultramafic + mineralized quartz vein
MG-T-107	9192060	692613	48.99-49.05	03-IT-36-PE	Sertãozinho, Itapetim-Central Domain	Schist with fractures filled by calcite + qz. + tu.
MG-T-110	9191837	692550	51.09-51.98	03-IT-21-PE	Pimenteiras, Itapetim-East Domain	Gneiss with fractures filled by feldsp. and qz. with py.
MG-T-111 B	9191911	692686	37.37-38.35	03-IT-03-PE	Pimenteiras, Itapetim-East Domain	Biotite-muscovite schist, with auriferous quartz vein intercalation
MG-T-112	9191911	692686	41.72-42.09	03-IT-03-PE	Pimenteiras, Itapetim-East Domain	Mafic- rock, large crystals of amphibole.
MG-T-113	9191861	692591	43.96-43.54	03-IT-06-PE	Pimenteiras, Itapetim-East Domain	Gneiss with mineralized quartz vein intercalated
MG-T-114	9191861	692591	43.54-44.38	03-IT-06-PE	Pimenteiras, Itapetim-East Domain	Quartz vein with tu. + py.+ gold
MG-T-115	9191861	692591	44.95-45.48	03-IT-06-PE	Pimenteiras, Itapetim-East Domain	Gneiss with fractures filled by calcite + qz.
MG-T-117	9193350	695950	1.34-2.55	03-IT-13-PE	Pimenteiras, Itapetim-East Domain	Mica schist, medium grained

MG-T-122	9193350	695950	11.01-12.65	03-IT-13-PE	Pimenteiras, Itapetim-East Domain	Mica schist, fine grained, light grey colour
MG-T-126 A	9193350	695950	16.97-21.80	03-IT-13-PE	Pimenteiras, Itapetim-East Domain	Mica schist, coarse grained.
MG-T-126 B	9193350	695950	16.97-21.80	03-IT-13-PE	Pimenteiras, Itapetim-East Domain	Quartz vein intercalated in mica gneiss
MG-T-129 A	9193350	695950	26.40-33.60	03-IT-13-PE	Pimenteiras, Itapetim-East Domain	Gneiss, coarse grained
MG-T-134	9193350	695950	43.84-45.69	03-IT-13-PE	Pimenteiras, Itapetim-East Domain	Gneiss, coarse grained
MG-T-135	9193350	695950	45.69-46.27	03-IT-13-PE	Pimenteiras, Itapetim-East Domain	Gneiss with quartz-feldspathic bands well developed, altered
MG-T-136	9193350	695950	46.27-47.25	03-IT-13-PE	Pimenteiras, Itapetim-East Domain	Mica gneiss, medium grained
MG-T-137	9193350	695950	47.25-48.67	03-IT-13-PE	Pimenteiras, Itapetim-East Domain	Amphibolite, dark colour, fine grained
MG-R-139	9177000	690500	-	-	S. Jose Egito/Brejinho road (3km from S.Jose Egito)	Calco-silicate intercalated in mica-gneiss (Irajaí Complex)
MG-R-140	9177500	690500	-	-	S. Jose Egito/Brejinho road (3km from S.Jose Egito)	Quartz vein cross-cutting Irajaí paragneiss
MG-R-141	9179480	691000	-	-	S. Jose Egito/Brejinho road (3km from S.Jose Egito)	Amphibolite, fine grained intercalated in Irajaí gneiss
MG-R-142	9180400	690540	-	-	S. Jose Egito/Brejinho road (3km from S.Jose Egito)	Mica-paragneiss, fine grained, Irajaí Complex
MG-R-143 A	9180700	691000	-	-	S. Jose Egito/Brejinho road (3km from S.Jose Egito)	Thin quartz vein, intercalated in Irajaí paragneiss
MG-R-143 B	9180700	691000	-	-	S. Jose Egito/Brejinho road (3km from S.Jose Egito)	Thin quartz vein, intercalated in Irajaí paragneiss
MG-R-144	9184500	690000	-	-	Ambó, SE of Brejinho	Biotite augen orthogneiss w/ stretched feldspar porphyroclast (ETG)
MG-R-144 A	9178000	674400	-	-	Serra do Machado	Biotite augen orthogneiss w/ stretched feldspar porphyroclast (ETG)
MG-R-145	9178480	709580	-	-	Cacimba de Dentro, close to Afogados da Ingazeira S.Z.	Biotite orthogneiss (ETG)
MG-R-146	9174000	709500	-	-	São Vicente, close to Afogados da Ingazeira shear zone	Biotite gneiss, feldspathic (Basement rock)
MG-R-147 A	9190000	695980	-	-	Cacimba Salgada	Biotite-granite with porphyroclast of zoned microcline (SLTG)
MG-R-147 B	9189880	696000	-	-	Cacimba Salgada	Quartz vein cross-cut granite, coarse text. w/ gold intercalated in SLTG
MG-R-148	9193000	697580	-	-	SE of Piedade Dam, Itapetim District-Central Domain	Biotite orthogneiss (ETG)
MG-R-148 A	9192620	697800	-	-	Sertãozinho, Itapetim-Central Domain	Biotite-muscovite paragneiss with calc-silicates intercalated (Irajaí Complex)
MG-R-148 B	9192620	697800	-	-	Sertãozinho, Itapetim-Central Domain	Mafic rock, large crystals of amphybole (Irajaí Complex)
MG-R-149	9199000	693500	-	-	Teixeira	Biotite-granite with enclaves of deformed mafic rock (SLTG)
MG-R-150 A	9196500	706900	-	-	NW of Serraria Dam, Itapetim-Central Domain	Sheet of biotite-monzogranite, mylonitic, (ESTG)
MG-R-150	9191200	685900	-	-	Vaca Morta Farm, NW of Desterro, Itapetim, East Domain	Biotite syeno-granite (protomylonite; ESTG)
MG-R-151 A	9191780	692760	35.00	-	Underground N-35, Sertãozinho, Itapetim-Central D.	Silicified schist, wallrock of qz. vein with visible gold (wallrock), level N-35
MG-R-151 B	9191780	692760	35.00	-	Underground N-35, Sertãozinho, Itapetim-Central D.	Quartz-tourmaline, wallrock alteration, level N-35 (underground)
MG-R-152 A	9191700	692600	-	-	Close to CPRM mill, Sertãozinho, Itapetim-Central Domain	Quartz vein intercalated in Irajaí mica gneiss
MG-R-152 B	9191700	692600	-	-	Close to CPRM mill, Sertãozinho, Itapetim-Central Domain	Quartz boudin intercalated in Irajaí mica gneiss
MG-R-153	9191540	691300	-	-	Sertãozinho, Jansen 'garimpo', Itapetim-Central Domain	Gneiss with quartz-tourmaline vein, dark colour, intensely silicifed
MG-R-154	9191160	691000	-	-	Sertãozinho, Jansen 'garimpo', Itapetim, Central Domain	Mineralized quartz vein, very thick, coarse texture
MG-R-155	9190120	691000	35.00	-	Underground N-35, Sertãozinho, Itapetim-Central Domain	Gneiss, dark grey, fine texture, with gold-bearing quartz vein (underground)
MG-R-156 A	9191660	692800	13.00	-	Underground N-13, Sertãozinho, Itapetim-Central Domain	Silicified schist, wallrock of mineraliz. quartz vein level N-13 (underground)
MG-R-156 B	9191660	692800	13.00	-	Underground N-13, Sertãozinho, Itapetim-Central Domain	Quartz vein intercalated in gneiss, level N-13
MG-R-157	9191520	692800	13.00	-	Underground N-13, Sertãozinho, Itapetim-Central Domain	Biot. schist wallrock of mineralized qz.-tu. vein, level N-13 (underground)
MG-R-158	9191640	692500	13.00	-	Underground N-13, Sertãozinho, Itapetim-Central Domain	Quartz-tourmaline vein mineralized with gold, level N-13 (underground)
MG-R-159	9191520	692800	35.00	-	Underground N-35, Sertãozinho, Itapetim-Central Domain	Quartz-tourmaline vein mineralized with gold, level N-35 (underground)
MG-R-160	9191400	691400	30.00	-	Shaft in Sertãozinho area, Itapetim-Central Domain	Gneiss with thin quartz vein intercalated
MG-R-161	9191200	691340	30.00	-	Shaft in Sertãozinho area, Itapetim-Central Domain	Gneiss, dark colour, fine grained, with thin quartz vein intercalated
MG-R-162 A	9192780	693900	-	-	Pedro Amancio 'garimpo' (Desterro), Itapetim-West Domain	Thick quartz vein, coarse text., mineralized with gold, intercalated in mica gneiss
MG-R-162 B	9192780	693900	-	-	Pedro Amancio 'garimpo' (Desterro), Itapetim-West Domain	Mica gneiss, wallrock of quartz vein mineralized with gold
MG-R-163 A	9196400	702000	-	-	Desterro area, Itapetim-East Domain	Leuco-gneiss (wallrock in hydrothermal alteration zone; east side)
MG-R-163 B	9196400	702000	-	-	Desterro area, Itapetim-East Domain	Quartz vein in contact with leuco-gneiss in hydrothermal alteration zone
MG-R-163 C	9196400	702000	-	-	Desterro area, Itapetim-East Domain	Quartz-tourmaline zone in contact with leuco-gneiss
MG-R-163 D	9196400	702000	-		Desterro area, Itapetim-East Domain	Wallrock alteration (quartz-feldspatic rock)

MG-R-163 E	9196400	702000	-	-	Desterro area, Itapetim-East Domain	Wallrock alteration (quartz-feldspatic rock)
MG-R-163 F	9196400	702000	-	-	Desterro area, Itapetim-East Domain	Quartz-tourmaline zone in contact with amphib. rock in hydroth. alteration zone
MG-R-163 G	9196400	702000	-	-	Desterro area, Itapetim-East Domain	Amphibolitic rock (wallrock in hydrother. alteration zone; west side)
MG-R-164	9195620	700100	-	-	Catole 'garimpo', Itapetim-East Domain	Mineralized thin quartz vein, medium texture, intercalated in mica gneiss
MG-R-165 A	9194000	698440	16.00	-	Shaft in Queiroz Galvão, Itapetim-East Domain	Quartz-tourmaline vein mineralized with gold (underground)
MG-R-165 B	9194000	698440	16.00	-	Shaft in Queiroz Galvão, Itapetim-East Domain	Alterated material in contact with mineralized quartz vein (east side)
MG-R-165 C	9194000	698440	16.00	-	Shaft in Queiroz Galvão, Itapetim-East Domain	Alterated material in contact with mineralised quartz vein (west side)
MG-R-166 A	9193680	696340	-	-	Shaft in Queiroz Galvão, Itapetim-East Domain	Thick quartz vein mineralized with gold
MG-R-166 B	9193680	696340	-	-	Shaft in Queiroz Galvão, Itapetim-East Domain	Mica schist with quartz vein mineralized with gold
MG-R-167 A	9193300	696000	-	-	Pimenteiras 'garimpo dos Franceses', Itapetim-East Domain	Thin quartz vein intercalated in mica schist
MG-R-167 B	9193300	696000	-	-	Pimenteiras 'garimpo dos Franceses', Itapetim-East Domain	Quartz-tourmaline intense silicified with quartz vein intercalated
MG-R-168 A	9193280	695020	-	-	Piedade 'garimpo', Itapetim-East Domain	Thin quartz vein intercalated in mica gneiss, coarse texture
MG-R-168 B	9193280	695020	-	-	Piedade 'garimpo', Itapetim-East Domain	Thick quartz vein, coarse texture, intercalated in mica gneiss
MG-R-169 A	9192560	694680	-	-	Piedade Dam, Itapetim-East Domain	Thick quartz vein intercalated in Irajaí mica gneiss
MG-R-169 B	9192560	694680	-	-	Piedade Dam, Itapetim-East Domain	Biotite-muscovite schist: Irajaí Complex
MG-R-169 C	9192560	694680	-	-	Piedade Dam, Itapetim-East Domain	Thin quartz vein, fine texture
MG-R-169 D	9192560	694680	-	-	Piedade Dam, Itapetim-East Domain	Mafic rock (biotite-muscovite schist; Irajaí Complex)
MG-R-170 A	9192840	692080	-	-	Piedade 'garimpo'; Itapetim-East Domain	Gold-bearing quartz vein, coarse text., intercalated in mica gneiss
MG-R-170 B	9192840	692080	-	-	Piedade 'garimpo'; Itapetim-East Domain	Mica schist, wall rock of gold-bearing quartz vein
MG-R-171 A	9191480	690050	-	-	CPRM trench, Degredo; Itapetim-West Domain	Thin quartz vein with gold, intercalated in mica gneiss
MG-R-171 B	9191480	690050	-	-	CPRM trench, Degredo; Itapetim-West Domain	Gneiss: silicified (host rock of quartz vein with gold)
MG-R-172 A	9191880	686820	-	-	Degredo; Sr. Camilo farm; Itapetim-West Domain	Quartz vein, medium-fine texture, intercalated in gneiss
MG-R-172 B	9191880	686820	-	-	Degredo; Sr. Camilo farm; Itapetim-West Domain	Gneiss, grey colour with quartz vein intercalated
MG-R-173	9190100	687640	-	-	Degredo; Sr. Raimundo 'garimpo'; Itapetim-West Domain	Quartz vein with gold intercalated in mica gneiss
MG-R-174 A	9188000	679640	-	-	Santo Aleixo area, Sta. Tereza 'garimpo'	Biotite schist with quartz vein intercalated
MG-R-174 B	9188000	679640	-	-	Santo Aleixo area, Sta. Tereza 'garimpo'	Thin quartz vein, medium-fine texture with Fe. ox., intercalated in gneiss
MG-R-174 C	9188000	679640	-	-	Santo Aleixo area, Sta. Tereza 'garimpo'	Quartz-tourmaline vein intercalated in biotite-gneiss
MG-R-175 A	9188880	679200	-	-	Santo Aleixo area, Sta. Tereza 'garimpo'	Mica schist, fine grained with quartz-tourmaline vein intercalated
MG-R-175 B	9188880	679200	-	-	Santo Aleixo area, Sta. Tereza 'garimpo'	Quartz-tourmaline vein intercalated in mica gneiss
MG-R-176	9189200	678900	-	-	Santo Aleixo area, Guilhermina 'garimpo'	Gneiss host rock of quartz-tourmaline vein with iron oxide
MG-R-177	9189300	678700	-	-	Santo Aleixo area, Guilhermina 'garimpo'	Thick quartz vein, coarse texture, intercalated in mica gneiss
MG-R-178 A	9189780	675580	-	-	Santo Aleixo area, São Gonçalo 'garimpo'	Porphyritic gneiss, grey colour
MG-R-178 B	9189780	675580	-	-	Santo Aleixo area, São Gonçalo 'garimpo'	Biotite-muscovite schist
MG-R-179 A	9187620	677100	-	-	Santo Aleixo area, Cassiano 'garimpo'	Biotite syenite-granite (protomylonite; ESTG)
MG-R-179 B	9187620	677100	-	-	Santo Aleixo area, Cassiano 'garimpo'	Mica gneiss, coarse grained
MG-R-179 C	9187620	677100	-	-	Santo Aleixo area, Cassiano 'garimpo'	Mica gneiss, intense silificated, fine-medium grained
MG-R-180 A	9191180	687580	-	-	CPRM trench, Degredo; Itapetim-West Domain	Thick quartz vein coarse texture intercalated in gneiss
MG-R-180 B	9191180	687580	-	-	CPRM trench, Degredo; Itapetim-West Domain	Gneiss, host rock of quartz-tourmaline vein: very coarse grained
MG-R-180 C	9191180	687580	-	-	CPRM trench, Degredo; Itapetim-West Domain	Thin quartz vein, fine texture intercalated in gneiss
MG-R-181 A	9188720	675020	-	-	Canafístula 'garimpo'	Biotite gneiss with quartz-tourmaline vein intercalated
MG-R-181 B	9188720	675020	-	-	Canafístula 'garimpo'	Mica schist, intensely silicified, fine grained
MG-R-183	9194950	694200	-	-	0.75 km from Fava Cheiro Farm to SE; Itapetim District	Biotite granite, undeformed, magmatic flow structure (SLTG)
MG-R-184	9194700	694500	-	-	Riacho Verde-Piedade road (3km from Riacho Verde)	Orthogneiss with stretched feldspar porphyroclast (ESTG)
MG-R-184A	9194500	694500	-	-	Riacho Verde-Piedade road (3km from Riacho Verde)	Mica schist with concordant quartz vein (foliation N70°E; 70°SE)
MG-R-186	9194000	694500	-	-	Riacho Verde-Piedade road (3km from Riacho Verde)	Augen orthogn., mylonit. foliation N75°E; 80°SE; deform. porph. (ESTG)
MG-R-190A	9193400	695000	-	-	Piedade town, toward to the dam, Itapetim-Central Domain	Mica schist, felsic/mafic banding, mylonitic foliation N75°E; 90°SE

MG-R-190B	9193400	695000	-	-	Piedade town, toward to the dam, Itapetim-Central Domain	Mica schist, felsic/mafic banding, mylonitic foliation N75°E; 90°SE
MG-R-191	9193400	695200	-	-	Piedade town, toward to the dam, Itapetim-Central Domain	Orthogneiss, mylon. foliation N65°SE; 80°SE, stretched feldsp. porph. (ETG)
MG-R-192	9193200	695900	-	-	Piedade-Dam road, Itapetim-Central Domain	Granite; streteched quartz, magmatic flow oriented at N60°E (SLTG)
MG-R-193	9192700	694600	-	-	Piedade Dam, Itapetim-Central Domain	Contact orthogneiss/supracrustal; mylonitic foliation N55°E; 85°SE
MG-R-196	9192100	694300	-	-	Ze Cabrinha dam, Itapetim District	Granite, magmatic flow oriented; mylonitic foliation N80°E; 85° SE; (SLTG)
MG-R-197A	9197000	673000	-	-	Garapa 'garimpo'	Granite; quartz veins with gold intercalated filling fractures N70°E (SLTG)
MG-R-197B	9197000	673000	-	-	Garapa 'garimpo'	Quartz vein with gold, mg. + py. + chp. filling fractures E-W in SLTG.
MG-R-197C	9197000	673000	-	-	Garapa 'garimpo'	Quartz vein with galena filling fractures in SLTG (Sample MG-R-197A)
MG-R-198	9190900	696400	-	-	Cacimba Salgada	Granite with diorite xenoliths orientated N60°E parallel to the shear (SLTG)
MG-R-200	9177000	690500	-	-	S. Jose Egito/Brejinho road (7km from S.Jose Egito)	Calc- silicate rock intercalated in metasediment of Irajaí Complex
MG-R-203	9189200	674000	-	-	Canafístula 'garimpo'	Mylonite with quartz vein with gold concordant with foliation N130°E; 70°NW
MG-R-203 AI	9189200	674000	-	-	Canafístula 'garimpo'	Mylonitic granitic rock foliation N130°E; 70°NW
MG-R-203 AII	9198200	674000	-	-	Canafístula 'garimpo'	Mylonitic granitic rock foliation N130°E; 70°NW
MG-R-203 B	9189200	674000	-	-	Canafístula 'garimpo'	Thick quartz vein in contact with tourmaline altered zone/mylonitic granitic rock
MG-R-203 C	9189200	674000	-	-	Canafístula 'garimpo'	Tourmaline zone (quartz-tourmaline vein with qz.+.k-feldsp. + op. min.)
MG-R-203 D	9189200	674000	-	-	Canafístula 'garimpo'	Quartz vein intercalated in tourmaline altered zone
MG-R-203 E	9189200	674000	-	-	Canafístula 'garimpo'	Potassic altered zone (biotite + k-feldsp.+ op. min.)
MG-R-203 F	9189200	674000	-	-	Canafístula 'garimpo'	Quartz vein intercalated in potassic altered zone
MG-R-203 G	9189200	674000	-	-	Canafístula 'garimpo'	Granitoid with foliation N150°E (ETG)
MG-R-203 H	9189200	674000	-	-	Canafístula 'garimpo'	Quartz vein in contact with granitoid (MG-R-203G)
MG-R-204 A	9189000	674000	-	-	Canafístula 'garimpo'	Mylonitic granite with stretched feldspar porphyroclasts
MG-R-204 B	9189000	674000	-	-	Canafístula 'garimpo'	As above, but the silicification is more intense
MG-R-204 DI	9189000	674000	-	-	Canafístula 'garimpo'	Tourmaline quartz vein with k-feldsp. + ser.+ Fe. ox. (tourmaline alteration zone)
MG-R-204 DII	9189000	674000	-	-	Canafístula 'garimpo'	As above, but the Fe. ox. is less abundant
MG-R-204 F	9189000	674000	-	-	Canafístula 'garimpo'	Tourmaline alteration zone (vein controlled) associated with qz. + k-feldsp.
MG-R-204 G	9189000	674000	-	-	Canafístula 'garimpo'	Quartz vein intercalated in tourmaline alteration zone
MG-R-204 H	9189000	674000	-	-	Canafístula 'garimpo'	Tourmaline alteration zone with quartz veins intercalated
MG-R-204 I	9189000	674000	-	-	Canafístula 'garimpo'	Quartz vein intercalated in tourmaline alteration zone
MG-R-204 J	9189000	674000	-	-	Canafístula 'garimpo'	Mylonitic granite with stretched feldspar porphyroclasts (ETG)
MG-R-205 A	9189300	677500	-	-	Santo Aleixo area, Guilhermina 'garimpo'	Augen gneiss with stretched feldsp. porphyroclast orientated N60°E
MG-R-205 B	9187200	677000	-	-	Ze Ferreira 'garimpo', Itapetim -West Domain	Quartz vein with galena orientated N60°E intercalated in gneiss (MG-R-205A)
MG-R-206	9189300	677500	-		Santo Aleixo area, Miro 'garimpo'	Grey gneiss, intensely silicified with pyrite
MG-R-207	9189200	679500	-	-	Santo Aleixo area, Guilhermina 'garimpo'	Quartz vein with sulphide and gold intercalated in gneiss
MG-R-208 A	9206000	593000	-	-	Boqueirão dos Cochos	Amphibolite with garnet; mylonitic foliation N120°E; 40°SW
MG-R-208B	9206000	593000	-	-	Boqueirão dos Cochos	Gneiss with amphibolite intercalation; mylonitic foliation N60°E; 75°SE
MG-R-208 C	9206000	593000	-	-	Boqueirão dos Cochos	Quartz vein mineralized with gold + py., preferred orientation N20°E
MG-R-209	9191700	692700	35.00	-	Underground N-35, Sertãozinho, Itapetim-Central Domain	Muscovite biotite schist; mylonitic foliation N40°E; 85°SE
MG-R-210	9191700	692700	35.00	-	Underground N-35, Sertãozinho, Itapetim-Central Domain	Sertãozinho ore, sulphide + gold in qz. vein hosted by muscovite biotite schist
MG-R-211	9192400	695100	-	-	Riacho Verde area, Itapetim District	Granite, magmatic flow structure; fractures (N20°E) with mylonite (SLTG)
MG-R-212	9192200	695100	-	-	Riacho Verde area, Itapetim District	As above SLTG (regional shear N70°E)
MG-R-214	9194700	694500	-	-	Riacho Verde area, Itapetim District	Augen gneiss, mylon. foliation, stretched porhpyroclasts feldsp. (SLTG)
MG-R-215	9192700	694600	-	-	Piedade, close to the dam, Itapetim-Central Domain	Biotite-muscovite gneiss; mylonitic foliation N80°E; Irajaí Complex
MG-R-216	9193300	695600	-	-	Piedade-Cacimba Salgada road (1 km from Piedade)	Granite (SLTG) with concordant and discordant qz. veins
MG-R-217	9192500	696600	-	-	Piedade-Cacimba Salgada road (2 km from Piedade)	Granite (SLTG) with magmatic flow structure N60°E
MG-R-218	9190900	696400	-	-	Cacimba Salgada	Granite (SLTG), magmatic flow orient. N80°E with qz. vein + gold N70°E
MG-R-219	9193300	696000	-	-	Pimenteiras 'garimpo'; Itapetim-East Domain	Biotite muscovite schist; (L1=N60°E; L2=N70°E; plunge 10°SW)
MG-R-222 A	9189200	679500	-	-	Santo Aleixo area, Guilhermina 'garimpo'	Biotite schist occuring along the fractures

MG-R-222 B	9189200	679500	-	-	Santo Aleixo area, Guilhermina 'garimpo'	Gneiss porphyr. with stretch. feldsp. porphyrocl. orient. N60°E (shear direction)
MG-R-222 C	9189200	679500	-	-	Santo Aleixo area, Guilhermina 'garimpo'	Gneiss porph. with qz. veins concord. with Sn (N65°E) & discord. Sn+1(N135°E)
MG-R-223	9189300	677500	-	-	Santo Aleixo area, Miro 'garimpo'	Grey gneiss, mylonitic foliation (N80°E) with quartz vein N30°E; 20° SE
MG-R-224 A	9160100	600100	-	-	Cachoeira de Minas mine, Covico area	Chlorite-biotite schist with foliation NE-SW (N60°E)
MG-R-224	9160200	600220	-	-	Cachoeira de Minas mine, Covico area	Galena in quartz vein intercalated in biotite-muscovite schist
MG-R-224 B	9160100	600100	-	-	Cachoeira de Minas mine, Covico area	Quartz vein, coarse and white colour intercalated in biotite-muscovite schist
MG-R-224 C	9160280	600100	-	-	Cachoeira de Minas mine, Covico area	Quartz vein very coarse texture with sulphides intercalated in schist
MG-R-224 D	9160100	600100	-	-	Cachoeira de Minas mine, Covico area	Biotite-muscovite schist, foliat. N60°E, dips 60°-70° SE, hosting qz. vein + gold
MG-R-224 E	9160200	600100	-	-	Cachoeira de Minas mine, Covico area	Biotite-muscovite schist, foliat. N60°E, dips 60°-70° SE, hosting qz vein + gold
MG-R-225 A	9339200	806200	-	-	São Francisco mine, Morro Pelado shear zone	Hematitic -silicified zone (qz.+ k-feldsp. + ch. + ser. + Fe ox.) interc. in schist
MG-R-225 B	9339200	806200	-	-	São Francisco mine, Morro Pelado shear zone	Hematitic-silicifed alteration zone consisting of quartz + Fe ox.
MG-R-225 C	9339280	806200	-	-	São Francisco mine, Morro Pelado shear zone	Wallrock alteration consisting of mica schist
MG-R-226	9339320	806200	-	-	São Francisco mine, Morro Pelado shear zone	Mica schist, mylonitic foliation N70°E; 40°SE with quartz vein intercalated
MG-R-226C	9339200	806200	-	-	São Francisco mine, Morro Pelado shear zone	Mica schist, mylonitic foliation N70°E; 40°SE with quartz vein intercalated
MG-R-227	9339345	806200	-	-	São Francisco mine, Santa Monica shear zone	Mica schist with garnet, mylonitic foliation N70°E; 40°SE
MG-R-227C	9339200	806200	-	-	São Francisco mine, Santa Monica shear zone	Mica schist with garnet, mylonitic foliation N70°E; 40°SE
MG-R-228	9339280	806300	-	-	São Francisco mine, Morro Pelado shear zone	Mica schist with cordierite; mylonitic foliation N40°E
MG-R-228C	9339200	806200	-	-	São Francisco mine, Morro Pelado shear zone	Mica schist with cordierite; mylonitic foliation N40°E
MG-R-229 A	9339200	806200	-	-	São Francisco mine, Morro Pelado shear zone	Quartz vein with sulphides intercalated in the hematitic-silicified-tourmaline zone
MG-R-229 B	9339400	806220	-	-	São Francisco mine, Morro Pelado shear zone	Quartz vein with sulphides intercalated in the hematitic-silicified-tourmaline zone
MG-R-229 C	9339200	806200	-	-	São Francisco mine, Morro Pelado shear zone	Quartz vein with sulphides intercalated in the hematitic-silicified-tourmaline zone
MG-R-230	9339200	806200	-	-	São Francisco mine, Morro Pelado shear zone	Mica schist with quartz vein segregation; mylonitic foliation N60°E; 40°SE
MG-R-231	9339300	806200	-	-	São Francisco mine, Morro Pelado shear zone	Quartz vein intercalated in mica schist with cordierite

Abbreviations:

ETG = Early-tectonic granite

ESTG = Early- to syn-tectonic granite

SLTG = Syn- and Late-tectonic granite

Grid reference based on UTM Projection (central meridien = 39°)

For further informations see List of Abbreviations

Appendix A4.1
Petrographic and Geochemistry Methods of Study

The analytical methods using for petrographic and geochemical studies comprised the following tecniques:

(i) Rock Cuting and Thin Sections Preparation

Samples collected during the fieldwork were broken into small chips using a hardened steel jaw crusher and after that thin sections were prepered (30 μm thick) for the microscopic investigation. This work was performed in the CPRM laboratories in Rio de Janeiro and Recife. Around 300 thin sections of rock were described for petrographic studies under the reflected light microscope.

(ii) Sample Preparation for Geochemistry Analysis

About 100 samples were crushing and powdered for the major and trace element analysis. Samples were broken into small chips and reduced to 2-3 pieces of 1-2 cubic inch volume for fine-grained rock. Samples were cleaned using first a tap water and then in an ultrasonic bath with distilled water. After that, dry clean pieces of rock (approximately 100 grams) were crushed using a steel reciprocating jaw crusher. The jaw crusher was cleaned with a wire brush, compressed air, a vacuum cleaner and then acetone. About 100 grams of crushed sample were placed in a tungsten carbide mill to produce the powder (< 200 mesh), after grinding for about 2.5 minutes at 1000 rpm.

This preparation was carried out in the CPRM laboratory in Rio de Janeiro.

(iii) Fused Glass Beads Sample

Major elements (SiO_2, Al_2O_3, Fe_2O_3, MgO, CaO, Na_2O, K_2O, TiO_2, MnO and P_2O_5) were determined on 100 fused glass beads using a Phillips PW 1480 X-ray fluorescence spectrometer at RHBNC. Approximatly 0.7 grams of powdered sample were used to make the beads, which precedure is depicted in Appendix A4. 1a. This preparation was performed at RHBNC.

(iv) Pressed Pellet Sample

Trace elements were analysed by a Phillips PW 1480 X-ray fluorescence spectrometer using pressed pellet samples (46 mm powder briquettes). 100 pellets were made using 0.7 grams of rock powder, at RHBNC. Trace elements were determined using rhodium (Pb, Rb, Sr, Th, Zr, Y, Nb, Cl and Ga) and tungsten (Sc, La, Ba,V, Nd, Ce, Cr, Ni, Cu and Zn) anode X-ray tubes. The first tube is operated at 90 kV and 30 mA and the second one operated at 60 kV and 45 mA. For further information see Appendix A4. 1b

(v) Processing Geochemical Data

The major and trace elements data were processed on a VAX/VMS system at the Computer Centre at RHBNC. Details of the XRF analytical error are given in Appendix A.4. 2. The results of the chemical analyses for major and trace elements are displayed in Appendices A4.3, and A4.6 to A.4.8).

(vi) Sample Preparation for Mineral Chemistry

Thirty rock samples were selected for mineral analysis. Around 50 polished thin sections (100 μm thick) were prepared and coated with carbon at RHBNC. Approximately 40 polished block of ore minerals were also coated with carbon at RHBNC. Quantitative microanalysis of ore and rock minerals was performed on an electron microprobe.

These analyses were carried out using three instruments:

(i) A Hitachi S-2400 SEM at Royal Holloway College using a Link systems energy dispersive detector (20 kv).

(ii) A Cambridge mark microprobe in the Department of Earth Sciences at the Open University using wavelength dispersive analysis (25kv).

(iii) A Caneca Sx50 microprobe in the Department of Mineralogy, Natural History Museum (London) using wavelength dispersive analysis (20 kv).

The analyses of native gold disseminated in a silicate matrix performed at Royal Holloway sometimes displayed very low amounts of Si, O and Na. This may be explained either by the small size of the gold grains, or that the gold grains are so thin that the beam (spot size = 1 μm diametre) from the electron microscope partly penetrates the surrounding silicate matrix. In these cases the results for gold, copper and silver were normalised taken removal of the values for Si, Na and O. (see Chapter 5, Appendices A5.1 and A5.2).

The detected limit for gold analysis was 0.10 % using the M line. Correction procedures were carried out using a ZAF correction program. Mineral standards were used as calibration and cobalt as primary reference standard.

Compositions of rock forming minerals were processing through the use of programs developed by Dr. Andy Tindle which mineral formula proportions were calculated on the basis:

23 O: Amphiboles; 32 O: Feldspar; 8 O: Plagioclase; 12 O: Garnet; 28 O: Chlorite;

22 O: Biotite; 22 O: Muscovite; 10 O: Sillimanite; 27 O: Tourmaline; 6 O: Jarosite

The classification of Leake (1978) for amphiboles was followed, whose standard formula is:

$A_{0-1}B_2C^{vi}_5T^{iv}_8O_{22}(OH,F,Cl)_2$. Each cation is assigned according to:

(i) T is summed to 8.00 using Si, then Al, then Cr^{3+}, then Fe^{3+} and then Ti^{4+};

(ii) C is summed to 5.00 using excess Al, Cr, Ti, Fe^{3+} from 1, then Mg, then Fe^{2+} and summed Mn;

(iii) B is summend to 2.00 using excess Fe^{2+}, Mn and Mg from 2, then Ca and then Na;

(iv) Excess Na from 3 is assigned to A, then all K.

On the basis of $(Ca + Na)_B$ the amphibolite is classified into one of four groups, each of which is subdivided into fields according to a series of diagrams using $Mg/Mg + Fe^{2+}$, Si, $(Na + K)_A$:

(i) $(Ca + Na)_B < 1.34$: Fe-Mg-Mn amphiboles.

(ii) $(Ca + Na)_B \geq 1.34$; $0.67 \leq (Na)_B \leq 1.34$: sodic-calcic amphiboles.

(iii) $(Ca + Na)_B \geq 1.34$; $(Na)_B < 0.67$: calcic amphiboles

(iv) $(Na)_B \geq 1.34$: alkali amphiboles

All the amphiboles analysed during this study meet the criteria for the calcic amphiboles, and then, they were classifed on the basis of $(Ca+Na)_B$ and each of them was classified into fields basing on the series of diagrams using the ratios: $Mg/Mg+Fe^{2+}$, Si and $(Na+K)_A$ as following:

(i) $(Na+ K)_A < 0.50$; $Ti < 0.50$

(ii) $(Na+ K)_A > 0.50$; $Ti < 0.50$; $Fe^3 < Al_{vi}$

(iii) $(Na+ K)_A > 0.50$; $Ti < 0.50$; $Fe^3 > Al_{vi}$

(iv) $Ti > 0.50$.

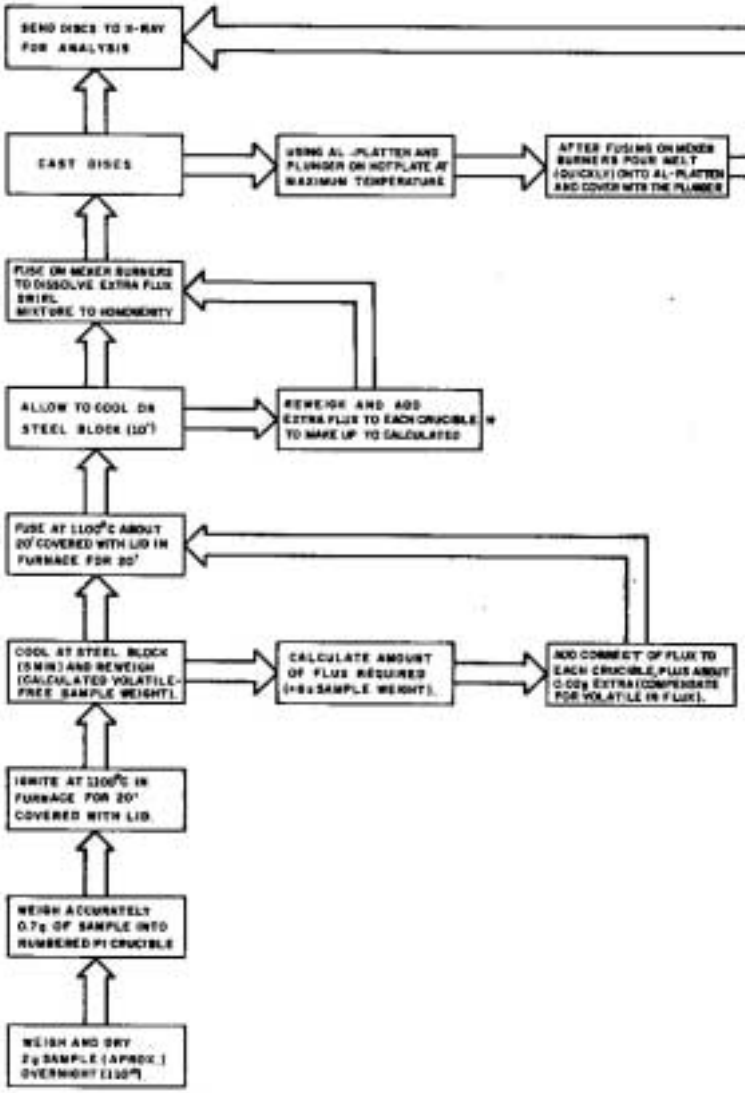

APPENDIX A4.1b

Procedure for Making Fusion Beads to X-Ray Fluorescence Analyses: Major Elements

* IF YOU NEED TO ADD MORE THAN 0.01g FLUX AT THIS STAGE, YOU SHOULD REPEAT STAGES 7,8,9.

APPENDIX A4.1a

Procedure for Pressed Pellet Preparation to X-Ray Fluorescence Analyses: Trace Elements

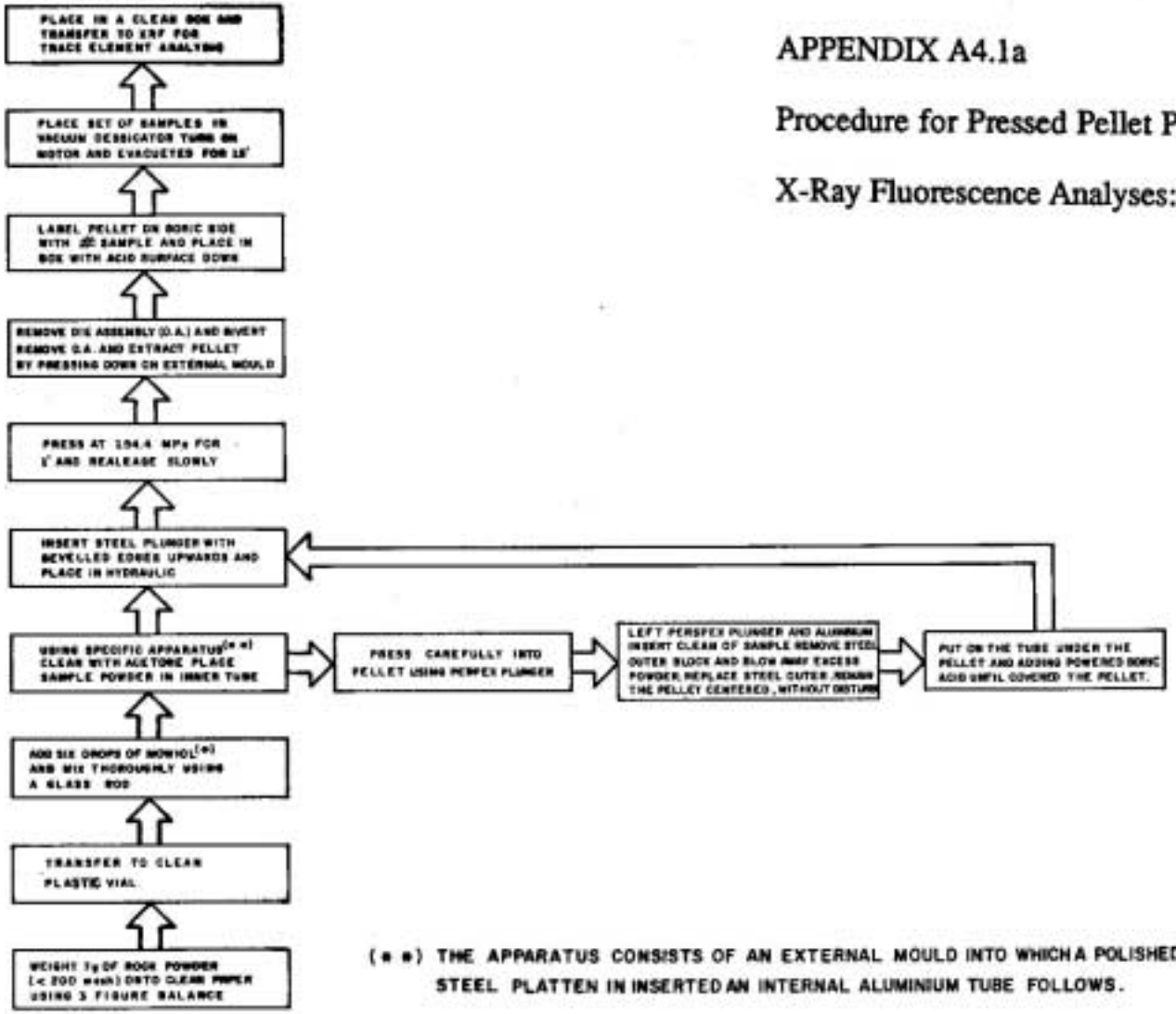

(* *) THE APPARATUS CONSISTS OF AN EXTERNAL MOULD INTO WHICH A POLISHED STEEL PLATTEN IN INSERTED AN INTERNAL ALUMINIUM TUBE FOLLOWS.

(*) MOWIOL IS 2% POLYVINYL ALCOHOL PREPARED BY DISSOLVING SOLID IN COLD DISTILLED WATER AND BRINGING TO THE BOIL

Appendix A4. 2

Chemical Analyses of Standares (X-Ray Fluorescence Data)

Sample	SiO2	Al2O3	Fe2O3	MgO	CaO	Na2O	K2O	TiO2	MnO	P2O5	LOI	Sc	La	Ba	V	Nd	Ce	Cr	Ni	Cu	Zn	Pb	Th	Rb	Sr	Y	Zr	Nb	Cl	Ga
Granite																														
ACOU	70.81	14.91	3.07	0.00	0.37	6.70	4.50	0.10	0.06	0.01	1.00	0	62	54	0	92	157	6	3	4	210	37	19	151	2	191	867	116	220	42
ACOU	70.25	14.82	2.55	0.00	0.38	6.63	4.45	0.11	0.06	0.01	1.00	1	64	44	0	92	158	6	2	4	211	38	19	151	3	189	890	114	0	42
ACOU	70.55	14.89	2.58	0.01	0.37	6.80	4.44	0.11	0.06	0.01	1.00	0	63	60	0	92	158	6	3	5	211	37	18	150	2	191	868	116	0	41
ACOU	70.82	14.83	2.54	0.02	0.38	6.70	4.53	0.11	0.06	0.01	0.00	0	63	56	0	92	159	6	4	3	211	38	20	150	2	197	881	116	178	41
ACOU	70.53	14.83	2.27	0.00	0.37	6.61	4.46	0.11	0.06	0.01	0.00	0	59	61	0	92	154	1	3	4	208	37	20	149	3	189	860	115	121	41
ACOU	70.52	14.83	2.57	0.05	0.37	6.76	4.48	0.12	0.01	0.02	0.00	-	-	-	-	-	-	-	-	-	-	37	19	149	3	190	859	116	126	42
mean	70.58	14.85	2.60	0.01	0.37	6.70	4.48	0.11	0.05	0.01	0.50	0	62	55	0	92	157	5	3	4	210	37	19	150	3	191	871	116	106	42
stand. dev.	0.20	0.04	0.17	0.04	0.00	0.01	0.04	0.01	0.00	0.00	0.43	0	2	6	0	0	8	2	0	1	1	1	0	1	0	2	11	1	33	1
no. samples	6	6	6	6	6	6	6	6	6	6	6	5	5	5	5	5	5	5	5	5	5	6	6	6	6	6	6	6	6	6
Nepheline Syenite																														
BCNS	57.35	24.43	2.92	0.00	0.78	10.81	4.58	0.90	0.08	0.03	1.00	1	40	227	3	16	60	9	2	17	33	4	2	100	215	5	81	33	139	18
BCNS	57.06	24.29	2.07	0.00	0.78	10.82	4.53	0.08	0.08	0.03	1.00	1	41	218	4	17	63	8	3	17	33	4	3	100	215	5	80	33	125	18
BCNS	57.18	24.50	2.08	0.03	0.79	10.95	4.46	0.08	0.08	0.03	1.00	0	41	226	4	17	62	8	2	18	33	4	4	100	214	5	79	33	120	19
BCNS	57.26	24.34	2.09	0.06	0.79	10.64	4.61	0.08	0.08	0.04	1.00	0	40	223	3	18	62	8	3	18	32	4	4	100	213	5	80	33	119	19
BCNS	57.52	24.42	2.06	0.08	0.78	10.77	4.59	0.08	0.08	0.03	0.00	0	41	214	3	16	62	8	3	18	33	4	3	100	212	6	79	33	116	19
BCNS	57.08	24.34	2.07	0.05	0.78	10.76	4.53	0.08	0.03	0.03	0.00	0	42	221	3	17	62	9	3	18	32	4	3	100	212	5	80	33	113	19
mean	57.24	24.39	2.22	0.04	0.79	10.79	4.55	0.22	0.07	0.03	0.67	0	41	222	3	17	62	8	3	18	33	4	3	100	214	5	80	33	122	19
stand. dev.	0.15	0.06	0.23	0.03	0.01	0.17	0.04	0.01	0.00	0.00	0.40	0	1	4	0	1	2	1	1	1	1	0	0	0	1	0	2	0	12	1
no. samples	6	6	6	6	6	6	6	6	6	6	6	6	6	6	6	6	6	6	6	6	6	6	6	6	6	6	6	6	6	6
Trachyte																														
AZSTD	52.14	16.10	9.06	3.75	7.11	3.86	4.14	2.93	0.14	0.50	1.00	13	58	1488	193	49	113	37	30	49	86	9	5	63	708	27	311	58	1372	22
AZSTD	51.95	16.03	9.15	3.68	7.12	3.87	4.14	2.92	0.14	0.50	1.00	13	58	1487	189	49	111	36	30	49	85	10	5	62	708	27	310	59	910	23
AZSTD	52.06	16.18	9.17	3.88	7.13	3.77	4.10	2.96	0.14	0.51	1.00	13	58	1497	180	50	111	39	30	49	84	11	5	63	709	27	310	58	1257	24
AZSTD	51.96	15.98	9.23	3.77	7.08	3.67	4.16	2.92	0.13	0.49	1.00	14	57	1480	181	49	113	37	30	49	84	10	5	63	711	28	311	58	1437	22
AZSTD	52.09	16.06	9.43	3.75	7.15	3.82	4.18	2.93	0.13	0.50	0.00	14	57	1486	180	50	111	40	31	48	83	10	6	62	707	27	313	59	1374	23
AZSTD	52.21	16.07	9.16	3.74	7.13	3.83	4.10	2.92	0.14	0.49	0.00	13	57	1476	181	50	110	37	30	46	85	10	6	63	709	28	312	58	1349	23
mean	52.07	16.07	9.20	3.75	7.12	3.80	4.14	2.93	0.14	0.50	4.00	13	58	1486	184	50	112	38	30	48	85	10	5	63	709	27	311	58	1283	23
stand. dev.	0.15	0.06	0.12	0.12	0.03	0.10	0.03	0.02	0.03	0.01	0.67	1	1	10	4	1	1	1	1	1	1	1	1	1	5	0	2	1	148	1
no. samples	6	6	6	6	6	6	6	6	6	6	6	6	6	6	6	6	6	6	6	6	6	6	6	6	6	6	6	6	6	6
Basalt																														
B0B1	50.94	16.74	8.56	7.56	11.17	3.31	0.37	1.29	0.15	0.16	1.00	33	5	37	237	9	15	277	108	62	65	1	0	5	197	28	105	5	496	16
B0B1	50.62	16.67	8.49	7.53	11.10	3.03	0.36	1.29	0.16	0.16	1.00	37	7	43	242	10	13	283	113	63	66	2	1	6	198	29	105	5	457	14
B0B1	50.83	16.69	8.60	7.76	11.07	2.97	0.36	1.29	0.15	0.17	1.00	35	5	39	247	10	14	283	112	63	67	1	2	6	200	28	106	5	464	16
B0B1	50.88	16.63	8.55	7.66	11.11	3.07	0.38	1.28	0.15	0.17	1.00	35	5	39	247	10	14	282	112	63	66	1	1	6	200	29	104	5	461	15
B0B1	51.08	16.77	8.48	7.71	11.17	3.18	0.37	1.29	0.15	0.17	0.00	37	6	34	247	11	15	282	111	64	66	2	0	5	200	29	107	5	480	16
B0B1	50.85	16.69	8.45	7.60	11.09	2.96	0.36	1.28	0.15	0.16	0.00	35	6	42	241	11	13	282	110	63	66	1	0	6	197	29	107	5	520	16
mean	50.87	16.70	8.52	7.64	11.12	3.09	0.37	1.29	0.15	0.16	0.67	35	6	39	244	10	14	282	111	63	66	1	1	6	199	29	106	5	480	15
stand. dev.	0.12	0.06	0.05	0.06	0.05	0.11	0.01	0.01	0.00	0.00	0.47	1	2	3	3	1	1	4	1	1	1	0	0	0	2	0	1	0	22	1
no. samples	6	6	6	6	6	6	6	6	6	6	6	6	6	6	6	6	6	6	6	6	6	6	6	6	6	6	6	6	6	6

Observations:

Major elements in wt %; Trace elements in ppm; Fe2O3 = total iron as Fe2O3; LOI = loss on ignition; (-) = not analysed

Appendix A4. 3

Chemical Analyses of Granites (X-Ray Fluorescence Data)

Sample	MG-R-144	MG-R-144A	MG-R-145	MG-R-148	MG-R-203AI	MG-R-203AII	MG-R-283G	MG-R-204J	MG-R-204B	MG-R-150	MG-R-150A	MG-R-184	MG-R-186	MG-R-192	MG-R-149	MG-R-147A	MG-R-198	MG-R-183	MG-R-197A
SiO2	73.52	72.27	73.63	73.31	80.23	78.03	74.11	73.86	76.04	72.29	71.29	70.75	69.73	74.16	65.08	65.39	62.94	70.78	77.17
Al2O3	13.38	14.03	14.44	13.36	11.45	12.04	13.81	13.61	13.53	13.50	15.41	15.07	13.93	13.19	17.17	16.09	15.12	14.88	11.14
Fe2O3	2.25	2.53	1.83	2.28	1.74	2.59	3.10	2.64	1.10	3.41	1.71	4.54	4.89	2.14	2.89	4.12	6.62	2.97	4.15
MgO	0.23	0.29	0.44	0.25	0.50	0.43	0.76	0.59	0.05	0.36	0.44	0.99	0.61	0.13	0.65	1.65	3.11	0.58	0.00
CaO	1.06	1.12	1.14	0.73	0.39	0.53	0.91	0.37	0.29	1.39	1.75	1.26	1.77	0.70	2.49	3.19	4.17	0.93	0.02
Na2O	2.47	2.56	2.89	2.97	3.06	2.42	4.02	4.09	4.40	2.99	4.47	2.89	2.62	2.95	5.60	3.68	3.49	3.14	2.64
K2O	6.13	6.63	4.62	6.14	2.86	4.13	3.30	4.75	4.43	5.49	4.49	4.42	5.13	6.24	4.52	4.39	2.98	5.29	4.16
TiO2	0.29	0.33	0.27	0.36	0.28	0.30	0.38	0.35	0.31	0.36	0.31	0.59	0.60	0.33	0.31	0.71	0.99	0.63	0.05
MnO	0.04	0.03	0.02	0.03	0.02	0.02	0.03	0.01	0.01	0.05	0.02	0.06	0.08	0.03	0.09	0.06	0.10	0.03	0.01
P2O5	0.09	0.11	0.07	0.07	0.05	0.05	0.07	0.09	0.04	0.10	0.12	0.07	0.14	0.06	0.10	0.18	0.26	0.12	0.01
Total	99.46	99.90	99.35	99.50	100.58	100.54	100.49	100.36	100.20	99.94	100.01	100.64	99.50	99.93	98.90	99.46	99.78	99.35	99.35
LOI	0.33	0.44	0.76	0.40	1.53	1.47	1.36	1.28	0.50	0.49	0.33	1.40	1.00	0.31	0.31	0.84	0.97	1.47	2.69
Ni	6	6	6	6	7	7	6	6	4	7	5	19	15	7	14	21	47	10	3
Cr	5	6	2	4	6	7	9	7	8	5	6	18	16	9	19	55	171	17	4
V	17	19	20	17	28	22	25	27	15	19	30	36	34	17	44	65	109	60	10
Sc	4	5	4	5	6	5	8	7	6	7	3	13	11	4	7	8	13	13	0
Cu	7	15	3	1	5	13	11	10	8	18	5	6	8	3	8	44	144	13	0
Zn	41	39	36	37	23	29	48	27	10	53	67	101	84	43	75	82	141	185	28
Cl	0	0	5	21	9	0	35	0	0	0	0	0	0	0	11	13	0	0	0
Ga	18	19	18	20	17	16	18	16	13	19	26	20	20	20	24	24	26	24	14
Pb	33	37	48	30	24	28	27	51	31	32	46	27	35	59	39	29	18	1035	117
Sr	64	88	298	34	95	140	269	228	206	94	480	101	149	42	2508	381	314	311	444
Rb	270	271	94	380	114	142	126	155	116	236	191	183	175	384	65	164	180	167	83
Ba	609	710	1923	299	527	736	745	2383	823	731	892	1322	922	274	5108	1031	333	1391	2644
Zr	167	199	241	321	212	220	286	260	240	269	161	405	403	335	185	183	236	425	42
Nb	13	14	10	19	14	15	18	17	13	18	11	24	24	18	11	13	14	20	3
Th	23	27	39	42	17	18	26	31	23	24	13	19	18	53	5	14	19	30	1
Y	42	49	11	44	78	60	70	81	47	65	6	47	61	47	13	22	21	39	1
La	43	42	66	41	50	48	53	75	45	64	35	47	47	35	44	44	57	36	1
Ce	115	99	120	73	95	96	110	146	95	119	71	600	94	81	72	75	98	91	0
Nd	38	38	41	35	48	51	52	70	43	59	31	44	45	34	29	34	36	49	2

Observations:

Early Tectonic Granites: MG-R-144 to MG-R-204B; Early-Syn-Tectonic Granites: MG-R-150 to MG-R-1192; Syn to Late Tectonic Granites: MG-R-149 to MG-R-197A

Appendix A4.4

Granites: CIPW Normalised Data

Mineral/ Sample	MG-R-144	MG-R-144A	MG-R-145	MG-R-148	MG-R-203AI	MG-R-203AII	MG-R-203G	MG-R-204J	MG-R-204B	MG-R-150
Quartz	33.30	29.23	36.31	30.71	49.73	45.28	34.64	30.09	32.87	30.19
Orthoclase	36.43	39.24	27.49	36.53	16.77	25.40	19.44	28.02	26.32	32.53
Albite	21.01	21.74	24.63	25.32	25.70	20.28	33.84	34.53	37.00	25.36
Anorthite	4.70	4.86	5.26	3.15	1.63	2.28	4.02	1.20	1.14	6.29
Corundum	0.99	0.87	2.80	0.68	2.71	2.51	2.14	1.29	1.06	0.34
Diopside	0.00	0.00	0.00	0.00	0.00	0.00	0.00	0.00	0.00	0.00
Hypersthene	1.25	1.45	1.58	1.18	1.64	1.81	2.85	2.17	0.14	2.03
Magnetite	1.56	1.74	1.27	1.57	1.19	1.77	2.19	1.81	0.76	2.35
Ilmenite	0.56	0.63	0.51	0.70	0.53	0.57	0.72	0.67	0.62	0.69
Apatite	0.21	0.25	0.16	0.17	0.11	0.11	0.16	0.22	0.11	0.22
TOTAL	100.00	100.00	100.00	100.00	100.00	100.00	100.00	100.00	100.00	100.00

Mineral/ Sample	MG-R-150A	MG-R-184	MG-R-1886	MG-R-192	MG-R-149	MG-R-147A	MG-R-198	MG-R-183	MG-R-197A
Quartz	23.91	32.30	30.08	31.39	9.60	18.17	18.19	29.79	45.48
Orthoclase	26.56	26.11	30.54	36.94	27.01	26.14	17.72	31.49	24.76
Albite	37.83	24.32	22.37	25.02	47.94	31.40	29.71	26.81	22.50
Anorthite	7.85	5.72	7.88	3.13	8.51	14.52	16.88	3.87	0.02
Corundum	0.32	3.40	1.21	0.44	0.00	0.00	0.00	2.60	2.32
Diopside	0.00	0.00	0.00	0.00	2.70	0.19	1.75	0.00	0.00
Hypersthene	1.46	3.75	3.08	0.85	1.38	4.95	8.69	1.91	1.93
Magnetite	1.18	3.10	3.39	1.47	2.01	2.85	4.57	2.06	2.87
Ilmenite	0.60	1.12	1.12	0.63	0.60	1.36	1.88	1.20	0.09
Apatite	0.30	0.18	0.34	0.13	0.24	0.43	0.61	0.27	0.03
TOTAL	100.00	100.00	100.00	100.00	100.00	100.00	100.00	100.00	100.00

Observation:

Samples processed according to the Geochemistry Lab. Program at RHBNC

Appendix A4.5

Ga / Al Ratios and their Interpretation for Granites

Pluton	Type	Ga/Al (ppm/%)	Data Source
Mumbulla suite	A-type	3.19-3.30; Av. = 3.20	Collins et al., (1982)
Bega batholith	I-type: 20 most felsic	Av. = 2.09	Collins et al., (1982)
Gabo suite	A-type	3.02-3.22; Av. = 3.14	Collins et al., (1982)
Bega batholith	48 wih similar SiO2 range to A-type Gabo suite	Av. = 2.08	Collins et al., (1982)
Mole granite, Torrington	Highly evolved	3.56 for unaltered 3.70 incipiently altered	Kleeman (1985)
Jindabyne KB22	Tonalite	1.88	Hine et al, 1978
Moonbi M551	Hornblende monzogranite	2.01	Chappell (1979)
Jillamatong KB32	Cordierite monzogranite	2.34	White et al., (1989)
Numbla Vale BB2	Cordierite monzogranite	1.94	White et al., (1989)
Granya VB140	Muscovite granodiorite	2.61	White (1990)
Bald Rock, Sierra Nevada	Trondjemite	2.13	White (1990)
Strathbogie WV 115	Monzogranite	2.56	White (1990)
Jeffcot	Monzogranite	2.67	White (1990)
Beridale BB34	Biotite-only granodiorite	1.96	White et al., (1977)
Temora G4-40	Aegirine-arfvedsonite granite (A-type granite)	5.35	Wormald and Price (1988)

Appendix A4. 6
Chemical Analyses of Gneisses (X-Ray Fluorescence Data)

Sample	MG-R-176	MG-R-205A	MG-R-222B	MG-R-222C	MG-R-223	MG-T-005	MG-T-014	MG-T-028	MG-T-035	MG-R-162B	MG-R-163A	MG-R-171B
SiO2	88.51	70.84	70.57	74.83	68.91	71.20	76.47	69.01	61.01	70.34	80.11	65.70
Al2O3	5.97	15.25	14.50	12.43	14.84	13.59	12.30	14.42	14.11	15.90	10.78	14.73
Fe2O3	1.84	1.40	5.02	4.17	4.59	4.20	1.71	4.04	8.43	4.50	1.30	6.41
MgO	0.47	0.57	0.80	1.03	0.88	0.74	0.02	0.84	2.14	0.64	0.52	1.51
CaO	0.16	1.04	2.34	1.45	1.99	1.62	0.50	1.77	3.89	0.22	0.69	1.46
Na2O	0.66	4.69	4.15	2.52	2.94	2.70	3.27	2.60	3.95	2.80	3.06	3.42
K2O	2.29	5.06	2.02	3.33	5.50	4.89	5.22	5.90	3.20	5.07	3.68	4.55
TiO2	0.11	0.18	0.59	0.53	0.58	0.60	0.11	0.65	1.78	0.84	0.10	1.00
MnO	0.01	0.04	0.09	0.07	0.07	0.06	0.02	0.06	0.14	0.22	0.02	0.10
P2O5	0.04	0.12	0.16	0.16	0.15	0.14	0.03	0.17	0.38	0.06	0.10	0.20
TOTAL	100.06	99.19	100.24	100.52	100.45	99.74	99.65	99.46	99.03	100.59	100.36	99.08
LOI	0.44	0.54	0.93	1.11	0.89	0.70	0.11	1.29	1.51	2.70	0.47	0.86
Ni	4	10	8	10	8	13	7	11	21	32	5	33
Cr	5	19	14	15	19	15	7	15	44	81	3	26
V	20	21	62	50	37	42	5	47	147	106	16	89
Sc	4	4	12	12	12	10	1	13	23	16	3	17
Cu	21	1	16	11	31	13	5	26	28	14	4	22
Zn	21	50	69	50	77	127	29	68	146	76	27	142
Cl	0	0	208	69	0	241	26	0	55	0	665	0
Ga	9	20	19	16	20	20	30	20	25	20	13	23
Pb	100	52	21	16	55	31	25	39	17	42	31	68
Sr	35	1359	156	94	95	93	27	97	121	115	39	110
Rb	76	124	77	121	209	202	217	185	237	302	184	254
Ba	474	3316	770	671	936	694	115	946	377	726	110	950
Zr	64	115	437	341	365	320	249	416	418	264	66	414
Nb	4	11	23	19	23	22	100	24	39	18	8	31
Th	13	6	17	16	21	20	31	18	16	14	15	17
Y	16	9	26	41	40	28	99	42	83	27	27	36
La	8	14	25	36	44	24	58	42	44	31	4	23
Ce	14	27	50	72	91	61	126	87	98	68	8	54
Nd	8	11	26	36	42	27	50	41	47	27	6	24

Observations:
Major elements in per cent; Trace elements in ppm; LOI = loss on ignition; Fe2O3 = total iron as F2O3

MG-R-180B	MG-T-077	MG-T-086	MG-T-115	MG-R-142	MG-R-153	MG-R-148A	MG-R-155	MG-R-157	MG-T-110	MG-T-113	MG-R-135	MG-R-181A	MG-R-208B
78.22	77.38	75.73	69.74	73.81	80.65	72.86	87.15	70.25	62.92	70.34	75.96	81.43	72.75
12.58	11.72	12.42	13.82	11.82	11.14	12.45	7.05	14.53	14.62	11.34	15.47	10.26	14.27
1.29	2.64	2.69	4.68	4.66	1.05	4.60	2.22	4.60	7.90	6.63	1.01	2.39	4.56
0.30	0.00	0.03	0.77	0.18	0.38	0.70	0.89	0.78	1.91	1.40	0.16	0.34	1.18
0.95	0.21	0.26	1.90	1.41	0.38	2.12	0.37	1.69	3.33	1.56	1.05	0.33	1.63
3.58	2.94	3.31	2.54	3.49	3.94	3.12	1.20	3.10	3.66	2.03	4.96	2.65	2.76
3.46	4.94	5.14	5.59	3.69	3.30	3.13	0.59	4.51	3.44	4.03	1.74	3.43	2.47
0.12	0.07	0.10	0.58	0.33	0.08	0.57	0.20	0.60	1.27	1.14	0.09	0.27	0.52
0.01	0.01	0.05	0.07	0.10	0.01	0.07	0.02	0.07	0.12	0.90	0.01	0.03	0.07
0.02	0.04	0.05	0.15	0.05	0.04	0.16	0.10	0.16	0.29	0.27	0.02	0.07	0.08
100.53	99.95	99.78	99.84	99.54	100.89	99.78	99.79	100.29	99.46	99.64	100.45	101.20	100.29
0.77	0.81	0.70	0.47	0.33	0.73	0.51	0.47	0.49	1.10	1.16	1.04	0.60	2.90
9	9	12	9	6	4	9	6	11	26	15	5	9	34
3	2	2	12	5	3	13	6	14	50	26	4	6	77
18	11	8	34	17	13	46	43	44	119	97	9	27	66
3	0	0	11	4	1	12	6	13	20	16	3	6	13
2	9	6	5	7	23	7	4	11	8	32	1	18	11
26	19	42	65	41	38	67	80	79	105	339	35	27	76
0	18	4	41	0	0	0	94	354	20	0	4	58	48
23	26	26	19	18	18	18	10	21	23	20	24	12	17
27	41	35	56	33	137	29	33	31	27	288	43	28	17
87	23	21	125	64	56	130	61	139	214	81	162	91	149
109	351	352	188	270	87	112	19	190	203	236	93	98	98
427	179	166	887	609	296	796	148	963	1033	596	333	1853	613
293	130	181	409	167	173	326	158	406	393	323	63	173	222
48	71	72	25	13	91	21	5	23	26	23	12	13	10
29	40	52	21	23	33	15	9	17	15	13	2	20	9
47	136	300	49	42	94	22	23	72	51	40	8	58	28
28	24	48	49	43	27	16	23	57	45	30	0	57	22
66	55	99	105	115	64	41	52	92	96	66	6	114	43
33	25	46	47	38	37	20	24	52	46	31	4	51	20

Appendix A4.7

Chemical Analyses of Schists (X-Ray Fluorescence)

Sample	MG-T-052	MG-T-089	MG-T-095	MG-T-107	MG-R-148B	MG-R-151A	MG-R-151B	MG-R-156A	MG-R-165B	MG-R-165C	MG-R-169D	MG-R-170B
SiO2	45.76	57.86	56.31	49.89	46.20	55.16	62.95	65.02	56.19	63.43	62.48	62.02
Al2O3	15.08	15.75	14.58	15.45	12.97	13.41	13.10	15.18	16.75	12.79	14.04	19.99
Fe2O3	16.44	11.46	12.09	13.39	17.61	12.30	10.30	7.12	11.10	14.67	8.38	8.07
MgO	5.94	4.43	4.40	7.63	5.11	3.61	1.97	1.73	8.62	3.12	2.00	1.39
CaO	3.71	2.44	1.99	3.74	5.90	6.10	2.67	1.42	0.81	0.45	3.02	0.60
Na2O	1.46	2.64	2.43	1.02	0.13	1.30	2.07	2.10	0.71	0.64	2.91	1.64
K2O	6.35	4.24	4.67	6.06	5.62	5.07	4.00	4.60	4.00	2.76	4.43	5.04
TiO2	3.39	1.10	2.40	2.06	4.22	2.55	2.03	1.20	1.19	2.26	1.49	0.84
MnO	0.25	0.28	0.24	0.18	0.23	0.22	0.20	0.11	0.27	0.15	0.13	0.29
P2O5	0.65	0.17	0.49	0.34	0.90	0.50	0.45	0.30	0.07	0.20	0.32	0.11
TOTAL	99.03	100.37	99.60	99.76	98.89	100.22	99.74	98.78	99.71	100.47	99.20	99.99
LOI	1.34	1.85	1.66	3.09	1.73	2.83	1.97	2.03	6.70	5.14	0.87	3.94
Ni	65	77	67	91	50	28	36	37	107	27	20	55
Cr	200	121	131	171	86	64	51	32	638	131	32	94
V	329	123	262	306	431	283	190	126	297	272	140	154
Sc	41	25	33	40	35	34	26	22	45	36	20	24
Cu	7	137	46	8	42	45	21	64	20	138	17	85
Zn	428	312	246	223	246	356	181	329	211	291	132	129
Cl	23	0	0	35	1	221	0	9415	846	1001	82	0
Ga	36	27	27	21	24	24	21	33	23	26	22	28
Pb	8	18	16	10	19	260	23	383	13	18	33	40
Sr	58	181	103	71	85	80	90	89	75	46	146	85
Rb	508	274	394	352	389	369	249	232	271	273	229	205
Ba	695	899	348	493	734	563	625	683	664	220	1017	1099
Zr	309	250	357	161	415	354	391	451	136	255	375	1776
Nb	43	19	37	14	33	28	26	28	8	43	27	17
Th	4	9	7	1	1	10	12	22	5	8	12	16
Y	76	34	74	41	89	51	74	144	39	25	47	40
La	24	23	39	11	45	26	51	100	23	10	39	33
Ce	56	73	78	28	96	59	90	178	74	22	84	69
Nd	32	25	41	16	52	31	58	90	30	10	42	31

Observations:

Major elements in per cent; Trace element in ppm; LOI = loss on ignition; Fe2O3 = total iron as Fe2O3

MG-R-190A	MG-R-190B	MG-T-117	MG-T-122	MG-R-126A	MG-R-166B	MG-R-167A	MG-R-169B	MG-T-111B	MG-R-222A	MG-R-174A	MG-R-175A	MG-R-181B	MG-R-225A
66.49	63.81	66.55	70.64	70.50	74.42	76.88	71.60	59.26	46.48	47.23	48.92	44.00	77.23
17.11	14.25	17.65	15.60	15.80	12.88	11.82	13.30	19.10	15.20	14.52	15.08	17.32	2.42
6.96	7.65	6.30	6.42	4.35	4.44	4.40	5.83	7.60	15.83	16.03	15.50	18.21	18.36
1.69	1.94	0.81	1.20	1.06	1.31	1.46	1.70	2.10	6.75	4.49	6.53	5.74	0.27
0.91	2.82	1.07	0.21	1.62	0.44	0.75	0.93	0.62	3.65	7.09	2.27	1.38	0.11
1.73	3.04	3.16	1.54	3.56	1.60	1.70	1.15	2.01	0.70	0.32	0.58	2.10	0.54
3.63	3.92	3.26	3.80	2.44	3.54	1.58	3.80	6.20	6.64	5.11	6.57	6.90	0.76
0.94	1.66	0.67	0.78	0.58	0.69	0.35	0.79	0.68	3.33	3.76	3.15	3.24	0.18
0.04	0.12	0.19	0.02	0.06	0.04	0.03	0.09	0.40	0.17	0.30	0.29	0.23	0.01
0.06	0.33	0.14	0.09	0.10	0.07	0.08	0.13	0.30	0.48	0.69	0.49	0.37	0.12
99.56	99.54	99.80	100.30	100.07	99.43	99.05	99.32	98.27	99.23	99.54	99.38	99.49	100.00
3.50	1.53	2.99	3.04	1.63	1.50	1.00	1.70	1.77	1.80	1.40	2.90	1.79	5.11
44	22	35	31	21	18	10	34	45	74	49	79	89	5
87	40	57	74	40	57	8	69	30	209	166	207	219	29
127	159	96	110	68	97	95	103	159	414	407	436	287	32
20	19	17	19	11	17	14	16	20	43	44	42	41	2
37	11	48	48	9	17	2	35	48	9	19	16	29	211
113	102	92	76	103	89	83	82	260	187	175	228	293	13
0	0	26	0	0	74	0	234	0	0	16	0	178	0
22	24	22	20	26	21	19	16	31	24	30	25	39	12
33	23	39	23	37	287	13	17	56	12	13	8	19	1561
997	148	172	68	190	93	97	59	221	89	59	49	106	23
169	209	111	157	112	152	44	183	290	365	573	627	659	9
719	896	546	675	661	602	264	710	1843	628	375	520	419	92
223	265	245	236	224	219	133	224	504	244	372	221	259	37
17	29	15	17	16	15	4	15	23	28	36	29	39	2
15	19	14	15	12	14	6	11	21	2	2	3	2	62
64	70	44	41	24	35	29	29	87	54	82	46	38	6
73	25	26	33	25	32	29	10	62	17	25	21	26	2
133	74	63	75	57	75	45	43	128	44	51	36	49	10
69	28	28	33	25	37	29	10	58	27	32	21	24	3

MG-R-226	MG-R-227	MG-R-228	MG-R-225C	MG-R-226C	MG-R-227C	MG-R-228C	MG-R-224A	MG-R-224D	Mg-R-224E
58.20	67.91	62.22	61.03	65.91	64.10	63.40	61.62	73.77	67.89
18.43	15.16	16.59	15.42	14.23	14.50	15.62	18.96	14.82	15.89
8.25	6.47	8.56	7.81	6.01	6.00	6.50	7.12	4.95	6.00
3.96	3.03	3.79	3.32	3.00	3.32	3.30	3.48	0.78	2.13
2.50	1.52	1.66	2.11	2.20	2.20	2.61	1.83	0.05	0.95
3.19	3.66	2.64	2.91	2.50	2.60	2.73	1.86	0.08	1.93
3.63	2.01	3.33	3.00	2.38	2.40	2.88	4.56	4.74	4.30
1.06	0.88	0.93	0.70	0.82	0.75	0.80	0.86	0.55	1.00
0.12	0.10	0.22	0.20	0.14	0.10	0.20	0.10	0.07	0.10
0.21	0.10	0.22	0.18	0.08	0.10	0.20	0.16	0.09	0.14
99.55	100.84	100.16	96.68	97.27	96.07	98.24	100.55	99.90	100.33
2.39	2.80	2.14	2.16	2.38	2.89	2.00	3.50	2.65	3.00
47	57	70	41	43	31	47	46	28	42
143	151	127	112	148	121	114	71	45	60
179	150	181	126	125	127	178	145	94	119
26	19	24	250	25	23	22	23	15	20
140	11	14	140	65	177	90	3	24	21
129	105	172	105	107	116	103	124	330	227
0	0	21	0	0	0	0	0	0	0
28	18	21	22	28	24	25	25	19	21
1174	13	17	17	18	13	16	30	145	83
232	334	132	150	170	170	152	133	30	103
103	70	103	82	73	43	79	190	171	182
658	537	583	243	311	409	438	809	630	629
224	216	197	141	190	168	159	206	170	188
8	10	12	10	9	110	12	18	13	14
14	5	7	14	12	13	6	16	13	14
39	31	37	30	32	31	38	33	30	30
19	13	14	19	13	13	12	33	24	31
43	30	33	42	30	32	31	78	51	60
22	15	18	21	20	20	18	33	23	28

Appendix A4.8

Chemical Analyses of Amphibolite (X-Ray Fluorescence Data)

Sample	MG-T-101	MG-T-112	MG-R-141	MG-R-163G	MG-R-208A
SiO2	47.67	54.08	46.01	51.29	53.55
Al2O3	13.88	13.73	16.09	15.55	12.50
Fe2O3	15.24	13.18	14.79	12.42	18.65
MgO	4.92	3.77	8.39	5.13	2.83
CaO	7.65	5.06	9.51	9.34	7.44
Na2O	1.10	1.45	1.65	2.99	2.36
K2O	3.67	4.34	0.74	0.80	0.46
TiO2	4.34	4.09	1.59	1.87	1.57
MnO	0.24	0.18	0.29	0.20	0.29
P2O5	0.82	0.87	0.16	0.28	0.20
TOTAL	99.53	100.75	99.22	99.87	99.85
LOI	1.86	2.56	1.93	1.31	0.03
Ni	35	143	151	57	4
Cr	75	89	101	117	7
V	495	379	271	303	96
Sc	50	47	38	42	51
Cu	13	88	48	166	9
Zn	208	385	129	101	178
Cl	42	0	0	1450	0
Ga	24	31	20	19	19
Pb	16	29	11	6	8
Sr	111	97	130	236	119
Rb	181	354	36	48	16
Ba	483	488	101	184	98
Zr	413	483	79	151	109
Nb	36	33	10	14	5
Th	2	5	1	3	1
Y	66	68	25	36	47
La	27	12	6	15	3
Ce	66	34	14	32	17
Nd	39	22	11	19	16

Observations:

Major elements in per cent; Trace elements in ppm; LOI = loss on ignition;
Fe2O3 = total iron as Fe2O3

Appendix A4.9

Microprobe Analyses of Amphibole

%wt Oxide	MG-R-208A1	MG-R-208AII	MG-R-208AIII	MG-R-208AIV	MG-R-208AV	MG-R-208AVI	MG-R-208AVII	MG-R-208AVIII	MG-R-208AIX	MG-R-208AX	MG-R-208AXI	MG-R-208AXII	MG-R-208AXIII
SiO2	41.81	41.74	41.37	42.12	42.09	42.17	41.75	41.79	41.86	41.50	42.15	41.57	41.86
TiO2	1.96	1.93	1.89	1.94	2.00	2.00	1.98	2.03	1.91	1.89	1.73	1.86	1.98
Al2O3	11.07	11.18	11.05	11.16	11.06	11.13	11.20	11.24	11.15	11.35	10.69	11.26	11.30
FeO	24.87	24.85	25.45	25.44	25.11	25.19	24.86	25.36	25.03	25.16	25.10	24.95	25.48
MnO	0.24	0.29	0.29	0.26	0.28	0.28	0.28	0.29	0.28	0.31	0.26	0.28	0.28
MgO	5.06	4.97	4.84	4.74	5.01	4.88	4.78	4.72	4.77	4.79	4.86	4.81	4.89
CaO	10.95	10.76	10.76	10.91	10.69	10.78	10.94	10.82	10.62	10.73	10.94	10.73	10.71
K2O	0.79	0.79	0.79	0.79	0.79	0.80	0.77	0.78	0.80	0.80	0.70	0.82	0.80
Na2O	1.65	1.78	1.72	1.71	1.73	1.57	1.61	1.69	1.59	1.71	1.56	1.76	1.75
F	-	-	-	-	-	-	-	-	-	-	-	-	-
Total	**98.40**	**98.29**	**98.16**	**99.87**	**98.76**	**98.80**	**98.17**	**98.72**	**98.01**	**98.24**	**97.99**	**98.04**	**99.05**
Formula Units:													
Si	6.402	6.402	6.354	6.419	6.408	6.419	6.412	6.394	6.423	6.360	6.475	6.400	6.357
Ti	0.230	0.221	0.222	0.220	0.229	0.229	0.231	0.230	0.221	0.221	0.203	0.213	0.228
Al	1.996	2.018	2.001	2.005	1.983	1.993	2.030	2.021	2.018	2.053	1.937	2.043	2.025
Fe2	3.183	3.187	3.264	3.241	3.199	3.210	3.192	3.243	3.207	3.222	3.219	3.209	3.238
Mn	0.028	0.037	0.037	0.037	0.037	0.037	0.037	0.037	0.037	0.037	0.037	0.037	0.037
Mg	1.159	1.133	1.107	1.080	1.133	1.107	1.098	1.075	1.087	1.095	1.116	1.100	1.104
Ca	1.794	1.769	1.771	1.785	1.746	1.756	1.799	1.773	1.742	1.758	1.798	1.766	1.742
K	0.156	0.157	0.157	0.156	0.156	0.156	0.148	0.156	0.157	0.157	0.138	0.157	0.155
Na	0.488	0.525	0.516	0.504	0.512	0.467	0.480	0.505	0.470	0.507	0.462	0.527	0.511
F	-	-	-	-	-	-	-	-	-	-	-	-	-
CatSum	15.436	15.449	15.429	15.447	15.403	15.374	15.427	15.434	15.362	15.410	15.385	15.452	15.397
Calculation:													
Si	6.404	6.398	6.359	6.420	6.412	6.422	6.416	6.388	6.423	6.366	6.484	6.394	6.364
Al (tet)	1.596	1.602	1.641	1.580	1.588	1.578	1.584	1.612	1.577	1.634	1.516	1.606	1.636
Al (oct)	0.402	0.419	0.362	0.425	0.398	0.419	0.444	0.413	0.440	0.418	0.422	0.436	0.390
Ti	0.226	0.223	0.218	0.222	0.229	0.229	0.229	0.233	0.220	0.218	0.200	0.215	0.226
Fe+++	0.505	0.519	0.632	0.487	0.577	0.564	0.451	0.535	0.574	0.586	0.484	0.517	0.633
Mg	1.155	1.136	1.109	1.077	1.138	1.108	1.095	1.075	1.091	1.095	1.114	1.103	1.108
Fe++	2.681	2.667	2.641	2.755	2.622	2.644	2.744	2.706	2.638	2.642	2.745	2.692	2.607
Mn	0.031	0.038	0.038	0.034	0.036	0.036	0.036	0.038	0.036	0.040	0.034	0.036	0.036
Ca	1.797	1.767	1.772	1.782	1.745	1.759	1.801	1.772	1.746	1.764	1.803	1.768	1.745
Na	0.490	0.529	0.513	0.505	0.511	0.464	0.480	0.501	0.473	0.509	0.465	0.525	0.516
K	0.154	0.155	0.155	0.154	0.154	0.155	0.151	0.152	0.157	0.157	0.137	0.161	0.155
F	0.000	0.000	0.000	0.000	0.000	0.000	0.000	0.000	0.000	0.000	0.000	0.000	0.000
OH	0	0	0	0	0	0	0	0	0	0	0	0	0
Si+Al+Ti+Fe+Mn+Mg	12.9999	13.0002	12.9991	13.0001	13.0000	13.0001	12.9992	13.0003	13.0001	13.0001	13.0002	12.9999	12.9998
FeO*, %	24.871	24.849	25.453	25.434	25.106	25.187	24.859	25.354	25.032	25.161	25.101	24.952	25.476
Fe2O3, %	4.38	4.50	5.46	4.25	5.03	4.92	3.90	4.65	4.97	5.08	4.18	4.47	5.53
FeO, %	20.93	20.80	20.54	21.61	20.58	20.76	21.35	21.17	20.56	20.59	21.34	20.93	20.50
FeO/(FeO+Fe2O3)	0.83	0.82	0.79	0.84	0.80	0.81	0.85	0.82	0.81	0.80	0.84	0.82	0.79
Formula 'A'	0.441	0.451	0.440	0.441	0.410	0.378	0.432	0.425	0.376	0.429	0.406	0.454	0.416
(Ca+Na)B	2	2	2	2	2	2	2	2	2	2	2	2	2
(Na)B	0.203	0.233	0.228	0.218	0.255	0.241	0.199	0.228	0.254	0.236	0.197	0.232	0.255
Mg/(Mg+Fe2)	0.301	0.299	0.296	0.281	0.303	0.295	0.285	0.284	0.293	0.293	0.289	0.291	0.298

Formulae for amphibole calculated on the basis of 23 oxygens

Not detected: nd; Not analysed:-

MG-R-208AXIV	MG-R-208AXV	MG-R-208XVI	MG-R-137	MG-R-141I	MG-R-141II	MG-R-141III	MG-T-101I	MG-R-163GI	MG-R-163GII	MG-R-163GIII	MG-R-056I	MG-R-056II	MG-R-056III
41.88	41.42	42.06	43.05	41.78	43.11	42.52	40.46	42.05	38.48	41.60	41.50	42.17	42.20
1.96	1.80	1.82	0.62	0.49	0.51	0.64	0.81	0.51	0.33	0.94	0.80	0.60	0.73
11.26	11.37	11.06	15.38	15.05	13.45	14.89	12.27	13.37	9.10	13.75	14.35	14.79	15.09
25.65	25.36	25.76	16.30	16.24	15.94	16.36	22.63	18.99	14.77	18.26	18.47	17.93	17.73
0.31	0.28	0.26	0.26	0.34	0.36	0.42	0.46	nd	nd	nd	0.10	0.30	0.30
4.82	4.62	4.82	9.21	9.32	9.85	9.35	6.24	7.70	6.97	7.35	7.44	7.80	8.34
10.61	10.97	10.75	10.74	11.03	11.43	11.06	11.49	11.13	7.10	11.39	12.10	11.82	11.88
0.79	0.78	0.75	0.47	0.37	0.35	0.34	1.72	0.97	0.50	0.99	1.12	1.02	1.00
1.68	1.73	1.54	1.14	1.47	1.29	1.51	1.30	1.10	0.56	1.21	1.20	1.50	1.54
-	-	-	0.13	nd	nd	nd	0.04	nd	0.09	0.04	nd	nd	nd
98.96	**98.33**	**98.82**	**97.30**	**96.09**	**96.29**	**97.09**	**97.42**	**95.82**	**77.98**	**95.53**	**97.08**	**97.93**	**98.81**
6.358	6.366	6.394	6.272	6.197	6.393	6.244	6.251	6.390	6.929	6.382	6.300	6.306	6.231
0.228	0.213	0.210	0.068	0.055	0.057	0.071	0.094	0.058	0.045	0.108	0.091	0.067	0.081
2.016	2.060	1.982	2.641	2.631	2.351	2.577	2.234	2.395	1.931	2.486	2.568	2.607	2.626
3.256	3.262	3.279	1.130	1.147	1.296	1.190	2.399	1.840	1.204	2.127	2.201	2.014	1.827
0.037	0.037	0.037	0.032	0.043	0.045	0.052	0.060	nd	nd	nd	0.013	0.038	0.038
1.095	1.063	1.096	2.000	2.061	2.177	2.047	1.437	1.744	1.871	1.681	1.684	1.739	1.836
1.724	1.811	1.754	1.677	1.753	1.816	1.740	1.902	1.812	1.370	1.872	1.968	1.894	1.879
0.155	0.157	0.146	0.087	0.070	0.066	0.064	0.339	0.188	0.115	0.194	0.217	0.195	0.188
0.493	0.517	0.457	0.322	0.423	0.371	0.430	0.389	0.324	0.196	0.360	0.353	0.435	0.441
-	-	-	0.060	nd	nd	nd	0.020	nd	0.051	0.019	nd	nd	nd
15.362	15.486	15.355	14.289	14.380	14.572	14.415	15.125	14.751	13.712	15.229	15.395	15.295	15.147
6.366	6.372	6.402	6.272	6.197	6.393	6.244	6.251	6.390	6.929	6.382	6.300	6.306	6.231
1.634	1.628	1.598	1.728	2.631	2.351	2.577	1.749	1.610	1.071	1.618	1.700	1.694	1.770
0.383	0.433	0.386	0.914	0.000	0.000	0.000	0.485	0.784	0.860	0.868	0.867	0.913	0.857
0.224	0.208	0.208	0.068	0.055	0.057	0.071	0.094	0.058	0.045	0.108	0.091	0.067	0.081
0.698	0.473	0.690	0.897	0.868	0.680	0.819	0.524	0.573	1.020	0.216	0.144	0.228	0.363
1.092	1.059	1.094	2.000	2.061	2.177	2.047	1.437	1.744	1.871	1.681	1.684	1.739	1.836
2.563	2.789	2.589	1.089	1.147	1.296	1.190	2.399	1.840	1.204	2.127	2.201	2.015	1.826
0.040	0.036	0.034	0.032	0.043	0.045	0.052	0.060	0.000	0.000	0.000	0.013	0.038	0.038
1.728	1.808	1.753	1.677	1.753	1.816	1.740	1.902	1.812	1.370	1.872	1.968	1.894	1.879
0.495	0.516	0.454	0.322	0.423	0.371	0.430	0.389	0.324	0.196	0.360	0.353	0.435	0.441
0.153	0.153	0.146	0.087	0.070	0.066	0.064	0.339	0.188	0.115	0.194	0.217	0.195	0.188
0.000	0.019	0.000	0.018	0.000	0.000	0.000	0.020	0.000	0.051	0.019	0.000	0.000	0.000
0	0	0	0	0	0	0	0	0	0	0	0	0	0
13.0001	13.0001	12.9999	13.0001	13.0000	13.0000	13.0000	12.9999	13.0000	13.0000	13.0000	13.0000	13.0000	13.0000
25.649	25.360	25.757	16.301	16.420	15.940	16.360	22.628	18.990	14.770	18.260	18.470	17.930	17.730
5.88	4.09	6.02	8.18	7.78	6.10	7.42	4.51	5.01	7.53	1.87	1.26	2.03	3.27
20.36	21.68	20.34	8.94	9.24	10.45	9.69	18.57	14.48	7.99	16.58	17.34	16.11	14.79
0.78	0.84	0.77	0.52	0.54	0.63	0.57	0.80	0.74	0.51	0.90	0.93	0.89	0.82
0.376	0.477	0.353	0.086	0.246	0.253	0.234	0.630	0.324	-0.320	0.426	0.538	0.524	0.509
2	2	2	2	2	2	2	2	2	insufficient	2	2	2	2
0.272	0.192	0.247	0.323	0.247	0.184	0.260	0.098	0.188	insufficient	0.128	0.032	0.463	0.121
0.299	0.275	0.297	0.647	0.642	0.627	0.632	0.375	0.487	0.608	0.441	0.433	0.106	0.501

Appendix A4.10
Method of Study for the Calculations of P-T Conditions

For this purpose samples minerals were probed, which data were acquired by wavelength dispersive energy (see Appendix A4.1). The following analytical methods using the microprobe analises were carried out for calculations of P-T metamorphic conditions:

(i) Chlorite Thermometry (Cathelineau, 1988)

Chorite thermometry is based on the cation site occupancy as a function of temperature, in particular the increase of Al $_{(iv)}$ on the tetrahedral site (Cathelineau, 1988). The equation used to calculate temperature from chlorite composition, on the basis of 14 oxygens, is:

$$T\ (°C) = -\ 61.92 + 321.98\ Al\ (iv)$$

(ii) Thermodynamic Dataset (Powell and Holland, 1988)

The computer program call Thermocalc consists of a list of dataset endmembers provided allows to identify all the mineral endmembers applicable for each example. The program estimates the P-T and also suggest all the reactions for each P-T pair.

(iii) Chlorite Solid Solution Model (Walshe, 1986)

The computer program based on a six-component chlorite solid solution model using the nonstoichiometry of chlorite represented by six thermodynamic components. These components were estimated making use of constraints imposed by the compositions of known chlorites. Two geothermometers have been calibrated and combined with mathematics equation (Gibbs-Duhem) allow the temperature of formation, the ferric iron content and the water content of chlorite coexisting with quartz and an aqueous phase at a known pressure to be calculated by probe analysis of cholite.

(iv) Experimental Calibrations (Thomas and Ernst, 1990; and Johnson and Rutherford, 1989)

The exterimantal calibration of Johnson and Rutherford (1989) based on the Al content of igneous horblende in equilibrium with melt, fluid, biotite, quartz, sanidine, plagioclase, sphene, and magnetite or ilmenite, for a pressure range 2-8 kbar at 740-780°C. The forluma is :

$$P = 4.23\ (Al_{total}) - 3.46.$$

The experimental of Thomas and Ernst (1990) was a function of pressure in the range 6-12 kbar based on the calibration for the total aluminium of hornblende as a function of aqueous fluid pressure at a constant, near solidus temperature was derived:

$$P = -\ 6.23 + 5.34\ (Al_{total})$$

Appendix A4.11

Microprobe Analyses used for P-T calculations
(Powell and Holland, 1988)

% Oxide/Sample	MG-R-208BI	MG-R-208BII	MG-R208BIII	MG-R-208BIV	MG-R-208BV	MG-R-208BVI	MG-R-208BVII	MG-R-208BVIII	MG-R-228I	MG-R-228II	MG-R-228III	MG-R-228IV
SiO2	37.94	37.91	62.07	60.07	62.16	34.92	34.97	34.92	37.62	37.54	62.64	62.09
TiO2	0.02	0.02	-	-	-	2.99	3.50	2.98	0.02	0.02	0.02	-
Al2O3	21.59	21.48	23.36	23.84	23.60	19.53	18.97	19.40	21.19	21.16	23.55	23.68
FeO	35.22	35.38	0.01	0.24	0.01	21.07	21.89	21.11	30.01	30.40	0.34	0.13
MnO	2.81	2.87	-	-	-	0.08	0.09	0.09	7.83	8.18	0.02	-
MgO	3.35	3.29	-	-	-	7.62	7.39	7.47	2.74	2.66	0.02	-
CaO	1.03	1.00	5.01	4.42	5.12	0.01	0.01	0.03	1.26	1.20	4.70	5.06
Na2O	0.02	nd	8.65	7.98	8.58	0.09	0.07	0.04	0.04	0.02	8.61	8.63
K2O	-	-	0.27	0.21	0.25	9.71	9.74	9.70	-	-	0.24	0.06
F	-	-	-	-	-	0.25	0.37	0.57	-	-	nd	-
Cl	-	-	-	-	-	0.04	0.04	0.04	-	-	0.01	-
Cr	-	-	-	-	-	0.03	0.06	0.03	-	-	-	-
Total	101.98	101.95	99.37	96.76	99.72	96.34	97.10	96.38	100.71	101.18	100.15	99.65
Formula/Sample	**MG-R-208BI**	**MG-R-208BII**	**MG-R208BIII**	**MG-R-208BIV**	**MG-R-208BV**	**MG-R-208BVI**	**MG-R-208BVII**	**MG-R-208BVIII**	**MG-R-228I**	**MG-R-228II**	**MG-R-228III**	**MG-R-228IV**
Si	2.995	2.990	2.768	2.745	2.762	5.326	5.323	5.342	3.011	3.000	7.622	2.760
Ti	0.001	0.001	-	-	-	0.342	0.400	0.343	0.001	0.001	0.002	-
Al	2.009	2.001	1.228	1.280	1.236	3.510	3.404	3.498	1.999	1.993	3.378	1.240
Fe	2.325	2.339	nd	0.009	nd	2.688	2.787	2.701	2.009	2.032	0.034	0.005
Mn	0.108	0.192	-	-	-	0.098	0.011	0.012	0.531	0.554	0.002	-
Ca	0.087	0.085	0.239	0.216	0.243	0.002	0.002	0.004	0.108	0.103	0.613	0.241
Mg	0.394	0.308	-	-	-	1.732	1.676	1.704	0.327	0.316	0.003	-
Na	0.003	nd	0.748	0.707	0.739	0.027	0.021	0.011	0.006	0.003	2.031	0.744
K	-	-	0.015	0.013	0.014	1.889	1.891	1.893	-	-	0.037	0.003
F	-	-	-	-	-	0.118	0.176	0.276	-	-	nd	-
Cl	-	-	-	-	-	0.009	0.009	0.009	-	-	0.003	-
Cr	-	-	-	-	-	0.004	0.007	0.003	-	-	-	-
Total	7.922	7.916	4.998	4.970	4.994	15.745	15.707	15.796	7.992	8.002	13.725	4.993
Mineral	**Garnet**	**Garnet**	**Plagioclase**	**Plagioclase**	**Plagioclase**	**Biotite**	**Biotite**	**Biotite**	**Garnet**	**Garnet**	**Plagioclase**	**Plagioclase**

Observations:
Formulae calculated on the basis of: Biotite = 22 oxygens; Garnet = 12 oxygens; Muscovite = 22 oxygens; Plagioclase = 8 oxygens; Sillimanite =10 oxygens
Boqueirão dos Cochos: MG-R-208BI to MG-R-208BVII; São Francisco mine area: MG-R-228I to MG-R-228VIII; Itapetim District: MG-R-169BI to MG-R-169X
Not detected: nd
Not analysed: -

MG-R-228V	MG-R-228VI	MG-R-228VII	MG-R-228VIII	MG-R-169BI	MG-R-169BII	MG-R-169BIII	MG-R-169BIV	MG-R-169BV	MG-R-169BVI	MG-R-169BVII	MG-R-169BVIII	MG-R169BXI	MG-R-169BX
35.59	35.71	45.61	37.14	45.85	45.48	37.50	37.61	37.31	59.41	59.31	59.37	35.06	33.25
2.07	1.92	0.19	-	0.76	0.84	0.07	0.07	0.03	-	-	-	1.52	1.44
19.53	19.82	37.00	56.97	33.19	33.49	21.17	20.92	20.90	24.10	24.31	23.81	18.62	18.05
18.63	18.68	0.81	2.87	1.85	1.81	34.11	33.60	34.35	0.10	0.15	0.08	18.85	20.35
0.20	0.20	0.02	0.05	0.02	nd	2.32	1.43	2.08	-	-	-	-	-
10.01	9.84	0.34	1.33	0.64	0.54	2.12	2.50	2.16	-	-	-	8.63	7.81
0.01	0.09	0.04	-	-	-	3.97	4.73	4.06	6.84	7.03	6.38	-	-
0.32	0.30	1.00	0.03	0.99	1.04	-	-	-	7.46	7.37	7.73	-	-
8.74	8.51	6.59	-	9.58	9.59	-	-	-	0.05	0.05	0.05	6.57	6.55
0.29	0.25	0.18	-	nd	0.05	-	-	-	-	-	-	0.13	0.25
0.01	0.01	0.01	-	0.01	nd	-	-	-	-	-	-	-	-
-	-	-	-	-	-	-	-						
95.40	95.33	91.79	98.39	92.89	92.84	101.26	100.86	100.89	97.96	98.22	97.42	89.38	87.70

MG-R-228V	MG-R-228VI	MG-R-228VII	MG-R-228VIII	MG-R-169BI	MG-R-169BII	MG-R-169BIII	MG-R-169BIV	MG-R-169BV	MG-R-169BVI	MG-R-169BVII	MG-R-169BVIII	MG-R169BXI	MG-R-169BX
5.385	5.395	6.143	2.070	6.261	6.220	2.991	3.000	2.991	2.299	2.689	2.710	5.582	5.482
0.235	0.218	0.019	-	0.078	0.086	0.004	0.004	0.002	-	-	-	0.182	0.190
3.484	3.530	5.875	3.742	5.343	5.398	1.991	1.967	1.975	1.290	1.299	1.281	3.496	3.508
2.357	2.359	0.092	0.134	0.211	0.206	2.275	2.241	2.303	0.004	0.006	0.003	2.511	2.806
0.026	0.026	0.002	0.002	0.002	nd	0.156	0.097	0.141	-	-	-	-	-
0.002	0.014	0.006	-	-	-	0.339	0.404	0.349	0.333	0.342	0.312	-	-
2.258	2.216	0.069	0.111	0.129	0.111	0.252	0.297	0.258	-	-	-	2.049	1.921
0.094	0.008	0.262	0.003	0.263	0.275	-	-	-	0.657	0.648	0.684	-	-
1.687	1.640	1.132	-	1.668	1.672	-	-	-	0.003	0.027	nd	1.335	1.378
0.137	0.117	0.076	-	nd	0.019	-	-	-	-	-	-	0.063	0.132
0.003	0.003	0.003	-	0.003	nd	-	-	-	-	-	-	-	-
-	-	-	-	-	-	-	-	-	-	-	-	-	-
15.668	15.526	13.679	6.062	13.958	13.987	8.008	8.010	8.019	4.586	5.011	4.990	15.218	15.417
Biotite	**Biotite**	**Muscovite**	**Sillimanite**	**Muscovite**	**Muscovite**	**Garnet**	**Garnet**	**Garnet**	**Plagioclase**	**Plagioclase**	**Plagioclase**	**Biotite**	**Biotite**

Appendix A4. 12

Chlorite Microprobe Analyses used for PxT calculations
(Cathelineau, 1988; and Walshe, 1986)

% Oxide/Sample	MG-R-224AI	MG-R-224AII	MG-R-224AIII	MG-T-056II	MG-T-056II
SiO2	25.77	25.75	25.91	25.38	24.65
TiO2	0.07	0.07	0.07	0.07	0.10
Al2O3	20.06	20.40	20.36	19.70	18.21
FeO	26.26	27.06	26.98	24.47	24.61
MnO	0.41	0.40	0.36	0.44	0.47
MgO	13.78	13.70	13.81	15.17	15.21
CaO	0.07	0.07	0.07	0.07	0.29
Na2O	0.02	0.02	0.02	0.02	0.02
K2O	0.13	0.10	0.10	0.02	0.01
Cl	0.01	0.01	0.01	-	-
F	nd	0.08	nd	-	-
Total	86.58	87.66	87.69	85.34	83.57
Formula Units /Sample					
Si	4.357	4.317	4.333	3.927	3.924
Ti	0.009	0.009	0.009	0.012	0.013
Al	3.997	4.032	4.014	3.592	3.417
Fe	3.712	3.794	3.774	3.166	3.276
Mn	0.059	0.056	0.052	0.057	0.064
Mg	3.472	3.423	3.443	3.499	3.608
Ca	0.013	0.012	0.012	0.012	0.050
Na	0.006	0.006	0.006	0.006	0.005
K	0.027	0.022	0.022	nd	0.002
Cl	0.003	0.003	0.003	-	-
F	nd	0.041	nd	-	-
Total	15.655	15.715	15.668	14.271	14.358
Formulae for chlorite calculated on the basis of 22 oxygens for the samples MG-R-224 and 20 oxygens for the sample MG-T-056 (c.f. Deer, Howie and Zussman, 1985: 28 oxygens = 1/R)					
R = 28/oxygens sample	1.2727	1.2727	1.2727	1.400	1.400
Si	4.36x1.2727 = 5.5490	4.32x1.2727 = 5.4981	4.33x1.2727 = 5.511	3.93x1.400 = 5.502	3.92x1.400 = 5.488
Al	4.00x1.2727 = 5.0908	4.03x1.2727 = 5.1290	4.01x1.2727 = 5.104	3.59x1.400 = 5.026	3.42x1.400 = 4.788
Fe	3.71x1.2727 = 4.7217	3.80x1.2727 = 4.8363	3.77x1.2727 = 4.798	3.17x1.400 = 4.438	3.28x1.400 = 4.592
Mg	3.47x1.2727 = 4.4163	3.42x1.2727 = 4.3526	3.44x1.2727 = 4.378	3.50x1.400 = 4.900	3.61x1.400 = 5.054
Al iv	5.5490-8.000 = 2.4510	5.4981-8.000 = 2.5019	5.511-8.000 = 2.489	5.502-8.00 = 2.498	5.488-8.00 = 2.512
Ratio Fe*/Fe*+Mg	0.520	0.526	0.520	0.480	0.480

Not detected: nd; Not analysed: -

Fe* as total iron

Appendix A 4.13 References for analyses used in compilation of geochemical database for Figures 4.23 to 4.26.

Authors	Reference
Atherton et al. (1979)	Atherton, M.P. & Tarney, J. (eds.)
Baker (1984)	JGSL 141: 401-411
Baker (1985)	JGSL 142: 279-295
Baker (1987)	Geol. Soc. Special Pub. 30: 293-311
Ball & Bland (1985)	JGSL 142: 889-898
Best et al. (1989)	BGSA 101: 1076-1090
Bevins et al. (1991)	JGSL 148: 719-729
Blake et al. (1992)	JGSL 149: 193-207
Bremond d'Ars et al. (1992)	JGSL 149: 701-708
Briand et al. (1991)	JGSL 148: 959-971
Brouxel et al. (1989)	Geology 17: 273-276
Camp et al. (1989)	BGSA 101: 71-95
Camp et al. (1991)	BGSA 103: 363-391
Camp et al. (1992)	BGSA 104: 379-396
Carlson & Moye (1990)	GSA Memoir 174: 375-394
Christe & Hannah (1990)	GSA Memoir 174: 315-329
Clift & Ryan (1994)	JGSL 151: 329-342
Cook et al. (1991)	BGSA 103: 829-841
Cullers et al. (1992)	BGSA 104: 316-328
D'Lemos (1992)	JGSL 149: 709-720
Defant et al. (1992)	JGSL 149: 569-579
Devey & Stephens (1991)	JGSL 148: 979-983
Ernst et al. 1991	BGSA 103: 56-72
Fitton (1987)	Geol. Soc. Spec. Pub. 30: 273-291
French et al. (1979)	Geol. Soc. Spec. Pub. 8: 635-642
Furnes et al. (1994)	JGSL 151: 91-109
Fyffe & Pickerill (1993)	BGSA 105: 897-910
Gamble et al. (1992)	JGSL 149: 93-106
Gibson (1990)	JGSL 147: 1071-1081
Glazner (1990)	GSA Memoir 174: 147-168
Harmon et al. (1984)	JGSL 141: 803-822
John & Wooden (1990)	GSA Memoir 174: 71-98
Jones et al. (1993)	JGSL 150: 1167-1181
Kanaris-Sotiriou & Webb (1989)	JGSL 146: 607-610
Kanaris-Sotiriou et al. (1993)	JGSL 150: 903-914
Kay et al. (1988)	J. S. Amer. Earth Sci. 1: 21-38
Lange & Carmichael (1991)	BGSA 103: 928-940
Linn et al. (1992)	BGSA 104: 1264-1279
Lipman (1988)	Trans. Roy. Soc. Edin. 79: 265-288
Lipman et al. (1989)	Geology 17: 611-614
Liverton (1992)	PhD Thesis, Univ. London
López-Ruiz et al. (1993)	JGSL 150: 915-922
Lyle & Preston (1993)	JGSL 150: 109-120
Macdonald et al. (1984)	JGSL 141: 147-159
Meyer et al. (1992)	BGSA 104: 1073-1085
Millward et al. (1984)	JGSL 141: 847-860
Mohr (1990)	JGSL 147: 1061-1069
Moore & Clague (1992)	BGSA 104: 1471-1484
Moore et al. (1994)	BGSA 106: 383-394
Mukasa & Henry (1990)	JGSL 147: 27-39
O'Brien et al. (1985)	JGSL 142: 1139-1157
Owen et al. (1992)	JGSL 149: 923-935
Petterson & Windley (1992)	JGSL 149: 107-114
Petterson et al. (1992)	JGSL 149: 889-906
Pichavant & Montel (1988)	Trans. Roy. Soc. Edin. 79: 197-207
Reavy et al. (1991)	BGSA 103: 392-401

Richards et al. (1990)	Geology 18: 958-961
Righter & Carmichael (1992)	BGSA 104: 1592-1607
Schandelmeier et al. (1994)	JGSL 151: 485-497
Sengupta et al. (1989)	JGSL 146: 491-498
Skulsky et al. (1991)	Geology 19: 11-14
Sloan & Bennett (1990)	JGSL 147: 1051-1060
Smith et al. (1990)	Geol. Soc. Amer. Memoir 174: 169-194
Stone (1990)	BGSA 102: 147-158
Tarney & Saunders (1979)	Atherton, M.P. & Tarney, J. (eds.) (1979)
Thirlwall & Burnard (1990)	JGSL 147: 259-269
Thirlwall & Graham (1984)	JGSL 141: 427-445
Thompson et al. (1993)	JGSL 150: 277-292
Thorkelson & Smith (1989)	Geology 17: 1093-1096
Wadge & Macdonald (1985)	JGSL 142: 297-308
Weaver et al. (1987)	Geol. Soc. Spec. Pub. 30: 253-267
Wobus et al. (1990)	Geology 18: 642-645

Abbreviations used: **B**, Bulletin; **GSA**: Geological Society of America; **JGSL**: Journal of the Geological Society, London; **Geol. Soc. Spec. Pub.**, Geological Society Special Publication; **Trans. Roy. Soc. Edin.**, Transactions of the Royal Society of Edinburgh; **J. S. Amer. Earth Sci.**, Journal of South American Earth Sciences.

Appendix A5.1

Electron Microscope Analyses of Sulphide: Pyrite

Wt % Element Concen.	MG-R-155-I	MG-R-155-II	MG-R-155-III	MG-R-155-IV	MG-R-155-V	MG-R-155-VI	MG-R-155-VII	MG-R-155-VIII	MG-R-155-IX	MG-R-155-X	MR-G-155-XI	MG-R-155-XII	MG-R-155-XIII	MG-R-155-XIV
S	53.88	53.72	54.28	53.74	53.41	53.75	53.85	52.63	49.44	54.07	51.78	55.19	55.54	48.99
Fe	46.99	46.93	47.58	46.16	46.70	46.21	46.48	45.46	42.10	46.15	44.88	48.00	47.94	43.06
Au	0.00	0.00	0.14	0.47	0.26	0.25	0.72	0.03	0.45	0.59	0.11	0.30	0.11	0.24
Si	0.23	2.89	0.41	1.19	0.44	0.42	0.45	0.43	6.57	0.25	4.36	0.37	0.39	4.88
Total	101.10	100.93	102.41	101.56	100.80	100.63	101.50	98.55	98.57	101.06	101.13	103.86	103.99	97.16
Wt % Normalized Atom.	**MG-R-155-I**	**MG-R-155-II**	**MG-R-155-III**	**MG-R-155-IV**	**MG-R-155-V**	**MG-R-155-VI**	**MG-R-155-VII**	**MG-R-155-VIII**	**MG-R-155-IX**	**MG-R-155-X**	**MR-G-155-XI**	**MG-R-155-XII**	**MG-R-155-XIII**	**MG-R-155-XIV**
S	66.42	66.33	66.13	65.80	66.13	66.52	66.34	66.43	60.90	66.80	62.73	66.32	66.49	61.78
Fe	33.25	33.27	33.28	32.45	33.19	32.83	32.87	32.94	29.77	32.73	31.21	33.11	32.95	31.17
Au	0.00	0.00	0.03	0.09	0.05	0.05	0.15	0.01	0.09	0.12	0.02	0.06	0.02	0.05
Si	0.23	0.41	0.57	1.66	0.63	0.60	0.64	0.62	9.24	0.36	6.03	0.51	0.54	7.02
Total	100.00	100.00	100.00	100.00	100.00	100.00	100.00	100.00	100.00	100.00	100.00	100.00	100.00	100.00
Normalised Element (wt %)	**MG-R-155-I**	**MG-R-155-II**	**MG-R-155-III**	**MG-R-155-IV**	**MG-R-155-V**	**MG-R-155-VI**	**MG-R-155-VII**	**MG-R-155-VIII**	**MG-R-155-IX**	**MG-R-155-X**	**MR-G-155-XI**	**MG-R-155-XII**	**MG-R-155-XIII**	**MG-R-155-XIV**
S	53.42	53.37	53.22	53.54	53.21	53.64	53.29	53.63	53.75	53.64	53.51	53.14	53.61	53.08
Fe	46.58	46.63	46.65	45.99	46.53	46.14	46.00	46.34	45.77	45.78	46.38	46.21	46.28	46.66
Au	0.00	0.00	0.13	0.47	0.26	0.25	0.72	0.03	0.49	0.58	0.11	0.29	0.11	0.26
Total	100.00	100.00	100.00	100.00	100.00	100.00	100.00	100.00	100.00	100.00	100.00	99.64	100.00	100.00

Observations:

Hitachi S-2400 Scanning Electron Microscope: Royal Holloway College
Operated at 20kv (accelerating voltage)
Element Lines: S; Fe and Si: K line; Au: M line
Data processed by ZAF Programme
Standard calibration: cobalt

Appendix A5.2

Electron Microscope Analyses of Native Gold

Wt% Element Concen.	MG-R-159-I	MG-R-159-II	MG-R-159-III	MG-R-159-IV	MG-R-159-V	MG-R-159-VI	MG-R-159-VII	MG-R-159-VIII	MG-R-159-IX
Au	89.44	86.68	86.49	89.69	89.69	87.89	93.63	87.61	93.78
Ag	5.41	5.07	5.07	3.88	3.88	4.62	4.85	4.62	4.45
Cu	0.00	0.19	0.19	0.00	0.00	0.00	0.00	0.00	0.00
Si	0.00	0.66	0.66	1.82	1.82	0.45	0.29	0.45	0.25
Na	0.31	0.26	0.00	0.00	0.00	0.32	0.00	0.00	0.00
O	4.14	8.28	8.17	6.00	6.00	4.53	4.49	4.41	4.42
Total	99.30	101.13	100.57	101.38	101.39	97.80	103.27	97.08	102.89

Wt % Normalized Atom.	MG-R-159-I	MG-R-159-II	MG-R-159-III	MG-R-159-IV	MG-R-159-V	MG-R-159-VI	MG-R-159-VII	MG-R-159-VIII	MG-R-159-IX
Au	3.51	1.70	1.72	2.43	2.43	3.15	3.39	3.23	3.45
Ag	0.39	0.18	0.18	0.19	0.19	0.30	0.32	0.31	0.30
Cu	0.00	0.01	0.01	0.00	0.00	0.00	0.00	0.00	0.00
Si	0.00	0.09	0.00	0.35	0.35	0.11	0.07	0.12	0.06
Na	0.11	0.04	0.00	0.00	0.00	0.10	0.00	0.00	0.00
O	2.00	2.00	2.00	2.00	2.00	2.00	2.00	2.00	2.00
Total	4.00	2.03	2.01	2.97	2.97	3.66	3.78	3.66	3.81

Wt% Normalized Elem.	MG-R-159-I	MG-R-159-II	MG-R-159-III	MG-R-159-IV	MG-R-159-V	MG-R-159-VI	MG-R-159-VII	MG-R-159-VIII	MG-R-159-IX
Au	94.30	94.28	94.28	95.86	95.85	95.00	95.08	94.99	95.48
Ag	5.70	5.52	5.52	4.14	4.15	5.00	4.92	5.01	4.53
Cu	0.00	0.20	0.20	0.00	0.00	0.00	0.00	0.00	0.00
Total	100.00	100.00	100.00	100.00	100.00	100.00	100.00	100.00	100.00

Observations:

Hitachi S-2400 Scanning Electron Microscope: Royal Holloway College
Operated at 20kv current
Element Lines: Si; Cu and O: K line; Au: M line; Ag: L line.
Data processed by ZAF Programme
Standard calibration: cobalt

Appendix A5.3

Electron Microscope Analyses of Maldonite

Wt% Element Conc.	MG-R-229I	MG-R-229-II	MG-R-229-III
Au	73.377	78.270	78.559
Ag	16.769	17.755	17.834
Bi	10.711	0.132	0.253
Total	100.857	96.157	96.646

Wt % Atom.	MG-R-229I	MG-R-229-II	MG-R-229-III
Au	64.313	70.632	70.543
Ag	26.838	29.256	29.242
Bi	8.848	0.112	0.214
Total	100.000	100.000	100.000

Observations:

Hitachi S-2400 Scanning Electron Microscope: Royal Holloway College
Operated at 20kv current
Element Lines: Au and Bi: M line; Ag: L line.
Data processed by ZAF Programme
Standard calibration: cobalt

Appendix A5.4

Microprobe Analyses of Sulphide: Pyrite

Wt% Element Concen.	MG-R-155-I	MG-R-155-II	MG-R-155-III	MG-R-155-IV	MG-R-155-V	MG-R-155-VI
S	52.63	51.66	51.66	52.48	52.10	51.79
Fe	47.74	47.56	47.56	47.65	47.19	46.81
Cu	0.04	0.05	0.05	0.02	0.04	0.09
Ag	0.04	0.00	0.00	0.00	0.04	0.07
Sn	0.04	0.02	0.02	0.00	0.00	0.01
Sb	0.00	0.02	0.02	0.00	0.00	0.00
Te	0.00	0.01	0.01	0.04	0.00	0.01
Au	0.16	0.00	0.00	0.00	0.00	0.01
Hg	0.08	0.32	0.32	0.00	0.39	0.07
Total	100.72	99.64	99.64	100.20	99.77	98.86
Wt % Normalized Atom.	**MG-R-155-I**	**MG-R-155-II**	**MG-R-155-III**	**MG-R-155-IV**	**MG-R-155-V**	**MG-R-155-VI**
S	65.69	65.35	65.35	65.72	65.71	65.76
Fe	34.21	34.54	34.54	34.26	34.17	34.13
Cu	0.03	0.03	0.03	0.01	0.03	0.06
Ag	0.01	0.00	0.00	0.00	0.02	0.03
Sn	0.01	0.01	0.01	0.00	0.00	0.00
Sb	0.00	0.01	0.01	0.00	0.00	0.00
Te	0.00	0.00	0.00	0.01	0.00	0.00
Au	0.03	0.00	0.00	0.00	0.00	0.00
Hg	0.02	0.07	0.07	0.00	0.08	0.01

Observations:
Cameca SX50 Microprobe: The Natural History Museum (British Museum); Wavelength-dispersive analysis.
Operated at 20kv and 20mA probe current
Element Lines: S; Fe and Cu: K line; As; Se; Ag; Cd; Sn; Sb; Te and Hg: L line; Au; Pb and Bi: M line
Standards: Troilite (FeS) for S and Fe; Pure Cu; Pure As; Lead selenide for Se and Pb; Pure Ag; Pure Cd; Pure Sb; Pure Te; Pure Au; Cinnabar for Hg and Pure Bi.

Appendix A5.5

Microprobe Analyses of Sulphides: Chalcopyrite

Wt% Elem. Concen.	MG-R-151AI	MG-R-151AII	MG-R-151AIII	MG-R-151AIV	MG-R-151AV	MG-R-151AVI	MG-R-151AVII	MG-R-151AVIII	MG-R-151AIX	MG-R-151AX
S	34.52	34.69	34.91	34.37	34.47	34.53	34.46	34.90	34.52	34.50
Fe	28.78	28.93	28.88	28.91	28.65	28.82	28.75	28.90	28.70	28.83
Cu	32.11	32.01	31.89	32.20	31.79	31.79	31.98	31.98	31.85	31.98
Ag	0.18	0.19	0.12	0.10	0.17	0.16	0.15	0.11	0.10	0.07
Sn	0.07	0.03	0.07	0.01	0.07	0.01	0.05	0.04	0.00	0.00
Sb	0.01	0.00	0.01	0.00	0.03	0.03	0.03	0.03	0.00	0.00
Te	0.01	0.06	0.04	0.05	0.00	0.00	0.00	0.00	0.01	0.02
Au	0.00	0.03	0.01	0.00	0.07	0.00	0.00	0.00	0.01	0.00
Hg	0.04	0.11	0.02	0.01	0.05	0.04	0.00	0.00	0.03	0.00
Total	95.72	96.05	95.95	95.64	95.30	95.38	95.42	95.95	95.23	95.40

Wt% Norm. Atom.	MG-R-151AI	MG-R-151AII	MG-R-151AIII	MG-R-151AIV	MG-R-151AV	MG-R-151AVI	MG-R-151AVII	MG-R-151AVIII	MG-R-151AIX	MG-R-151AX
S	51.37	51.45	51.71	51.19	51.51	51.50	51.41	51.67	51.55	51.43
Fe	24.45	24.49	24.41	24.58	24.43	24.53	24.48	24.42	24.45	24.53
Cu	24.06	23.90	23.77	24.16	23.91	23.86	24.02	23.83	23.94	24.00
Ag	0.08	0.09	0.06	0.04	0.08	0.07	0.07	0.05	0.05	0.03
Sn	0.03	0.01	0.03	0.00	0.03	0.01	0.02	0.02	0.00	0.00
Sb	0.00	0.00	0.00	0.00	0.01	0.01	0.01	0.01	0.00	0.00
Te	0.00	0.02	0.01	0.02	0.00	0.00	0.00	0.00	0.00	0.01
Au	0.00	0.01	0.00	0.00	0.02	0.00	0.00	0.00	0.00	0.00
Hg	0.01	0.03	0.00	0.00	0.01	0.01	0.00	0.00	0.01	0.00

Observations:

Cameca SX50 Microprobe: The Natural History Museum (British Museum); Wavelength-dispersive analysis
Operated at 20kv and 20mA probe current
Element Lines: S; Fe and Cu: K line; As; Se; Ag; Cd; Sn; Sb; Te and Hg: L line; Au; Pb and Bi: M line
Standards: Troilite (FeS) for S and Fe; Pure Cu; Pure Ag; Pure Sb; Pure Te; Pure Au; and Cinnabar for Hg

Appendix A5.6

Microprobe Analyses of Ore Minerals: Bismuth Minerals, Native Gold and Selenide/Telluride Minerals

Wt% Element	MG-R-229I	MG-R-229II	MG-R-229III	MG-R-229IV	MG-R-229V	MG-R-229VI	MG-R-229VII	MG-R-229VIII	MG-R-229IX	MG-R-229X
S	0.01	0.06	0.04	0.04	18.10	17.23	12.06	3.78	0.13	0.06
Fe	0.13	0.29	0.37	0.30	1.04	0.72	0.33	0.58	0.15	0.15
Cu	0.21	0.49	0.71	0.55	0.25	0.35	0.59	0.96	0.41	0.32
As	0.00	0.00	0.00	0.00	0.00	0.00	0.00	0.00	0.01	0.01
Se	0.02	0.00	0.01	0.00	0.07	0.05	1.62	2.38	0.04	0.05
Ag	0.03	0.09	0.04	0.03	0.00	0.05	0.32	0.10	20.15	21.15
Cd	0.16	0.02	0.12	0.06	0.13	0.01	0.00	0.16	0.21	0.27
Sn	0.01	0.05	0.05	0.02	0.00	0.05	0.04	0.09	0.00	0.02
Sb	0.01	0.09	0.06	0.02	0.01	0.03	0.03	0.19	0.03	0.02
Te	0.06	0.01	0.06	0.03	0.10	0.14	0.91	15.79	0.04	0.05
Au	0.99	0.08	0.00	0.12	0.37	0.04	0.28	0.00	79.02	78.82
Hg	0.00	0.00	0.08	0.00	0.00	0.27	0.00	0.11	0.00	0.00
Pb	0.13	0.08	0.12	0.05	0.00	0.00	79.87	10.49	0.03	0.17
Bi	98.96	99.84	97.98	99.96	82.82	82.01	5.17	64.70	0.00	0.00
Total	100.70	101.09	99.64	101.18	102.88	100.93	101.22	99.33	100.22	101.08
Wt% Norm. Atom.	**MG-R-229I**	**MG-R-229II**	**MG-R-229III**	**MG-R-229IV**	**MG-R-229V**	**MG-R-229VI**	**MG-R-229VII**	**MG-R-229VIII**	**MG-R-229IX**	**MG-R-229X**
S	0.05	0.39	0.23	0.23	57.13	56.40	45.10	17.79	0.69	0.28
Fe	0.46	1.05	1.33	1.09	1.89	1.35	0.71	1.57	0.43	0.44
Cu	0.67	1.55	2.26	1.75	0.40	0.58	1.11	2.27	1.06	0.82
As	0.00	0.00	0.00	0.00	0.00	0.00	0.00	0.00	0.03	0.03
Se	0.05	0.00	0.03	0.00	0.09	0.06	2.45	4.55	0.09	0.10
Ag	0.05	0.17	0.08	0.06	0.00	0.05	0.36	0.14	30.90	32.13
Cd	0.29	0.04	0.23	0.11	0.12	0.00	0.00	0.21	0.31	0.39
Sn	0.01	0.09	0.09	0.03	0.00	0.04	0.04	0.12	0.00	0.02
Sb	0.02	0.14	0.09	0.04	0.00	0.02	0.02	0.24	0.04	0.02
Te	0.09	0.02	0.09	0.05	0.08	0.11	0.85	18.68	0.05	0.06
Au	1.03	0.08	0.00	0.12	0.19	0.02	0.17	0.00	66.37	65.57
Hg	0.00	0.00	0.08	0.00	0.00	0.14	0.00	0.08	0.00	0.00
Pb	0.12	0.08	0.11	0.05	0.00	0.00	46.21	7.64	0.03	0.13
Bi	97.14	96.41	95.36	96.48	40.11	41.20	2.97	46.71	0.00	0.00
Classification	**Native Bismuth (A)**	**Native Bismuth**	**Native Bismuth**	**Native Bismuth (D)**	**Bismuthinite**	**Bismuthinite**	**Unc. Bi+Se+Te (B)**	**Unc.Te+Bi+S+Se (C)**	**Native Au+Ag**	**Native Au+Ag**

Observations:

Cameca SX50 Microprobe: The Natural History Museum (British Museum) operated at 20 kv and 20mA probe current; Wavelength-dispersive analysis;
Element Lines: S; Fe and Cu: K line; As; Se; Ag; Cd; Sn; Sb; Te and Hg: L line; Au; Pb and Bi: M line
Standards: Troilite (FeS) for S and Fe; Pure Cu; Pure As; Lead selenide for Se and Pb; Pure Ag; Pure Cd; Cassiterite;
Note: A, B, C and D analyses refer to the points plotted in the Figure 5.17 b

Appendix A5.7

Microprobe Analyses of Gangue Minerals: Jarosite and Tourmaline

Wt% Oxide/Sample	MG-R-151BI	MG-R-151BII	MG-R-151BIII	MG-R-151BIV	MG-R-151BV	MG-R-151BVI
SiO2	0.60	0.52	0.25	0.30	0.44	35.30
Al2O3	2.00	0.64	0.84	0.70	0.46	30.05
TiO2	1.06	1.32	1.10	0.95	-	0.59
FeO	38.00	34.85	39.32	36.10	41.42	12.21
MnO	nd	nd	nd	nd	0.03	0.03
MgO	0.10	nd	0.14	0.05	nd	4.38
CaO	0.30	0.05	0.12	0.05	0.10	0.34
K2O	6.44	5.49	5.67	4.87	4.95	0.04
Na2O	0.36	nd	54.00	0.30	-	2.27
S	17.36	18.65	19.83	19.54	10.01	-
P2O5	3.06	0.73	0.74	0.53	-	-
Cr2O3	nd	nd	0.05	nd	-	-
F	-	-	-	-	-	0.13
Total	69.28	62.70	68.60	63.39	57.41	85.30

Wt% Norm.Atom. / Sample	MG-R-151BI	MG-R-151BII	MG-R-151BIII	MG-R-151BIV	MG-R-151BV	MG-R-151BVI
Si	0.19	0.19	0.09	0.11	0.07	6.62
Al	0.76	0.28	0.34	0.30	0.08	6.64
Ti	0.26	0.37	0.28	0.26	nd	0.08
Fe	10.27	10.86	11.21	11.11	5.24	1.92
Mn	nd	nd	nd	nd	nd	nd
Mg	0.05	nd	0.07	0.03	nd	1.22
Ca	0.09	0.02	0.05	0.02	0.02	0.07
K	2.66	2.61	2.46	2.29	0.96	0.01
Na	0.22	nd	0.36	0.21	nd	0.83
S	7.02	8.69	8.46	8.99	8.84	-
P	0.84	0.23	0.21	0.16	-	-
Cr	nd	nd	0.02	nd	-	-
Ni	nd	nd	nd	nd	-	-
F	-	-	-	-	-	0.08
Total	22.36	23.25	23.55	23.48	15.21	17.47
Classification	Jarosite	Jarosite	Jarosite	Jarosite	Jarosite	Tourmaline

Observations:

Formulae calculated on the basis of : Jarosite = 06 oxygens; Tourmaline = 27 oxygens; Not detected: nd; Not analyesd: -

Appendix A5.8

Chemical Analyses of Wallrock Alteration Assemblages (X-Ray Fluorescence Data)

Sample	MG-R-163B	MG-R-163A	MG-R-163C	MG-R-163F	MG-R-163G	MG-R-225A	MG-R-225B	MG-R-225C	MG-R-226	MG-R-227	MG-R-228	MG-R-204DI	MG-R-204DII	MG-R-204F
SiO2	98.07	80.11	57.92	58.86	51.29	77.23	99.06	62.01	58.20	67.91	62.22	61.85	72.52	65.03
Al2O3	0.68	10.78	13.71	16.86	15.55	2.42	0.35	23.44	18.43	15.16	16.59	12.77	15.09	16.53
Fe2O3	0.52	1.30	11.78	9.50	12.42	18.36	0.69	5.31	8.25	6.47	8.56	13.59	2.13	7.87
MgO	0.04	0.52	4.20	3.36	5.13	0.27	0.23	0.66	3.96	3.03	3.79	0.64	0.43	2.72
CaO	0.10	0.69	5.04	3.30	9.34	0.11	0.01	0.34	2.50	1.52	1.66	0.21	0.36	0.45
Na2O	0.00	3.06	0.90	3.36	2.99	0.54	0.09	1.25	3.18	3.66	2.64	3.00	4.89	1.18
K2O	0.03	3.68	3.26	2.40	0.80	0.76	0.05	4.66	3.62	2.01	3.33	5.10	3.42	0.10
TiO2	0.04	0.11	2.01	1.37	1.87	0.19	0.02	1.11	1.10	0.88	0.94	0.28	0.28	0.48
MnO	0.04	0.02	0.25	0.14	0.20	0.01	0.01	0.08	0.12	0.10	0.22	0.03	0.02	0.03
P2O5	0.02	0.11	0.32	0.18	0.29	0.12	0.03	0.28	0.21	0.10	0.23	0.13	0.03	0.01
Total	99.54	100.38	99.39	99.33	99.88	100.01	100.54	99.14	99.57	100.84	100.18	97.60	99.17	94.40
LOI	0.30	0.47	3.14	3.20	1.31	5.11	0.74	5.94	2.39	2.80	2.14	3.65	0.75	1.75
Ni	4	5	43	41	57	5	3	7	47	57	70	17	4	15
Cr	2	3	76	97	117	29	4	137	143	151	127	7	7	24
V	9	16	237	206	303	32	3	244	179	150	181	70	35	163
Sc	0	3	26	35	42	2	0	31	26	19	24	7	7	18
Cu	5	4	78	324	166	211	15	168	140	11	14	127	8	3
Zn	8	27	214	98	101	13	4	106	129	105	172	39	27	126
Cl	80	665	3340	2045	1450	0	0	1594	0	0	21	0	0	0
Ga	2	13	29	24	19	12	0	54	28	18	21	16	17	33
Pb	0	31	12	13	6	15561	92	4441	1174	13	17	47	26	12
Sr	2	39	54	129	236	23	2	70	232	334	132	279	167	155
Rb	5	184	547	357	48	9	3	82	103	70	103	111	81	7
Ba	86	110	150	213	184	92	29	933	658	537	583	15757	1608	168
Zr	3	66	173	112	151	37	3	216	224	216	197	170	269	47
Nb	0	8	21	31	14	2	1	7	8	10	12	13	10	2
Th	0	15	7	8	3	62	17	40	14	5	7	14	22	1
Y	3	27	50	104	36	6	0	32	39	31	37	70	60	12
La	0	4	31	19	15	2	1	19	19	13	14	42	49	4
Ce	6	8	53	23	32	10	0	46	43	30	33	84	105	10
Nd	2	6	29	15	19	3	1	22	22	15	18	47	50	5

Observations:

Major elements in per cent; Trace elements in ppm

Fe2O3 = Total iron as Fe2O3; LOI = loss on ignition

Samples: MG-R-163B to MG-R-163G = Itapetim area; MR-225A to MG-R-228 = São Francisco mine; MG-R-204DI to MG-R to MG-R-204B = Canafítula 'garimpo'; MG-R-203E to MG-R-203G = Canafístula 'garimpo'

MG-R-204H	MG-R-204J	MG-R-204A	MG-R-204B	MG-R-203E	MG-R-203C	MG-R-203AI	MG-R-203AII	MG-R-203G
95.95	73.86	74.03	76.04	53.61	61.39	80.43	78.23	74.11
1.94	13.61	13.83	13.53	13.28	17.47	11.45	12.04	13.81
0.63	2.64	2.74	1.10	15.17	6.67	1.74	2.59	3.20
0.05	0.59	0.24	0.05	7.88	2.79	0.50	0.43	0.76
0.04	0.37	0.91	0.29	0.10	0.14	0.39	0.53	0.91
0.19	4.09	3.14	4.42	0.29	0.94	3.06	2.42	4.02
0.64	4.75	5.13	4.43	6.04	8.81	2.85	4.33	3.30
0.07	0.35	0.34	0.32	2.95	1.25	0.28	0.30	0.38
0.01	0.01	0.04	0.01	0.13	0.06	0.01	0.02	0.03
0.02	0.09	0.08	0.04	0.05	0.05	0.04	0.04	0.07
99.54	100.36	100.48	100.22	99.50	99.57	100.75	100.93	100.59
0.19	1.28	0.55	0.50	3.41	2.70	1.53	1.47	1.36
4	6	6	4	210	57	7	7	6
6	7	6	8	261	80	6	7	9
10	27	21	15	193	110	28	22	25
1	7	8	6	21	15	6	5	8
0	10	12	8	22	8	5	13	11
9	27	49	10	275	118	23	29	48
0	0	0	0	455	0	9	0	35
2	16	19	13	29	22	17	16	18
5	51	29	31	19	55	24	28	27
15	228	200	206	43	191	95	140	269
16	155	201	116	618	328	114	142	126
228	2383	2050	823	606	2117	527	736	745
9	260	256	240	227	335	212	220	286
2	17	18	13	58	25	14	15	18
10	31	23	23	5	20	17	18	26
9	81	62	47	111	68	78	60	70
7	75	56	45	50	48	50	48	53
11	146	105	95	106	104	95	96	110
7	70	46	43	70	61	48	51	52

APPENDIX A6.1: LEAD ISOTOPIC EXTRACTION

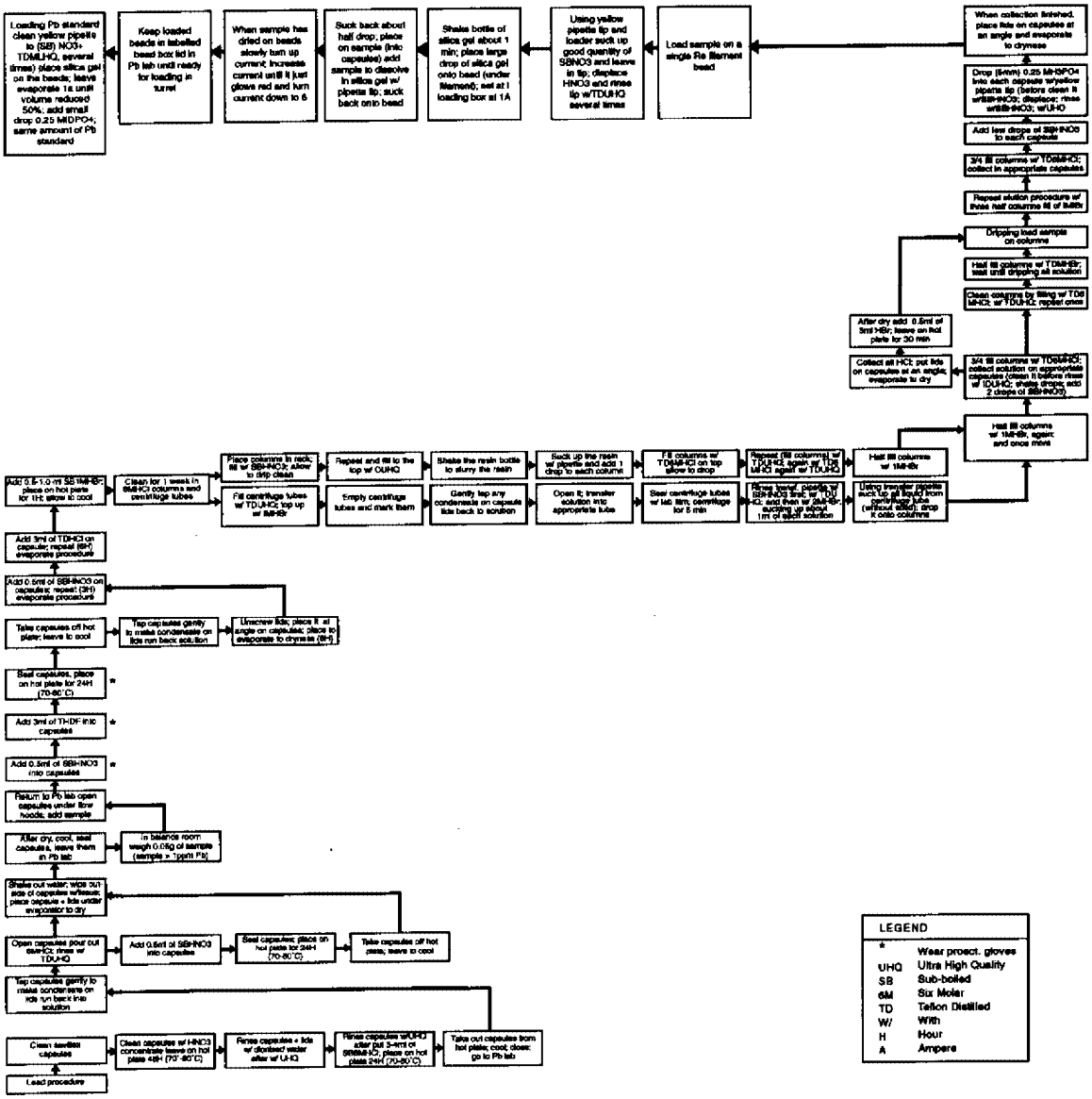

Appendix A7.1
Microthermometric Standards

Critical Temperature of Homogenization of pure H_2O (°C)	Melting of CO_2 (°C)	Melting of Ice (°C)	Date of Measurement
395	-56.9	3.3	16.07.93
393	-57.7	4.2	23.07.93
394	-56.8	4.1	30.07.93
398	-57.9	4.2	06.07.93
398	-57.9	3.9	07.08.93
398	-57.5	3.8	14.08.93
400	-57.8	3.9	21.08.93
400	-57.6	3.9	28.08.93
400	-57.1	3.9	03.09.93
400	-57.0	4.0	10.09.93
400	-57.1	3.9	17.09.93
399	-56.6	4.5	24.09.93
399	-56.6	4.5	04.10.93
400	-56.6	4.3	11.10.93

Observation:
Type of Standards: Synthetic
Period of time of measurements: July to October/ 1993

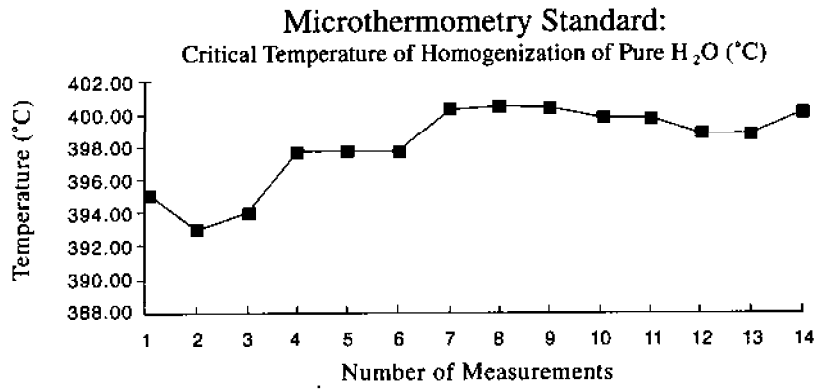

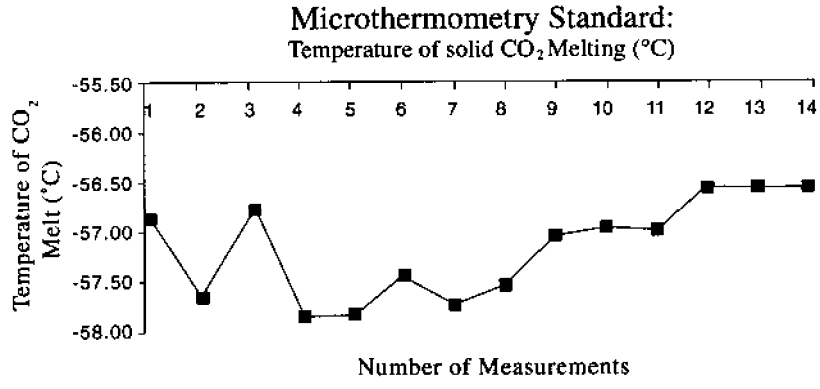

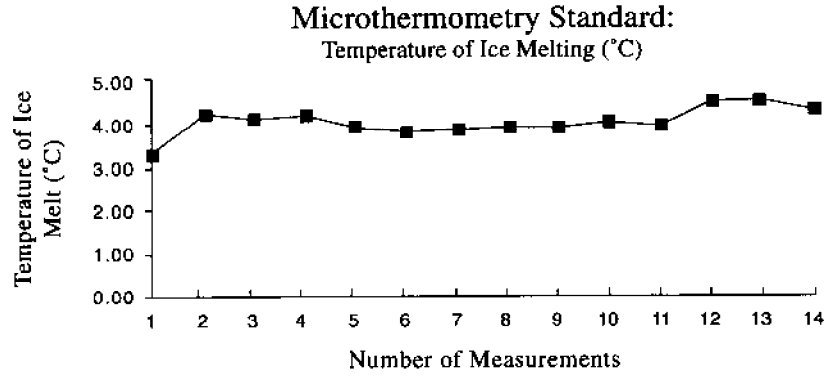

Appendix A7.1 Curves used to make corretion in the microthermometric measuremnets

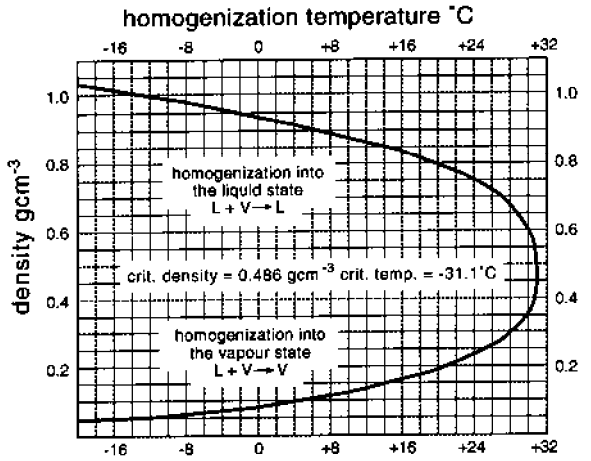

Appendix 7. 2a Graph showing the relationship between temperature of homogenization of liquid and vapour CO_2 (Th CO_2) and density of CO_2 . This diagram is used for calculating the density of CO_2 for both states whether CO_2 homogenizes into the liquid or vapour states. (After Shepherd et al., 1985).

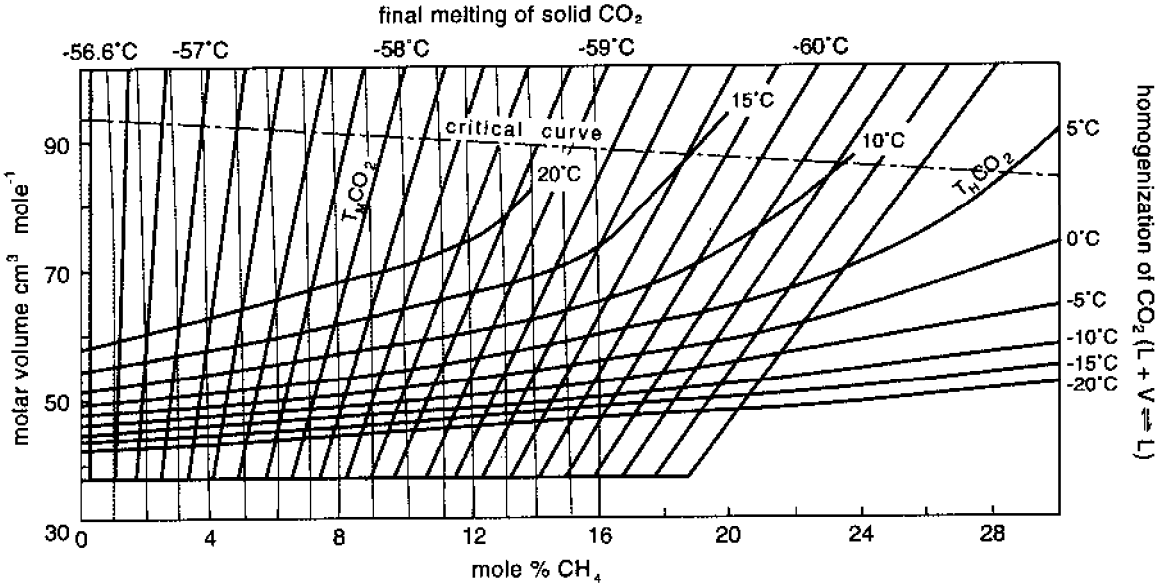

Appendix A7. 2b Graph for calculating the mole composition of CO_2 - CH_4 mixtures using the final melting temperature of solid CO_2 (Tm CO_2) and the temperature of liquid-vapour homogenization (Th CO_2). The mole % CH_4 is given by the intersection of the appropriate Th CO_2 and Tm CO_2. This graph refers to inclusions which homogenize into the liquid state. (as above).

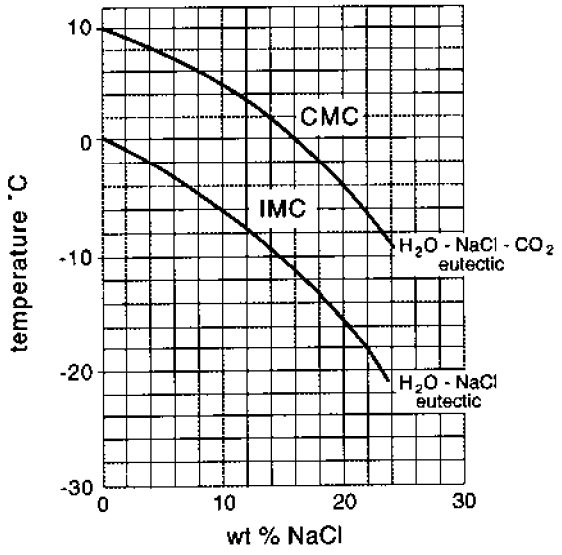

Appendix A7. 2c Graph for calculating the salinity of the aqueous phase using the clathrate melting curve (CMC) or the ice melting curve (IMC). (as above)

Appendix A7.2 Graphs used to calculate (**a**) density; (**b**) the amount of CH_4 and (**c**) the salinity according to Shepherd et al., (1985).

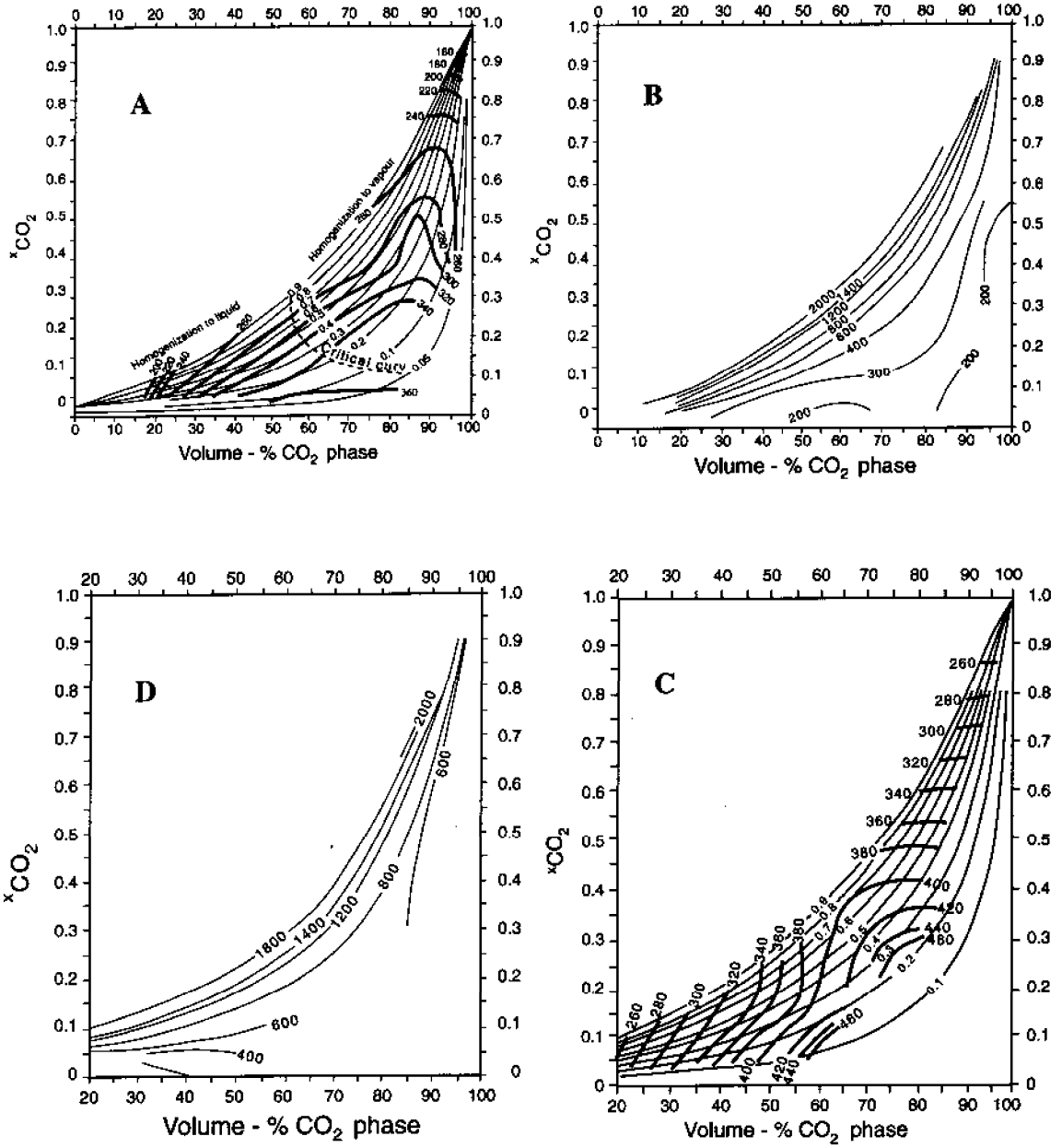

Appendix A7.3 Diagrams from Schwartz (1989) showing the relationships between: (**A**) mole % CO2, the vol. % CO2, the density of the CO2, and the isotherms T-Th of the CO2-H2O miscibility gap (160°-360°C) in mixed CO2-H2O inclusions; In (**B**) the mole % CO2, the vol. % CO2 phase at 40°C, and pressure of 200-2000 bars at total homogenization in mixed CO2-H2O inclusions; In (**C**) mole % CO2, the vol % CO2 phase at 40 °C, and the isotherms T-Th of the miscibility gap (260-460°C) in CO2-H2O-NaCl inclusions with 6 wt % NaCl relative to H2O + NaCl; In (**D**) the mole % CO2, the vol. % CO2 phase at 40°C, and the pressure of 400-20000 bars at total homogenization in mixed CO2-H2O-NaCl inclusions with 6 wt % NaCl relative to H2O + NaCl. Diagram (**A**) was used for predicted the T-Th and the vol. wt % of the CO2; and (**B**) the pressure for the CO2 monophase inclusions, knowing the density and the mole % of CO2.
Digram (**C**) was used to calculated the vol. % of the CO2 for the H2O-CO2 inclusions knowing the T-Th, the density and the mole wt % of CO2; (**D**) permited calculated the pressure for this type of inclusions knowing the mole % CO2 and th vol. % CO2.

Appendix A7.4

Microthermometric Data for H2O-CO2 Fluid Inclusions in Quartz Vein Hosted by Syn- and Late Tectonic Granite

Sample	Size (μm)	DF	Tm CO2 (°C)	Tm Cl (°C)	Th CO2 (°C)	T-Th (°C)	D (*) (g cm-3)	CH4 (*) (mole % CO2)	S (NaCl eq. *) (wt %)	CO2 (*) (wt % of total fluid)
MG-R-197B	25	0.90	-58.6	5.8	22.0	322	0.78	10.5	8.0	8.0
MG-R-197B	15	0.95	-58.8	5.6	16.7	331	0.81	11.5	8.0	4.1
MG-R-197B	15	0.95	-57.3	6.3	20.3	267	0.78	3.5	8.0	3.9
MG-R-197B	20	0.70	-56.8	5.8	18.7	273	0.83	1.0	8.0	26.2
MG-R-197B	10	0.70	-56.7	6.2	18.9	267	0.81	0.5	8.0	25.8
MG-R-197B	25	0.50	-58.0	6.5	23.0	316	0.76	7.5	6.8	41.9
MG-R-197B	15	0.90	-56.6	6.7	16.0	292	0.84	0.2	6.0	8.5
MG-R-197B	45	0.90	-58.5	6.6	23.2	263 *	0.76	9.0	6.0	7.8
MG-R-197B	50	0.95	-58.2	7.1	21.5	264	0.79	8.5	6.0	4.0
MG-R-197B	25	0.70	-57.8	6.3	14.0	255	0.85	5.5	8.0	26.7
MG-R-197B	20	0.70	-58.0	6.0	17.0	260	0.83	7.0	8.0	26.3
MG-R-197B	25	0.70	-58.0	6.3	18.2	248	0.81	7.0	8.0	25.8
MG-R-197B	25	0.90	-57.8	6.3	14.0	220	0.85	6.0	8.0	8.2
MG-R-197B	25	0.90	-58.0	7.0	15.3	299	0.85	6.5	6.0	8.6
MG-R-197B	25	0.90	-58.0	7.0	15.3	279	0.84	7.0	6.0	8.5
MG-R-197B	25	0.50	-58.6	8.5	26.1	415	0.72	7.5	4.5	41.9
MG-R-197B	40	0.50	-59.2	8.0	14.6	314	0.84	13.0	4.0	45.7
MG-R-197B	40	0.50	-59.0	8.0	14.6	352	0.84	12.0	4.0	45.7
MG-R-197B	25	0.90	-58.2	4.4	14.8	316	0.85	8.0	10.0	8.6
MG-R-197B	45	0.90	-58.2	6.3	22.6	316	0.76	8.5	8.0	7.8
MG-R-197B	25	0.90	-58.0	5.8	18.2	349	0.81	7.5	7.8	8.3
MG-R-197B	25	0.70	-58.2	9.1	22.3	207	0.74	8.5	2.0	24.1
MG-R-197B	25	0.70	-58.1	9.4	22.8	207	0.77	7.5	1.5	24.8
MR-R-197B	25	0.70	-58.2	9.6	22.9	214	0.76	8.5	0.8	24.5
MG-R-197B	40	0.70	-58.2	6.1	23.0	352	0.76	8.5	8.0	24.5
MG-R-197B	15	0.70	-56.8	6.1	23.0	353	0.76	1.5	8.0	24.5
MG-R-197B	15	0.90	-57.0	7.2	23.0	354	0.76	2.5	6.0	7.8
MG-R-197B	15	0.90	-57.5	7.2	23.0	354	0.76	3.5	6.0	7.8
MG-R-197B	40	0.90	-58.5	9.4	16.7	216	0.81	9.5	2.0	8.3
MG-R-197B	25	0.90	-58.0	6.0	17.0	232	0.83	7.5	8.0	8.4
MG-R-197B	25	0.90	-58.4	6.3	13.0	374	0.87	9.0	8.0	8.8
MG-R-197B	25	0.90	-58.2	6.2	10.1	242	0.88	8.0	8.0	8.8
MG-R-197B	25	0.90	-57.4	9.0	10.1	194	0.88	4.0	2.0	8.8

* Decrepitation temperature; NFI = 33 (Number of fluid inclusion measurements)

Abbreviations:

DF = degree of fill; Tm CO2 = temperature of CO2 melting; Tm Cl = temperature of clathrate melting; Th CO2 = temperature of homogenization of CO2; T-Th = tempera of the fluid inclusion; D = density; CH4 = methane; S (NaCl equiv.) = salinity (halite equivalent); CO2 = carbon dioxide.

(*) Data calculated using the microthermometric measurements and fit it in the plot (Shepherd, et el.,1985)

Appendix A7.5

Microthermometric Data for H2O-CO2 Fluid Inclusions in Quartz Vein Hosted by Syn- and Late Tectonic Granite

Sample	Size (μm)	DF	Tm CO2 (°C)	Tm Cl (°C)	Th CO2 (°C)	T-Th (°C)	D (*) (g cm-3)	CH4 (*) (mole % CO2)	S (NaCl eq.*) (wt %)	CO2 (*) (wt % of total fluid)
MG-R-147B	25	0.90	-58.2	7.1	23.0	220 *	0.77	8.5	6.0	7.9
MG-R-147B	25	0.90	-58.2	7.1	23.5	220 *	0.76	8.5	6.0	7.8
MG-R-147B	45	0.70	-58.1	5.6	23.8	225	0.75	8.0	8.5	24.3
MG-R-147B	45	0.70	-58.1	5.6	23.0	225	0.77	8.0	8.5	24.8
MG-R-147B	45	0.70	-58.1	5.6	13.0	223	0.87	7.5	8.5	27.2
MG-R-147B	45	0.70	-58.1	5.5	23.0	295	0.77	8.0	8.6	24.8
MG-R-147B	45	0.70	-57.9	5.3	24.0	295	0.75	6.5	9.0	24.3
MG-R-147B	45	0.70	-58.8	8.4	18.7	244	0.82	11.5	4.0	26.0
MG-R-147B	25	0.90	-58.0	5.0	10.0	232	0.88	6.5	9.0	8.9
MG-R-147B	25	0.90	-57.8	6.6	10.0	308	0.88	5.5	6.5	8.9
MG-R-147B	25	0.90	-57.5	5.3	10.0	282	0.88	4.5	8.5	8.9
MG-R-147B	25	0.90	-56.8	6.2	13.0	226	0.87	1.0	8.0	8.8
MG-R-147B	25	0.90	-56.6	6.2	12.5	223	0.84	0.2	8.0	8.5
MG-R-147B	25	0.90	-56.6	6.2	11.7	226	0.86	0.2	8.0	8.7
MG-R-147B	45	0.90	-57.5	5.3	13.9	255	0.85	4.5	8.5	8.6
MG-R-147B	45	0.90	-57.5	5.3	10.3	220	0.88	4.5	8.5	8.9
MG-R-147B	45	0.90	-57.0	7.0	9.8	233	0.89	1.0	6.0	9.0
MG-R-147B	50	0.70	-57.2	5.0	9.8	220	0.89	1.0	9.0	27.6
MG-R-147B	20	0.90	-57.3	5.3	10.0	380	0.88	3.0	8.5	8.9
MG-R-147B	45	0.90	-57.5	9.5	8.9	385	0.89	3.5	2.0	9.0
MG-R-147B	20	0.95	-58.0	5.0	10.0	232	0.88	6.5	8.0	4.4
MG-R-147B	25	0.95	-57.3	7.5	9.0	232	0.89	3.5	4.5	4.5
MG-R-147B	20	0.95	-58.9	8.4	10.0	232	0.88	11.0	4.0	4.4
MG-R-147B	20	0.95	-57.8	6.5	10.0	232	0.88	5.5	7.0	4.4
MG-R-147B	25	0.90	-56.6	5.0	13.5	274	0.84	0.2	8.5	8.5
MG-R-147B	45	0.90	-56.8	5.8	13.0	287	0.87	0.2	8.0	8.8

* Decrepitation temperature; NFI = 26 (Number of fluid inclusion measurements)

Abbreviations:

DF = degree of fill; Tm CO2 = temperature of CO2 melting; Tm Cl = temperature of clathrate melting; Th CO2 = temperature of homogenization of CO2; T-Th = temperature of total homogenization of fluid inclusion; D = density; CH4 = methane; S (NaCl equiv.) = salinity (halite equivalent); CO2 = carbon dioxide.

(*) Data calculated using the microthermometric measurements and fit it in the plot (Shepherd, et el.,1985)

Appendix A7.6

Microthermometric Data for H2O-CO2 Fluid Inclusions in Quartz Vein Hosted by Early-Syn- Tectonic Granite

Sample	Size (μm)	DF	Tm CO2 (°C)	Tm Cl (°C)	Th CO2 (°C)	T-Th (°C)	D (*) (g cm-3)	CH4 (*) (mole % CO2)	S (NaCl eq. *) (wt %)	CO2 (*) (wt % of total fluid)
MG-R-174B	35	0.70	-57.5	4.9	22.0	354	0.76	3.5	10.0	24.6
MG-R-174B	25	0.70	-57.2	5.0	19.4	248	0.81	3.0	8.5	25.8
MG-R-174B	25	0.70	-57.2	4.9	25.0	326	0.73	3.5	8.5	23.8
MG-R-174B	25	0.70	-59.2	8.1	20.0	210	0.73	15.0	4.0	23.8
MG-R-174B	15	0.90	-57.5	5.3	19.4	212	0.81	4.5	8.5	8.3
MG-R-174B	25	0.70	-57.5	5.3	21.0	248	0.77	4.5	8.5	24.8
MG-R-174B	25	0.70	-57.3	5.3	21.5	268	0.77	3.5	8.5	24.8
MG-R-174B	25	0.70	-57.9	5.4	25.0	234	0.73	7.0	8.5	23.8
MG-R-174B	15	0.70	-57.9	5.4	23.5	317	0.76	6.5	8.5	24.7
MG-R-174B	25	0.70	-57.8	6.7	22.0	228	0.78	12.0	6.0	25.0
MG-R-174B	25	0.70	-57.9	6.7	22.0	228	0.78	7.0	6.0	25.0
MG-R-174B	25	0.70	-57.2	4.8	22.2	304	0.78	3.5	10.0	25.0
MG-R-174B	25	0.70	-57.2	4.1	22.2	253	0.78	3.5	11.0	25.0
MG-R-174B	40	0.70	-56.9	6.0	16.5	279	0.81	1.5	8.0	25.8
MG-R-174B	40	0.70	-57.8	6.6	19.5	279	0.80	6.0	8.0	25.5
MG-R-174B	25	0.70	-57.8	6.6	16.5	200	0.83	6.0	8.0	26.2
MG-R-174B	25	0.70	-56.7	5.8	16.5	200	0.83	0.5	8.0	26.2
MG-R-174B	25	0.70	-56.8	5.8	16.5	279	0.83	1.0	8.0	26.2
MG-R-174B	40	0.70	-57.0	7.4	16.0	298	0.84	2.0	6.0	26.5
MG-R-174B	40	0.70	-56.6	7.6	16.0	258	0.84	0.5	6.5	26.5
MG-R-174B	40	0.70	-56.6	7.6	16.0	258	0.84	0.5	6.5	26.5
MG-R-174B	45	0.70	-57.3	5.3	15.0	200	0.79	3.5	8.5	25.3
MG-R-174B	40	0.70	-57.3	6.7	17.5	200	0.82	3.5	6.0	26.0
MG-R-174B	45	0.70	-56.6	5.3	16.5	200	0.83	0.2	8.5	26.2
MG-R-174B	45	0.90	-56.6	7.2	16.2	200	0.83	0.5	6.0	8.4
MG-R-174B	25	0.70	-57.1	7.7	15.8	354	0.84	2.5	4.0	26.5
MG-R-174B	25	0.70	-57.1	7.7	17.5	354	0.82	2.5	4.0	26.0
MG-R-174B	25	0.70	-56.9	7.7	17.0	376	0.83	1.5	4.0	26.2
MG-R-174B	25	0.70	-56.9	7.7	15.8	376	0.84	1.5	4.0	26.5
MG-R-174B	25	0.70	-57.2	7.0	16.5	372	0.81	3.0	6.0	25.8
MG-R-222C	45	0.70	-56.7	7.1	15.0	313	0.85	0.5	6.0	26.7
MG-R-222C	45	0.70	-57.4	7.3	16.2	224	0.83	4.0	5.8	26.2
MG-R-222C	45	0.70	-58.8	6.8	18.2	212	0.81	11.0	6.0	25.8
MG-R-222C	25	0.90	-59.1	8.0	13.1	287	0.87	13.0	4.0	8.8
MG-R-222C	25	0.90	-58.6	9.4	13.1	298	0.87	11.0	2.0	8.8
MG-R-222C	25	0.90	-58.6	9.2	13.1	350	0.87	10.0	2.0	8.8
MG-R-222C	25	0.90	-58.6	6.3	13.2	298	0.87	10.0	8.0	8.8
MG-R-222C	25	0.90	-59.1	8.0	13.2	374	0.87	12.0	4.0	8.8
MG-R-222C	40	0.90	-57.2	7.0	13.8	365	0.85	3.0	6.0	8.6
MG-R-222C	50	0.70	-57.2	8.0	15.2	275	0.84	3.0	4.0	26.5
MG-R-222C	50	0.90	-57.2	7.0	12.1	365	0.86	3.0	8.0	8.7
MG-R-222C	45	0.90	-57.8	6.6	11.3	393	0.87	10.5	8.0	8.8
MG-R-222C	25	0.90	-56.9	7.0	11.3	395	0.87	1.5	6.0	8.8
MG-R-222C	25	0.90	-57.2	7.0	11.3	353	0.87	3.0	8.0	8.8

NFI = 44 (Number of fluid inclusion measurements)

Abbreviations:

DF = degree of fill; Tm CO2 = temperature of CO2 melting; Tm Cl = temperature of clathrate melting; Th CO2 = temperature of homogenization of CO2; T-Th = temperature of total homogenization of fluid inclusion; D = density; CH4 = methane; S (NaCl equiv.) = salinity (halite equivalent); CO2 = carbon dioxide.

(*) Data calculated using the microthermometric measurements and fit it in the plot (Shepherd, et el.,1985)

Appendix A7.7
Microthermometric Data for H2O-CO2 Fluid Inclusions in Quartz Vein Hosted by Early Tectonic Granite

Sample	Size (μm)	DF	Tm CO2 (°C)	Tm Cl (°C)	Th CO2 (°C)	T-Th (°C)	D (*) (g cm-3)	CH4 (*) (mole % CO2)	S (NaCl eq.*) (wt %)	CO2 (*) (wt % of total fluid)
MG-R-203D	25	0.70	-57.5	6.0	20.5	324	0.78	4.5	8.0	25.1
MG-R-203D	25	0.70	-57.9	5.3	22.4	356	0.76	6.5	8.5	24.6
MG-R-203D	25	0.70	-57.9	5.3	22.4	332	0.76	6.5	8.5	24.6
MG-R-203D	15	0.70	-58.3	6.8	16.9	290	0.81	8.5	6.0	25.8
MG-R-203D	15	0.70	-58.3	6.8	16.8	221	0.81	8.5	6.0	25.8
MG-R-203D	25	0.70	-57.1	8.0	13.7	376	0.85	2.5	4.0	26.7
MG-R-203D	25	0.70	-58.0	8.2	12.3	326	0.84	6.5	3.5	26.5
MG-R-203D	25	0.70	-57.1	7.0	26.6	201	0.72	2.5	5.0	23.6
MG-R-203D	15	0.70	-57.1	9.0	17.5	201	0.83	2.5	2.0	26.2
MG-R-203D	25	0.70	-59.3	8.0	18.5	373	0.81	14.5	4.0	25.8
MG-R-203D	25	0.70	-57.9	5.3	18.5	371	0.81	7.0	8.5	25.8
MG-R-203D	25	0.70	-58.5	6.9	20.1	324	0.78	8.5	6.0	25.1
MG-R-203D	25	0.70	-58.5	6.9	20.2	356	0.78	8.5	6.0	25.1
MG-R-203D	25	0.70	-57.6	7.9	20.7	324	0.77	5.0	4.0	24.8
MG-R-203D	25	0.70	-57.6	7.8	20.8	326	0.77	5.0	4.0	24.8
MG-R-203D	50	0.70	-57.4	7.2	22.2	331	0.76	4.5	6.0	24.6
MG-R-203D	15	0.70	-57.0	5.2	20.0	366	0.78	2.0	9.0	25.1
MG-R-203D	15	0.70	-57.4	7.7	23.1	341	0.76	4.5	4.0	24.6
MG-R-203D	15	0.70	-58.0	8.0	18.6	338	0.81	7.0	4.0	25.8
MG-R-203D	15	0.70	-56.7	5.3	17.3	317	0.83	0.5	9.0	26.2
MG-R-203D	15	0.70	-56.7	5.3	17.3	273	0.83	0.5	9.0	26.2
MG-R-203D	15	0.70	-56.7	5.3	17.3	287	0.83	0.5	9.0	26.2
MG-R-203D	15	0.70	-56.7	5.3	17.3	287	0.83	0.5	9.0	26.2
MG-R-203D	35	0.70	-57.0	4.5	18.7	370	0.81	3.0	8.0	25.8
MG-R-203D	35	0.70	-56.6	7.8	20.8	370	0.78	0.2	6.0	25.1

NFI = 25 (Number of fluid inclusion measurements).

Abbreviations:

DF = degree of fill; Tm CO2 = temperature of CO2 melting; Tm Cl = temperature of clathrate melting; Th CO2 = temperature of homogenization of CO2; T-Th = temperature of total homogenization of fluid inclusion; D = density; CH4 = methane; S (NaCl equiv.) = salinity (halite equivalent); CO2 = carbon dioxide.

(*) Data calculated using the microthermometric measurements and fit it in the plot (Shepherd, et el.,1985)

Appendix A7.8

Microthermometric Data for H2O-CO2 Fluid Inclusions in Quartz Vein Hosted by Supracrustal Rock (Cachoeira de Minas Mine)

Sample	Size (μm)	DF	Tm CO2 (°C)	Tm Cl (°C)	Th CO2 (°C)	T-Th (°C)	D (*) (g cm-3)	CH4 (*) (mole % CO2)	S (NaCl eq.*) (wt %)	CO2 (*) (wt % of total fluid)
MG-R-224C	25	0.70	-57.1	9.0	26.0	320	0.72	2.5	0.5	23.6
MG-R-224C	20	0.90	-57.0	9.0	23.5	260	0.76	2.5	0.5	7.8
MG-R-224C	20	0.90	-57.0	9.0	23.5	260	0.76	2.5	0.5	7.8
MG-R-224C	20	0.70	-57.0	5.0	15.5	312	0.85	2.0	9.0	26.7
MG-R-224C	15	0.90	-57.0	5.2	15.5	287	0.85	2.0	8.9	8.6
MG-R-224C	20	0.90	-56.9	5.7	25.5	258	0.73	1.5	8.0	7.5
MG-R-224C	20	0.90	-56.9	5.7	21.0	260	0.79	1.5	8.0	8.1
MG-R-224C	20	0.90	-57.4	4.6	17.5	317	0.83	4.0	9.0	8.4
MG-R-224C	20	0.90	-59.6	8.0	22.0	226	0.78	17.0	4.0	4.0
MG-R-224C	20	0.90	-56.8	5.3	22.1	226	0.78	1.5	9.0	9.0
MG-R-224C	20	0.90	-58.6	6.8	26.0	258	0.68	11.5	6.0	7.0
MG-R-224C	20	0.90	-58.0	6.9	23.0	320	0.76	7.5	6.1	7.8
MG-R-224C	20	0.90	-57.9	7.3	21.8	294	0.78	6.5	6.2	8.0
MG-R-224C	15	0.90	-56.9	7.2	21.8	301	0.78	1.5	6.0	8.0
MG-R-224C	15	0.90	-57.0	7.1	26.0	240	0.60	2.5	6.0	6.3
MG-R-224C	15	0.90	-57.5	7.2	25.2	230	0.73	4.5	6.0	7.5
MG-R-224C	20	0.90	-57.5	6.3	25.2	238	0.73	5.0	8.0	7.5
MG-R-224C	25	0.90	-58.5	5.8	22.5	260	0.76	10.5	8.0	7.8

NFI =18 (Fluid inclusion number of measurements).

Abbreviations:

DF = degree of fill; Tm CO2 = temperature of CO2 melting; Tm Cl = temperature of clathrate melting; Th CO2 = temperature of homogenization of CO2; T-Th = temperature of total homogenization of fluid inclusion; D = density; CH4 = methane; S (NaCl equiv.) = salinity (halite equivalent); CO2 = carbon dioxide.

(*) Data calculated using the microthermometric measurements and fit it in the plot (Shepherd, et el.,1985)

Appendix A7.9

Microthermometric Data for H2O-CO2 Fluid Inclusions in Quartz Vein Hosted by Supracrustal Rock (São Francisco Mine)

Sample	Size (μm)	DF	Tm CO2 (°C)	Tm Cl (°C)	Th CO2 (°C)	T-Th (°C)	D (*) (g cm-3)	CH4 (*) (mole % CO2)	S (NaCl eq.*) (wt %)	CO2 (*) (wt % of total fluid)
MG-R-229C	25	0.95	-57.0	7.6	23.5	326	0.76	2.5	5.5	4.1
MG-R-229C	25	0.70	-57.3	7.0	26.0	276	0.72	3.0	6.0	23.6
MG-R-229C	25	0.70	-57.3	9.3	22.5	281	0.76	4.0	2.5	24.6
MG-R-229C	50	0.70	-57.6	9.9	23.0	296	0.76	5.5	1.0	24.6
MG-R-229C	25	0.70	-57.2	7.1	25.0	288	0.73	3.5	6.4	23.8
MG-R-229C	25	0.70	-57.4	9.1	25.4	279 *	0.73	4.5	2.0	23.8
MG-R-229C	15	0.70	-57.4	9.1	23.3	278 *	0.76	4.5	2.0	24.6
MG-R-229C	20	0.90	-57.5	9.2	23.5	279	0.76	4.5	2.0	7.8
MG-R-229C	20	0.70	-57.4	7.1	25.8	310	0.72	4.5	6.0	23.6
MG-R-229C	20	0.70	-57.4	7.1	26.0	293	0.72	4.5	6.0	23.6
MG-R-230	20	0.70	-57.3	7.1	25.8	313	0.76	3.5	6.0	24.6
MG-R-230	20	0.70	-57.3	7.1	26.0	293	0.72	4.0	6.0	23.6
MG-R-230	20	0.70	-57.4	7.1	26.0	294	0.72	4.5	6.0	23.6
MG-R-230	25	0.70	-57.4	7.1	26.0	296	0.72	4.5	6.0	23.6
MG-R-230	25	0.70	-57.4	7.1	26.0	278	0.72	4.5	6.0	23.6
MG-R-230	15	0.70	-57.9	7.1	25.8	260	0.72	7.0	6.0	23.6
MG-R-230	15	0.90	-57.9	6.7	22.5	249	0.76	7.0	6.0	7.8
MG-R-230	15	0.70	-57.9	9.3	22.5	239	0.76	7.0	2.5	24.6
MG-R-230	45	0.70	-57.9	9.3	21.4	200	0.77	7.0	2.5	24.8
MG-R-230	45	0.70	-58.6	9.3	22.3	227	0.78	10.5	2.5	25.0
MG-R-230	45	0.70	-57.8	9.3	22.0	250	0.78	6.5	2.5	25.0
MG-R-230	25	0.50	-58.6	6.0	21.4	203	0.77	10.5	7.0	43.5
MG-R-230	25	0.50	-58.6	6.8	21.4	203	0.77	10.5	7.0	43.5
MG-R-230	25	0.70	-58.3	9.0	26.7	311	0.66	9.0	2.0	22.1
MG-R-230	25	0.70	-58.3	7.7	26.7	311	0.66	9.0	4.0	22.1

* Decrepitation temperature; NFI = 25 (Number of fluid Inclusion measurements)

Abbreviations:

DF = degree of fill; Tm CO2 = temperature of CO2 melting; Tm Cl = temperature of clathrate melting; Th CO2 = temperature of homogenization of CO2; T-Th = temperature of total homogenization of fluid inclusion; D = density; CH4 = methane; S (NaCl equiv.) = salinity (halite equivalent); CO2 = carbon dioxide.

(*) Data calculated using the microthermometric measurements and fit it in the plot (Shepherd, et el.,1985)

Appendix A7.10

Microthermometric Data for H2O-CO2 Fluid Inclusions in Quartz Vein Hosted by Supracrustal Rock (Itapetim)

Sample	Size (μm)	DF	Tm CO2 (°C)	Tm Cl (°C)	Th CO2 (°C)	T-Th (°C)	D (*) (g cm-3)	CH4 (*) (mole % CO2)	S (NaCl eq.*) (wt %)	CO2 (*) (wt % of total fluid)
MG-R-159	15	0.90	-56.7	5.0	16.0	246	0.81	1.0	9.0	8.3
MG-R-159	15	0.70	-56.7	5.0	15.0	381	0.85	1.0	9.0	26.7
MG-R-159	15	0.70	-56.7	7.2	17.0	408	0.83	1.0	6.0	26.2
MG-R-159	15	0.70	-56.7	7.0	17.0	402	0.83	1.0	6.0	26.2
MG-R-159	25	0.70	-57.0	7.2	16.0	380	0.81	2.0	6.0	26.3
MG-R-159	25	0.70	-57.0	7.0	13.6	322	0.85	2.0	6.0	26.7
MG-R-159	25	0.70	-57.0	7.0	13.6	346	0.85	2.0	6.0	26.7
MG-R-159	25	0.70	-57.0	8.0	13.7	322	0.85	2.0	9.0	26.7
MG-R-159	25	0.70	-56.7	8.0	13.7	322	0.85	0.5	9.0	26.7
MG-R-166A	20	0.70	-56.6	8.3	18.0	375	0.82	0.5	4.0	26.0
MG-R-166A	20	0.70	-56.9	6.0	21.0	375	0.79	1.5	8.0	25.3
MG-R-166A	20	0.70	-56.9	6.0	21.0	375	0.79	1.5	8.0	25.3
MG-R-166A	20	0.70	-56.9	6.0	21.0	375	0.79	1.5	8.0	25.3
MG-R-166A	20	0.70	-56.9	7.0	21.0	375	0.79	1.5	8.0	25.3
MG-R-166A	20	0.70	-56.9	6.0	19.0	341	0.81	0.5	8.0	26.3
MG-R-166A	20	0.70	-57.1	6.5	19.0	361	0.81	2.5	7.5	26.3
MG-R-166A	20	0.70	-57.1	6.5	19.0	303	0.81	2.5	7.5	26.3
MG-R-166A	20	0.70	-57.0	7.5	19.0	233	0.81	3.0	5.5	26.3
MG-R-166A	20	0.70	-57.0	7.9	25.0	233	0.73	2.5	4.0	23.8
MG-R-166A	20	0.70	-56.8	6.0	23.0	365	0.76	1.5	8.0	24.6
MG-R-166A	20	0.70	-56.7	7.6	21.0	283	0.79	0.5	5.5	25.3
MG-R-166A	20	0.70	-57.0	6.6	21.1	275	0.79	2.0	6.0	25.3

NFI = 22 (Number of fluid inclusion measurements).

Abbreviations:

DF = degree of fill; Tm CO2 = temperature of CO2 melting; Tm Cl = temperature of clathrate melting; Th CO2 = temperature of homogenization of CO2; T-Th = temperature of total homogenization of fluid inclusion; D = density; CH4 = methane; S (NaCl equiv.) = salinity (halite equivalent); CO2 = carbon dioxide.

(*) Data calculated using the microthermometric measurements and fit it in the plot (Shepherd, et el.,1985)

Appendix A7.11

Microthermometric Data for H2O-CO2 Fluid Inclusions in Quartz Vein Hosted by Amphibolite (Boqueirão dos Cochos)

Sample	Size (μm)	DF	Tm CO2 (°C)	Tm Cl (°C)	Th CO2 (°C)	T-Th (°C)	D (*) (g cm-3)	CH4 (*) (mole % CO2)	S (NaCl eq.*) (wt %)	CO2 (*) (wt % of total fluid)
MG-R-208B	25	0.7	-57.5	8.1	22.0	394	0.80	4.5	4.0	25.5
MG-R-208B	25	0.7	-57.5	6.0	22.0	404	0.80	4.5	8.0	25.5
MG-R-208B	25	0.7	-56.8	7.0	19.4	393	0.82	1.0	6.0	26.0
MG-R-208B	25	0.7	-56.8	7.0	19.4	370	0.82	1.0	6.0	26.0
MG-R-208B	25	0.9	-56.8	6.0	22.0	370	0.80	1.5	8.0	8.2
MG-R-208B	20	0.9	-56.8	9.5	22.0	390	0.80	1.5	1.5	8.2

NFI = 6 (Fluid inclusion number of measurements); Fluid inclusions very rare

Abbreviations

DF = degree of fill; Tm CO2 = temperature of CO2 melting; Tm Cl = temperature of clathrate melting; Th CO2 = temperature of homogenization of CO2; T-Th = temperature of total homogenization of fluid inclusion; D = density; CH4 = methane; S (NaCl equiv.) = salinity (halite equivalent); CO2 = carbon dioxide.

(*) Data calculated using the microthermometric measurements and fit it in the plot (Shepherd, et el.,1985)

Appendix 7.12

Microthermometric Data for CO2 Monophase Fluid Inclusions in Quartz Veins Hosted by Granites

Sample	Size (μm)	Tm CO2 (°C)	Th CO2 (°C)	D (*) (g cm -3)	CH4 (*) (mole % CO2)	CO2 (**) (wt % of total fluid)
MG-R-147B	45	-59.2	-16	1.00	11.5	88.5
MG-R-147B	45	-59.3	-2	0.95	12.5	88.0
MG-R-147B	45	-58.9	7	0.90	10.5	89.5
MG-R-147B	45	-59.2	-2	0.95	12.5	88.5
MG-R-147B	45	-58.9	-17	1.20	9.5	90.5
MG-R-147B	45	-58.2	-10	0.87	8.0	92.0
MG-R-147B	45	-58.2	-5	0.98	7.0	93.0
MG-R-147B	45	-58.8	-3	0.95	10.0	90.0
MG-R-147B	45	-58.8	10	0.85	11.0	89.0
MG-R-147B	45	-58.8	10	0.85	11.0	89.0
MG-R-147B	45	-58.9	-16	0.84	9.5	90.5
MG-R-147B	45	-58.2	8	0.90	8.0	92.0
MG-R-147B	45	-58.2	16	0.85	8.0	92.0
MG-R-203D	15	-57.6	10	0.86	4.5	95.5
MG-R-203D	15	-57.9	10	0.86	4.5	95.5
MG-R-174B	25	-57.6	15	0.85	5.0	95.0
MG-R-174B	25	-57.6	9	0.85	4.5	95.5
MG-R-174B	25	-57.6	7	0.85	4.5	95.5

N = 18 (number of fluid inclusion measurements)
MG-R-147B = SLTG (Cacimba Salgada); MG-R-203D = ETG (Canafístula 'garimpo'); MG-R-174B = SLTG (Santo Aleixo)

Appendix 7.13

Microthermometric Data for CO2 Monophase Fluid Inclusions in Quartz Veins Hosted by Granites

Sample	Size (μm)	Tm CO2 (°C)	Th CO2 (°C)	D (*) (g cm -3)	CH4 (*) (mole % CO2)	CO2 (**) (wt % of total fluid)
MG-R-166A	20	-57.9	8	0.90	5.5	94.5
MG-R-166A	20	-57.9	8	0.90	5.5	94.5
MG-R-166A	25	-57.4	13	0.87	4.0	96.0
MG-R-166A	40	-57.6	12	0.86	4.5	95.5
MG-R-229C	25	-57.9	12	0.86	6.0	94.0
MG-R-229C	25	-57.9	16	0.85	6.0	94.0
MG-R-229C	25	-57.5	16	0.85	4.5	95.5
MG-R-224C	15	-57.7	13	0.87	5.5	94.5
MG-R-224C	15	-57.4	13	0.87	4.0	96.0
MG-R-224C	15	-57.9	13	0.87	6.0	94.0
MG-R-224C	15	-57.8	11	0.87	6.0	94.0

N = 11 (number of fluid inclusion measurements)
MG-R-166A = Itapetim District; MG-R-229C = São Francisco mine; MG-R-224C = Cachoeira de Minas mine

Observations:
Tm CO2 = temperature of solid CO2 melting; Th CO2 = temperature liquid-vapour homogenization of CO2; D = density
(*) Data calculated using the microthermomerty measurements and fit it in the plot (Shepherd et al., 1985; see Appendix A7.14)
(**) Data calculated: CO2 = 100 - CH4, based on the approach of: Crawford and Hollister, (1986); and Van der Kerkhof (1988); see text for details.

Apppendix A7.14

Microthermometric Data for H2O Fluid Inclusions in Quartz Vein Hosted by Granitoids

Sample	Size (μm)	DF	T fm Aq (°C)	T lm Aq (°C)	T-Th (°C)	S (NaCl eq. wt %)
MG-R-197B	25	0.70	-22.3	-1.4	207	2.0
MG-R-197B	25	0.70	-21.7	-0.6	207	1.5
MG-R-197B	25	0.70	-21.7	-1.1	214	2.0
MG-R-197B	40	0.70	-16.5	-2.8	352	4.4
MG-R-197B	20	0.70	-16.5	1.4	352	14.0
MG-R-197B	20	0.70	-22.0	-2.0	354	4.0
MG-R-197B	20	0.90	-22.0	-1.1	354	2.0
MG-R-197B	40	0.90	-18.9	-0.3	216	1.3
MG-R-203D	25	0.70	-12.4	-0.5	324	1.5
MG-R-203D	25	0.70	-12.4	-0.8	356	1.8
MG-R-203D	25	0.70	-22.4	-0.3	332	2.0
MG-R-203D	20	0.70	-22.4	-0.4	290	1.4
MG-R-203D	20	0.70	-20.9	-1.5	221	1.5
MG-R-203D	20	0.70	-18.7	0.7	201	1.7
MG-R-203D	25	0.70	-18.7	-0.6	373	1.6
MG-R-174B	20	0.90	-19.6	-0.8	212	1.8
MG-R-174B	20	0.70	-18.2	1.8	248	10.0
MG-R-174B	20	0.70	-19.5	2.9	268	10.5
MG-R-174B	20	0.70	-17.5	1.8	234	10.0
MG-R-174B	25	0.70	-16.5	-1.4	317	1.4
MG-R-174B	25	0.70	-16.8	-2.4	228	4.0
MG-R-174B	20	0.70	-22.0	-2.3	228	4.0
MG-R-222C	25	0.70	-26.8	2.7	215	12.0
MG-R-222C	50	0.70	-28.0	-0.3	361	1.3
MG-R-147B	45	0.70	-22.0	-0.7	295	1.7
MG-R-147B	45	0.70	-22.0	-2.1	295	4.0
MG-R-147B	45	0.70	-28.0	-0.7	223	2.0
MG-R-147B	45	0.70	-21.5	-0.8	295	1.8
MG-R-147B	45	0.70	-28.0	-2.4	244	4.5
MG-R-147B	45	0.70	-28.0	-2.0	295	4.0

Observations:
NFI = 30 (Number of fluid inclusion measurements)
DF = degree of fill; T-fm Aq = temperature of first melting of aqueous phase; T lm Aq = temperature of last melting of aqueous phase
T-Th = temperature of homogenization of fluid inclusion; S = salinity (NaCl equivalent)
(*) approminately

Apppendix A7.15

Microthermometric Data for H2O Fluid Inclusions in Quartz Vein Hosted by Supracrustal Rocks

Sample	Size (μm)	DF	T fm Aq (*) (°C)	T lm Aq (°C)	T-Th (°C)	S (NaCl eq. wt %)
MG-R-159	10	0.50	-12.0	-0.3	416	1.00
MG-R-159	10	0.50	-13.9	-1.9	402	4.00
MG-R-159	10	0.50	-13.7	-1.9	402	4.00
MG-R-159	10	0.50	-13.7	-1.9	315	4.00
MG-R-159	15	0.70	-11.9	-2.3	291	4.10
MG-R-166A	15	0.70	-47.7	0.0	379	0.00
MG-R-166A	15	0.70	-47.5	-0.7	408	1.70
MG-R-166A	15	0.70	-46.0	-0.7	408	1.70
MG-R-166A	15	0.70	-43.0	-0.6	291	1.60
MG-R-166A	20	0.70	-40.0	-0.6	291	1.60
MG-R-166A	20	0.70	-43.0	-0.7	330	1.70
MG-R-166A	20	0.90	-42.4	-0.4	294	1.40
MG-R-224C	20	0.70	-27.5	-0.9	317	1.90
MG-R-224C	20	0.90	-26.3	-0.2	230	1.20
MG-R-224C	20	0.90	-26.3	-0.3	226	1.30
MG-R-224C	20	0.90	-22.9	-1.4	343	3.00
MG-R-224C	20	0.90	-22.9	-1.4	320	3.00
MG-R-224C	20	0.90	-23.0	0.6	294	12.50
MG-R-224C	25	0.70	-23.0	1.9	340	14.00
MG-R-224C	15	0.90	-26.0	1.7	240	14.00
MG-R-224C	15	0.90	-28.5	1.7	230	14.00
MG-R-224C	20	0.90	-16.5	0.8	260	1.80
MG-R-229C	45	0.70	-22.7	0.4	227	1.40
MG-R-229C	45	0.70	-22.7	-0.4	228	1.40
MG-R-229C	45	0.70	-22.7	-0.5	250	1.50
MG-R-229C	25	0.50	-22.8	-0.5	203	1.50
MG-R-229C	25	0.50	-22.8	-3.0	203	4.00
MG-R-229C	15	0.70	-21.0	2.0	311	14.00
MG-R-229C	15	0.70	-21.0	0.0	311	1.00
MG-R-229C	15	0.90	-20.3	-0.4	249	1.40
MG-R-208B	20	0.70	-22.5	-0.2	291	1.20
MG-R-208B	20	0.70	-22.0	-0.1	230	1.10

Observations:
NFI = 32 (Number of fluid inclusion measurements)
DF = degree of fill; T-fm Aq (*) = temperature of first melting of aqueous phase; T lm Aq = temperature of last melting of aqueous phase
T-Th = temperature of homogenization of the inclusion; S = salinity (NaCl equivalent)
(*) approximately

Appendix A7.16

Mole % Composition Calculation for H2O-CO2 Fluid Inclusion in Gold-Bearing Quartz Veins

Sample	T-Th ** (°C)	T-Th ** (°C) (mean value)	Density (a) (g cm -3)	Density (a) (g cm -3) (mean value)	CH4 (a) (mole %)	S (a) (NaCl wt %)	CO2 (a) (wt %)	H2O (b) (wt %)	NaCl (c) (mole %)	NaCl (c) (mole %) (mean value)	H2O (d) (wt %)	CO2 (e) (mole %)	CO2 (f) (mole %)	CO2 (f) (mole %) (mean value)	CH4 (g) (mole %)	CH4 (g) (mole %) (mean value)	H2O (h) (mole %)	H2O (h) (mole %) (mean value)
MG-R-197B	322	289	0.78	0.82	10.5	8.0	8.0	92.0	7.4	6.2	84.6	0.03	2.9	2.9	0.3	0.2	95.5	90.7
MG-R-197B	331	267	0.81	0.76	11.5	8.0	4.1	95.9	7.7	3.1	88.2	0.02	1.5	9.5	0.2	0.6	97.0	86.8
MG-R-197B	267	291	0.78	0.80	3.5	8.0	3.9	96.1	7.7	5.2	88.4	0.01	1.4	13.6	0.0	0.7	97.2	80.5
MG-R-197B	273	333	0.83	0.84	1.0	8.0	26.2	73.8	5.9	2.2	67.9	0.13	11.6	23.2	0.1	3.0	87.3	71.6
MG-R-197B	267		0.81		0.5	8.0	25.8	74.2	5.9		68.3	0.13	11.1		0.1		87.8	
MG-R-197B	316		0.76		7.5	6.8	41.9	58.1	4.0		54.1	0.24	19.4		1.5		78.5	
MG-R-197B	292		0.84		0.2	6.0	8.5	91.5	5.5		86.0	0.03	3.3		0.0		95.8	
MG-R-197B	264*		0.76		9.0	6.0	7.8	92.2	5.5		86.7	0.03	2.7		0.2		96.1	
MG-R-197B	264		0.79		8.5	6.0	4.0	96.0	5.8		90.2	0.01	1.4		0.1		97.5	
MG-R-197B	255		0.85		5.5	8.0	26.7	73.3	5.9		67.4	0.14	12.1		0.7		86.2	
MG-R-197B	260		0.83		7.0	8.0	26.3	73.7	5.9		67.8	0.13	11.6		0.8		86.5	
MG-R-197B	248		0.81		7.0	8.0	25.8	74.2	5.9		68.3	0.13	11.1		0.8		87.1	
MG-R-197B	220		0.85		6.0	8.0	8.2	91.8	7.3		84.5	0.03	3.3		0.2		95.3	
MG-R-197B	299		0.85		6.5	6.0	8.6	91.4	5.5		85.9	0.03	3.4		0.2		95.5	
MG-R-197B	279		0.84		7.0	6.0	8.5	91.5	5.5		86.0	0.03	3.3		0.2		95.5	
MG-R-197B	415		0.72		7.5	4.5	41.9	58.1	2.6		55.5	0.22	18.2		1.4		80.0	
MG-R-197B	314		0.84		13.0	4.0	45.7	54.3	2.2		52.1	0.30	23.2		3.0		73.5	
MG-R-197B	353		0.84		12.0	4.0	45.7	54.3	2.2		52.1	0.30	23.2		2.8		73.7	
MG-R-197B	316		0.85		8.0	10.0	8.6	91.4	9.1		82.3	0.04	3.5		0.3		94.6	
MG-R-197B	316		0.76		8.5	8.0	7.8	92.2	7.4		84.8	0.03	2.8		0.2		95.7	
MG-R-197B	349		0.81		7.5	7.8	8.3	91.7	7.2		84.5	0.03	3.2		0.2		95.4	
MG-R-197B	207		0.74		8.5	2.0	24.1	75.9	1.5		74.4	0.10	8.9		0.8		90.0	
MG-R-197B	207		0.77		7.5	1.5	24.8	75.2	1.1		74.1	0.11	9.5		0.7		89.6	
MR-R-197B	214		0.76		8.5	0.8	24.5	75.5	0.6		74.9	0.10	9.2		0.8		89.9	
MG-R-197B	352		0.76		8.5	8.0	24.5	75.5	6.0		69.5	0.11	9.9		0.8		88.2	
MG-R-197B	353		0.76		1.5	8.0	24.5	75.5	6.0		69.5	0.11	9.9		0.1		88.9	
MG-R-197B	354		0.76		2.5	6.0	7.8	92.2	5.5		86.7	0.03	2.7		0.1		96.3	
MG-R-197B	354		0.76		3.5	6.0	7.8	92.2	5.5		86.7	0.03	2.7		0.1		96.2	
MG-R-197B	216		0.81		9.5	2.0	8.3	91.7	1.8		89.9	0.03	3.0		0.3		96.4	
MG-R-197B	232		0.83		7.5	8.0	8.4	91.6	7.3		84.3	0.03	3.3		0.2		95.2	
MG-R-197B	374		0.87		9.0	8.0	8.8	91.2	7.3		83.9	0.04	3.6		0.3		94.8	
MG-R-197B	242		0.88		8.0	8.0	8.8	91.2	7.3		83.9	0.04	3.6		0.3		94.8	
MG-R-197B	194		0.88		4.0	2.0	8.8	91.2	1.8		89.4	0.04	3.4		0.1		96.1	

MG-R-147B	221*	258	0.77	0.86	8.5	6.0	7.9	92.1	5.5	7.0	86.6	0.03	2.8	3.1	0.2	0.1	96.0	89.8
MG-R-147B	221*	260	0.76	0.75	8.5	6.0	7.8	92.2	5.5	8.7	86.7	0.03	2.7	9.8	0.2	0.7	96.1	80.8
MG-R-147B	225	241	0.75	0.82	8.0	8.5	24.3	75.7	6.4	7.7	69.3	0.11	9.7	11.5	0.8	0.8	88.4	80.0
MG-R-147B	225	-	0.77	-	8.0	8.5	24.8	75.2	6.4	-	68.8	0.11	10.2	-	0.8	-	87.9	-
MG-R-147B	223		0.87		7.5	8.5	27.2	72.8	6.2		66.6	0.15	12.7		1.0		85.3	
MG-R-147B	295		0.77		8.0	8.6	24.8	75.2	6.5		68.7	0.11	10.2		0.8		87.9	
MG-R-147B	295		0.75		6.5	9.0	24.3	75.7	6.8		68.9	0.11	9.8		0.6		88.4	
MG-R-147B	244		0.82		11.5	4.0	26.0	74.0	3.0		71.0	0.12	10.9		1.3		87.3	
MG-R-147B	232		0.88		6.5	9.0	8.9	91.1	8.2		82.9	0.04	3.7		0.2		94.6	
MG-R-147B	308		0.88		5.5	6.5	8.9	91.1	5.9		85.2	0.04	3.6		0.2		95.2	
MG-R-147B	282		0.88		4.5	8.5	8.9	91.1	7.7		83.4	0.04	3.7		0.2		94.8	
MG-R-147B	226		0.87		1.0	8.0	8.8	91.2	7.3		83.9	0.04	3.6		0.0		95.1	
MG-R-147B	223		0.84		0.2	8.0	8.5	91.5	7.3		84.2	0.03	3.4		0.0		95.4	
MG-R-147B	226		0.86		0.2	8.0	8.7	91.3	7.3		84.0	0.04	3.5		0.0		95.2	
MG-R-147B	256		0.85		4.5	8.5	8.6	91.4	7.8		83.6	0.04	3.5		0.2		95.1	
MG-R-147B	220		0.88		4.5	8.5	8.9	91.1	7.7		83.4	0.04	3.7		0.2		94.8	
MG-R-147B	233		0.89		1.0	6.0	9.0	91.0	5.5		85.5	0.04	3.7		0.0		95.3	
MG-R-147B	220		0.89		1.0	9.0	27.6	72.4	6.5		65.9	0.15	13.2		0.1		85.5	
MG-R-147B	380		0.88		3.0	8.5	8.9	91.1	7.7		83.4	0.04	3.7		0.1		94.9	
MG-R-147B	385		0.89		3.5	2.0	9.0	91.0	1.8		89.2	0.04	3.5		0.1		96.0	
MG-R-147B	232		0.88		6.5	8.0	4.4	95.6	7.6		88.0	0.02	1.8		0.1		96.8	
MG-R-147B	232		0.89		3.5	4.5	4.5	95.5	4.3		91.2	0.02	1.8		0.1		97.4	
MG-R-147B	232		0.88		11.0	4.0	4.4	95.6	3.8		91.8	0.02	1.7		0.2		97.5	
MG-R-147B	232		0.88		5.5	7.0	4.4	95.6	6.7		88.9	0.02	1.8		0.1		97.0	
MG-R-147B	274		0.84		0.2	8.5	8.5	91.5	7.8		83.7	0.03	3.4		0.0		95.3	
MG-R-147B	287		0.87		0.2	8.0	8.8	91.2	7.3		83.9	0.04	3.6		0.0		95.1	
MG-R-174B	354	324	0.76	0.86	3.5	10.0	24.6	75.4	7.5	5.4	67.9	0.11	10.1	3.4	0.4	0.2	88.2	91.0
MG-R-174B	248	257	0.81	0.73	3.0	8.5	25.8	74.2	6.3	5.3	67.9	0.13	11.2	9.4	0.3	0.8	87.4	84.5
MG-R-174B	326	274	0.73	0.81	3.5	8.5	23.8	76.2	6.5	5.2	69.7	0.10	9.3	11.1	0.3	0.4	89.3	83.3
MG-R-174B	210	-	0.73	-	15.0	4.0	23.8	76.2	3.0	-	73.2	0.10	8.9	-	1.3	-	89.3	-
MG-R-174B	212		0.81		4.5	8.5	8.3	91.7	7.8		83.9	0.03	3.2		0.1		95.4	
MG-R-174B	248		0.77		4.5	8.5	24.8	75.2	6.4		68.8	0.11	10.2		0.5		88.3	
MG-R-174B	268		0.77		3.5	8.5	24.8	75.2	6.4		68.8	0.11	10.2		0.4		88.4	
MG-R-174B	234		0.73		7.0	8.5	23.8	76.2	6.5		69.7	0.10	9.3		0.6		89.0	
MG-R-174B	317		0.76		6.5	8.5	24.7	75.3	6.4		68.9	0.11	10.0		0.7		88.2	
MG-R-174B	228		0.78		12.0	6.0	25.0	75.0	4.5		70.5	0.11	10.2		1.2		87.8	
MG-R-174B	228		0.78		7.0	6.0	25.0	75.0	4.5		70.5	0.11	10.2		0.7		88.4	
MG-R-174B	304		0.78		3.5	10.0	25.0	75.0	7.5		67.5	0.12	10.6		0.4		87.8	

MG-R-174B	253		0.78		3.5	11.0	25.0	75.0	8.3		66.8	0.12	10.7		0.4		87.5		
MG-R-174B	279		0.81		1.5	8.0	25.8	74.2	5.9		68.3	0.13	11.1		0.2		87.7		
MG-R-174B	279		0.80		6.0	8.0	25.5	74.5	6.0		68.5	0.12	10.9		0.7		87.5		
MG-R-174B	200		0.83		6.0	8.0	26.2	73.8	5.9		67.9	0.13	11.6		0.7		86.7		
MG-R-174B	200		0.83		0.5	8.0	26.2	73.8	5.9		67.9	0.13	11.6		0.1		87.3		
MG-R-174B	279		0.83		1.0	8.0	26.2	73.8	5.9		67.9	0.13	11.6		0.1		87.3		
MG-R-174B	298		0.84		2.0	6.0	26.5	73.5	4.4		69.1	0.13	11.6		0.2		87.4		
MG-R-174B	258		0.84		0.5	6.5	26.5	73.5	4.8		68.7	0.13	11.7		0.1		87.4		
MG-R-174B	258		0.84		0.5	6.5	26.5	73.5	4.8		68.7	0.13	11.7		0.1		87.4		
MG-R-174B	200		0.79		3.5	8.5	25.3	74.7	6.3		68.4	0.12	10.7		0.4		87.9		
MG-R-174B	200		0.82		3.5	6.0	26.0	74.0	4.4		69.6	0.13	11.1		0.4		87.7		
MG-R-174B	200		0.83		0.2	8.5	26.2	73.8	6.3		67.5	0.13	11.6		0.0		87.3		
MG-R-174B	200		0.83		0.5	6.0	8.4	91.6	5.5		86.1	0.03	3.2		0.0		95.8		
MG-R-174B	354		0.84		2.5	4.0	26.5	73.5	2.9		70.6	0.13	11.4		0.3		87.8		
MG-R-174B	354		0.82		2.5	4.0	26.0	74.0	3.0		71.0	0.12	10.9		0.3		88.3		
MG-R-174B	376		0.83		1.5	4.0	26.2	73.8	3.0		70.8	0.13	11.2		0.2		88.2		
MG-R-174B	376		0.84		1.5	4.0	26.5	73.5	2.9		70.6	0.13	11.4		0.2		87.9		
MG-R-174B	372		0.81		3.0	6.0	25.8	74.2	4.5		69.7	0.12	10.9		0.3		88.0		
MG-R-222C	313		0.85		0.5	6.0	26.7	73.3	4.4		68.9	0.13	11.9		0.1		87.3		
MG-R-222C	224		0.83		4.0	5.8	26.2	73.8	4.3		69.5	0.13	11.3		0.5		87.5		
MG-R-222C	212		0.81		11.0	6.0	25.8	74.2	4.5		69.7	0.12	10.9		1.2		87.1		
MG-R-222C	287		0.87		13.0	4.0	8.8	91.2	3.6		87.6	0.04	3.5		0.4		95.5		
MG-R-222C	298		0.87		11.0	2.0	8.8	91.2	1.8		89.4	0.04	3.4		0.4		95.9		
MG-R-222C	350		0.87		10.0	2.0	8.8	91.2	1.8		89.4	0.04	3.4		0.3		96.0		
MG-R-222C	298		0.87		10.0	8.0	8.8	91.2	7.3		83.9	0.04	3.6		0.4		94.8		
MG-R-222C	374		0.87		12.0	4.0	8.8	91.2	3.6		87.6	0.04	3.5		0.4		95.5		
MG-R-222C	365		0.85		3.0	6.0	8.6	91.4	5.5		85.9	0.03	3.4		0.1		95.6		
MG-R-222C	275		0.84		3.0	4.0	26.5	73.5	2.9		70.6	0.13	11.4		0.3		87.7		
MG-R-222C	365		0.86		3.0	8.0	8.7	91.3	7.3		84.0	0.04	3.5		0.1		95.1		
MG-R-222C	393		0.87		10.5	8.0	8.8	91.2	7.3		83.9	0.04	3.6		0.4		94.8		
MG-R-222C	395		0.87		1.5	6.0	8.8	91.2	5.5		85.7	0.04	3.5		0.1		95.5		
MG-R-222C	353		0.87		3.0	8.0	8.8	91.2	7.3		83.9	0.04	3.6		0.1		95.0		
MG-R-203D	324	-	0.78	-	4.5	8.0	25.1	74.9	6.0	-	68.9	0.12	10.4	-	0.5	-	88.1	-	
MG-R-203D	356	305	0.76	0.76	6.5	8.5	24.6	75.4	6.4	4.3	69.0	0.11	10.0	9.5	0.6	0.4	88.3	85.8	
MG-R-203D	332	323	0.76	0.81	6.5	8.5	24.6	75.4	6.4	4.8	69.0	0.11	10.0	11.0	0.6	0.6	88.3	83.6	
MG-R-203D	290	-	0.81	-	8.5	6.0	25.8	74.2	4.5	-	69.7	0.12	10.9	-	0.9	-	87.4	-	
MG-R-203D	221		0.81		8.5	6.0	25.8	74.2	4.5		69.7	0.12	10.9		0.9		87.4		
MG-R-203D	376		0.85		2.5	4.0	26.7	73.3	2.9		70.4	0.13	11.7		0.3		87.6		
MG-R-203D	326		0.84		6.5	3.5	26.5	73.5	2.6		70.9	0.13	11.4		0.7		87.4		

MG-R-203D	201		0.72		2.5	5.0	23.6	76.4	3.8		72.6	0.10	8.7		0.2		90.4	
MG-R-203D	201		0.83		2.5	2.0	26.2	73.8	1.5		72.3	0.12	11.0		0.3		88.5	
MG-R-203D	373		0.81		14.5	4.0	25.8	74.2	3.0		71.2	0.12	10.7		1.6		87.2	
MG-R-203D	371		0.81		7.0	8.5	25.8	74.2	6.3		67.9	0.13	11.2		0.8		87.0	
MG-R-203D	324		0.78		8.5	6.0	25.1	74.9	4.5		70.4	0.11	10.2		0.9		88.1	
MG-R-203D	356		0.78		8.5	6.0	25.1	74.9	4.5		70.4	0.11	10.2		0.9		88.1	
MG-R-203D	324		0.77		5.0	4.0	24.8	75.2	3.0		72.2	0.11	9.8		0.5		89.2	
MG-R-203D	326		0.77		5.0	4.0	24.8	75.2	3.0		72.2	0.11	9.8		0.5		89.2	
MG-R-203D	331		0.76		4.5	6.0	24.6	75.4	4.5		70.9	0.11	9.7		0.4		89.0	
MG-R-203D	366		0.78		2.0	9.0	25.1	74.9	6.7		68.2	0.12	10.5		0.2		88.1	
MG-R-203D	342		0.76		4.5	4.0	24.6	75.4	3.0		72.4	0.11	9.6		0.4		89.5	
MG-R-203D	339		0.81		7.0	4.0	25.8	74.2	3.0		71.2	0.12	10.7		0.8		88.0	
MG-R-203D	317		0.83		0.5	9.0	26.2	73.8	6.6		67.2	0.13	11.7		0.1		87.1	
MG-R-203D	273		0.83		0.5	9.0	26.2	73.8	6.6		67.2	0.13	11.7		0.1		87.1	
MG-R-203D	287		0.83		0.5	9.0	26.2	73.8	6.6		67.2	0.13	11.7		0.1		87.1	
MG-R-203D	287		0.83		0.5	9.0	26.2	73.8	6.6		67.2	0.13	11.7		0.1		87.1	
MG-R-203D	370		0.81		3.0	8.0	25.8	74.2	5.9		68.3	0.13	11.1		0.3		87.5	
MG-R-203D	370		0.78		0.2	6.0	25.1	74.9	4.5		70.4	0.11	10.2		0.0		89.0	
MG-R-224C	320	265	0.72	0.76	2.5	0.5	23.6	76.4	0.4	5.8	76.0	0.09	8.4	2.7	0.2	0.1	91.3	91.4
MG-R-224C	260	320	0.76	0.72	2.5	0.5	7.8	92.2	0.5	0.5	91.7	0.03	2.6	8.4	0.1	0.2	97.3	90.9
MG-R-224C	260	312	0.76	0.85	2.5	0.5	7.8	92.2	0.5	6.6	91.7	0.03	2.6	12.2	0.1	0.2	97.3	81.0
MG-R-224C	312	-	0.85	-	2.0	9.0	26.7	73.3	6.6	-	66.7	0.14	12.2	-	0.2	-	86.4	-
MG-R-224C	287		0.85		2.0	8.9	8.6	91.4	8.1		83.3	0.04	3.5		0.1		95.1	
MG-R-224C	258		0.73		1.5	8.0	7.5	92.5	7.4		85.1	0.03	2.6		0.0		96.1	
MG-R-224C	260		0.79		1.5	8.0	8.1	91.9	7.4		84.5	0.03	3.0		0.0		95.7	
MG-R-224C	317		0.83		4.0	9.0	8.4	91.6	8.2		83.4	0.03	3.3		0.1		95.1	
MG-R-224C	226		0.78		17.0	4.0	8.0	92.0	3.7		88.3	0.03	2.8		0.5		96.1	
MG-R-224C	226		0.78		1.5	9.0	8.0	92.0	8.3		83.7	0.03	3.0		0.0		95.6	
MG-R-224C	258		0.68		11.5	6.0	7.0	93.0	5.6		87.4	0.02	2.2		0.3		96.6	
MG-R-224C	320		0.76		7.5	6.1	7.8	92.2	5.6		86.6	0.03	2.7		0.2		96.1	
MG-R-224C	294		0.78		6.5	6.2	8.0	92.0	5.7		86.3	0.03	2.9		0.2		96.0	
MG-R-224C	301		0.78		1.5	6.0	8.0	92.0	5.5		86.5	0.03	2.9		0.0		96.1	
MG-R-224C	240		0.60		2.5	6.0	6.3	93.7	5.6		88.1	0.02	1.7		0.0		97.3	
MG-R-224C	230		0.73		4.5	6.0	7.5	92.5	5.6		87.0	0.03	2.5		0.1		96.4	
MG-R-224C	238		0.73		5.0	8.0	7.5	92.5	7.4		85.1	0.03	2.6		0.1		96.0	
MG-R-224C	260		0.76		10.5	8.0	7.8	92.2	7.4		84.8	0.03	2.8		0.3		95.7	
MG-R-229C	326	285	0.76	0.76	2.5	5.5	4.1	95.9	5.3	4.2	90.6	0.01	1.4	2.2	0.0	0.1	97.7	93.5
MG-R-229C	276	279	0.72	0.73	3.0	6.0	23.6	76.4	4.6	3.2	71.8	0.10	8.8	9.0	0.3	0.5	90.1	87.3

MG-R-229C	281	-	0.76	-	4.0	2.5	24.6	75.4	1.9	-	73.5	0.10	9.4	-	0.4	-	89.9	-
MG-R-229C	296	203	0.76	0.77	5.5	1.0	24.6	75.4	0.8	4.0	74.6	0.10	9.3	20.7	0.5	2.3	90.1	73.0
MG-R-229C	288		0.73		3.5	6.4	23.8	76.2	4.9		71.3	0.10	9.1		0.3		89.8	
MG-R-229C	279*		0.73		4.5	2.0	23.8	76.2	1.5		74.7	0.10	8.7		0.4		90.7	
MG-R-229C	279*		0.76		4.5	2.0	24.6	75.4	1.5		73.9	0.10	9.4		0.4		89.9	
MG-R-229C	279		0.76		4.5	2.0	7.8	92.2	1.8		90.4	0.03	2.6		0.1		97.0	
MG-R-229C	310		0.72		4.5	6.0	23.6	76.4	4.6		71.8	0.10	8.8		0.4		90.0	
MG-R-229C	293		0.72		4.5	6.0	23.6	76.4	4.6		71.8	0.10	8.8		0.4		90.0	
MG-R-230	313		0.76		3.5	6.0	24.6	75.4	4.5		70.9	0.11	9.7		0.3		89.1	
MG-R-230	293		0.72		4.0	6.0	23.6	76.4	4.6		71.8	0.10	8.8		0.4		90.0	
MG-R-230	294		0.72		4.5	6.0	23.6	76.4	4.6		71.8	0.10	8.8		0.4		90.0	
MG-R-230	296		0.72		4.5	6.0	23.6	76.4	4.6		71.8	0.10	8.8		0.4		90.0	
MG-R-230	278		0.72		4.5	6.0	23.6	76.4	4.6		71.8	0.10	8.8		0.4		90.0	
MG-R-230	260		0.72		7.0	6.0	23.6	76.4	4.6		71.8	0.10	8.8		0.6		89.8	
MG-R-230	249		0.76		7.0	6.0	7.8	92.2	5.5		86.7	0.03	2.7		0.2		96.1	
MG-R-230	239		0.76		7.0	2.5	24.6	75.4	1.9		73.5	0.10	9.4		0.7		89.6	
MG-R-230	200		0.77		7.0	2.5	24.8	75.2	1.9		73.3	0.11	9.6		0.7		89.4	
MG-R-230	227		0.78		10.5	2.5	25.0	75.0	1.9		73.1	0.11	9.8		1.0		88.8	
MG-R-230	250		0.78		6.5	2.5	25.0	75.0	1.9		73.1	0.11	9.8		0.6		89.2	
MG-R-230	203		0.77		10.5	7.0	43.5	56.5	4.0		52.5	0.26	20.7		2.2		76.5	
MG-R-230	203		0.77		10.5	7.0	43.5	56.5	4.0		52.5	0.26	20.7		2.2		76.5	
MG-R-230	311		0.66		9.0	2.0	22.1	77.9	1.6		76.3	0.08	7.2		0.7		91.8	
MG-R-230	311		0.66		9.0	4.0	22.1	77.9	3.1		74.8	0.08	7.4		0.7		91.4	
MG-R-159	246	246	0.81	0.81	1.0	9.0	8.3	91.7	8.3	8.3	83.4	0.03	3.2	3.2	0.0	0.0	95.4	88.5
MG-R-159	381	279	0.85	0.75	1.0	9.0	26.7	73.3	6.6	4.1	66.7	0.14	12.2	9.4	0.1	0.2	86.5	86.7
MG-R-159	408	345	0.83	0.82	1.0	6.0	26.2	73.8	4.4	5.2	69.4	0.13	11.4	11.3	0.1	0.2	87.8	83.3
MG-R-159	402	-	0.83	-	1.0	6.0	26.2	73.8	4.4	-	69.4	0.13	11.4	-	0.1	-	87.8	-
MG-R-159	380		0.81		2.0	6.0	26.3	73.7	4.4		69.3	0.13	11.2		0.2		87.8	
MG-R-159	323		0.85		2.0	6.0	26.7	73.3	4.4		68.9	0.13	11.9		0.2		87.1	
MG-R-159	346		0.85		2.0	6.0	26.7	73.3	4.4		68.9	0.13	11.9		0.2		87.1	
MG-R-159	323		0.85		2.0	9.0	26.7	73.3	6.6		66.7	0.14	12.2		0.2		86.4	
MG-R-159	323		0.85		0.5	9.0	26.7	73.3	6.6		66.7	0.14	12.2		0.1		86.6	
MG-R-166A	375		0.82		0.5	4.0	26.0	74.0	3.0		71.0	0.12	10.9		0.1		88.5	
MG-R-166A	375		0.79		1.5	8.0	25.3	74.7	6.0		68.7	0.12	10.6		0.2		88.2	
MG-R-166A	375		0.79		1.5	8.0	25.3	74.7	6.0		68.7	0.12	10.6		0.2		88.2	
MG-R-166A	375		0.79		1.5	8.0	25.3	74.7	6.0		68.7	0.12	10.6		0.2		88.2	
MG-R-166A	375		0.79		1.5	8.0	25.3	74.7	6.0		68.7	0.12	10.6		0.2		88.2	
MG-R-166A	341		0.81		0.5	8.0	26.3	73.7	5.9		67.8	0.13	11.4		0.1		87.5	
MG-R-166A	361		0.81		2.5	7.5	26.3	73.7	5.5		68.2	0.13	11.3		0.3		87.4	

MG-R-166A	303	0.81	2.5	7.5	26.3	73.7	5.5	68.2	0.13	11.3	0.3	87.4
MG-R-166A	233	0.81	3.0	5.5	26.3	73.7	4.1	69.6	0.13	11.1	0.3	87.9
MG-R-166A	233	0.73	2.5	4.0	23.8	76.2	3.0	73.2	0.10	8.9	0.2	90.4
MG-R-166A	365	0.76	1.5	8.0	24.6	75.4	6.0	69.4	0.11	9.9	0.1	88.9
MG-R-166A	283	0.79	0.5	5.5	25.3	74.7	4.1	70.6	0.12	10.4	0.1	88.9
MG-R-166A	275	0.79	2.0	6.0	25.3	74.7	4.5	70.2	0.12	10.4	0.2	88.6

Observations:

* decreptation temperature; For further sample label information see Appendix A1.1

** Microthermometric measurements (see Appendices A7.4 to A7.11)

(a) = data calculated using the microthermometric measurements and processing according to the approach of Shepherd et al., (1985).

Note: (b) to (h) refer to the calculation of the mole %

(b) H_2O = 100 - CO_2 (a) % wt

(c) S = [NaCl wt % (a) x H_2O (b) wt %] / 100

(d) H_2O wt % = 100 - [NaCl wt % (c) + CO_2 (a) wt %]

(e) mole % CO_2 = [CO_2 (a) wt % x D(a) / H_2O (d) wt %] x 18/44

(f) mole % CO_2 = CO_2(e) mole % / [CO_2(e) mole % +1)] x 100

(g) mole % CH_4 = [CH_4 (a) mole % of CO_2 x mole % CO_2 (f) /100]

(h) mole % H_2O = 100 - [NaCl (c) wt % / 5.85 + mole % CO_2 (f) + mole % CH_4 (g)]

Mean values are expressed for each sample as four mole % CO_2 intervals: < 5%; 5-10 % ; 10-20 %; > 20 %; (-) = interval not present

Appendix A7.17

Mole % Composition Calculation for CO2 Monophase Fluid Inclusion In Gold-Bearing Quartz Vein

Sample	Density (a) (g cm -3)	Density (a) (g cm -3) (mean value)	CO2 (a) (wt % of total fluid)	CH4 (a) (mole % of CO2)	CO2(b) (mole %)	CO2 (c) (mole %)	CO2 (mole %) (mean value)	CH4 (d) (mole %)	CH4 (mole %) (mean value)	H2O (e) (mole %)	H2O (mole %) (mean value)
MG-R-147B	1.00	0.86	88.5	11.5	3.6	78.4	76.0	9.0	7.4	12.6	16.7
MG-R-147B	0.95	0.94	88.0	12.5	3.4	77.4	77.5	9.7	9.9	13.0	14.2
MG-R-147B	0.90	1.10	89.5	10.5	3.3	76.7	80.0	8.1	8.4	15.2	13.0
MG-R-147B	0.95		88.5	12.5	3.4	77.5		9.7		12.8	
MG-R-147B	1.20		90.5	9.5	4.4	81.6		7.8		10.6	
MG-R-147B	0.87		92.0	8.0	3.3	76.6		6.1		17.3	
MG-R-147B	0.98		93.0	7.0	3.7	78.8		5.5		15.6	
MG-R-147B	0.95		90.0	10.0	3.5	77.8		7.8		14.5	
MG-R-147B	0.85		89.0	11.0	3.1	75.6		8.3		16.1	
MG-R-147B	0.85		89.0	11.0	3.1	75.6		8.3		16.1	
MG-R-147B	0.84		90.5	9.5	3.1	75.7		7.2		17.1	
MG-R-147B	0.90		92.0	8.0	3.4	77.2		6.2		16.6	
MG-R-147B	0.85		92.0	8.0	3.2	76.2		6.1		17.7	
MG-R-203D	0.86	-	95.5	4.5	3.4	77.1	77.1	3.5	3.5	19.5	19.5
MG-R-203D	0.86	0.86	95.5	4.5	3.4	77.1	-	3.5	-	19.5	-
MG-R-174B	0.85	0.85	95.0	5.0	3.3	76.8	76.8	3.8	3.6	19.4	19.6
MG-R-174B	0.85	-	95.5	4.5	3.3	76.9	-	3.5	-	19.7	-
MG-R-174B	0.85	-	95.5	4.5	3.3	76.9	-	3.5	-	19.7	-
MG-R-166A	0.90	-	94.5	5.5	3.5	77.7	-	4.3	-	18.1	-
MG-R-166A	0.90	0.88	94.5	5.5	3.5	77.7	77.5	4.3	3.8	18.1	18.8
MG-R-166A	0.87	-	96.0	4.0	3.4	77.4	-	3.1	-	19.6	-
MG-R-166A	0.86		95.5	4.5	3.4	77.1		3.5		19.5	
MG-R-229C	0.86	0.85	94.0	6.0	3.3	76.8	76.7	4.6	4.3	18.6	18.9
MG-R-229C	0.85	-	94.0	6.4	3.3	76.6	-	4.9	-	18.5	-
MG-R-229C	0.85	-	95.5	4.5	3.3	76.9	-	3.5	-	19.7	-
MG-R-224C	0.87	-	94.5	5.5	3.4	77.1	-	4.2	-	18.7	-
MG-R-224C	0.87	0.87	96.0	4.0	3.4	77.4	77.1	3.1	4.2	19.6	18.8
MG-R-224C	0.87	-	94.0	6.0	3.3	77.0	-	4.6	-	18.4	-
MG-R-224C	0.87		94.0	6.0	3.3	77.0		4.6		18.4	

Observations:

Mean values refer to the intervals of CO2 mole %: < 77 %; 77-79 %; >79 % for each sample ; (-) = intervale not present.

For further sample label information see Apppendix A1.1; For data information see Appendix A7.12 and A7.13.

Salinity is = 0 ; H2O = 10 % wt (see text for details)

(a) = data calculated using the microthermometric measurements and processing according to the approach of Shepherd et al, (1985)

Note: (b) to (e) refer to the calculation of the mole %

(b) mole % CO2 = [CO2 (a) % wt x D (a) / H2O % wt] x 18/44

(c) mole % CO2 = CO2 (b) mole % wt / [(CO2 (b) mole % + 1)] x 100

(d) mole % CH4 = [CH4 (a) mole % of CO2 x mole % CO2 (c) / 100]

(e) mole % H2O = 100 - [mole % CO2 (c) + mole % CH4 (d)]

Appendix A7.18

δ 13 C Data for Fluid Inclusions in Gold-Bearing Quartz Veins

Sample	T° C	t	pCO2	ng C	δ 45	δ 46	δ13C	sd	δ18 O	sd	ppm C	%CO2	PNC	δ 13 C mean values
MG-R-203E	300	30	0.0027	86	5.562	10.964	-26.678	72	-9.676	329	0	0.000	0.0254	**-0.34**
MG-R-203E	400	30	0.0017	54	-7.529	24.976	-40.764	201	4.361	651	0	0.000	0.0020	**-0.33**
MG-R-203E	500	30	0.0025	80	-69.138	59.307	-105.138	996	38.169	762	0	0.000	0.0007	**-1.24**
MG-R-203E	600	30	0.0023	64	-14.062	3.108	-46.799	255	-17.074	295	0	0.000	0.0007	**-0.44**
MG-R-203E	700	30	0.0023	74	-11.060	12.647	-44.009	213	-7.724	463	0	0.000	0.0007	**-0.48**
MG-R-203E	1200	30	0.0200	6400	18.198	-5.620	-13.129	15	25.705	48	29	0.011	0.0070	**-12.43**
MG-R-197B	300	30	0.0210	672	9.473	4.969	-22.510	21	-15.300	17	3	0.001	0.0027	**-4.42**
MG-R-197B	400	30	0.0230	736	16.698	5.965	-15.070	18	-14.338	21	3	0.001	0.0020	**-3.24**
MG-R-197B	500	30	0.0140	448	13.372	10.722	-18.660	17	-9.665	10	2	0.001	0.0011	**-2.44**
MG-R-197B	600	30	0.0200	640	18.453	7.279	-13.290	13	-13.053	46	3	0.001	0.0009	**-2.48**
MG-R-197B	700	30	0.0140	448	17.122	6.256	-14.640	25	-14.053	47	2	0.001	0.0009	**-1.92**
MG-R-197B	800	30	0.0150	480	-1.856	98.924	-32.140	155	76.885	645	2	0.001	0.0008	**-4.51**
MG-R-197B	1000	30	0.0190	-	-	-	-	-	-	-	-	-	-	-
MG-R-222C	300	30	0.0070	224	0.303	7.467	-32.086	17	-12.830	106	1	0.000	0.0035	**-6.61**
MG-R-222C	400	30	0.0035	-	-	-	-	-	-	-	-	-	0.0027	-
MG-R-222C	500	30	0.0060	304	0.950	-0.124	-31.158	62	-20.277	163	1	0.001	0.0025	**-8.71**
MG-R-222C	600	30	0.0034	-	-	-	-	-	-	-	-	-	0.0015	-
MG-R-222C	700	30	0.0050	-	-	-	-	-	-	-	-	-	0.0025	-
MG-R-222C	800	30	0.0075	240	-11.480	0.155	-41.877	148	-19.976	296	1	0.000	0.0025	**-9.24**
MG-R-222C	1200	30	0.0100	320	11.368	-9.396	-20.071	41	-29.393	117	2	0.001	0.0560	**-5.90**
MG-R-229C	300	30	0.0101	323	7.315	8.835	-24.869	22	-11.502	174	1	0.001	0.0014	**-5.45**
MG-R-229C	400	30	0.0220	704	11.549	11.487	-19.556	31	-8.911	63	3	0.001	0.0019	**-9.33**
MG-R-229C	500	30	0.0140	448	9.140	10.055	-21.891	28	-10.310	21	2	0.001	0.0016	**-6.65**
MG-R-224C	300	30	0.0298	954	11.671	2.477	-20.151	19	-17.749	14	4	0.002	0.0067	**-1.23**
MG-R-224C	400	30	0.0800	2560	17.158	-5.113	-14.222	71	-25.205	75	11	0.004	0.0030	**-2.33**
MG-R-224C	500	30	0.1333	4266	23.524	2.904	-7.900	12	-17.355	36	18	0.007	0.0052	**-2.16**
MG-R-224C	600	30	0.1009	3229	18.225	9.162	-13.591	16	-11.206	13	14	0.005	0.0050	**-2.81**
MG-R-224C	700	30	0.0060	192	-2.295	25.302	-35.359	480	4.669	323	1	0.000	0.0040	**-0.43**
MG-R-224C	800	30	0.0009	-	-	-	-	-	-	-	-	-	0.0080	-
MG-R-224C	1200	30	0.1380	4416	18.456	1.652	-13.103	16	-18.572	43	19	0.007	0.0019	**-3.70**
MG-R-166A	300	30	0.0510	1632	17.647	13.144	-14.320	11	-7.299	20	7	0.002	0.0025	**-4.28**
MG-R-166A	400	30	0.0440	1408	19.521	13.042	-12.378	13	-7.403	28	6	0.002	0.0011	**-3.19**
MG-R-166A	500	30	0.0008	-	-	-	-	-	-	-	-	-	0.0009	-
MG-R-166A	600	30	0.0300	960	20.026	11.165	-11.794	29	-9.245	34	4	0.001	0.0020	**-2.07**
MG-R-166A	700	30	0.0100	320	16.601	14.151	-15.436	42	-6.309	65	1	0.000	0.0020	**-0.91**
MG-R-166A	800	30	0.0055	176	15.619	12.956	-16.413	41	-7.479	105	1	0.000	0.0020	**-0.53**
MG-R-166A	1200	30	0.0300	960	13.194	2.612	-18.579	26	-17.620	22	4	0.001	0.0065	**-3.27**
MG-R-159	400	30	0.0230	736	5.242	-7.605	-26.470	18	2.384	34	3	0.001	-	**-6.56**
MG-R-159	500	30	0.0290	928	15.463	8.016	-16.410	17	18.156	13	4	0.002	-	**-5.13**
MG-R-159	600	30	0.0100	320	15.144	-2.385	-16.397	38	7.639	67	1	0.001	-	**-1.77**
MG-R-159	800	30	0.0170	544	18.053	-9.951	-13.136	20	-0.017	27	3	0.001	-	**-2.41**
MG-R-159	1000	30	0.0138	442	17.313	-8.057	-13.964	17	1.900	43	2	0.001	-	**-2.08**
MG-R-208C	300	30	0.0260	832	6.612	12.516	-25.718	244	-7.890	90	4	0.001	0.0030	**-5.69**
MG-R-208C	400	30	0.0270	864	8.813	4.808	-23.186	37	-15.456	40	4	0.002	0.0060	**-5.33**
MG-R-208C	500	30	0.0160	512	13.469	9.953	-18.539	27	-10.420	51	2	0.001	0.0030	**-2.52**
MG-R-208C	600	30	0.0205	656	14.020	12.720	-18.060	51	-7.707	44	3	0.001	0.0016	**-3.15**
MG-R-208C	700	30	0.0070	224	2.169	8.781	-30.193	47	-11.545	159	1	0.000	0.0013	**-1.80**
MG-R-208C	800	30	0.0060	192	-3.285	7.405	-35.790	51	-12.882	51	1	0.000	0.0014	**-1.82**
MG-R-208C	1200	30	0.0150	480	4.190	-0.859	-27.782	25	-21.004	37	2	0.001	0.0154	**-3.55**

Observations:

T = temperature; t = interval of 30 minutes; p = pressure; sd = standard deviation; PNC = pressure of non condensables (CH4, N2, etc); ng = nanograms.

Samples analysed in the Stabe Isotope Laboratory at Royal Holloway and Bedford New College